

RĒZEKNES TEHNOLOĢIJU AKADĒMIJA
Inženieru fakultāte

REZEKNE ACADEMY OF TECHNOLOGIES
Faculty of Engineering

ISSN 1691-5402

VIDE. TEHNOLOĢIJA.
RESURSI

XI starptautiskās zinātniski praktiskās konferences materiāli
2017.gada 15.-17.jūnijs

3. SĒJUMS

ENVIRONMENT. TECHNOLOGY.
RESOURCES

Proceedings of the 11th International Scientific and Practical Conference
June 15–17, 2017

Volume III

Rēzekne
2017

VIDE. TEHNOLOĢIJA. RESURSI: 11. starptautiskās zinātniski praktiskās konferences materiāli 2017. gada 15.-17. jūnijs. 3. sējums. Rēzekne: Rēzeknes Tehnoloģiju akadēmija, 2017. 362 lpp.

ENVIRONMENT. TECHNOLOGY. RESOURCES: Proceedings of the 11th International Scientific and Practical Conference June 15-17, 2017. *Volume III*. Rezekne: Rezekne Academy of Technologies, 2017. p 362.

Rekomendējusi publicēšanai Rēzeknes Tehnoloģiju akadēmijas Zinātnes padome 2017. gada 23.maijā. *Recommended for publication by the Scientific Council of Rezekne Academy of Technologies on May, 23rd, 2017.*

11. starptautiskās zinātniski praktiskās konferences „Vide. Tehnoloģija. Resursi” materiālu trijos sējumos ir pārstāvēti jaunākie pēdējo divu gadu pētījumi vides inženierzinātnē, vides un dabas aizsardzībā, ilgtspējīgā lauksaimniecībā, enerģētikā, materiālzinātnē, mehānikā, metālapstrādē, lāzeru tehnoloģijās, matemātiskajā modelēšanā, elektrotehnikā, vides ekonomikā un vadībā, informācijas tehnoloģijās un sociotehnisko sistēmu modelēšanā, vides izglītībā un ilgtspējīgās attīstības procesos. Krājumā pārstāvēto pētījumu joma ir daudzpusīga un strapdisciplināra, balstīta uz starptautisko zinātnieku kolektīvu sasniegumu rezultātiem. Konferences materiālos iekļauti 152 zinātniskie raksti, kuru autori pārstāv 14 valstis.

Proceedings of the 11th International Scientific and Practical Conference “Environment. Technology. Resources” include studies of the last two years in fields of engineering, environmental and nature protection, sustainable agriculture, energy, material science, mechanics, metalworking, laser technologies, mathematical modelling, electrical engineering, environmental economics and management, information technologies and sociotechnical systems modelling, environmental education and sustainable development. The research area presented in the proceedings is comprehensive and cross disciplinary, based on advances of international researchers. The proceedings comprise 152 scientific papers from 14 countries.

Par raksta saturu atbild raksta autors.

The author of the paper takes responsibility for the content of the paper.

Conference Organizing Committee:

Chairman:

Dr.habil.geol. Gotfrids Noviks - Latvia, Rezekne Academy of Technologies

Co-Chairmen:

Dr.sc.ing. Edmunds Teirumnieks - Latvia, Rezekne Academy of Technologies

Dr.sc.ing. Artis Teilans - Latvia, Rezekne Academy of Technologies

Dr.sc.ing. Andris Martinovs - Latvia, Rezekne Academy of Technologies

Members:

PhD Andres Annuk - Estonia, Estonian University of Life Sciences

Dr.habil.sc.ing. Dagnija Blumberga - Latvia, Riga Technical University

Dr.habil.sc.comp. Juris Borzovs - Latvia, University of Latvia

Dr. Xiao Chen - China, Hefei University

Dr.-Ing. Horst Exner - Germany, Mittweida University of Applied Sciences

Dr.sc.ing. Egils Ginters - Latvia, Riga Technical University

Dr.sc.ing. Peteris Grabusts - Latvia, Rezekne Academy of Technologies

DSc. Dimitar Grekov - Bulgaria, Agricultural University - Plovdiv

Dr.habil.sc.ing. Janis Grundspenkis - Latvia, Riga Technical University

DSc. Raycho Ilarionov - Bulgaria, Technical University of Gabrovo

DSc. Hristo Ivanov Beloev - Bulgaria, "Angel Kanchev" University of Ruse

Dr.habil.chem. Maris Klavins - Latvia, University of Latvia

Dr. Linas Kliucininkas - Lithuania, Kaunas University of Technology

Dr.sc.ing. Eriks Kronbergs - Latvia, Latvia University of Agriculture

Dr. Walter Leal - Germany, Hamburg University of Applied Sciences

PhD Eng. Valeri Markov Mladenov - Bulgaria, Technical University of Sofia

Dr.sc.ing. Vladislav Morozov - Russia, Geophysical Centre of the Russian Academy of Sciences

Dr.sc.ing. Alla Anohina-Naumeca – Latvia, IEEE Latvia Section, Riga Technical University

Dr.geogr. Olgerts Nikodemus - Latvia, University of Latvia

Dr.sc.ing. Igor Plokhov - Russia, Pskov State University

Vilnis Rantins - Latvia, Chairman of the Management Board of the Association of Mechanical Engineering and Metalworking Industries

Dr.sc.ing. Andrejs Romanovs - Latvia, IEEE Latvia Section, Riga Technical University

Dr.geol. Valdis Seglins - Latvia, University of Latvia

Dr.sc.ing. Victor Tatarinov - Russia, Geophysical Centre of the Russian Academy of Sciences

Dr-Ing. Josef Timmerberg - Germany, Jade University of Applied Sciences

Dr.sc.ing. Olegs Uzga-Rebrovs - Latvia, Rezekne Academy of Technologies

PhD Pepo Yordanov - Bulgaria, Technical University of Sofia Branch Plovdiv

PhD Veiko Karu – Estonia, Tallinn University of Technology

Reviewers:

PhD Nikolaj Angelov - Bulgaria, Technical University of Gabrovo

Dr. Dragen Antic - Serbia, University of Nis

Dr.oec. Dzintra Atstaja - Latvia, BA School of Business and Finance

Dr.sc.ing. Jurijs Cizovs - Latvia, Riga Technical University

Dr.sc.ing. Edgars Cubars - Latvia, Rural Support Service

PhD Peteris Daugulis - Latvia, Daugavpils University

PhD Hristina Deneva - Bulgaria, Technical University of Gabrovo

Dr.oec. Sandra Ezmale - Latvia, Rezekne Academy of Technologies

Dr.sc.ing. Peteris Grabusts - Latvia, Rezekne Academy of Technologies
Dr. Ants Kallaste - Estonia, Tallinn University of Technology
PhD Julieta Kaleicheva - Bulgaria, Technical University of Sofia
Dr.paed. Ilmars Kangro - Latvia, Rezekne Academy of Technologies
Dr. Vasyliy Karasev - Russia, Russian Academy of Sciences
Dr.paed. Aivars Kaupuzs - Latvia, Rezekne Academy of Technologies
Dr. Lars Kempt - Germany, Technical University Chemnitz
Dr.habil.chem. Maris Klavins - Latvia, University of Latvia
Dr.sc.ing. Sergejs Kodors - Latvia, Rezekne Academy of Technologies
Dr.sc.ing. Eriks Kronbergs - Latvia, Latvia University of Agriculture
Dr.sc.ing. Andris Martinovs - Latvia, Rezekne Academy of Technologies
PhD Petko Mashkov - Bulgaria, "Angel Kanchev" University of Ruse
Dr.iur. Liga Mazure - Latvia, Rezekne Academy of Technologies
Dr.phys. Pavels Narica - Latvia, Rezekne Academy of Technologies
PhD Galina Nikolcheva - Bulgaria, Technical University of Sofia
Dr. Vlastimir Nikolic - Serbia, University of Nis
Dr.habil.geol. Gotfrids Noviks - Latvia, Rezekne Academy of Technologies
Dr.sc.ing. Imants Nulle - Latvia, Latvia University of Agriculture
Dr.sc.ing. Lyubomir Lazov - Latvia, Rezekne Academy of Technologies
Dr.oec. Lienite Litavniece - Latvia, Rezekne Academy of Technologies
PhD Angel - Lengerov - Bulgaria, Technical University, Plovdiv
Dr. Nenad Pavlovic - Serbia, University of Nis
Dr.habil.sc.ing. Igor Plokhov - Russia, Pskov State University
Dr. Svetlana Polukosko - Latvia, Ventspils University College
Dr.geol. Janis Prols - Latvia, SIA "Geo Consultants", Rezekne Academy of Technologies
Dr. Anton Rassolkin - Estonia, Tallinn University of Technology
Dr.sc.ing. Andrejs Romanovs - Latvia, Riga Technical University
Dr.biol. Arturs Skute - Latvia, Daugavpils University
Dr.habil.phys. Vladimir Solovyev - Russia, Pskov State University
Dr.paed. Aina Strode - Latvia, Rezekne Academy of Technologies
Dr.paed. Gunars Strods - Latvia, Rezekne Academy of Technologies
Dr.-Ing. Josef Timmerberg - Germany, Jade University of Applied Sciences
Dr.sc.ing. Artis Teilans - Latvia, Rezekne Academy of Technologies
Dr.sc.ing. Edmunds Teirumnieks - Latvia, Rezekne Academy of Technologies
Dr.biol. Rasma Tretjakova - Latvia, Rezekne Academy of Technologies
Dr.paed. Svetlana Usca - Latvia, Rezekne Academy of Technologies
Dr.sc.ing. Olegs Uzga-Rebrovs - Latvia, Rezekne Academy of Technologies
Dr. Toomas Vaimann - Estonia, Tallinn University of Technology
Dr.habil.sc.ing. Janis Viba - Latvia, Riga Technical University

Steering Committee:

Mg.chem. Erika Teirumnieka - Latvia, Rezekne Academy of Technologies
Mg.sc.env. Sintija Augule - Latvia, Rezekne Academy of Technologies
Mg.chem. Inese Bernane - Latvia, Rezekne Academy of Technologies
Mg.comp. Gundega Berina - Latvia, Rezekne Academy of Technologies



**ENGINEERING SCIENCES
AND PRODUCTION
TECHNOLOGIES**

SATURS

CONTENTS

Yordanka Angelova, Lyubomir Lazov, Silvija Mezinska INNOVATIVE LASER TECHNOLOGY IN TEXTILE INDUSTRY: MARKING AND ENGRAVING	15
Ilze Baltina, Ausma Vilumsone, Anna Tarasenko, Liene Silina FABRIC SELECTION FOR WORK WEAR DURING PROCUREMENT PROCEDURE	22
Tingting Cheng, Jun Chen, Ke Wu, Jianguo Liu, Siheng Lu, Shouchuang Hu ANALYSIS AND COUNTERMEASURE OF VOCS SOURCE IN AUTOMOBILE PRODUCTION PROCESS IN CHINA	27
Edgars Čubars, Liena Poiša ANALYSIS OF ASH CONTENT IN COMPOSITE BIOMASS FUELS	31
A. V. Cvetkov, V. I. Gerbreders, S. D. Khanin, A. E. Lukin, A. S. Ogurcovs, S. G. Romanov, V. G. Solovyev, A. I. Vanin, M. V. Yanikov STRUCTURE AND OPTICAL PROPERTIES OF HYBRID METAL- DIELECTRIC COLLOIDAL PHOTONIC CRYSTALS	37
Inga Dāboliņa, Ausma Vilumsone, Eva Lapkovska ANTHROPOMETRIC PARAMETRIZATION OF UNIFORMS FOR ARMED FORCES	41
Pēteris Druķis, Līga Gaile, Vadims Goremikins CASE STUDY OF STRUCTURAL RELIABILITY OF EXISTING BUILDING	47
Galitskov S.Ya., Mizuryaev S.A., Chiknovoryan A.G. HEAT RESISTANT BUILDING ENVELOPES MADE OF LIGHTWEIGHT CONCRETE WITH THE USE OF POROUS GRANULAR WASTES	53
Galitskov K.S., Samokhvalov O.V., Fadeev A.S. OPTIMIZATION OF BURNING PRODUCTION PROCESS OF CERAMSITE WITH SPECIFIED DENSITY	57
Aleksandrs Gorbunovs, Zanis Timsans, Atis Kapenieks, Rudolfs Gulbis DEVELOPMENT OF HUMAN BALANCE CAPABILITY TESTING PROTOTYPE	62

Armands Grickus, Sharif E. Guseynov	
ON A MATHEMATICAL MODEL DESCRIBING OPTIMAL PROCESSING MECHANISM OF DISPERSED GRANULAR MATERIALS IN GRAVITATIONAL FLOW WITH HORIZONTAL OR INCLINED VIBRATING SIEVE CLASSIFYING SCREENS	69
Guryanov A.M., Korenkova S.F., Sidorenko Yu.V.	
STRUCTURE FORMATION PROCESS OF HYDRATED PORTLAND CEMENT COMPOSITIONS: NANOSCALE LEVEL CONTROL	77
Sharif E. Guseynov, Ruslans Aleksejevs, Jekaterina V. Aleksejeva, Raufs Guseinovs	
DETERMINING COUNTRIES' POTENTIALS FOR SUCCESSFUL EXPORT OF LUXURIOUS AND BANKING SERVICES	83
Sharif E. Guseynov, Janis S. Rimshans	
ON THE GINZBURG-FEINBERG PROBLEM OF FREQUENCY ELECTROMAGNETIC SOUNDING FOR UNAMBIGUOUS DETERMINATION OF THE ELECTRON DENSITY IN THE IONOSPHERE	89
Shouchuang Hu, Jun Chen, Ke Wu, Zhongkai Zhou, Tingting Cheng, Dongbiao Wu	
OPTIMIZATION OF MUNICIPAL SOLID WASTE COLLECTION SYSTEM IN HEFEI CITY OF CHINA	97
Alexander Ilyin, Igor Plokhov, Igor Savraev, Oksana Kozyreva, Nikita Kotkov	
FORMING AND OVERLAPPING MICRORELIEFS IN SLIDING CONTACT SIMULATION MODEL	102
Krasimir Marinov Ivanov, Tsviatko Kolev Varbov, Georgi Tsonev Velev	
CALCULATION OF LOSSES OF ACTIVE POWER AND ENERGY IN TRANSMISSION LINES AND TRANSFORMERS, AS A PART OF THE ELECTRICAL DISTRIBUTION POWER NETWORK	107
Irina Ivanova, Deniss Sceulovs	
COMPETENCE AS A FACTOR OF EMOTIONAL CAPITAL	111
Tsvetan Kaldashev, Petar Hadzhiyski, Galina Nikolcheva	
STUDY WEAR TOOL WITH HIGH-SPEED MILLING	117
Julieta Kaleicheva, Valentin Mishev, Zdravka Karaguiozova, Galina Nikolcheva	
STRUCTURE AND MECHANICAL PROPERTIES OF SPHEROIDAL GRAPHITE CAST IRON WITH NANOSIZED ADDITIVES	122

Ilmārs Kangro, Harijs Kalis, Ērika Teirumnieka, Edmunds Teirumnieks ON MATHEMATICAL MODELLING OF THE 2-D FILTRATION PROBLEM IN POROUS AXIAL SYMMETRICAL CYLINDER	129
Andrei Khitrov, Alexander Khitrov, Evgeny Veselkov, Vyacheslav Tikhonov INVESTIGATIONS OF ELECTRIC POWER QUALITY IN AUTONOMOUS LOW POWER PLANT	139
Vladimir Konevtsov, Lilia Motaylenko NON-LINEAR TRANSFORMATION OF SIGNALS IN SOFTWARE DESIGN OF DIGITAL CONTROL SYSTEMS COMPLEX	140
Tarmo Koppel, Inese Vilcane, Viktor Mironov, Andrei Shiskin, Sanita Rubene, Piia Tint AERATED CONCRETE MICROWAVE REFLECTION AND TRANSMISSION PROPERTIES IN A WET ENVIRONMENT	145
Oksana Kozyreva, Igor Plokhov, Nikita Kotkov, Igor Savraev, Alexander Ilyin EXPERIMENTAL INVESTIGATIONS OF EFFECT OF LC-CIRCUITS ON SPARKING AND THERMAL STATE OF SLIDING ELECTRIC CONTACT UNIT	150
Kaspars Kroics, Janis Zakis, Oleksander Husev CAPACITANCE REDUCTION USING RIPPLE SUPPRESSION CONTROL OF SINGLE PHASE ENERGY STORED QUASI-Z-SOURCE INVERTER	154
Lyubomir Lazov, Hristina Deneva, Erika Teirumnieka STUDY OF AUXILIARY GAS PRESSURE ON LASER CUTTING TECHNOLOGY	159
Lyubomir Lazov, Hristina Deneva, Erika Teirumnieka INFLUENCE OF DEFOCUS POSITION ON LASER CUTTING PROCESS IN SHEET STEEL	163
Lyubomir Lazov, Pavels Narica, Janis Valiniks, Antons Pacejs, Hristina Deneva, Dainis Klavins OPTIMIZATION OF CO ₂ LASER PARAMETERS FOR WOOD CUTTING	168
Lyubomir Lazov, Peter Uzunov MINIMIZING THE DETENT FORCE IN PERMANENT MAGNET LINEAR SYNCHRONOUS MOTOR FOR DRIVING OF 2D LASER MARKING TABLE	174

Angel Lengerov, Galina Nikolcheva, Julieta Kaleycheva, Lyubomir Lazov COMPUTER CONTROL THE ACCURACY OF THE PARTS PROCESSED ON CNC MACHINE TOOLS BASED ON STATISTICAL PROCESS CONTROL	179
Angel Lengerov, Galina Nikolcheva, Lyubomir Lazov STATISTICAL CONTROL OF ACCURACY AT MACHINING	183
Sergei Loginov, Yuri Zhuravlyov, Yulia Domracheva, Dmitriy Fedorov ADAPTIVE CONTROL OF THE 1-DOF ACTIVE MAGNETIC BEARING	188
SiHeng Lu, Chang Pan, YuJuan Jin, Xiang Wang, Xinlai Wei, ZhiMin Yu EVALUATION OF HEAVY METALS AROUND THE MINING OF DECORATIVE STONE ORE IN SUSONG COUNTY LIAOHE RIVER	192
Andris Martinovs, Rasma Tretjakova, Rene Castro, Vladimir Solovyev, Josef Timmerberg, Alexander Cvetkov, Sergey Gango, Angelika Borkenstein, Paul Beckmann, Helmut Schütte, Nikolai Puchkov, Sergey Trifonov EFFECT OF HEAT TREATMENT ON ELECTRICAL AND MECHANICAL PROPERTIES OF THE SOLID SAPROPEL	200
Petko Mashkov, Hristo Beloev, Berkant Gyoch, Tamara Pencheva LED LAMP FOR APPLICATION IN MEDICAL CENTERS – DESIGN AND THERMAL MANAGEMEN	207
Veslava Matikevičienė, Saulius Grigiškis, Erika Lubytė, Gervydas Dienys PARTIAL PURIFICATION AND CHARACTERIZATION OF BACTERIOCIN- LIKE PEPTIDE PRODUCED BY <i>STAPHYLOCOCCUS XYLOSUS</i>	213
Ziedonis Miklašėvičs THE IMPACT OF HARVESTER CALIBRATION ON THE ACCURACY OF BIRCH VENEER LOGS MEASUREMENTS BY MEASURING DIAMETER IN SHORT INTERVALS USING ELECTRONIC 3D SYSTEMS	217
Eva Namsone, Genadijs Sahmenko, Elvija Namsone, Aleksandrs Korjakins THERMAL CONDUCTIVITY AND FROST RESISTANCE OF FOAMED CONCRETE WITH POROUS AGGREGATE	222
Pavels Narica, Jurijs Komkovs STUDY OF LASER SOURCE OUTPUT CHARACTERISTICS	229
Igor Nikiforov, Pavel Maltsev, Sergey Loginov ENHANCING THE TECHNOLOGICAL CAPABILITIES OF UNIVERSAL GRINDING EQUIPMENT	234

Aleksandrs Oks, Aleksey Katashev, Edgars Bernans, Valters Abolins SMART SOCKS SYSTEM AS AN EQUIPMENT TO ANALYZE TEMPORAL PARAMETERS OF HUMAN GAIT AND RUNNING	238
Alexander Pavlov, Igor Plohov, Sergei Drozdov, Vadim Smirnov STUDY AND OPTIMIZATION OF ELECTRIC HEATING FOR OIL AND PETROLEUM PRODUCTS PIPELINE	242
Aigars Paze, Janis Rizhikovs, Prans Brazdausks, Maris Puke, Juris Grinins, Ramunas Tupciauskas, Ance Plavniece PROCESSING POSSIBILITIES OF BIRCH OUTER BARK INTO GREEN BIO-COMPOSITES	249
A. Petrov, A. Rassõlkin, T. Vaimann, A. Belahcen, A. Kallaste, I. Plokhov BASIC ALGORITHM FOR INDUCTION MOTORS ROTOR FAULTS PRE-DETERMINATION	254
Igor Plokhov, Igor Savraev, Alexander Markov, Alexander Ilyin, Oksana Kozyreva, Nikita Kotkov INDUSTRIAL TESTS OF CURRENT DISTRIBUTION DYNAMICS IN THE BRUSH-CONTACT APPARATUS OF THE TURBO-GENERATOR	258
Svetlana Polukoshko, Andris Martinovs, Svetlana Sokolova AGING, FATIGUE AND DURABILITY OF RUBBER VIBRATION ISOLATION ELEMENTS	269
Sanita Reinerte, Martins Andzs, Ramunas Tupciauskas, Andris Veveris, Janis Gravitis STEAM EXPLOSION AS A PRE-TREATMENT METHOD FOR BIO-REFINED HYBRID ASPEN LIGNOCELLULOSE	276
Janis Rizhikovs, Aigars Paze, Ance Plavniece, Kristaps Stankus, Inguss Virsis A NOVEL METHOD FOR BIRCH OUTER BARK QUALITY CONTROL USING HIGHER HEATING VALUE	282
Genadijs Sahmenko, Sandis Aispurs, Aleksandrs Korjakins EXPERIENCE OF APPLICATION HIGH PERFORMANCE CEMENT COMPOSITES FOR CREATING DURABLE SCULPTURAL ELEMENTS	286
Arta Seile, Dana Beļakova NONWOVEN DEVELOPMENT BY THE MULTILAYER STRUCTURE	292

Sergej Semyonov, Sergej Tikhonov, Mihail Donchenko, Jurij Lukyanov, Andrej Perminov	
ANALYSIS METHOD OF CALCULATION PARAMETERS OF HEAT AND MASS TRANSFER PROCESSES IN THE STIRLING ENGINE	298
Janis Šliseris, Līga Gaile, Leonids Pakrastiņš, Kārlis Rocēns	
NONLINEAR NUMERICAL MODELLING OF BASALT REBAR REINFORCED CONCRETE STRUCTURES	304
Sergei Trashchenkov, Victor Astapov	
SPURIOUS ACTIVATION ASSESSMENT OF THERMAL POWER PLANT'S SAFETY-INSTRUMENTED SYSTEMS	310
Eva Trumsina, Zane Zelca, Silvija Kukle-1570	
POLY(VINYL ALCOHOL) AND POLY(VINYL ALCOHOL) /ZINC OXIDE COMPOSITE NANOFIBRE WEBS: QUALITY CONTROL WITH CONDUCTOMETER	316
Yulia Usherenko, Sergei Usherenko, Vladimir Dashkevich, Javad Yazdani	
USING DYNAMIC PRE-ACTIVATION OF STEEL SURFACES FOR NITRIDING INTENSIFICATION	321
Peter Uzunov, Lyubomir Lazov	
DESIGN OF PERMANENT MAGNET LINEAR SYNCHRONOUS MOTOR DRIVING 2D TABLE FOR LASER MARKING	325
Sergei Verteshev, Vladimir Konevtsov	
PROCESSES CONTROL WITH FUZZY INITIAL INFORMATION IN A COMPLEX OF SOFTWARE DESIGN OF DIGITAL CONTROL SYSTEMS	332
Sergei Verteshev, Vladimir Konevtsov	
DIRECT DIGITAL CONTROL IN A COMPLEX OF SOFTWARE DESIGN OF DIGITAL CONTROL SYSTEMS	337
Sanita Vitolina, Galia Shulga, Brigita Neiberte, Skaidrite Reihmane, Elina Zhilinska	
NEW ENVIRONMENTALLY FRIENDLY DUST SUPPRESSANT BASED ON LIGNOCELLULOSIC BIOMASS FROM WOOD PROCESSING WASTEWATER	343
Uldis Zaimis, Sharif E. Guseynov	
SCIENTIFICALLY SUBSTANTIATED GUIDELINES FOR PHYSICO-MATHEMATICAL MODELLING OF LASER SURFACE-TREATMENT OF WEAR-RESISTANT IMPLANTS FOR HUMAN JOINT REPLACEMENTS	350

**Yury Zhuravlev, Andrey Perminov, Yury Lukyanov, Sergey Tikhonov,
Alexander Ilyin, Sergey Semyonov**

**OPTIMIZATION OF MECHANICAL STRENGTH OF ROTARY-VANE
ENGINE**

357

Innovative Laser Technology In Textile Industry: Marking and Engraving

Yordanka Angelova¹, Lyubomir Lazov², Silvija Mezinska²

Technical University of Gabrovo, 4.H.Dimitar Str., 5300 Gabrovo, Bulgaria¹,

Rezekne Academy of Technologies, Faculty of Engineering, Atbrivosanas aleja 115, Rezekne, Latvia²

Abstract. The advent of laser technology in textiles industry has established a new innovative solution, which successfully prevents some of the weaknesses in the conventional technologies. Lasers are being used in Laser Marking (Only the surface of fabric is processed, fading), Laser Engraving (Controlled cutting to depth). It has been used extensively as the replacement of some conventional dry processes like sand blasting, hand sanding, destroying, and grinding etc., which are potentially harmful and disadvantageous for the environment.

The article considers some innovative laser technologies, such as marking and engraving on various textile materials. The laser applications for leather and textile processing were analysed. The report overviews systems and ways of laser marking and engraving implementations. Classification of markings was proposed. The advantages of laser marking and engraving technologies in textile fields were pointed.

Keywords: laser technologies, marking, engraving, textiles, denim clothing.

I. INTRODUCTION

Laser marking and engraving are innovative technologies. Furthermore, they discover additional horizons for the textile sector by providing prospects for development of new production technologies [4, 38, 39]. Laser technologies take place on modern laser systems on fabric, ready-made clothes, logos, labels and others. Some information (alpha-numeric, graphics or encoded) is applied to almost all types of materials including textiles and leather. It is an important element in the modern manufacture and consumption of goods with certain functions: identification, information, warning, aesthetic, etc.

In recent years, the use of lasers for textile material marking is increasing because of the speed, accuracy and flexibility of this modern technique [29]. Many traditional methods of textile and clothing finishing consume significant energy amounts, water and other supplies. Compared to them, the laser technology is adequate to achieve good results at low cost. The laser methods are used extensively as a replacement of some conventional processes which are ones of the most environment polluting technologies, potentially harmful and disadvantageous in some manner [16, 26, 34].

Laser technologies, such as marking and engraving are considered in this article. Applications of laser for various textile material processing are analysed. The report overviews systems and ways of laser marking and engraving implementations. The advantages of laser marking and engraving technologies in textile fields are pointed.

II. WAYS OF LASER MARKING AND ENGRAVING IMPLEMENTATION

Laser marking and engraving are implemented through three main ways: raster, vector and projection. When image is obtained by raster marking, laser beam moves sequentially in rows, similar to dot matrix printers, but instead of an ink there is a laser beam "Fig.1". This method was used mainly for marking alpha-numeric information, more rarely for graphic images [2, 8, 22, 24].

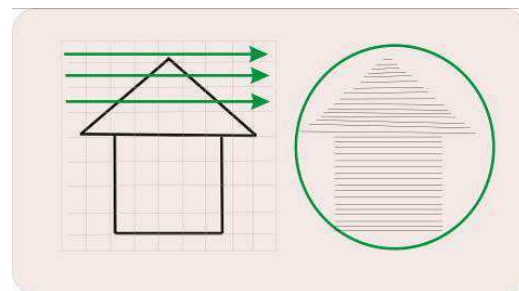


Fig. 1. Way of Raster Marking

In vector marking the mark is written by focused laser beam, which follows the contour, guided by an optical system, operated by a computer program "Fig. 2". Vector marking applies to all kinds of information: numeric-codes, bar-codes, 2D codes, logos, and almost any other type of image. This is the most common and versatile method of laser marking.

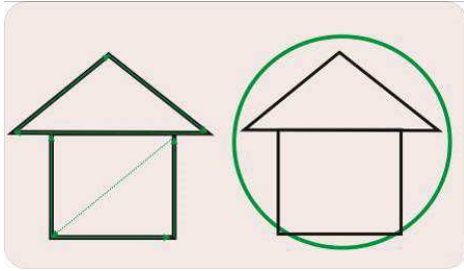


Fig. 2. Way of Vector Marking

Projection marking is implemented with mask (stencil). Laser beam passes through it and is projected onto the working area “Fig. 3”.

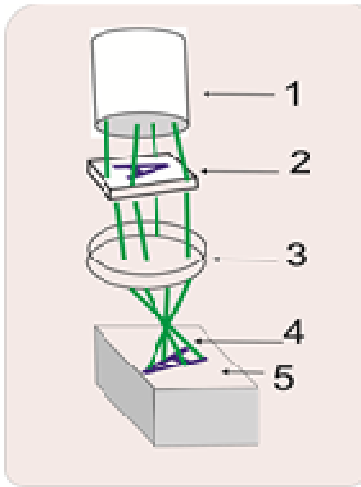


Fig. 3. Projection Marking

where: 1-laser, 2-mask, 3-lens, 4-image, 5-work area [3].

Raster and vector marking can be realized by a plotter “Fig. 4” or a scanner system “Fig. 5”.

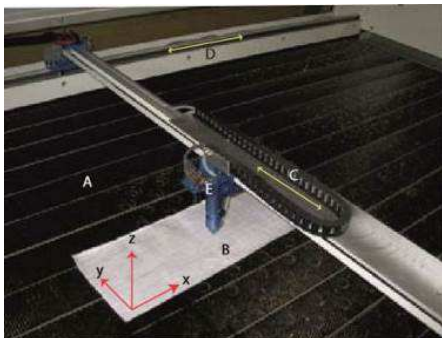


Fig. 4. Plotter system for marking [25]

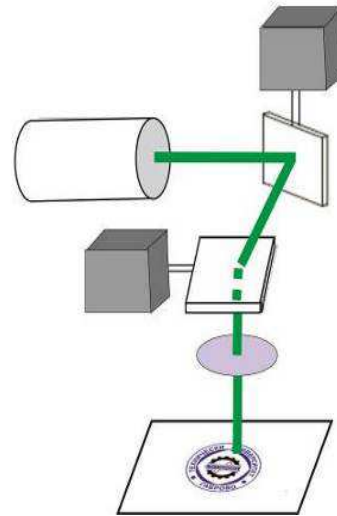


Fig. 5. Scanner system for marking [3].

Systems that combine plotter and scanner system are used increasingly “Fig.6” [8, 22, 24]. Each of the three systems for laser marking has its advantages and disadvantages. According to the specific case of marking the most appropriate way is selected depending on the requirements for speed, size of the treated area, flexibility and investment costs.

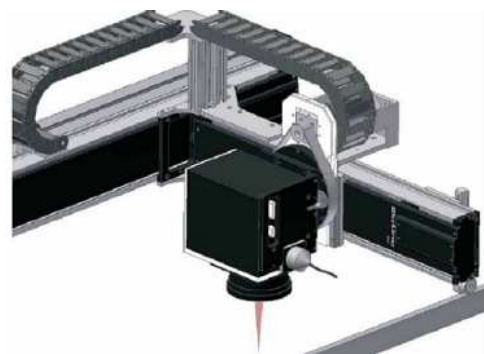


Fig. 6. Plotter&scanner system for marking.

III. FACTORS INFLUENCING THE QUALITY OF LASER MARKING

In order to achieve the best marking results, it is necessary to obtain optimum combination of laser parameters and parameters of the technological process for the relevant material. The main factors that influence, to a greater or lesser extent, the quality of marking may be presented in the following groups, relating respectively to: the properties of the material for marking, the parameters of the laser source (laser properties) and parameters of the technological process [2, 3, 10].

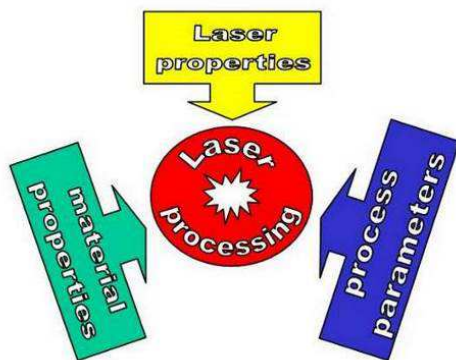


Fig. 7. Factors that influence laser technology in the textile industry [10]

Optical characteristics of different materials, as: reflectance capacity, absorption capacity, transmission efficiency, relevant coefficient and their interconnection are basic to the process of laser marking. Heat transfer in treated area of the material takes place during the laser marking process. Therefore, it is essential to have knowledge of its main thermal-physical properties: coefficient of thermal conductivity, specific heat capacity, ratio of temperature-conductivity. Textile material and leathers behaviour to heating is very important for setting up laser system in order to obtain the desired results.

The variety of textile materials is vast. In general, they can be divided into two groups: of natural origin (such as cotton, wool, etc.) and synthetic (polyester, polyamide, etc.). The key is to know their properties very well, especially what happens when they are admitted to heat in different temperatures.

For example: The cellulose (the content of cotton is about 91-95% cellulose) carbonizes (burns) without melting at high temperature. Thermal destruction occurs from 150°C÷180°C, the fibre strength decreases significantly and the color changes. As a result of cellulose destruction, the polymer chain breaks, as its length decreases and respectively its

average molecular mass reduces. At about 220°C the vitrification happens and cellulose passes from viscoelasticity to pseudo-plasticity state. At 300°C the result is carbonation. When the polyester fibres heat to temperature 80÷90°C they vitrificate, at about 250°C they become soft and at 260°C - melt. When temperature reaches 350°C – evaporate [9].

Marking depends on the following characteristics of laser source: wavelength - λ , the diameter of the minimum focal spot, average power, impulse power, pulse duration, pulse frequency, surface power density of laser radiation impulse power, pulse duration, pulse frequency, surface power density of laser radiation parameter of quality of the laser beam.

From factors related to the technological process, the most crucial are: speed of marking, step of marking, number of repetition and defocusing.

IV. LASER SOURCES FOR TEXTILE MATERIAL MARKING

A vast variety of laser sources and laser technological systems with different characteristics and application are offered on the world market [6, 7, 45]. This requires, for a case-by-case basis, to select good quality laser beam with a corresponding wavelength. The wavelength determines good absorption of a specific color material. Technological process of laser marking is complex and to get good results with economically justified costs, it is necessary to find the right laser for corresponding production. Textile polymer marking requires lasers with a wavelength that is absorbed best by the material, low impulse energy and lower power density than used for marking metals. The average power of the laser doesn't have to be high, enough is at the range of 10-50W. Good results are achieved in diameter of the minimum focal spot about 0.03-0.2 mm

Basic parameters of some lasers for marking are given in table 1. [2, 35, 41, 42, 45, 46].

Table I
 Key features of some lasers, applied for textile and leather materials

№	Parameters	Type of laser			
		CuBr	CO ₂	Fiber	Excimer
1	Wavelength of laser $\lambda, \mu\text{m}$	0,511-0,578	10,64	1,064	0,193
2	Average power P, W	10	50	10-40	24
3	Impulse power P_p, kW	17-34	10	5,32-17,8	1700
4	Impulse energy E_p, mJ	0,50-1,02	0,20	0,16-1,33	24
5	Pulse duration τ, ns	30	20	30-250	14
6	Pulse frequency ν, kHz	1-20	0,20-50	20-30	1
7	Diameter of the minimum focal spot d_f, mm	0,03	0,15	0,15	0,2
8	Quality of the laser beam M^2	1,7	1,5÷2	1,1	2
9	Positioning accuracy μm	< 2,5	< 10	< 2,5	< 2,5
10	Coefficient of efficiency COP,%	10	20	40	10

V. METHODS OF LASER MARKING

Today all organic polymers, such as the textiles and leather, can be treated by one or another manner, by means of laser radiation. When the laser beam is

focused on the material, its energy is absorbed by the surface layer, modified in depth from parts of micron to hundreds micron "Fig. 8". As a result of the reaction, caused by heat and according to the type of

material, different results can be achieved [15, 16, 25, 29].



Fig. 8. Laser bleaching on Denim Jeans [21].

Depending on the depth of processing two processes can be distinguished and defined: laser marking and laser engraving. Laser marking is surface impact in very little depth. Laser engraving is impact in much greater depth and most cases besides the color, also relief effect is obtained.

The textile fabrics are more often with small thickness from 0.1 mm to 5.0 mm [10]. For them more appropriate is to apply laser marking process. For materials with greater thickness it is recommended to choose engraving process. These kinds of textile, so called 3D fabrics, are woven, knitted or non-woven fabrics and composites. A large part of industrial materials are textile polymer materials.

Laser marking and laser engraving can be realized through a variety of methods, such as:

- change of color by bleaching (depigmentation) “Fig. 11”, “Fig. 12”;
- change of surface as a result of destruction;
- change of surface as a result of vitrification;
- change of color and structure through carbonation (burning) “Fig. 9a”;
- melting of surface layer material “Fig. 9b”;
- evaporation of surface layer material (ablation) “Fig. 10”, “Fig. 14”.

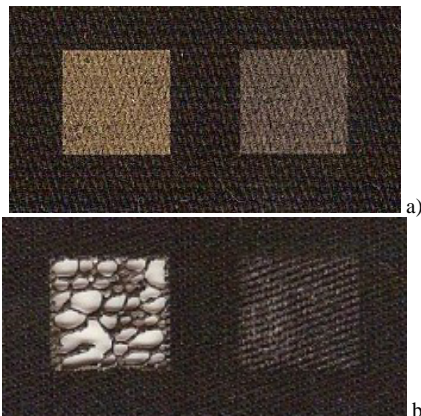


Fig. 9. Laser treating by: a) carbonation; b) melting.

Laser methods become increasingly popular and are applied as a substitute for traditional finishing

processes in textile industry nowadays [16,26,34,36]. One of the most workable textile laser treating, especially for denim, is bleaching method [20]. Bleaching (fading) surface of denim fabric by conventional chemical and mechanical processes (sandblasting, stone washing, enzyme washing, bleach washing, grinding and etc.) causes environmental pollution, while laser whitening is an ecologically clean process [18,19,31]. By controlling laser parameters, such as amount of energy applied on the fabric, the color changes on the surface, affecting its appearance without unacceptable damage to the material. The firm 'SEI Laser' presents a revolutionary technology 'Flexi Denim' for laser finishing that can replace traditional methods of manual discoloration, wearing out, decoration, marking, engraving and cutting of jeans and ready-to-wear clothes, at the textile show ITMA'2015, Milan, Italy. This technology reduces water consumption by 80% and removes toxic chemicals used for treatment of denim fabrics in traditional methods. It reduces the cost of energy consumption at three times higher performance relative to the conventional methods - to 160 pairs of jeans per hour [32].



Fig. 10. Laser treating by evaporation (ablation) on polar fabric.

VI. APPLICATIONS OF LASER MARKING AND ENGRAVING

Laser technologies marking and engraving can be used for different applications. Depending on function for which they are intended, images are: **decorative** and **informative**.



Fig. 11. Graphic design: decorative image at denim reached by the bleaching method [12].

Currently decorating clothes with laser is the most economical and creative technology of its artistic meaning. Decorating with the help of laser technology allows to create truly unusual, complicated in many ways and certainly completely unique models in fashion design [37]. Through opportunities for computer controlled laser beam and the application of different methods of marking, expression of graphical information, in the art sphere on fabric surfaces, is unlimited actually “Fig. 11”.

Laser marking allows obtaining the so-called 3D pictures (paintings) on the fabric. They look very real thanks to the receipt of light and dark areas and numerous shades “Fig.12a [15]”&“Fig.12c [47]” or whiskers “Fig.12d [26]”. It is easy to combine cutting out lace and marking 3-D effects together on jeans “Fig.12b” [17].

Similar well-known technologies are applying an image screen printing and thermal transfer printing, but they have limitations on the range of materials used and the end result does not provide a completeness of light and shadow transmission [1].



Fig. 12. Laser marking applications by varied of effects at jeans

Also, a very important laser marking application is to express technical information. With the help of laser information on fabric surface is put very easily: signs, identification symbols (letters and digits), bar codes, 2D matrix code “Fig.13” special characters, serial numbers, logos “Fig.14” and so on.



Fig. 13. 2D matrix code directly on the article [44].

About the user, marking comprises all important information on the main characteristics of the product, such as manufacturer identification, size, ingredients, care and maintenance of the product, instructions for possible allergic substances, flammability, environmental requirements and so on [11]. European and world markets require marking as an integral part of the offered products.



Fig. 14. Laser marking of logo on a leather

On the other hand, for manufacturer, marking is required to control production process-tracing at the stages of creation and removal of defects with the aim of good production quality.

VII. ADVANTAGES OF LASER MARKING

Laser marking and engraving of textile materials are fundamentally different and greatly superior to conventional. The following advantages can be indicated [2, 8, 30, 32, 33]:

- Automated process of production reporting and control - reading with electronic tracking devices on the marked product during manufacturing process and throughout the retail chain [5, 13, 23, 30, 29, 40, 43];
- Ability to process almost all textile materials;
- Ensure the authenticity of the product and protect it against counterfeiting;
- Allows storage of large amounts of data;
- The density of marked information is very big;
- The ability to read at different angles and even after a partial demolition, which is very typical for textile products during exploitation life;
- Flexibility - integration in production and automated lines allows marking on the fly;
- Extremely accurate and qualitative, with clear contours, very fast and precise method;
- Minimal heat affected zone;

- Contactless - missing mechanical impact on the treated material, and the result is getting the permanent, contrasting image;
- Very good quality, due to the stability and manageability of the laser source;
- Environmentally friendly process;
- High performance of the process;
- Profitable method as for large series and for single piece;
- Economical - low production and operating costs without the use of consumables, there are not necessary nor chemicals, nor ink ribbons or other materials;

Laser technologies work with better precision and higher productivity but also, they should be optimized and investigated for each specific process and material.

VIII. CLASSIFICATION OF MARKINGS

Marking has various purpose and is made according to the specific requirements.

The classification of marks can be made in different indicators "Fig. 15". Types of markings obtain by laser radiation are a part of the main classification.

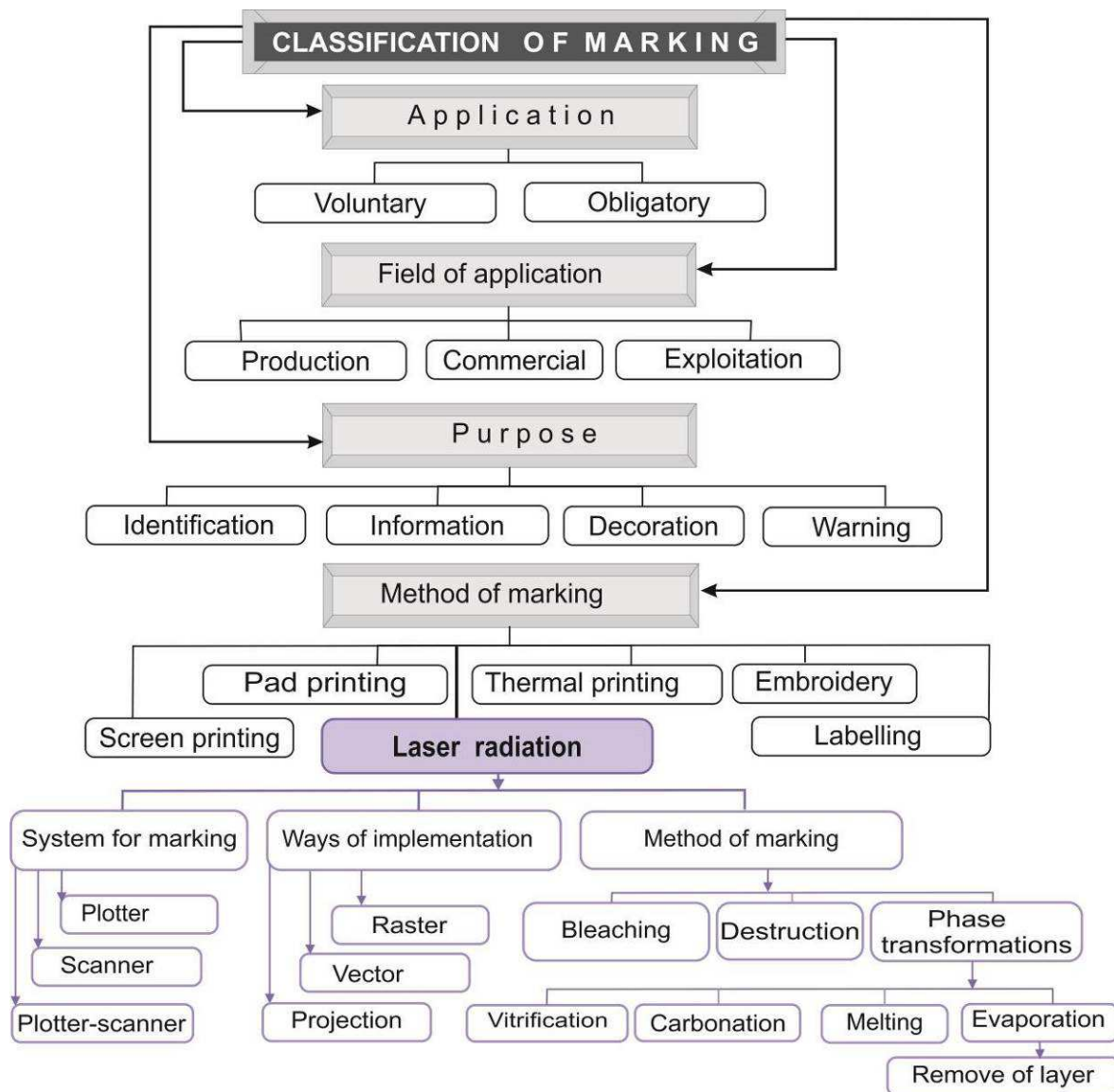


Fig. 15. Classification of the markings by various indicators [3]

IX. CONCLUSIONS

The laser-based marking and engraving are complex physical processes with a great scientific and applied importance. Laser radiation provides high quality processing because of its technical characteristics. Laser marks can be successfully used

for artistic decorating and unique design of any surfaces of textile products, so popular in fashion industry.

As well they are used for important, indelible technical information, which is useful for both manufacturers and consumers. Marks contain some

data about the textile product and allow tracking sources of raw materials, monitoring and controlling the state of proceedings and their impact on the environment.

For all textile materials, also for leather materials, marking and engraving can be successfully applied. The choice of laser process is determined by the desired final result.

In this research, the laser applications for leather and textile processing are analysed. The advantages of innovative laser technology in textile fields were pointed.

REFERENCES

- [1] Абуталипова Л.Н., Гатиятуллина Р.Ф. Модификация поверхности полимерных текстильных материалов под воздействием
- [2] Angelov, N., "Optimization of the marking process with a laser radiation of the tool steel specimens", PhD Thesis, 2011
- [3] Angelova, Y., "Investigation on Laser Marking Process of Industrial Materials", PhD Thesis, 2017.
- [4] Angelova, Y., L. Lazov, "Laser technology in textile industry", 46 International Congress IFKT, 6-8 Sept. 2012, Sinaia, Romania
- [5] Валиулин А., С.Горный, Ю.Гречко, М.Патров, К.Юдин, В.Юревич, "Лазерная маркировка материалов", Научно-технический журнал Фотоника, № 3/2007, с.16-22, 2007
- [6] Вебер, Х., Г. Херцигер, Лазери - физически основы и приложения, Наука и искусство, София, 1984
- [7] Вейко, В., Технологические лазеры и лазерное излучение, ГУ ИТМО, Санкт-Петербург, 2007
- [8] Динев, Ст., Лазерите в модерните технологии, Алфа, София, 1993
- [9] Кеворкян, А., Текстилно материалознания и изпитвания, Техн., София, 1977
- [10] Лазов Л., Приложение на лазерите в машиностроенето, МК, АМТЕХ 07, ТУ Габрово, 2007 г. II с. 33-39
- [11] Наредба за маркировката за съответствие със съществените технически изисквания към продуктите, Приета с ПМС № 164, обн., ДВ, бр. 66 от 11.08.2000
- [12] Хисамиева, Л., и др. "Декорирование поверхности текстильных полимерных материалов с помощью лазерной технологии" Журнал Вестник Казанского технологического университета, стр 127,128, 2012.
- [13] Belforte, D., 2015 industrial laser market outperforms global manufacturing instability, Industrial lasers Solutions,
- [14] Belforte, D., Marks & Spencer to become first British retailer to use innovative laser labeling, 18.06.2014,
- [15] Bosman, J., Processes and strategies for solid state q-switch laser marking of polymers, PhD Thesis, 2007
- [16] Csanák, E., "Sustainable Concepts And Eco-Friendly Technologies In The Denim Industry", 19–20 Nov. 2014, Budapest, Hungary
- [17] Gaebler, Fr., M. Schulze, "Sealed CO₂ Laser Update Product Trends Driven by Diverse Applications". LTJ June No.3, WILEY-VCH Verlag GmbH & Co., Weinheim, 2007
- [18] Esterves, F, Alonso H., "Effect of CO₂ laser radiation on surface properties of synthetic fibres". Research Journal of Textile and Apparel, 11(3):42, 2007
- [19] Ferrero F, Testore F, Innocenti R, Tonin C., "Surface degradation of linen textiles induced by laser treatment: comparison with electron beam and heat source", AUTEX Research Journal. Vol.2(3), 2002
- [20] Juciene, M., V. Urbelis, Ž. Juchnevičienė, L. Čepukonė, "The effect of laser technological parameters on the color and structure of denim fabric", TRJ, Vol. (2013) July 12, 2013
- [21] Khalil, El., "Sustainable and Ecological Finishing Technology for Denim Jeans", AASCIT Communications (American Association for Science and Technology), 2015, Vol.2, Issue 5 July 10, pp. 159-163
- [22] LATI Industria Termoplastici S.p.A., Italy, Laser Marking of Thermoplastics, 05.01.2016
- [23] Laser marking technologies, Sintec Optronics Technology Pte Ltd, 2016
- [24] Lazov, L., Hr. Deneva, P. Narica, Laser Marking Methods, ISSN 1691-5402, © Rezekne Higher Education Institution (Rēzeknes Augstskola), Rezekne 2015
- [25] Matthews, J., "Textiles in Three Dimensions: An investigation into processes employing laser technology to form design-led three-dimensional textiles", PhD thesis, Loughborough University, 28 February 2011
- [26] Nayak, R., R. Padhye, The use of laser in garment manufacturing: an overview, Fashion and Textiles, Springer Open Journal, 2016
- [27] Nourbakhsh, S. & Ashjarian, A., 2012, 'Laser Treatment of Cotton Fabric for Durable Antibacterial Properties of Silver Nanoparticles', Materials, 5, Pp. 1247-1257
- [28] Ortiz-Morales, M., et al., "Comparison between Characteristics of Various Laser-based Denim Fading Processes", Optics and Lasers in Engineering, Elsevier, 39, p.15–24, 2003
- [29] Overton, G., D. Belforte, A. Noguee, C. Holton, Laser Marketplace 2015: Lasers surround us in the Year of Light, Tulsa, 01.16.2015
- [30] Schuöcker D., Handbook of the Eurolaser Academy, Chapman & Hall, London, 1998
- [31] Schuöcker, D., G. Schuocker, Advanced Laser Materials Processing, CO₂ Laser,
- [32] SEI Laser Introduces Digital And Eco Sustainable Laser Solutions At ITMA'2015, TWM, 18 January 2016
- [33] Siegman, A., LASERS, Mill Valley University Science Books, CA, 1986
- [34] Solaiman, Md., J. Saha, Comparative Analysis of Manual Fading and Laser Fading Process on Denim Fabric, Science Discovery, Vol.3(6), pp 44-49, Dec. 2015
- [35] Steen, M. W., J. Mazumder, Laser Material Processing, Springer, 2010
- [36] Štěpánková, M. et al., "Impact of laser thermal stress on cotton fabric". Fibers and Textiles in Eastern Europe, Vol.18, N3, p.70-73, 2010
- [37] Yuan, G., Jiang, S., Newton, E., Fan, J. & Au, W., 'Fashion Design Using Laser Engraving Technology', 8ISS Symposium-Panel on Transformation, Pp. 65-69
- [38] Laserschneiden und -gravieren von Textilien, Eurolaser GmbH, avr, 2009, 2 www.avronline.de
- [39] Laserbearbeitung für das Automobil-Interieur, urolaser GmbH, avr, 2010, 9 www.avronline.de
- [40] US 6753501 B1, Processing of textile materials using laser beams and material sized in larger widths, Jun 22, 2004
- [41] www.sp-laser.ru/aktualnye-woprosy-otwety.html , [Accessed: 30.10.2016]
- [42] www.trumpf.com/en.html TRUMPF Laser Technology, [Accessed: 28.10.2016]
- [43] www.markpro.ru/lazer.html Лазерная маркировка, [Accessed: 28.08.2015]
- [44] www.dapramarking.com/data-matrix.htm 2D Data Matrix Code Products [Accessed: 26.10.2015]
- [45] www.cemark.bg/bg/lazeri/ , [Accessed: 21.11.2016]
- [46] www.pulslight.net/laser-marking/ , Pulslight-Laser systems, [Accessed: 20.12.2014]
- [47] http://www.goldenlaser.cc/gallery/page/4 [Accessed: 17.04.2017]

Fabric Selection for Work Wear During Procurement Procedure

Ilze Baltina, Ausma Vilumsons, Anna Tarasenko, Liene Silina

*Riga Technical University, Faculty of Material Science and Applied Chemistry, Institute of Design Technologies,
Address: Kipsalas 6 - 222, Riga, LV-1048, Latvia*

Abstract. Nowadays, more and more importance is given to labour protection, health and safety. One of the protective means is suitable clothing. Often workwear serves as a uniform, which characterizes the position of the worker and represents the organization. Basically, such types of workwear are sewn or purchased using the procurement procedure. Usually procurement procedure is carried out for the entire sewn product as a whole. When workwear is worked out great importance should be paid to basic fabrics and their protective quality. In order to provide the most suitable choice of the fabric, the procurement procedure of it should be done separately from the sewing service purchase. Fabric production and garment sewing in most cases take place at different companies. In this case, does not always match the probability that the best sewing service provider will offer the best quality fabrics.

Technical specification of fabrics should be worked out very carefully. It should include fabric fibre content, structure characteristics, type of finishing, mechanical and physical properties. Fabric supplier selection can be made after the applicant submitted fabric technical description, which specifies all nominal values of requested technical characteristics. The procurement procedure must include testing of actual characteristics and its comparison with nominal values.

Field uniform fabrics are analysed as an example in scientific study. The procurement procedure of these fabrics should be especially accurate. During procurement procedure is important to check conformity of supplied fabric directly to offered characteristics.

Keywords: fabric, procurement procedure, work wear.

I. INTRODUCTION

A big part of the time is spent in a workplace. Thus, the working conditions, comfort and working tools are the ones that largely affect the quality of life and one's working capacity. Nowadays, work wear plays a very important role. It performs a variety of functions. One of the most important is the safety function, as well as representation. Workwear often serves as a uniform which also performs the tasks of protection.

The standard LVS EN ISO 31688:2013 "Protective clothing. General requirements" stipulates that protective clothing is clothing including protectors which cover or replace personal clothing, and which is designed to provide protection against one or more hazards [1]. Protective clothing shall not only provide protection against all types of threats, but also be comfortable, its' body size and design, as well as the appropriate choice of materials is of great importance. It should be done very carefully, by precisely developing appropriate requirements. It is important to not only make demands, but to observe and provide them accurately.

Sewn product procurements primarily involve sewing companies, offering both product manufacturing services, as well as providing materials for manufacturing. In most cases, for the basic material procurement procedure a technical

specification and requirements are developed. The supplier, by submitting a tender, is required to demonstrate the compliance of the potential materials and to submit a sample. Unfortunately, the real samples are rarely tested, and the materials actually used in sewing are tested even more rarely. Mainly this kind of control is related to the damages of sewn products in order to obtain the required sample fineness of the material for testing.

Failing to test the actual materials, hidden defects whose causes are ambiguously interpreted often appear in articles over time. Consequently, it is not always clear whether the defects are caused by the wearer's fault or the defects are due to the quality of the fabric. Causes are difficult to be determined precisely, but in any case, the loser is the consumer. If the fabric's non-compliance is even determined, it is still a long and complicated process.

II. MATERIALS AND METHODS

The compliance of the fabric used in the supplied field uniform with the requirements of the technical specification and the sample submitted within the tender is analysed. The geometric characteristics, structural characteristics, as well as mechanical and physical properties of the fabrics are experimentally determined. The fabrics are tested according to European and international test methods. The

acquired characteristics and used test methods are summarized in Table I.

Table I
Test Methods.

Geometric and structural characteristics	Test method	Mechanical and physical characteristics	Test method
Fibre content	European Parliament and Council Regulation (EU) No. 1007/2011[2]	Tensile properties of fabric	LVS EN 13934-1:2013 [7]
Fabric width	LVS EN 1773:2001[3]	Tear properties of fabric	LVS EN 13937-2:2001[8]
Mass of 1m ²	LVS EN 12127:2001 [4]	Air permeability	LVS EN 9237:2001 [9]
Warp and weft density	LVS EN 1049-2:2001 [5]	Fabric stiffness	BS 3356:1990 [10]
Warp and weft linear density	ISO 7211-5:1984 [6]	Fabric surface wetting	LVS EN ISO 4920:2012 [11]
		Fabric water – vapour resistance	LVS EN ISO 11092:2014 [12]

III. RESULTS AND DISCUSSION

The geometric and structural characteristics acquired during testing are summarized in Table II.

The table also contains requirements of the technical specification raised within the procurement procedure.

Table II
Geometric And Structural Characteristics Of Fabrics

Characteristics	Requirement of the technical specification	Submitted sample	Supplied fabric
Fibre content, %	65% cotton 35% polyester	Not fixed	63.4±3% cotton 36.6±3% polyester
Fabric type	Ripstop	Ripstop	Ripstop
Fabric width, cm	150 cm±10%	155	149
Fabric weave	Plain with rip stop	Plain with rip stop	Plain with rip stop
Mass of 1m ² , g	200	217 ±11	214±11
Warp density, warp/10cm	Not fixed	413	429
Weft density, weft/10cm	Not fixed	228	213
Warplinear density, tex	Not fixed	32,2	32,8
weft linear density, tex	Not fixed	34,5	32,9

The technical specification of fabrics indicates two geometrical characteristics: fabric width and weight of 1m².

The fabric width is indicated as 1500mm ± 10%, which means that it can be 135 to 165 cm wide. Such amplitude of fabrics can cause problems during cloth construction; moreover, if the fabric is 135 cm wide, additional material could be necessary. When drawing up the technical specification, it would be desirable to provide a deviation amplitude that is not greater than ±5cm and that is not dependent on the average width (is not expressed as a percentage of the average width).

In the technical specification, a constant value is determined regarding the weight of 1m² of fabric – 200 g/m². In fact, it is very rarely that a fabric is produced that corresponds to the value so accurately. It usually varies within 5% of the average value. Also, in this particular case the values of both tested materials (for 1m²) are slightly greater than set out in the requirements of the technical specification, but this deviation is so small that it can be ignored.

In the technical specification, two structural characteristics are determined: fibre composition and fabric type. Characteristics of both the fabric sample and the supplied fabric correspond to the set requirements. In the paper, the following structural characteristics

- Warp density in the fabric;
- Weft density in the fabric;
- Warp linear density;
- Weft linear density.

Comparing the warp and weft density of the two fabrics, we must conclude that the parameters are different, which could be due to the different fabric contraction during printing. It is the fabric width that lets us think of such a possibility. Regarding the potentially possible unevenness of yarn, the linear density of warp and weft is relatively close.

The mechanical and physical characteristic of both fabric are summarized in Table III.

Table III
Characteristics of the Fabric's Mechanical and Physical Properties

Characteristics	Requirement of the technical specification	Submitted sample	Supplied fabric
Tensile strength, N • warp • weft	No less than 1050 N No less than 450 N	1106±111 N 552±55 N	1260±126 N 547±55 N

Extension, % • warp • weft	Not fixed	22,2 % 11,7 %	15,5 % 12,7 %
Tear strength, N • warp • weft	Not fixed	27 N 20 N	19 N 15 N
Air permeability at a pressure difference of 100Pa	No less than 150mm/s	30 mm/s	22 mm/s
Fabric water – vapour resistance	Up to 3.5 m ² K/W	3.4 m ² K/W	4.2 m ² K/W
Fabric stiffness, • warp • weft	0.7-2.4	17 μNm 23μNm	18 μNm 49 μNm
Fabric surface wetting	Not fixed	Grade 1	Grade 4

The technical specification of fabrics sets the requirements for the following mechanical and physical characteristics:

- tensile strength in a longitudinal and transverse direction;
- air permeability;
- bending rigidity;
- changes of linear dimensions;
- water vapour resistance;
- thermal resistance;
- vapour permeability index.

Additional mechanical and physical characteristics set out in the paper:

- elongation;
- tear strength;
- abrasion resistance
- fabric surface wetting.

Tensile Strength indicators for both longitudinal and transverse direction correspond to the ones indicated in the technical specification. It must be taken into account that tensile strength values border values in both directions set out in the technical specification are different. Essentially, the tensile strength border value in the transverse direction is very low and therefore is not suitable for field uniforms that are work also at active physical activities. The tensile strength is tested according to the standard LVS EN ISO 13934-1. In the standard method, by simultaneously determining the tensile strength, the absolute extension of the fabric is also determined and the relative extension is calculated. Consequently, these indicators do not require investing great additional work or resources, but provide information about the fabric maximum capacity to be extended up to the breaking moment and the possible free movement during wearing. The elongation values indicated in the paper prove the low elongation capability of the given fabric. In the recommendation of the European apparel and textile confederation EURATEX "Recommendations Concerning Characteristics And Faults in Fabrics To Be Used For Clothing" [14] it has been suggested that the trouser fabric elongation capacity should be

between 12.5 and 55% in each direction. This value of the supplied fabric is close to the minimum value, but for the transverse fabric sample – even lower than the minimum allowable value. In this case, it can be concluded that from the view of fabric prolongation this fabric is not suitable for active physical activities, where clothing is exposed to high elongation.

The technical specification does not provide requirement on the fabric tear strength. Since field uniforms are worn in active physical conditions, two investigational fabric tear strength values are defined in the paper. The values obtained are very low and are not appropriate to the product that may not restrict freemovement.

The air permeability of both the fabric sample and the supplied fabric is at least 5 time lower than required in the technical specification. Such air permeability is not allowed for clothing that is worn in active physical conditions in summer.

Vapour resistance of the fabric sample meets the values set out in the technical specification, but the value for the supplied fabric it is higher than the set value. Thus, during physical activity in warm weather conditions the fabric in the lower clothing layer accumulates a high level of humidity. Due to the high humidity, low air permeability and low tear strength of the lower clothing layer, the sewn product bends to the body, does not pass the additional strength of physical activities, and thereby breaks.

The rigidity in the transverse direction of the supplied fabric is substantially increased (more than 2 times) compared to the fabric sample. It is too large for fabrics of field uniforms. Such fabric might be unpleasant to the wearer when in contact with skin.

The surface of both the fabric sample and the supplied fabric is tested regarding its resistance against wetting. Results for both fabrics are dramatically different. If the surface of the sample fabric moistens strongly and its resistance against wetting can be evaluated with grade 1, the surface of the supplied fabric is almost water-repellent and can be evaluated with grade 4 (see Figure 1).



Fig. 1. Surface soaking of the fabric sample (a) and the supplied fabric (b)

Given the above, it can be concluded that neither the analysed fabric sample, nor the fabric actually used in the sewn products does not meet the requirements of the technical specification. Therefore, it can be already predicted that, first, the uniforms will outwear soon and, secondly, the wearer will feel discomfort due to the low air permeability of the fabric.

Procurement procedures of sewn product purchasing can be arranged in two ways. Traditionally, companies participate in procurements by offering ready-made products from their own materials. At the beginning, this options seems very good and acceptable, since nowadays people are usually buying manufactured foods that correspond to their needs, and only rarely purchase their own fabric and go to the tailor. By realizing manufactured goods, the manufacturer is eager to retain its customers and to as much as possible to make the customer return. In most cases customers are able to appreciate good quality. Consequently, manufacturers are interested in meeting consumer expectations with a vengeance by introducing new technologies, achievement and conclusions acquired while working.

Unfortunately, the procurement procedure focuses on one-time deals. A potential supplier is usually thinking of offering the lowest price but still meeting the minimum technical requirements set out in the specification. He does not think whether this order will be followed by another one. Materials chosen for protective work wear play an important role and they provide a large part of protective functions. Meanwhile, raw materials account for a large part of the unembroidered product's cost. Consequently, the procurements often face situations where potential suppliers offer fabrics of the lowest possible price that meet the technical specifications. Since fabric characteristics are affected by lots of different factors, ranging the smallest unit of fibre, its fineness, length, winding, thread type, coarseness, twist, fabric structure and process parameters, up to the type of finish and technological processes, it is virtually

impossible for the fabric technical specification to be fully covered. Usually the most important factors are included. Unfortunately, just as in the analysed example, the suppliers not only offer the least expensive materials, but also ultimately use other similar materials, which do no longer meet the specified requirements, for sewing the products. If the supplier has to send ready-made products, it acts with confidence that the compliance of fabrics will no longer be tested, because without damaging the products in most cases it is simply not possible.

Consequently, it could be resolved by dividing the procurement into two parts. First, purchasing the fabric, testing its compliance with the requirements of the procurement procedure and the submitted sample, and then organizing a procurement for sewing services. Such a division of the procurement process would enable one to improve the protective characteristics of the material, avoid the hidden defects of the product, as well as avoid delivery of different fabrics in different delivery times. In case of army field uniforms, it would provide protection of the masking prints, originality and a narrower range of companies, to whom restricted access information should be provided.

III. CONCLUSIONS

Given the above analysis, we recommend to consider dividing the procurement of protective work wear into two parts: first, buying fabrics, secondly, sewing products from the purchased fabrics.

When concluding the fabric procurement, the fabrics should be tested and their conformity with technical specifications should be approved mandatory.

It is important to include structural and geometric characteristics, as well as physical and mechanical properties in the technical specification of the fabric procurement.

Traditionally, one of the most important characteristics in the technical specifications is fabric weight per 1m^2 , but it may be equal to fabrics of a very different structure. Consequently, technical

specification should also determine requirements for the warp and weft density or the warp and weft linear density.

The technical specification of any work wear should include such characteristics as tensile strength, elongation, tear strength, abrasion resistance, air permeability, and water vapour permeability.

IV. ACKNOWLEDGMENT

This research work was partially financed by the European Union's European Regional Development Fund, through the INTERREG BSR Programme, which awarded a grant to the SWW project (#R006). The authors gratefully acknowledge the received financial support.

REFERENCES

- [1] LVS EN ISO 31688:2013 Aizsargapģērbs. Vispārīgās prasības.
- [2] Regulation (EU) No 1007/2011 of the European Parliament and of the Council of 27 September 2011 on textile fibre names and related labelling and marking of the fibre composition of textile products.
- [3] LVS EN 1773:2001 Textiles - Fabrics - Determination of width and length
- [4] LVS EN 12127:2001 Textiles - Fabrics - Determination of mass per unit area using small samples
- [5] LVS EN 1049-2:2001 Textiles - Woven fabrics; construction - Methods of analysis - Part 2: Determination of number of threads per unit length
- [6] ISO 7211-5:1984 Textiles Woven fabrics Construction Methods of analysis
- [7] LVS EN 13934-1:2013 Textiles - Tensile properties of fabrics - Part 1: Determination of maximum force and elongation at maximum force using the strip method
- [8] LVS EN 13937-2:2001 Textiles - Tear properties of fabrics - Part 2: Determination of tear force of trouser-shaped test specimens (Single tear method)
- [9] LVS EN 9237:2001 Textiles - Determination of the permeability of fabrics to air
- [10] BS 3356:1990 Method for determination of bending length and flexural rigidity of fabrics
- [11] LVS EN ISO 4920:2012 Textile fabrics - Determination of resistance to surface wetting (spray test)
- [12] LVS EN ISO 11092:2014 Textiles - Physiological effects - Measurement of thermal and water-vapour resistance under steady-state conditions (sweating guarded-hotplate test)
- [13] Euratex Technical Clothing Group, "Recommendations concerning characteristics and faults in fabrics to be used for clothing," *Euratex TCG Recommendations, Proposal March 2006* [Online]. Available: https://s3-eu-west-1.amazonaws.com/frantic/stjm/ECLA_suositus_kankaiden_1_aatuvaatimukset_2006.pdf [Accessed: Feb. 16, 2017].

Analysis and Countermeasure of VOCs Source in Automobile Production Process in China

Tingting Cheng¹, Jun Chen¹, Ke Wu^{1*}, Jianguo Liu², Siheng Lu¹, Shouchuang Hu¹

1 - Department of Biological and Environmental Engineering, Hefei University; Collaborative Invention Center for Environmental Pollution Precaution And Restoration of Anhui, Hefei 230601, P. R. China.

2 - Hefei Institutes of Physical Science, Chinese Academy of Sciences, Hefei 230031, P. R. China

*Address: No. 99, Jinxiu Road, Hefei 230601, P. R. China. * Corresponding author. e-mail: wuke@hfu.edu.cn*

Abstract. *This article describes the hazards and causes of VOCs as well as the state of VOCs. It is the main culprit in the production of VOCs, which is the main culprit of the production of VOCs source materials in automobile, and analyzes the production of VOCs in the raw material production process from the source. Finally, proposed reduction measures from three aspects of the raw materials, production, management.*

Keywords: *VOCs, coatings, adhesives, plastic parts, rubber parts.*

I. INTRODUCTION

Recently, The air pollution situation is becoming increasingly serious in China, volatile organic compounds (VOCs) emissions seriously affected the ambient air quality. Volatile Organic Compounds (VOCs) refer to the general term of a class of organic compounds with high vapor pressure and volatile at room temperature and atmospheric pressure [1], including various combinations of alkenes, olefins, Oxygen and halogenated hydrocarbons, such as "Three benzene", formaldehyde and ethyl acetate [2]. Studies have shown that VOCs are O₃ and PM_{2.5} form one of the important precursor materials [3], VOCs can react with the atmosphere NO_x in the ultraviolet radiation, produce ozone and other secondary pollutants, which resulting in photochemical pollution [4]. At the same time, VOCs also have an impact on human health, of which n-hexane, heptane and octane will affect the human central nervous system [5]; polycyclic aromatic hydrocarbons and many chlorine-containing organic due to carcinogenic, teratogenic and mutagenicity. Long-term exposure to high concentrations of VOCs can cause headaches, nausea, vomiting, coma and other symptoms, and damage the liver, kidney, brain and other vital organs [6]-[8]. All in all, VOCs are one of the key pollutants that endanger the atmospheric environment and human health, and it is imperative to control VOCs emissions.

According to the results of 2015 national human source results listing the emissions of volatile organic compounds, that the main sources of industrial sources are traffic, the source of life, agricultural sources in artificial source VOCs emissions constitute [9]. At present, China's annual emissions of anthropogenic

VOCs has been as high as 30 million tons. Among them, the industrial source emissions accounted for the proportion of the entire human source of 55.5 %, is the most important source of emissions [10]. At the same time, on July 8, 2016, the Ministry of Industry and the Ministry of Industry organized the " Action Plan for Volatile Organic Compounds in Key Industries " indicated that, industry is a priority area for VOC emissions is the focus of industrial areas to reduce VOCs with emissions accounting for more than 50 % of total emissions, Complex, with high strength, high concentration and many other types of pollutants, recycling difficult with high cost. At present, the air pollution control situation is grim. It is of great significance to accelerate the key industry VOC reduction to promote industrial green development and promote the improvement of atmospheric environment quality and keep human health.

The production of volatile organic compounds is more complex in the process of automobile production, resulting in hundreds of VOCs, including hydrocarbons, aldehydes, ketones and so on. The resulting VOCs are directly related to the types of parts used in the production of automobiles and the accessories of the automobile manufacture process. The influence of the VOCs is automotive coatings, adhesives, plastic parts and rubber parts and so on.

II. ANALYSIS OF VOCS SOURCE MATERIAL IN AUTOMOBILE PRODUCTION PROCESS

Coatings

In the developed countries of the automobile industry, the amount of paint used in the paint production occupies an extremely important place [11]. Coatings produce large amounts of malodorous and VOCs in transporting and using processes because of the large amount of organic solvents in the production. Therefore, the paint industry is an important industrial source of atmospheric VOCs [12].

Paint is mainly composed of film-forming materials, pigments, organic solvents, additives [13]. The main components of film-forming substances include acidic phenolic resin, phenolic resin, urea-formaldehyde resin, etc., these organic compounds in the process can be used to release benzene, methanol, chlorinated ethylene, hydrogen chloride and phenols and other toxic and harmful gases [14]. Most of these related solvents are strong organic solvents, commonly used solvents include alcohols, esters, ethers, ketones, aliphatic hydrocarbons and chlorine-containing organic matter. In principle, these solvents are not part of the coating and not present in the coating but acting primarily to dissolve the film-forming material used in the coating in a liquid environment to facilitate application and to form a solid coating. After the formation of the volatile to the atmosphere. So the main source of pollution in the paint production process is the solvent [14].

A total of fifteen major VOCs were detected in the automotive coating production workshop, including benzene, toluene, ethylbenzene, xylene, ethyl acetate, butyl acetate, methyl isobutyl ketone, propylene glycol methyl ether acetate and Diol butyl ether and so on, the concentration of detection range of 0.51 ~ 593.14 mg / m³. The concentration of TVOCs in the production stations was significantly different, and the concentration of VOCs in the gas samples of different batches in the same production chain was different. Xylene and butyl acetate are the main VOCs for the production of indoor air [15].

Adhesive

Automotive adhesives in the application of the car is very wide, Coverage is about 20 kg per car. The application of coating technology in automobile manufacturing can enhance the structure of automobile structure, heat and vibration, but also can replace some parts of the welding, riveting and other traditional crafts, simplify the production process, optimize the product structure [16], with The use of the automotive industry towards energy-saving lightweight, high-speed environmental protection, comfort and safety, low-cost trends, glue and related materials in the automotive manufacturing will become more prominent and key.

The volatile organic compounds (methanol, acetone, methyl acetate, tert-butanol, vinyl acetate,

ethyl acetate) in the adhesive were analyzed. The linear range of the six volatile organic compounds was methanol 40 ~ 400 ug/g, acetone 4 to 40 ug / g, methyl acetate 9.2 to 92 ug/g, t-butanol 3.2 to 32 ug/g, vinyl acetate 7.5 to 75 ug / g, and ethyl acetate 4.5 to 45 ug / g [17]. At the same time, the results show that the main components of the welding glue are butyl rubber, processed oil and carbon black, and the influence of the three on the content of VOC is the processing oil > carbon black > butyl rubber; the main component of the coating is (PVC) resin, DOP (dioctyl phthalate) plasticizer and organic solvent, which has a great impact on the emission of automotive VOCs. The main components of the total glue are isocyanate, polyether polyol And so on, its ethylbenzene content is relatively high and have great impact on vehicle VOCs emissions [18].

Plastic parts

With the progress of science and technology, the status of plastic parts in automobile production is more and more important, and its effect on improving vehicle performance, appearance and light weight is obvious [19]. The results show that the vehicle quality can be reduced by 10 %, the fuel consumption can be reduced by 6 % ~ 8 %, the fuel efficiency is improved by 5.5 % and the emission is reduced by 5 % ~ 6 %; the vehicle mass is reduced by 100 kg [20]. October 2016, China Automotive Engineering Society released "energy and new energy vehicle technology road map." The road map pointed out that by 2020, 2025, 2030, the vehicle quality than in 2015 were 10 %, 20 %, 35 %. At present, the average use of bicycle bicycles in developed countries is more than 150 kg, accounting for 12 % to 20 % of the total weight of the car, while the use of bicycles in China accounts for about 7 % to 10 % of the weight of vehicles [21]. Thus, the application of automotive plastic parts will be more and more widely. Over the past 30 years, the amount of plastic used in automobiles has risen from about 10 kg in the early 1960s to 200 kg at the beginning of the 21st century. At present, the application of plastic in the car is divided into three categories: external parts, interior parts and functional structural parts [22], including automotive dashboard, car handrails, handles, liner, car bumpers and so on.

The main components of automotive plastics are polypropylene (PP), ABS, polycarbonate (PC), polyethylene (PE), polyurethane (PU) and polyvinyl chloride (PVC) [23]. Polypropylene plastic in automotive plastic parts of the most widely used, polypropylene (PP) with good mechanical properties, low relative density, easy processing and other excellent characteristics. Because of its excellent heat resistance, it is widely used in automobile production, but PP materials in the production and use of the process will inevitably produce some monomer, oligomers and other pollutants [24]. A total of 28 components were detected in their volatile gases, including alkanes, aldoxones, alkoxides and olefins,

with acetone (14.12 %) and 2, 4 - dimethylheptane (12.97 %) of the most [25].

Rubber products

Rubber products in the use of automotive production accounted for about 5% of the weight of the vehicle, the amount can not be underestimated. In addition to the main components of rubber tires, there are also rubber seal products, rubber shock products, hoses, tape and other rubber products in the car.

Rubber products used in the production of raw materials are mainly raw rubber with agents and as a skeleton material of fiber and metal materials. Raw rubber includes natural rubber and synthetic rubber (silicone rubber, styrene-butadiene rubber, cis-methyl rubber, isoprene rubber, etc.) [26]. The compounding agent is an auxiliary material added to improve the properties of the rubber, according to the function can be divided into curing agent, curing accelerator, anti-aging agent, anti-scorching agent, plasticizer, with thousands of complex ingredients, complex composition. These materials are masticated (according to different types of raw rubber, the temperature is usually 30-40 °C), kneaded (temperature 80-160 °C or so), rolled out pressure, petaled, molded and other processes finally got rubber products. In this process, due to high temperature and high pressure, they will make the organic ingredients in the volatile or cracked and resulting in a large number of odor VOCs exhaust. VOCs waste gas in the mixing, pressing, rolling, curing and other processes is accounted for about 20% of the total emissions of rubber products production process with high temperature and complex composition, low concentration characteristics, which composed mainly by carbon disulfide, Carbon, hexane, toluene, hydroquinone and other components [27]. According to the American Rubber Manufacturers' Association, the emission of VOCs in the production process of rubber products is the largest, and the pollutants emitted by the vulcanization process include toluene, m-xylene, p-xylene and carbon disulfide. Other processes are mainly polluted it is carbon disulfide, carbon tetrachloride and hexane [28].

III. REDUCTION MEASURES

In the context of environmental protection, automobile manufacturing industry as a labor and knowledge-intensive industries, reducing the production of atmospheric environmental pollution has become the industrial development needs to bear the important social responsibility. Automotive production industry VOCs cut not only in the production process to optimize the production process, but also from the source of VOCs - the production of raw materials, choose clean green materials for the automotive production process to contribute to control VOCs emissions. In this regard, the car companies and the relevant departments can make some improvements:

Both government and enterprises should strengthen VOC emissions management. Government departments should strengthen the emission requirements of industrial production, improve the laws and regulations to restrict emissions of production enterprises. Enterprises should not only strengthen the managerial requirements of emission of pollutants in the producing process and establish strict policies but also increase the VOCs post-treatment facilities that can burn or wash waste gases and then emit them. There is a remarkable example of RTO device in Hefei Economic Development Zone. One of car manufacturing plant use the RTO device to burn the organic waste gases emitted from the spray room, natural drying room and industrial drying room. A large amount of organic waste gases produced in the coating process are oxidized and decomposed in the case of natural gas combustion and becomes non-toxic CO₂ and H₂O. The heat of the oxidized high-temperature gas is "stored" by the ceramic generator for preheating the new organic waste gas and saving the fuel consumption required for the temperature rise. The purification efficiency is generally greater than 98 %.

In order to take the road of cleaner production, enterprises have to choose new technologies, new materials and new technology. They should initiate environmental protection activities from the source to the process, every step of the production. They should better control the amount of pollutants from the resource and pay attention to the process and process transformation and select the optimal coating ratio and spraying process to reduce the use of related raw materials and emissions. In addition, they ought to use green production materials and select coatings and adhesives of aqueous solvent type to reduce the VOCs emissions from organic solvents. In term of automotive plastic parts, they should utilise long-chain polymer materials to reduce the plastic parts pyrolyzed in high temperature environment and producing VOCs gas.

Enterprises must speed up the improvement of the existing process, controlling the amount of pollutants from the parts and assembly process to the use of source materials. They should pay attention to the process and process transformation and select the optimal coating ratio and spraying process to reduce the relevant use of raw materials and emissions. For example, After a car manufacturing plant Hefei Economic Development Zone take the lead in the use of environmentally friendly water-based paint, the third factory has adopted the most environmentally friendly water-based B1B2-free coating process, which is the shortest spray process today. Through the optimization of coating, these enterprises have reserved the anti-UV and anti-stone attack function of floating coat, which not only can subtract the equipment caused by the equipment investment and energy costs, but also make a significant reduction in VOC pollution to the

environment. It is reported that the use of water-based B1B2 exemption technology not only can save 25% to 30% of the energy and reduce 15% to 20% of the CO₂, 20% to 25% of the waste, but also reduce the consumption of coating about 2kg per car. The enterprise has adopted green technology to reduce the pollution emissions to the minimum.

IV. ACKNOWLEDGMENTS

This research was supported by Municipal Solid Waste Disposal Innovation Team of Anhui Province ([2015]49), Collaborative Innovation Center for Environmental Pollution Control and Ecological Restoration of Anhui Province ([2014]28), Major Scientific and Technological Projects of Anhui Province (16030801119).

REFERENCE

- [1] Wang H.L., Zhang G.N., Nie L., et al. Control and management of industrial VOCs in China. *Environmental Science* 32. 2011, pp. 3462-3468. (in Chinese)
- [2] Hunter P, Oyama S T. Control of volatile organic compound emissions: conventional and emerging. New York: John Wiley & Sons, Inc., 2000.
- [3] Song Y., et al. Characteristics of Fine Particles in Beijing. *Environmental Science* 2002 , pp. 11-16. (in Chinese)
- [4] Shi Y.Z. Simulation of Photochemical Smog in Suburbs of Beijing City. *Journal of climate and environmental research* 2008, pp. 84-92. (in Chinese)
- [5] Zhang C.N., Ye D.Q., Wu J.L. Adsorption and Catalytic Purification Technology of Advanced and Practical Volatile Organic Waste Gas. *Energy Environmental Protection* 2005, pp. 5-8. (in Chinese)
- [6] Zhou J, You Y, Bai Z P, et al. Health risk assessment of personal inhalation exposure to volatile organic compounds in Tianjin, China. *Science of the Total Environment* 409.2011, pp. 452-459.
- [7] Shirasu M, Touhara K. The scent of disease: volatile organic compounds of the human body related to disease and disorder. *The Journal of Biochemistry*, 150. 2011, pp. 257-2.
- [8] Rudnicka J, Kowal kowski T, Ligor T, et al. Determination of volatile organic compounds as biomarkers of lung cancer by SPME-GC-TOF / MS and chemometrics. *Journal of Chromatography B: Biomedical Sciences and Applications* 879. 2011, pp. 3360-3366.
- [9] Ning M., Sun Y.M. Thanks and Approaches to the Prevention and Control of Volatile Organic Compounds in the 13th Five-Year Plan. *World Environment* 2016, pp. 27-29. (in Chinese)
- [10] Anonymous. About the cutting action plan for key industries volatile organic compounds (2016-2018) interpretation of the Chinese tyres resources comprehensive utilization 2016, pp. 23-24. (in Chinese)
- [11] Zhang W.Y., Hou S.Z. Development and Application of Automotive Coatings. *Modern Coatings and Coatings* 16. 2013, pp. 23-25. (in Chinese)
- [12] Chen Y., Ye D.Q., Liu X.Z., et al. Study on source tracking and industry characteristics of VOC emission from industrial sources in China . *China Environmental Science* 32. 2012, pp. 48-55. (in Chinese)
- [13] Liu H., Hu W.Q. Production and application of iron white powder. Science and Technology Press, 1992. (in Chinese)
- [14] Lin H. Synthesis and Technology of Acrylic Resin in Clean Production of UV Coatings. Hunan University, 2007. (in Chinese)
- [15] Zeng P.Y., Li J.J., Liao D.Q., et al. Emission characteristics and safety evaluation of VOCs in the production of automotive coatings // The 16th National Symposium on Environmental Microbiology. 2013, pp. 4592-459. (in Chinese)
- [16] Shen F., Chen Y., Wu S.Z. Introduction of Automotive Adhesive and Sealant // 2004 Beijing International Adhesive Technology Seminar. pp. 608-617. (in Chinese)
- [17] Zhang Y.M., Zha L., Fang J.L., et al. Determination of Volatile Organic Compounds in Tobacco Adhesives by Headspace-Gas Chromatography. *Fine Chemical Industry* 29. 2012, pp. 717-720. (in Chinese)
- [18] Xu S.Y., Jin Y.M., LI L., et al. Effects of vehicle adhesives on air quality in the vehicle. *China Adhesives* 2013 pp. 14-17. (in Chinese)
- [19] An S.X. Analysis of automotive plastic materials application and development trend. Urban construction theory: electronic version, 2013, pp. 132-133. (in Chinese)
- [20] Liu J.C., Cao D., Li J., et al. Application of Plastic Composites in Automobile Lightweight. *Modern Parts and Components*, 2013, pp. 39-42. (in Chinese)
- [21] Yang T. Application and prospect of plastic material application in automobile industry. *New Materials for Chemical Industry*, 2013, pp. 1-4. (in Chinese)
- [22] Cao J.Y. Application of plastic material in automobile interior and exterior decoration. *Heilongjiang Science and Technology*, 2016, pp. 13. (in Chinese)
- [23] Yang Z.M. Automotive waste plastics and its recycling // National Plastics modification and alloy industry technology exchange annual meeting. 2006. (in Chinese)
- [24] Huang J.B., Li J.J., Yang B., et al. Preparation of Low TVOC Polypropylene Materials for Vehicles. *Plastics Industry* 39. 2011, pp. 113-115. (in Chinese)
- [25] Cui W., Tao R., Li R.H. Study on Volatile Gas Produced by Polypropylene by Solid Phase Microextraction and Chromatography-Mass Spectrometry. *Plastics* 39. 2010, pp. 139-141. (in Chinese)
- [26] Zeng W.Y. Source and purification technology of organic waste gas in heavy polluting industry. Zhejiang University, 2014. (in Chinese)
- [27] Fang M.Q., Huang Y., Liu Z.Z., et al. Ozone Oxidation Chemical Absorption Research Safety and Environmental Engineering 17. 2010, pp. 23-25. (in Chinese)
- [28] Zhang Z.L. Emission coefficient of organic waste gas in the production of rubber products. *Rubber Industry* 53. 2006, pp. 682-683. (in Chinese)

Analysis of Ash Content in Composite Biomass Fuels

Edgars Čubars¹, Liēna Poiša².

¹Rezekne Academy of technologies, Geo technology and Eco industry Research center, Atbrīvošanas aleja 115/k-4, LV 4601, email: edgars.cubars@inbox.lv; ²email: lienapoisa@inbox.lv

Abstract. The study reveals research of ash content in different composite biomass fuels. It contains analysis of samples obtained from various local Latvian biomass types, i.e. reed, wood, hemp, flax shives and peat, by combining them in different proportions. Ash is a by-product derived from combustion process consisting mostly of inorganic substances that are left after a fuel is burnt. High level of ash content in a fuel is undesirable because it causes problems in automation of biomass combustion process. Previous studies carried out by the author show that average ash content in reeds is 2%, which is a high index comparing with wood where ash content is approximately 0,5-1%. Thus, the high ash content in reeds may cause problems in reed combustion in solid fuel boilers. Besides, it is not possible to ensure permanent reed collection that would ensure continuous reed fuel generating process all year long. In order to reduce the ash content to the optimal level and to diversify raw materials necessary for biomass fuel generating process, the author suggests using composite fuels by combining different biomass types. The study contains optimal combining proportions of different biomass types for composite fuel production basing on the ash content in them.

Keywords: ash content in fuels, common reed, wood, peat, hemp, flax shives, composite fuels.

I. INTRODUCTION

One of the most popular renewable energy sources (RES) is biomass. Use of the biomass takes a considerable part in energy industry, mainly due to the use of timber that is one of the main natural resources in Latvia. However, recently an increased attention has been paid to the use of cultivable energy plants and water plants.

The use of such non-traditional sources is disrupted by the fact that in Latvia there is no any thorough assessment of the amount of RES, potential and long-term availability of each energy source in the respective regions. For a rational and appropriate long-term use of RES, the available amount and quality parameters of the respective RES should be assessed [1]. Thus far, the potential of water plant biomass in Latvia as an energy resource has not been taken into account. There is also insufficient interest in peat and various cultivable energy plants. Given Latvian conditions, reeds (*Phragmites australis* (Cav.) Trin. Ex Steud.) growing in natural or artificial water bodies could be used for energy generation [2,3,4]. Researches conducted by foreign scientists also indicate that reeds can be used as a raw material for fuel generation. [5,6]. Overall, reeds from more than 2000 lakes located in Latvia may be used for energy generation. [7] Use of reeds, compared with cultivable energy plants, has its advantages and disadvantages. The main advantage is the fact that it is not necessary to occupy areas of agricultural lands and that no expenses are needed for settlement of plantations. The main disadvantage is the fact that no

subsidies are paid for cultivation of these plants, or for energy plants; besides, it is relatively complicated to gather such plants mechanically and a special equipment is needed.

Flax processing residues, i.e. shives, straw, hemp fibres, peat, hay, as well as other energy plants can also be used. The main problem related to their use is the fact that these resources are available seasonally; besides, their thermal qualities are often worse if compared to timber. Therefore, it can be suggested to use composite fuels where timber is used as a base, while other energy plants are added as supplementary fuels, e.g. in pellet production. Thus, when resources are provided irregularly, they could be easily replaced by other types of biomass.

One of the most important fuel characteristics is ash content. Ash is a by-product of fuel combustion mainly consisting of inorganic substances obtained after fuel combustion. High ash content is a negative feature because it makes the automation of biomass combustion process more difficult [8].

The paper studies the ash content in fuels, depending on the amount of fuel added to wood. Ash content in fuels was assessed according to the Standard ISO 17225-1: 2014 Solid biofuels. Fuel specifications and classes. Part 1: General requirements [9]. According to this standard, the quality of composite fuel was evaluated basing on ash content.

Basic material for the research consisted of industrially produced wood pellets, which can be purchased in trading venues in Latvia; various types

of local biomass, i.e. reeds, flax shives, peat, hemp fibre, hay, as well as fossil fuel, i.e. coal dust, were added.

II. MATERIALS AND METHODS

The study used industrially produced wood pellets ground into powder using a mill. Various types of local biomass available in Latgale region were added to the wood chips, i.e. reeds, flax shives, peat, hay, hemp fibre, as well as coal dust, that had previously been dried and ground into powder. In order to determine the ash content dependence on the amount of various types of biomass added to the wood, respective samples were prepared and analysed in the following proportions. Sample 1: 100% wood; Sample 2: 90% of wood and 10% of other fuels; Sample 3: 80% of wood and 20% of other fuels; Sample 4: 60% of wood and 40% of other fuels; Sample 5: 40% of wood and 60% of other fuels; Sample 6: 20% of wood and 80% of other fuels; Sample 100% other fuels. Ash content in the samples was determined using the standard method CEN/TS 14775:2004 [10]. The samples were dried at the temperature of 105°C. They were later placed into crucibles and weighted (Fig. 1).



Fig. 1. Samples analysed to determine the ash content

For combustion of samples the furnace “Nabertherm” was used (Fig. 2).



Fig. 2. The furnace used to determine the ash content

After combustion in the furnace at the temperature of 550°C the crucibles with ash (Fig. 3) were taken out, cooled and weighted, the respective calculations of ash content were also performed. Each sample was

analysed twice, measurement error assessment was also carried out [10].



Fig. 3. Samples after combustion

III. RESULTS AND DISCUSSION

According to the Standard ISO 17225-1: 2014 Solid biofuels. Fuel specifications and classes. Part 1: General requirements (see the Standard below), fuels, basing on the ash content, are divided into ten classes. See Table 1.

Table 1
Classes of solid biofuels basing on ash content [9]

Class	A 0.5	A 0.7	A 1.0	A 1.5	A 2.0	A 3.0	A 5.0	A 7.0	A 10.0	A10.0+
Ash content, %	≤ 0,5 %	≤ 0,7 %	≤ 1,0 %	≤ 1,5 %	≤ 2,0 %	≤ 3,0 %	≤ 5,0 %	≤ 7,0 %	≤ 10 %	>10 % (maximum value to be stated)

Ash content in timber without bark is around 0.3%, it is higher in the bark and amounts to 4-5% [12.9] Ash content in wood pellets analysed in our study amounted to $0.43 \pm 0.01\%$, which is a good indicator. Pellets, basing on the ash content, correspond to the highest class A 0.5. Ash content grows when reed biomass is added to the wood (Figure 3). Ash content in 100% reed biomass amounted to $2.39 \pm 0.11\%$, which corresponds to the class A 3.0. In another study, ash content in reeds was also similar, i.e. 2.76% [13]. Thus, it can be concluded that adding reed biomass to the wood increases ash content and deteriorates fuel quality.

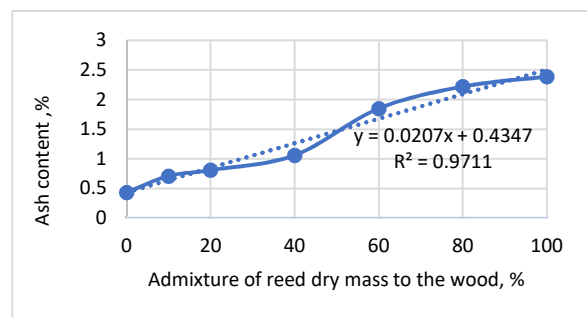


Fig. 3. Ash content in the wood-reed composite fuel

In order to determine the proportions of wood and reeds in the composite fuel to meet certain quality standards, the following equation (Equation 1) was used:

$$A = 0,0207R + 0,4347 \quad (1.)$$

Where, A- Ash content in composite wood-reed fuel, %

R- admixture of reed dry mass to the wood %

This equation can be used to find critical ash content values for each class. In the class A 0.5 reed admixture to the wood may amount to 3.2%, in the class A 0.7 it may range from 3.3% to 12.8%, in the class A 1.0 reed admixture may amount to 12.9 – 27.3%, in the class A 1.5 from 27.4% to 51.5%, in the class A 2.0 from 51.6% to 75.6%, while reed admixture exceeding 75.6%, basing on the reed content, corresponds to the class A 3.0.

Thus, 3.2% of reed biomass may be added to wood pellets without decreasing fuel quality in terms of ash content. If such a high quality is not necessary, the amount of reed biomass admixture may be increased in accordance with the above-mentioned ranges.

Adding flax shives to the wood increased rapidly the ash content (Figure 4). Ash content in the biomass of pure flax shives was high, it amounted to $17.76 \pm 1.05\%$, which ranks flax shives into the class A 10+. Other researchers have also found such a high ash content in rice straw, i.e. about 1 –20% [14] Adding flax shives to the wood increases rapidly ash content and deteriorates fuel quality. Using flax shives in production of biomass fuel might be difficult and uneconomical because of the high ash content.

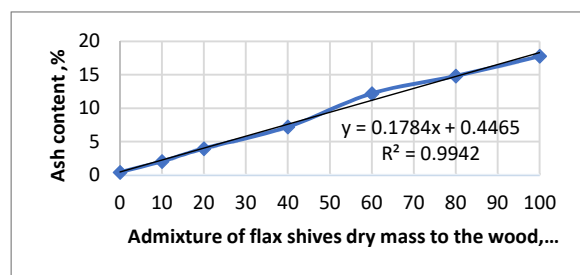


Fig. 4. Ash content in the wood-flax shives composite fuel

In order to determine the proportions of wood and flax shives in the composite fuel to meet certain quality standards, the following equation (Equation 2) was used:

$$A = 0,1784R + 0,4465 \quad (2.)$$

Where, A- Ash content in composite wood-flax shives fuel, %; R- admixture of flax shives dry mass to the wood, %.

This equation can be used to find critical ash content values for each class. In the class A 0.5 admixture of flax shives dry mass to the wood may

not exceed 0.3 %. In the class A 0.7 admixture of flax shives may amount to 0.3-1.4%, in the class A 1.0 admixture of flax shives may amount to 1.5-3.1%, in the class A 1.5 it may amount to 3.2%-5.9 %, in the class A 2.0 it may amount to 6% - 8.7%, in the class A 3.0 it may amount to 8.8%-14.3 %, in the class A 5.0 it may amount to 14.4-25.5%, in the class A 7.0 it may amount to 25.6%-36.7 %, in the class A 10.0 it may amount to 36.8-53.6 %, while flax shive-wood composite fuel where content of flax shives exceeds 53.6 % corresponds to the class A 10+. Therefore, flax shives form a biomass with a high ash content, growth in the proportion of this material increases rapidly the ash content in the composite fuel. Ash content in flax shives is almost eight times higher than the ash content in reeds and forty times higher than in wood. The high ash content can cause problems in automation of combustion process. Adding peat to the wood increases the ash content (Figure 5). In our research, ash content in the biomass of pure peat amounted to $4.13 \pm 0.21\%$, which ranks peat, basing on the ash content, into the class A 5.0. Adding peat to the wood increases ash content.

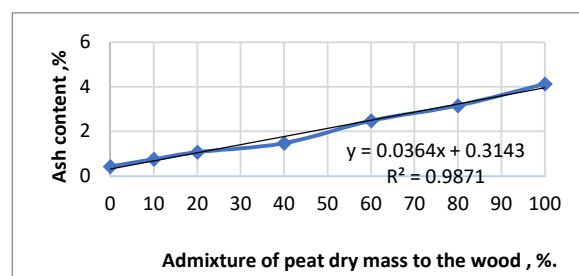


Fig. 5. Ash content in wood-peat composite fuel

In order to determine the proportions of wood and peat in the composite fuel to meet certain quality standards, the following equation (Equation 3) was used:

$$A = 0,0364R + 0,3143 \quad (3.)$$

Where, A- Ash content in composite wood-peat fuel, %

R- Admixture of peat dry mass to the wood, %.

This equation can be used to find critical ash content values for each class. In the class A 0.5 admixture of peat to the wood may not exceed 5.1 %. In the class A 0.7 admixture of peat may amount to 5.2-10.6 %, in the class A 1.0 admixture of peat may amount to 10.7-18.8%, in the class A 1.5 it may amount to 18.9-32.6 %, in the class A 2.0 it may amount to 32.7-46.3%, in the class A 3.0 it may amount to 46.4-73.8%. Admixture of peat to the wood chips exceeding 73.9% corresponds to the class A 5.0.

In 2016, in order to receive area payments for tidying up permanent grasslands, the grass had to be mowed and removed from the field. Thus, the farms without livestock faced the problem of hay

overproduction, which could be solved by using hay as additional fuel. Ash content in canary seed may range from 2.5 to 10%. [9] Overall ash content in dry grass is about 7% [12]. Festulolium, timothy, and meadow fescue also have high ash content, i.e. 6-8%. [15] In our research, ash content in pure straw amounted to $7.73 \pm 0.01\%$, which ranks pure straw, basing on the ash content, into the class A 10.0. Adding straw to the wood increased ash content in the fuel (Figure 6).

In order to determine the proportions of wood and straw in the composite fuel to meet certain quality standards, the following equation (Equation 4) was used:

$$A = 0,0728R + 0,2346 \quad (4.)$$

Where, A- Ash content in composite wood-straw fuel, %

R - admixture of straw dry matter to the wood, %.

This equation can be used to find critical ash content values for each class.

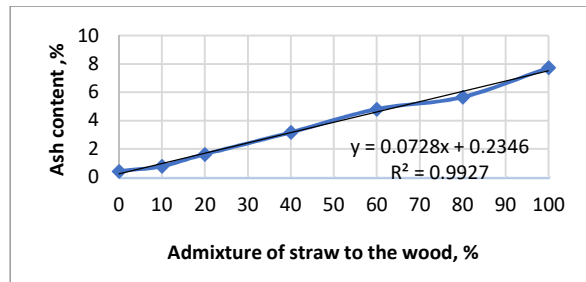


Fig. 6. Ash content in wood-straw composite fuel

In class A 0.5 maximum amount of straw admixture to the wood may be 3.6 %. In class A 0.7 straw admixture may amount to 3.7- 6,3 %, in class A 1.0 it may amount to 6.4- 10.5 %, in class A 1.5 it may amount to 10.6-17.4 %, in class A 2.0 it may amount to 17.5-24.2%, in class A 3.0 it may amount to 24.3-38%, in class A 5.0 it may amount to 38.1-65.4 %, in class A 7.0 it may amount to 65.5- 93%. If straw admixture to the wood exceeds 93%, it corresponds to the class A 10. One of the most promising energy plants for cultivation is hemp. Ash content in hemp varies in different studies: it may be 2% [16] or around 3% [13]. In addition, it may also vary for different parts of the plant, such as leaves, stems, etc., as it was revealed before in the study of corn plants, where ash content in leaves was 2 times higher than in its trunk [17]. Furthermore, the ash content in plants depends on the time of harvesting, it is recommended to harvest the cultivated energy plants as late as possible in the autumn [18]. In our study, ash content in hemp fibres was higher and amounted to $3.78 \pm 0.09\%$, which ranks pure hemp fibre into the class A 5.0, basing on its ash content. Adding hemp fibre to the wood increased ash content in the fuel (Figure 7).

Figure 7. Ash content in wood-hemp fibre composite fuel.

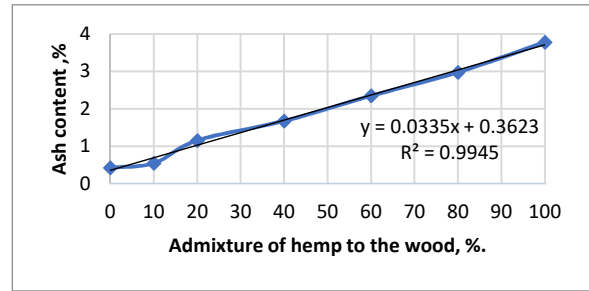


Fig. 7. Ash content in wood-hemp fibre composite fuel.

In order to determine the proportions of wood and hemp fibre in the composite fuel to meet certain quality standards, the following equation (Equation 5) was used:

$$A = 0,0335R + 0,3623 \quad (5.)$$

Where, A- Ash content in composite wood-hemp fuel, %

R- Admixture of hemp fibre dry mass, %.

This equation can be used to find critical ash content values for each class. In class A 0.5 maximum amount of hemp fibre admixture to the wood may be 4.1%. In class A 0.7 admixture of hemp fibre may amount to 4.2-10.0%, in class A 1.0 it may amount to 10.1-19.0%, in class A 1.5 it may amount to 19.1- 34 %, in class A 2.0 it may amount to 34.1-48.9%, in class A 3.0 it may amount to 49-78.8%. If the amount of hemp fibre admixture exceeds 78.9 %, it corresponds to the class A 5.0. Wood may be also mixed with various fossil fuels, which would increase its energy value. Coal dust may be used as one of the components in composite fuels. Ash content in coal available in Latvian markets was established. Ash content in pure coal dust was high, it amounted to $8.27 \pm 0.39\%$, which ranks it into class A 10.0. Adding coal dust to the wood increases ash content in the fuel (Figure 8).

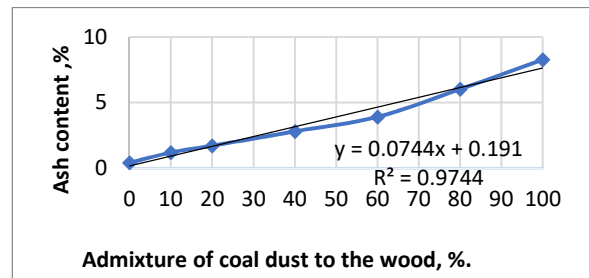


Fig. 8. Ash content in wood-coal dust composite fuel.

In order to determine the proportions of wood and coal dust in the composite fuel to meet certain quality standards, the following equation (Equation 6) was used:

$$A = 0,0744R + 0,191 \quad (6.)$$

Where, A-Ash content in composite wood-coal fuel, %

R- Admixture of coal dust to the wood, %.

This equation can be used to find critical ash content values for each class.

In class A 0.5 maximum amount of coal dust admixture to the wood may be 4.1%. In class A 0.7 admixture of coal dust may amount to 4.2-6.8%, in class A 1.0 it may amount to 6.9-10.9%, in class A 1.5 it may amount to 11-17.6%, in class A 2.0 it may amount to 17.7- 24.3%, in class A 3.0 it may amount to 24.4-37.8%, in class A 5.0 it may amount to 37.9- 64.6%, in class A 7.0 it may amount to 64.7-91.5%. If the amount of coal dust admixture to the wood exceeds 91.5%, it corresponds to the class A 10.0.

High ash content is a negative feature in fuels, because it makes the automation of combustion process more difficult. Combustion of fuel with a high ash content involves additional expenses related to ash disposal and maintenance of combustion equipment. It has been concluded that mixing wood and other biofuels or fossil fuels inevitably increases the ash content therein (Figure 9).

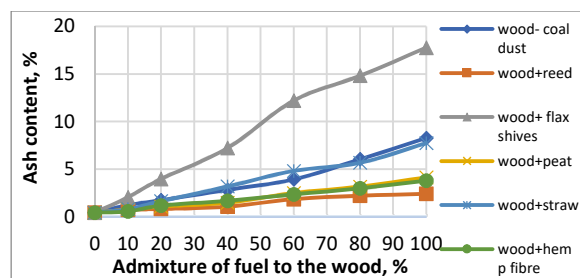


Fig. 9. Ash content in different composite fuels depending on the amount of fuel added to the wood

As we can see from the Figure 9, analysis of ash content in fuels revealed that the best results (lowest ash content) was in the wood-reed composite fuel; ash content in the fuel containing admixture of peat and hemp was also relatively low. The study results indicate that the wood, in order to keep ash content of the class A 0.5, can be mixed with a relatively small amount of these fuels, i.e. 3-5%. If the final product is intended for use in furnaces, which allows for a higher ash content, the added amount of biomass can be increased according to the estimates above. To keep the ash amount corresponding to class A 1.0, the wood may be mixed with 27% of reed, 18% of peat and 19% of hemp. The second group, basing on the results of the study, contains wood-straw composite fuel and wood-coal dust composite fuel. In order to correspond to the class A 0.5, wood can be mixed with about 3 or 4% of these fuels. For the ash content in class A 0.5, 10% of straw and coal dust may be added. Use of such composite fuels is possible, but the increased amount of ash should be considered.

Given that the heat of combustion of coal dust is higher than that of the wood, such a combination could improve the overall fuel quality. In addition, changes in the heat of combustion should be examined in the future.

The highest ash content was found in flax shives, it exceeds the characteristics of wood by approximately 40 times. Consequently, the use of flax shives in composite fuels is not recommended.

IV. CONCLUSION

Wood is a fuel with a low ash content, and admixture of various biomass types available in Latvia, as well as admixture of coal dust to the wood in composite fuels, increases ash content in the respective fuels.

The lowest ash content was found in reeds, peat and hemp fibre, therefore these types of biofuels are the most appropriate to be added to wood in composite fuels.

Basing on experimental studies, equations have been created for calculation of amounts of fuels to be added to the wood.

The studied wood pellets, looking at the ash content, correspond to the highest class A 0.5. In order to keep ash content within the limits of class A 0.5, it is possible to add 3-4% of reeds, peat, hemp fibre, coal or straw. Ash content in flax shives ash content is forty times higher than ash content in wood, therefore the use of flax shives in composite fuels rapidly increases the overall ash content and is not recommended.

REFERENCES

- [1] Noviks G., Zorins A. (2011) National recommendation report. In: *Joint European-Latin American Universities Renewable energy Project*, Rēzeknes Augstskola Rēzekne, Latvija p.6-8.
- [2] Čubars E. (2008) Lubānas ezera niedru resursu izvērtējums un to izmantošanas enerģijas ieguvei pamatojums/ *Zinātniskais darbs maģistra grāda ieguvei*/ Rēzeknes Augstskola, Inženieru fakultāte. Zin.vad. Gotfrīds Noviks. Rēzekne, 70 lpp.
- [3] Enerģētisko augu audzēšana un izmantošana (2007) Adamovičs A., Agapovs J., Aršanica A. u. c. Valsts SIA „Vides projekti”, Rīga, 43-133. lpp.
- [4] Kronbergs E., Šmits M. (2009) Cutting properties of common Reed biomass. In: *8th international scientific conference “Engineering for rural development”*, May 28.-29., Jelgava, Latvia, p.207.
- [5] Komulainen M., Simi P., Hagelberg E., Ikonen I., Lyytinen S. (2008) Reed energy-Possibilities of using the Camnon Reed for energy generation in Southern Finland. In: *Turku university of applied sciences reports 67*. p.5-75.
- [6] Reed up on Reed (2007) Ikkonen I., Roosaluuste E., Pitkanen T.at.al. Southwest Finland regional Environment centre, Turku 2007. , p. 5-115.
- [7] Kronbergs A., Kronbergs E., Siraks E., Dalbins J. (2012) Cutting properties of arranged stalk biomass In: *Proceedings of the International Scientific Conference „Renewable Energy and Energy Efficiency”*, p. 145.
- [8] Tardenaka A., Spince B. (2006) Characterization of fuel granules and briquettes produced from fine-dispersed wastewood. In: *International conference Eco-Balt 2006*, Riga, Latvia, p. 37-38.
- [9] LVS EN ISO 17225-1:2014:Solid biofuels- Fuel specifications and classes-Part 1: General requirements.

- [10] Arhipova I., Bāliņa S.(2006) *Statistika ekonomikā. Risinājumi ar SPSS un Microsoft Excel*. 2.izdevums. Rīga: Datorzinību centrs, 352. lpp.
- [11] LVS CEN/TS 14775:2004: Solid biofuels- Method for the determination of ash content.
- [12] Biedermann F., Obernberger I. (2005) Ash-related Problems during Biomass Combustion and Possibilities for a Sustainable Ash utilisation., p.2-3. [12.01.2016] Available: <http://www.bios-bioenergy.at/uploads/media/Paper-Biedermann-AshRelated-2005-10-11.pdf>
- [13] Kakitis A., Ancans D., Nulle I.(2014) Evaluation of combustion properties of biomass mixtures. In: *Engineering for rural development*, Jelgava, 29.-30.05.2014, p. 423-425.
- [14] Jenkins B.M., Baxter L.L., Miles Jr T.R., Miles T.R.(1998) Combustion properties of biomass. In: *Fuel processing Technology* 54, p.22;
- [15] Platače R., Adamovičs A (2014) The evaluation of ash content in grass biomass used for energy production. In: *Energy Production and menegment in the 21st Century*, Vol.2 .p.1060.
- [16] Marques G., Rencoret J., et.all.(2010) Evaluation of the Chemical Composition of Different Non-Woody Plant Fibers Used for Pulp and Paper Manufacturing. In: *The Open Agriculture Journal*, 2010, pp.93-101
- [17] Lizotte P., Savoie F., De Champlain A. (2015) Ash content and calorific Energy of Corn Stover Components in Eastern Canada. In: *Energies* 2015, 8. p.4827-4838.
- [18] Rancane S., Karklins A., Lazdina D., Berzins P.(2015) Biomass yield and chemical composition of perennial grasses for energy production. In: *Engineering for Rural development*. Jelgava, 20.-22.05.2015., p. 550.

Structure and Optical Properties of Hybrid Metal-Dielectric Colloidal Photonic Crystals

A. V. Cvetkov¹, V. I. Gerbreders², S. D. Khanin³, A. E. Lukin¹, A. S. Ogurcovs²,
S. G. Romanov⁴, V. G. Solovyev¹, A. I. Vanin¹, M. V. Yanikov¹

¹Department of Physics, Faculty of Physics and Mathematics, Pskov State University, Lenin Square 2, 180000 Pskov, Russia;

²G. Liberts' Innovative Microscopy Centre, Daugavpils University, Vienibas Street 13, LV-5400 Daugavpils, Latvia;

³Department of Physical Electronics, Faculty of Physics, Herzen State Pedagogical University of Russia, Moyka-river embankment 48, 191186 St. Petersburg, Russia;

⁴Ioffe Physical Technical Institute, Polytechnicheskaya Street, 26, 194021 St. Petersburg, Russia

Abstract. Metal-dielectric nanocomposite optical materials based on colloidal crystals have been prepared by electro-thermo-diffusion or magnetron sputtering of silver. Optical properties of these photonic crystals have been studied by angle-resolved reflectance and transmission spectroscopy. The interpretation of observed spectra has been made taking into account the Bragg diffraction, Fano resonance, Fabry-Perot resonance and surface plasmon-polaritons, which excitations contribute to the optical properties of plasmonic-photonic crystals.

Keywords: colloidal crystal, photonic crystals, photonic glasses, plasmonic crystal, nanostructures.

I. INTRODUCTION

Hybrid metal-dielectric photonic crystals have been fabricated on the basis of colloidal crystals [1] with the aim to design the next generation of optical materials.

Novel 3-dimensional *Ag / opal* nanocomposites have been prepared by electro-thermo-diffusion of silver in opal templates [2]. Their reflectance spectra $R_{Ag/opal}(\lambda)$ demonstrate the diffraction resonances. These resonances are red-shifted compared to those of $R_{opal}(\lambda)$ spectra due to higher effective refractive index $n_{Ag/opal} > n_{opal}$. The most striking observation is the pronounced distortion of diffraction resonance band in reflectance spectra of *Ag / opal* nanocomposite with high metal content that contrasts to almost symmetric Bragg resonance shape of a bare opal. This phenomenon has been interpreted in [2, 3] as the manifestation of the Fano resonance [4, 5] between zero-order diffracted electromagnetic waves and those resonantly scattered by silver dendrites in *Ag / opal* composite.

Alternative approach to metal-dielectric architectures assumes integration of continuous metal films with colloidal crystals [6]. In particular, slab 2-dimensional photonic crystals represented by monolayers (ML) of spheres have been sandwiched between flat and corrugated thin metal films that

terminate their bottom and the top sides, respectively, to produce *Ag / ML / Ag* architecture. Further this structure has been equipped with a corrugated Fabry-Perot microcavity, by adding a silica film and another metal film on top of *Ag / ML / Ag* to achieve *Ag / cavity / Ag / ML / Ag* hybrid. The role of the metal layers here is two-fold – to form a microresonator across the structure and to guide surface plasmon polaritons (SPP) along the structure. This approach can be considered as the prototype fabrication technology for the optical chip production.

II. MATERIALS AND METHODS

Synthetic opals under study consist of silica (SiO_2) beads that are self-assembled in closely packed face centered cubic (FCC) lattice [7].

Silica opal samples were characterized by «VEGA // LMU Tescan» Scanning Electronic Microscope (SEM). According to SEM images, the mean sphere diameter of the studied opal is $D \approx 280$ nm. Moreover, some lattice disorder takes place (Fig. 1).

The electro-thermo-diffusion of silver in the 0.8mm thick opal slab has been carried out under electric field of $E=3.75$ kV/cm at temperature $T \approx 800$ K.

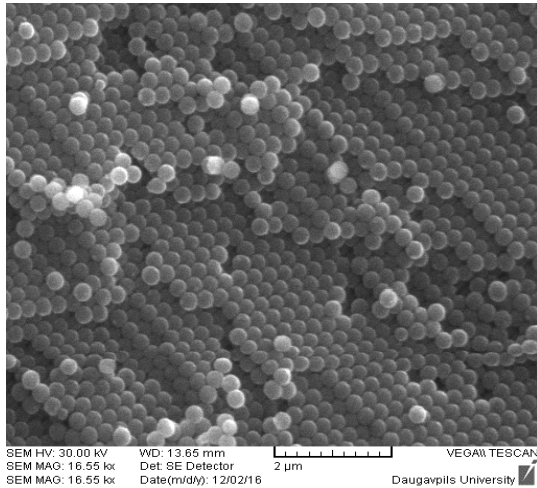


Fig. 1. SEM image of the silica opal matrix under study.

Hexagonally packed monolayer-based metal-dielectric colloidal crystals $Ag/ML/Ag$ and $Ag/cavity/Ag/ML/Ag$ have been prepared by magnetron sputtering of Ag in ATC ORION SERIES SPUTTERING SYSTEM [6] and characterized by “ZEISS FIB-SEM GEMINI” Scanning Electronic Microscope.

Angle-resolved reflectance and transmission spectra of the parent opal template and metal-dielectric nanocomposites have been measured using white light illumination from a tungsten lamp. Spectra have been acquired by USB650 Red Tide spectrometer (Ocean Optics).

III. RESULTS AND DISCUSSION

Figure 2 shows SEM image of the silver infiltrate in one of the defect regions of the $Ag/opal$ composite, confirming infiltration of opal. Silver concentration within these defect regions (e.g., near microscopic cracks, grain boundaries etc.) may be rather high (up to few atomic %).

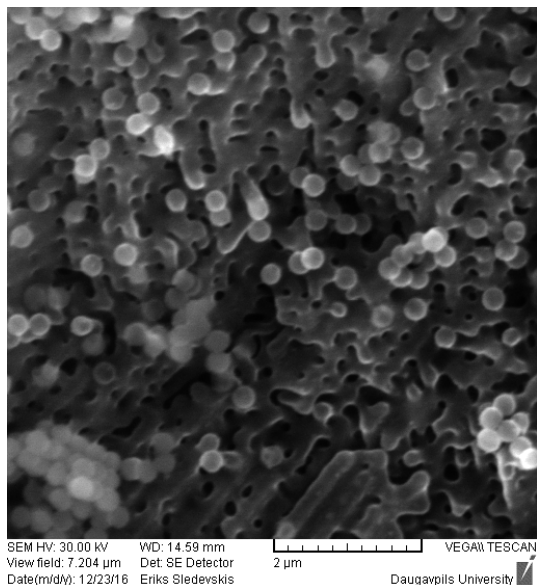


Fig. 2. SEM image of the defect region of the $Ag/opal$ composite.

Reflectance spectra of opal template and those of nanocomposite $Ag/opal$ at two different angles of light incidence are shown in Fig. 3.

One can see three maxima in the reflectance spectra of the opal template (Fig. 3, curves 1, 2), but only one of them (the left one in Fig. 3) demonstrates distinct angular dispersion. At small angles, the resonance wavelength is $\lambda \approx 2dn \approx 600$ nm, where $d = 0.816D$ is the interplane distance of (111) planes in FCC lattice and n represents the effective refractive index of the photonic crystal. Hence, the maximum centred at ~ 600 nm can be attributed to the zero-order (111) Bragg diffraction resonance.

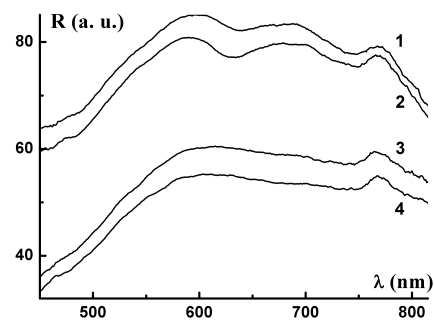


Fig. 3. Reflectance spectra of silica opal template (1, 2) and those of nanocomposite $Ag/opal$ (3, 4) at the angles of incidence 25° (1, 3) and 30° (2, 4).

The positions of two other maxima (near 690 nm and 770 nm – see Fig. 3) seem insensitive to the angle of light incidence. These maxima are presumably attributed to light scattering in partially disordered opal lattice structure (“photonic glass” [8] – [10]).

The diffraction band in the reflectance spectra of $Ag/opal$ composite (Fig. 3, curves 3, 4) differs from the Bragg resonance shape in the spectra of a bare opal (Fig. 3, curves 1, 2). As we already mentioned in Section I, this phenomenon is the manifestation of the Fano resonance [2] – [5] between two flows of electromagnetic waves: one is diffracted in the photonic crystal and the other is resonantly scattered by silver dendrites.

Figure 4 demonstrates SEM image of the hybrid colloidal plasmonic-photonic crystal [6]. This image shows the $Ag/ML/Ag$ hybrid integrated with $Ag/cavity/Ag$ resonator that is formed on top of the monolayer surface.

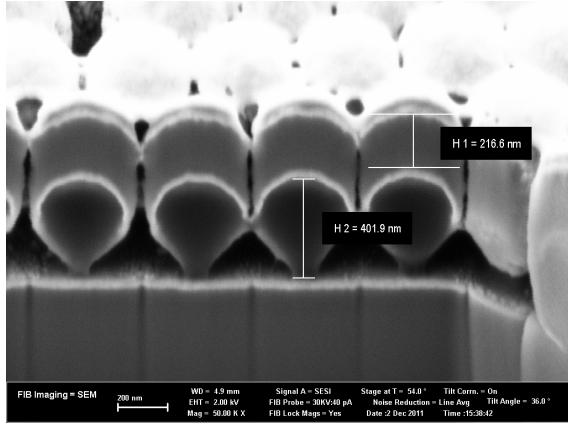


Fig. 4. SEM image of the focused ion beam cut of the $Ag/cavity/Ag/ML/Ag$ hybrid colloidal plasmonic-photonic crystal under study [6].

The bare monolayer of spheres shows several resonances that correspond to the diffraction of guided resonances propagating along the monolayer (Fig. 5a, curve 1). Sandwiching a monolayer between Ag films results in the surprisingly weak transmission reduction, which is counteracted by two extraordinary transmission peaks (EOT) at 596 and 489 nm. These peaks appear due to excitation of surface plasmon polaritons (SPPs) propagating at the interfaces of flat and corrugated silver films with ML and air, respectively (curve 2). The transmission enhancement manifests the enhancement of the optical density of states in surface plasmon polaritons. Peak at 400 nm is due to the intraband transitions of silver. Curve 5 in Fig. 5b illustrates relative changes introduced by metal films represented by the ratio $r_5(\lambda) = T_2(\lambda)/T_1(\lambda)$.

If another resonator $Ag/cavity/Ag$ with resonances at 770 and 385 nm (curve 3, Fig. 5a) is series connected to $Ag/ML/Ag$ one, the transmission is further reduced, but this reduction occurs selectively stronger at the Fabry-Perot resonances of the cavity (curve 4). Remarkably, the transmission peaks of the microcavity are converted in transmission minima of the hybrid architecture. This is clearly illustrated by the ratio $r_6(\lambda) = T_4(\lambda)/(T_2(\lambda) \times T_3(\lambda))$, which demonstrates further enhancement of the EOT peaks and minima for cavity resonances (curve 6 in Fig. 5b). This effect can be tentatively interpreted as the extraordinary absorption (EOA). It occurs due to excitations of SPPs in the corrugated cavity in contrast to SPP absence in a microcavity with flat mirrors. Overall, one and the same architecture is capable of both enhancing and suppressing light transmission. Since both effects relate to guided SPP resonances, one can say that the transmission is enhanced owing to “bright” SPPs, whereas the absorption is enhanced owing to the cavity-related activation of normally “dark” SPPs.

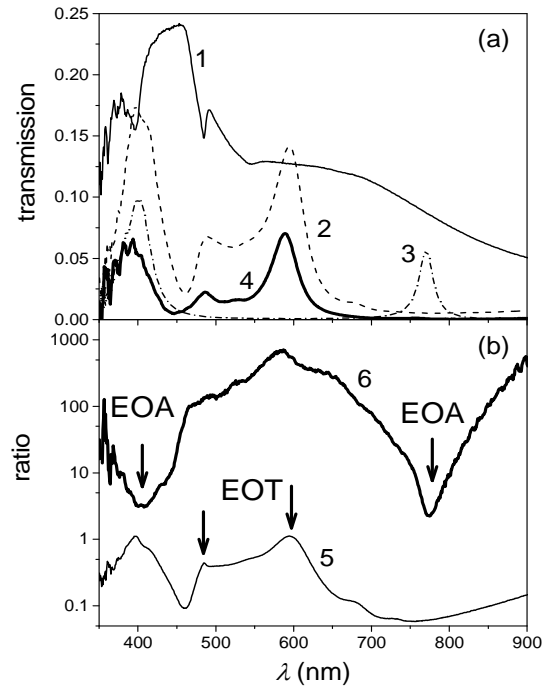


Fig. 5. (a) Transmission spectra of the monolayer ($T_1(\lambda)$, curve 1), plasmonic-photonic crystal $Ag/ML/Ag$ ($T_2(\lambda)$ curve 2), microresonator ($T_3(\lambda)$, curve 3), plasmonic-photonic crystal with microresonator $Ag/cavity/Ag/ML/Ag$, ($T_4(\lambda)$, curve 4) at the normal light incidence $\theta = 0^\circ$. (b) The ratios $r_5(\lambda) = T_2(\lambda)/T_1(\lambda)$ (curve 5), $r_6(\lambda) = T_4(\lambda)/(T_2(\lambda) \times T_3(\lambda))$ (curve 6).

IV. CONCLUSIONS

The light diffraction in $Ag/opal$ photonic crystals is affected by the light scattering at silver species. This interaction leads to Fano-type distortion of the Bragg resonance shape.

Engineering of optical properties of plasmonic-photonic crystals has been achieved via the architecture topology. Hybridization of different resonances results in either the extraordinary transmission or extraordinary absorption of light.

ACKNOWLEDGEMENTS

Authors thank M. I. Samoilovich for providing high-quality bulk opals, U. Peschel and D. Ploss for obtaining SEM images of a hybrid crystal.

This work was supported by the Ministry of Education and Science of Russian Federation under the “Development of Scientific Potential of Higher Educational Institutions” program and by German Academic Exchange Service (DAAD)

REFERENCES

- [1] S. G. Romanov, A. V. Korovin, A. Regensburger, U. Peschel, “Hybrid colloidal plasmonic-photonic crystals”, *Advanced Materials*, vol. 23, pp.2515–2533, 2011.
- [2] V. L. Veisman, S. G. Romanov, V. G. Solovyev, M. V. Yanikov, “Optical properties of nanostructured silver embedded by electro-thermo-diffusion in opal photonic

- crystal”, *Environment. Technology. Resources: Proceedings of the 10th International Scientific and Practical Conference, Rezekne, Latvia*, vol. 1, pp. 230-231, 2015.
- [3] A. I. Vanin, V. G. Solovyev, “Modelling of Fano resonance in nanostructured material”, *Proceedings of VI International Conference on Photonics and Information Optics, Moscow*, pp. 140-141, 2017.
- [4] U. Fano, "Effects of configuration interaction on intensities and phase shifts", *Phys. Rev.*, vol. 124, pp. 1866–1878, 1961.
- [5] A. E. Miroschnichenko, S. Flach, Yu. S. Kivshar, "Fano resonances in nanoscale structures", *Reviews of Modern Physics*, vol. 82, pp. 2257–2298, 2010.
- [6] S. G. Romanov, V. G. Solovyev, D. Ploss, U. Peschel, “Non-invasive management of photonic crystal resonances”, *Abstracts of the 4th International Topical Meeting on Nanophotonics and Metamaterials, Seefeld, Austria*, p. 26, 2013.
- [7] V. G. Balakirev, V. N. Bogomolov, V. V. Zhuravlev, Y. A. Kumzerov, V. P. Petranovskii, S. G. Romanov, L. A. Samoilovich, "Three-dimensional superlattices in opals", *Crystallography Reports*, vol. 38, pp. 348–353, 1993.
- [8] O. L. J. Pursiainen, J. J. Baumberg, H. Winkler, B. Viel, P. Spahn, T. Ruhl, “Nanoparticle-tuned structural color from polymer opals”, *Optics Express*, vol. 15, pp.9553-9561, 2007.
- [9] P. D. Garcí’a, R. Sapienza, C. Lo’pez, “Photonic glasses: A step beyond white paint”, *Advanced Materials*, vol. 22, pp. 12-19, 2010.
- [10] Y. Takeoka, “Angle-independent structural coloured amorphous arrays”, *Journal of Materials Chemistry*, vol. 22, pp. 23299-23309, 2012.

Anthropometric parametrization of Uniforms for Armed Forces

Inga Dāboliņa, Ausma Viļumsone and Eva Lapkovska

*Rīga Technical University, FMSAC, Institute of Design Technologies,
Kīpsalas street 6-220, Rīga, LV-1048, Latvia; E-mail: inga.dabolina@rtu.lv*

Abstract. Planning manufacture of uniforms decisions must be taken as to how many and in what size a particular model series should be manufactured, how they should be labeled and to what body-dimensions garment sizes should correspond. The purpose of anthropometric parametrization is to introduce garment size classification for mass production clothing, so as to representatively depict wearers' body figure diversity. It is in the interests of manufacturers (design time and costs, logistics etc.) and buyers/procurement service alike to confine themselves with a minimum garment sizes and to use a possibly less complicated garment size classification. The aim of this research is to gather different impact factors for anthropometric parametrization for Uniforms of Armed Forces.

Research is formed from anthropometric data and end user survey exploring data set of 150 soldiers. Anthropometrics are performed by non-contact anthropometric methods (3D anthropometrical scanner Vitus Smart XXL® is used in the study), data processing automation systems, pattern making CAD/CAM systems, etc. National Armed Forces (NAF) technical specification provides for manufacture of a wide range of garment sizes (by height indifference interval of 6 cm). Manufacturers labeling system and charts of finished products are subjected to comparative analysis and evaluation of corresponding standard recommendations is included.

The study indicates the need to optimize the currently used anthropometry method in the Latvian Army, anthropometric data registration and application, thus improving the performance of military personnel and the procurement process and the use of resources, thus promoting resource planning and environmental protection. Also improvements are needed in uniform labeling and instructing of the military personnel on selection of uniform and equipment components.

Proper anthropometric parametrization and labeling of Uniforms for Armed Forces would minimize expenses of Uniforms as well as the negative waste impact to the environment.

Keywords: anthropometry, clothing industry, design automation/CADCAM, mass customization.

I. INTRODUCTION

The most important problems with designing and producing uniforms for National Armed Forces (NAF) is the lack of proper anthropometric data of wearers – soldiers. Generally procedure of ordering and supplying uniforms are based on normal distribution (Gaussian function) with standard deviation +/- 10%. EN 13402 [1] is a European standard for labelling clothes sizes. It is based on body dimensions, measured in centimeters. It replaces many older national dress-size systems in popular use before the year 2007. Cabinet of Ministers of the Republic of Latvia Regulation No.519 [2], paragraph 25 reads that uniforms are issued corresponding to garment sizes based on anthropometric measurements, which are taken upon person joining the service, and later every two years, while paragraph 28 stipulates that tailoring of field uniforms shall be organized on an individual basis, if soldier anthropometric measurements do not correspond to the standard size. However, neither the Latvian Republic Ministry of Defense nor other uniformed services regulatory technical documents

contain any definite references to the requirements of these “standards” and availability, procedure of obtaining anthropometric data standardization [3].

The right clothing and equipment is vital importance to the survival and effectiveness of military personnel [4]. One of initial aspects is appearance and fit of uniforms [5] and now the information necessary to ensure it can be obtained and processed using non-contact technologies.

This anthropometric research [6] was carried out by using data of the NAF units. According to the National Defense Concept, the number of NAF personnel in professional service does not exceed 5,800, which was respectively equated with the general group in the anthropometric research. The sample set consisted of at least 3350 measurements. Research results confirmed the conformity of the NAF personnel anthropometric data to the normal distribution.

End users claims about uniforms – fitting of field uniforms are partly weak, defects such as seam-stitching splits and fabric splits are often found in the area of the crotch during the use of soldiers' trouser.

Therefore, the aim of the research in purpose to do anthropometric parametrization for Uniforms of Armed Forces is to identify potential reasons for defects by analyzing the fitting of the products as well as the design and the wearing habits of trousers.

II. MATERIALS AND METHODS

A. Anthropometrics – 3D Scanning

In the research, measurements have been gathered by Vitus Smart XXL human body 3D scanner, which conforms to the ISO 20685 standard. This equipment is designed to capture the surface of the human body in a twelve seconds. The scanning volume is 210 cm in height by 100 cm by 110 cm in depth and width. Resolution in X, Y, and Z is 27 points in cm in the middle of the scanning base for human subjects. 3D Human Body Scanner uses optical triangulation as the basis for measurement extraction. For this purpose, combination of camera and laser (laser sensor) is used. The lasers are switched on (pulsed) when the measurement begins. During the measurement, the slides travel vertically at a defined speed.

Standard anthropometry (traditional contact methods) dimensions are measured from one point on the body (or fixed surface such as the floor) to another. In the case of circumferences, the dimension is measured around a part of the body at a specified level. These measurements are taken with specific instruments: anthropometer, measurement tape, caliper.

Principal component analysis was used to create a plan for anthropometric data gaining for end-user group. The results of this study showed that there are differences in fit to the test person of these prototypes (all selected in size M), also clarified scenario to measurement activities to be gathered from end-user group.

3D human body scanning and measuring activities of end-user group has been held.

The prerequisite for reliable body measurements is the correct position and posture of the subject during the scanning process. Instructions about the correct posture, both verbally and by means of an illustrated poster and presentation was given. Also anthropometrist checked out the position before scanning starts. The correct scanning posture was defined as follows: The end users stands on the scanner platform with his or her feet on “footprints” painted on the platform. The soldier forms fists, slightly bends the arms at the elbows, and positions the hands slight away from the hips. The subject looks straight ahead with the head held in a position to the Frankfurt plane. The soldier breathes normally and stands relaxed without flexing his or her muscles.

All end users were asked to wear tight-fitting underwear. Tight cap was used to produce smooth head shape if needed (hair-dress conditions).

B. Measurements used

Main measurements to analyse human body are three circumferences (bust, waist and hip circumference) and three lengths/heights (body height, waist height and crotch height).

Bust/chest girth - The circumference of the chest is measured across the bust point landmarks. The circumference is measured parallel to the standing surface (scanner code 4515). Waist girth - The circumference of the waist is measured in the height of the natural waist (if feasible). The natural waist height is determined by extracting a contraction point on the side. The circumference is measured parallel to the standing surface (scanner code 6510). Hip girth - The circumference of the Hip is measured slightly underneath the buttock girth at a maximal girth location. The circumference is measured parallel to the standing surface (scanner code 7525). Body height - Vertical height from standing surface to the visual top of the head. The vertical distance is measured between the standing surface and the top of the head. Waist height - Vertical height of the waist girth (scanner code 6510) measurement to the standing surface. Crotch height - Vertical height of the crotch point to the standing surface (scanner code 0100).

C. Experimental procedure

The average statistical data of NAF soldiers in accordance with the general sample measurements are as follows: height – 179 cm (measurements of 3360 soldiers), chest circumference – 106 cm (measurements of 3351 soldiers), waist circumference – 94 cm (measurements of 3351 soldiers) [6]. One of the reasons for defects of clothes may be the unsuitability of clothing sizes with the dimensions of the human body. In the case of individual orders a correct measurement of the body is sufficient, but in mass production - careful planning of the type and number of sizes of a batch to be produced by taking into consideration anthropometric features of a consumer group is necessary.

In the framework of the process of 3D scanning of soldiers 150 uniform wearers were asked to indicate sizes of worn products (trousers and jackets of a field uniform). In the reports 87% (131) of respondents were able to indicate trouser sizes, however, types of labelling of sizes differ - 87% (114) indicate one-size letter designations (XS-3XL). Moreover, 11% (12) of them had doubts and indicated two labels (e.g. L/M), 6% (8) indicated two-dimensional numeric labelling (e.g. 92/182), and only 7% (9) two-dimensional letter designation, which had been implemented by the manufacturer and used in supply (e.g., L/REG). By taking into consideration that some of the respondents were unable to indicate trouser size (13% (19)) and different types of labels, it was apparent that in the supply of this research group there was no common approach to labelling of clothing sizes to be worn or

wearers themselves were confused over the types of labelling of trousers that may encourage receiving unsuitably-sized trousers.

In order to examine how appropriate the indicated sizes were with the body measures of each person (in total, 123 had a letter indicated), trouser sizes have been reviewed according to the measurement chart of the manufacturer on the basis of waist circumferences of wearers obtained in 3D scanning (primary key dimension). When these were compared it was apparent that 51% of trouser sizes (63) comply, according to primary key dimension - waist circumference. 31% (38) indicated a smaller size, but 18% (22) larger. As an overall result 49% (60) of the clothing worn by the 123 participants found that size is non-compliant with measurements of waist circumference (see Fig.1).

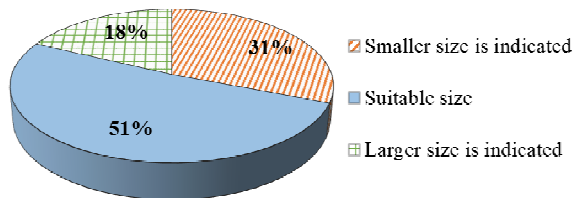


Fig. 1. Sizes of trousers - comparison of those indicated in the record and measurements in the charts of the manufacturer.

In the figure below (Fig.2.) differences are clearly demonstrated between the frequency of sizes (key dimension - waist circumference) developed according to reported and already reviewed measurements; moreover, more distinctive differences are observed exactly in the broadly represented size groups M, L and XL.

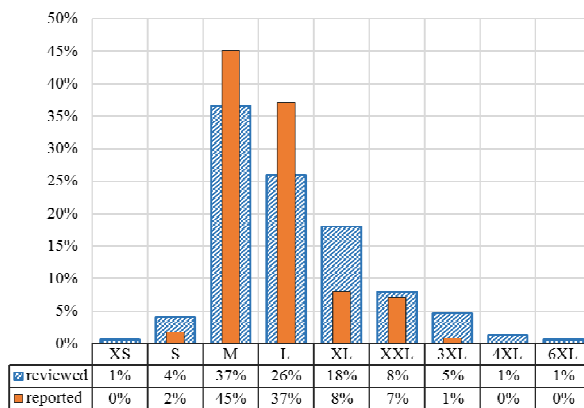


Fig. 2. Sizes of trousers - waist circumference frequency analysis.

When such unsuitability of trouser sizes with actual body measures exists, then a waist circumference is taken as a key dimension; it may be predicted in the framework of a specific research group as a reason for different defects during use.

Chest circumference, waist circumference, and body height are indicated in the measurement charts of the manufacturer's finished products as being the key dimensions for matching trouser size group and

drawing up of a label for nether garments. If the application of a waist circumference is clearly justified in the design of trousers then there is no clear justification for chest circumferences to be included in a chart for drawing up of trouser sizes, as this body measurement is not used and does not affect the calculations of trouser design. The lengths of the inseam and side seam are classified by choosing body height as a key dimension (secondary).

As a result, finished trouser products are labelled by taking a waist circumference as the primary key dimension by classifying them into 7 sizes (XS-3XL), but as a secondary - body height, by classifying leg lengths (for inseam and side seam) into 7 lengths (2XSH-2XLO). In general, it provides 49 combined types of sizes (7 x 7 = 49).

This means that the inseam and side seam length will be determined by referring a test person to some body height interval. During anthropometric researches it has been established that persons referring to one body height interval may have different leg lengths i.e. proportion of legs in relation to a body height by classifying into, e.g. types of extra short legs, short legs, normal legs, long legs and extra-long legs.

III. RESULTS AND DISCUSSION

A. Measurements

When matching trousers/leg length intervals of the charts of the manufacturers determined by body height and leg length measurements (see chart), it is apparent that by individually examining existing leg lengths in some body height group not all wearers refer to these set intervals. However, averages are close to those set by the manufacturers.

In the framework of specific research group classification has been made according to body measurements and manufacturer charts by determining suitable labels for leg lengths (the other side of a two dimensional label). First, a label according to a body height has been found and afterwards according to measurement of inside leg length. (See example in Table I.)

Table I.
 Measurement of inside leg length

Trouser size - recorded	Body height	Range to which refers according to body height	Inside leg length - body measurement	Range to which refers according to inside leg length
XXL/REG	181.0	REG (179-185)	79.6	SHO (80)

When comparing, it has been established that in 72% (108) of the cases labels will not comply, i.e. a label will be affected by whether body height or inside leg length was taken as a key dimension of trouser length. Differences in leg proportions are also apparent when comparing frontal views of body images of people included in one body height interval (see Fig.3).

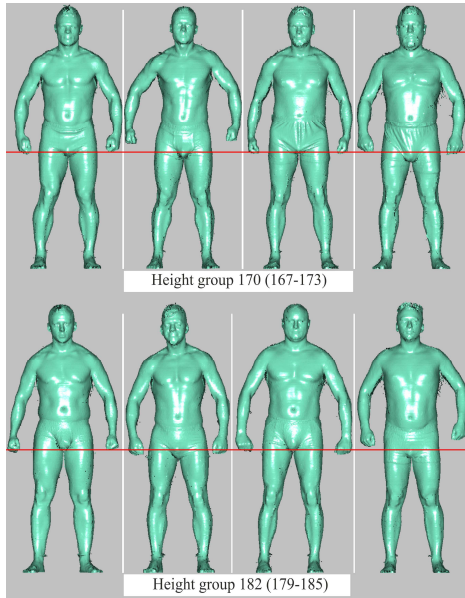


Fig. 3. Differences in leg proportions

It should be noted that according to instructions of the standard EN 13402-2:2002 (Size Designation of Clothes - Part 2: Primary and Secondary Dimensions] as key dimensions for men’s trousers and shorts, a waist circumference (as a primary key dimension) and body height and/or inside leg length (as secondary key dimensions) should be used.

B. Tests on teared trousers

As one of the methods to gain proper result of analysis is to research existent product. Field Uniforms trousers from real field usage are analysed (seven samples).

When starting the experiment data on trouser sizes worn by the test persons was collected according to the manufacturer’s chart (see Table II).

Table II.
Data on Sizes of Trousers Worn by Test Persons

No.	No. in general list	Sex	Age	Trousers size (indicated)	Size			Product control measurements			
					Size group	Chest circumference	Waist circumference	Waist (1/2)	Crotch seam (1/2)	Side seam	Inseam
18	143	M	28	XXL/REG	XXL	116-120	104-108	53.5	42.5	112	82
19	144	M	27	XXL/REG	XXL	116-120	104-108	53.5	42.5	112	82
20	145	M	29	L/REG	L	100-104	88-92	45.5	38.5	110	82
21	146	M	25	L/REG	L	100-104	88-92	45.5	38.5	110	82
22	147	M	23	L/XSH	L	100-104	88-92	45.5	38.5	110	80
23	148	M	23	L/REG	L	100-104	88-92	45.5	38.5	110	82
24	149	M	22	XL/REG	XL	108-112	96-100	49.5	40.5	111	82

In almost all labels (except No.22), test persons trouser lengths (in the charts see - inseam) are indicated as REG, i.e. Regular length of a value of 82 cm, according to the charts. One of the hypothesis which has been put forward for the reason for defects is a choice of unsuitable inseam length. Firstly, on the basis of inside leg length suggested in standards as a necessity of separately selected secondary body measure for accurate determination of trouser size. Secondly, in the chart by summarising waist circumference, body height measurements and inside

leg length measurements of test persons it has been apparent that there is a deviation of measurements of a wearer from the measurement chart made by the manufacturer and subsequent non-compliance with the chosen size.

In the summarised table (see Table III) size designations that have already been reviewed, as well as comments on established non-compliance are included.

Table III.
Summarised analysis data

No.	Body height	Trousers size (indicated)		Inseam according to the measurement chart	Inside leg length - measurement	Deviation	Waist circumference (according to label)	Waist circumference - measurement	Trousers size (reviewed)	
		XXL	REG						3XL	SHO
18	181.0	XXL	REG	82	79.6	-2.4	104-108	117	3XL	SHO
Actual waist circumference does not comply with range of selected size XXL (104-108 cm) but it should be included in the next size, 3XL, instead. If, according to a body height range (179-185) an inseam refers to REG range, then according to actual inside leg length a wearer should be referred to the size SHO instead (by rounding up 80 not 82 as REG). When changing a size, a wearer will obtain a nether garment with larger waist circumference and shorter inseam.										

No.	Body height	Trousers size (indicated)		Inseam according to the measurement chart	Inside leg length - measurement	Deviation	Waist circumference (according to label)	Waist circumference - measurement	Trousers size (reviewed)	
19	188.4	XXL	REG	82	88.2	+6.2	104-108	104.2	XXL	XLO
	Waist circumference complies with charts of the manufacturer and size XXL. According to the body height range (185-191), the inseam refers to LON range but even more according to actual inside leg length a wearer should be rather referred to the size XLO instead (by rounding up 88, not 82 as REG). When changing a size a wearer will obtain a nether garment with a longer inseam.									
20	180.0	L	REG	82	84.5	+2.5	88-92	84.5	L	LON
	Waist circumference complies with charts of the manufacturer and size L. If, according to the body height range (179-185), an inseam refers to REG range then, according to actual inside leg length, a wearer should be referred to the size LON instead (by rounding up 85 not 82 as REG). When changing a size a wearer will obtain a nether garment with a longer inseam.									
21	184.3	L	REG	82	82.4	+0.4	88-92	84.3	L	REG
	Waist circumference complies with charts of the manufacturer and size L. REG size is correctly chosen for a wearer according to both the body height range (179-185) and actual inside leg length.									
22	166.6	L	XSH	80	71.7	-8.3	88-92	88.4	L	3XSH
	Waist circumference complies with charts of the manufacturer and size L. According to the body height range (161-167), an inseam refers to 2XSH range but even more according to actual inside leg length a wearer should be referred to the size 3XSH instead (by rounding up 72 not 78 as XSH). When changing a size a wearer will obtain a nether garment with a shorter inseam.									
23	175.6	L	REG	82	76.3	-5.7	88-92	86.3	L	XSH
	Waist circumference according to charts of the manufacturer and size L. According to the body height range (173-179), an inseam refers to SHO range but even more according to actual inside leg length a wearer should be referred to the size 2XSH instead (by rounding up 76 not 82 as REG). When changing a size a wearer will obtain a nether garment with a shorter inseam.									
24	181.9	XL	REG	82	77.2	-4.8	96-100	99.3	XL	XSH
	Waist circumference complies with charts of the manufacturer and size XL. If, according to a body height range (179-185), an inseam refers to REG range then, according to actual inside leg length, a wearer should be referred to the size XSH instead (by rounding up 77 not 82 as REG). When changing a size a wearer will obtain a nether garment with a shorter inseam.									

In summarising existing and reviewed trouser sizes, it is apparent that in only one of seven cases there is compliance of product size with data on body measurements (No.21). In three cases it is apparent that by using only a body height as a secondary key dimension, a correct length is not always matched as an inside leg length. Values should be taken into consideration that may vary among persons within one body height range.

In addition, to clearly establish such non-compliance frontal views of body images (Fig.4) of test persons in scale are organised according to size groups of relevant clothes worn by indicating different heights of a seat seam. i.e. levels of inside leg lengths (classification according to the charts of the manufacturer).

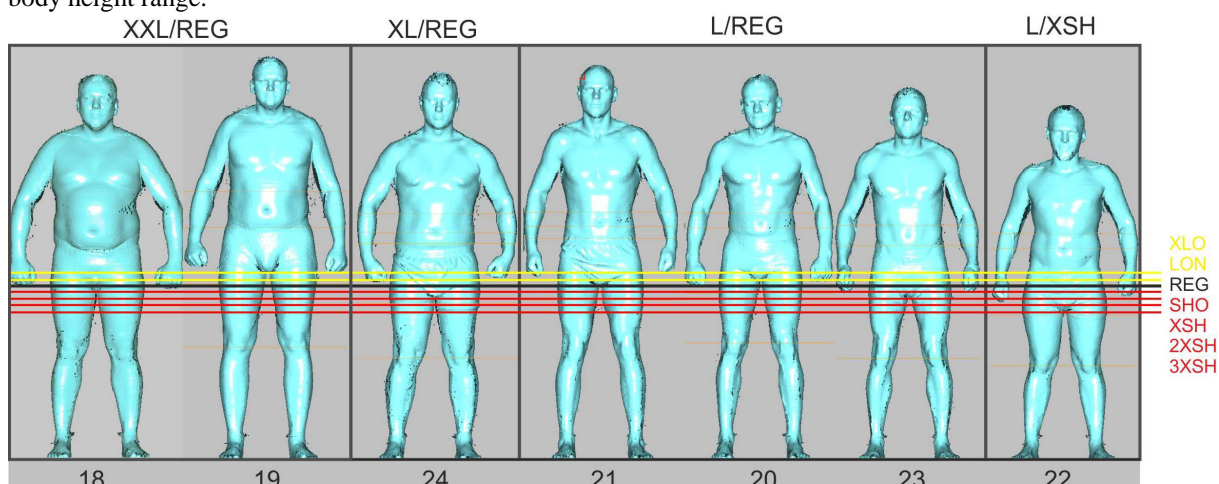


Fig. 4. Frontal views of body images in scale – indicating different levels of inside leg length

As a reference level, inside leg length REG (black line) has been chosen, which refers to test person No. 21, according to all body measurements. It is clear that the remaining persons who also wear trousers of length REG do not refer to this level and

distinguishing differences are seen in relation to test person No. 22, who wears trousers of length XSH. Therefore, according to both body measurements, and visually, it should be established that in one size range

wearers may have different measurements of inside leg lengths.

All this analysis leads to lack of obvious system for choosing uniforms. For clarity, labelling of clothes in accordance with EN 13402-3:2014 [Size Designation of Clothes. Part 3: Body measurements and intervals], interval pictograms supplemented by letter designations may be used (see example Fig.5) [1]. For example, when trying on clothes it would enable products suitable to body measurements to be accurately chosen, provided that the wearer knows their sizes - both the more suitable label and separate body measures.

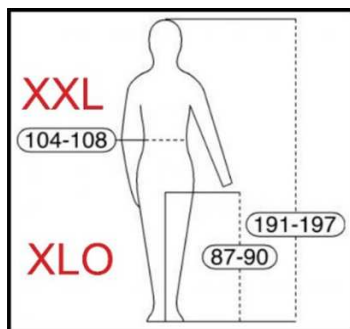


Fig. 5. A label pictogram relevant to test person No.19

Article 25 of the Regulation of the Cabinet of Ministers of the Republic of Latvia No. 519 (09.16.2003) "On Support Conditions, Norms and Procedures by which Soldiers shall be provided with Financial, Material and Technical Resources", it was defined (not effective) as "uniforms are provided according to "sizes" (or body sizes) on the basis of anthropometric measurements. Anthropometric measurements are taken during enlistment, as well as every two years thereafter." However, Article 28 states that: "If anthropometric sizes of soldiers are non-standard... sewing of field uniforms is organised individually" [2]. However, certain instructions in relation to requirements and availability of these standards are not in the normative technical documents of either the Ministry of Defence of the Republic of Latvia or of other uniformed agencies of the Republic of Latvia. Orders of clothes of soldiers are implemented according to developed normal distribution and choice of wear is made by trying on existing delivered products in warehouses.

IV. CONCLUSION

Sufficient difference shows the necessity to review classification of general sizes, however, it should be taken into consideration that collection and research of body measures of a wider target audience is required as 150 persons measured in the research is an insufficient data set which is unable to clearly demonstrate statistically, anthropometric features of the target population (army and Civil Guard).

In order to credibly demonstrate data of any population a complete overview of the population should be made at the best or a selection should be at least 10% of all the population subject to review (approximate values, e.g.: ~5000 army + ~8000 Civil Guard = 13000, 10%=1300 people).

For a general analysis of the population data on body measurements is required before implementing the order in order to duly classify wearers and avoid non-compliance. Moreover, by taking into consideration suggestions that the inside leg length measurement is important for determining a size that is established in the experiment, developed charts may be reviewed by taking the waist circumference as a primary key dimension, but inside leg length and body height (or only inside leg length) - as a secondary, and by classifying lengths of intervals.

It is obvious that by implementing inside leg length as a general secondary measurement the number of sizes, i.e. types of specific test person groups has increased (from 4 to 7) that in the case of larger group of people this may affect planning of orders.

As mentioned above, it would be required to develop a database of body measurement values of a target audience in order to make an analysis of and duly plan division of orders. To date, when soldiers enlist, the only information on their body measurements is obtained from the soldiers themselves by asking them about their body height and chest circumference.

ACKNOWLEDGMENTS

This research work was partially financed by the European Union European Regional Development Fund, through the INTERREG BSR Programme, which awarded a grant to the SWW project (#R006). The authors gratefully acknowledge the received financial support.

REFERENCES

- [1] EN 13402-2:2014 Size designation of clothes – Part 3: Body measurement and intervals.
- [2] Ministru kabineta noteikumi Nr.519, Rīgā 2003.09.16. (prot. Nr.49, 9.§), Noteikumi par apgādes nosacījumiem, normām un kārtību, kādā karavīri nodrošināmi ar finanšu un materiāltehniskajiem līdzekļiem., 2003 / CM Regulation No.519, Rīga 2003.09.16 (Prot.No.49,§9), Regulations on requirements for supply conditions, rules and procedures for providing soldiers with financial and logistics resources.
- [3] LVS EN ISO 20685 Latvijas Standarts 3D skenēšanas metodoloģijas starptautiski saderīgām antropometrisko datu bāzēm/ 3D scanning methodologies for internationally compatible anthropometric databases. - Brisele : CEN - European Committee for Standardization. - ISO 20685:2005.
- [4] E Sparks *Advances in Military Textiles and Personal Equipment* ISBN: 9781845696993, Woodhead Publishing, 2012.
- [5] J.C.Tsan-Ming *Information Systems for the Fashion and Apparel Industry* ISBN: 978-0-08-100571-2, Elsevier, 2016
- [6] Šitvjenkins, Igors. *Enhancement of the Combat Individual Protection System*. PhD Thesis. Rīga: [RTU], 2014. 265 p.

Case Study of Structural Reliability of Existing Building

Pēteris Druķis*, Līga Gaile, Vadims Goremikins

Kaļķu Street 1, Riga, Latvia. Riga Technical University, Institute of Structural Engineering and Reconstruction.

*Corresponding author: peteris.drukis@gmail.com, +371 29233300.

Abstract. Structural reliability of buildings has become an important issue after the collapse of a shopping centre in Riga 21.11.2013, caused the death of 54 people. The reliability of a building is the practice of designing, constructing, operating, maintaining and removing buildings in ways that ensure maintained health, ward suffered injuries or death due to use of the building. Evaluation and improvement of existing buildings is becoming more and more important.

For a large part of existing buildings, the design life has been reached or will be reached in the near future. The structures of these buildings need to be reassessed in order to find out whether the safety requirements are met. The safety requirements provided by the Eurocodes are a starting point for the assessment of safety. However, it would be uneconomical to require all existing buildings and structures to comply fully with these new codes and corresponding safety levels, therefore the assessment of existing buildings differs with each design situation. This case study describes the simple and practical procedure of determination of minimal reliability index β of existing steel structures designed by different codes than Eurocodes and allows to reassess the actual safety level of different structural elements of existing buildings under design load.

Keywords: Structural reliability, existing buildings, assessment of safety, steel structures, partial factors, reliability index.

I. INTRODUCTION

Existing buildings in operation, if properly operated, are considered to be safe for people, even if these buildings are more than 100-year-old, or the so called heritage buildings [1]. However, due to technological progress, as well as changes in laws and regulations related to the integration in the European Union, the roles for both employees and maintenance staff regarding the use of buildings are becoming more and more strict. Existing buildings are designed according to the safety requirements of the decade they were built. However, the requirements of the respective safety level today are generally higher. New requirements have been introduced, the provision of which requires proper attention and resources from the building owner [2], and nowadays building safety requires special attention [3].

A lot of buildings depending on their time of construction in Latvia have different safety levels. Taking into consideration that users of the building expect the same level of safety, situations leading to severe accidents can occur. In Latvia there are buildings in operation, most of which were built more than 20 years ago in accordance with the Soviet building norms (SNiP) [4]. Furthermore, there are also buildings which were built before 2010 in accordance with national building norms (LBN) [5] whilst there are also buildings built during the last years already in accordance with the European

Union's construction standards or Eurocodes (EC) [6].

Furthermore, the operational duration of the building is longer than life-time of any other system and equipment in the building, which means that the building solutions, their operation and safety lag behind up-to-date technologies. If the condition of existing buildings will not be improved in accordance with contemporary requirements and safety level, the number of accidents occurring may rise.

Taking into consideration the above-mentioned circumstances, in the Construction Law [7], Article 21, Clause 4 the Parliament of Latvia has laid down the obligation of the owner of the building to provide proper maintenance of the building and its components during the operation thereof in the condition compliant with the essential requirements defined in the Construction Law, Article 9, Clause 4. These essential requirements are identical to the basic requirements defined by the European Parliament and EU Council Regulation Nr.305/2011 [8]:

- mechanical resistance and stability;
- safety in case of fire;
- hygiene, health and the environment;
- safety and accessibility in use;
- protection against noise;
- energy economy and heat retention;
- sustainable use of natural resources.

In order to meet the above-stated requirements, the responsibility of the building owner is to make sure that:

- the building is safe for its users and building maintenance staff;
- the building is being properly maintained;
- essential risk factors are evaluated during the use of the building;
- relevant improvement measures are carried out in accordance with the results of technical surveys.

Therefore, it is extremely important for the owner of the building to get proper answers from engineers and technical auditors about the condition of existing structures [9-14]. Before the decision of refurbishment or disposal of a building not only economical or technical aspects are to be considered. An important factor due to the climate changes is sustainability [15]. That's why there are a lot of methods worldwide used for the grading of buildings based of sustainability criteria [16]. Also, improvement of energy efficiency of buildings gives a challenge to improve the condition of existing structures [17].

This paper is in the scope of the first essential requirement for buildings - mechanical resistance and stability. There are a lot of publications worldwide about the proper manner for retrofitting existing structures [18-23]. All those publications give researches of different studies of existing structures and they have one particular issue in common – the question of what is the right safety level of existing structures or the important question of “how safe is safe enough”? [24]

Reliability index β is associated with the probability of failure in many publications. For example, in publications [25-27], it is shown as one of the main quantifiers of the reliability and it is also the main approach to reliability concepts in the structural codes of last decades.

An important reason to assess existing structures is the existence of a doubt concerning the actual reliability of a structure and its elements. In the case of retrofitting or repairing the structure, the set of the partial safety factors (a function of the reliability index β) per current design codes should be established.

This study proposes a simple procedure to derive the reliability index β in line with Eurocode of the existing structure that originally was designed by earlier structural design codes. This makes it possible to comparable the reliability levels of existing structures to the target values of the current design practice.

The developed procedure is applied to the case study and the reliability index β is derived for differently stressed elements of existing building roof truss.

II. MATERIALS AND METHODS

A. Structural reliability in Eurocodes

Generally, it is known that the target reliability levels are calibrated to the existing practice that is proven to be satisfactory and partly introduced through the structural design codes. The most common method is the partial factor design method where partial safety factors are a function of the reliability level [28]. Eurocode uses two safety factors performing the standard design procedures. These are safety factors for the material property γ_m and safety factor for loads γ_f . A simple method to obtain the relevant partial factor γ_f is to divide the design value of a variable action Q_d by its representative or characteristic value Q_k . Similarly, could be obtained material partial factor γ_m . The normal distribution is normally used for characteristic and design values of material properties [29] and for permanent loads G , but for snow loads Gumbel redistribution is used [29] (see Table 1).

Table 1.

Value	Redistribution	Equation
R_k	Normal	$\mu_R \cdot \exp(-1,645V_R)$
R_d	Normal	$\mu_R \cdot \exp(-\alpha_R \beta_d V_R)$
G_k	Normal	μ_G
G_d	Normal	$\mu_G (1 + 0,7 \beta_d V_G)$
Q_k	Gumbel	$\mu_Q (1 - V_Q (0,45 + 0,78 \ln(-\ln(0,98))))$
Q_d	Gumbel	$\mu_Q (1 - V_Q (0,45 + 0,78 \cdot \ln(-\ln(\Phi^{-1}(\alpha_E \beta))))$
$\gamma_R =$		$\frac{\exp(-1,645V_R)}{\exp(-\alpha_R \beta_d V_R)}$ (1)
$\gamma_G =$		$(1 + 0,7 \beta_d V_G)$ (2)
$\gamma_Q =$		$\frac{1 - V_Q (0,45 + 0,78 \cdot \ln(-\ln(\Phi^{-1}(\alpha_E \beta))))}{1 - V_Q (0,45 + 0,78 \ln(-\ln(0,98)))}$ (3)

In these expressions μ , σ and V are, respectively, the mean value, the standard deviation and the coefficient of variation of a given variable, α is FORM (First Order Reliability Method) sensitivity factor and β is reliability index, Φ^{-1} is failure probability function; γ is relevant partial factor.

B. Determination of reliability index

The newly developed simple procedure of determination of reliability index β for existing structures is presented via case study. For the case study a steel roof truss and one supporting beam of an existing building in Liepaja, Latvia is chosen. The span of the truss is 32m, but the span of the simply supported beam is 10,8m. The configuration of the truss is presented in the Figure 1.

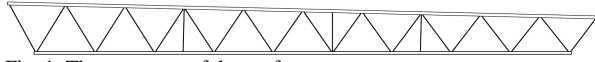


Fig. 1. The geometry of the roof truss.

The roof truss is loaded by the permanent load and snow load uniformly distributed over the truss length. Wind load influence has not been considered as it produces negligible internal forces in truss elements. The simply supported beam supports the truss and is loaded in three-point bending. All cross sections of truss elements are square hollow sections, but the beam is made of one I section. The three most loaded elements of the truss under different loading conditions are selected for the analysis: the element of the top chord under compression and bending, truss compression diagonal and bottom chord under tension.

Before starting to determine the reliability index β it is recommended to calculate the utilization factor U (design effect / characteristic effect) of each element according to the design codes that were valid during building construction time (SNiP system [30]).

When calculating according to the SNiP structural design code three safety partial factors should be used in this case. These are - the safety factor for material properties γ_m equal to 1,025, safety factor γ_c that takes into account exploitation conditions and is equal to 1 for elements in compression, compression and bending, and bending only. For the tension elements, it is equal to 0,95. The third safety factor for loads γ_f equal to 1,6 for snow loads (on light roofs) and 1,3 for permanent loads excluding steel self-weight when it is 1,05.

Applied loads on trusses for the case study are presented in Table 2.

Table 2.

Applied load	According to SNiP in Liepaja, kN/m	According to SNiP in Riga, kN/m	According to Eurocode NA in Liepaja and Riga, kN/m
G_k	2,4	2,4	2,4
G_d	2,8	2,8	N/A
Q_k	2,7	3,8	5,4
Q_d	4,3	6,1	N/A

G and Q is permanent and variable (snow) load and subscripts denote whether it is characteristic or design load.
N/A – not applied (calculated later from reliability index β)

For the given example, the maximum design force in the tension chord (loading is applied according to (SNiP for Liepaja) is 401.9kN and calculated design resistance of SHS 140x140x4 ($R_y=335\text{MPa}$) (according to SNiP) is 679kN makes utilization factor $U=59\%$. This utilization factor is just information needed to assess stress level in the member. Correspondingly it is possible for the element under consideration to determine reliability index β by using the equations given in Table 1 when the

utilization factor U is near 100%. This implies calculating the design loads and resistances according to general Eurocode design procedures. For the same element SHS 140x140x4 ($f_y=345\text{MPa}$) according to Eurocode design load is 633,2kN and design resistance is 637,99. Therefore the utilization factor is 99,2%. This is reached when partial factors corresponding to $\beta=4,3$ is used. Two partial safety factors are used performing reliability design – the safety factor for material resistance γ_R and load partial safety factor γ_m .

The first step is to determine the required cross section according to the SNiP when the utilization factor U is also about 100%. Then for the tension element in consideration, the cross section of the element should be reduced to SHS 90x90x4.

Now in the next step it is possible to obtain the reliability index β using the same Eurocode procedure as before. Eurocode characteristic loads should be applied iteratively and β could be found when the utilization factor U is about 100%. For the previously discussed element β is found to be 2,5, which corresponds to probability of failure equal to 0.621%.

The predetermined reliability indexes β could be compared with target reliability indexes depending on consequence classes according to EN1990 ($\beta=3.8$ for building under consideration). In the case of the tension member of roof truss in Liepaja, the safety level difference is 34% which could be regarded as considerable. The corresponding probability of failure will increase from 0.0072 % to 0.62%, respectively.

The summary of the proposed procedure of the determination of minimal reliability index β for structures that are designed in accordance to different structural codes than Eurocodes is presented in Figure 2.

In this case-study, the following coefficients of variation were used: for snow load $V_Q=0,6$; for permanent load $V_G=0,1$ and for material properties $V_R=0,08$. The sensitivity factors chosen according to ISO 2394 [31] and equal to $\alpha_Q=0,7$ for snow load, $\alpha_G=0,7$ for permanent load and $\alpha_R=0,8$ for material properties.

III. RESULTS AND DISCUSSION

A. Minimal reliability index of existing structure designed by different codes than Eurocodes

Table 3 to 6 presents results of the case study obtained by the simple and practical procedure developed as the result of the current research. Results are presented per element phenomena.

The calculated actual reliability index β for the analyzed elements of the case-study under Eurocode design loads and design resistances varies from 4,3 to 3,3. The reliability index β target value according to Eurocode for a 50-year design life and 50-year reference period of variable loads for buildings with reliability class RC2 is 3,8.

The calculated theoretical reliability index β for the analyzed elements with a utilization factor $U=100\%$ according to SNiP design loads and design resistances in city Liepaja varies from 2,5 to 2,8, but in Riga from 3,2 to 3,5.

B. Discussion

Although in general the load bearing capacity of analysed elements is higher when using the Eurocode design system due to the utilizing the plastic geometrical properties of cross sections, the reliability index β for elements is considerably lower when using the SNiP design code system. Mostly it is because the design loads in the Eurocode system are

noticeably higher. Moreover, it has been discovered that the safety level varies among the region of the country considered since the climatic snow load maps are not the same for the SNiP and Eurocode systems.

The target reliability index β given in EN 1990 [28] is provided for new buildings. For the existing structure, target reliability levels can be modified in respect to the current code values assumed for new structures [32]. These modifications are still under discussion in the industry and the next researches will examine the context of geographical location and national traditions.

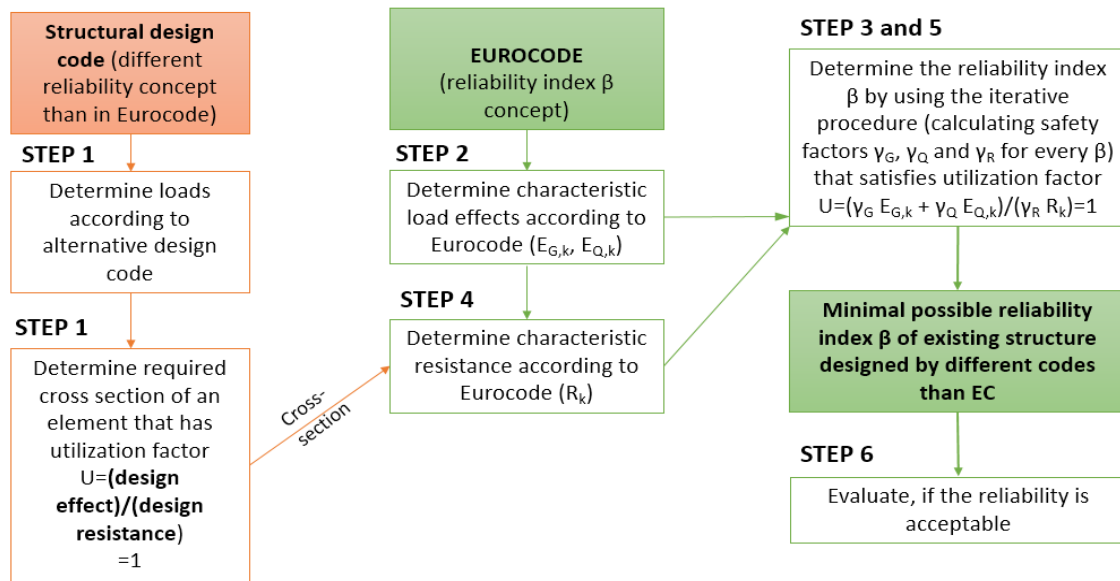


Fig. 2. Determination procedure of minimal reliability index β of existing structure designed by different codes than EC

Table 3. Element of truss top chord under compression and bending

City	As built Liepaja		If designed with ~100% utilization			
	SNiP	Eurocode	Liepaja		Riga	
Code	SNiP	Eurocode	SNiP	Eurocode	SNiP	Eurocode
β	-	3.8	-	2.6	-	3.2
γ_Q	-	1.30	-	0.90	-	1.09
γ_G	-	1.27	-	1.18	-	1.22
γ_R	-	1.12	-	1.04	-	1.08
Internal loads	$N_d = 388$ kN $M_d = 4.89$ kNm	$N_{Ed} = 546.9$ kN $M_{s,Ed} = 6.9$ kNm $M_{h,Ed} = 8.6$ kNm	$N_d = 388$ kN $M_d = 4.89$ kNm	$N_{Ed} = 418.1$ kN $M_{s,Ed} = 5.3$ kNm $M_{h,Ed} = 6.6$ kNm	$N_d = 483$ kN $M_d = 6.08$ kNm	$N_{Ed} = 478.4$ kN $M_{s,Ed} = 6.0$ kNm $M_{h,Ed} = 7.5$ kNm
Utilization factor U	68%	98%	98%	100%	95%	99%
Cross-section	□160x160x4		□130x130x4		□150x150x4	

Table 4. Element of truss bottom chord under tension

City	As built Liepaja		If designed with ~100% utilization			
	SNiP	Eurocode	Liepaja		Riga	
Code	SNiP	Eurocode	SNiP	Eurocode	SNiP	Eurocode
β	-	4.3	-	2.5	-	3.2
γ_Q	-	1.50	-	0.87	-	1.09
γ_G	-	1.30	-	1.18	-	1.22
γ_R	-	1.15	-	1.03	-	1.08
Internal loads	$N_d = 401.9$ kN	$N_{Ed} = 633.2$ kN	$N_d = 401.9$ kN	$N_{Ed} = 424.2$ kN	$N_d = 500$ kN	$N_{Ed} = 496.3$ kN
Utilization factor U	59%	99.2%	95%	98%	96%	97.5%
Cross-section	□140x140x4		□90x90x4		□90x90x5	

Table 5.
Compressed element of truss diagonal

City	As built Liepaja		If designed with 100% utilization			
			Liepaja		Riga	
Code	SNiP	Eurocode	SNiP	Eurocode	SNiP	Eurocode
β	-	3.3	-	2.8	-	3.3
γ_Q	-	1.12	-	0.96	-	1.12
γ_G	-	1.23	-	1.20	-	1.23
γ_R	-	1.08	-	1.05	-	1.08
Internal loads	$N_d = 99.2$ kN	$N_{Ed} = 125.2$ kN	$N_d = 99.2$ kN	$N_{Ed} = 111.9$ kN	$N_d = 123.4$ kN	$N_{Ed} = 125.2$ kN
Utilization factor U	81%	98%	95%	98%	100%	97.5%
Cross-section	□80x80x3		□80x80x2.5		□80x80x3	

Table 6.
Beam in bending

City	As built Liepaja		If designed with 100% utilization			
			Liepaja		Riga	
Code	SNiP	Eurocode	SNiP	Eurocode	SNiP	Eurocode
β	-	3.5	-	2.7	-	3.5
γ_Q	-	1.19	-	0.93	-	1.19
γ_G	-	1.25	-	1.19	-	1.25
γ_R	-	1.10	-	1.04	-	1.10
Internal loads	$M_d = 589$ kNm	$M_{Ed} = 777.5$ kNm	$M_d = 589$ kNm	$M_{Ed} = 650$ kNm	$M_d = 732$ kNm	$M_{Ed} = 777$ kNm
Utilization factor U	80%	99%	100%	98%	99%	99%
Cross-section	IPE600		IPE550		IPE600	

IV. CONCLUSION

The developed simple and practical procedure of determination of minimal reliability index β of existing structure designed by different codes than Eurocodes allows to assess the actual safety level of different structural elements of buildings. It is very important to Latvia, as most of the existing buildings are designed to different structural codes and actual safety level generally is unknown. Therefore, often arises the question do some parts of buildings needs to be strengthened to reach the safety level of the current design codes in force.

The case study of the existing building with light weight roof in the city Liepaja and Riga revealed that the reliability index β and therefore safety level of elements varies even between the regions of Latvia. It is since climatic snow maps are changed relatively recently.

The reliability index β of the structural elements depending on the phenomena varies in limits of 2,5 to 2,8 for Liepaja and 3,2 to 3,5 for Riga. That are lower values than target reliability index β set in the ISO 13822 [33] for buildings with medium consequences of failure and minimum standard period for safety 50 years. This target safety level for existing buildings varies from different aspects and will be analysed in the next researches to look for the optimal ways to reduce it as most of the existing building elements seems to fall below the value denoted in current ISO standard.

V. REFERENCES

- [1] Dalia Abdelaziz Elsorady, Assessment of the compatibility of new uses for heritage buildings; Journal of Cultural Heritage 15 (2014) 511–521.
- [2] Simone Ferrari, Federica Zagarella, Costs assessment for building renovation cost-optimal analysis Energy Procedia 78 (2015) 2378 – 2384.
- [3] Francesca Cappelletti, Tiziano Dalla Mora, Fabio Peron, Piercarlo Romagnoni, Paolo Ruggeri, Building renovation: which kind of guidelines could be proposed for policy makers and professional owners? Energy Procedia 78 (2015) 2366 – 2371.
- [4] National Construction Programme [online]. Riga, Cabinet of Ministers. 2002. [cited 30 August 2002]. Available, from Internet: <http://likumi.lv/doc.php?id=65990u> (in Latvian).
- [5] The Latvian Eurocode National Implementation plan for 2013-2014 years [online]. Riga, Cabinet of Ministers. 2012. [cited 10 January 2013]. Available from Internet: <http://www.likumi.lv/doc.php?id=247907> (in Latvian).
- [6] Liga Gaile, Andina Sprince, Leonids Pakrastinsh, Specific Challenges of Adopting Eurocodes in Latvia, Procedia Engineering 57 (2013) 294 – 301.
- [7] Construction Law [online]. Riga, Latvian Parliament, 2013 [cited 30 July 2013]. Available, from Internet: <http://likumi.lv/doc.php?id=258572> (in Latvian).
- [8] Regulation (EU) No 305/2011 of the European Parliament and of the Council of 9 March 2011 laying down harmonised conditions for the marketing of construction products and repealing Council Directive 89/106/EEC, Strasbourg, 9 March 2011. Available, from Internet: <http://eur-lex.europa.eu/legal-content/EN/TXT/?uri=CELEX:32011R0305>
- [9] Bertram Kühn Assessment of existing steel structures - Recommendations for estimation of the remaining fatigue life Procedia Engineering 66 (2013) 3 – 11
- [10] Dir.u.Prof.Dr.W.Rücker, Dipl.-Ing. F.Hille, Dipl.-Ing.R.Rohrmann, F08a Guideline for the Assessment of Existing Structures, Federal Institute of Materials Research and Testing (BAM), Samco 2006;
- [11] Dimitris Diamantidis; Paolo Bazzurro Safety acceptance criteria for existing structures, University of Applied Sciences, Regensburg
- [12] M.Sykora, M.Holicky, Target reliability levels for the assessment of existing structures
- [13] Quanwang Li, Bruce R. Ellingwood, Damage inspection and vulnerability analysis of existing buildings with steel moment-resisting frames, Engineering Structures 30 (2008) 338–351
- [14] Daniel W.M. Chan, Tracy N.Y. Choi, Difficulties in executing the Mandatory Building Inspection Scheme (MBIS) for existing private buildings in Hong Kong, Habitat International 48 (2015) 97-105.

- [15] Sophie I.Hallstedt Sustainability criteria and sustainability compliance index for decision support in product development, *Journal of Cleaner production* 140 (2017) 251-266
- [16] Raji Banani, Maria.M.Vahdati, Mehdi Shahrestani, Derek Clements-Croome, The development of building assessment criteria framework for sustainable non-residential buildings in Saudi Arabia; *Sustainable Cities and Society* 26 (2016) 289-305;
- [17] Zhenjun Ma, Paul Cooper, Daniel Daly, Laia Ledo, Existing building retrofits: Methodology and state-of-the-art; *Energy and Buildings* 55 (2012) 889-902
- [18] Nuno Pereira, Xavier Romão; Assessment of the concrete strength in existing buildings using a finite population approach, *Construction and Building Materials* 110 (2016) 106–116.
- [19] *Szigeti, F. and Davis, G*, Using the ASTM/ANSI Standards for Whole Building Functionality and Serviceability for major asset and portfolio decisions, CIB World Building Congress, April 2001, Wellington, New Zealand, Paper: CLI 16.
- [20] Ki-Uhn Ahn, Deuk-Woo Kim, Young-Jin Kim, Cheol-Soo Park, In-Han Kim, Gaussian Process model for control of an existing building, *Energy Procedia* 78 (2015) 2136 – 2141.
- [21] B. Radhika, C.S. Manohar, Reliability models for existing structures based on dynamic state estimation and data based asymptotic extreme value analysis, *Probabilistic Engineering Mechanics* 25 (2010) 393_405
- [22] Wei Gao, Chongmin Song, Francis Tin-Loi, Probabilistic interval analysis for structures with uncertainty, *Structural Safety* 32 (2010) 191–199.
- [23] Starr, Ch.: "Social Benefit versus Technological Risk"; *Science*, Vol. 165, No. 19, S. 1232, 1969
- [24] R.D.J.M.Steenbergen, A.C.W.M.Vrouwenvelder; Safety philosophy for existing structures and partial factors for traffic loads on bridges, TNO, Built Environment and Geosciences, Delft , the Netherlands, *HERON* Vol.55 (2010) No.2 125-139
- [25] Dr.Nico P.M.Scholten, Prof.Ton.C.W.M Vrouwenvelder, Eurocodes and structural safety of the existing buildings – considering the publication of the Dutch NEN 8700, 4th International Conference Civil Engineering 13, Proceeding Part II, Building and Renovation
- [26] V.V.Nadolskiy, M.Sykora, M.Holicky, Comparison of Reliability levels provided by the Eurocodes and standards of the Republic of Belarus, *Vestnik MGSU*, 2013
- [27] Paul Luechinger; Juerg Fischer, New European Technical Rules for the assessment and retrofitting of existing structures, European Commission, Joint Research Centre, Institute for the Protection and Security of the Citizen, 2015
- [28] EN 1990:2002 Eurocode: Basis of structural design
- [29] Implementation of Eurocodes. Handbook 2. Reliability background. Guide to basis of structural reliability and risk engineering related to Eurocodes, supplemented by practical examples. Leonardo da Vinci pilot project CZ/02/B/F/PP-134007, Prague 10, 2005
- [30] SNIP 2.01.07-85* Building regulations. Loads and actions. USSR State Building. 1987.
- [31] ISO 2394: 2015 General principles on reliability for structures
- [32] CEN/TC/250/WG2 Assessment and retrofitting of existing structures, Bases. Report N2032, 2014
- [33] ISO 13822:2010 Bases for design of structures – Assessment of existing structures

Heat Resistant Building Envelopes Made of Lightweight Concrete with the use of Porous Granular Wastes

Galitskov S.Ya., Mizuryaev S.A., Chiknovoryan A.G.

Samara State Technical University, Institute of Architecture and Civil Engineering

Address: Molodogvardeyskaya St., 194, Samara, 443001, Russia

Abstract. The paper focuses on building envelopes for industrial thermal generating units, their efficiency and its increase. Building envelopes made of lightweight heat-resistant concretes are considered most effective from the point of their building construction, maintenance, repair and cost-effectiveness. One of the unresolved problems here is that porous granular materials suitable for use as concrete fillers operating at temperatures over 1000 °C are not industrially manufactured at the moment. The article also characterises commonly used heat resistant porous fillers. It indicates that the use of exhaust zeolites is potentially perspective. General properties and characteristics of zeolites are also given. The paper demonstrates that it is quite possible to use exhaust zeolites in building envelopes of lightweight heat-resistant concretes. The work describes testing experiments of typical exhaust zeolites (petrochemical and oil refining industries wastes) in Samara region and the Republic of Tatarstan. Their stress-strain properties and chemical compositions as well as X-ray crystallographic analysis (including analysis under high temperature) are presented. They prove that zeolites are heat-resistant and fire-proof because of corundum formation. Phosphate binder was used for testing in heat-resistant concretes. The composition of the concrete mixture is given in the paper. As a result, concrete with the following characteristics was obtained: 1550 kg/m³ density, with compressive strength of approximately 21 MPa, having high thermal resistance and maximum permissible application temperature of 1450° c.

Keywords: lightweight concretes, heat resistance, exhaust zeolites, concrete mixture, physical and thermal properties.

I. INTRODUCTION

Nowadays hardly any production can do without thermal units of different application, for which the most effective lining is usually constructions of lightweight heat-resistant concrete. Nevertheless, the overall volume of concrete linings compared to single-piece refractories, is extremely small and is less than 10% of the total. One of the reasons here is the lack of industrial production, i.e. large quantity production of heat-resistant porous fillers for concrete, which are able to work at a temperature over 1000 °C [1-5]. Such porous fillers as expanded clay, ceramsite, agglomerite, vermiculite, perlite are sometimes referred to as heat-resistant, but their maximum application temperature does not exceed 1000-1100 °C. It is important to note that several types of heat-resistant porous fillers as well as the technology for their production have already been invented for concretes used at temperatures 1000-1500 °C [5-13]. The methodology of producing such aggregates is based on very scarce and expensive high-aluminous raw materials and their clinker formation, melting and swelling at high temperatures. Therefore, searching and discovering of available porous, preferably granulated, materials with high fire resistance is now of considerable interest.

II. THEORY AND EXPERIMENTS

Some of the most promising materials, in terms of their use as heat-resistant fillers, are exhausted zeolite-containing adsorbents which are wastes of petrochemical industry and oil refining factories.

Such materials include exhaust zeolites, zeosorbs and other zeolite-like catalysts, hereinafter referred to as "zeolites".

Zeolites are referred to the class of hydroalumosilicates with space-framed structure. Such tetrahedra as AlO_4 or SiO_4 with negative charges balanced by Ca, Mg, Na, K and sometimes Ba or Sr ions serve as the basis of the frame. All zeolites have one and the same typical structure: their crystal lattice is penetrated by micropores of a certain size, enabling anions and cations move to the center of the structure, or, vice versa, to its periphery [14-16].

Wide application of zeolites in petrochemical and refining industries is brought about by the following characteristic properties:

a) zeolites are "cations", i.e. capable of ion exchange of cations with surrounding environment. This characteristic makes possible to use them for regulating water hardness;

b) a definite diameter of zeolite pores can be used for gaseous and liquid substances clearance from various impurities or for separation of substances with different size of their molecules. Therefore, zeolites are often referred to as "molecular sieves";

c) the volumes of zeolite-containing wastes are quite substantial. According to our information, 2-3.5 thousand tons of such zeolite-containing wastes are generated only in the Samara region. Almost all of these exhaust zeolites look as granules of 1-8 mm size with the bulk density up to 850 kg/m³ and refractory property of 1550-1800 °C.

Research and testing of exhaust zeolites generated by industrial enterprises of Samara region (Z-1) and the Republic of Tatarstan (Z-2) were carried out in accordance with standard methodologies and the Standard of the Russian Federation № 20955 "Heat-resistant concretes and their aggregate and fillers". The influence of high-temperature heating on these wastes was studied by means of X-ray crystallographic analysis.

Physical and mechanical characteristics of exhaust zeolites are presented in Table 1.

Table I
Physical mechanical properties of used adsorbents

Indicators	Value of indicators	
	Zeolite type	
	Z-1	Z-2
Density:		
- absolute, g/cm ³	2.8	2.7
- in the lump, g/cm ³	1.18	1.37
- bulk, kg/m ³	640	810
Porosity:		
- true, %	58	49
- intergranular, %	46	41
Water absorption by weight, %	75	47
Sieve residue percentage, %		
10 mm	2.6	3.7
5 mm	77.4	88.8
2.5 mm	19.4	7.5
1.25 mm	0.6	-
0.63 mm	-	-
0.315 mm	-	-
0.14 mm	-	-
Cylinder compressive strength, MPa	2.7	4.64

According to their chemical composition (see Table 2), the zeolites in question are high-aluminous materials with a minimum content of fluxing oxides. This fact predetermines their high refractory properties.

Table 2
Physical mechanical properties of used adsorbents

Zeolite type	Oxide								
	SiO ₂	Al ₂ O ₃	FeO _{gen}	Fe ₂ O ₃	FeO	RO	SO ₃	R ₂ O	PPP
Z-1	4.93	76.57	3.46	2.36	1.11	2.51	0.3	0.23	12.0
Z-2	5.24	72.6	6.59	5.55	1.04	3.51	0.96	0.31	9.78

X-ray crystallographic analysis made it possible to prove that tested exhaust zeolites at a temperature of 20 °C contain mostly boehmite γ -AlO (OH) (see Figure 1). The analysis results prove the results of chemical composition of zeolites determinations and conclusions that high-aluminous compounds of high refractory properties make the large part of zeolites composition.

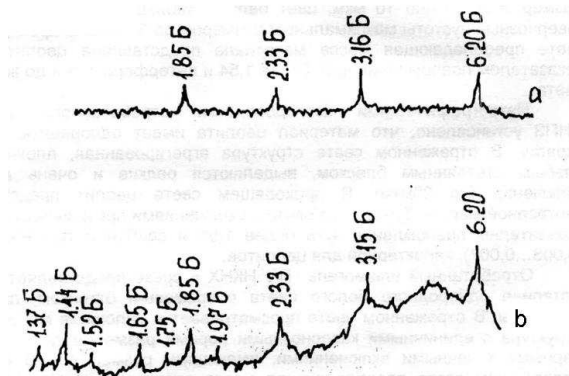


Fig. 1. X-ray diffraction pattern of exhausted adsorbents at 20°C: a – Z-1; b – Z-2

It goes without saying that heat resistant fillers for concrete should have certain physical and thermal characteristics. Physical and thermal characteristics of exhaust zeolites are presented in Table 3. For a comparative analysis we also give here similar characteristics of specially manufactured agglomerite (A) generated from high refractory raw charge with refractoriness of 1710 ... 1750 °C.

The obtained data show that the wastes in question are similar by their physical and thermal properties to specially produced high-resistant agglomerite with very energy-consuming production technology. For the final determination of maximum permissible temperature of lightweight concrete application on tested zeolites we tested concretes to determine their deformation under load when heated.

Table 3
 Special physical and thermal properties of exhaust zeolites

Zeolite type	Indicators	
	Heat resistance, thermal When heated to 1000 °C and cooled in air jet	Fire Resistance, °C
Z-1	41	1750
Z-2	46	1850
A	25	1710-1750

For materials designed to operate at high temperatures, it is necessary have data on the nature of the processes occurring in these materials when heated. To do that we applied X-ray crystallographic analysis of exhaust zeolites Z-1 and Z-2 at temperatures of 300, 500, 800, 1000 and 1200 °C. The results of the tests are given in Figures 2 and 3.

The results show that at a temperature of 300 °C the tested zeolites are presented as «bemites» AlO(OH) (see Figures 2a and 3a). When zeolites are heated to 500, 800 and 1000 °C they are dehydrated and amorphized. At these temperatures they have only the traces of γ -alumina (see Figures 2b, 2c, 2d and 3b, 3c, 3d). When zeolites are further heated to 1200 °C they form corundum α -Al₂O₃ (see Figures 2e and 3e). Corundum formation at high temperatures is beneficial, because it is a stable high temperature form of alumina that has high strength and thermal characteristics.

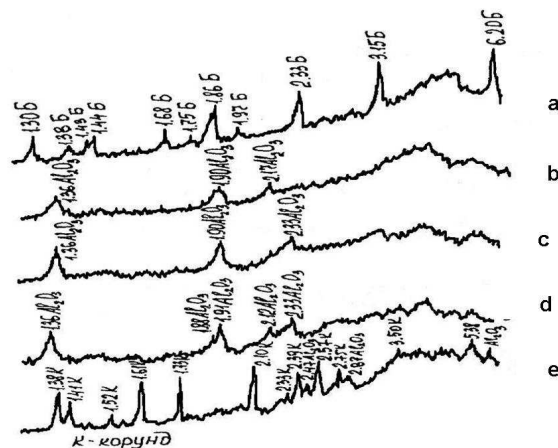


Fig. 2. Exhaust zeolite Z-1 X-ray diffraction pattern a – at 300; b – at 500; c – at 800; d – at 1000; e – at 1200 °C.

The analysis of the obtained results showed that for the manufacture of heat-resistant concretes the most effective binder (for the purpose of working together with the filler) is the phosphate binder based on phosphoric acid and floured chamotte.

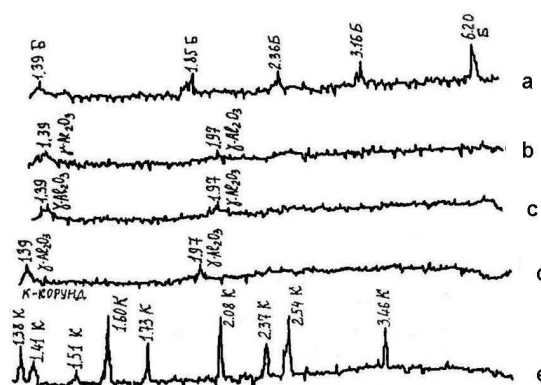


Fig. 3. Exhaust zeolite Z-2 X-ray diffraction pattern: a – at 300, b – at 500, c – at 800. d – at 1000, e – at 1200 °C.

The analysis of the obtained results showed that for the manufacture of heat-resistant concretes the most effective binder (for the purpose of working together with the filler) is the phosphate binder based on phosphoric acid and floured chamotte.

In the course of the experiments the following composition of the concrete mix (for 1 cub.m. of concrete) was suggested:

- exhaust zeolites – 660 kg;
- floured chamotte – 530 kg;
- 65% orthophosphoric acid – 560 l.

As the result we obtained concrete with 1550 kg/m³ density and with compressive strength of approximately 21 MPa. The designed lightweight heat-resistant concrete had the following thermal characteristics:

- heat resistance after heating to 800 °C is 45-55 air thermal shifts;
- the maximum permissible temperature of use corresponding to 4% of deformation is 1450°C.

III. RESULTS

The research yielded the following conclusions:

- Exhaust zeolites density makes it possible to refer them to aggregate and fillers suitable for manufacturing lightweight concrete. Exhaust zeolites are characterized by comparatively high compressive strength (2.7 ... 4.6 MPa).
- According to their chemical composition, exhaust zeolites are high-aluminous-containing materials (over 70% of Al₂O₃) with a minimum content of oxides of RO and R₂O.
- When exhaust zeolites are heated, they generate a high temperature form of alumina – corundum – characterized by high heat-resistant, strength and fire-resistant properties.
- The exhaust zeolites under analysis have high fire-resistant properties: 1750-1850 °C.
- Characteristics exhaust zeolites correspond to the requirements of the Standard of the Russian Federation № 20955 "Heat-resistant concretes and their aggregate and fillers" and

can be used as porous fillers in lightweight heat-resistant concretes.

- Heat-resistant lightweight concrete obtained on the basis of exhaust zeolites has excellent physical and thermal characteristics and is suitable for manufacturing structures, designed to operate at temperatures up to 1450 °C.

REFERENCES

- [1] Gorin V.M. Extension of the scope of ceramsite gravel usage. *Construction materials*, 11, 2003, pp. 19-21.
- [2] Vytchikov Yu.S. Improving energy efficiency of buildings and facilities. *Intercollegiate scientific paper*, Samara State University of architecture and civil engineering, 7, 2012, pp. 245-249.
- [3] Balabanov M.S. Influence of aggregate properties on the properties of concrete. *Collection of works*. Samara State University of architecture and civil engineering, 2013, pp. 13-14.
- [4] Kudyakov A.I., Radina T.N., Ivanov M.Yu. Granular insulating material on the basis of modified water glass of microsilicasuspension. *Construction materials*, 11, 2004, pp. 12-13.
- [5] Mizuriaev S.A., Zhigulina A.Yu., Mamonov A.N., Ivanova N.V. Expansion of nomenclature of synthetic porous fillers. *Construction materials*, 7, 2011, pp. 12-13.
- [6] Galickov S.Ya., Galickov K.S., Samokhvalov O.V., Fadeev A.S. Simulation study ofceramsite burning in the rotating kiln with angular velocity as control object. *Scientific Survey*, 2015, pp. 227-237.
- [7] A.Yu. Zhigulina, S. A. Mizuryaev. Composition for production of porous filler, patent. 2003, No. 2211196 RU.
- [8] S. A. Mizuryaev, A.Yu. Zhigulin, Construction designs and materials. *Express information*, 16, 2002, pp. 1-3.
- [9] Guryanov A.M., Mizuriaev S.A., Lebedev V.M., Lebedev V.T. Nanostructured porous materials on the basis of soluble sodium glass. *Proceedings of the V Eurasian scientific-practical Conference "Strength of non-homogeneous structures"*, 2010, pp. 136-137.
- [10] Ivashchenko Yu.G., Surmin, A.A., Zobkova N.V., Pavlova I.L. Composition for manufacturing spherical granules for thermal insulation material, patent. 2000, No. 2158716RU.
- [11] Korotayev S.A., Erofeev V.T. Obtaining lightweight concrete based on solid glassy binder. *Bulletin of Mordovskiy University*, 4, 2008, pp. 54-59.
- [12] Kudyakov A.I., Radina T.N., Ivanov M.Yu. Granular insulating material on the basis of modified water glass of microsilicasuspension. *Construction materials*, 11, 2004, pp. 12-13.
- [13] Mizuriaev S.A., Zhigulina A.Yu., Mamonov V.N. Development of an effective fire-resistant insulation of cellular structures. *Industrial and civil engineering*, 6, 2015, pp. 47-50.
- [14] Kubasov A.A. Zeolites – boiling stones. *Soros educational journal*, Vol. 3, 5, 2006, pp. 58-65.
- [15] Romanovskiy B.V., Makshina E. V. Nanocomposites as functional materials. *Soros educational journal*, Vol. 8, 2, 2004, pp. 50-55.
- [16] Konkova T.V., Lieberman E.Yu., Alekhina M.B., Pochitalkina I.A. Adsorption processes. *Encyclopedia of engineer-chemist*, 2, 2007, pp. 12-17.

Optimization of Burning Production Process of Ceramsite with Specified Density

Galitskov K.S., Samokhvalov O.V., Fadeev A.S.

Samara State Technical University, Institute of Architecture and Civil Engineering
Address: Molodogvardeyskaya St., 194, Samara, 443001, Russia

Abstract. The paper goes into peculiarities of using developed mathematical models of ceramsite burning and computational models created on their basis. The work is done in the light of analysis and synthesis of multivariate control system of kiln angular velocity and kiln charge with volumetric thermal capacity burners. It is shown that computational models of burning as an object of control are problem-oriented on producing ceramsite with specified density. Mathematical model of ceramsite burning process as an object with distributed parameters is synthesized. The transition from model with distributed parameters to the mode with lumped parameters is performed. Then the authors used a model with three bearing cross-sections along Z-axis in Matlab software and created a computational model of multivariate object of control with inter-channel connections. The paper presents experimental computational set up methods and methods of ceramsite burning optimal curve identification on the criterion of minimizing energy consumption for burning. The developed method of staging computational experiments makes it possible to predict the strength of ceramsite if values of control actions are known. The results of modeling help create methodology of choosing optimal modes of ceramsite burning with the required mark of strength and with minimum energy consumption.

Keywords: claydite, rotary kiln, strength and bulk density of ceramsite, mathematical model.

I. INTRODUCTION

Ceramsite production is in itself a sequential execution of technological processes, among which the most significant process is that of burning. It is usually performed in a rotary drum kiln, with the length (L) of 40 m [1]. In the kiln, raw clay moving from the download zone to the zone of unloading final product undergoes multiple technological transitions: drying, heating, swelling, and, finally, cooling [2]. Strength and density of ceramsite is determined mainly by two factors: physical-chemical characteristics of the original clay raw materials and a burning curve, which shows the dependence of ceramsite temperature changes T from its position along the axis of the kiln T (z), where $z \in 0, \dots, L$. In existing structures of kilns a burning curve is formed by a specialist (called "a burner") who implements heuristic algorithms of thermal power control of the burner Q_b , loading of the kiln q_L and, less frequently, of angular velocity of the kiln ω_k . In some installations, used to control a burning curve, double-drum kilns with drums rotating with different speeds are applied [1, 2].

Most famous publications, devoted to ceramsite production, describe technological issues covering the evaluation of clay characteristics [3-6], their influence on swelling, bulk density and ceramsite strength [7-10] and experimental research of burning curves and the like [11-14].

Ceramsite burning is a complex, energy-consuming process which is difficult to formalize. Therefore,

experimental determination of desired modes of kiln operation, providing production of ceramsite with specified strength in conditions of minimal energy consumption while using existing technological equipment, requires a lot of time and money, and does not always produce optimal results. Under current conditions it is reasonable to solve this important production task by using mathematical modeling.

This paper is a further step in research previously carried out by the authors and aimed at automation of technological-processes of ceramsite burning. This work describes the basic stages for solving tasks of automatic control of burning by using mathematical models. It also demonstrates different ways of finding optimal decisions with important practical application at each of these stages.

II. DYNAMICS MODEL OF CERAMSITE BURNING IN ROTARY KILN

Papers [15, 16] within known assumptions and simplifications introduce a physical model of the kiln as a rotating multilayer cylinder of Length L (see Figure 1). This cylinder consists of a steel jacket (1), fireclay bricks (2), ceramsite raw material (3), flue gases (4) of D1-D4 diameters, respectively. Raw ceramsite granules move along Axis z of the cylinder from a charging door to a transporting out zone at v^m speed. Gas-fired burner (5) creates flue gases moving with speed v^{fg} toward the material. This process results in ceramsite burning. In this case,

thermodynamics of flue gases can be described by a system of equations:

$$\left. \begin{aligned} \rho^{\text{fg}} \left(\frac{\partial v_z^{\text{fg}}}{\partial \tau} + v_z^{\text{fg}} \frac{\partial v_z^{\text{fg}}}{\partial z} \right) &= Z - \frac{\partial p^{\text{fg}}}{\partial z} + \frac{\partial}{\partial z} \left(\mu^{\text{fg}} \frac{4 \partial v_z^{\text{fg}}}{3 \partial z} \right), \\ \frac{\partial p^{\text{fg}}}{\partial \tau} + \frac{\partial (\rho^{\text{fg}} v_z^{\text{fg}})}{\partial z} &= 0, \\ \rho^{\text{fg}} c_p^{\text{fg}} \frac{DT^{\text{fg}}}{D\tau} &= \frac{Dp^{\text{fg}}}{D\tau} + \left[\frac{\partial}{\partial x} \left(\lambda^{\text{fg}} \frac{\partial T^{\text{fg}}}{\partial x} \right) + \frac{\partial}{\partial y} \left(\lambda^{\text{fg}} \frac{\partial T^{\text{fg}}}{\partial y} \right) + \frac{\partial}{\partial z} \left(\lambda^{\text{fg}} \frac{\partial T^{\text{fg}}}{\partial z} \right) \right] + \mu^{\text{fg}} \Phi + Q(\tau), \\ p^{\text{fg}} - \rho^{\text{fg}} RT^{\text{fg}} &= 0, \\ \mu^{\text{fg}} &= \mu_0^{\text{fg}} (T^{\text{fg}}) \end{aligned} \right\} (1)$$

and dynamics of heat transfer in a solid body, in particular between the layers of rotary kiln and ceramsite, by the following equations:

$$\left. \begin{aligned} \frac{\partial T_m(z,r,\tau)}{\partial \tau} &= a_m(z) \left(\frac{\partial^2 T_m(z,r,\tau)}{\partial r^2} + \frac{1}{r} \frac{\partial T_m(z,r,\tau)}{\partial r} + \frac{\partial^2 T_m(z,r,\tau)}{\partial z^2} \right) - v_m \frac{\partial T_m(z,r,\tau)}{\partial z}, \\ \frac{\partial T_f(z,r,\tau)}{\partial \tau} &= a_f \left(\frac{\partial^2 T_f(z,r,\tau)}{\partial r^2} + \frac{1}{r} \frac{\partial T_f(z,r,\tau)}{\partial r} + \frac{\partial^2 T_f(z,r,\tau)}{\partial z^2} \right), \\ \frac{\partial T_w(z,r,\tau)}{\partial \tau} &= a_w \left(\frac{\partial^2 T_w(z,r,\tau)}{\partial r^2} + \frac{1}{r} \frac{\partial T_w(z,r,\tau)}{\partial r} + \frac{\partial^2 T_w(z,r,\tau)}{\partial z^2} \right) \end{aligned} \right\} (2)$$

Here, v^{fg} , p^{fg} , ρ^{fg} , T^{fg} , λ^{fg} , c_p^{fg} , μ^{fg} are respectively velocity, pressure, density, thermal conductivity coefficient, temperature, specific thermal capacity (at constant pressure) and viscosity coefficient of flue gases; X , Y , Z are force media projection of flue gases, related to the unit of volume; τ – time; $Dv^{\text{fg}}/D\tau$, $Dp^{\text{fg}}/D\tau$, $DT^{\text{fg}}/D\tau$ – substantial derivative of velocity, temperature and pressure; Φ is dissipative function (dissipation), T_m , a_m , v_m – temperature, heat transfer coefficient and material velocity, respectively; T_f , a_f , T_w , a_w – temperature and heat transfer coefficient of the lining of shells and steel walls of the kiln, respectively.

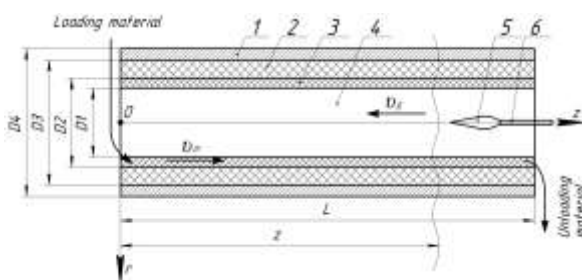


Fig. 1. Design scheme of rotary kiln

The solution of equations (1) and (2), supplemented by boundary conditions [15, 16] was carried out by a numerical method in SolidWorks computer software. A rotary kiln with 40×2.5 m dimensions, equipped with a gas burner C199-08-100 was taken by way of example. Creating a computer model of the kiln in SolidWorks computer software includes the following steps: a) heat transfer: heat transfer in solid bodies, radiative heat transfer, volumetric heat source (simulating the torch of the

kiln) with temperature of 1200°C , rotation of the kiln; b) the composition of flue gases: CO_2 – carbon dioxide, N_2 – nitrogen, O_2 – oxygen, Ar – argon, H_2O – water vapor; c) type of gas flow – laminar; g) material of kiln layers: framework – steel St.3, lining – refractory brick, material being burnt – raw ceramsite; d) initial conditions of gas environment: temperature – 20°C , speed – 30 m/s, e) initial and boundary conditions of the kiln; k) parameters of computational grid. The researchers worked with two types of raw materials: the first was from easily swelling clay from Smyshlyaevka, the second was from iron clay with little swelling properties [15, 16].

The developed computational model makes it possible to perform two phases of testing the kiln. The main objective of the first phase is to assess the adequacy of models and optimization of coordinates choice of the kiln bearing cross-sections. Firstly, modeling of dynamics of kiln preheating in conditions of its rotating at a constant angular velocity is done. In this case, we should specify time (for example, 24 hours) of expected time interval necessary for the kiln to achieve steady temperature. As a result of these calculations, we found static temperature distribution of flue gases along the length of the rotary kiln. Comparison of the results obtained with empirical data makes it possible to evaluate the adequacy of the model in this technological mode.

Then we explored burning curves of ceramsite. In the calculation model, the adequacy of which was confirmed by the previous experiment, we specify the following parameters of raw material: moisture, density, thermal conductivity. For example, computational experiments to evaluate the impact of speed ω_k on the strength R were performed with 3-x values $\omega_k = 0.26; 0.13; 0.08 \text{ s}^{-1}$. Comparison of burning curves, obtained in computational experiments [17], with the results obtained on the existing kiln, demonstrated that they differed by no more than 5%, which confirms the adequacy of designed mathematical model.

The analysis of the multitude of burning curves allows to solve the first task of optimization – choice of coordinates for three bearing cross-sections F, A and C along the length of the kiln [18]. It makes possible to justified the following three control actions: angular velocity of the kiln and its load, thermal power of the burner. In the second phase, we investigated dynamics of the burning process as a multivariate control object with distributed parameters, in which the temperature of ceramsite is controlled in three selected cross-sections.

The main objective of this phase is to justify the possibility of transition from kiln model as an object with distributed parameters to its model as a multivariate object of control with lumped parameters.

III. DYNAMICS MODEL OF CERAMSITE BURNING IN ROTARY KILN AS A MULTIVARIATE CONTROL OBJECT

The second phase of the tests represents, in fact, identification of the kiln transfer function and transfer functions of the links of ceramsite burning process as multidimensional (especially 3D) object of control (see Figure 2) in its relation to both the vector $\bar{U} = [\Delta\omega_k, \Delta q_L, \Delta Q_b]^T$ of control actions, and to the vector $\bar{H} = [\Delta w, T_c]$ of disturbances.

Here T is the vector of the output coordinates $\bar{T} = [T_F, T_A, T_C]$, where T_F, T_A, T_C – the temperature of clay in selected sections of the kiln. The object structure is supplemented by the developed operator S_1 through which the projected strength R and bulk density of ceramsite ρ , which is baked from clay with generalized characteristic of γ , raw material is characterized with moisture w and the burning curve is represented by the vector \bar{T} .

To solve the described tasks by using our model (which adequacy was estimated in the first stage of the tests) the following experiments were performed:

1) Research of response functions (curves of the transition process) of ceramsite temperature in cross-sections F, A and C of the kiln to the step change "in the small" of one of the vector elements of control actions at constant values for the remaining elements of this vector and disturbances. Identification of separate links and inter-channel links of a multivariate object with respect to control in the form of dynamic models with lumped parameters.

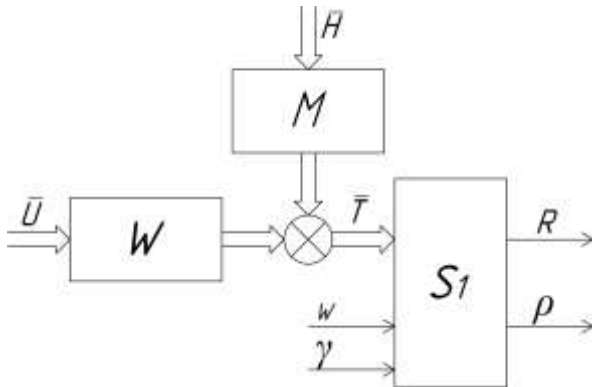


Fig. 2. Structural scheme of the object of control Here W is its own transfer functions, M is transfer functions of links for control, H is transfer functions in relation to disturbance.

2) Research of response functions (curves of the transition process) of ceramsite temperature in cross-sections F, A and C of the kiln to the step change "in the small" of one of the disturbance areas (raw material moisture w , external environment temperature T_c) at constant values for the remaining control effects and disturbances. Identification of separate channels and inter-channel links of a multivariate object with respect to disturbance in the form of dynamic models with lumped parameters.

3) Forecasting of strength R and bulk density of ceramsite ρ by using a computational model created in Matlab software and based on synthesized structure of multidimensional object of control (see Figure 2).

IV. OPTIMIZATION METHODOLOGY OF CONTROL OF CERAMSITE BURNING PROCESS

Based on the developed model of the dynamics of the control object we synthesized a structure (see Figure 3) and created a computational model of multidimensional system of control of burning process in Matlab software.

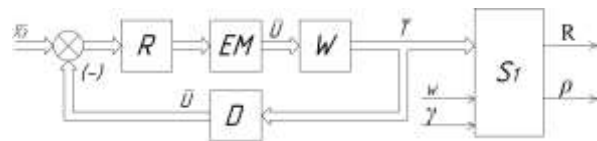


Fig. 3. The structure of a multidimensional control system for ceramsite burning: EM – an electromechanical part; \bar{X}_s – a vector specifying exposure; D – a temperature sensor

The practical application of this model makes it possible, firstly, to perform parametric synthesis of regulators R of separate channels of multidimensional systems in conditions of inter-channels links and, secondly, to solve the problem of determining optimal control of ceramsite burning with account of achieving the required strength values in conditions of the least possible value of consumed energy [19-21].

The use of Operator S_1 makes it possible to calculate permitted deviation values of elements \bar{T} . These values still make possible to burn ceramsite of certain brands. As a result, in the space $OT_F T_A T_C$ we built a set of parallelepiped (see Figure 4) Π_i ($i \in 1, \dots, n$, where n is the number of possible standard ceramsite grades according to its strength which can be produced by the oven). Here Volume $K_i L_i M_i N_i K'_i L'_i M'_i N'_i$ includes countless combinations of values of Vector $T_i = [T_{Fi}, T_{Ai}, T_{Ci}]^T$, specifying temperatures which makes it possible to produce ceramsite of Π_i grade.

When a working point (that is, a spherical solid) of a system of automatic control of ceramsite burning is inside one of these parallelepipeds, ceramsite of the brand corresponding to this volume will be produced.

It lies in the following assumption. Suppose we know the desired value of ceramsite brand P strength and the properties of raw materials loaded into the kiln, as well as its humidity. We have to find the optimum value of a vector element \bar{T} in which burning will be performed at the lowest achievable energy consumption. In conditions, when for each brand P in accordance with All Union State Standard (GOST) there exists some fairly significant in magnitude variation of strength R , the unique solution of the task is impossible. Using the operator S_1 makes

it possible to calculate permitted deviation values of elements \bar{T} . These values still make possible to burn ceramsite of certain brands. As a result, in the space $O_T T_A T_C$ a family of boxes (parallelepipeds) was built (see Figure 4).

When a working point of a system of automatic control of ceramsite burning is inside one of these parallelepipeds, ceramsite of the brand corresponding to this volume will be produced.

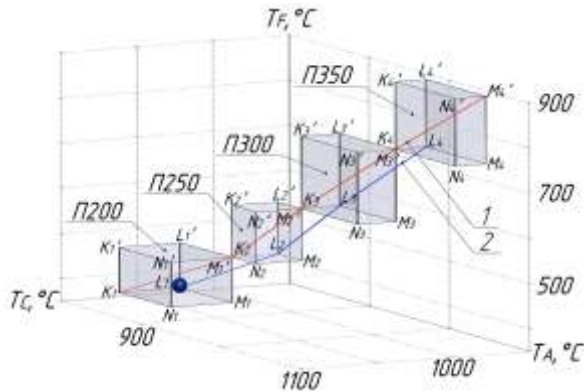


Fig. 4. The brand of ceramsite according to its strength in space $O_T T_A T_C$, 1 – a polygonal curve of maximum strength, 2 – an energy efficient polygonal curve

We believe that the synthesized system allows to provide ceramsite temperature stabilization in three selected sections of the kiln to the specified accuracy. Figure 3 shows that the research on the model proved that production of ceramsite with specified strength will have the lowest energy consumption, if the working point of the automatic control system is in point (L) (shown in Figure 5) of the parallelepiped in question.

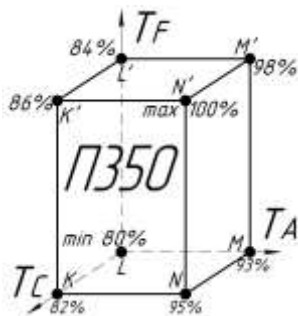


Fig. 5. Relative costs of gas (%) for burning 1m^3 of ceramsite P 350 Brand in relation to the boundary points of the multi-dimensional phase space of the developed system of automatic control of ceramsite burning

V. RESULTS AND DISCUSSION

The research and its results show that the proposed approach to solving the problem of ceramsite with specified strength production in conditions of the minimum achievable energy consumption by applying the developed mathematical models of the kiln as an object of control, models of synthesized automatic control system of the burning process and the use of these models allows to use

them while solving practical tasks to optimize the process of ceramsite burning.

The obtained results of solving this multi-criteria task of optimization also include the assessment of the adequacy of mathematical model of ceramsite burning as an object with distributed parameters, selection of bearing cross-sections coordinates of the kiln along its central axis, justification for the move from models with distributed parameters to the model with lumped parameters, selection of the optimal position (on the criterion of minimizing energy consumption for burning) of the working point of the system of automatic control in the limited space $O_T T_A T_C$, corresponding to production of ceramsite with specified strength P. The test results of research carried out on a specific example show that production of ceramsite with specified strength makes it possible to reduce energy consumption up to 20%.

VI. CONCLUSION

Theoretical aspects of optimization of ceramsite burning technological processes, described in the paper, are aimed to solve important practical tasks of automating production of ceramsite with specified strength (or density) by synthesis and implementation of multidimensional system control for the thermal field in the rotary kiln. Optimization of kiln operation was performed by using mathematical models of the burning process.

REFERENCES

- [1] Lisienko V.G., Shchelokov Ya.M., Ladygichev M.G. Rotary kilns: heat engineering, management and ecology, Book 1, Moscow, Heating engineer, 2004, 688 p.
- [2] Lisienko V.G., Shchelokov Ya.M., Ladygichev M.G. Rotary kilns: heat engineering, management and ecology, Book 2, Moscow, Heating engineer, 2004, 592 p.
- [3] Yıldız M., Soğancı A.S. Effect of freezing and thawing on strength and permeability of lime-stabilized clays. Scientia Iranica, Vol. 19, Is. 4, 2012, pp. 1013–1017.
- [4] Chuan Wang, n-Xin Chen, Chao Dang Yuan-Zhe Li, Aruna, Hai-Chao Li, Yu Huang Preparation of Ceramsite from C&D Waste and Baiyunebo Tailings. Procedia Environmental Sciences, Vol. 31, 2016, pp. 211–217.
- [5] Fan Tie-lin, Chen Mi-mi, Zhao Feng-qing The preparation of phase change energy storage ceramsite from waste autoclaved aerated concrete. Procedia Environmental Sciences, Vol. 31, 2016, pp. 227–231.
- [6] Metin Davraza, Murat Korub, Ali Ekrem Akdağ. The Effect of Physical Properties on Thermal Conductivity of Lightweight Aggregate Procedia Earth and Planetary Science, Vol. 15, 2015, pp. 85–92.
- [7] Kartushina Yu. N., Shaikhiev I. G., Ananyev D. Waste treatment plants and charcoal production wastes as a corrective additive in the production of ceramsite. Vestnik of Kazan Technological University, Vol.17, Is.21, 2014, pp. 195-198.
- [8] Sokolov L.I., Fomenko A.I. Reclamation of Waste Products in Aglite Production. Industry ecology. Vol. 19, 9, 2015, pp. 30-34.
- [9] Kislenco T.A., Koshkarev S.A., Sidyakin P.A., Eremyan S.P. The Basic Significance Of Parameters Of Inertial Devices Cleaning Ventilation Emissions In Claydite Manufacturing. Modern problems of science and education, 1, 2014.
- [10] Toropkov N.E. Influence of molding conditions clay matters for claydite and waste treatment methods of claydite production. Scientific Almanac, 8 (10), 2015, pp. 1039-1045.

- [11] Maksimova I.N., Makridin N.I. Technological Features Of Light Concretes Structure And Properties Formation. *Regional architecture and engineering*, 2, 2012, pp 45-48.
- [12] Castrodale R.W., Harmon, K.S. Increasing Design Efficiency Using Lightweight Concrete for Prestressed Girder Bridges. Paper 55, Proceedings, 2005 National Bridge Conference, Palm Springs, CA, PCI, October 16-19, 2005.
- [13] Castrodale R.W., Eriksson R.L., Barngrover B. Comparative Bridge Designs Using Normal Weight and Lightweight Concrete. Paper 45, Proceedings, 2009 National Bridge Conference, San Antonio, TX, PCI, September 13-15, 2009.
- [14] Vaiana R., Capiluppi G.F., Gallelli V., Iuele T., Minani V. Pavement Surface Performances Evolution: an Experimental Application. *Procedia - Social and Behavioral Sciences*, Vol. 53, 3 October, 2012, pp. 1149–1160.
- [15] Galitskov S.Ya., Galitskov K.S., Samohvalov O.V. Modelling Operating Area of Condition and Management of High Strength Bloating Clay, Stoving in a Rotary Kiln. *Procedia Engineering, XXV R-S-P Seminar, Theoretical Foundation of Civil Engineering (25RSP)*, Vol. 111, 2016, pp. 233–235.
- [16] Galitskov S.Ja., Galitskov K.S., Samohvalov O.V., Fadeev A.S. Modeling the calcination of ceramsite in a rotary furnace with regulated speed as a control object. *Science Review*, 7, 2015, pp. 227-237.
- [17] Galitskov S. Y., Samokhvalov O. V., Fadeev A. S. Structural synthesis of a multi-dimensional system for automated control of claydite baking in a rotary furnace. *Science Review*, 12, 2013, pp. 204-208.
- [18] Galitskov K.S., Samohvalov O.V. Strength properties of expanded clay and their reflection in the range of various temperature modes of three supporting cross-sections of kiln. *Promyshlennoe i grazhdanskoe stroitelstvo [Industrial and Civil Engineering]*, 9, 2015, pp. 91—94.
- [19] Vorobyov V.A., Ilyukhin A.V., Kolbasin O.M., Popov V.P. Automating preparation of concrete mixtures and manufacturing of reinforced-concrete products and structures. Publishing House of the Russian Academy of engineering, 2016, 660 p.
- [20] Vorobyov V.A., Ilyukhin A.V., Kolbasin O.M., Popov V.P. Automating the production of concrete mixtures for road construction. Publishing House of the Russian Academy of engineering, 2014, 420 p.
- [21] Rapoport, E.Ya., Pleshivtseva Yu.E. Optimal control of thermal management of induction heating. Moscow, Science, 2012, 309 p.

Development of Human Balance Capability Testing Prototype

Aleksandrs Gorbunovs, Zanis Timsans, Atis Kapenieks, Rudolfs Gulbis

Riga Technical University, Distance Education Study Centre¹, Address: Kronvalda Blvd.1, Riga, LV-1010, Latvia

Abstract. The detection of human balance functional disorders may provide some kind of awareness or even warning about potential problems for human health both in organs responsible for ensuring the balance function and in organs related to fulfilment of other important life functions. Modern world offers some sophisticated solutions which enable not only determination of the human balance functional capacity but also offer some kind of training environment to provide corresponding rehabilitation. Unfortunately, such systems are very expensive. And this make limitations of their accessibility and practical usability for a wide range of the target group / population. Software solutions, including mobile applications, on the other hand, are incomparably cheaper. However, they do not allow to make precise balance capability measurements, limiting to simplified balance retention simulators.

During implementation of the Latvian National State Research Program VPP INOSOCTEREHI from 2015 to 2017 three human balance capability testing prototypes were developed using a variety of electronic and mechatronic solutions. The last one was successfully approbated during two pilots in Latvian schools in 2016 and demonstrated at the International Invention and Innovation Exhibition MINOX-2016. This paper analyses benefits and disadvantages of approaches used in creating of these prototypes. Besides, authors make initial comparison of developed third prototype version against the BioSway system offered in the market. The paper gives also insight into particular system interface development and new effective graphic portrayal of the balance testing output data, as well as sets the goals for further possible commercialization of the developed balance testing prototype.

Keywords: balance disorder; circuit; microcontroller; sensor.

I. INTRODUCTION

Modern society benefits from innovations in technology. Life expectancy is growing due to advances in medical, care and rehabilitation services. However, about one billion people, according to the World Bank and World Health Organization report, suffer from different kinds of disabilities [1], [2]. Each year this number increases. One part of persons with disabilities are born with the hereditary illnesses and functional disorders, but another one – got disability during life: due to some illnesses or at work; for example, approximately 3 per cent of employees in Europe got injured at the workplace [3]. World countries are faced with more than 9 health year losses in an average caused due to population disabilities and chronic illnesses [4]. State and local authorities take measures to reintegrate these people into work and society activities, enhance social inclusion processes [3]. Moreover, the world population is aging. This phenomenon impacts their ability to walk, care themselves, actively participate in everyday activities. It means that also this social group requires society attention and care.

In many cases functional disorders and injuries restrict ability of persons with disabilities to be involved in society activities, and decrease their life quality. Walking and postural ability trainings

become essential, especially for elderly people and persons after stroke [5].

Social rehabilitation ought to be considered as the key component to improve the quality of life of elderly people, persons with disabilities and special needs. Taking into account that many physical disabilities and illnesses are closely tied with central nervous system functionality, and postural stability in particular [6], the human balance capability assessment equipment could be considered as the one of the tools which may help in early diagnosis of possible functional disorders.

At the moment, the industry offers a variety of systems and tools which can test patient postural stability. Unfortunately, they are rather expensive to be used in all involved respective rehabilitation organisations. This make limitations of their accessibility and practical usability for a wide range of the target group / population.

Software solutions, including mobile applications, on the other hand, are incomparably cheaper. However, they do not allow to make precise balance capability measurements, limiting to simplified balance retention simulators.

Our aim is to propose solutions and ensure development of portable, efficient and low-cost human balance disorder assessment equipment which

would be accessible for the wide range of social groups not only at the rich medical centres, but also at all public and private medical, social rehabilitation and care organisations, schools, sport teams, army bases, and even at home.

II. MATERIALS AND METHODS

In order to reach defined goals, we have investigated the newest technical solutions which were implemented or offered for implementation in practice. Existing commercial systems and mobile applications were also studied. These findings helped us to develop a few human balance disorder assessment prototype models.

It was found that one of the most important market leaders in balance assessment field is the Biodex company. In particular, its Biosway system allows assessing person's balance capability rather precise [7]. It includes balance assessment part, consisting of the balance board with the hard and foam surfaces and the monitor to follow up on exercise implementation process and results. Training via gaming modes are also included. The system provides reporting about fulfilled tests. System's disadvantage – its expensive cost.

The Nintendo Wii Balance Board, mainly known as a gaming console, due to embedded pressure sensors, may also serve as an equipment for balance disorders assessment, postural stability training and improvement [8], [9]. Video games in combination with postural stability exercises in a form of physical activities, so called – exergaming, can improve human balance capabilities. Especially it applies for elderly people [10]. Despite apparent advantages this system has also some limitations in hardware and software caused by its commercial base.

One of promising findings and developments in the field of balance disorder assessment in a form of the balance board device for home care and exergaming was presented by Italian researchers [11], [12], who demonstrated very encouraging results in rehabilitation of post-stroke patients. However, still there is a set of research directions to be covered in order to solve early balance disorder assessment problem, for instance, availability to assess possible postural sways by appropriate scientifically recognized tests [13], use of different foam pads, ensure patient safety and stability during exercises.

Available on the market mobile applications, such as iBEST and similar ones [14], offer various ways to train personal balance capability. They successfully utilize potentialities of built-in sensors to determine possible balance disorders, monitor test, exercise or game fulfilment and provide feedback. Though, the validity of obtained postural sway data by mobile applications needs to be improved in order to give for a patient credible recommendations regarding further rehabilitation and / or visiting a doctor.

Pursuant to abovementioned considerations it was decided to start development of the new balance capability testing prototype. It ought to be rather inexpensive, easy to use, and ensure efficient postural sway detection.

Necessary programming tools for the prototype creation were chosen from available open source software in order to decrease project expenses. Wooden materials were used to create three prototype constructions. Used materials, including electronics, are shown in the next section together with the description of developed models and achieved results.

Developed prototypes were approbated in test-beds at the university and the first trials in schools, as well at the international exhibition. Obtained feedback and lessons identified gave the directions for further improvements.

Human balance assessment was made by employing Modified Clinical Test of Sensory Organization and Balance (mCTSIB) test [15] series. Test results were collected and displayed in graphs.

III. RESULTS AND DISCUSSION

Altogether three different types of human balance testing boards were developed from 2015 to 2017 by researchers of Riga Technical University. Initially two balance functional capability diagnostic and improvement system prototype versions (based on employing of joystick and potentiometer sensors in conjunction with microcontrollers Arduino and other necessary electronics, such as signal amplifiers) were developed during the year of 2015.

However, both models did not allow getting enough reliable statistical data which would be comparable with existing solutions in balance testing field, such as data obtained by BioSway and similar systems. As a result, it was decided to find new solutions which were realized in development of the third version of the prototype in 2016 as well as further updates and improvements in 2017. All created balance testing systems included balance board platform with embedded electronic equipment. The persons being tested were asked to stand on these boards and accomplish certain balance testing tasks. Next subsections give an overview of developed prototype models.

A. *The first, mini joystick based, model*

In the first created model (Fig. 1) the mini joystick was used as an information reader. Operating principle – mechanical movements in horizontal (X) and vertical (Y) axes were transferred into electrical signals. It allowed reading the surface shift from rotation axes. Principal scheme included microcontroller Arduino Uno and joystick linkage according recommendations provided by microcontroller producer [16].

However, the system repeatability was concluded as moderately complicated. The problem emerged

due to difficulties to create rotation axes frame of the movable platform.

During experiments it was concluded that the shift of motion axes is too small to provide reliable enough data quantity for the joystick movements to obtain significant readable data. Besides, it was recognized that the problems with mechanical strength of the joystick could create additional problems for the long-term exploitation.

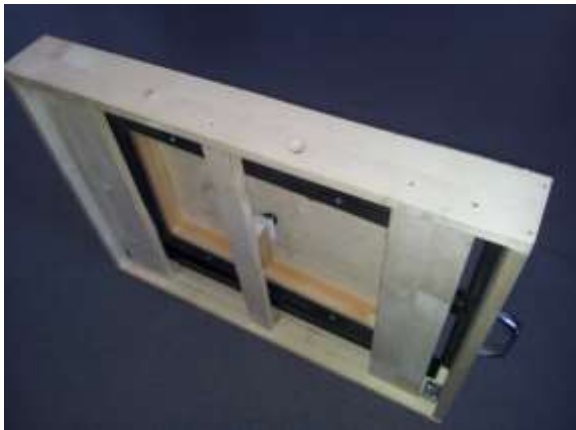


Fig. 1. Joystick mounted into the rotation centre of the platform

B. The second, potentiometers based, model

In the developed second prototype model the joystick was substituted by potentiometers which were mounted in rotation axes of the platform. The platform was taken from the first prototype model. Principal scheme included microcontroller Arduino Uno and potentiometers connection according recommendations provided by microcontroller producer [16]. To achieve the aim of diagnosis and improvement of person balance functional capabilities, consequently, for person's motion recording, the respective potentiometer mechanical transmission mechanism was implemented in this prototype model. In order to maximize the amount of movement in rotation axes, mechanical gear transmission was set with a coefficient 1:4. Practical development of the model and its realization led to the consideration that the complexity of system creation is too big, but system resistance against external electromagnetic impacts is rather high.

Taking into account recognized shortcomings of the first two developed prototype models in a prospective case of the wide spread out and massive implementation of such systems in social rehabilitation, it was decided to start development of the third prototype version of balance diagnostic and improvement system, based on utilization of the load sensor capacities. Comparative assessment of developed prototype models was made, analysing their mechanical repeatability, signal resistance against external electromagnetic impacts, mechanical strength, and system components risks (Table 1).

Table I
Comparative parameters of the developed balance testing models

Factors	Model 1	Model 2	Model 3
Type	Mechanical	Mechanical	Piezoelectric
Reader	Joystick	Potentiometers	Pressure sensors
Mechanical repeatability	Moderate complex	Complex	Simple
Signal resistance against external electromagnetic impacts	High	High	Low
Mechanical strength	Moderate	Moderate	Moderate
System components risks	Creation of mechanical part	Creation of mechanical part	Purchase of tensor sensor's amplifier; system shielding

C. The third, load sensor based, model

We decided to choose four load sensors (tenzoresistors), mounted in balance testing board platform (a simple 2.5 cm thick particleboard plywood) and connected with Arduino Uno microcontroller and signal amplifiers, as these sensors are the most widely used devices for deformation measurement. To secure a place for the circuit of microcontroller and amplifiers, a special recess at the bottom of the plywood was milled hiding all sensitive parts of the system. In order to manage and monitor balance tests, the circuit of four tenzoresistors, two amplifiers and one microcontroller was connected to a laptop through USB port; this also ensured power supply for the whole system.

Operating principle of tenzoresistors is based on the electrical resistance of the driver reliance on cross-sectional area changes to mechanical deformation. Usually electrical conductor (metal wire) is glued with an insulating adhesive to the deformable material. At the loading, the material is deformed together with the adhesive layer and the electrical conductor. Deformation size shall be determined by measuring the electrical conductor resistance changes.

Further research showed, that for successful determination of the sensor output signal, tenzoresistors are connected in a certain circuit. For example, in digital scales, to determine the resistance changes, as the most common case, the resistive Wheatstone bridge circuit is used (Fig. 2).

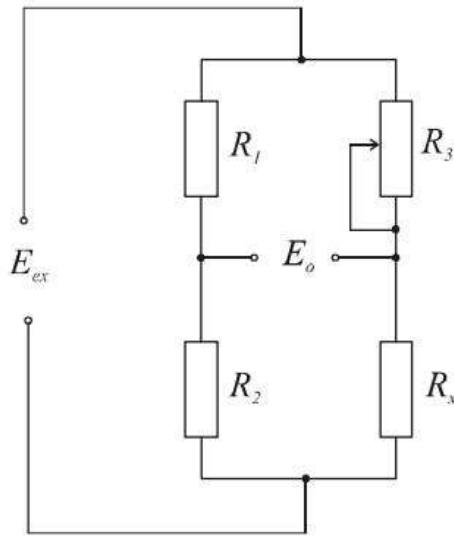


Fig. 2. Resistive Wheatstone bridge circuit

Resistive bridge theory is based on the voltage divider principles. Bridge circuit basis consists of four resistors R_1 , R_2 , R_3 un R_X . Resistors R_1 and R_2 usually has a high accuracy with known values, R_3 – with variable resistance, and R_X – with unknown resistance, which is associated with measurement transducer outputs. The voltage E_{ex} is connected for the bridge feeding, and the bridge is balanced with the resistor R_3 .

Using a multi-meter, electrical signal changes, which depend on the applied pressure, were measured. During our findings, as it was expected, we realized that the resulting signal was weak (a few millivolts) and with a low power. To ensure that this signal could be used to regulate the processes, the signal should be amplified.

This problem was solved by adding two amplifiers HX711 to the microcircuit which took care of data storage, calculation and transmission, as well amplified and transformed the obtained signal. The functionality of amplifiers allowed not only to get and amplify data from different types of sensors, but also transform them into a digital format and further transfer to “Arduino Uno” microcontroller [17].

Initially it was argued that there would be a need for four amplifiers HX711 – one for each sensor. A reason for that was following: unlike commercial scales, where the main approach was based on an implementation of the Wheatstone bridge (Fig. 2) to obtain a single value or weight, in our case we had to obtain four different values which would help reproducing the movement in the coordinate plane. In this case, it would be necessary to place appropriate resistance for each sensor which could build a quarter-bridge circuit.

Realised experiments revealed a more effective way to achieve four different values. Since the obtained data in the case of implemented half-bridge circuit (Fig. 3) can be both a positive and a negative

numeral, depending on the sensor, which the power is exposed on ($\Delta R_1 = -\Delta R_3$), then these, now already two, values might be easily displayed on the coordinate plane as the X and Y positive and negative values, accordingly visualizing the movement on the plane.

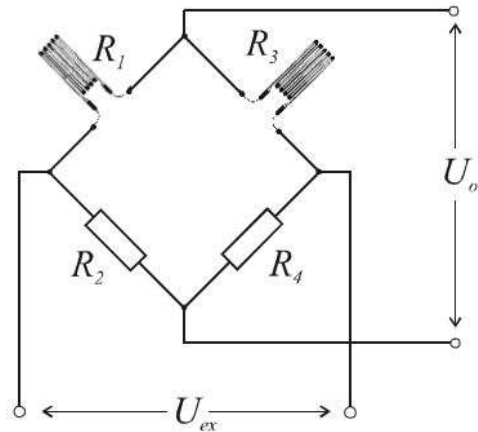


Fig. 3. Half-bridge circuit

Sensors were mounted into previously prepared particle plywood in the way to ensure that the volatility in coordinate plane could be determined as much effective as possible – each of them would give either a positive or negative value. To ensure reliability of measurement data while testing of heavy weight persons, each of four load sensors should be able to measure at least 50 kg. Since the sensor arrangement consisted of a relatively unstable surface, the safety was provided by fitting supporting legs at each corner, which had to facilitate and improve the use of the platform.

One of the most important things, which ought to be done, is the calibration of sensors by implementing of the HX711 calibration code, which is loaded into Arduino Uno micro-controller. During modification the code is adapted for the processing from the half-bridge circuit using two amplifiers instead of one. After processing of received signal the micro-controller sends it to computer, where it is further processed by the code, created by “Processing 3.0.2” open source programming tools, which helps to interpret the received values as a moving sphere in the coordinate plane (Fig. 5 and 6).

Since gained values could be either a positive or negative numbers, it was necessary to make appropriate modifications in the previously created program. It was crucial that its newly acquired values were able to reflect also on the negative axis direction. However, “Processing” desktop started displaying from zero in the positive direction. In this case, there was defined a new zero point, which was located in the middle of the desktop instead of in the upper left corner, as usually. As a result, this approach allowed us to reflect sphere’s movement also in the negative plane directions.

Before balance functions assessment the following personal data ought to be input in the system: name and surname, age, height, duration of the test, the number of repeatable tasks / measurements and the type of the test. This information is displayed on the laptop monitor during data input (Fig. 4).

After person's data input the balance testing can start (Fig. 5 and 6). The person is asked to fulfil certain four tasks according to Modified Clinical Test of Sensory Organization and Balance (mCTSIB) test modes which already approbated in many clinical studies demonstrating test's simplicity, accessibility, usability and efficiency in balance disorder measurements [15], [18], [19].

The duration of each of four tests is set for 30 sec, the number of tasks / measurements – four times, and the person is asked to keep the moving sphere in the centre of coordinate plane precisely as much as possible (Fig. 6 and 7):

- On a hard surface, eyes open;
- On a hard surface, eyes closed;
- On a foam surface, eyes open;
- On a foam surface, eyes closed.

Test fulfilment interface (Fig. 5) gives both for the patient and medical personnel a possibility to follow all tests paces. Moving sphere's trajectories are tracked by remaining colour traces in the circle. The interface has equipped with calibration, starting, test mode selection, data acquiring and exit buttons. It displays also the patient's name and test remaining time.

Fig. 4. Data input interface



Fig. 5. Test fulfilment interface

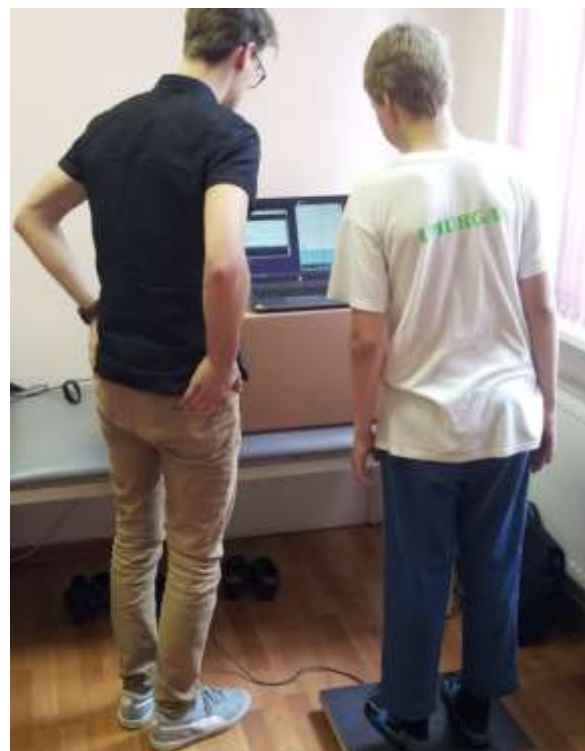


Fig. 6. Ongoing mCTSIB test

The resulting data can be summarized in the form of an Excel table (it has already carried out over two pilots / approbations as noted below in the next subsection) for further analysis and providing recommendations and guidance to the person being tested, as well to medical staff, parents and responsible personnel in educational organizations.

Balance test results already are visualized in order to make them more usable, tangible and understandable for immediate analysis of the balance capability at the test site.



Fig. 7. Data visualization

Test results (Fig. 7) are represented in the four graphs which show patient's test results in accordance with fulfilled mCTSIB test modes: on a hard surface – eyes open and eyes closed, and on a foam surface – eyes open and eyes closed. Each of fulfilled tasks is marked by the sway index. An average sway index also is shown – the smaller the better should be. For each of test mode corresponding measurement scale ought to be developed in the next project implementation phase, allowing detection of any balance disorder.

The first trials (40 tested persons) demonstrated system ability to detect balance sways depending on test mode and person's physical capabilities. However, further large scale pilots could bring more statistical data which would allow to draw conclusions and offer practical rehabilitation instrument to be used in social rehabilitation organisations, hospitals, schools, sport teams, armed forces and so on.

D.Approbation

In 2016 two approbation pilots of the developed balance testing prototype were launched in Latvian schools in 5 – 7 class pupil groups:

- 05.05.2016, in Riga Catholic Gymnasium (High School) 23 persons (22 pupils and 1 teacher) were tested;
- 26.05.2016, in Rezekne Speech Therapy Boarding Elementary School-Development Centre 17 pupils were tested.

Project group participated also in the International Invention and Innovation Exhibition MINOX-2016 in Riga in October 2016 providing valuable insight in the developed prototype capabilities. Moreover, in the fourth quarter of 2016 four broadcasts on Latvian National Television (LTV-7 Channel) were dedicated

to disseminate project results and demonstrate created equipment to a wider public.

Obtained approbation data at the first estimation confirm developed balance testing third version prototype's ability to achieve defined objectives. Moreover, it should be noted that our developed balance assessment prototype is able to perform also the tasks which cannot cope commercial and more expensive system BioSway – for example, testing persons with the weight less than 40 kg.

IV. CONCLUSIONS

Developed prototype offers fast, demonstrative and effective human balance capability assessment. The main aim of this balance testing prototype is the early raw detection of any balance disorder. Any deflection from pre-defined sway index scale intervals will serve as a basis to make recommendations for a patient to visit a doctor.

Test results highlighted the necessity to develop corresponding measurement interval scale which would give a message about possible balance disorder. Besides, it would be useful to find relationships and correlations between person's ability to keep the balance when different external disturbing factors influence test fulfilment.

Series production of the created prototype could decrease its costs. It might be about almost ten times cheaper than existing BioSway equipment which costs around USD 7 000. Affordable price can promote prototype employment in the wide range of organisations and even at home, and as result, enhance social rehabilitation services and improve quality of life of persons with balance function disabilities.

ACKNOWLEDGEMENTS

This study has been supported by the Latvian National Research Program "Innovative solutions in social rehabilitation in Latvian schools in the context of inclusive education" (in Latvian: „Inovātīvi risinājumi sociālajā telerehabilitācijā Latvijas skolās iekļaujošās izglītības kontekstā – VPP INOSOCTEREHI”); project No.2 „Development, approbation and implementation of new prototypes and innovative methodology (approaches, methods, techniques, ways) in social rehabilitation for the rendering of new services” (in Latvian: „Jaunu prototipu, inovatīvas metodikas (pieeju, metožu, tehniku, paņēmieni) sociālajā rehabilitācijā izstrāde, aprobācija un ieviešana jaunu pakalpojumu sniegšanai”). Contract No. 10-4/VPP-8-7 (RTU PVS ID 1868).

REFERENCES

- [1] World Health Organization, “Disability and rehabilitation: World report on disability,” WHO, 2017. [Online]. Available: http://www.who.int/disabilities/world_report/2011/en/. [Accessed Mar. 14, 2017].
- [2] World Health Organization and The World Bank, “World report on disability,” WHO and WB, p.325, 2011. [Online].

- Available:
<http://documents.worldbank.org/curated/en/665131468331271288/pdf/627830WP0World00PUBLIC00BOX361491B0.pdf>
.[Accessed Jan. 16, 2017].
- [3] W. Oortwijn, E. Nelissen, S. Adamini, S. van den Heuvel, G. Geuskens, L. Burdof, "Social determinants state of the art reviews - Health of people of working age - Summary Report," European Commission Directorate General for Health and Consumers, Luxembourg, p. 40, 2011.
- [4] [4] The World Bank, "World Report on Disability: Dataset," WB, 18 October, 2013. [Online]. Available: <http://data.worldbank.org/data-catalog/world-report-on-disability>. [Accessed January 16, 2017].
- [5] J.-M. Belda-Lois, S. Mena-del Horno, I. Bermejo-Bosch, J. Moreno, J. Pons, D. Farina, M. Iosa, M. Molinari, F. Tamburella, A. Ramos, A. Caria, T. Solis-Escalante, C. Brunner, and M. Rea, "Rehabilitation of gait after stroke: a review towards a top-down approach," *Journal of NeuroEngineering and Rehabilitation*, vol. 8, issue 1, article 66, Dec. 2011.
- [6] B. G. Travers, P. S. Powell, L. G. Klinger, M. R. Klinger, "Motor Difficulties in Autism Spectrum Disorder: Linking Symptom Severity and Postural Stability," *Journal of Autism and Developmental Disorders*, vol. 43, issue 7, pp. 1568–1583, July 2013.
- [7] Biodex Medical Systems, Inc., "Balance System SD and BioSway: Software Manual – User's Guide", Biodex, pp.1-64, 2016. [Online]. Available: http://www.biodex.com/sites/default/files/950440man_add_14074revb.pdf. [Accessed Mar. 14, 2017].
- [8] C. H. Shih, C. T. Shih, M. S. Chiang, "A new standing posture detector to enable people with multiple disabilities to control environmental stimulation by changing their standing posture through a commercial Wii Balance Board," *Research in Developmental Disabilities*, vol. 31, issue 1, pp. 281–286, Jan.-Feb. 2010.
- [9] R. A. Clark, A. L. Bryant, Y. Pua, P. McCrory, K. Bennell, & M. Hunt, "Validity and reliability of the Nintendo Wii Balance Board for assessment of standing balance," *Gait & posture*, vol. 31, issue 3, pp. 307-310, Mar. 2010.
- [10] P. Scaglioni-Solano, & L. F. Aragón-Vargas, "Validity and reliability of the Nintendo Wii Balance Board to assess standing balance and sensory integration in highly functional older adults," *International Journal of Rehabilitation Research*, vol. 37, issue 2, pp. 138-43, June 2014.
- [11] P. Arpaia, P. Cimmino, E. De Matteis, G. D'Addio. *A balance board device for home care telerehabilitation exergaming: XX IMEKO World Congress: Metrology for Green Growth*, Sep. 9–14, 2012, Busan, Republic of Korea.
- [12] P. Arpaia, P. Cimmino, E. De Matteis, G. D'Addio, "A low-cost force sensor-based posturographic plate for home care telerehabilitation exergaming," *Measurement*, vol. 51, pp. 400–410, May 2014.
- [13] H. S. Cohen & K. T. Kimball, "Usefulness of some current balance tests for identifying individuals with disequilibrium due to vestibular impairments," *Journal of Vestibular Research*, vol. 18, no. 5, 6, pp. 295-303, 2008.
- [14] A. A. Wai, P. D. Duc, C. Syin, H. Zhang. *iBEST: Intelligent balance assessment and stability training system using smartphone: Engineering in Medicine and Biology Society (EMBC): The 36th Annual International Conference of the IEEE*, pp. 3683 – 3686, Aug. 26-30, 2014, Chicago, USA.
- [15] M. K. Park, K.-M. Kim, J. Jung, N. Lee, S. J. Hwang, & S. W. Sung, "Evaluation of Uncompensated Unilateral Vestibulopathy Using the Modified Clinical Test for Sensory Interaction and Balance," *Otology & Neurotology*, vol. 34, issue 2, pp. 292-296, Feb. 2013.
- [16] Arduino, "What is Arduino?" Arduino, 2017. [Online]. Available: <https://www.arduino.cc/en/Guide/Introduction/>. [Accessed Feb. 1, 2017].
- [17] SparkFun, "SparkFun Load Cell Amplifier - HX711," SparkFun, 2016. [Online]. Available: <https://www.sparkfun.com/products/13230>. [Accessed June 7, 2016].
- [18] N. Murray, A. Salvatore, D. Powell, and R. Reed-Jones, "Reliability and Validity Evidence of Multiple Balance Assessments in Athletes with a Concussion," *Journal of Athletic Training*, vol. 49, no. 4, pp. 540–549, Aug. 2014.
- [19] A. Kaupuzs, V. Larins, & L. Rizakova. *Effects of Vestibular Exercises on Postural Balance for Children: International Scientific Conference "Society. Integration. Education (SIE-2016)*, vol. 3, pp. 453-463, Rezekne, May 27-28, 2016.

On a Mathematical Model Describing Optimal Processing Mechanism of Dispersed Granular Materials in Gravitational Flow with Horizontal or Inclined Vibrating Sieve Classifying Screens

Armands Grickus^{1,2,a}, Sharif E. Guseynov^{1,2,3,b}

¹Institute of Fundamental Science and Innovative Technologies, Liepaja University, Liepaja LV-3401, Latvia;

²Faculty of Science and Engineering, Liepaja University, 4 Kr.Valdemar Street, Liepaja LV-3401, Latvia;

³"Entelgine" Research & Advisory Co., Ltd., Kleistu Street 2-53, Riga LV-1067, Latvia;

^aarmands.grickus@liepu.lv, ^bsh.e.guseinov@inbox.lv

Abstract. *The investigation of motion and gravitational processing of disperse granular materials is very important for solution of a wide spectrum of technological processes, including the chemical technology of treatment (with or without the decoration-compression procedure) of granular mineral fertilizers and their drying and sorting/separation by means of vibrating sieve classifying screens, in particular. In this work, we have used the apparatus of the theory of continuous media for the mathematical modelling of dynamics of disperse granular materials, and by this we assume that a property of these materials is the distribution of a solid granular component inside of them. The elaborated mathematical model is based on the volume conservation law for granular components, on the momentum conservation law, as well as on the equations for stress tensor in the granular mineral fertilizers and equations for description of the Coulomb granular mineral fertilizers.*

Keywords: *dispersed granular material, gravitational flow, vibrating sieve classifying screen, continuum mechanics, mathematical model.*

I. INTRODUCTION

The investigation of the motion and mechanics of the gravitational processing of disperse granular materials is important for solution of a wide spectrum of technological processes, including the chemical technology of treatment (with or without the decoration-compression procedure) of granular mineral fertilizers and their drying and sorting/separation by means of vibrating sieve classifying screens, in particular. Apart from technological processes of different kind, the investigation of dynamics of disperse granular media is extremely important for solution of such problems as mineral extraction, engineering, geology – the motion and erosion of soils, in particular, and so on (for instance, see [1]-[7] and the references therein). Currently, there exist two methods for mathematical modelling of the dynamics of disperse granular materials: the first method – this is the consideration of disperse granular media on the level of separate unconnected, but interacting particles ([5], [7]); the second method – this is the consideration of this media from the point of view of continuum mechanics ([3], [4], [6]). When the first method of modelling is used, the flux of finite-size particles is considered, these particles being represented as rigid or elastic geometric figures, e.g., spheres, and it is

attempted to derive rules, describing the behaviour of the particle flux as a whole. Significant contributions to the theory of dynamics of disperse granular media have been provided in foreign works (see [8]-[15]) by Reynolds O., Faraday M., Deresiewicz H., Rowe P.W. and Winterkorn H.F., where problems related to artificially excited vibrations, as well as questions of different kind concerning the natural sand flow, have been investigated. Despite of these and other results and their interpretations, which have been obtained by experts in different fields in framework of the first method of modelling, up to now the mechanism of motion of disperse granular media have not provided a satisfactory explanation of many unusual phenomena, arising in motion of such media. When the second method of modelling is used, it is assumed that the properties of particle flux, considered as continuum, can be represented by continuous functions, in such way that any infinitesimal part of disperse granular medium has properties of each separate particle. For example, those mathematical models, which use the apparatus of plasticity theory, are based on criteria of Coulomb-Mohr fluidity; those mathematical models, which use the apparatus of the theory of fluidized boiling beds, are based on thermodynamic principles for particle distribution in bulk, and so on. In this work, the apparatus of

ISSN 1691-5402

© Rezekne Academy of Technologies, Rezekne 2017
<http://dx.doi.org/10.17770/etr2017vol3.2547>

continuum mechanics we will use for elaboration of corresponding mathematical models, describing the dynamics of disperse granular materials.

II. MATHEMATICAL MODELLING

A. The volume conservation law for granular components and the momentum conservation law

As it was stated in the introduction, we will investigate the dynamics of disperse granular media in gravitational flows from the point of view of continuum mechanics and, hence, we can state that the property of a disperse granular material is the presence of solid granular component, distributed inside of it. Therefore, to take into account the distribution of solid phase in bulk of a continuous granular body (we denote this body by D_{solid}), we have to introduce the bulk distribution function $U = U(x, y, z; t)$, which is a kinematic variable and is continuously defined in the whole region occupied by the body. This function can be interpreted as the porosity, i.e. as the volume fraction of empty spaces (relative free volume), although in reality it is the inverse of this volume fraction. The introduced here function $U(x, y, z; t)$ can be defined as $U(x, y, z; t) = 1 - \Pi(x, y, z; t)$, where $\Pi(x, y, z; t)$ denotes the porosity. Obviously, the volume of the granular components in the body D_{solid} can be defined by the formula

$$V_{\text{granule}}(t) \stackrel{\text{def}}{=} \int_{D_{\text{solid}}} U(x, y, z; t) dv. \quad (1)$$

Introducing the notion of mass density $W(x, y, z; t)$ of granular components, we can determine the total mass M_{granule} of granular components in the body D_{solid} by the formula

$$M_{\text{granule}}(t) \stackrel{\text{def}}{=} \int_{D_{\text{solid}}} U(x, y, z; t) \cdot W(x, y, z; t) dv, \quad (2)$$

where $\rho_{\text{v.d.}}(x, y, z; t) \stackrel{\text{def}}{=} U(x, y, z; t) \cdot W(x, y, z; t)$ is the volume density of the investigated disperse granular medium. Further on, since we consider the investigated disperse medium as a continuous media, the mass of the interpore space in the body D_{solid} is negligibly small. Consequently, the total mass $M_{\text{granule}}(t)$ of the granular components can be considered as the total mass of the granular material and, therefore, the following continuity equation for the considered granular material can be obtained from the equation (2):

$$\frac{\partial \rho_{\text{v.d.}}(x, y, z; t)}{\partial t} = -\rho_{\text{v.d.}}(x, y, z; t) \operatorname{div}(\vec{\mathcal{G}}(x, y, z; t)), \quad (3)$$

where $\vec{\mathcal{G}} = \vec{\mathcal{G}}(x, y, z; t)$ is the spatial vector of the velocity with three Cartesian components \mathcal{G}_x , \mathcal{G}_y , \mathcal{G}_z ; and $\operatorname{div}(\vec{\mathcal{G}}(x, y, z; t))$ is the divergence of the vector field $\vec{\mathcal{G}}$.

Remark 1. If the granular components (in our case the granular mineral fertilizers) of the body D_{solid} are incompressible, then mathematically it means that $\frac{\partial W(x, y, z; t)}{\partial t} = 0$ holds. Consequently, in this case the equation

$$\frac{\partial U(x, y, z; t)}{\partial t} = -U(x, y, z; t) \cdot \operatorname{div}(\vec{\mathcal{G}}(x, y, z; t)), \quad (4)$$

which describes the volume conservation law for the granular components in the body D_{solid} , must be used instead of (3).

It has to be noted that the conservation law (4) can be derived directly from (1). In addition, it is important to notice that, although the volume of granular components is constant, the total volume needs not to be constant, i.e. the total volume can be varied: the positive/negative dilatancy (it is the increase or decrease of the volume at shear deformation) can serve as a natural example in disperse systems of high concentrations, for example, in natural fertilizers. Consequently, in equation (4), as well as in equation (3), $\operatorname{div}(\vec{\mathcal{G}})$ needs not to be zero. Further on, since the total mass of granular mineral fertilizers is calculated from (2), we can write the momentum conservation law in the form of

$$\rho_{\text{v.d.}}(x, y, z; t) \cdot \left(\frac{\partial \vec{\mathcal{G}}(x, y, z; t)}{\partial t} - \vec{F} \right) = \operatorname{div}(\vec{\sigma}(x, y, z)) \quad (5)$$

or componentwise in the form of

$$\rho_{\text{v.d.}}(x, y, z; t) \cdot \left(\frac{\partial \mathcal{G}_i(x, y, z; t)}{\partial t} - F_i \right) = \sigma_{ij,j},$$

where $\vec{\sigma}$ is the Cauchy stress tensor with nine direct and tangential stresses $\sigma_{xx} = \sigma_{11}$, $\sigma_{xy} = \sigma_{12}$, $\sigma_{xz} = \sigma_{13}$, $\sigma_{yx} = \sigma_{21}$, $\sigma_{yy} = \sigma_{22}$, $\sigma_{yz} = \sigma_{23}$, $\sigma_{zx} = \sigma_{31}$, $\sigma_{zy} = \sigma_{32}$, $\sigma_{zz} = \sigma_{33}$; \vec{F} is the vector of mass forces with Cartesian components $F_x = F_1$, $F_y = F_2$, $F_z = F_3$; and the covariant derivative is expressed by $\sigma_{ij,j}$.

B. Equation for the stress tensor in granular mineral fertilizers

In this subsection, we will consider stresses in the case of non-dissipative granular medium, as well as in the case, where this media is dissipative, i.e. when the energy of ordered macroscopic motions or fields transforms irreversibly into the energy of disordered (i.e. chaotic) motions or fields. Let us assume that specific Helmholtz free energy $A_{H.f.e.}$ of granular mineral fertilizers depends on the bulk distribution function $U(x, y, z; t)$ and on its time derivative, as well as on the density of granular components of the body D_{solid} and temperature T , i.e.

$A_{H.f.e.} = A_{H.f.e.}\left(U, \frac{\partial U}{\partial t}, \rho_{v.d.}, T\right)$. We can now introduce from thermodynamic considerations the following dynamic quantities:

– pressure $P_{m.p.}$ of the investigated disperse granular media :

$$P_{m.p.} \stackrel{def}{=} U \cdot W^2 \cdot \frac{\partial A_{H.f.e.}}{\partial W}; \quad (6)$$

– spatial pressure $P_{s.p.}$, which is related to the distribution of granular components in the bulk:

$$P_{s.p.} \stackrel{def}{=} U^2 \cdot W \cdot \frac{\partial A_{H.f.e.}}{\partial U}; \quad (7)$$

– effort vector $\vec{f}_{e.v.}$, which is the vector of the balancing stress (as it is related to the system of self-balancing forces, applied either at the pressure centre or shift centre; see e.g. [1]):

$$\vec{f}_{e.v.} \stackrel{def}{=} U \cdot W \cdot \frac{\partial A_{H.f.e.}}{\partial U}. \quad (8)$$

Then, from thermodynamic considerations, we can write

$$P_{m.p.} \stackrel{def}{=} U \cdot \text{div}(\vec{f}_{e.v.}) = P_{s.p.} - P_{m.p.}. \quad (9)$$

Equation (9) is a fundamental equation and, being determined by expressions (6)-(8), the dynamical quantities $P_{m.p.}$, $P_{s.p.}$, $\vec{f}_{e.v.}$ characterize just the non-dissipative part of the stress

$$\vec{\sigma}^* \stackrel{def}{=} U \cdot \text{div}(\vec{f}_{e.v.}) - P_{s.p.} \cdot \vec{I} - \vec{f}_{e.v.} \otimes \text{grad}(U), \quad (10)$$

where the symbol \otimes means the tensor product; the spatial gradient of the scalar function

$U = U(x, y, z; t)$ is denoted by $\text{grad}(U)$. It follows from the equation (10) and expressions (6)-(8) that the stress is completely determined by Helmholtz energy function in the non-dissipative case: this fact is analogous to the corresponding relation for the equilibrium stress in compressible fluids.

Now, in order to determine the dissipative part of the stress in granular mineral fertilizers, we will use the corresponding equation from the theory of viscous liquid:

$$\vec{\sigma} - \vec{\sigma}^* = \nu_1 \text{tr}(\mathcal{G}_{s-t.}) \vec{I} + 2\nu_2 \mathcal{G}_{s-t.}, \quad (11)$$

where $\mathcal{G}_{s-t.}$ is the strain-rate tensor, determined as the symmetrical part of the spatial gradient of velocities; the notion $\text{tr}(\mathcal{G}_{s-t.})$ means the trace of the tensor $\mathcal{G}_{s-t.}$ of the second rank (one time covariant rank and one time contravariant rank); quantities $\nu_1 = \nu_1(U, W)$ and $\nu_2 = \nu_2(U, W)$ are viscosity coefficients.

C. Equation for the description of Coulomb granular mineral fertilizers

The obtained in the previous subsection equation (10) is the general equation for the non-dissipative part of the stress, and just because of this general form it cannot be used for solution of the actual problem: precise expressions are necessary for pressures $P_{m.p.}$ and $P_{s.p.}$, as well as for the balancing vector of stresses $\vec{f}_{e.v.}$. In this section, the required expressions will be obtained. For this purpose, we will assume that specific Helmholtz energy per unit volume $U \cdot W \cdot A_{H.f.e.}$ is an isotropic function (i.e. it is a tensor function, the symmetry group of which agrees with complete orthogonal group; tensor function – it is a mapping, relating several tensors of different ranks to one tensor of certain rank), which can be expanded in Taylor series in vicinity of $\text{grad}(U)|_{U=U_{l.d.}} = 0$, where $U_{l.d.}$ is the limiting

distribution in bulk, which corresponds to the limiting relative fraction of empty spaces in granular mineral fertilizers (the limiting relative fraction of empty spaces in granular mineral fertilizers corresponds to such a state, where volume does not change under shear action; some kinds of granular mineral fertilizers, having larger or smaller relative fraction of empty spaces as compared to its critical value, correspondingly decrease or increase their volume under the shear action, see Remark 1). In addition, we assume that the deviation of $\|\text{grad}(U)\|$ from zero and the deviation of quantity U from $U_{l.d.}$ is negligibly small. Consequently, within accuracy up to

terms of the third and higher orders of smallness we can expand the function $U \cdot W \cdot A_{\text{H.f.e.}}$ as follows:

$$U \cdot W \cdot A_{\text{H.f.e.}} = \sum_{i=0}^2 c_i \cdot (U - U_{\text{l.d.}})^i + c_3 \cdot \text{grad}(U) \cdot \text{grad}(U_{\text{l.d.}}), \quad (12)$$

where $c_i = c_i(U, U_{\text{l.d.}})$, $i = \overline{1, 3}$.

In view of the natural requirements of positiveness of the Helmholtz energy $U \cdot W \cdot A_{\text{H.f.e.}}$ per unit volume and of its minimum at the condition $\text{grad}(U)|_{U=U_{\text{l.d.}}} = 0$, we can write down the following restrictions for the coefficients c_i , $i = \overline{0, 3}$:

$$c_1 = 0, \quad c_i \geq 0, \quad i \in \{0, 2, 3\}. \quad (13)$$

Now, substituting the expansion (12) with coefficients (13) into expressions (6)-(8), we obtain:

$$P_{\text{m.p.}} = \left(W \cdot \frac{\partial \xi}{\partial W} - \xi \right) \cdot (\text{grad}(U))^2 + W \cdot \frac{\partial \xi_0}{\partial W} - \xi_0, \quad (14)$$

$$P_{\text{s.p.}} = -\eta_0 + \eta \cdot U^2 - \xi \cdot (\text{grad}(U))^2, \quad (15)$$

$$\vec{f}_{\text{e.v.}} = 2 \cdot \xi \cdot \text{grad}(U), \quad (16)$$

where the following notations are used:

$$\left. \begin{aligned} \xi_0 &= c_0 + c_2 \cdot (U - U_{\text{l.d.}})^2, \\ \eta_0 &= c_0 + c_2 \cdot U_{\text{l.d.}}^2, \\ \xi &= c_3, \quad \eta = c_2. \end{aligned} \right\} \quad (17)$$

Equation (10) for the stress in non-dissipative situation together with equations (14) and (16) require that non-dissipative direct and tangential stresses, which act on certain area at some point, have a special mutual relation. Note that in the hydrostatics, where the tangential stress must be completely absent, a similar result takes place.

At non-dissipativeness of the considered granular media, the tangential stress has a characteristic nonzero value, which is related to the value of the direct stress. In order to establish this relation mathematically, we will consider an arbitrarily chosen and fixed spatial point and an arbitrary fixed plane with the normal \vec{n}_{out} . Taking into account the equations (10) and (16), the direct stress $\vec{\sigma}$, acting on the fixed plane, is calculated by the following formula:

$$\vec{\sigma} = \vec{n} \cdot (\vec{\sigma}^* \cdot \vec{n}) = -P_{\text{m.p.}} - 2 \cdot \xi \cdot (\text{grad}(U) \cdot \vec{n}). \quad (18)$$

The determined by formula (18) direct stress $\vec{\sigma}$ is related to the tangential stress $\vec{\sigma}_{\text{tang.}}$, acting on the same area, by the following rule:

$$\begin{aligned} \vec{\sigma}^2 + \vec{\sigma}_{\text{tang.}}^2 &= (\vec{\sigma}^* \cdot \vec{n})^2 = P_{\text{m.p.}}^2 + \\ &4 \cdot \xi \cdot P_{\text{m.p.}} \cdot (\text{grad}(U) \cdot \vec{n})^2 + \\ &4 \cdot \xi^2 \cdot (\text{grad}(U))^2 \cdot (\text{grad}(U) \cdot \vec{n})^2. \end{aligned} \quad (19)$$

Now, using expressions (18) for exclusion of the term $(\text{grad}(U) \cdot \vec{n})^2$ in equation (19) and keeping squares in the final expression, we obtain the following relation:

$$\vec{\sigma}_{\text{tang.}}^2 + (\vec{\sigma} - \omega)^2 = r^2, \quad (20)$$

with the introduced here notations

$$r \stackrel{\text{def}}{=} \xi \cdot (\text{grad}(U))^2, \quad \omega \stackrel{\text{def}}{=} -P_{\text{m.p.}} - r. \quad (21)$$

Further on, taking into account equation (14), the second relation in (21) for the pressure $P_{\text{m.p.}}$ takes the following form:

$$r = \lambda \cdot (\beta - \omega), \quad (22)$$

$$\frac{1}{\lambda} \stackrel{\text{def}}{=} \frac{W}{\xi} \cdot \frac{\partial \xi}{\partial W}, \quad \beta = \xi_0 - W \cdot \frac{\partial \xi_0}{\partial W}. \quad (23)$$

Finally, comparing the expressions (20) and (22), we will find the required relation between the tangential stress $\vec{\sigma}_{\text{tang.}}$ and the direct stress $\vec{\sigma}$, acting on the considered area in the given point of granular mineral fertilizers in the state of non-dissipativeness.

Remark 2. If $\vec{\sigma}$ and $\vec{\sigma}_{\text{tang.}}$ are considered as Cartesian coordinates, then the equation (20) represents a circle with centre at the point $(0, \omega)$ and radius r . Besides, the requirement that the radius of this circle must be a function of the shift of its centre from the origin of the coordinate system follows from equation (22), which has been obtained from (20), taking into account (14). If equation (22) is chosen as the necessary and sufficient condition of the non-dissipativeness of the media, then this result can be considered as a generalization of the Coulomb condition on stresses at the limiting equilibrium in granular mineral fertilizers, in which the angles of internal friction and bonding are functions of density W and bulk distribution function U . Finally, note that in the case if quantities λ and β , determined by formulas (23), are constant, equation (22) becomes an equation of straight line, whereas equation of circle

(20) transforms into the usual Coulomb-Mohr condition, which is well known as the criterion of fluidity. In this case, the Mohr's circle (20) is tangent to the straight line (22); the scalar functions ξ_0 , ξ , η_0 and η , given by formulas (17), can be easily found from the differential equations (23). For example, if η_0 is a constant, then the relation $\eta_0 = \beta$ follows from the system of equations, consisting of the second formula in (23) and of the first and the third formulas in (17). Its physical interpretation is the following: η_0 corresponds to the bonding of the granular mineral fertilizer and is a strictly positive quantity due to the condition (13) and formulas (17). Thus, if the system of equations, consisting of (10), (11), (15), (16) and the Coulomb condition, is used for representation of the stress tensor in the non-dissipative case, then the general determining equation has the form:

$$\left. \begin{aligned} \mathcal{G}_{\text{strain-rate tensor}} \neq 0 \Rightarrow: \\ \bar{\sigma} = \nu_1 \cdot \text{tr}(\mathcal{G}_{\text{s.r.t.}}) \cdot \vec{I} + 2 \cdot \nu_2 \cdot \mathcal{G}_{\text{s.r.t.}} - \\ 2 \cdot \xi \cdot \text{grad}(U) \otimes \text{grad}(U) + (\eta_0 - \eta \cdot U^2 + \\ \xi \cdot (\text{grad}(U))^2 + 2 \cdot U \cdot \text{div}(\xi \cdot \text{grad}(U))) \cdot \vec{I}; \\ r = \lambda \cdot (\beta - \omega). \end{aligned} \right\} (24)$$

The medium, described by equations (24), is called Coulomb granular material.

D. The basic mathematical model of the dynamics of unconnected Coulomb granular materials (with granular mineral fertilizers as an example) with constant density in the regions of dissipative medium.

In this subsection, the dynamics of unconnected Coulomb granular mineral fertilizers is considered with constant density $W(x, y, z; t) \equiv \text{const}$ in the regions, where the medium is not in the state of non-dissipativeness. First of all, we note that the non-connectedness of granular materials (in our case Coulomb granular mineral fertilizers) in mathematical notions means that $\beta = \eta_0 = 0$ holds. Obviously, quantities, characterising the investigated here materials in such regions, are the functions ξ and η . Consequently, the general determining equation (24), which has been obtained in the previous subsection, takes the following form:

$$\left. \begin{aligned} \bar{\sigma} = \nu_1 \cdot \text{tr}(\mathcal{G}_{\text{s.r.t.}}) \cdot \vec{I} + 2 \cdot \nu_2 \cdot \mathcal{G}_{\text{s.r.t.}} - \\ 2 \cdot \xi \cdot \text{grad}(U) \otimes \text{grad}(U) - (\eta \cdot U^2 - \\ \xi \cdot (\text{grad}(U))^2 - 2 \cdot U \cdot \text{div}(\xi \cdot \text{grad}(U))) \cdot \vec{I}; \\ r = -\lambda \cdot \omega. \end{aligned} \right\} (25)$$

The obtained equation (25) is a dynamic relation for the tensor of stresses. The substitution of the equation (25) into the momentum balance equation (5) gives us the following differential equation:

$$\begin{aligned} \rho_{\text{v.d.}} \cdot \frac{\partial \vec{g}}{\partial t} = -\eta \cdot \text{grad}(U^2) + \\ 2 \cdot \xi \cdot U \cdot \text{grad}((\text{grad}(U))^2) + \\ (\nu_1 + \nu_2) \cdot \text{grad}(\text{div}(\vec{g})) + \\ \nu_2 \cdot (\text{grad}(U))^2 + \rho_{\text{v.d.}} \cdot \vec{F}. \end{aligned} \quad (26)$$

The system of equations, consisting of the equations (4), (5) and (26), describes the cases, where the medium is not in the state of equilibrium, i.e. when it is the dissipative medium. If one analysis the dimensions of differential equations (26) (the equation (26) is a tensorial differential equation and, consequently, it does not consist of a single equation), then it becomes clear that, in addition to the usual dimensionless quantities, appearing in the theory of viscous fluids, it is necessary to consider two extra dimensionless parameters:

- the dimensionless parameter L , which is called the relative length and is defined as the characteristic geometric size ℓ , normalized to the characteristic length of the material, i.e.

$$L \stackrel{\text{def}}{=} \ell \cdot \sqrt{\frac{\eta}{\xi}}; \quad (27)$$

- the dimensionless parameter

$$M \stackrel{\text{def}}{=} \frac{W \cdot g \cdot \ell}{\eta}, \quad (28)$$

where g is gravitational acceleration; the meaning of parameter M - this is the ratio of gravitational forces and forces, responsible for the spatial distribution of granular mineral fertilizers in bulk.

For mathematical completeness and correctness of the elaborated mathematical model (4), (5), (26), it must be completed with the allowed boundary conditions, which ensure the existence (the question of solvability) and uniqueness of the solution. Conditions on the basic variable fields U and W , fluxes $\vec{\sigma}$ and $\vec{f}_{\text{e.v.}}$, or on their combination can be used as boundary conditions. For example, the boundary conditions for fluxes

$$\left. \begin{aligned} \vec{\sigma} \cdot \vec{n} = \vec{h}; \\ \vec{f}_{\text{e.v.}} \cdot \vec{n} = \tau \end{aligned} \right\} \quad (29)$$

can be used, where \vec{h} is the usual effort vector and τ is the tension, which is related to the vector of stresses. It should be noted here that, since the tension τ refers to the system of self-balancing forces, the resulting forces are vanishing on the surface and, consequently, there is no need to set $\tau=0$ in the case where free surface is present. However, one should be also noted that the balancing tension is related to the surface energy per unit area, and it influences the effect of surface tension. In the case if both the balancing tension τ and the effort vector \vec{h} are zero on the boundary, such a boundary is called tension-free boundary.

III. NUMERICAL EXPERIMENT

Carrying out the numerical experiment, a two-phase medium of homogeneous solid particles sized 0.5-10 mm was chosen as the granular medium, in which the granular medium is a dispersed phase, and the dispersion phase is liquid. To simplify the mathematical model (4), (5), (26), (29), the corresponding technological process was considered only on the plane design mesh (see Fig. 1) under the condition that the technological process proceeds at invariable geometry of the inclined vibration classifier, at isothermal conditions and at absence of chemical reactions..

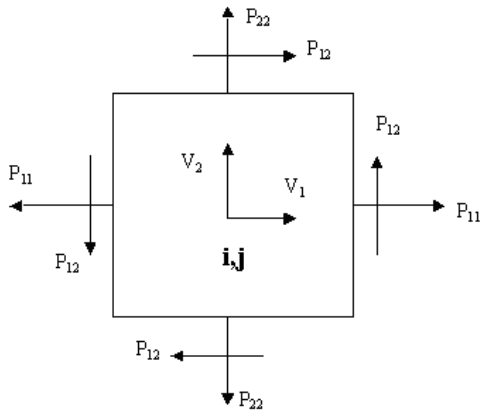


Fig. 1. Plane design mesh for coarse particle of granular dispersion medium.

After taking into account aforesaid suggestions we have got the following simplified mathematical model ($i = 1, 2; j = 3 - i$):

$$\frac{\partial \mathcal{G}_{i1}}{\partial t} + \mathcal{G}_{i1} \cdot \frac{\partial \mathcal{G}_{i1}}{\partial x_1} + \mathcal{G}_{i2} \cdot \frac{\partial \mathcal{G}_{i1}}{\partial x_2} = \ddot{\mathcal{Q}}_1 - g_1 + \frac{1}{c_i \cdot \rho_0} \cdot \left(\frac{\partial P_{i11}}{\partial x_1} + \frac{\partial P_{i12}}{\partial x_1} + F_{ji1} \right),$$

$$\begin{aligned} & \frac{\partial \mathcal{G}_{i2}}{\partial t} + \mathcal{G}_{i1} \cdot \frac{\partial \mathcal{G}_{i2}}{\partial x_1} + \mathcal{G}_{i2} \cdot \frac{\partial \mathcal{G}_{i2}}{\partial x_2} = \ddot{\mathcal{Q}}_2 - g_2 + \\ & \frac{1}{c_i \cdot \rho_0} \cdot \left(\frac{\partial P_{i12}}{\partial x_1} + \frac{\partial P_{i22}}{\partial x_2} + F_{ji2} \right), \\ & \frac{\partial c_i}{\partial t} + \frac{\partial (c_i \cdot \mathcal{G}_{i1})}{\partial x_1} + \frac{\partial (c_i \cdot \mathcal{G}_{i2})}{\partial x_2} = 0, \\ & P_{111} = \alpha_0 + \alpha'_0 \cdot \left(\frac{\partial \mathcal{G}_{11}}{\partial x_1} + \frac{\partial \mathcal{G}_{12}}{\partial x_2} \right) + \\ & (\alpha''_0 + \alpha'_1) \cdot \frac{\partial \mathcal{G}_{11}}{\partial x_1} \cdot \frac{\partial \mathcal{G}_{12}}{\partial x_2} - \alpha''_0 \cdot \left(\frac{\partial \mathcal{G}_{11}}{\partial x_2} + \frac{\partial \mathcal{G}_{12}}{\partial x_1} \right)^2 + \\ & \alpha_1 \cdot \frac{\partial \mathcal{G}_{11}}{\partial x_1} + \alpha'_1 \cdot \left(\frac{\partial \mathcal{G}_{11}}{\partial x_1} \right)^2 + \alpha''_1 \cdot \left(\frac{\partial \mathcal{G}_{11}}{\partial x_1} \right)^2 \cdot \frac{\partial \mathcal{G}_{12}}{\partial x_2} - \\ & \alpha''_1 \cdot \frac{\partial \mathcal{G}_{11}}{\partial x_1} \cdot \left(\frac{\partial \mathcal{G}_{11}}{\partial x_2} + \frac{\partial \mathcal{G}_{12}}{\partial x_1} \right)^2, \\ & P_{112} = \left(\frac{\partial \mathcal{G}_{11}}{\partial x_1} + \frac{\partial \mathcal{G}_{12}}{\partial x_2} \right) \cdot \left(\alpha_1 + \alpha'_1 \cdot \left(\frac{\partial \mathcal{G}_{11}}{\partial x_2} + \frac{\partial \mathcal{G}_{12}}{\partial x_1} \right) \right) - \\ & \alpha'_1 \cdot \left(\frac{\partial \mathcal{G}_{11}}{\partial x_2} + \frac{\partial \mathcal{G}_{12}}{\partial x_1} \right) \cdot \left(\frac{\partial \mathcal{G}_{11}}{\partial x_1} + \frac{\partial \mathcal{G}_{12}}{\partial x_2} - \left(\frac{\partial \mathcal{G}_{11}}{\partial x_2} + \frac{\partial \mathcal{G}_{12}}{\partial x_1} \right)^2 \right), \\ & P_{122} = \alpha_0 + \alpha'_0 \cdot \left(\frac{\partial \mathcal{G}_{11}}{\partial x_1} + \frac{\partial \mathcal{G}_{12}}{\partial x_2} \right) + \\ & (\alpha''_0 + \alpha'_1) \cdot \frac{\partial \mathcal{G}_{11}}{\partial x_1} \cdot \frac{\partial \mathcal{G}_{12}}{\partial x_2} - \alpha''_0 \cdot \left(\frac{\partial \mathcal{G}_{11}}{\partial x_2} + \frac{\partial \mathcal{G}_{12}}{\partial x_1} \right)^2 + \\ & \alpha_1 \cdot \frac{\partial \mathcal{G}_{12}}{\partial x_2} + \alpha'_1 \cdot \left(\frac{\partial \mathcal{G}_{12}}{\partial x_2} \right)^2 + \alpha''_1 \cdot \left(\frac{\partial \mathcal{G}_{12}}{\partial x_2} \right)^2 \cdot \frac{\partial \mathcal{G}_{11}}{\partial x_1} - \\ & \alpha''_1 \cdot \frac{\partial \mathcal{G}_{12}}{\partial x_2} \cdot \left(\frac{\partial \mathcal{G}_{11}}{\partial x_2} + \frac{\partial \mathcal{G}_{12}}{\partial x_1} \right)^2, \\ & P_{211} = -P + 2 \cdot \mu \cdot \frac{\partial \mathcal{G}_{21}}{\partial x_1}, \quad P_{212} = \mu \cdot \left(\frac{\partial \mathcal{G}_{22}}{\partial x_1} + \frac{\partial \mathcal{G}_{21}}{\partial x_2} \right), \\ & P_{222} = -P + 2 \cdot \mu \cdot \frac{\partial \mathcal{G}_{22}}{\partial x_2}, \\ & F_{211} = F_{212} = \begin{cases} 4 \cdot \pi \cdot d^2 \cdot \rho_{2i} \cdot \mathcal{G}_{21}^2 \cdot f_1 & \text{if } c_\infty \geq 2 \cdot c_1, \\ -\nabla P \cdot c_1 + \frac{6 \cdot c_1}{d} \cdot f_2 & \text{if } c_\infty < 2 \cdot c_1, \end{cases} \\ & F_{121} = F_{122} = \pi \cdot d \cdot \mathcal{G}_{12} \cdot (0.042 \cdot d \cdot \mathcal{G}_{12} \cdot \rho_{12} + \\ & 0.45 \cdot \mu \cdot \sqrt{(d \cdot \mathcal{G}_{12} \cdot \rho_{12})^5 + 3 \cdot \mu}), \end{aligned}$$

$$f_1 = 0.042 \cdot d \cdot \varrho \cdot \rho_{21} + 0.45 \cdot \mu \cdot \sqrt[5]{(d \cdot \varrho_{21} \cdot \rho_{21})^5} + 3 \cdot \mu,$$

$$f_2 = \left(\frac{12 \cdot c_1}{1 - c_1} + 3 \right) \cdot \frac{\mu \cdot (1 - 2.57 \cdot c_1)^2 \cdot (\varrho_{21} - \varrho_{12})}{d} +$$

$$0.03 \cdot \rho_{12} \cdot d \cdot \frac{\partial(\varrho_{21} - \varrho_{12})}{\partial t}.$$

Below there are some graphical results of the numerical implementation of the simplified mathematical model on the application package MathCAD 14.0 (version 14.0.0.163).

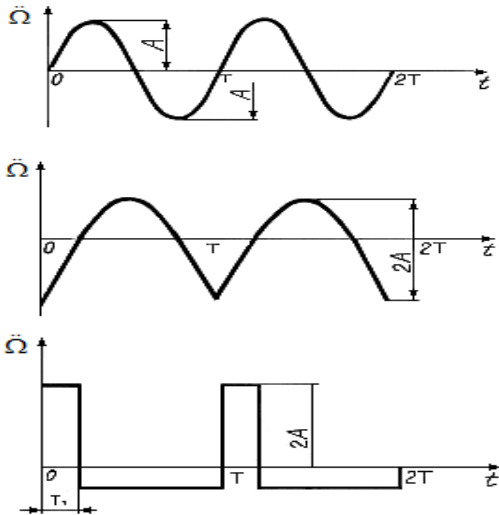


Fig.2. Three different laws of vibration acceleration.

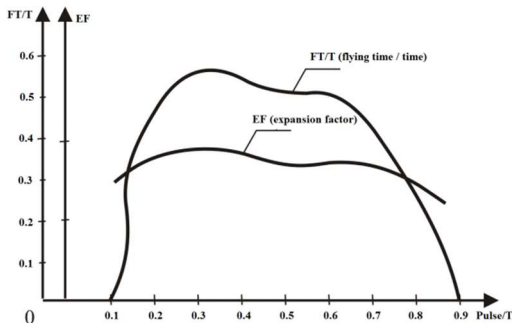


Fig. 3. Dependence of the flight time and the expansion coefficient of granular materials on duration of positive vibration pulse.

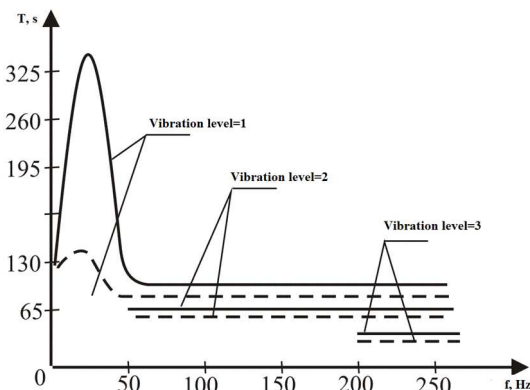
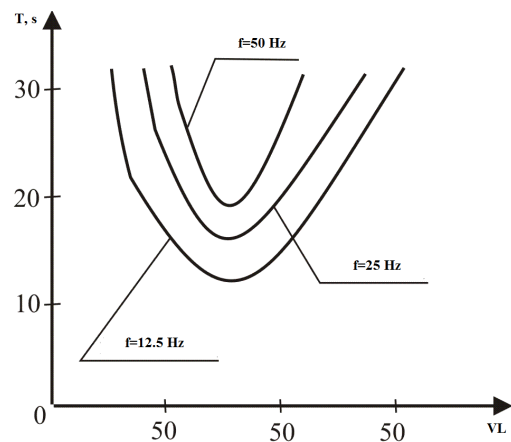
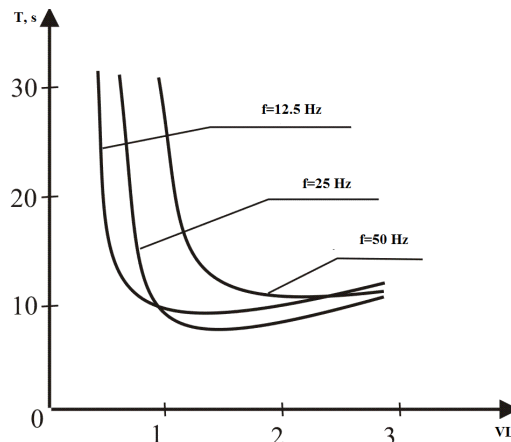


Fig. 4. Dependence of the condensation time of granular structures on the vibration frequency under fixed vibration level ($VL = \dot{\Omega}/g$): solid line shows harmonic excitation; dashed line shows polyharmonic excitation.



(a): Harmonic excitation



(b): Polyharmonic excitation

Fig. 5. Dependence of the separation time of granular materials on the vibration level $VL = \dot{\Omega}/g$: (a) harmonic excitation; (b) polyharmonic excitation.

IV. CONCLUSION

In this paper, the mechanism of processing granular disperse materials in gravitational flows, using horizontal or inclined vibrating sieve horizontal or inclined vibrating sieve classifying screens, is investigated. The apparatus of continuum mechanics is chosen as the apparatus of mathematical modelling of the investigated problem and, consequently, we assume that the properties of the particle flow, considered as continuum, can be presented in the form of continuous functions in such a way that each infinitesimal part of the disperse granular medium has characteristic properties of each separate particle.

In the actual paper, based on: (a) volume conservation law of granular components, (b) momentum conservation law, (c) equations, describing Coulombic interactions of granular disperse materials in gravitational flows, (d) equations for the stress tensor in the granular mineral fertilizers (both in the case of non-dissipativeness of granular medium and in the case of its dissipativeness), a mathematical model is built up, which consists of 7 equations (4), (5), (26) and

boundary conditions (29). In this work, we have analysed also the possibility to consider other boundary conditions, which enable to ensure the existence and uniqueness of the solution for the system of equations (4), (5), (26). The necessity of arising different from (29) boundary conditions is related to the practical point of view: for instance, for a specific type of horizontal (or inclined) vibrating sieve classifying screens, the ensuring of boundary conditions (3) can appear to be unprofitable (economically and/or technically) or even impossible.

It has to be outlined that the elaborated mathematical model describes only the mechanism of motion of granular disperse materials in gravitational fields, but not drying, sorting etc., which are other important problems arising in practice.

V. ACKNOWLEDGMENTS

For the second co-author the present article was executed within the framework of The State Research Programme "Next generation Information and Communication Technologies" ("NextIT"), Project No. 4.

REFERENCES

- [1] I. I. Blekhman, *Vibration Mechanics*. Moscow, Russian Federation: Science, 1994, 374 p.
- [2] P. V. Klassen, I. G. Grishaev, and I. P. Shomin, *Granulation*. Moscow, USSR: Chemistry, 1991, 240 p.
- [3] V. M. Dmitriyev, E. A. Sergeyeva, L. S. Tarova, and S. P. Rudobashta, "The Mathematical Modelling of Mass Transfer in Polydisperse Granular Materials Used in Environment Protection", Herald of the TSU, vol. 9, No. 4, pp. 456-460, 2004.
- [4] S. Savage, "Gravity Flow of Cohesionless Granular Materials in Chutes and Channels", Journal of Fluid Mechanics, vol. 92, No. 1, pp. 53-96, 1979.
- [5] P. Evesque, "A Simple Incremental Modelling of Granular-Media Mechanics", Poudres & Grains, vol. 9, pp.1-12, 1999.
- [6] A. L. Svistkov and B. Lauke, "Differential Constitutive Equations of Incompressible Medium at Finite Strains", Applied Mechanics and Theoretical Physics, vol. 50, No. 3, pp. 158-170, 2009.
- [7] F. G. Akhmediev and R. F. Gizzjatov, "Mathematical modelling and optimization of separation processes of disperse materials multistoreyed sith classifier", Proceedings of the Kazan State University of Architecture and Engineering, vol. 18, No. 4, pp. 330-340, 2011.
- [8] A. Lyav, *Mathematical Theory of Elasticity*. Moscow, USSR: ONTI, 1935, 647 p.
- [9] H. Deresiewicz, "Mechanics of Granular Matter", Advances in Applied Mechanics, vol. 5, pp. 233-306, 1958.
- [10] M. Faraday, "On a Peculiar Class of Acoustical Figures; and on Certain Forms Assumed by Groups of Particles upon Vibrating Elastic Surfaces", Philosophical Trans. Royal Soc. London, vol. 52, pp. 299-340, 1831.
- [11] O. Reynolds, "On the Dilatancy of Media Composed of Rigid Particles in Contact", The London, Edinburgh and Dublin Philosophical Magazine and Journal Science, vol. 20, No. 127, pp. 469-483, 1885.
- [12] H. M. Jaeger and S. R. Nagel, "Physics of the Granular State", Science, vol. 255, No. 3, pp. 1523-1531, 1995.
- [13] P. K. Haff, "Grain Flow as a Fluid-Mechanical Phenomenon", Journal of Fluid Mechanics, vol. 134, pp. 401-430, 1992.
- [14] P. W. Rowe, "The Stress Dilatancy Relation for Static Equilibrium of an Assembly of Particles in Contact", Proceedings of the Royal Society of London, A269, pp. 500-527, 1962.
- [15] J. C. Dutertre and H. F. Winterkorn, "Shear Phenomena in Natural Granular Materials", Princeton Soil Engineering Resources, Series 6, Princeton University Press, Princeton, USA, Contract No AFCRRL-66-771, 1966.

Structure Formation Process of Hydrated Portland Cement Compositions: Nanoscale Level Control

Guryanov A.M., Korenkova S.F., Sidorenko Yu.V.

Samara State Technical University, Institute of Architecture and Civil Engineering

Address: Molodogvardeyskaya St., 194, Samara, 443001, Russia

Abstract. Durability of cement-like construction materials, as well as durability of cement stone, depends on their humidity resistance, frost resistance, corrosion resistance. All of these properties depend not only on the composition of the original clinker, but also on structural organization at micro-and nanoscale level of hydrated portland cement compositions. In this research the authors used the method of small-angle neutron scattering to define structural parameters of hydrated portland cement compositions on nanoscale level, distribution of calcium hydrate silicate nanoparticles in size, medium nanoparticles radius, fractal dimension. It is shown, that introduction of modifying nanoadditives into portland cement compositions affects structural parameters of a cement stone. The following nanoadditives were used: of artificial (alpha aluminium oxide, gamma aluminum oxide) and of anthropogenic (carbonate and alumo-alkaline sludges) origin, as well as integrated nanoadditives containing surfactants. The change in structural parameters of portland cement compositions with nanoadditives in the process of hydration is investigated. It is shown that use of nanoadditives allows to control the process of forming the structure of hydrated portland cement composition on the nanoscale level, directly affect the values of structural parameters and, as a result, modify properties of cement stone.

Keywords: Portland cement, cement composition, nano additives, surfactants, small-angle neutron scattering, fractal dimension.

I. INTRODUCTION

Hydration of cement clinker leads to formation of complex gel-like frame of calcium hydrate silicate particles (C-S-H) [1, 2]. Parameters describing C-S-H particles structure and as well as parameters of the cement matrix itself, affect the properties of cement stone which is formed during the process [3, 4]. Strength and durability (which are closely connected with water resistance, frost resistance, corrosion resistance and other properties of cement stone) are influenced by shape and size distribution of C-S-H nanoparticles, by the ratio of free and bound water, by the presence of pores and their distribution in shape and size, that is, structural parameters of the material at micro-and nanoscales [5-7].

Certain specified properties of cement-like construction materials can be obtained by using different additives (fillers, modifiers) of artificial (e.g., carbon materials, other fine and ultra-fine powders) and of man-made (slimes, slags etc.) origin [5-7]. Additives affect structure formation in the process of initial hydration of portland cement clinker, and thus, affect operational properties of obtained materials [8-11]. This is especially evident when there are nanodispersed components present in cement compositions of additives. According to

characteristic features of their influence on the properties of resulting building materials, such additives can be described as nanoadditives or nanomaterials.

From the point of view of their effects, raw sludges, in their turn, can be referred to as filling additives (e.g., carbonate slimes) or as structure-forming additives (for example, alumoalkaline sludges). Sludges are formed as a result of processes of chemical reactions, dispersing and mixing, as well as adsorption, coagulation and sedimentation of particulate matters from oversaturated sewage solutions while their cleaning or water softening in industrial plants of metal industry, oil refining factories, thermal power plants. Slimes are a suspension, characterized by structure stability, homogeneity and consistency of composition [12]. Compliance with conditions of sludges by sol-gel technology, as well as the existence of nanodispersed components allows to refer them to nanotechnogenic raw materials.

In this paper, the authors used a method of small-angle neutron scattering (SANS), carried out a study of structures formation at the nanoscale of hydrated portland cement compositions, modified with nanoadditives of both artificial (Alpha aluminium

oxide nanoparticles, gamma alumina) and of man-made (carbonate and aluminosilicate sludges), and identified structural parameters of portland cement compositions. The influence of surfactants on structural parameters was also studied. It was proved that a combination of nanoadditives of different focus makes it possible to control the process of structures formation (structural parameters) of portland cement compositions during the process of hydration.

II. EXPERIMENTAL METHODS

Hydration of cement clinker leads to formation of complex gel-like frame of calcium hydrate silicate particles (C-S-H) [1, 2]. Parameters describing C-S-H particles structure and as well as parameters of the cement matrix itself, affect the properties of cement stone which is formed during the process [3, 4]. Strength and durability (which are closely connected with water resistance, frost resistance, corrosion resistance and other properties of cement stone) are influenced by shape and size distribution of C-S-H nanoparticles, by the ratio of free and bound water, by the presence of pores and their distribution in shape and size, that is, structural parameters of the material at micro- and nanoscales [5-7].

It is possible to use a method of small-angle neutron scattering (SANS) to determine parameters of over-atomic structure of samples of portland cement compositions applicable to distances from 1 nm to 100 nm [13]. This method is quite applicable to the investigation of nanoobjects of different physical nature because of the dependence of the intensity of SANS from scattering ability of inhomogeneities in the structure of substances and contrast at the borders of phase interface. The method of small-angle neutron scattering was firstly introduced in 1938 by A. Guinier in his works on over-atomic metallic structure. In 1950-ies this method was further developed in the works by G. Porod, O. Kratky and V. Luzzati. Now SANS is successfully used for research at the nanoscale of various materials, including the definition of structural parameters of hydrated cement compositions [14-16].

The intensity of SANS $I(q)$ depends on the transmitted neutron pulse.

$$q = \frac{4\pi}{\lambda} \sin \frac{\theta}{2}, \quad (1)$$

where θ is the scattering angle which carries information about over-atomic structure of scattering particles.

When performing the condition $qR_c < 1$ (Guinier regime) small angle scattering intensity $I(q)$ is defined by a characteristic particles size and shape of scattering particles or their inhomogeneities:

$$I(q) = I(0) \exp\left(-\frac{R_g^2 q^2}{3}\right). \quad (2)$$

where R_g is the radius of particles gyration. From experimental data on low-angle scattering in Guinier regime it is possible to estimate the radius of gyration R_g of the particles and their characteristic size R_c .

When performing the condition $qR_c > 1$ (Porod regime) for small angle scattering intensity there exists power-law dependence from transmitted neutron pulse.

$$I(q) \propto q^{-n}. \quad (3)$$

Deviation of exponent n from Porod asymptotics ($n = 4$) points to the fractal properties of the scattering objects and makes it possible to determine their fractal dimension. In the case of bulk or mass fractals the exponent coincides with the fractal dimension $n = D_V$ and takes a value from the interval $1 < D_V < 3$. In the case of scattering objects with fractal surface, fractal dimension equals $D_S = 6 - n$ and takes a value from the interval $2 < D_S < 3$. Accordingly, the exponent lies in the interval $3 < n < 4$.

Thus, according to the slope of straight-line portions of SANS dependencies, built in a double logarithmic scale, it is possible to determine whether the scattering objects belong to a specific type of fractal (volumetric or surface) and their fractal dimension [17-19].

According to data on low-angle scattering for polydisperse systems, it is possible to restore distribution functions of scattering objects for distances $G(R)$, on the basis of spectra of pair correlations $\gamma(R)$, obtained by Fourier transforms of data for cross sections. These functions are related to the forms of particles and describe quantitatively a set of line segments connecting the elements of the volume of particles, and also depend on the distribution of inhomogeneities within particles. Distribution function by distances $G(R)$ can be presented as follows:

$$G(R) = R^2 \gamma(R) = \frac{1}{2\pi^2} R^2 \int \frac{d\sigma(q)}{d\Omega} \frac{\sin(qR)}{qR} q^2 dq. \quad (4)$$

The function $G(R)$ shows whether particles of the radius R exist in the test material.

Processing of SANS experimental data is implemented by use software complex ATSAS 2.8.0 [20, 21].

III. EXPERIMENTS

Spectra intensities SANS from samples of cement compositions were measured in Petersburg nuclear physics Institute (the town of Gatchina) with a diffractometer "Membrane-2" installed on the WWR-

M reactor [22]. Wavelength of neutrons was equal to $\lambda = 0.3\text{nm}$ with linewidth $\Delta\lambda/\lambda = 0,25$. Range of registered elastic transferred neutron pulses q was ranging from 0.03 nm^{-1} to 0.8 nm^{-1} . Scattered specimens of neutrons were recorded in the range of angles $\theta = \pm 0.017\text{ rad}$. The detector consisted of forty one ^3He -counter. The intensity of the beam on the sample was measured while using two counters (monitors), installed in front of the model above and below the axis of the beam of neutrons.

Samples of hydrated portland cement compositions were placed in a target device representing the cavity in a cadmium plate. The volume of the cavity was 0.52 cm^3 . The thickness of the sample was equal to the cadmium plate thickness $d_s = 2\text{mm}$. With this thickness of the samples, values of transmission coefficient (transmission) of the beam of neutrons were $T = 0.4-0.9$.

The results obtained from the experiment data were standardized with monitors readings and transmission values. Background subtraction was carried out, as well as the effect of neutrons which had passed through the sample without scattering. The obtained distributions of scattering intensities $I_S(q)$ were then standardized with scattering intensities obtained under the same conditions $I_{ST}(q)$ from the standard sample, which was a light water layer of $\delta_{ST} = 1\text{mm}$ thickness. Differential cross-sections of portland cement compositions samples scatterings per 1cm^3 of the volume of the sample in absolute units was calculated by the formula

$$\frac{d\sigma(q)}{d\Omega} = \frac{I_S(q)}{I_{ST}(q)} \frac{d_{ST}}{d_S} \frac{d\sigma_{ST}}{d\Omega}. \quad (5)$$

From the obtained cross sections of neutrons scattering, by means of Fourier transformation (4) we restored the distribution of scattering objects in the approximation of homogeneous areas.

When fitting experimental data, the maximum radius of scattering objects was ranged from 50 to 100 nm. When the maximum radius was equal to 50 nm, the points corresponding to minimal neutron pulses fell through. This part of the test is not described and taken into account. When the maximum radius was equal to 100 nm, the points corresponding to maximum neutron pulses fell through. This part of the test is not described and taken into account either. The general description of scattering data was quite correct, if the maximum size of the dispersal areas was about 80 nm. The average radius of the scattering objects for tested samples of cement compositions was ranging from 30 nm to 65 nm.

Samples of cement compositions were made on the basis of portland cement D0-500 with no additives. During the process of of Portland cement hydration, nanoadditives in the amount of 2,5÷5% were put into it. They were nanopowders $\alpha\text{-Al}_2\text{O}_3$ и $\gamma\text{-Al}_2\text{O}_3$, carbonate or alumoalkaline sludge, as well as about 0.5% of surface acting agents. Nanopowder $\alpha\text{-Al}_2\text{O}_3$ was characterized by an average particle size of 80 nm with a specific surface area of not less than $10\text{ m}^2/\text{g}$. Nanopowder $\gamma\text{-Al}_2\text{O}_3$ had average particle size of 20 nm and specific surface area of not less than $160\text{ m}^2/\text{g}$. The composition of the sludge used in this work is given in Table 1. As surface acting agents superplasticizing agent of brand C-3 was used.

Table I
 Mineral composition of raw sludges

A sample of raw sludge	Al ₂ O ₃ [%]	CaO [%]	MgO [%]	Fe ₂ O ₃ [%]	SiO ₂ [%]	Losses at steam curing [%]
Carbonate	10	43	6	2	4	35
Alumoalkaline	52	2	2	2	0	40

Water/cement ratio was ranged from 0.27 to 0.30. When raw sludges and surface acting agents were added, water/cement ratio decreased to values of 0.18-0.24.

Periodically measurement of neutron scattering intensities of manufactured samples was done. According to the charts of neutron scattering intensities the following calculations were performed: According to formula (2) the average radii of scattering objects were calculated; according to formula (3) – fractal dimensions; according to formula (4) – differential cross-sections of scattering; according to formula (5) – distribution function of scattering objects by distances.

Calculated structural parameters of samples were compared. The time interval of measurement cycles was 28 days.

IV. DISCUSSION AND RESULTS

Table 2 shows the composition of the samples of tested cement compositions. For all samples we observed power dependence of the scattering intensity from the transmitted neutron pulse. As an example, Figure 1 presents graphs of the neutron scattering intensities of three samples after 28 days from the start of hydration. Sample 1 is made portland cement D0-500 with no additives. Sample 8 is a cement composition with 5% of $\gamma\text{-Al}_2\text{O}_3$ additive. Sample 10 is a cement composition with 5% of $\alpha\text{-Al}_2\text{O}_3$ additive.

Figure 2 shows graphs of calculated functions of scattering objects distribution by distances for samples 8 and 10.

Characteristics of the tested samples of portland cement compositions, calculated values of fractal

dimensions D_s and average particles size R_c are shown in Table 2.

In sample 2 and 3, 4 and 5, 6 and 7 (as shown in Table 2) added sludges had similar chemical compositions. Average particle size R_c was calculated on the 28th day after cement compositions gauging.

Table 2 demonstrates that nanoadditives in portland cement compositions change structural parameters of materials at the nanoscale. All nanoadditives in the range of distances up to 80 nm reduce the average size of the scattering objects. In the specified range of distances, scattering of neutrons occurs on fractal surfaces. Increase of the fractal dimensions in the process of hydration points to the strength increase in the surface area in the process of portland cement hydration of calcium silicate particles. Influence of structural parameters of nanoadditives is connected not only with

nanodimensions of their particles. An important factor here is also the target of the impact on the process of hydration. Carbonate slimes and nanopowders $\alpha\text{-Al}_2\text{O}_3$ и $\gamma\text{-Al}_2\text{O}_3$ are of low chemical activity. They, most likely, can be attributed to the filling nanoadditives. On the other hand, alumoalkaline sludges as well as complex nanoadditives containing surfactants, or two-component (a mixture of carbon and alumoalkaline sludges) can be attributed to the modifying nanoadditives. They have a greater influence on the structural parameters. Target-specific change of structural parameters of cement compositions by introduction of surfactants is determined by the absorption mechanism of modification of dispersion systems.

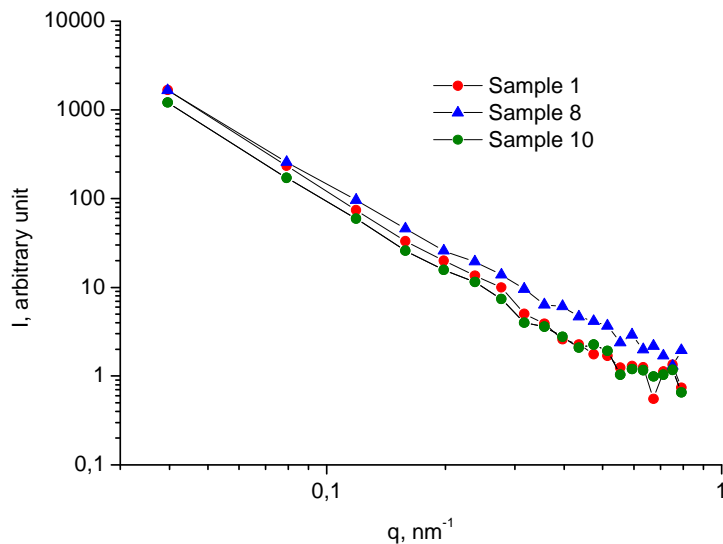


Fig.1. Experimental spectra of SANS intensities of cement compositions samples. Sample 1 – cement without additives; Sample 8 – cement with $\gamma\text{-Al}_2\text{O}_3$ additive (5%); Sample 10 – cement with $\alpha\text{-Al}_2\text{O}_3$ additive (5%).

Table II
Structural parameters of samples of portland cement compositions

Sample number	Type of additive (raw sludge)/[%]	PAV [%]	D_s , 1 day	D_s , 7 days	D_s , 14 days	D_s , 28 days	R_c , nm
1	-	-	2.31	2.35	2.39	2.49	65
2	Carbonate / 5.0	-	2.35	2.40	2.52	2.55	60
3	Carbonate / 5.0	0.25	2.37	2.41	2.55	2.58	45
4	Alumoalkaline / 4,5	-	2.44	2.50	2.62	2.76	42
5	Alumoalkaline / 4,5	0.25	2.48	2.58	2.71	2.85	40
6	Carbonate / 3.0 + Alumoalkaline / 3.0	-	2.40	2.48	2.56	2.62	52
7	Carbonate / 3.0 + Alumoalkaline / 3.0	0.25	2.41	2.52	2.58	2.68	43
8	$\gamma\text{-Al}_2\text{O}_3$ / 5,0	-	2.40	2.50	2.58	2.60	48
9	$\gamma\text{-Al}_2\text{O}_3$ / 5,0	0.25	2.41	2.54	2,	2.68	44
10	$\alpha\text{-Al}_2\text{O}_3$ / 5,0	-	2.30	2.35	2.36	2.48	52
11	$\alpha\text{-Al}_2\text{O}_3$ / 5,0	0.25	2.38	2.40	2.41	2.52	50

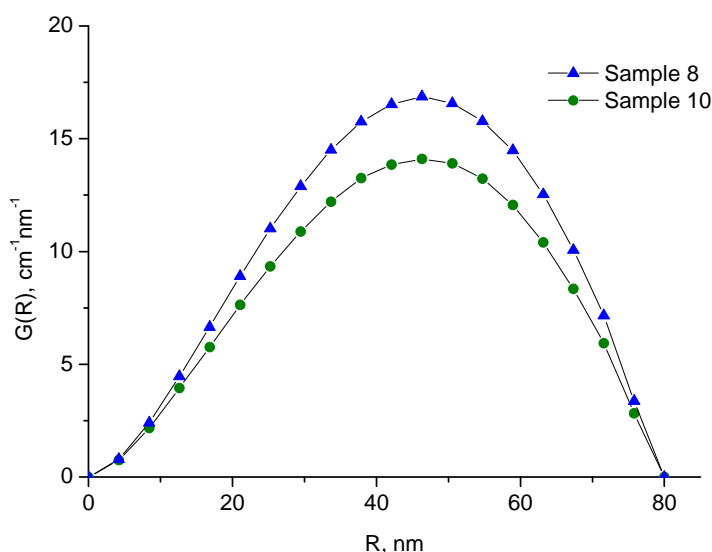


Fig. 2. Distribution functions of scattering objects by distances of samples of cement compositions. Sample 8 – cement with γ -Al₂O₃ additive (5%); Sample 10 – cement with α -Al₂O₃ additive (5%).

V. CONCLUSION

Nanoadditives influence structural parameters of hydrated portland cement compositions in the following ways: the distribution of nanoparticles in size, average size of nanoparticles, fractal dimension. Application of filling and modifying nanoadditives makes it possible to purposefully influence on the process of hydration, thereby driving the process of formation of structural parameters of hydrated portland cement compositions and, ultimately, affect the properties of cement stone.

The obtained dependences of structural parameters values of portland cement compositions point to the fact that sludges used as additives, as well as such nanopoders as alpha and gamma of corundum enhance the strength of particles surface area, increase frost resistance, water resistance and corrosion resistance of cement stone, which has a positive effect on the durability of the cement-like construction materials.

REFERENCES

- [1] Bullard J.W., Jennings H.M., Livingston R.A., Nonat A., Scherer G.W., Schweitzer J.S., Scrivener K.L., Thomas J.J. Mechanisms of cement hydration. *Cement and Concrete Research*, Vol. 41, 2011, pp. 1208-1223.
- [2] Nonat A. The structure and stoichiometry of C-S-H. *Cement and Concrete Research*, Vol. 34, 2004, pp. 1521-1528.
- [3] Skinner L.B., Chae S.R., Benmore C.J., Wenk H.R., Monteiro P.J.M. Nanostructure of calcium silicate hydrates in cements. *Physical Review Letters*, Vol. 104, 195502, 2010, pp. 1-4.
- [4] Raki L., Beaudoin J., Alizadeh R., Makar J., Sato T. Cement and concrete nanoscience and nanotechnology. *Materials*, Vol. 3, 2010, pp. 918-942.
- [5] Guryanov A.M. Nanoscale investigation by small angle neutron scattering of modified portland cement compositions. *Procedia Engineering*, Vol. 111, 2015, pp. 283-289.
- [6] Guryanov A.M. Investigation of hydrated portland cement structure formation by means of small angle neutron scattering. *Procedia Engineering*, Vol. 153, 2016, pp. 217-222.
- [7] Guryanov A., Korenkova S., Sidorenko Yu. Research on the nanolevel influence of surfactants on structure formation of the hydrated portland cement compositions. *MATEC Web of Conference*, Vol. 86, 04011, 2016, pp. 1-5.
- [8] Phair J.W., Schulz J.C., Bertram W.K., Aldridge L.P. Investigation of the microstructure of alkali-activated cements by neutron scattering. *Cement and Concrete Research*, Vol. 33, 2003, pp. 1811-1824.
- [9] Thomas J.J., Allen A.J., Jennings H.M. Density and water content of nanoscale solid C-S-H formed in alkali-activated slag (AAS) paste and implications for chemical shrinkage. *Cement and Concrete Research*, Vol. 42, 2012, pp. 377-383.
- [10] Chiang W.-S., Fratini E., Ridi F., Lim S.-H., Yeh Y.-Q., Baglioni P., Choi S.-M., Jeng U.-S., Chen S.-H. Microstructural changes of globules in calcium-silicate-hydrate gels with and without additives determined by small-angle neutron and X-ray scattering. *Journal of Colloid and Interface Science*, Vol. 398, 2013, pp. 67-73.
- [11] Trapote-Barreira A., Porcar L., Cama J., Soler J.M., Allen A.J. Structural changes in C-S-H gel during dissolution: Small-angle neutron scattering and Si-NMR characterization. *Cement and Concrete Research*, Vol. 72, 2015, pp. 76-89.
- [12] Korenkova S.F., Sheina T.V. *Foundations and the concept of recycling of chemical precipitation in the construction industry*. Samara, SGASU, 2004.
- [13] Avdeev M.V., Aksenov V.I. Small-angle neutron scattering in structural studies of ferrofluids. *Success of physical sciences*, Vol. 180, 2010, pp. 1009-1034.
- [14] Thomas J.J., Chen J.J., Allen A.J., Jennings H.M. Effects of decalcification on the microstructure and surface area of cement and tricalcium silicate pastes. *Cement and Concrete Research*, Vol. 34, 2004, pp. 2297-2307.
- [15] Allen A.J., Thomas J.J., Jennings H.M. Composition and density of nanoscale calcium-silicate-hydrate in cement. *Nature Materials*, Vol. 6, 2007, pp. 311-316.
- [16] Allen A.J., Thomas J.J. Analysis of C-S-H gel and cement paste by small-angle neutron scattering. *Cement and Concrete Research*, Vol. 37, 2007, pp. 319-324.
- [17] Ficker T. Fractal strength of cement gels and universal dimension of fracture surfaces. *Theoretical and Applied Fracture Mechanics*, Vol. 50, 2008, pp. 167-171.
- [18] Zeng Q., Luo M., Pang X., Li L., Li K. Surface fractal dimension: An indicator to characterize the microstructure of cement-based porous materials. *Applied Surface Science*, Vol. 282, 2013, pp. 302-307.

- [19] Gao Y., Jiang J., Schutter G.D., Ye G., Sun W. Fractal and multifractal analysis on pore structure in cement paste. *Construction and Building Materials*, Vol. 69, 2014, pp. 253-261.
- [20] Konarev P.V., Petoukhov M.V., Volkov V.V., Svergun D.I. ATSAS 2.1, a program package for small-angle scattering data analysis. *Journal of Applied Crystallography*, Vol. 39, 2006, pp. 277-286.
- [21] Petoukhov M.V., Franke D., Shkumatov A.V., Tria G., Kikhney A.G., Gajda M., Gorba C., Mertens H.D.T., Konarev P.V., Svergun D.I. New developments in the ATSAS program package for small-angle scattering data analysis. *Journal of Applied Crystallography*, Vol. 45, 2012, pp. 342-350.
- [22] Lebedev V.M., Lebedev V.T., Ivanova I.N., Kolkhidashvili M.R., Orlova D.N. *Measuring and analysis system of small angle neutron diffractometer "Membrane-2"*. Preprint PNPI-2785, 2008.

Determining Countries' Potentials for Successful Export of Luxurious and Banking Services

Sharif E. Guseynov^{1, 2, 3,a}, Ruslans Aleksejevs^{4,b}, Jekaterina V. Aleksejeva^{1,c},
Raufs Guseinovs^{5,d}

¹Institute of Fundamental Science and Innovative Technologies, Liepaja University, Liepaja LV-3401, Latvia;

²Faculty of Science and Engineering, Liepaja University, 4 Kr.Valdemar Street, Liepaja LV-3401, Latvia;

³"Entelgine" Research & Advisory Co., Ltd., Kleistu Street 2-53, Riga LV-1067, Latvia; ⁴Riga State Gymnasium No. 1, 8 Raina Boulevard, Riga LV-1050, Latvia; ⁵Faculty of Humanities, Leiden University, Rapenburg 70,

2311 EZ Leiden, the Netherlands; ; ^ash.e.guseynov@inbox.lv; ^bruslan.alekseyev.1998@gmail.com;

^cjekaterina.v.aleksejeva@gmail.com; ^dr.guseinovs@umail.leidenuniv.nl

Abstract. Country's economic potential implies joint capability of the country's economy, its branches and enterprises to carry out production and economic activity, to create goods and services, to supply the demand of the population, to stimulate production and consumption development. Country's economic potential is defined by estimating different economic, social, ecological, scientific and technical, political and other criteria, which, as a rule, are interconnected and correlated. Each of these criteria includes heterogeneous set of economic, financial, social, political, juridical, educational, scientific and innovational, ecological, cultural and other factors, every single of which can consist of independent or indirectly correlated subfactors called indices or indicators. In this work we investigate the problem of estimating economic potentials of groups of countries according to their measurable economic, financial, social and other indicators in order to export bank and other luxurious services. The approach to solving the problem offered in this work is based on the apparatus of the theory of inverse and ill-posed problems.

Keywords: economic attractiveness, export of service, mathematical model, inverse problem, stable solution.

I. INTRODUCTION

Country's economic potential is defined by estimating different economic, social, ecological, scientific and technical, political and other criteria, which, as a rule, are interconnected and correlated. Each of these criteria includes heterogeneous set of economic, financial, social, political, juridical, educational, scientific and innovational, ecological, cultural and other factors, every single of which can consist of independent or indirectly correlated subfactors called indices or indicators. For instance, ([1]), the factor of the level of attractiveness of running a business in a country consists of six independent indices; the factor of the level of democracy in a country also consists of six independent indices; the factor of global competitiveness of a country contains only one index called Global Competitiveness Index; the factor of corruption level in a country is defined by one to nine indices, among which there are both independent and indirectly correlated indices; the factor of the level of market relations and commercial infrastructure development contains at least five indices (depending on the region, where the investigated country is situated, and on the technique of estimation, the number of indices can reach

seventeen); the factor of economic freedom of a country consists of seven to nine indices depending on the technique of estimation; the factor of global understanding of risks and conditions of running a business consists of six independent indices; the factor of the level of ecology and understanding of ecological risks in a country contains at least ten (depending on the region, where the investigated country is situated, and on the technique of estimation) independent and indirectly correlated indices; three indirectly correlated indices – index of literacy, index of longevity, index of life quality (actually, this index is often considered a separate factor containing many subfactors due to its significance) – describe the factor of human development of a country (this factor is often called Human Development Index); the demographic factor is described by one to five independent and indirectly correlated indices; the factor of the level of economic development of a country can contain up to twenty indices, the majority of which are indirectly correlated; etc.

Country's economic potential should be considered as a generic description of the level of economic, social and juridical development of the country (see [2]-[6] and respective references given in these). If we try to

emphasize only the level of economic development of the country then this level includes two factors – economic resources and economic results of the country ([6]). Economic resources of a country, which are described by total volume, structure and quality, consist of all material assets, scientific, intellectual, informational and labor resources the country accumulated on its territory as well as abroad (including entrepreneurial ability and natural resources). Economic results of a country, which are described by total volume, structure, quality and technical level of production and services, make Gross domestic product (GDP), Gross national product (GNP), national income (NI), structures GDP, GNP and NI as well as physical amount of production of these types of goods which are the most significant for the country at this stage of history.

There exist many methods for estimation of country's economic potential, for example, method of sum of places, method of numerical scores, method of multidimensional mean, method "Pattern", method of multidimensional comparative analysis, different by the level of complexity methods of deterministic and stochastic factor analysis, big amount of methods of expert evaluation, etc. (see [2], [5]-[9] and respective references given in these). Analysis of the most popular of those shows that none of them allows to determine, for example, which indices have considerable effects (and how big they are) on economic potential of a specific country or group of countries with more or less identical subjective, economic, technological, social, political and other conditions in a specific period of time. In addition, these methods do not help to unambiguously and objectively determine how different same indices are in different countries, where the values of economic potential differ drastically or, on the contrary, are very close. In other words, all these extensively used methods do not allow to objectively distinguish influence of every economic, financial, social etc. index on economic potential both by time unit and for every country by different sets of indices. This means that unambiguous and objective partitioning of a group of investigated countries according to the popular methods is impossible (for instance, see the fundamental work [2]). The main reason of lack of relevant methods for unambiguous and objective estimation of country's economic potential, in our opinion, is subjectivity of methods for finding a priori not given weighted coefficients of indices (let us remind that weighted coefficient of an index describes its relative significance in overall evaluation). Authors of the present work are sure that the above mentioned subjectivity can be eliminated using the powerful apparatus of the theory of inverse and ill-posed problems, which is successfully used in different problem of mathematical physics: at present, application of this apparatus to economic analysis, particularly, to the problem of estimation of economic

potential or economic attractiveness of a country, unfortunately, does not exist.

In this work we investigate the problem of estimation of economic potentials of groups of countries according to their measurable economic, financial, social etc. indices in order to export bank and other luxurious to these countries. We construct a mathematical model of the considered problem and develop an iteration method which allows finding solution of the constructed model. In addition to it, we carry out a computing experiment ([10]), which implements the constructed model: in this experiment the initial data are values of 30 indices of 8 Central and Eastern Europe's countries for years 2012-2014.

II. STATEMENT OF THE INVESTIGATED PROBLEM AND ITS MATHEMATICAL MODEL

A. Verbal statement of the investigated problem

In this section it is assumed that during n years we estimate k economic, financial, social etc. indices of m countries, and that in i -th year each of k indices of the j -th investigated country is estimated by one number $a_{i,j}$, which integrally describes many factors which directly or indirectly influence these indices. It is required to:

- determine countries' economic potentials and rank the investigated countries according to the package of found economic potentials;
- determine "Degree of favorability of the year" for every year for all indices together as well as for each of them separately;
- rank the years by "Degree of favourability of the year" and by "Degree of succession of the year";
- to detect influence of "Degree of succession of the year" on economic potentials of the investigated countries.

Before we go to the mathematical model of just formulated problem, let's make the following assumptions on the values of the initial indices

$\{a_{i,j}\}_{i=1,n}^{j=1,m}$: some indices $a_{i,j}$ can be equal to zero or

negative numbers and then, likewise in the theory of zero-sum matrix games zero and negative elements of payoff array are transformed into strictly positive numbers, in our problem we will transform zero and negative indices into positive numbers. It can always be done, for example, by increasing every element $a_{i,j}$

by one number, for instance, by $\left| \min_{\substack{i=1,n \\ j=1,m}} \{a_{i,j}\} \right| + 1$, i.e.

instead of initial values of indices $\{a_{i,j}\}_{i=1,n}^{j=1,m}$ we will have new values

$$\left\{ \hat{a}_{i,j} \right\}_{i=1,n}^{j=1,m} \stackrel{def}{=} \left\{ a_{i,j} + \left| \min_{\substack{i=1,n \\ j=1,m}} \{ a_{i,j} \} \right| + 1 \geq 1 \right\}_{i=1,n}^{j=1,m}. \quad (1)$$

Obviously, after this operation we receive a problem which is equivalent to the original one. That is why from now onwards, without loss of generality, we will consider that for $\forall (i = \overline{1, n}; j = \overline{1, m})$ holds true $a_{i,j} > 0$. Let us show another way of securing positiveness of indices. Its essence consists in a special standardization of values of initial indices $\{a_{i,j}\}_{i=1,n}^{j=1,m}$ using the formula

$$\hat{a}_{i,j} = \frac{a_{i,j}}{\Delta_i} - \delta_{i,j}, \quad (2)$$

where $\Delta_i \stackrel{def}{=} \sup_{j=1,m} \{a_{i,j}\} - \inf_{j=1,m} \{a_{i,j}\}$ stands for i -th saltus/leap; $\delta_{i,j} \stackrel{def}{=} \frac{\Delta_i - \varepsilon \cdot a_{i,j}}{\varepsilon \cdot \Delta_i}$ ($0 < \forall \varepsilon \ll 1$) means oscillation. Also it is obvious that this procedure creates new package of standardized positive data $\{\hat{a}_{i,j}\}_{i=1,n}^{j=1,m}$, where $0 < \varepsilon \leq \hat{a}_{i,j} \leq 1 + \varepsilon$.

B. Mathematical model

The offered mathematical model of the above formulated problem has the following form:

$$\begin{cases} x_j = p \cdot \sum_{i=1}^n w_i \cdot \hat{x}_{i,j}, \quad \forall j = \overline{1, m}; \\ w_i = w_{\max} - ss \cdot \sum_{j=1}^m |\hat{x}_{i,j} - x_j|, \quad \forall i = \overline{1, n}, \end{cases} \quad (3)$$

where

$\{\hat{x}_{i,j}\}_{i=1,n}^{j=1,m}$ is the result of standardization of initial indices according to any known procedure, for example, according to the formula (2), or the formula

$$\hat{x}_{i,j} = \frac{a_{i,j} - \min_{i=1,m} \{a_{i,j}\}}{\max_{i=1,m} \{a_{i,j}\} - \min_{i=1,m} \{a_{i,j}\}},$$

or the formula $\hat{x}_{i,j} = \frac{a_{i,j} - m_j}{\sigma_j}$,

in which m_j denotes average deviation of j -th index, and σ_j denotes mean-square deviation of j -th index;

- x_j is the desired economic potential of j -th country;

- vector $x = (x_1, \dots, x_m)^T$ is the desired ranking of the investigated countries by the values of standardized indices $\{\hat{x}_{i,j}\}$ during n years;
- parameter w_i is the desired "Degree of favorability of the year" for i -th year;
- vector $w = (w_1, \dots, w_n)^T$ is the desired "Degree of influence of years' favorability";
- parameter $w_{\max} \stackrel{def}{=} \max_{i=1,n} \{w_i\}$ is maximal possible estimate "Degree of favorability of the year" by all years: this parameter also is unknown, because $w_i (i = \overline{1, n})$ are unknown;

- parameter ss is "Sensitivity switch", which means sensitivity coefficient of the model (1) to the package "Degree of succession of the year", i.e. sensitivity of (1) to residual $\sum_{j=1}^m |\hat{x}_{i,j} - x_j|$;

obviously, for $ss = 0$ the model (1) becomes a model, using which the decision-maker makes his decision concerning countries' rankings by their economic potentials by the way of reduction of values of standardized indices during n years without taking into account their correlation in every year; when the coefficient ss in the model (1) increases, increases also significance of correlation of standardized indices' values during n years for decision making concerning rankings of countries according to their economic potentials.

- parameter $p > 0$ is a controlled parameter and it plays the role of proportionality coefficient of the desired economic potential for each of the investigated countries to the weighted sum of standardized indices of all investigated countries. This controlled parameter is chosen arbitrarily, for example, it can be equal to the number of investigated countries, that is $p = m$.

III. DEVELOPMENT OF ITERATION

ALGORITHM FOR SOLVING THE CONSTRUCTED MATHEMATICAL MODEL

In order to solve the constructed mathematical model (1), first of all, let's rewrite it in a compact matrix form. To do this, we introduce a matrix $X_{Residual}$ of residuals of size $n \times m$, defines as

$X_{Residual} \stackrel{def}{=} \left\{ \left| \hat{x}_{i,j} - x_j \right| \right\}_{i=1,n}^{j=1,m}$. Also, we introduce a

constant vector $W_{\max} \stackrel{def}{=} \left(\underbrace{w_{\max}, \dots, w_{\max}}_n \right)^T$ of size $n \times 1$,

and a matrix $X \equiv \left\{ \hat{x}_{i,j} \right\}_{i=1,n}^{j=1,m}$ of size $n \times m$, whose meaning is obvious. Then the model (1) allows the following matrix notation with parameter ss :

$$\begin{cases} x = p \cdot X^T w; \\ w = W_{\max} - ss \cdot X_{Residual} I, \end{cases} \quad (3)$$

where I denotes column vector of size $m \times 1$, consisting only of units.

In the model (3) the unknown are vectors x and w , and in order to find them we offer the following iterative process:

$$\begin{cases} x^0 = I; w^0 = W_{\max}; \\ x^{l+1} = p \cdot \frac{X^T w^l}{\sum_{i=1}^m \left| \sum_{j=1}^n \hat{x}_{i,j} \cdot w_j^l \right|}, \quad \forall l = 0, 1, \dots; \\ w^{l+1} = W_{\max} - ss \cdot X_{Residual}^{l+1} I, \quad \forall l = 0, 1, \dots; \end{cases} \quad (4)$$

Remark 1. The offered iterative process (4) is, generally speaking, somewhat incorrect as we a priori assume that we know W_{\max} , while this does not obligatory correspond to the truth and restricts power of the (1) (and (3)): in the model (1) w_i ($i = \overline{1, n}$) are the desired unknown elements, thus, constant $w_{\max} \equiv \max_{i=1,n} \{w_i\}$ cannot be a priori known, which makes unknown also W_{\max} . In the offered iterative process (4), whose aim is to find the desired elements $\{x_1, \dots, x_m; w_1, \dots, w_n\}$ from the model (1) (or (3)), a priori is assumed that we know the vector

$$W_{\max} \stackrel{def}{=} \left(\underbrace{\max_{i=1,n} \{w_i\}, \dots, \max_{i=1,n} \{w_i\}}_n \right)^T.$$

That is exactly why values of found by the iterative process (4) elements $\{x_1, \dots, x_m; w_1, \dots, w_n\}$ can differ from the real values, i.e. from the values we get from the model (1) (or (3)) not by use of the iterative process (4), but by use of any other algorithm which does not have the above mentioned assumption about us a priori W_{\max} .

Now let's investigate convergence of the iterative process (4). Let's separately consider cases $ss = 0$ and $ss \in (0, 1]$. For $ss = 0$ the iterative process (4) does converge. Indeed, in this case we have:

$$\begin{cases} x^0 = I; w^0 = W_{\max}^{l+1} = W_{\max}; \\ x^{l+1} = p \cdot \frac{X^T \cdot W_{\max}}{\sum_{i=1}^n \left| \sum_{j=1}^m \hat{x}_{i,j} \cdot W_{\max j} \right|}, \end{cases}$$

where $W_{\max j}$ means j -th coordinate of the vector W_{\max} . Then we can write:

$$\lim_{l \rightarrow \infty} x^{l+1} = \lim_{l \rightarrow \infty} \frac{p \cdot X^T \cdot W_{\max}}{\sum_{i=1}^n \left| \sum_{j=1}^m \hat{x}_{i,j} \cdot W_{\max j} \right|} = \frac{p \cdot X^T \cdot W_{\max}}{\sum_{i=1}^n \left| \sum_{j=1}^m \hat{x}_{i,j} \cdot W_{\max j} \right|} = x,$$

which confirms convergence of the iterative process (4) for $ss = 0$.

Now, as all discrete functions which participate in the iterative process are continuous by parameter ss , it is not difficult to see that the iterative process (4) does converge for $ss \in (0, 1]$ unconditionally. Indeed, from (4) we get recurrent function

$$x^{l+1} = p \cdot \frac{X^T \cdot w^l}{\sum_{i=1}^n \left| \sum_{j=1}^m \hat{x}_{i,j} \cdot (W_{\max} - ss \cdot X_{Residual}^l \cdot I) \right|},$$

which may have a point of break only if the denominator equals zero, i.e.

$$\sum_{i=1}^n \left| \sum_{j=1}^m \hat{x}_{i,j} \cdot (W_{\max} - ss \cdot X_{Residual}^l \cdot I) \right| = 0. \quad \text{On the}$$

other hand, according to the conditions of use of the mathematical model (1), elements of the initial matrix of estimates X must be strictly positive, i.e. $\hat{x}_{i,j} > 0 \quad \forall i = \overline{1, n}, \forall j = \overline{1, m}$. Thus, the condition of

existence of break point of function x^{l+1} is the condition $W_{\max} - ss \cdot X_{Residual}^l \cdot I = 0$. As deviation of

w_i from w_{\max} is proportional to the sum of residuals between rankings of the investigated countries and estimates of k parameters, we can write

$$w^{l+1} - W_{\max} = -ss \cdot X_{Residual}^{l+1} \cdot I. \quad \text{Obviously,}$$

$w^{l+1} - W_{\max} < 0$ for $\forall l = 0, 1, 2, \dots$. Consequently,

$$ss = \frac{w^{l+1} - W_{\max}}{-X_{Residual}^{l+1} \cdot I} > 0, \quad \text{which is true only for}$$

$w_i^{l+1} > 0$. That is why, function x^{l+1} has no points of break, i.e. $W_{\max} - ss \cdot X_{Residual}^l \cdot I \neq 0$. In other words, we can write

$$\lim_{l \rightarrow \infty} x^{l+1} = \lim_{l \rightarrow \infty} \frac{p \cdot X^T \cdot w^l}{\sum_{i=1}^n \left| \sum_{j=1}^m \hat{x}_{i,j} \cdot (W_{\max} - ss \cdot X_{Residual}^l \cdot I) \right|} = x,$$

which finishes the proof of unconditional convergence of the iterative process (4) for $ss \in (0, 1]$.

The questions concerning stability and convergence rate of the iterative process (4) are not investigated in this work.

Remark 2. As we can see from the model (3) and iterative process (4), the dependence of components of vector w from the sensitivity coefficient ss has a more complicated nature than the dependence of vector x from the parameter p . The value of sensitivity coefficient $ss \in (0, 1]$ can also be chosen arbitrarily, but it must secure fulfilment of conditions $w_i^{l+1} > 0$ for $\forall (i = \overline{1, n}; l \in \{0\} \cup \mathbb{N})$.

IV. RESULTS OF COMPUTING EXPERIMENT

A. Choice of the group of countries and time interval, selection of necessary indices

In this section the computing experiment ([10]) is described. As the investigated countries were chosen 8 countries of Central and Eastern Europe: Republic of Bulgaria, Republic of Croatia, Czech Republic, Hungary, Romania, Republic of Serbia, Slovak Republic, Republic of Slovenia; as the investigated time interval was chosen the interval [2012, 2014]; as the economic indices were chosen 30 economic, financial, social, demographic etc. indices: P1 – Population size of country (thousands); P2 – Population size of largest cities (thousands); P3 – Population of the largest urban agglomeration in the range of $>200\ 000$ (thousands); P4 – Urbanization (thousands); P5 – Number of adults (thousands); P6 – Total wealth (billion EUR); P7 – Wealth per adult (EUR); P8 – Wealth of adults in the range of $\leq 10\ 000$ EUR (percentage); P9 – Wealth of adults in the range of $10\ 000 \div 100\ 000$ EUR (percentage); P10 – Wealth of adults in the range of $100\ 000 \div 1\ 000\ 000$ EUR (percentage); P11 – Wealth of adults in the range of $>1\ 000\ 000$ EUR (percentage); P12 – Gini index; P13 – GDP (billion EUR); P14 – Growth rate in Real GDP (percentage); P15 – GDP (at purchasing power parity) per capita (EUR); P16 – Unemployment rate published by the EU Labour Force Survey (percentage); P17 – Consumer prices per annum (percentage); P18 – Foreign direct investment (FDI) net inflows (million EUR); P19 – Exchange rate stability; P20 – Ease of doing business index (+1 for position); P21 – Economic Development Board (EDB)/ Paying Taxes (EUR); P22 – Economic Development Board (EDB)/Tax Burden (percentage); P23 – Economic Development Board (EDB)/Trading Across Borders (position); P24 – Corruption Perceptions Index (CPI); P25 – Credit rating ($0 \div 100$); P26 – Net international

investment position (billion EUR); P27 – Capital flight (CF) (million EUR); P28 – Quality of Life Index; P29 – Offshore concentration defined on indirect indications (+1 for each indication); P30 – Ratio of financial and non-financial wealth.

Remark 3. It is necessary to mention that this set of 30 indices does not claim to be "the fullest and absolutely true" set, having which is necessary and sufficient to estimate customer segment of the investigated countries of Central and Eastern Europe in order to carry out potential export of bank and other luxurious services. In other words, authors of this work admit that respective specialists (for example, specialists in investment and financial services) may not agree with the choice of exactly this list of indices and may offer a more adequate list, which could seriously differ from the one we offer. However, it is worth noting that authors of this work have chosen 30 indices out of 43 economic, financial, social, demographic, political, educational etc. indices (extensively used by The World Bank and other transnational organizations of relevant profile), beforehand analyzing their "suitability" in our investigation – estimation of economic potential of a group of countries for possible export of bank and other financial luxurious services to these countries.

Remark 4. Indices P8, P12, P16, P19, P20, as opposed to other 25 indices, have the following property: big value of each of them causes smaller economic potential for export of bank and other luxurious services.

Remark 5. Before implementing the necessary procedure of standardization to all 30 indices, we used the following simple scaling to the indices P8, P12, P16, P19, P20 and P26:

- the values of indices P8, P12, P16, P20 are scaled according to the rule $\tilde{a}_{ij} = 100 - a_{ij}$;
- the values of index P19 are scaled according to the rule $\tilde{a}_{ij} = 1.1 - a_{ij}$;
- the values of index P26 are scaled according to the rule $\tilde{a}_{ij} = -a_{ij}$.

This scaling, obviously, conserves distributional similarity of these 6 indices, however it allows to eliminate the inverse proportionality of these 6 indices to the potential of export of bank services.

Remark 6. As method of standardization of initial values of all 30 indices we chose the formula (2), which implies implementation of the mathematical model (1), (2) both for finding economic potentials of the 8 investigated countries and for finding the weighted coefficients of 30 indices.

B. Results

The results (in brief) of the conducted computing experiment are reflected below. Let's note that as the initial data the real values of P1-P30 indices ([1]) for 8 above-listed countries in three years (2012-2014) are taken.

Table 1.
The ratings and the economic potentials of the investigated 8 countries

Country	Abridged results	
	Rating	Economic potential
Republic of Bulgaria	7	2.986
Republic of Croatia	6	3.230
Czech Republic	1	5.359
Hungary	2	4.303
Romania	5	3.474
Republic of Serbia	8	2.542
Slovak Republic	4	3.879
Republic of Slovenia	3	4.225

Table 2.
The ratings of the years by the found potentials' power

Ordered rating	Year	Value of rating
1	2012	9982.33295056359
2	2013	9982.80211546073
3	2014	9983.07377612381

Table 3.
Years-averaged standardized weighting coefficients values of indices

Index	Weight	Index	Weight
P1	0.401	P16	0.2862
P2	0.3345	P17	0.5536
P3	1.1	P18	0.7475
P4	0.2878	P19	0.2768
P5	0.3347	P20	0.4571
P6	0.6591	P21	0.3833
P7	0.6294	P22	0.3363
P8	0.3605	P23	0.386
P9	0.4164	P24	0.5681
P10	0.9553	P25	0.542
P11	1.1	P26	0.4783
P12	0.5578	P27	0.2944
P13	0.4987	P28	0.3921
P14	0.4081	P29	0.3223
P15	0.3744	P30	0.303

V. CONCLUSION

In this work we investigate the problem of estimation of economic potentials of a group of countries by their measurable economic, financial, social etc. indices with the aim of export of bank and other luxurious services to these countries. In the work, in order to solve the assigned problem, we offer (and justify) a qualitatively other approach based on the apparatus of the theory of inverse and ill-posed problems and differing from the traditional approaches, where a priori not given weighted coefficients of the measurable indices are set by the use of additional information, which, from the point of view of mathematical rigor, in no way can claim to be objective: for example, by the use of surveys among involved experts and other subjective procedures.

It is important to emphasize that our approach allows not only to find the desired economic potentials

of the countries, but also the weighted coefficients of all indices without any subjective assumptions and additional information, using only value of indices, which form our initial data.

VI. ACKNOWLEDGMENTS

Authors of the present paper express sincere gratitude to the colleagues Andris Nātriņš and Kristaps Lešinskis from BA School of Business and Finance, Riga, Latvia for their valuable remarks on selection of the necessary indices in order to carry out computing experiment; as well as Dr. Ivars Driķis from University of Latvia for his detailed discussion and help in order to computer realization of the developed by the present paper's authors the mathematical model and method.

For the first and the third co-authors the present article was executed within the framework of The State Research Programme "Next generation Information and Communication Technologies" ("NextIT"), Project No. 4.

REFERENCES

- [1] Various economic, financial, social, political, legal, educational, scientific innovative, ecological, cultural, etc. factors. [Online]. Available: <http://www.worldbank.org/>, <http://www.eiu.com/home.aspx>, <https://www.weforum.org/>, <http://www.transparency.org/>, <http://www.heritage.org/>, <https://www.ihs.com/industry/economics-country-risk.html>, <http://www.prosperity.com/>, <http://hdr.undp.org/en> [Accessed: March 13, 2017].
- [2] P. R. Krugman and M. Obstfeld, *International Economics: Theory & Policy*, 8th Edition. Boston-San Francisco-New York, USA: Pearson Addison Wesley, 2007, xxviii+687 p.
- [3] P. R. Krugman and R. Wells, *Economics*, 4th Edition. New York, USA: Worth Publishers, 2015, xlili+1016 p.
- [4] P. R. Krugman, R. Wells, and K. Graddy, *Essentials of Economics*, 2nd Edition. New York, USA: Worth Publishers, 2011, xxvii+604 p.
- [5] A. Chalenko, "Methodology for determining the economic potential", February 2013. [Online]. Available: http://kapital-rus.ru/articles/article/metodika_opredeleniya_ekonomicheskogo_potenciala/ [Accessed: March 13, 2017].
- [6] O. S. Puzikov, *Course of Lectures on socio-economic forecasting*. Rostov-on-Don, Russian Federation: Don State Technical University Press, 2000, 124 p.
- [7] A. N. Asaul and N. I. Pasyada, *Investment attractiveness of the region*. Saint-Petersburg, Russian Federation: Saint-Petersburg State University of Architecture and Civil Engineering Press, 2008, 120 p.
- [8] N. I. Klimova, *Investment attractiveness of the region*. Yekaterinburg, Russian Federation: Ural Division of the Russian Academy of Sciences Press, 2003, 276 p.
- [9] E. A. Blyum, "Review of methodologies for assessing the investment potential of the region", *Young Scientist*, vol. 54, No. 7, pp. 137-141, 2013.
- [10] A. Natrinss, I. Deikis, Sh. E. Guseynov, K. Leshinskis, and A. Sarnovichs, *Fundamental Principles of Creation of Attractiveness Principles of Central and Eastern European Countries for Evaluation of Customer Segment and Financial Services Potential*. Riga, Latvia: Business and Financial Research Centre Press, 2015, 107 p.

On the Ginzburg-Feinberg Problem of Frequency Electromagnetic Sounding for Unambiguous Determination of the Electron Density in the Ionosphere

Sharif E. Guseynov^{1, 2, 3,a}, Janis S. Rimshans^{1,2}

¹Institute of Fundamental Science and Innovative Technologies, Liepaja University, Liepaja LV-3401, Latvia;

²Faculty of Science and Engineering, Liepaja University, 4 Kr. Valdemar Street, Liepaja LV-3401, Latvia;

³"Entelgine" Research & Advisory Co., Ltd., Kleistu Street 2-53, Riga LV-1067, Latvia; ^ash.e.guseinov@inbox.lv

Abstract. In the present work, we investigate an inverse problem of frequency electromagnetic sounding for unambiguous determination of the electron density in the ionosphere. Direct statement of this problem is known as the Ginzburg-Feinberg problem that has, in general case, an essential nonlinearity. Inverse statement of the Ginzburg-Feinberg problem has the boundary-value formulation relative to two functions: the sought-for electric-field strength and the distribution of the electron density (or rather two-argument function appearing in the additive decomposition formula for distribution of the electron density) in the ionosphere. In the present work, we prove the existence and uniqueness of the solution of the Ginzburg-Feinberg problem as well as we propose the analytical method, permitting: first, to reduce it to the problem of integral geometry, and, thereupon, having applied the adjusted variant of the Lavrentiev's theorem, to reduce the obtained problem of integral geometry to the first kind matrix integral equation of Volterra type with a weak singularity.

Keywords: frequency electromagnetic sounding, electron density, Ginzburg-Feinberg problem, inverse boundary-value problem.

I. INTRODUCTION

The term "ionosphere" was introduced by Scottish physicist Sir R.A. Watson-Watt in 1926 in one of his letters, which was published only in 1969 in the English multidisciplinary scientific journal "Nature Magazine" ([1]). Apparently, the beginning of the history of studies of ionosphere is tied to the work of Italian electrical engineer and radio technician G. Marconi (awarded Nobel prize in Physics in 1909), who, in the end of December 1901, conducted a unique experiment and managed to get transatlantic radio signal, using a 152m tall antenna. In 1902, English physicist O. Heaviside supposed that the atmosphere has an ionized layer. His theory claimed that a radio signal can travel across the Earth despite its curvature. Independently from O. Heaviside, American electrical engineer A.E. Kennelly was conducting his own experiments to study transmission of short waves over Atlantics ([2]). The experiments conducted by O. Heaviside and A.E. Kennelly indicated that somewhere around the Earth there should an ionized layer of the atmosphere, which is capable of reflecting radio waves (now that layer is named "Kennelly-Heaviside layer" or just "E-region"). Possibly, the ideas of O. Heaviside and A.E. Kennelly together with the law of radiation of black body, which was formulated by German theoretical physicist M. Planck

(awarded Nobel prize in Physics in 1918), contributed to the rapid development of radio astronomy starting with 1932. Also, it served as the founding point in the development of high frequency systems of the receiver-transmitter. In 1924, English physicist E.V. Appleton (awarded Nobel prize in Physics in 1947) together with his colleagues from the Cavendish Laboratory, University of Cambridge, and King's College London conducted the famous experiment (having strongly defined the theoretical basis for it, presenting that in advance) when the approximate height of ionosphere was detected for the first time ever. Then, in 1924-1927, Sir E.V. Appleton did prove the existence of the Earth's ionosphere, focusing his work and studies on that fundamental issue. In 1924, American geophysicist and engineer (one of the most notable specialists in the domains of Earth magnetism and ionosphere) L.V. Berkner did measure electronic density of ionosphere for the first time. Later, in 1933-1934, together with the colleagues from the Brookhaven National Library, Long Island, USA ([3]-[6]) he studied the fundamental physical issues tied to the effect of magnetoionic birefringence effect of radio waves in ionosphere and magnetoionic splitting of E-region, using critical frequency. Also, they proved the existence of substratification of F-region (proved the existence of the F₁ layer under the

ISSN 1691-5402

© Rezekne Academy of Technologies, Rezekne 2017
<http://dx.doi.org/10.17770/etr2017vol3.2561>

main F₂ layer). The results obtained by L.V. Berkner later appeared to be crucially important for creation of the short radio waves theory. Innovative studies of influential British radio physicist J.A. Ratcliffe and British physicist M.V. Wilkes (further – notable scientist in the domain of computer sciences) did stimulate creation of the theory of spread of very long radio waves in ionosphere ([7]-[10]). In 1940-1960, Soviet theoretical physicist and astrophysicist V.L. Ginzburg (awarded Nobel prize in Physics in 2003) developed the theory of spread of electromagnetic waves in plasma, in particular – in ionosphere.

In the current paper, authors study a non-linear problem of detection of density of electrons in ionosphere by the method of frequency electromagnetic probing. Its mathematical formulation can be found in the fundamental [11] and [12]. Apparently, authors of these monographs independently each from another did formulate and study the current non-linear problem, full solution of what is absent, as for now. In our paper, we study the issues of the existence and uniqueness of solution of the stated problem.

II. STRUCTURE AND KEY PARAMETERS OF THE IONOSPHERE, BASIC INVESTIGATION METHODS

Ionosphere is defined as border part of the Earth's atmosphere where the level of ionization is big enough to make notable impact on the spread of radio waves. ([4], [7], [11], [13], [14]). The lower border of ionosphere is at the height of around 50-60 km from the surface of the Earth, while its upper border is at the level of approximately 1000 km and transcends into plasmasphere and other magnetospheric plasma formations. The main parameters of ionosphere are its ionic composition, temperature, and concentration of electrons; and these parameters have complex dependence from the height. ([11], [13], [14]). If we are limited with consideration of only one parameter – concentration of electrons in ionosphere, then, usually, there are three spaces of the maximal concentration of electrons:

- D-region, which is about 60÷90 km above the ground and has maximal concentration of electrons 10^3 cm^{-3} ;
- E-region, which is sometimes called Kennelly-Heaviside Layer, being 90÷120 km above the ground and having maximal concentration of electrons 10^5 cm^{-3} . Such a dense concentration is achieved only in a thin space (as thin as 0.5÷1 km), it is called E_s layer (100÷110 km above the ground);
- F-region, often called Appleton-Barnett layer, 120÷300 km above the ground, maximal concentration of electrons 10^6 cm^{-3} . Such concentration of electrons is achieved in the so-called F₂ layer (170÷300 km above the ground), while in the layer F₁ (120÷170 km above the

ground) the maximal concentration of electrons can be observed only in daytime, as it is caused by strong sun ultraviolet radiation, and it can drop up to 10^4 cm^{-3} level.

Worth underlining that the values mentioned above are presented as landmarks, since the heights of layers as well as concentration of electrons in them do experience strong regular sporadic ([11], [13]-[15]). Sporadic variations of the three main spaces of ionosphere – ion composition, temperature, and concentration of electrons – are tied to the interaction of particles and radiations generated in the sun or magnetospheric flare events. Sudden ionospheric disturbances in E- and D-regions are caused by X-ray burst generated in the Sun during chromospheric flares, which last only few minutes, while concentration of electrons in D-region can increase in dozen times; in E-region – it can increase twice. The effects and collateral phenomena are observed only in the enlightened part of ionosphere. When solar space beams reach the Earth, it causes an ionospheric disturbance known as Polar Cap Absorption (PCA). PCA belongs to D-region of ionosphere where concentration of electrons can double. Length of PCA is defined by the length of the event, which causes it. So, it can last up to several days. Development of auroral substorm causes notable changes in the entire ionosphere and changes the conditions of transmission of radio signals up to total absorption.

Now, the main methods of study if ionosphere are being presented. First, it is worth being mentioned that study of ionosphere is one of the actual scientific problems, which is tied both to the issues of fundamental problems of the physics of space plasma as well as to the applied problems. Impermanence of ionosphere (especially that in the high latitudes) attracted much attention, because of the importance of stable radio connection for both military and civil operations. Studies of ionosphere until the time, when opportunities for direct with rockets and satellites were provided, were based on its ability to absorb, reflect, and spread radio signals. The main methods of study of ionosphere are: method of particular electromagnetic probing; methods of vertical, incline, and reverse-incline probing; riometric and radiolocational methods; method of incoherent dissolution; method of spread of superlong waves. Worth mentioning that ionospheric methods are applied not only in the studies of the ionosphere itself, and its parameters, but also for studies of magnetospheric processes.

III. MATHEMATICAL STATEMENT OF THE ORIGINAL PROBLEM

As it was already mentioned in the introduction, concentration of electrons is one of the three main parameters for studying ionosphere ([7], [11], [16]). In the current section, we study the reverse problem for the sought-for concentration of electrons in the

ionosphere with frequency electromagnetic probing of the ionosphere.

So, we approach the following boundary-value inverse problem: it is required to determine the function $E(x, z; \omega)$ and $V(x, z)$, where $(x, z; \omega) \in [0, L] \times \mathbb{R}_{++}^1 \times [0, \omega_{\max}]$, which fit the equation

$$\left\| \nabla_{x,z} E(x, z; \omega) \right\|_{\mathbb{R}^2}^2 - \varepsilon(x, z; \omega) = 0, \quad (1)$$

$$x \in (0, L), \quad z \in \mathbb{R}_{++}^1, \quad \omega \in (0, \omega_{\max}),$$

the Dirichlet boundary conditions

$$E(x, z; \omega) \Big|_{(x,z)=(0,0)} = 0, \quad \omega \in [0, \omega_{\max}], \quad (2)$$

$$E(x, z; \omega) \Big|_{(x,z)=(L_j, 0)} = E_j(\omega), \quad \omega \in (0, \omega_j) \quad j = \overline{0, n}, \quad (3)$$

and additional condition

$$0 \leq |V(x, z)| \ll U(z), \quad x \in [0, L], \quad z \in \mathbb{R}_+^1, \quad (4)$$

where sought-for $E(x, z; \omega)$ is the electric-field strength; the dielectric permeability of the ionosphere is designated as

$$\varepsilon(x, z; \omega) \stackrel{\text{def}}{=} \frac{m \cdot (\omega^2 + \nu_{\text{effective}}^2) - 4 \cdot \pi \cdot e^2 \cdot N(x, z)}{m \cdot (\omega^2 + \nu_{\text{effective}}^2)};$$

m is the electron mass; $\omega = \omega(z)$ is the cyclic/angular frequency of the electromagnetic field; e is the elementary electronic charge; $\nu_{\text{effective}}$ is the effective number of collision of an electron with molecules or ions per second, and at each collision an electron on the average passes to a molecule or ion the pulse of the order $m \cdot \bar{v}^2$, where \bar{v} means an ordered velocity imparted to the electron by electromagnetic field \vec{E} ; $N(x, z) \stackrel{\text{def}}{=} U(z) + V(x, z)$ is sought-for distribution of the electron density in the ionosphere, where $U(z) \in D^1(\mathbb{R}_{++}^1)$ is a priori given function, and $V(x, z) \stackrel{\text{def}}{=} \sum_{i=0}^n \varphi_i(z) \cdot x^i$ is unknown; the boundary functions $E_j(\omega)$, $\omega \in (0, \omega_j) \quad \forall j = \overline{0, n}$ are experimentally measurable functions, and the essence of these values consists in the field phase, i.e. an eikonal (for instance, see [17]) at the measuring points $A_i(x = L_i, z = 0)$, $\forall i = \overline{0, n}$ relative to the phase of some measuring device located at the point $O(x = 0, z = 0)$; $\omega_{\max} \in \mathbb{R}_{++}^1$; $L \in \mathbb{R}_{++}^1$; $n \in \mathbb{N}$;

$$L_j \in (0, L) \quad \forall j = \overline{0, n}; \quad \omega_j \in (0, \omega_{\max}) \quad \forall j = \overline{0, n};$$

$$\mathbb{R}_+^1 \stackrel{\text{def}}{=} [0, +\infty); \quad \mathbb{R}_{++}^1 \stackrel{\text{def}}{=} (0, +\infty).$$

IV. TRANSFORMATION OF THE ORIGINAL PROBLEM TO A PROBLEM OF INTEGRAL GEOMETRY

First, shall we note that the additional information (4) cause study of the two mutually exclusive cases:

$$V(x, z) \equiv 0, \quad (x, z) \in [0, L] \times \mathbb{R}_{++}^1, \quad (5)$$

$$V(x, z) \neq 0, \quad (x, z) \in [0, L] \times \mathbb{R}_{++}^1. \quad (6)$$

In the beginning, let us assume that the case (5) is the actual situation. Then, evidently, the initial problem (1)-(4) becomes direct: we need to define only the function $E(x, z; \omega)$. By the actual check, it is possible to find out that $\lambda(x)$ of the equation (1) is the solution for the Bernoulli equation ([18])

$$\lambda''(x) + C(z) \cdot (\lambda'(x))^2 = -A(z), \quad (7)$$

where

$$C(z) \stackrel{\text{def}}{=} \frac{2 \cdot \pi \cdot e^2 \cdot U'(z)}{m \cdot (\omega^2 + \nu_{\text{effective}}^2) - 4 \cdot \pi \cdot e^2 \cdot U(z)},$$

$$U(z) = \begin{cases} 0, & z \in [0, Z]; \\ U(z) \in D^3(Z, +\infty), \\ 0 < c \equiv \text{const} < U'(z), \end{cases} \quad z \in [Z, +\infty) \quad (8)$$

So, in the case (5) the problem of definition of the function $E(x, z; \omega)$ from the direct (1)-(4) results ([19]) to the problem of finding the function $\lambda(x)$ from (7), (8) with the boundary conditions

$$\lambda(x) \Big|_{x=0} = 0; \quad \lambda(L) \Big|_{x=0} = 0. \quad (9)$$

Since the solution of the boundary-value problem (7)-(9) depends from the parameter ω , as the result we have set of characteristics $\lambda = \lambda(x; \omega)$, linking the point $O(x = 0, z = 0)$ of the location of the measurement device with the point $A(x = L, z = 0)$ of the measurement, which depends on the cyclic frequency ω of the electromagnetic field $\vec{E}(x, z; \omega)$. Since the problem (7)-(9) is solved in quadrants, study of the case (5) is fully accomplished, and now we can switch to the study of the case (6). For that purpose, we introduce the functional first

$$\Omega[S(z)] \stackrel{\text{def}}{=} \frac{m \cdot (\omega^2 + \nu_{\text{effective}}^2) - 4 \cdot \pi \cdot e^2 \cdot S(z)}{m \cdot (\omega^2 + \nu_{\text{effective}}^2)}$$

and consider the equation

$$\|\nabla_{x,z} E_U(x, z; \omega)\|_{\mathbb{R}^2}^2 = \Omega[U(z)]. \quad (10)$$

Evidently that when $z_0 \in [0, Z]$ we can write

$$\frac{4 \cdot \pi \cdot e^2 \cdot V(x, z(x, z_0))}{m \cdot (\omega^2 + v_{\text{effective}}^2) \cdot \Omega[U(z(x, z_0))]} = O\left(\frac{V(x, z(x, z_0))}{U(z(x, z_0))}\right),$$

so consequently, with an accuracy up to infinitesimal of the second order of the fraction $\left[\frac{V(x, z(x, z_0))}{U(z(x, z_0))}\right]^2$ on the characteristic curves of the equation (10) there is an equality

$$\varepsilon(x, z; \omega) = \frac{\sqrt{\Omega[U(z(x, z_0))]} - 2 \cdot \pi \cdot e^2 \cdot V(x, z(x, z_0))}{m \cdot (\omega^2 + v_{\text{effective}}^2) \cdot \sqrt{\Omega[U(z(x, z_0))]}}.$$

Theorem (Lavrentyev, [20]). Let $u_i(x_1, x_2) = u_{i,1}(x_1, x_2) + u_{i,2}(x_1, x_2)$, ($i = 1; 2$) where $u_{1,j}(x_1, x_2) \in D^2\{X_1 \times X_2\}$, ($j = 1; 2$) and function $u_{2,2}(x_1, x_2)$ are the solution of the equation

$$\left(\frac{u_{2,1}(x_1, x_2)}{\partial x_1}\right)^2 + \left(\frac{u_{2,1}(x_1, x_2)}{\partial x_2}\right)^2 = u_{1,1}^2(x_1, x_2). \quad (11)$$

Then, with an accuracy up to infinitesimal of the 2nd order of $u_{1,1}^2(x_1, x_2)$, we can present the function

$u_{2,1}(x_1, x_2)$ as

$$u_{2,2}(A) = \int_{\Gamma_{OA}} u_{1,1}(x_1, x_2) d\gamma_{OA},$$

where Γ_{OA} as characteristic curve of the equation (11), linking points $O(x_1 = 0, x_2 = 0)$ and $A(x_1, x_2)$.

For being able to use the above mentioned Lavrentiev's Theorem in our study, we consider the solution of equation (1) in relation to the parameter ω at the point $(x = L, z = 0)$, in advance switching the parameter ω for z_0 : such substitution is possible, since from the evident formula

$$\sqrt{\frac{m \cdot (\omega^2 + v_{\text{effective}}^2) \cdot \Omega[U(z_0)]}{4 \cdot \pi \cdot e^2}} \cdot \int_0^{z_0} \frac{d\xi}{\sqrt{U(z_0) - U(\xi)}} = \frac{L}{2},$$

which is the consequence of the equation (7) and from the fact that $\lambda(x)$ is symmetrical function in relation to the straight line $x = \frac{L}{2}$, which is

$$\lambda\left(\frac{L}{2} - x\right) = \lambda\left(\frac{L}{2} + x\right) \Leftrightarrow \lambda(x) = \lambda(L - x), \quad (12)$$

so it is that each z_0 has only one value of $\omega = \omega(z_0)$

corresponding. Then, we can write that $E = E(L, 0; z_0)$. An analogical approach lets us define the function $E_U = E_U(L, 0; z_0)$ as the relevant solution of the equation (9) in relation to the parameter ω at the point $(x = L, z = 0)$, also introducing in advance the parameter ω instead of z_0 . Further, we introduce the function

$E(L, 0; z_0) \stackrel{\text{def}}{=} E_V(L, 0; z_0) + E_U(L, 0; z_0)$, and again consider the Lavrentiev's Theorem. Then, we can formulate the following theorem:

Theorem 1. With an accuracy up to infinitesimal of the second order of the fraction $\left[\frac{V(x, z(x, z_0))}{U(z(x, z_0))}\right]^2$ the function $E_V(L, 0; z_0)$ with $z_0 \in [0, Z]$ can be presented as

$$E_V(L, 0; z_0) = -\frac{2 \cdot \pi \cdot e^2}{\sqrt{m \cdot (\omega^2(z_0) + v_{\text{effective}}^2)}} \times \int_{\Gamma_{OA}} \frac{V(x, z(x, z_0)) dx}{\sqrt{m \cdot (\omega^2 + v_{\text{effective}}^2) \cdot \Omega[U(z(x, z_0))]}}. \quad (13)$$

So, in the case (6), the initial problem (1)-(4) is presented as the following problem of integral geometry: it is required to restore the function $V(x, z)$ by its integrals by the series of curves

$$\int_{\Gamma_{OA}} K(z(x, z_0)) \cdot V(x, z(x, z_0)) dx = f(L, z_0), \quad (14)$$

where

$$K(z(x, z_0)) \stackrel{\text{def}}{=} \frac{1}{\sqrt{\Omega[U(z(x, z_0))]}}, \quad (15)$$

$$f(L, z_0) \stackrel{\text{def}}{=} -\frac{\sqrt{m \cdot (\omega^2(z_0) + v_{\text{effective}}^2)} \cdot E_V(L, 0; z_0)}{2 \cdot \pi \cdot e^2}. \quad (16)$$

V. SOLVING THE OBTAINED PROBLEM OF INTEGRAL GEOMETRY

The study of the problem (14)-(16) of integral geometry is done in two stages: first, we formulate and solve the auxiliary problem of integral geometry, where it is required to restore the function $V(x, z)$ by the measurement of intensity of electric field $E(x, z; \omega)$, $\omega \in (0, \omega_0)$, $\omega_0 \in (0, \omega_{\text{max}})$ only at one point; secondly, based on the data what we get in the first problem we study the general problem of integral geometry, where it is required to restore the function

$V(x, z)$ by measurement of intensity of electric field $E(x, z; \omega)$, $\omega \in (0, \omega_j)$, $\omega_j \in (0, \omega_{\max})$, $\forall j = \overline{1, n}$ by measurements at $(n+1)$ points.

A. The auxiliary problem and its investigation

Supposing that we know values $E(\omega) \stackrel{\text{def}}{=} E(x, z; \omega)|_{(x,z)=(L,0)}$, for $\forall \omega \in (0, \omega_0)$, $\omega_0 \in (0, \omega_{\max})$, from the problem (14)-(16) it is required to define the function

$$\varphi(z) = \begin{cases} 0, & z \in [0, Z]; \\ \varphi(z) \in C[Z, +\infty), & z \in [Z, +\infty), \end{cases} \quad (17)$$

which, then, means the function $V(x, z) \stackrel{\text{def}}{=} \varphi(z) \cdot x$.

Theorem 2. There is no more than one function $\varphi(z)$ of the kind (17), which corresponds to each given first part $f(L, z_0)$ of the kind (16) of the equation (14).

Proof of the Theorem 2. From (12) and from the fact that

$$\alpha(z, z_0) \stackrel{\text{def}}{=} \sqrt{\frac{m \cdot (\omega^2(z_0) + v_{\text{effective}}^2) \cdot \Omega[U(z_0)]}{4 \cdot \pi \cdot e^2}} \times \int_z^{z_0} \frac{d\xi}{\sqrt{U(z_0) - U(\xi)}} \in D^2[Z, +\infty),$$

we can claim

$$\int_0^{z_0} \alpha'_z(z, z_0) \cdot \varphi(z) dz = \frac{f(L, z_0)}{L}. \quad (18)$$

Since

$$\alpha'_z(z, z_0) = \sqrt{\frac{m \cdot (\omega^2(z_0) + v_{\text{effective}}^2) \cdot \Omega[U(z_0)]}{\pi \cdot e^2 \cdot U'_z(z)|_{z=z_0}}} \times \frac{2 \cdot (z_0 - z) \cdot \beta'_z(z, z_0) - \beta(z, z_0)}{2 \cdot \sqrt{z_0 - z}},$$

where

$$\beta(z, z_0) \stackrel{\text{def}}{=} \frac{\alpha(z, z_0)}{\sqrt{(z_0 - z)}} \times \sqrt{\frac{\pi \cdot e^2 \cdot U(z_0)}{m \cdot (\omega^2(z_0) + v_{\text{effective}}^2) \cdot \Omega[U(z_0)]}}, \quad (19)$$

Then equation (18) takes the following form:

$$\int_0^{z_0} \frac{\tilde{K}(z, z_0)}{\sqrt{z_0 - z}} \cdot \varphi(z) dz = F(z_0), \quad (20)$$

where the core $\tilde{K}(z, z_0)$ and the right part $F(z_0)$ are defined by formulas

$$\tilde{K}(z, z_0) \stackrel{\text{def}}{=} 2(z_0 - z) \beta'_z(z, z_0) - \beta(z, z_0);$$

$$F(z_0) \stackrel{\text{def}}{=} \frac{2}{L} \sqrt{\frac{\pi e^2 U'_z(z)|_{z=z_0}}{m(\omega^2(z_0) + v_{\text{effective}}^2) \Omega[U(z_0)]}} f(L, z_0). \quad (21)$$

Due to arbitrariness of the point $z_0 \in [Z, +\infty)$, the obtained integral equation (20) is the first kind Volterra integral equation with a weak singularity. Consequently, in the space $C[Z, +\infty)$ of continuous function, the problem (20), (21) can have only one solution ([21]). With that, the proof of the Theorem 2 is finished.

Remark. The Theorem 2, which was just proved, does not give an answer to the question of existence of solution of the problem (20), (21), so, consequently, also to the above mentioned auxiliary problem of integral geometry, too. Any condition, which guarantees smoothness of the function $F(z_0)$ from (21) is the sufficient condition for solution of the auxiliary problem of integral geometry.

B. The original general problem and its investigation

Supposing that for $\forall j = \overline{0, n}$ we know values

$E_j(\omega) \stackrel{\text{def}}{=} E(x, z; \omega)|_{(x,z)=(L_j,0)}$ for $\forall \omega \in (0, \omega_j)$, $\omega_j \in (0, \omega_{\max})$, it is required from the problem (14)-(16) to define the function

$$\varphi_j(z) = \begin{cases} 0, & z \in [0, Z]; \\ \varphi_j(z) \in C[Z, +\infty), & z \in [Z, +\infty), \end{cases} \quad (22)$$

and, by that, the function $V(x, z)$.

Theorem 3. There is no more than one collection of functions $\{\varphi_j(z)\}_{j=\overline{1, n}}$ of the kind (22), corresponding to each set of the right-hand side $\{f_j(L_j, z_0)\}_{j=\overline{0, n}}$ of the kind (22) of the equation (14).

Proof of the Theorem 3. We consider a randomly chosen point L_k from the given set $\{L_j\}_{j=\overline{0, n}}$ and consider $V(x, z)$ in the equation (14) of integral geometry:

$$\int_0^{L_k} \left\{ \sum_{i=0}^n \varphi_i(z_k(x, z_0)) \cdot x^i \right\} dx = \int_0^{z_0} \left[\alpha_k(z, z_0) \right]'_z \cdot \sum_{i=0}^n \left\{ \left(\alpha_k(z, z_0) + \frac{L_k}{2} \right)^i - \left(\alpha_k(z, z_0) - \frac{L_k}{2} \right)^i \right\} \cdot \varphi_i(z) dz = f_k(L_k, z_0), \quad (23)$$

where $\alpha_k(z, z_0) \stackrel{\text{def}}{=} \alpha(z(L_k, z_0), z_0)$.

Applying to the equation (23) the method analogical to the one applied at the first stage, while we were formulating the formulas (18)-(21), we get the following integral equation:

$$\int_0^{z_0} \sum_{i=0}^n \frac{L_k^i \cdot \tilde{K}_{k,i}(z, z_0)}{2^{i-1} \cdot \sqrt{z_0 - z}} \cdot \varphi_i(z) dz = F_k(z_0), \quad (24)$$

where we mark

$$\left. \begin{aligned} \tilde{K}_{k,i}(z, z_0) &\stackrel{\text{def}}{=} \tilde{K}^i(z(L_k, z_0), z_0); \\ F_k(z_0) &\stackrel{\text{def}}{=} \frac{2}{L_k} \cdot \sqrt{\frac{\pi \cdot e^2 \cdot U'_z(z)|_{z=z_0}}{m \cdot (\omega^2(z_0) + v_{\text{effective}}^2)} \cdot \Omega[U(z_0)]} \end{aligned} \right\}$$

We introduce the following marking:

$$- M \stackrel{\text{def}}{=} \left\{ \frac{L_i^j}{2^{j-1}} \right\}_{i=0, \overline{n}}^{j=0, \overline{n}} \text{ is the quadratic matrix of size } (n+1) \times (n+1);$$

$$- \tilde{K} \stackrel{\text{def}}{=} \left\{ \tilde{K}_{i,j} \right\}_{i=0, \overline{n}}^{j=0, \overline{n}} \text{ is the quadratic matrix of size } (n+1) \times (n+1), \text{ constituents of which are calculated by the formula}$$

$$\tilde{K}_{i,j} = \left(2 \cdot (z_0 - z(L_j, z_0)) \cdot \beta'_z(z(L_j, z_0), z_0) - \beta(z(L_j, z_0), z_0) \right)^i,$$

where the function $\beta(z(L_j, z_0), z_0)$ is defined by the formula (19);

- I is an identity matrix of size $(n+1) \times (n+1)$;

- $\Phi \stackrel{\text{def}}{=} \{ \varphi_i \}_{i=0, \overline{n}}$ is a column-vector of size $(n+1) \times 1$, constituents of which are sought-for functions of the equation (24) (consequently, of the original general problem of integral geometry);

- $F \stackrel{\text{def}}{=} \{ F_i \}_{i=0, \overline{n}}$ is the column-vector of size $(n+1) \times 1$, constituents of which are calculated by the formula

$$F_j \stackrel{\text{def}}{=} \frac{2}{L_j} \cdot \sqrt{\frac{\pi \cdot e^2 \cdot f^2(L_j, z_0) \cdot U'_z(z)|_{z=z_0}}{m \cdot (\omega^2(z_0) + v_{\text{effective}}^2)} \cdot \Omega[U(z_0)]},$$

where $f(L_j, z_0)$ is a function in the form (16).

The above stated lets rewrite the integral equation (24) in a matrix form:

$$M \int_0^{z_0} \frac{\tilde{K}I\Phi(z, z_0)}{\sqrt{z_0 - z}} dz = F(z_0). \quad (25)$$

Due to arbitrariness of the point $z_0 \in [Z, +\infty)$ obtained matrix integral equation (25) is the first kind Volterra equation with a weak singularity. Therefore, in the space $C[Z, +\infty)$ of continuous functions this equation can have unique solution. Also, the remark made above at the first stage remains correct also for the matrix integral equation (25): guaranteeing smoothness of the right side of the F equation (25) guarantees the existence of its solution, so, it also guarantees the existence of the solution of the initial problem of integral geometry. The proof of the Theorem 3 is finished.

Solution of the Abel's integral equation (25) is the following vector-function (for instance, see [29]):

$$\tilde{K}I\Phi(z, z_0) \Big|_{z=z_0} = \frac{1}{\pi} \cdot \frac{d}{dz_0} \int_0^{z_0} \frac{M^{-1}F(z, z_0)}{\sqrt{z_0 - z}} dz.$$

From here follows the following system of linear algebraic equations with respect to sought-for functions $\varphi_i(z)$, $i = \overline{0, n}$ at each point $z_0 \in [Z, +\infty)$:

$$\sum_{j=0}^n \tilde{K}_{i,j}(z, z_0) \Big|_{z=z_0} \cdot \varphi_j(z_0) = \frac{1}{\pi} \cdot \frac{d}{dz_0} \int_0^{z_0} \frac{(M^{-1}F(z, z_0))_i}{\sqrt{z_0 - z}} dz, \quad i = \overline{0, n}. \quad (26)$$

Having solved this system by some kind of direct methods, for $\forall i = \overline{0, n}$ we can find

$$\varphi_i(z_0) = \frac{1}{\pi} \cdot \left(\tilde{K}(z, z_0) \Big|_{z=z_0} \cdot \frac{d}{dz_0} \int_0^{z_0} \frac{M^{-1}F(z, z_0)}{\sqrt{z_0 - z}} dz \right)_i^{-1}.$$

However, it will be better to solve the system (26) by Tikhonov's regularization method for finding its stable solution (for instance, see [30], [31]).

VI. CONCLUSION

In the present work, we prove the existence and uniqueness of the solution of the inverse problem (1)-(4) as well as we propose the analytical method permitting: firstly, to reduce it to the problem of integral geometry, and thereupon, having applied the

adjusted variant of the Lavrentiev's theorem, to reduce the obtained problem of integral geometry to the first kind matrix integral equation of Volterra type with a weak singularity.

Let's note that the considered problem arises, generally, at study of the following problems (for instance, see [22]-[28] and respective references given in these): propagation of various low-frequency electromagnetic waves in the ionosphere, exosphere and adjacent to its regions of interplanetary space; propagation of radio waves in the ionosphere, i.e. in the upper layers of the Earth's atmosphere; propagation of radio waves of cosmic origin in the solar atmosphere, in the nebulae as well as in the interstellar and interplanetary spaces; propagation of radio waves at laser ranging of the Sun, the Moon and some planets as well as in case of communication with the distant artificial Earth satellites and space rockets; propagation of low-frequency magneto-hydrodynamic and acoustic waves in space environment; propagation of plasma waves both on the ionosphere and the solar corona; propagation of various types of electromagnetic waves in plasma created in vitro (i.e. at the laboratory conditions) at study of gaseous discharge as well as in installations meant for study of controlled thermonuclear reactions, etc.

It is appropriate also to mention here that by now the comprehension and the solid knowledge of the ionosphere have in many respects well-composed and completed character, and therefore, many sections of the discipline about the Earth's atmosphere is unlikely to undergo a change in the future. However, at present there are variety of investigated issues having the corresponding theoretical foundations only in a state of becoming: such fundamental issues as the formation of the ionosphere, the processes in the transition region between the ionosphere in the interplanetary medium, cloud formation mechanisms, wave excitation mechanisms, etc. have not yet been resolved in a satisfactory extent, and even there are variety of gaps and contradictions in the theories constructed for them.

VII. ACKNOWLEDGMENTS

For the first co-author the present article was executed within the framework of The State Research Programme "Next generation Information and Communication Technologies" ("NextIT"), Project No. 4.

REFERENCES

- [1] "Ionosphere". [Online]. Available: <https://en.wikipedia.org/wiki/Ionosphere> [Accessed: March 11, 2017].
- [2] "Kennelly-Heaviside Layer". [Online]. Available: http://ethw.org/Kennelly-Heaviside_Layer [Accessed: March 11, 2017].
- [3] W. R. Piggott and K. Rawer, *URSI Handbook of Ionogram Interpretation and Reduction*. Amsterdam, The Netherlands: Elsevier Publishing Company, 1961, 192 p.
- [4] H. R. Mimno, "The Physics of the Ionosphere", *Reviews of Modern Physics*, vol. 51, No. , pp. 1-43, 1937.
- [5] J. A. Pierce, and H. R. Mimno, "Unusual Range of Radio Signals", *Reviews of Modern Physics*, vol. 54, No. 6, pp. 475-477, 1938.
- [6] J. A. Pierce and H. R. Mimno, "The Reception of Radio Echoes From Distant Ionospheric Irregularities", *Physics Reviews*, vol. 57, No. 2, pp. 95-104, 1940.
- [7] J. A. Ratcliffe, *An Introduction to the Ionosphere and Magnetosphere*. Cambridge, UK: Cambridge University Press, 1972, 265 p.
- [8] J. A. Ratcliffe, "The Interaction of Radio Waves", *Journal of the Institution of Electrical Engineers*, vol. 95, No. 37, pp. 325-342, 1948.
- [9] J. A. Ratcliffe and I. J. Shaw, "A Study of the Interaction of Radio Waves", *Proceedings of the Royal Society A: Mathematical, Physical and Engineering Sciences*, vol. 193, No. 1034, pp. 311-343, 1948.
- [10] R. N. Bracewell, "The Ionospheric Propagation of Low- and Very-Long-Frequency Radio Waves Over Distances Less Than 1000 km", *Proceedings of the Institute of Electrical and Electronics Engineers, Part III: Radio and Communication Engineering*, vol. 98, No. 53, pp. 221-236, 1951.
- [11] V. L. Ginzburg, *Propagation of Electromagnetic Waves in Plasma*. Oxford, UK: Pergamon Press, 1971, 624 p.
- [12] E. L. Freinberg, *Radio-Wave Propagation along the Earth's Surface*. Moscow, Russian Federation: "Nauka" Publishing House, 1999, 496 p.
- [13] B. E. Bryunelli and A. A. Namgaladze, *Ionospheric Physics*. Moscow, USSR: "Nauka" Publishing House, 1988, 527 p.
- [14] L. I. Miroshnichenko, *Physics of Solar and Solar-Terrestrial Relation*. Moscow, Russian Federation: Lomonosov Moscow State University Press, 2011, 174 p.
- [15] F. G. Bass and Yu. G. Gurevich, "Nonlinear Theory of Electromagnetic Wave Propagation in Solid-State Plasma, and Theory of Gaseous Discharge", *Advances in Physical Sciences*, vol. 103, No. 3, pp. 447-468, 1971.
- [16] N. Jakowsky, R. Leitinger, and L. Ciraolo, "Behaviour of large scale structures of the electron content as a key parameter for range errors in GNSS applications", *Annals of Geophysics*, vol. 47, No. 2/3, pp. 1031-1047, 2004.
- [17] M. Born and E. Wolf, *Principles of Optics: Electromagnetic Theory of Propagation, Interference and Diffraction of Light*. Cambridge, UK: Cambridge University Press, 1999, 985 p.
- [18] M. I. Zelikin, *Homogeneous Space and the Riccati Equation in Calculus of Variations*. Moscow, Russian Federation: "FACTORIAL Publishing House, 1998, 351 p.
- [19] L. S. Pontryagin, *Ordinary Differential Equations*. Moscow, USSR: "Nauka" Publishing House, 1974, 331 p.
- [20] M. M. Lavrentyev, V.G. Vasilyev, and V.G. Romanov, *Multivariate Inverse Problems for Differential Equations*. Novosibirsk, RF: "Nauka" Publishing House, 1969, 73 p.
- [21] I. C. Gokhberg and M.G. Krein, *Theory of Volterra Operators in Hilbert Space and its Applications*. Moscow, RF: "Nauka" Publishing House, 1967, 508 p.
- [22] Y. L. Alpert, *Radio Wave Propagation and the Ionosphere. Volume 2: Propagation of Electromagnetic Waves Near the Earth*. New York, USA: Springer, 1974, 268 p.
- [23] Y. L. Alpert, *The Near-Earth and Interplanetary Plasma. Volume 1: General Properties and Fundamental Theory*. Cambridge, UK: Cambridge University Press, 1983, 311 p.
- [24] Y. L. Alpert, *Space Physics with Artificial Satellites*. New York, USA: Springer, 2013, 252 p.
- [25] Yu. M. Timofeev and A.V. Vasilev, *Theoretical foundations of Atmospheric Optics*. St.Petersburg, RF: "Nauka" Publishing House, 2003, 476 p.
- [26] I. R. Gekker, *Interaction of Strong Electromagnetic Fields with Plasmas*. Oxford, UK: Oxford University Press, 1978, 350 p.
- [27] H. G. van Buerne, *Imperfections in Crystals*. Whitesh, USA: Literary Licensing LLC, 2013, 740 p.
- [28] K. V. Shalimova, *Semiconductor Physics*. Moscow, USSR: "ErgoAtomIzdat" Publishing House, 1985, 392 p.
- [29] E. T. Whittaker and G. N. Watson, *A Course of Modern Analysis*. Cambridge, UK: Cambridge University Press, 1996, 608 p.

- [30] A. N. Tikhonov and V. Ya. Arsenin, *Solutions of ill-posed problems*, Washington, USA: Winston & Sons., 1977, xiii+258 p.
- [31] Sh. E. Guseynov and M. Okruzhnova, "Choice of a quasi-optimal regularization parameter for the first kind operator equations", *Journal of Transport and Telecommunication*, vol. 6, No. 3, pp. 471-486, 2005.

Optimization of Municipal Solid Waste Collection System in Hefei City of China

Shouchuang Hu¹, Jun Chen², Ke Wu^{3*}, Zhongkai Zhou¹, Tingting Cheng¹, Dongbiao Wu⁴

1- Department of Biological and Environmental Engineering, Hefei University, Hefei 230601, P. R. China.

2- Anhui Key Laboratory of Sewage Purification and Ecological Rehabilitation Materials, Hefei 230601, P. R. China.

3- Collaborative Innovation Center for Environmental Pollution Control and Ecological Restoration of Anhui Province, Hefei University, Hefei 230601, P. R. China.

4- Anhui Urban Construction Design Institute Co., Ltd., Hefei 230051, P. R. China.

Address: No. 99, Jinxiu Road, Hefei 230601, P. R. China. * Corresponding author. E-mail: wuke@hfuu.edu.cn

Abstract. The refuse collection spot is the central part in the municipal solid waste collecting system. The wrong collecting way would lead to environmental problem and disturb the life of citizens. With the demand of source separation in China, the waste collecting sites need to be improved. Nowadays there have three different types of wastes collecting in Hefei, capital city in Anhui province, China. The advantages and disadvantages of such waste collection system were compared and discussed. The suggestions were put forward. Concerning about special example for agricultural market waste collection, taking Hefei Wanguo market as a sample, the research was made to optimize the present collection system. Compared with traditional waste collecting sites, the results showed the agricultural market waste collecting sites were better in both environmental and social efficiency.

Keyword: solid waste collection, market, changes.

I. INTRODUCTION

Hefei is the capital city of Anhui province in China. It refers as the center of provincial politics economy culture education and transportation. Hefei is also the city in the center of Anhui in geography. The area of the city is about 11445.1 square kilometers, the population is 7.79 million. The development of economy in Hefei is rapid, it produces large amount of solid waste, about 3616 tons, each day. According to the prediction, the output of solid waste will increase to 2.22 million tons in 2030 [1]. In fact, the Hefei city collected the solid waste daily since 1997 [2]. Moreover, the city achieved the waste direct from household in package gradually, making use of it in an environmental way. In 2000, the domestic garbage disposal fee was implemented [3].

So much solid waste may be a burden to Hefei city, but if appropriate collection system and technology can be choosed, it not only can make waste profitable, but also can produce enormous economic benefits. So this paper studied the present solid waste collection system in Hefei and tried to find a suitable municipal solid waste collection mode.

II. MATERIALS AND METHODS

A. Materials

In order to analyse the physical component of municipal solid waste in Hefei, we sampled municipal

solid waste from eight districts and the materials of analysis are including the following three.

1 –sample sieve : diameter of the hole is 10mm

2 –scale: the minimum division value is 50g

3 –Platform scales : the minimum division value is 5g [4]

B. Methods

Method for sampling and analysis is The National Standard of the People's Republic of China, sampling and analysis method for municipal solid waste. The standard provides that physical component analyse must be done immediately after sampling, otherwise, the samples must be paved on the clean concrete floor with impermeable plastic in the shatered and shady room, the thickness is limited within 50mm. And in case of the loss of samples and mixture of other substance, it must be prevented within 24h. The physical component analyse are including six steps. [4]

1 –Weigh the sample of municipal solid waste

2 –Sort the ingredients of municipal solid waste samples according to the categories in the standard

3–After sorting, the remaining samples are fully sieved, and then subdivide.

4–Easy to be dismantled should be disassembled before classification

5–Determine whether to subdivide according to the purpose of the measurement

6-The last step, weigh the weight of each component

The physical components of household waste are calculated as follows

$$C_i = \frac{M_i}{M} \times 100$$

$$C'_i = C_i \times \frac{100 - C_{i(w)}}{100 - C_{(w)}}$$

C_i -Wet base content of a component (%)

M_i - Wet base weight of a component (KG)

M - Total weight of sample (KG)

C'_i - Dry base content of a component (%)

$C_{i(w)}$ - Moisture content of a component (%)

$C_{(w)}$ - Sample moisture content (%)

Results retain two significant digits.

III. RESULTS AND DISCUSSION

C. Experimental results

The physical components of municipal solid waste in Hefei are shown in Table 1. From the table we can see that organic waste is a large percentage, about 70%~80% and inorganic waste is about 20%.

Table 1
The composition of municipal solid waste in hefei (%)

location	Kitchen waste	Paper	Plastic	Rubber	Textiles	Wood and bamboo	Brick and tile	Glass	Metal	Lime soil
Yaohai District	28.43	23.37	19.56	0.94	5.24	1.34	2.73	3.68	1.14	13.58
Baohu District	31.36	15.72	21.03	0.77	5.68	1.65	3.04	4.15	0.72	15.90
Luyang District	36.46	13.20	20.55	0.91	4.81	1.54	2.32	3.84	1.51	14.87
Jingkai District	32.43	15.58	19.19	1.60	4.84	1.60	2.86	4.05	1.05	16.81
Xinzhan District	32.20	16.81	21.00	0.81	4.76	1.49	2.82	4.16	0.85	15.09
Shushan District	32.80	17.25	20.77	0.80	5.60	1.51	3.05	3.54	1.04	13.66
Gaoxin District	34.37	16.44	16.35	1.15	5.74	1.84	2.95	3.69	0.99	16.49
Zhengwu District	32.46	28.00	19.19	1.45	4.83	1.75	2.51	2.97	2.14	4.70

D. The present collection way of municipal solid waste

The main sources of the daily waste can be classified as residence waste, hotel waste and farmers' market waste. At present, the main gathering way in Hefei is using mobile garbage compressor, garbage storage machine and trash can. The terminal treatment technologies for solid waste were complexity. They are incineration technology, landfill and compost [5]–[6]. Different technology guides the different collection way. Fig. 1 shows the present waste collection way in Hefei. At present, the main problem in Hefei is solid waste collected in a mixing way, resulting in resource utilization not very high. With the demand of source separation, the municipal solid waste management should be strengthened, and the municipal solid waste collection system should be optimized.

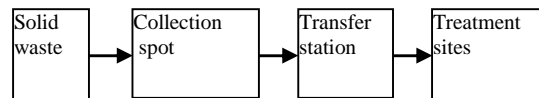


Fig.1. The existing collection system

E.

F. Types of municipal solid waste collection system in Hefei

At present, there are three types of garbage collection in Hefei, such as mobile waste collection container; garbage storage machine and trash can. Mobile waste collection box has the functions of loading, compression and transportation municipal solid waste [7]. The garbage storage machine has the functions of collection, storage and automatic unloading [8]. The trash can was used to collect and store solid waste. All of them can be commonly used for urban sanitation collection stations, residential areas, communities, schools and other large public

places. Three type collection devices shown as Table. 2. Their advantages and disadvantages were listed in Table 3.

TABLE 3
 COMPARISON OF THREE COLLECTION WAYS

Serial number	Project	Mobile garbage collection	Garbage storage machine	Trash can
1	Area	Big	Small	Big
2	Cost of the machine	30-50 million	25-40 million	200 trash cans, to be 40,000 Yuan and often need to update
3	Sewage	Less and filter before discharge into the sewage pipe network	Less and filter before discharge into the sewage pipe network	More and discharged arbitrarily outdoor
4	Applicable conditions	Indoor or outdoor	Indoor or outdoor	
5	Supporting vehicles	Detachable container garbage collector	Truck with compactor	Truck with compactor
6	Operation method	Automatic	Automatic	Artificial
7	Closed and compressed	Double confined and horizontal compression	Double confined and Horizontal compression	not sealed and No compression
8	Service life	Designed for 10 years	Designed for 10 years	Need to be updated
9	Compression ratio	3 : 1	2.5~3:1	No compression capability

The garbage storage machine and the mobile waste compressor have many advantages, such as easy to operate, container tightness and high degree of mechanization [7]-[8]. The use of environmentally friendly garbage collection points is more conducive to the future clearance work.

G. Optimization of refuse collection spot in Hefei city

With the implementation of source separation project in China, the present municipal solid waste management system faces many challenges. The traditional collection and transportation model should be changed gradually. In China, the popular guide for solid waste source separation from household classified as dry and wet [9], the resident can separate daily waste with different bags in such simple way. The waste source separation action needs the support of treatment technologies. It is important that the separated municipal solid waste can be dealt with next step into a useful cycle to reduce environmental pollution [10].

There are three kinds of technologies, such as incineration, composting and landfill [11], for solid waste treatment in Hefei. The capacities of these waste treatment plants are sufficient to the daily waste disposal. In order to establish a sustainable solid waste management system, appropriate municipal solid waste collection and transportation system is more important. At present, Hefei has been established the city kitchen waste collection and transportation system, the waste produced from hotels, restaurants and cafeteria, etc., by special container collection, is collected and transported directly to the composting plant by the kitchen garbage truck [12], but, the resident solid waste and agricultural market waste are collected together in designed locations, then optimization. Table 4 shows the result.

transported by truck to the waste transfer station, and finally be sent to the landfill plant or incineration plant. The mixed collection mode is low resource utilization and unfriendly to the environment. How to separate the waste with large amount of organic fraction from the municipal solid waste maybe a big problem or challenge for government in the larger city.

To buy the vegetable directly from agricultural market is the Chinese tradition. There are many larger scales of agricultural markets in each city in China. Every day a large amount of waste are produced from there. This waste contains mainly organic fraction. It has the characteristics of high water content (>80%), high volatile solid content (>95%, mass fraction) and high biodegradability [13], according to relevant research, kitchen waste and agricultural market waste can be mixed thermophilic anaerobic digestion [14]. In addition, the waste generated from large farmer's market has feasibility of implementing garbage classification [15]–[17]. It is good material for composting. So it is easier to establish the collection and transportation system for agricultural market. As to the resident waste source separation, the idea of “dry and wet” shall be publicized. It will take a few years to practice. Fig.2 shows the suitable way for municipal solid waste management in the future for Hefei city.

The practice for agricultural market waste collection was investigated. In Hefei binhu new district, Wanguo agricultural market collection point was used as research object. Wanguo farmers market is called "super vegetable basket project", the daily garbage production is about 10-15 tons. The garbage storage machine was selected to collect the waste. Using the method of comparatively research [8], we select different indexes to compare the effect before and after

Table 4
Comparison of the effect of collection point before and after optimization

Serial number	Project	Before	After
1	Area	About 200m ²	About 40m ²
2	Sewage	Sewage any discharge	Three-level filter into the sewage pipe network
3	Stench	Most of the trash cans are open, the stench smells and spreads wide	Very little odor and no overflow
4	Noise	Operating time mostly night or early morning, noisy	low noise, meet the national standards
5	Clearance time	Mostly on night or morning	Not subject to time constraints
6	City appearance	Affect the image of the city	Integrated with the surrounding buildings, become the highlight of the city
7	Citizen Complaints	Often complained by residents	No complaints, be praised
8	Operating efficiency	Low	Higher
9	Economy	Uneconomical	Good economy

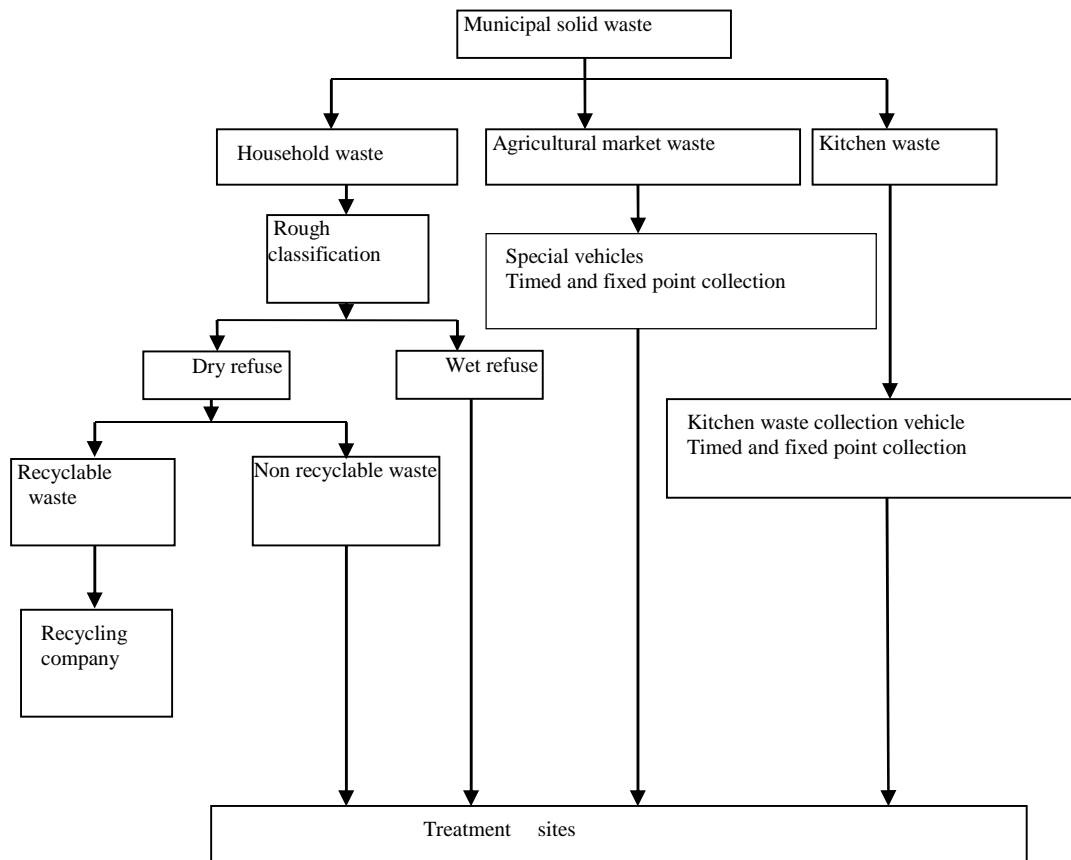


Fig.2 Refuse management optimization

IV. CONCLUSION

Hefei classification work of solid waste can be taken from easy to difficult. At present, Hefei has

established a kitchen waste management system from source collection to terminal processing, and it will be gradually improved. On the basis of the Hefei Wanguo agricultural market research, the new mode is suitable

and can be popularized. The heavy difficult point of Hefei city is still built a good system of household waste classification management and it also has a long way to go.

V. ACKNOWLEDGMENTS

This research was supported by Municipal Solid Waste Disposal Innovation Team of Anhui Province ([2015]49), Collaborative Innovation Center for Environmental Pollution Control and Ecological Restoration of Anhui Province ([2014]28), the project of Key University Science Research Project of Anhui Province (KJ2016A877).

REFERENCES

- [1] Shu Y. Grey model predication of urban refuse in Hefei city. *Environmental Science and Management* 9.2007, pp. 5- 8. (In Chinese)
- [2] Ye S.Y., Sun S. Q., Wu K. Consideration of all location and construction of municipal solid waste transportation stations in Hefei. *Environmental Science and Management* 32.2007, pp. 1- 4. (In Chinese)
- [3] Wu K., Cai J.M., Yu Z.M., et al. Status and perspective of municipal domestic waste management in Hefei city. *Environmental Sanitation Engineering* 13.2005, pp. 4- 6. (In Chinese)
- [4] Sampling and analysis method for municipal solid waste, 2009, CJ/T313- 2009. (In Chinese)
- [5] Yang L., Wang L.C., Zhu X.C. A study on the present management and strategy of MSW in Nanjing city. *Sichuan Environment* 4. 2001, pp. 529- 529. (In Chinese)
- [6] Wu K, Yu Z.M., Jin J., et al. A discussion of selection of schemes for municipal solid waste treatment in Hefei City. *Journal of Hefei University* 18. 2008, pp. 56- 58. (In Chinese)
- [7] Deng W.C. Improvement meat of sealing structure of unloading door of mobile garbage compressor, *Equipment Manufacturing Technology* 9. 2015, pp. 222- 223. (In Chinese)
- [8] Lian X.J., D Y.P., Tian Y. The design of a new kind of garbage compressing and storing device. *Development & Innovation of Machinery & Electrical Products* 21.2008, pp. 121- 122. (In Chinese)
- [9] Xu J.X. Research on pilot phrase of dry and wet waste sorting collection in pudong new area. *Journal of Green Science and Technology* 9.2011, pp. 118- 120. (In Chinese)
- [10] Wu K., Yu Z.M., Jin J., et al. Recycle and utilization of municipal solid waste in Hefei. *China Resources Comprehensive Utilization* 26. 2008, pp. 23- 25. (In Chinese)
- [11] Liu S.P., Cai J.M., Wu k., Jin J. status and count measure of municipal solid waste treatment. *Journal of Hefei University* 15. 2005, pp. 53- 57. (In Chinese)
- [12] Gong C. Study on hefei city kitchen waste collection and transportation system. Hefei University, 2015. (In Chinese)
- [13] Wang S.R., Zhan M.L., Sun Y.J., et al. Study on thermophilic anaerobic digestion of vegetable market waste in Qingdao. *Environmental Pollution & Control* 33. 2011, pp. 39-43. (In Chinese)
- [14] Zhan M.L., Dong L., Sun Y.J., et al. Study on thermophilic anaerobic digestion of mixture of kitchen wastes and vegetable market wastes in Qingdao. *Chinese Journal of Environmental Engineering* 7. 2013, pp. 1945- 1950. (In Chinese)
- [15] Gunaseelan V N. Anaerobic digestion of biomass for methane production: a review. *Biomass and bioenergy* 13. 1997, pp. 83-114.
- [16] Wang Y.Y. Research on process parameters of anaerobic fermentation of vegetable waste for biogas production and comprehensive utilization of anaerobic fermentation residues. Shanghai Jiao Tong University, 2008. (In Chinese)
- [17] Ma Z.D. Research on the vegetable market waste in its reduce and reuse. Suzhou University, 2014. (In Chinese)

Forming and Overlapping Microreliefs in Sliding Contact Simulation Model

Alexander Ilyin, Igor Plokhov, Igor Savraev, Oksana Kozyreva, Nikita Kotkov
Pskov State University, Department of Electric Drive and Automation Systems.
Address: Lenina 8, Pskov, 180000, Russia.

Abstract. Sliding contacts are widely used in electrical machines despite the trend towards non-contact methods of the electrical current transfer. In some cases, using of brush-contact devices is indispensable due to low cost and continuity of operations. One of methods to improve reliability of sliding contact is simulation modeling. This approach can significantly reduce the amount of expensive practical experiments in the study of different contact pairs characteristics.

The paper introduces and describes a few new algorithms for simulation model of sliding contact which allow to improve precision and take into account more physical processes occurring in contact transient layer.

Keywords: sliding electrical contact, simulation model, microrelief.

I. INTRODUCTION

Sliding electrical contacts are widely used in industry. Operating modes and application environment of the contacts vary from micromachines to large turbo-generators.

For selecting the best brushes and brush holders for specific instance usually engineering calculations or experiments are used. The full-scale experiments are often very time-consuming and expensive. Modeling of processes in sliding electrical contacts helps to do better choice and cut the cost.

Most of the developed sliding contact models use different approaches and have restricted application [1–7]. The simulation modeling lets to describe complex physical phenomena taking place in transient layer of sliding electrical contact. The most comprehensive description of simulation model introduced in [8–10].

Based on this model two computer programs was created. The first one allows calculating and plotting volt-ampere characteristics of the sliding contact [8]. The second program shows thermal spikes and distribution diagrams of temperature and electrical current density in the transient layer [11].

However, for some time past, new submodels for the simulation model were suggested and several algorithms were enhanced. These developments are described in the article.

II. MODELS AND ALGORITHMS

Discrete contact element

Each contact surface is described as a system of the surface discrete elements (DSE). The surface discrete elements are located in the rectangular array of size $N_{br}^{(x)}$ to $N_{br}^{(y)}$ for the static brush contact and

$N_r^{(x)}$ to $N_r^{(y)}$ for the moving rotor contact. The upper indexes (x) and (y) are used for the tangential and axial directions of the contacts. DSE has length Δx and width Δy . For simplicity, we assume $\Delta x = \Delta y$. The area of the element is $\Delta S = \Delta x^2$.

The Fig. 1 shows the discrete contact element (DCE) that has formed by the two lying opposite and interacting surface elements.

Each surface element presents a hemisphere of radius $\Delta x/2$ based on a Δx square face of a rectangular parallelepiped with the height $h - \Delta x/2 + \Delta h/2$, where h is the height of the surface element from the center line, Δh is the distance between two neighbor layers of the contact body. The hemispheres of interacting DSE overlap on the distance δ depending on its heights and applied load. The oxide film of the contact element has thickness $f_{br} + f_r - \delta$, where f_{br} and f_r are the oxide film thicknesses of the brush and the rotor contacts. If the value of $f_{br} + f_r - \delta$ is less than zero then the contact element does not have the oxide film and it conducts the current directly. The initial distance between the centre lines H_0 is calculated by approaching the contact surfaces without load.

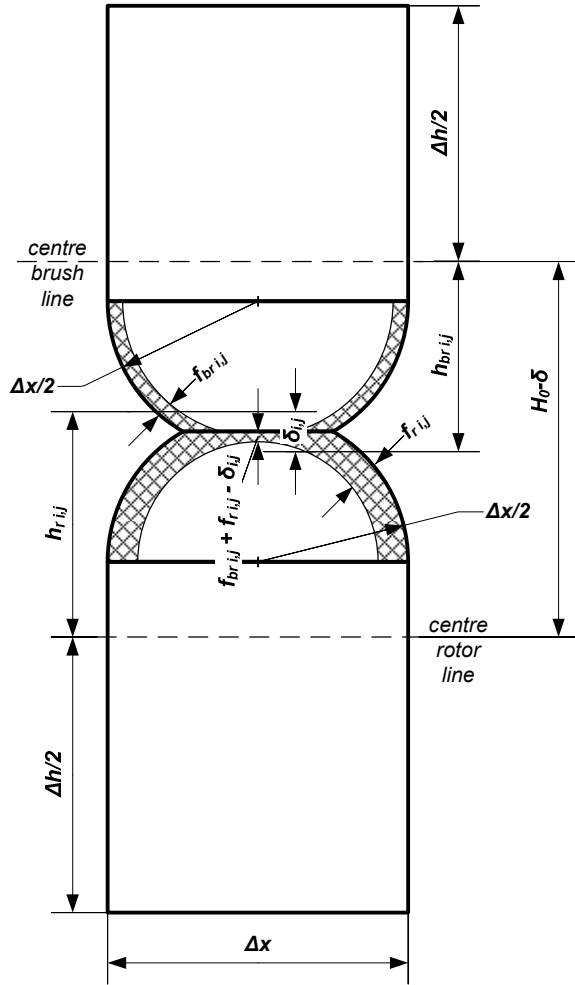


Fig. 1. The discrete contact element

Forming microreliefs

In the process of the contacts manufacturing and operation the deformations are formed on the surface and define the microrelief: macrodeviations, waviness, roughness and subroughness. The microreliefs of two interacting rough surfaces affecting by friction and the transmission of electric current through the contact is a result of complex action of a set of mechanical, electrical, chemical and thermal factors. Whereas mechanical factors have the leading role in the formation of a waviness, deformation and fracture of microroughnesses are accompanied by electroerosion and thermoplastic processes, oxidation-reduction reaction. As a result, over time the microrelief becomes steady state having determined statistical characteristics. While the process of generating roughness is stochastic, a number of deterministic factors, which separately affect the geometric characteristics of the axial and tangential profiles, can identify the formation of waviness.

We suggest to use new algorithm to form the contact microrelief based on the Kotelnikov's sampling function [12]:

$$h_i = \sum_{k=1}^M \frac{\sin\left(2\pi f \frac{i}{N} - \pi k\right)}{2\pi f \frac{i}{N} - \pi k} \cdot A_k,$$

where $i=1...N$ – samples of the random process; $k=1...M$ – process local points, heights of which depends by the vector A random values; f – upper frequency of the random process spectrum; A – vector of random values distributed by assigned probability law.

Selection of the upper frequency f and the probability distribution law for vector A allows us obtain different microreliefs with desired waviness and roughness. As far as more than one factor takes place in forming microreliefs then finite equation is:

$$h_{i,j} = \sum_{n=1}^C \sum_{k=1}^{M_n^{(x)}} \sum_{m=1}^{M_n^{(y)}} \left[\frac{\sin\left(2\pi f_n^{(x)} \frac{i}{N^{(x)}} - \pi k\right)}{2\pi f_n^{(x)} \frac{i}{N^{(x)}} - \pi k} \times \frac{\sin\left(2\pi f_n^{(y)} \frac{j}{N^{(y)}} - \pi m\right)}{2\pi f_n^{(y)} \frac{j}{N^{(y)}} - \pi m} A_{n,k,m} \right] + R_{i,j}, \quad (1)$$

where $i=1...N^{(x)}$ и $j=1...N^{(y)}$ – samples of the random process by X and Y axis; $n=1...C$ – factors take place in the microrelief formation; $k=1...M_n^{(x)}$ and $m=1...M_n^{(y)}$ – process local points for n -th factor; $f_n^{(x)}$ и $f_n^{(y)}$ – upper frequency for n -th factor; A_n – matrix of random values distributed by assigned law with size $M_n^{(x)} \times M_n^{(y)}$ for n -th factor; R – matrix of random values with size $N^{(x)} \times N^{(y)}$ used for the roughness formation.

Analysis and comparing results of performed computational experiments with the real sliding contacts allows us select optimal distribution law for matrixes A_n and R . It is normal probability distribution with zero mathematical expectation and standard deviation proportional to mean-square values for each factor waviness and roughness.

The Fig. 2 shows example of the realistic contact microrelief formed by three factors modeled in Mathcad.

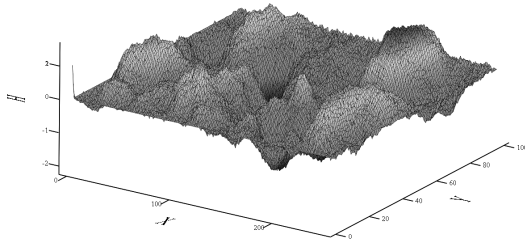


Fig. 2. The contact microrelief depending on three factors

Approaching and overlapping microreliefs

An approach algorithm is needed for searching the first touch of the contacting surfaces. On the Fig. 3 the scheme of the approach and overlap algorithms is shown, where O_r , O_{br} – centre lines of the contacting microreliefs; H_0 – distance between the centre lines in the radial direction without deformation.

We start the search with the initial distance

$$H_{0max} = R_{pbr} + R_{pr},$$

that equals to the sum of maximum microreliefs heights, and the minimal distance $H_{0min} = 0$. Then we count the number of contact points for the height $H_{0k} = (H_{0max} - H_{0min})/2$:

$$N_{cont} = \sum_{j=1}^{N^{(y)}} \sum_{i=1}^{N^{(x)}} h_{bri,j} + h_{ri,j} - H_{0k} \geq 0.$$

Further we use bisection method: if the number of contact points $N_{cont} > 1$, then $H_{0min} = H_{0k}$; else if the number of points equal zero (no contact) $N_{cont} = 0$, then $H_{0max} = H_{0k}$. After that, we define the next height $H_{0k} = (H_{0max} - H_{0min})/2$. The procedure repeats until we find the height H_0 , where there is only one contact point.

The overlapping algorithm uses Hertzian theory for elastic contact between two spheres. When the microreliefs is overlapping, the spheres of the opposite contact elements interact and its elastic deformation occurs. The process continues until contact load will equal to the sum of reactions (Fig. 3): δ – overlap of the microreliefs under the load; $H_0 - \delta$ – distance between the centre lines under the load; $\Delta h_{i,j} = (h_{bri,j} + h_{ri,j}) - (H_0 - \delta)$ – overlap of a contact element (if $\Delta h_{i,j} \geq 0$) or distance between surface elements (if $\Delta h_{i,j} < 0$).

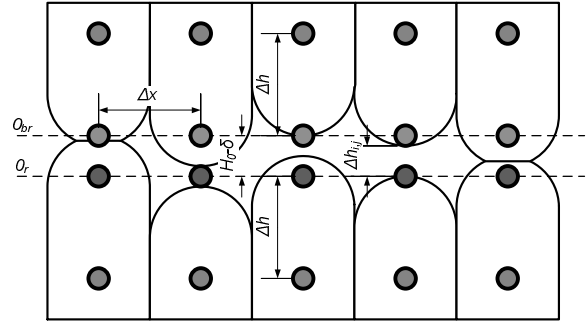


Fig. 3. The approach and overlap of two-contact microreliefs scheme

After calculating the initial distance between the microreliefs H_0 , we start searching the overlap δ using an initial value based on the waviness and roughness parameters of the contact surfaces. Further, for each discrete contact element with the positive overlap $\Delta h_{i,j} > 0$ we calculate:

–relative elastic modulus

$$K_{i,j} = \left(\frac{1 - \mu_{br}^2}{E_{br}} + \frac{1 - \mu_r^2}{E_r} \right)^{-1},$$

where μ_{br} and μ_r – Poisson's ratio, a E_{br} and E_r – elasticity modulus;

–relative radius of curvature

$$R_{i,j} = \left(\frac{1}{R_{bri,j}} + \frac{1}{R_{ri,j}} \right)^{-1} = \frac{\Delta x}{4},$$

where R_{br} and R_r – sphere radiuses equal to $\Delta x/2$;

–force (reaction)

$$F_{i,j} = \frac{4}{3} K_{i,j} \sqrt{\Delta h_{i,j}^3 R_{i,j}} = \frac{2}{3} K_{i,j} \sqrt{\Delta h_{i,j}^3 \Delta x};$$

–radius of contact spot

$$a_{i,j} = \sqrt{\Delta h_{i,j} R_{i,j}} = \frac{1}{2} \sqrt{\Delta h_{i,j} \Delta x};$$

–contact area

$$A_{i,j} = \pi a_{i,j}^2 = \frac{\pi}{4} \Delta h_{i,j} \Delta x;$$

–average pressure

$$p_{i,j} = \frac{F_{i,j}}{A_{i,j}}.$$

After summing the reactions for all overlapping contact elements we use bisection method for the next overlap δ and repeat the calculations iteratively until the reaction will be equal to the contact load with the specified accuracy.

Fig. 4 shows experimental example of microreliefs overlapping [13]. As we see the overlap approximation (dashed line) has the exponential dependence on the contact load that is corresponding to the Hertzian theory solution for two spheres.

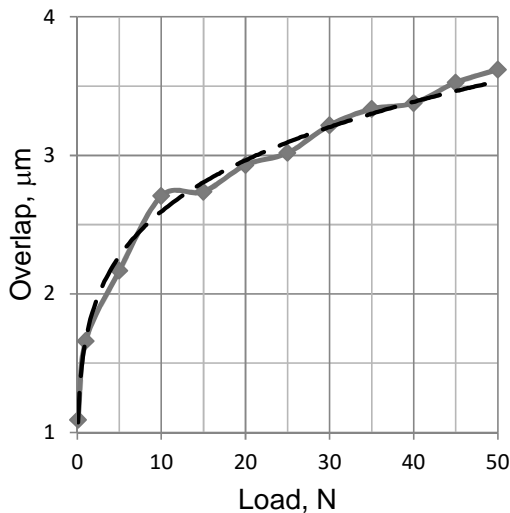


Fig. 4. Experimental results of overlapping

Contact areas

It should be noted, that the actual contact area of the sliding contact is larger than for static contacts and can be calculated as

$$A_{ck} = A_{cm} \sqrt{1 + \mu^2},$$

where A_{sl} – sliding contact area, A_{st} – static contact area, μ – friction coefficient [14]. However, the difference for real slip-ring assemblies is only a few percent and can be neglected in the calculations.

The sum of all contact spots areas $A_{i,j}$ forms the bearing contact area A_b . This area is much less than the apparent contact area A_c . Usually the bearing area A_b partially is covered by insulating films. The electrical current will flow through the film only in the contact elements in which $f_{br,i,j} + f_{ri,j} - \Delta h_{i,j} \leq f_{tun}$, where f_{tun} – maximum film thickness when tunneling effect is possible. The sum of direct conductivity areas and tunneling conductivity areas forms the actual contact area A_a (Fig. 5).

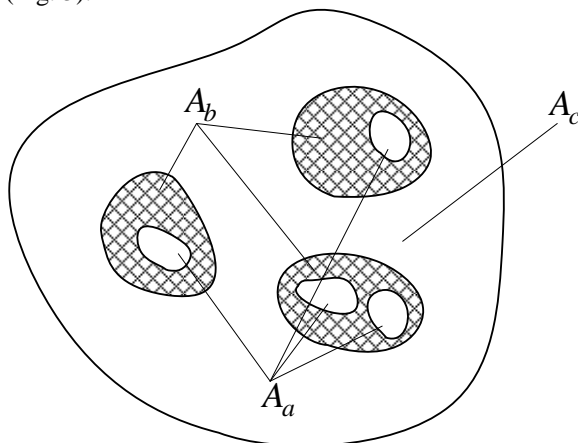


Fig. 5. The apparent, bearing and actual contact areas

III. CONCLUSION

Thus, a few new algorithms for the simulation model of sliding contact have been introduced and described in the paper.

The new models of discrete surface element and discrete contact element provide improving calculation precision of mechanical, electrical and thermal processes occurring in contact transient layer. In the work [15] these models were used for calculating time dependent thermal processes taking into account heat generation due to the friction and the electrical current, the constriction resistance, oxide films, heat flow to the neighbor elements and contact bodies.

Using equation (1) for contact microrelief generation allows take into account any external influences that form waviness and roughness of contact surfaces, such as: brush assembly design, mechanical vibrations of electrical machine parts, natural oscillation frequency of contacts [16].

Using Hertzian theory for the overlapping algorithm allows improving calculation precision of the reaction, pressure and contact spot area for interacting contact elements. As consequence, it improves calculation precision of constriction resistance, electrical and thermal processes. Also, it can be used in contact wear modeling.

REFERENCES

- [1] Тарановский В. Р., *Исследование коммутационной устойчивости коллкторных электрических машин на основе моделирования электрофизических свойств скользящего контакта*, Самара: Изд-во СамГТУ, 2007.
- [2] Саблуков В. Ю., *Модели, методы и средства для оценки механического состояния скользящего контакта электрических машин*, СПб., 2008.
- [3] Никулин С. В., *Улучшение свойств щеточного контакта электрических машин*, Киров: Изд-во ВятГУ, 2007.
- [4] Колесов С. Л., *Улучшение трибохарактеристик твердощеточного контакта электрических машин с помощью дисульфида молибдена*, Москва, 2001.
- [5] Качин О. С., *Повышение ресурса скользящего контакта универсальных коллекторных электродвигателей*, Томск, 2008.
- [6] Деева В. С., *Анализ и исследование динамического поля проводимости щеточного контакта*, Томск, 2013.
- [7] Gomez M. F., *Characterization and Modeling of Brush Contacts*, Hamburg, 2005.
- [8] Плохов И. В., *Комплексная диагностика и прогнозирование технического состояния узлов скользящего токосъема*, СПб.: СПбГПУ, 2001.
- [9] Ilyin A., Plokhov I., Isakov A., "The simulation model of a sliding contact", in *Environment. Technology. Resources: Proceedings of the 9th International Scientific and Practical Conference June 20-22, 2013. Volume II*, Rezekne, Latvia, 2013.
- [10] Plokhov I., Kozyreva O., Savraev I., Ilyin A., "The simulation model of sliding contact with three degrees of freedom and distributed parameters of the transition layer", in *Environment. Technology. Resources: Proceedings of the 10th International Scientific and Practical Conference June 18-20, 2015. Volume I*, Rezekne, Latvia, 2015.
- [11] Ильин А. В., Плохов И. В., "Верификация вычислительной модели электрофрикционного взаимодействия в щеточно-контактных аппаратах турбогенераторов", *Математические модели и методы исследования надежности либерализованных систем*

- энергетики: сб. статей международной конференции "Методические вопросы исследования надежности больших систем энергетики", Вып. 58, М./Н. Новгород: изд-во Волго-Вятской академии государственной службы, 2008.
- [12] Войнов К. Н., Ходаковский В. А., Шварц М. А., "Математическое моделирование шероховатых поверхностей", *Трение, износ, смазка №41*, 2009.
- [13] Ильин А. В., Плохов И. В., Козырева О. И., "Моделирование процессов электрофрикционного взаимодействия в узлах скользящего токосъема", *Научно-технический вестник Поволжья №4*, Казань, 2013.
- [14] Чичинадзе А. В., Браун Э. Д., Буше Н. А. и др., *Основы трибологии (трение, износ, смазка): Учебник для технических вузов*. 2-е изд. переработ. и доп. / Под общ. ред. А. В. Чичинадзе, Москва: Машиностроение, 2001.
- [15] Ilyin A., Plokhov I., Savraev I., Kozyreva O., "Modeling of time dependent thermal process in sliding electrical microcontact", in *Environment. Technology. Resources: Proceedings of the 10th International Scientific and Practical Conference June 18-20, 2015. Volume III*, Rezekne, Latvia, 2015.
- [16] Ильин А. В., Плохов И. В., Козырева О. И., "Моделирование микрорельефа поверхностей контактирующих деталей", *Научно-технический вестник Поволжья №5*, Казань, 2013.

Calculation of Losses of Active Power and Energy in Transmission Lines and Transformers, as a Part of the Electrical Distribution Power Network

Krasimir Marinov Ivanov, Tsviatko Kolev Varbov, Georgi Tsonev Velev
Technical University of Gabrovo, Gabrovo, Bulgaria

Abstract. The paper inhere discusses the impact of renewable distributed generation sources upon the power and energy losses in electrical distribution power networks where these sources are attached. In addition a set of mathematical expressions to calculate these active power and energy losses are presented with the respective examples and implementation.

Keywords: renewable power sources, active power loss, active energy losses, distribution power network.

I. INTRODUCTION

The processes of generation, transmission and distribution of electricity are in no doubt, associated with active power and energy losses. In the conditions of sustainable energy resources, it is especially important the reliable determination of these active power and energy losses, in order to resolve issues related with the planning and optimal distribution of electricity.

In the recent years, the deal of renewable energy sources connected to the distribution power network, as a part of the entire energy production, has a significant increase. The transmission of electricity generated from these sources is associated with additional losses of power and energy that has to be calculated and taken into account in regard with the optimal power flow, and the quality of electricity.

II. CALCULATION OF POWER AND ENERGY LOSSES

In Germany and Austria under the provisions for attachment of generation sources from renewable energy to the distribution power grid, the maximum installed generating capacity that is allowed to be connected to the grid is calculated taking into consideration of the voltage increase in the node of connection according to the following expression:

$$\Delta U_{aV} = \frac{S_{Wmax}}{S_{kV}} \cos(\psi_k + \varphi) \quad (1)$$

where: S_{kV} - short-circuit power at the connection

point; ψ_k - short-circuit impedance phasor angle at the connection point; S_{Wmax} - maximum power capacity of the generating source attached at the connection point; φ - phase difference between voltage and current at the connection point.

The voltage increase, according to (1) doesn't have to exceed 2% in regard to the German regulations [3]

The power factor may be in the range 0.95 (CAP) ... 1 ... 0.95 (IND). In this way, a further increase in the generating capacity could be achieved and the respective source could be involved in the voltage regulation.

Using the above formula, an expression is derived for calculation of the maximum permissible power rating of newly installed generating power sources in the case of limiting the voltage increase within 2% at the point of connection.

$$S_{Wmax} = \frac{0,02 S_{kV}}{\cos(\psi_k + \varphi)} \quad (2)$$

Medium voltage distribution power networks (in Bulgaria mainly 20 kV) as a rule are supplied by substations 110kV/20kV. The average subtransient short-circuits power for the 110kV power grid in the country is within 3200MVA. Most often, the substations have two power transformers in operation. The power rating of these transformers may be 6.3, 10, 12.5, 16, 25, 31.5 or 40 MVA.

Under parallel operation, on the low-voltage side, these transformers have bigger values for the short-

circuit power: 116.02, 180.65, 222.93, 280.35, 419.15, 512.195 and 580.03 MVA.

In separate operation, on the low-voltage side, the transformers subtransient short-circuits power decreases and has the following values: 58.99, 115.13, 146.02, 222.92, 276.315, 316.38 MVA.

The predetermined maximum power rating of renewable generation sources, that can be connected to the grid is also a subject to compliance with the electricity quality requirements for voltage deviation of the Energy and Water Regulatory Commission (EWRC), i.e. the voltage deviation should be within +/- 10% and also the addition condition has to be met that the voltage increase in the point of installation has to be limited up to 2%.

In regard with the German regulations, the maximum allowable capacities of electrical power plants, connected to the busbars 20 kV, depending on the rated power and the number (1 or 2) of power transformers are represented graphically in Figure 1.

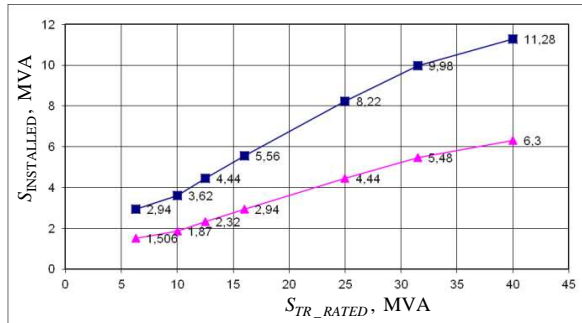


Fig. 1. Maximum allowed generating capacity, installed at the low-voltage buss bar of a substation HV / MV

The calculation of active power and energy losses in medium-voltage power lines and power transformers with attached-in renewable energy generating sources is beneficial in regard with the determination of their efficiency.

In order to calculate the energy losses, it is expected that the source's generated power deviation in time is known. Figure 2 shows the Equivalent diagram of the respective study:

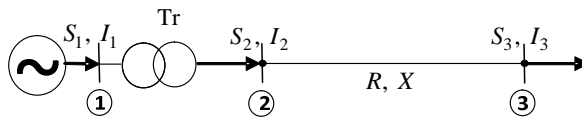


Fig. 2. Equivalent diagram of the system, according to the respective study

Losses of active and reactive power at the end of the line are calculated as:

$$\Delta \dot{S}_w = \Delta P_w + j\Delta Q_w = \frac{P_2^2 + Q_2^2}{U_2^2} \cdot (R + jX) \quad (3)$$

wherein: R and X are the parameters of the line, $\dot{S}_2 = P_2 + jQ_2$ - complex power at the beginning of the line.

The losses of active energy in the line depend on the variation of the generated energy considered for the time interval - T.

In general, the active energy loss is:

$$\Delta A = \int_0^T \Delta P(t) \cdot dt = R \int_0^T I_k^2(t) \cdot dt = R \int_0^T \frac{S_k^2(t)}{U^2} \cdot dt \quad (4)$$

$$\Delta A = R \cdot \left(\frac{S_{\text{mean.sq}}}{U} \right)^2 \cdot T \approx R \cdot \left(\frac{S_{\text{mean.sq}}}{U_n} \right)^2 \cdot T$$

where T - period of time for which the energy losses are determined; $I_k(t)$ - alteration of line current in the time domain for the respective period of time; U - operating voltage; $S_k(t)$ - alteration of the apparent power in the time domain for the respective time period; $S_{\text{mean.sq}}$ - mean square apparent power for the period.

The mean square apparent power for the period is obtained by formula (5), where n is the number of power measurements.

$$S_{\text{mean.sq}} = \sqrt{\frac{S_1^2 + S_2^2 + \dots + S_n^2}{n}} \quad (5)$$

Taking into account the deviation of the operating voltage U in relation to the rated voltage U_n , expression (4) is transformed to:

$$\Delta A_l = R \cdot \left(\frac{S_{\text{mean.sq.}}}{U} \right)^2 \cdot T \cdot \left(\frac{U}{U_n} \right)^2 \quad (6)$$

Transformers passport data in regard with the core and the winding losses are used in order to determine their power and energy losses.

The total active power losses of a transformer are calculated according to:

$$\Delta P_{tr} = \Delta P_0 + \Delta P_k \cdot \left(\frac{S_2}{S_n} \right)^2 \quad (7)$$

where: ΔP_0 - transformer no-load power loss; ΔP_k - transformer short-circuit power loss; S_2 - apparent power load of the transformer; S_n - rated power capacity of the transformer.

Considering the deviation of the operating voltage U, expression (7) is transformed to:

$$\Delta P_{tr} = \Delta P_0 \cdot \left(\frac{U}{U_n} \right)^2 + \Delta P_k \cdot \left(\frac{S_2}{S_n} \right)^2 \cdot \left(\frac{U_n}{U} \right)^2 \quad (8)$$

If concrete data is available about the alteration of transformer's load in regard with time, the active energy loss of a power transformer can be calculated taking into account the mean square value of transformer's power load:

$$\Delta A_{ir} = \Delta P_0 \cdot T \cdot \left(\frac{U}{U_n}\right)^2 + \Delta P_k \cdot \left(\frac{S_{mean_sq}}{S_n}\right)^2 \cdot T \cdot \left(\frac{U_n}{U_{av}}\right)^2 \quad (9)$$

where T is the operation time in hours for one year or for a specific period.

III. DEFINING THE MEAN SQUARE APPARENT POWER OF A RENEWABLE ENERGY SOURCE PER ONE YEAR

The software product Microsoft Excel has been used in order to process the generating power load data, collected from a renewable power source. The sequence of work is as follows:

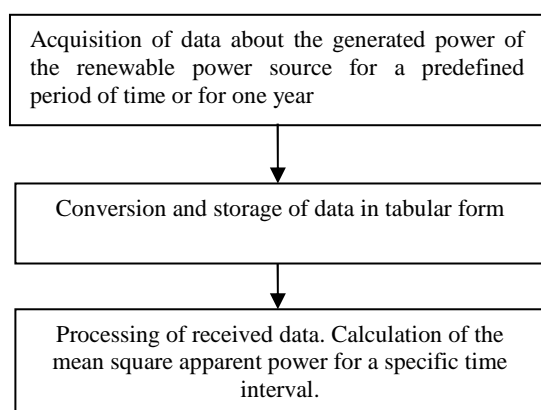


Fig. 3. Algorithm for data processing

A photovoltaic system, connected to the grid is used as an example. The data about the operation of the PV system is collected by the software product PVGIS [4] for a photovoltaic system with rated

installed power 1.0 kWp.

Table 1 shows the calculations of the mean square power of a photovoltaic system with a rated output of 1.0 kWp for an operation period of 1 year. The data has been obtained from the software product PVGIS-CMSAF.

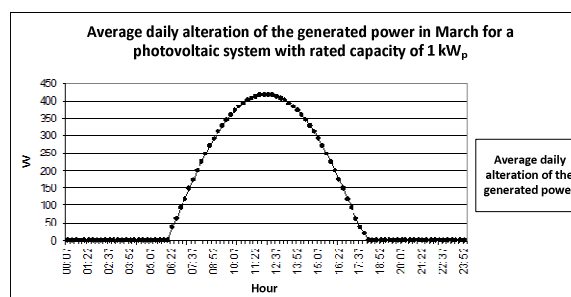


Fig. 4. Average daily power output change in March for a photovoltaic system with a rated power of 1.0 kW_p, obtained by PVGIS-CMSAF

The power output has been taken in every 15min and the total number of indications per year is 35,040.

If a certain photovoltaic system has an installed power rating that is different than 1.0 kWp, the results in Table 1 are multiplied by the square of its installed power capacity in kWp i.e. $(S_{pv})^2$. In this case, expression (5) changes as follow:

$$\Delta A_i = R \cdot \left(\frac{S_{mean_sq_1kWp}}{U_n}\right)^2 \cdot (S_{PV})^2 \cdot T \cdot \left(\frac{1}{U/U_n}\right)^2 \quad (10)$$

Table I

Day of the year	hour:minutes	Power output	Mean square power
-	h:min	W	W ²
01.01	07:37	56,56	3199,29
01.01	07:52	81,97	6719,78
01.01	08:07	109,03	11886,62
01.01	08:22	130,34	16988,27
-	-	-	-
01.03	06:22	38,85	1509,02
01.03	06:37	62,15	3863,10
01.03	06:52	93,23	8691,98
01.03	07:07	119,65	14315,20
-	-	-	-
31.12	15:37	114,65	13143,93
31.12	15:52	90,25	8145,78
31.12	16:07	25,21	635,35
31.12	16:22	17,89	319,99
Sum			1653731868,8
S_{mean_sq}			217,245

The following example comprises calculations regarding a photovoltaic system with a rated installed capacity of 600 kWp connected to the power system through a power transformer with power rating 630kVA and via an overhead power line with rated

voltage of 20 kV. The power line consists of aluminum steel conductors AC-50 with a length of 5 km [8].

Substituting in (10) under nominal operation

parameters and $\frac{U_n}{U} = 1$, the total annual active energy losses are calculated to be 1107 kWh.

Table 2 shows the change of the energy loss in regard with the voltage deviation, as reflected in expression (10). It should be taken in consideration that for the case from fig. 2(Table 2), the voltage of the power line increases from node 3 to node 1, where the generating source is connected. It is obvious that if the voltage in node 3 increases by 10% over the rated voltage U_n the energy losses in the power line ΔA decrease by 17.7%.

Taking into account a photovoltaic system with an installed capacity, different than 1.0 kWp, the values from Table 1 are multiplied by (S_{pv}) and expression (9) regarding the power transformer energy losses will change according to:

$$\Delta A_{tr} = \Delta P_0 \cdot T \cdot \left(\frac{U}{U_n}\right)^2 + \Delta P_k \cdot \left(\frac{S_{mean_sq} \cdot (S_{pv})}{S_n}\right)^2 \cdot T \cdot \left(\frac{U_n}{U}\right)^2 \quad (11)$$

Substituting in (11) with the transformer's passport data ($S_n = 630$ kVA; $\Delta P_0 = 600$ W; $\Delta P_k = 6500$ W) and $S_{pv} = 600$ kWp, $T = 1$ year = 8760 h and $\frac{U}{U_n} = 1$, the obtained annual transformer energy losses will be 7693,5 kWh.

$$\begin{aligned} \Delta A_{SUM} &= \Delta A_l + \Delta A_{tr} = 1107 + 7693,5 = \\ &= 8800,5 \text{ kWh} \end{aligned} \quad (12)$$

The annual production of a photovoltaic system with installed capacity of 600kWp under the program PVGIS-CMSAF for the geographic region of Gabrovo is 714360kWh.

According to the above calculations, the resulting total active energy loss in the entire system will be around 1.23% in regard with the annual production.

If the ratio $\frac{U_n}{U}$ changes, this will result in a change of power transformer's energy losses, as shown in Table 2.

Table 2 also reflects the nodes' voltage alteration as a result of the voltage drop along the line.

A voltage increase of 10% over U_n results in an increase of power transformer's energy losses ΔA_{tr} with 8.9 %.

In case the system voltage increases U over the rated value U_n , energy losses in transformer's core increase, while the energy losses in the transformer's windings are reduced.

Table II

$\frac{U}{U_n}$	Electrical Power line	Power transformer			Total energy losses
	ΔA_l kWh	ΔA_0 kWh	ΔA_K kWh	ΔA_{tr} kWh	ΔA_{SUM} kWh
0,9	1366,62	4304,83	2976,03	7280,86	8647,49
0,95	1226,55	4794,47	2672,10	7466,57	8693,13
1	1106,96	5310,59	2412,41	7723,00	8829,96
1,05	1004,05	5853,16	2188,78	8041,95	9046,00
1,1	914,85	6422,21	1994,85	8417,06	9331,90

IV. CONCLUSIONS

The transmission of electricity, produced in photovoltaic systems is associated with the respective active power and energy losses. Calculation of these losses in the power lines and the power transformers, with connected to the electrical distribution power network renewable energy sources allows to determine the efficiency of their use.

The method described inhere allows determination of the active energy losses in electrical power lines and transformers, with connected to them renewable energy sources, by means of preliminary calculation of the mean square apparent power of these generating sources.

The suggested methodology can be used also to determine the energy losses in electrical power networks.

REFERENCES

- [1] Stiebler, Manfred: Wind energy systems for electric power generation, Springer-Verlag Berlin Heidelberg, 2008
- [2] Volker Quaschnig: Regenerative Energiesysteme, Technologie – Berechnung – Simulation, Hanser Verlag Muenchen, 7. aktualisierte Auflage, 2011
- [3] Technische Richtlinie Erzeugungsanlagen am Mittelspannungsnetz, Richtlinie für Anschluss und Parallelbetrieb von Erzeugungsanlagen am Mittelspannungsnetz Ausgabe Juni 2008, BDEW Bundesverband der Energie- und Wasserwirtschaft e.V.
- [4] <http://re.jrc.ec.europa.eu/pvgis/apps4/pvest.php> - European Commission, Joint Research Centre Institute for Environment and Sustainability Ispra (VA), Italy.
- [5] http://re.jrc.ec.europa.eu/pvgis/cmapi/eu_opt/PVGIS-EuropeSolarPotential.pdf.
- [6] Zhelezko, YU.S. AB Artemyev, OB Savchenko, Calculation, Analysis and standards regarding the energy losses in electrical power networks, Moscow, NCENAS, 2002, 280 p.
- [7] Genov, L.G., Electrical Power Engineering, Sofia, Tehnika, 1979.
- [8] www.energo-pro-grid.bg/uploads/files.../Prilozhenie_1_79.pdf

Competence as a Factor of Emotional Capital

Irina Ivanova, Deniss Sceulovs

Riga Technical University, Faculty of Engineering Economics and Management,
Department of Engineering Economics and Management
Contactpoint. Address: Kalnciema street 1, Rīga LV-11048, Latvija.

Abstract. Use of modern knowledge and technologies determines market development which grows with high rates. Today's business environment cause changes that affect the formation of the modern technologies, including business models, which generates changes not only the competencies, but I soft skills, including emotional capital, as a factor influencing the development of modern companies. Article investigates configuration during company growth process. Researching relevance and justification, the purpose of work is conception of factors, which positively influenced development of the entity, organization developments influencing on the productive direction.

The aim of the article is to provide the competence concept and its components to identify interrelationship with knowledge and skills which is related to emotional intelligence as a part of emotional capital. And as the result, the emotional equity as element of competence, acting as the regulator, carries out a role of positive feedback within strategic management.

Keywords: emotional capital, competence, resource, emotional intelligence.

I. INTRODUCTION

The question of the value of competences and their formation is one of the ways to study factors required to create a set of competencies that is associated with the efficiency of the organization. The company's ability to compete and be resilient to changes in the external environment in the modern practice of entrepreneurship focuses on strengthening the elements of competencies which may include a combination of key competencies skills, abilities, technologies, allowing the company to provide its consumers with certain values [1].

In this paper we consider the notion of competence and identify factors of emotional capital as the basis of forming a framework of competencies for effective development of the organization and the achievement of related goals.

As result of literature review it is necessary to indicate that a different definition or understanding of the meaning of competence, use different classifications of the set of competencies its define for scientific and practical purposes, and to determine their use and significance in connection with the concept of emotional capital. According to research out the basic set, which includes elements such as knowledge, skills and abilities, and it is also necessary to determine the readiness of the application of these elements, which are interconnected with the concept of emotional capital.

The object of research is competence and its elements.

The subject of research is interaction of competence elements such as knowledge, skill and capabilities.

The methodology: literature overview comprising and interpretation.

Exploring sources consider the meanings and elements of competencies in various fields related to management, social sciences and human resources.

II. MATERIALS AND METHODS

General definition of *competence* is often cited from David McClelland as the founder of the modern competences movement. In his paper "Testing for competence rather than for intelligence" McClelland (1973) introduced the concept of "competency" to replace the more limited concept of "skill" and also include behavioural aspects and technical capabilities.

The linguistic roots of the word competence come from Latin "competens" – as being able and allowed by law/regulation, and "competentia" as capability and permission. The use of the West European words "competence" and "competency" dates back to the early 16th century. The same word competence can be found also in ancient Greek – "ikanotis". It is translated as the quality of being "ikanos" (capable), having the ability to achieve something; a skill. "Epangelmatikes ikanotita stands for stands for professional/vocational capability or competence. (Mulder, 2007)[2].

The widely accepted definition of the competency model used by managers of Anglo-Saxon countries is

the set of desired competencies – skills, knowledge, attitudes, underlying characteristics or behaviour – that differentiate effective performers from ineffective ones (Boyatzis, 1982; McLagan, 1996). Moreover, the discussion continues on whether the term “competency” (plural –“competencies”) and “competence” (plural – “competences”) bear the same or a different meaning. According to some dictionaries, both concepts have the same meaning while others highlight certain differences. Supporters of the latter approach claim that “competency” concentrates on how people behave while “competence” focuses on what people do. In addition, “competency” corresponds to behaviour-based aspects whereas “competence” – to skill-based ones (Sanghi, 2007) [2].

Mayer and Salovey (1997), for example, define emotional intelligence as “the ability to perceive emotion, use emotion to facilitate thought, understand emotions, and manage emotion” (p. 3). This is not unlike Kanning (2002), who regards social competence as containing the behavioral control of emotions, meaning the ability to control one’s feelings both internally and externally. These incongruities and overlaps necessitate a great deal of effort to find a shared vocabulary. They are a sign that these constructs derive from a common theoretical basis of underlying skill, competence and intelligence dimensions that need to be precisely defined. A “concept clean-up” (Organ, 1997) is needed [3].

The competencies of perception, understanding, utilizing and managing emotions effectively in the self and others comprise the core of emotional intelligence (Maul, 2012; Mayer, Salovey & Caruso, 2004; 2008). Competency in perception of emotion

involves recognizing emotion-related facial and voice cues of others and awareness of one’s own body states relating to emotion. Competency in understanding one’s own and others’ emotions consists of knowing the causes and consequences of different emotions as well as being able to differentiate between varying emotions. Utilizing emotions involves harnessing the effects of emotions, for example by drawing on positive mood to enhance creative thought [4].

Emotional intelligence consists of adaptive emotional functioning involving inter-related competencies relating to perception, understanding, utilizing and managing emotions in the self and others. Researchers in diverse fields have studied emotional intelligence and found the construct to be associated with a variety of intrapersonal and interpersonal factors such as mental health, relationship satisfaction, and work performance. This article reviews research investigating the impact of training in emotional-intelligence skills. The results indicate that it is possible to increase emotional intelligence and that such training has the potential to lead to other positive outcomes. The paper offers suggestions about how future research, from diverse disciplines, can uncover what types of training most effectively increase emotional intelligence and produce related beneficial outcomes [4].

Unfortunately, the authors do not reveal the weight of each part of the value of competences, which does not reflect the significance and interaction of emotional capital and talent in general. To form an objective opinion about the value of competencies, in addition to literature overview view, the authors used the research that was done in the framework of the projects and conducted the triangulation.

III. RESULTS AND DISCUSSION

Table 1.
Competence Concepts

No	Author/Publication title	Concepts	Findings: Keyword
1.	Leading public service organizations: how to obtain high employee self-efficacy and organizational performance Christian Bøtcher Lotte Bøgh Andersen Political Science, Aarhus University, Aarhus C, [5]	Competence provide positive feedback on performance to strengthen feelings, getting conditional rewards	Positive feedback on performance
2.	Innovation and international business John Cantwell [6]	Competence-creating capabilities - the presence or absence of local knowledge in either direction.	Competence-creating capabilities to knowledge
3.	The Roles of Sustainability Orientation and Market Knowledge Competence in New Product Development Success Marius C. Claudy, Mark Peterson [7]	competence is an important capability, which helps firms to balance social and ecological objectives with economic goals such as profitability and market share.	Capability to balance objectives
4.	The Core Competence of the Corporation C. K. Prahalad, G. Hamel[1]	Core competencies are the organization's collective learning and ability to coordinate and integrate multiple production skills and technology streams; they are also about the organization of work and delivery of value in services and manufacturing.	Competencies - collective learning and ability to coordinate and integrate multiple production skills

5.	Competency modelling targeted on boosting configuration of virtual organisations Ekaterina Ermilova, Hamideh Afsarmanesh[8]	Formation of Virtual Organizations as the base of organizations' competencies defined;• "4C-model" (Capabilities + Capacities + Costs + Conspicuities), developed to comprehensively specify competencies of VBE member organizations.	Capabilities + Capacities + Costs + Conspicuities
6.	Handbook of Competence and Motivation Andrew J. Elliot, Carol S. Dweck [9]	Need for competence is mediated, organized, and satisfied through cognitive processes. These cognitive processes include beliefs, expectations, and inferences about competence; schemas or goals oriented toward acquiring or demonstrating competence; and beliefs about the importance or value of different competence domains.	Cognitive processes include beliefs, expectations, and inferences about competence
7.	Towards a Competence Theory of the Firm Nicolai J. Foss, Christian Knudsen [10]	By competence - typically idiosyncratic knowledge capital that allows its holder to perform activities - in particular, to solve problem in certain ways, and typically do this more efficiently than others, because its skill-like character, competence has a large component and is asymmetrically distributed.	Knowledge capital that allows its holder to perform activities - in particular
8.	Personality and intellectual competence Chamorro-Premuzic, T; Furnham, A [11]	Personality and Intellectual Competence is an outstanding account of the relationship between major individual differences constructs.	Intellectual Competence- the relationship between major individual differences constructs
9.	The assessment of professional competence: building blocks for theory development C.P.M. van der Vleuten, , Schuwirth, , F. Scheele, E.W. Driessen, B. Hodges [12]	Assessment of professional competence based on Miller's pyramid, a distinction is made between established assessment technology for assessing 'knows', 'knowing how' and 'showing how' and more recent developments in the assessment of (clinical) performance at the 'does' level.	Professional competence based for assessing 'knows', 'knowing how' and 'showing how' - skills
10.	A Personality-Competence Model of Opinion Timo Gnams; [13]	Results emphasize two major sources of domain-specific opinion leadership (DSOL) which is related to personal competence: personality in the form of a general, domain-independent influencer trait and competencies in terms of product-specific knowledge;	Leadership - which is related to personal competence: personality independent influencer trait and competencies in terms of product-specific knowledge;
11.	Digital competence – an emergent boundary concept for policy and educational research Minna Lakka laLiisa Ilomäki Saami Paavola Anna Kantosalo [14]	Elements of competence - a variety of skills and competences, and its scope is wide, as is its background;	Elements of competence - a variety of skills
12.	Concept of competence: A conceptual clarification. Weinert, Franz Emanuel [15]	The concept of competence, mentioning specific competencies including: economic, technological, technical, and methodological competencies; social competencies; creativity and innovation skills; and mobility and flexibility combined with persistence, reliability, and precision.	The concept of competence creativity and innovation skills; and mobility and flexibility combined with persistence, reliability, and precision.
13.	The Limits of Competence: Knowledge, Higher Education and Society. Barnett, Ronald [16]	The competence focuses on some ideas either disappearing from public debate or defunct as apparently unworthy of serious attention, including understanding, critical thought, interdisciplinary, and wisdom. Two ideologies of competence--operational and academic--against each other and sketches an alternative definition of human being. This idea of human being is relatively unconstrained by sectional interests, contains a sense of knowing not derived from mere instrumentality, and looks to promote human beings in situations and conditions unimaginable because the human beings concerned will be doing the imagining.	The competence focuses critical thought, understanding, interdisciplinary, and wisdom, sense of knowing.
14.	The skill element in decision making under uncertainty: Control or competence? Judgment and Decision Making Adam S. Goodie, Diana L. Young [17]	The competence elements control increased risk taking markedly with all statistical properties held constant, decisions made in domains of varying difficulty, and by individuals of varying ability, yielded further qualified support for the role of competence. The role of control was replicated, and participants' perceptions	The competence elements control varying difficulty, and by individuals of varying ability, yielded further qualified support for the role of competence.
15.	Motivation reconsidered: The concept of competence. White, Robert W. [18]	The new motivational concept of "competence" is introduced indicating the biological significance of such behavior. It furthers the learning process of effective interaction with the environment.	"competence" is introduced indicating the biological significance of such behavior and further interaction with the environment.

The main components of competence are knowledge, skills and capabilities. Unfortunately, the literature review showed only the presence of components of competencies, but it is not clear that proportional division and proportion. To understand the importance of each identified component, the authors used the results of three studies conducted in the framework of the EU projects in which one of the authors of the article took an active part.

Research results of three EU projects are included in this paper:

1) LLP Transfer of Innovation, Multilateral Projects, Leonardo da Vinci project “Employability and Skills Anticipation Policies: a Social ROI Approach” (thereafter - ESAP).

2) Erasmus+ KA 2 Cooperation for innovation and the exchange of good practices strategic partnership project „Coaches of SMEs: 5POINTS Trainings” (thereafter – 5POINTS)

3) Erasmus+ KA 2 Cooperation for innovation and the exchange of good practices strategic partnership project “Innovative strategic partnership for European higher education” (thereafter – ISPEHE).

1. Project: The 5POINTS

Programme: The justification for the basic objectives of the project is explained by acting as coach to enable the SMEs to produce their own solutions and embed the understanding of innovative SMEs within their organizational structures.

Table 2. Managerial Skills

Areas	Turkey	Hungary	Latvia	Finland	Spain
Self-awareness, self recognition, entrepreneurship and leadership skills (personal characteristics, value priorities, time perspective, resistance against stress, leading style etc.)	4	3	4	4	2
Interpersonal relationships, communication and specific communication skills (written and verbal presentation skills, managing the meetings etc.)	3	4	4	3	3
Problem solving and effective decision making skills	5	4	3	3	4
Negotiation and conflict management skills	4	5	3	4	4

In the report published by the European Commission in 2012 regarding SMEs, it is indicated that SMEs play a key role in shaping European economy with a share of 98%. 5POINT Coaches of SMEs: 5POINTS Trainings research and development and management of financial tools and developing problem solving abilities of SMEs, including the solution of financial problems, constitutes an important point which should be highlighted by the government as the public authority, as well as a vital issue which the

academicians working in this area in universities should emphasize. This issue is taken as basis when determining the rationality of the project. The justification for the basic objectives of the project is explained by acting as coach to enable the SMEs to produce their own solutions and embed the understanding of innovative SMEs within their organizational structures[5].

2. Project:

Innovative Strategic Partnership For EU Higher Education. Programme:

Erasmus Plus Action KA2: Cooperation For Innovation And The Exchange Of Good Practices.

The main purpose of the Strategic Integration of Learning Modes (hereinafter SILM), as the first innovative project component, is to establish joint contemporary educational practices and produce a long-term strategic learning model based on the existing curricula adopted and successfully implemented in each partnering institution.

The Needs Assessment Analysis is the first element in preparing the SILM. The Needs Assessment presents an integrated report of the individually conducted analysis in each of the partnering institutions. The objectives of analysis are aligned with the specific objectives of SILM, and support their accomplishment. They are stated as follows:

- Identify the factual situation in each of the partnering HEIs
- Provide assistance for making needed decisions related to establishing optimal learning models and best practices
- Obtaining a participatory approach in constructing SILM from relevant stakeholders.

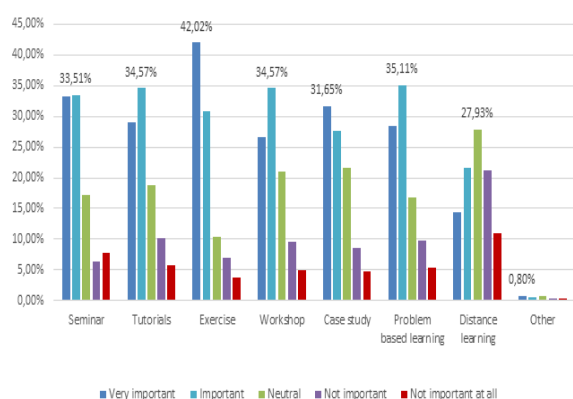


Fig. 1. Integrated results from all five partnering institutions.

Additional research shows that an important aspect of knowledge in their practical application, which require not only knowledge in its original form, but also skills. This conclusion discovers the importance of acquiring skills for students.

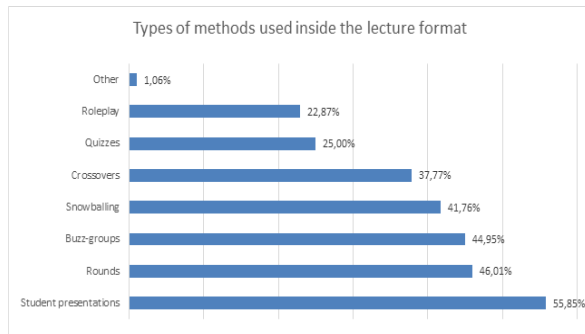


Fig. 2. Integrated results from all five partnering institutions.

The results of the research, students prefer the presentation and Buzz-groups that require the development of skills.

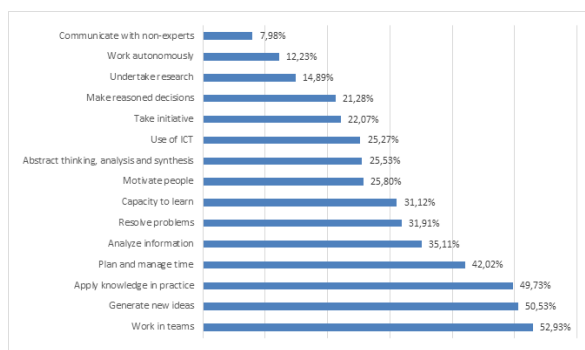


Fig. 3. Integrated results from all five partnering institutions.

The result of this study shows that it is necessary to improve quality skills such as: work in teams, apply knowledge in practice, generation of new ideas. Figure 3 shows areas of potential improvement of the students in order to get optimal use of the teaching methods utilized in classes. The areas of improvement, identified by the students for tackling in the future in order to optimize the utilization of teaching methods are: Working in teams with 52,93%, followed by Generating new ideas with 50,53% and Applying the acquired knowledge in practice with 49,73%. The areas whose improvement doesn't coincide with optimizing the teaching methods, by the students are: Communication with non-experts with 7,98% and Working autonomously with 12,23%.[6]

3. Project

The companies were asked about the abilities, skills and knowledge considered essential for the development of the current and future predictable jobs. They rated the importance of the proposed skills from 1 (not important) to 4 (very important).

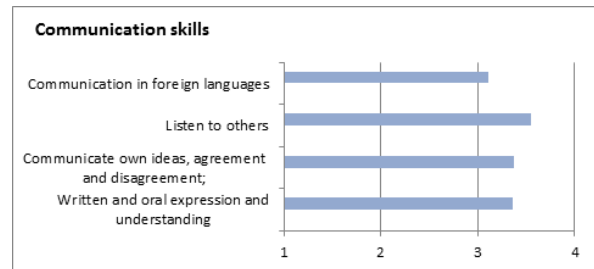


Fig. 4. Most valued Communication skills in all partnered countries.

The results of the research require the development of skills. The results of the analysis of all three studies show the importance of two elements of competencies - skills and knowledge are inseparably linked, which in turn dominates the value of the skills[7].

To perform competence, skills and knowledge relationship authors of the paper used Kulkki & Kosonen framework. Analyzing project researches projektov authors of the article think that Skills (S) based on Knowledge (K) are main elements of C (competence). Due to the inseparable connection of knowledge and skills, underlined the value of dispersed and knowledge. Following the thoughts of Hayek and Tsoukas discusses the fact that knowledge is dispersed primarily because it is an individual possession. Although the stock of knowledge of the firm is a reflection of individuals' stock of knowledge, it is destined to stay dispersed and local because there are few means to control processes when knowledge is emerging all over the firm. Tsoukas declares that "rational economic calculation" cannot take into account the factual knowledge of the particular circumstances of time and space. [22]

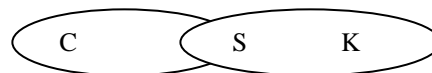


Fig. 5. Relationship of competence (C) and skills (S) based on knowledge (K) [done by authors based on X]

IV. CONCLUSION

The authors of the paper conclude that the main dominant element of competence are knowledge and skills.

The results of the study the hypothesis was not confirmed at this stage. Triangulation showed the importance of knowledge and skills for competence creation. In turn, the factor of emotional intelligence has not been performed. This requires detailed in-depth analysis, which will be revealed in future studies. Hypothesis: emotional intelligence influences the creation of competencies

As a first step of our research, there is not yet fully approved direct correlation between competence and emotional capital, and therefore authors are forced to use in future researches more detailed and deep analysis to get more information about explored problem.

V.ACKNOWLEDGMENTS

This paper includes three different surveys results conducted by projects have been funded with support from the European Commission:

1) Erasmus+ Key Action 2 „Cooperation for innovation and the exchange of good practices” strategic Partnership project „Coaches of SMEs: 5POINTS Trainings”, Nr: 2014-1-TR01-KA202-013033

2) Lifelong Learning Programme Transfer of Innovation, Multilateral Projects, Leonardo da Vinci project “Employability and Skills Anticipation Policies: a Social ROI Approach”, Nr: 2011-1-PT1-LEO05-08605.

3) Erasmus+ Key Action 2 „Cooperation for innovation and the exchange of good practices” strategic Partnership project “Innovative strategic partnership for European higher education”, Nr: 2014-1-MK01-KA203-000275

This publication reflects the views only of the authors, and the European Commission cannot be held responsible for any use that may be made of the information contained therein.

REFERENCES

- [1] Prahalad C. K., G.Hammel *The Core of Competence* , 2011, pp. 23–65.
- [2] Lapiņa, I., Aramina, D.”Development of Human Capital based on Competencies and Quality of Education”. *Economics and Business*. Vol.21, 2011, pp.60-66.
- [3] Monnier, M, “Difficulties in Defining Social-Emotional Intelligence, Competences and Skills--A Theoretical Analysis and Structural Suggestion” *International Journal for Research in Vocational Education and Training*, v2 n1, 2015 p59-84
- [4] Nicola S., Schutte, J, M. Malouff and Einar B. Thorsteinsson “Increasing Emotional Intelligence through Training: Current Status and Future Directions” *International Journal of Emotional Education* , Vol 5, Nr 1, April 2013 pp. 56.
- [5] Bøtcher C and Andersen L.B, “Leading public service organizations: how to obtain high employee self-efficacy and organizational performance”, *Political Science, Public Management Review*, vol 19.2017 pp 253-273
- [6] Cantwell J, “Innovation and international business” vol.24 2017, pp 41-63
- [7] Claudy M.C and Peterson M, “The Roles of Sustainability Orientation and Market Knowledge Competence in New Product Development Success”, *Journal of Product Innovation Management* 33 (S1), 2016, pp 72-85.
- [8] Ermilova E and Afsarmanesh H, “Competency modelling targeted on boosting configuration of virtual organisations” *Production Planning and Control, The Management of Operations*, vol.21, 2010 - Issue 2, pp 103-118
- [9] Elliot A.J and Dweck C S., *Handbook of Competence and Motivation* , Guilford Press, NY, 2005, pp 92-114
- [10] Foss N.J, Knudsen C, *Towards a Competence Theory of the Firm* , Routledge, 1996, pp 62-101
- [11] Chamorro-Premuzic, T; Furnham, A., *Personality and intellectual competence*, Lawrence Erlbaum Associate, 2009
- [12] C.P.M. van der Vleuten., Schuwirth, Scheele F, E.W. Driessen, B. Hodges “The assessment of professional competence: building blocks for theory development “, *Best Practice and Research*, vol.24, Issue 6, Pages 703–719
- [13] Gnamb T; A Personality-Competence Model of Opinion Minna L, Paavola I.S, Kantosalo A, “Digital competence – an emergent boundary concept for policy and educational research”, *Education and Information Technologies* May 2016, vol.21, Issue 3, pp 655–679
- [14] Weinert F.E, *Concept of competence: A conceptual clarification*, Munich , Germany, 1999
- [15] Ronald B, *The Limits of Competence: Knowledge, Higher Education and Society*. The Society for Research Into Higher Education and Open University Press; Reprint edition, 1999
- [16] Goodie A. S. and Young D. L.” The skill element in decision making under uncertainty: Control or competence? “ *Judgment and Decision Making* , *Judgment and Decision Making*, vol. 2, No. 3, June 2007, pp183-211
- [17] White, R.W. Motivation reconsidered: “The concept of competence”. *Journal: Psychological review*, 1959/09
- [18] Ganite K. Tuğba Uçma U. 5POINTS Coaches of SMEs: 5POINTS Trainings, Tech. Rep. Nr: 2014-1-TR01-KA202-013033, 2014
- [19]. ISPEHE, SILM Needs Assessment Analysis Tech. Rep 2014-1-MK01-KA203-000275, 2014
- [20] “Employability and Skills Anticipation Policies: a Social ROI Approach”, Tech. Rep ,Nr: 2011-1-PT1-LEO05-08605, 2011
- [21] Kulkki S., Kosonen, M. How Tacit Knowledge Explains Organizational Renewal and Growth: the Case of Nokia. *Managing Industrial Knowledge*. Edited by Nonaka, I., Teece, D.2001.p.249.

Study Wear Tool with High-speed Milling

Tsvetan Kaldashev, Petar Hadzhiyski, Galina Nikolcheva

Technical university of Sofia, Address: Blvd. "Kl. Ohridski" 8, Sofia, Bulgaria

Abstract. This report examined tool wear in high-speed machining of tool steel with a hardness of HRC 63. Wear monitored periodically using the device for automatic geometric correction tool (length and radius) situated in the working area of the machine. The study was conducted on milling machine RAIS M400 with CNC Heidenhain iTNC 530i.

Keywords: wear, high-speed milling, cutting tool, milling machine, CNC.

I. INTRODUCTION

Rotary dies for the production of sanitary absorbents (Figure 1) in the process of work wear [1,2], which requires their periodic sharpening i.e. reconstruction of cutting power. They are made of tool steel, where after quenching reached hardness between 60 and 63 HRC. Resharpener of these components is carried out by grinding the side surface where the process compared to the milling has a low performance [3].



Fig. 1 Rotary die for sanitary absorbents

Taking into account the stiffness of the rotary die from HRC 63 it is possible to increase productivity by using high-speed milling. When sharpening the cutting edge of the rotary die due to different wear have capture greater added. This, together with the great length of the cutting edge may lead in turn to an unacceptable wear of the cutting tool and breakage. The aim of the study is to check the wear of the tool to be able to answer the question whether high-speed milling can replace grinding.

II. STUDY OF THE WEAR OF THE TOOL AT HIGH SPEED MILLING

To conduct the study used a cutting tool company SGS Series Power-Carb with AlTiN coating. This series is recommended for machining of molds for injection molding of forms for casting and the production of dies [4, 5]. Tools of this series are characterized by high quality of the machined surface of hardened steel with a hardness of 65 HRC. The

study is done on milling machine RAIS M400 with CNC Heidenhain iTNC 530i [6]. Fig. 2 shows the establishment of a workpiece, which is essentially a rotary die obsolete.



Fig. 2 Establish a workpiece

Wear on the tool radius is controlled using the findings in the working area of the machine device for automatically determining the length and tool radius (Tool Touch Probe TT140). This is a built-in CNC cycles. The measurement of the tool radius is performed with cycle 482 (Fig.3), wherein the measurement is possible to carry out in two ways - with continuous rotation of the instrument and measurement of each tooth separately, in which case it must first be set to the number of the teeth of the tool. In this way, the system automatically determines the highest tooth and it introduces a correction. After measurement, the values recorded in the sub-instruments.

Study of measurement accuracy Tool Touch Probe TT140

The study of the accuracy of the TT 140 is necessary to examine to what extent will be reliable survey data. It will be held by being made 20 measurements for each of the aforementioned methods.

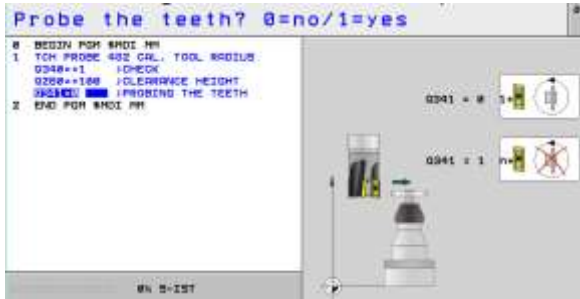


Fig. 3 Measuring cycle 482

Accuracy in the rotating tool

Used measurement cycle 482 (fig. 3). This cycle is only measured tool radius. Depending on what is set in parameter 341 (fig. 3) measured on the rotating tool (parameter 341 = 0) or measured each tooth individually (parameter 341 = 1). In Table 1 shows the measurement results.

Table 1
Results of measurement in rotating tool

№	Tool radius [mm]	Deviations DR [mm]	№	Tool radius [mm]	Deviations DR [mm]
1	4	-0,0155	11	4	-0,0176
2	4	-0,0156	12	4	-0,0217
3	4	-0,0219	13	4	-0,0157
4	4	-0,0181	14	4	-0,0210
5	4	-0,0104	15	4	-0,0218
6	4	-0,0227	16	4	-0,0165
7	4	-0,0247	17	4	-0,0161
8	4	-0,0262	18	4	-0,0108
9	4	-0,0225	19	4	-0,0212
10	4	-0,0108	20	4	-0,0134

Results are processed statistically to determine what is the accuracy of the measurement. Arithmetical mean value $\bar{\Delta}$ is defined by equation (1) and residual errors in equation (2).

$$\bar{\Delta} = \frac{1}{n} \sum_{i=1}^n \Delta_i \quad (1)$$

$$\delta_i = \Delta_i - \bar{\Delta} \quad (2)$$

With the obtained values are determined standard deviation equation (3) and mean square deviation S_x in equation (4).

$$s = \sqrt{\frac{1}{n-1} \sum_{i=1}^n \delta_i^2}, \text{ at } n < 30 \quad (3)$$

$$s_{\bar{x}} = \frac{s}{\sqrt{n}} \quad (4)$$

Confidence limits $\pm \varepsilon$ is defined in equation (5) at the confidence level $\gamma = 0,99$, then determine confidence limits in equation (6).

$$\varepsilon = t_{\gamma} \cdot S_x \quad (5)$$

$$(\bar{X} - t_{\gamma} \cdot s_{\bar{x}}) < E < (\bar{X} + t_{\gamma} \cdot s_{\bar{x}}) \quad (6)$$

The results are presented graphically in fig. 4.

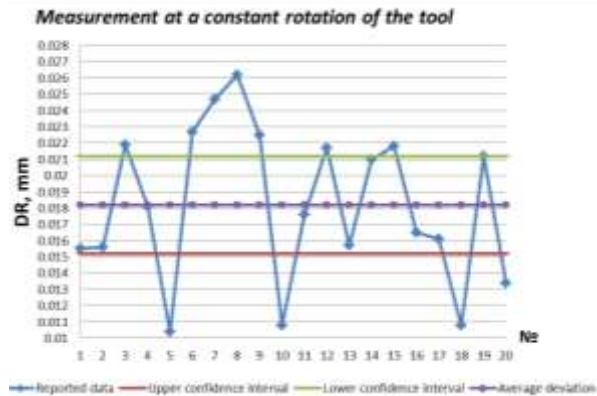


Fig. 4 Graphical representation of the accuracy of the rotating tool

Accuracy of each tooth individually

Again using the measuring cycle 482 as a parameter 341 is set to 1. In the table parameters of the tool set number of teeth.

Table 2
Measurement results for each tooth individually

№	Tool radius [mm]	Deviations DR [mm]	№	Tool radius [mm]	Deviations DR [mm]
1	4	-0,0166	11	4	-0,0172
2	4	-0,0132	12	4	-0,0160
3	4	-0,0134	13	4	-0,0170
4	4	-0,0128	14	4	-0,0149
5	4	-0,0141	15	4	-0,0133
6	4	-0,0176	16	4	-0,0166
7	4	-0,0168	17	4	-0,0168
8	4	-0,0165	18	4	-0,0179
9	4	-0,0160	19	4	-0,0174
10	4	-0,0158	20	4	-0,0173

The measurement results are presented in Table. 2. In Fig. 5 presents graphically the data processed statistically by the equations (1) to (6).

The standard deviation of the first case (a rotating tool) is $S = 0.0047$, and in the second case, $S = 0.0016$. Mean square error in the measurement of rotation of the tool is $SX = 0.0011$, while the second case when measured each tooth individually, the mean square error is $SX = 0.0004$.

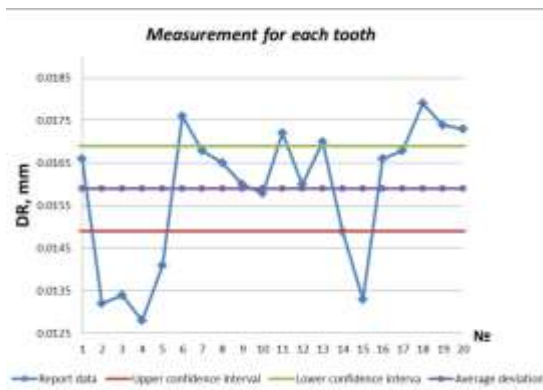


Fig. 5 Graphical representation of accuracy in measuring each tooth individually

From these results, it is found that the method which measures each cutting tooth individually is more accurate and will be used in the experiment to check the wear of the cutting tool at high-speed cutting of steel with a hardness of 63 HRC.

Study of wear on the cutting tool at high speed milling

SGS is used tool Series Power-Carb coated with AlTiN and tooth 6, wherein the treatment is performed with circular interpolation. Control program is implemented with the help of parameters and cycles meeting certain logical conditions. At the beginning of the control program introduces parameters such as diameter and height of the workpiece feeding speeds jutting out into the addition and routing, cross-filing and more. After each pass of 5 instrument is measuring its radius. Fig. 6 shows the control program.

```

0 BEGIN PGM M400 MM
1 FN 0: Q1 =+156
2 FN 0: Q2 =+300
3 FN 0: Q3 =+152
4 FN 0: Q4 =+0.25
5 FN 0: Q5 =+0
6 FN 0: Q6 =+0
7 FN 0: Q7 =+0
8 FN 0: Q8 =+5
9 FN 0: Q9 =+4
10 FN 0: Q10 =+3000
11 FN 0: Q11 =+3000
12 FN 0: Q12 =+6000
13 FN 0: Q13 =+0
14 FN 4: Q14 =+Q1 DIV +2
15 BLK FORM 0.1 Z X-Q14 Y-Q14 Z-Q2
16 BLK FORM 0.2 X+Q14 Y+Q14 Z+0
17 TOOL CALL 2 Z SQ12
18 LBL "IZMERVANE"
19 TCH PROBE 482 CAL. TOOL RADIUS ~
    Q340=+1 ;CHECK ~
    Q260=+100 ;CLEARANCE HEIGHT ~
    Q341=+1 ;PROBING THE TEETH
20 L X+0 Y+0 Z+80 R0 FMAX
    
```

```

21 FN 0: Q13 =+0
22 LBL 0
23 LBL "FREZOVANE"
24 FN 1: Q5 =+Q5 + +Q4
25 FN 2: Q6 =+Q1 - +Q5
26 FN 1: Q7 =+Q6 + +Q4
27 FN 1: Q13 =+Q13 + +1
28 CYCL DEF 257 CIRCULAR STUD ~
    Q223=+Q6 ;FINISHED PART DIA. ~
    Q222=+Q7 ;WORKPIECE BLANK DIA. ~
    Q368=+0 ;ALLOWANCE FOR SIDE ~
    Q207=+Q10 ;FEED RATE FOR MILLNG ~
    Q351=+1 ;CLIMB OR UP-CUT ~
    Q201=-Q9 ;DEPTH ~
    Q202=+Q9 ;PLUNGING DEPTH ~
    Q206=+Q11 ;FEED RATE FOR PLNGNG ~
    Q200=+2 ;SET-UP CLEARANCE ~
    Q203=+0 ;SURFACE COORDINATE ~
    Q204=+50 ;2ND SET-UP CLEARANCE ~
    Q370=+1 ;TOOL PATH OVERLAP
29 CYCL CALL POS X+0 Y+0 Z+0 FMAX
M3
30 LBL 0
31 FN 15: PRINT Q108 /Q7 /Q5 /Q6 /Q13
32 FN 9: IF +Q13 EQU +Q8 GOTO LBL
"IZMERVANE"
33 FN 11: IF +Q6 GT +Q3 GOTO LBL
"FREZOVANE"
34 END PGM M400 MM
    
```

Fig. 6 Control program

The study was realized, it was made five attempts to change the regime of cutting. In Table. 3 shows the results of well skilled in mode 1 cutting: cut feed 3000 mm / min (feed per tooth 0.083 mm), spindle speed 6000 min⁻¹, step over 0.25 mm, diameter of the workpiece Dw = 158.85 mm.

Table 3
 Result of Experiment 1

Experiment 1			
Tool radius, [mm]	DR, [mm]	Dw, [mm]	Distance L, [mm]
4		158.6	498.2566
		158.35	497.4712
		158.1	496.6858
		157.85	495.9004
	0.0147	157.6	495.1150
	ΣL , [mm]		2483.4290
	Wear, [mm]		-0.0026

A negative sign is accidentally received and due to the dissipation of the measurement results with Tool Setter TT140.

Experiment 2 was conducted in the following mode: cut feed 2000 mm / min (feed per tooth 0.055), spindle speed 6000 min⁻¹, step over 0.32 mm, diameter of the workpiece Dw = 157,6 mm (Table. 4)

Table 4
Result of Experiment 2

Experiment 2			
Tool radius, [mm]	DR, [mm]	Dw, [mm]	Distance L, [mm]
4		157.28	494.1097
		156.96	493.1044
		156.64	492.0991
		156.32	491.0938
	0.0147	156.00	490.0884
$\Sigma L, [mm]$			2460.4954
Wear, [mm]			0.0059

Experiment 3 was conducted in the following mode: cut feed 3000 mm / min (feed per tooth 0.083), spindle speed 6000 min-1, step over 0.25 mm, diameter of the workpiece Dw = 156 mm (Table. 5)

Table 5
Result of Experiment 3

Experiment 3				
Tool radius, [mm]	DR, [mm]	Dw, [mm]	Distance L, [mm]	Wear [mm]
4	0.0201	157.28	2434.73	-0.0005
	0.0231	156.96	2419.03	0.003
$\Sigma L, [mm]$			4853.76	
Wear, [mm]				0.0025

Experiment 4 - mode: cut feed 3000 mm / min (feed per tooth 0.071), spindle speed 7000 min-1, step over 0.25 mm, feed per tooth 0.055, diameter of the workpiece Dw = 153.25 mm (Table. 6)

Table 6
Result of Experiment 4

Experiment 4			
Tool radius, [mm]	DR, [mm]	Distance L, [mm]	Wear [mm]
4	0.0268	4684.9	0.0043
	0.0273	3691.37	0.0005
	0.0282	5061.89	0.0009
	0.0299	4983.35	0.0017
	0.0305	4904.81	0.0006
	0.0318	4826.27	0.0016
	0.0363	8347.99	0.0013
	0.0394	8093.52	0.0048
$\Sigma L, [mm]$		51733.36	
Wear, [mm]			0.0163

In the last 5 Experiment was changed only step over = 0.15 mm. The results are shown in Table. 7

Table 7
Result of Experiment 5

Experiment 5			
Tool radius, [mm]	DR, [mm]	Distance L, [mm]	Wear [mm]
4	0.0407	4384.87	0.0013
$\Sigma L, [mm]$		4384.87	
Wear, [mm]			0.0013

When the last attempt tool was completely worn out. In the treated surface was obtained yellowish-brown mark (fig. 7), from which it is clear that the tool is worn. This path is obtained by burning the material in the cutting zone. Fig. 8 is visible wear of the tool.



Fig. 7 Marks on the treated surface related to tool wear



Fig. 8 Wear the instrument after completion of the study

The results of the experiment are summarized in Table. 8. From these data it is clear that the parameters used tool travels nearly 66 meters before being completely worn out.

Table 8
Summarized Results of the Study

Total distance, [mm]	66 000
Total wear, [mm]	0.0234

Fig. 9 is a graph of tool wear compared traveled road. The amount of volume of the milled material is 45 492 mm³.

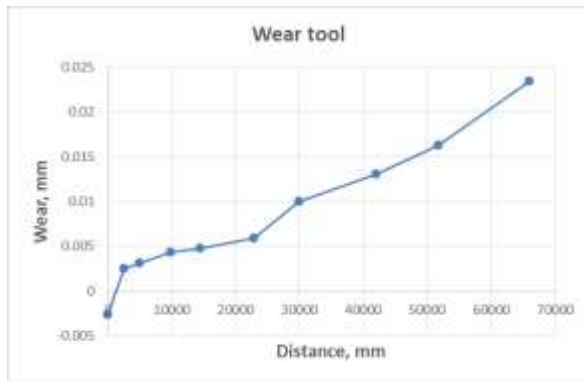


Fig. 9 Wear the instrument to the covered distance

III. CONCLUSION

From the results can be drawn the following conclusions:

1. In high-speed milling filled with these modes, tool wear is minimal compared to the distance covered;

2. From Fig. 9 it can be seen that with some initial wear, there is a slow minimum wear increase as compared to the way traveled. It is explained by the fact that in the initial stage of operation the wear of the tool is more intense and it is not in line with the way traveled;

3. Wear compared to the distance covered is negligible, and the life of the tool is much longer than prescribed by the manufacturer;

4. High-speed milling can replace the grinding operation at sharpening the cutting edge of the rotary die;

5. With high-speed milling, productivity increases about 2-3 times compared to grinding.

REFERENCES

- [1] Хаджийски П., Маринов Ив., Анализ на износването на режещият клин на ротационни щанцови инструменти със сложна форма. 25-та Юбилейна научна конференция, МТФ, 2007, Созопол.
- [2] Hadzhiyski P., Knives for rotary dies with variable geometry, Проблеми машиностроения и автоматизации, 2011, №4, стр. 132-136, ISSN 0234-6206.
- [3] Хаджийски П., Анализ на възможностите за повишаване на производителността при шлифване на режещи ръбове със сложна геометрия върху металорежещи машини с CNC, Тринадесета национална научно-техническа конференция „Автоматизация на дискретното производство“ АДП 2004 г., София, стр. 60-62, ISSN 1310-3946.
- [4] SGS High Performance Catalog.
- [5] www.sgstool.com.
- [6] User's manual Heidenhain Conversational format, 2002

Structure and Mechanical Properties of Spheroidal Graphite Cast Iron with Nanosized Additives

Julieta Kaleicheva¹, Valentin Mishev¹, Zdravka Karaguiozova², Galina Nikolcheva¹

¹ Technical University of Sofia, boulevard Kliment Ohridski 8, 1000 Sofia, Bulgaria,
e-mail: jkaleich@tu-sofia.bg

² Space Research and Technology Institute, Bulgarian Academy of Sciences, Acad. G. Bonchev str., Bl.1,
Sofia-1113, Bulgaria, e-mail: karazuzi@yahoo.com

Abstract: *The microstructure and properties of spheroidal graphite cast irons and austempered ductile irons with nanosized additives of titanium carbonitride and titanium nitride (TiCN+TiN), titanium nitride TiN and cubic boron nitride cBN are investigated. The microstructure of the patterns is observed by optical metallography, quantity metallographic analysis, X-Ray analysis, SEM analysis and EDX analysis. Hardness measurement, impact strength and abrasion wear test on fixed abrasive are performed. The influence of the nanosized additives on the microstructure, mechanical and tribological properties of the cast irons are examined.*

Keywords: *spheroidal graphite iron, austempering, titanium nitride, titanium carbonitride, cubic boron nitride, wear resistance, hardness, structure, bainite, austenite.*

I. INTRODUCTION

Spheroidal graphite cast iron is a structural material, characterized with a high strength, toughness and wear resistance. Graphite in the cast iron provides resistance to mechanical wear and improves the processability. Application of an alloying, thermal treatment or both of these processes influence the graphite morphology and substrate structure and allows achieving optimal properties of the iron [1-5]. Austempering is a thermal treatment process leading to a bainitic structure of the substrate material with high strength, increased ductility and high toughness [1-4]. The addition of small quantities of nanosized particles into the iron melt increases graphite quantity [9] and changes its morphology [8], which combined with the changes in the structure of the substrate enhances the wear resistance of the cast iron [7-10].

The aim of the present study is investigation of the microstructure, mechanical and tribological properties of spheroidal graphite cast iron and austempered ductile iron samples with nanosized additives of titanium carbonitride and titanium nitride (TiCN+TiN), titanium nitride TiN and cubic boron nitride cBN.

II. MATERIALS AND METHODS

The composition of the spheroidal graphite cast iron samples is: Fe-3,55C-2,67Si-0,31Mn-0,009S-0,027P-0,040Cu-0,025Cr-0,08Ni-0,06Mg wt%. Samples with and without nanosized additives of

titanium carbonitride and titanium nitride (TiCN+TiN), titanium nitride TiN and cubic boron nitride cBN are investigated (Table 1). For the improvement of the particles wetting and their uniform distribution into the casting volume the electroless nickel coating is plated on the particles surface. EFTTOM-NICKEL method is used for electroless plating [11].

The microstructure of the spheroidal graphite cast iron samples is investigated by quantity metallography, scanning electronic microscopy (SEM), and Energy dispersive microanalysis (EDX). Scanning microscope EVO® MA10 „Carl Zeiss” with X-Ray micro analyzer „Bruker“ is used. The software „Olympus MicroImage” is used for the quantity metallographic analysis. Data for the average diameter D_{mid} of the graphite particles, their roundness and the volume parts of the graphite, pearlite and ferrite are received.

The spheroidal graphite cast iron samples are subjected to the austempering, including heating at 900°C for an hour, after that isothermal retention at 280°C, 2 h and at 380°C, 2 h. The austempered ductile iron samples' microstructure is observed by means of an optical metallographic microscope GX41 OLIMPUS. The samples surface is treated with 2 vol. % nital solution. The austempered ductile iron samples are tested by X-Ray diffraction analysis for measurement of the retained austenite quantity in the structure. The retained austenite quantity before and after abrasive wear is determined. X-ray powder

ISSN 1691-5402

© Rezekne Academy of Technologies, Rezekne 2017
<http://dx.doi.org/10.17770/etr2017vol3.2605>

diffraction patterns for phase identification were recorded in the angle interval $20 \div 103^\circ$ (2θ), on a Philips PW 1050 diffractometer, equipped with Cu $K\alpha$ tube and scintillation detector. Data for cell refinements and quantitative analysis are collected in θ - 2θ , step-scan mode in the angle interval from 20 to 103° (2θ), at steps of 0.03° (2θ) and counting time of 3s/step. Quantitative analysis is carried out by BRASS - Bremen Rietveld Analysis and Structure Suite [12].

The hardness test by Brinell method (for cast samples) and by Vickers method (for austempered samples) is performed. The impact strength test is carried out by a Charpy hammer.

The friction wear investigation on fixed abrasive by kinematic scheme “thumb-disc” is performed using accelerated testing [9, 10]. The impregnated material *Smirdex 330 Duraflex P80, 117SV* is used for the spheroidal graphite cast iron. The test data are: nominal contact pressure $P_a = 0,21 \cdot 10^6$ [Pa]; average sliding speed, $V = 26,38$ [cm/s]; nominal contact surface, $A_a = 50,24$ [mm²]; density, $\rho = 7,80 \cdot 10^3$ [kg/m³] [9]. The impregnated material Corundum 220 is used for the austempered ductile iron samples. The test data are: nominal contact pressure, $P_a = 0,4 \cdot 10^6$ [Pa]; average sliding speed, $V = 24,5$ [cm/s]; nominal contact surface, $A_a = 50,24$ [mm²]; density, $\rho = 7,80 \cdot 10^3$ [kg/m³] [10].

III. RESULTS AND DISCUSSION

The structure of the tested iron after casting consists of ferrite, pearlite, and graphite [9]. The quantity metallographic analysis is performed for the evaluation of the influence of the nanosized particles on the graphite quantity, size and morphology. Also the quantity ratio between ferrite and pearlite is defined (Table 1). Nanosized additives in the spheroidal graphite cast iron don't change the graphite shape. They decrease the average diameter of the graphite sphere D_{mid} from $11,00$ to $10,34 \mu\text{m}$ (Figure 1). The increase of the quantity of the graphite phase with 35÷94% and the change of the pearlite and ferrite quantity in the iron structure (Table 1) are observed in the presence of the nanosized particles (Figure 2). The quantity ratio between structural elements with different hardness is changed (the pearlite hardness is highest and the graphite hardness is lowest). This is the reason for the changes in the total iron hardness (Table 1, Figure 3). The impact strength of the samples increases with 14÷37% for the irons with nanosized additives (Figure 4).

SEM analysis of the fracture of the impact destructed spheroidal graphite cast iron sample with TiCN+TiN nanoparticles additives (Figure 5) and EDX analysis of the graphite phase (Figure 6), show the nanoparticles presence in the graphite. These results and that achieved from the quantity metallographic analysis prove the modifying influence of the nanoparticles on the size and shape

of the graphite phase in the iron samples.

In the wear resistance assessing of the iron base structure is necessary to take into account its ability to be changed as a result of a complex set of processes in operation. Graphite in the gray cast iron structure has an essential role in their wear. In case of dry friction virtually no wear was observed on some individual sections of the contact surface. This is related to the presence of graphite in the structure, which has a lubricating ability and acts as a lubricant material.

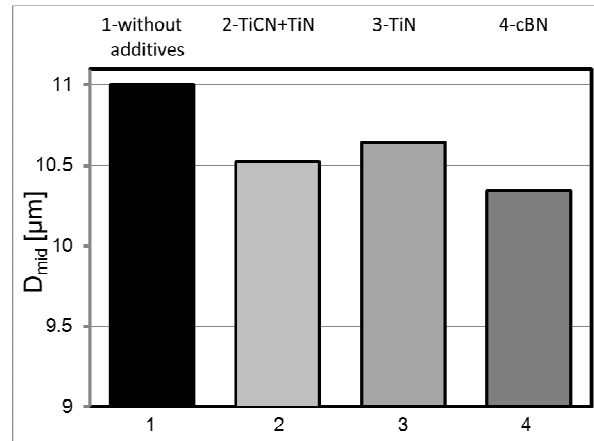


Figure 1. Average diameter of the graphite spheres D_{mid} in spheroidal graphite cast irons: 1,2, 3, 4 – sample number

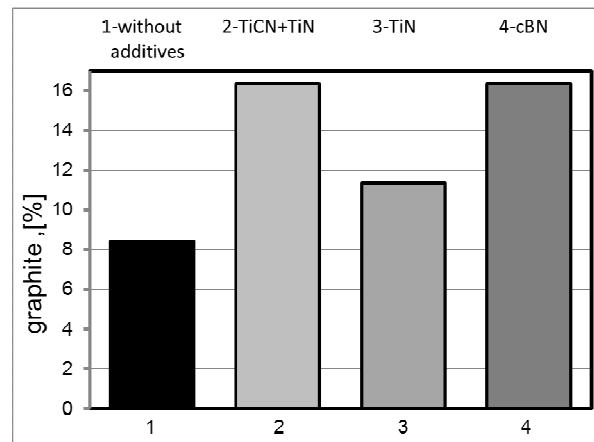


Figure 2. Graphite quantity in spheroidal graphite cast irons: 1,2, 3, 4 – sample number

The wear resistance of the irons with pearlite base at specified conditions of wear (contact pressure and sliding speed) is inversely proportional to the average distance between graphite grains. By reducing the distance between the graphite grains protective properties of the surface carbon layer is improved and the wear resistance of the iron is increased.

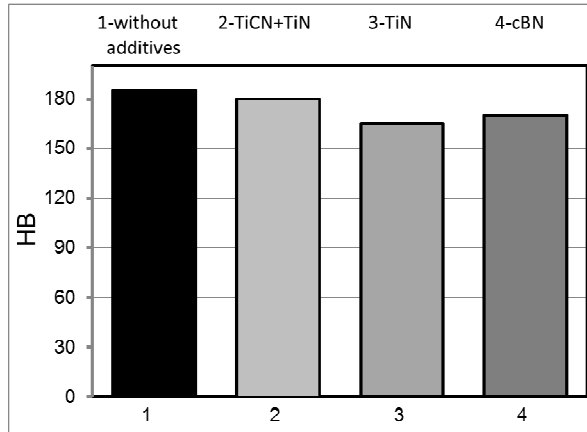


Figure 3. Hardness HB of spheroidal graphite cast irons: 1,2, 3, 4 – sample number

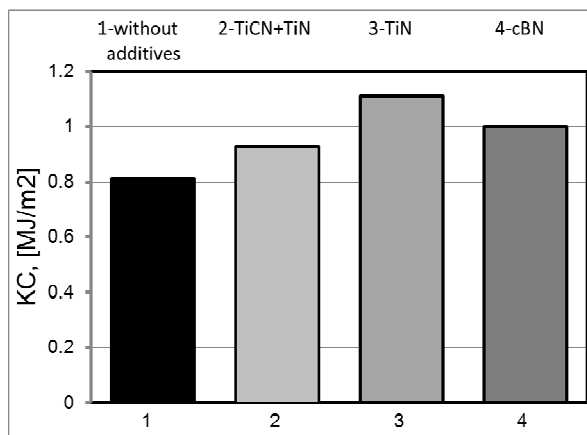


Figure 4. Impact strength KC of spheroidal graphite cast irons: 1,2, 3, 4 – sample number

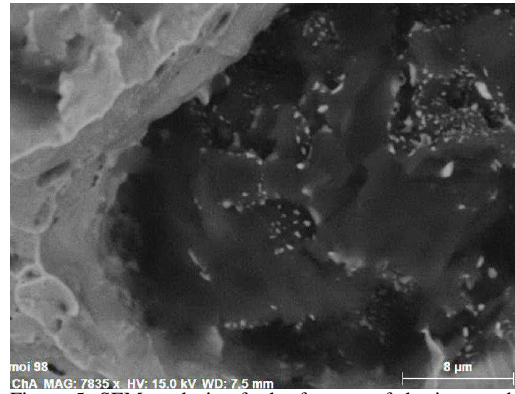
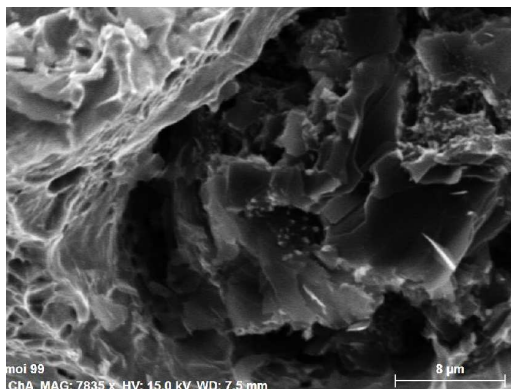
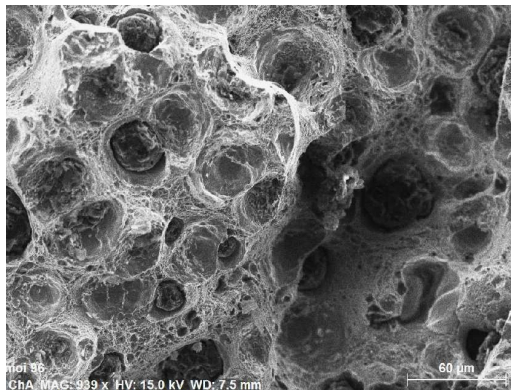


Figure 5. SEM analysis of the fracture of the impact destructed sample of spheroidal graphite cast irons with nanoadditives of TiCN+TiN (sample 2)

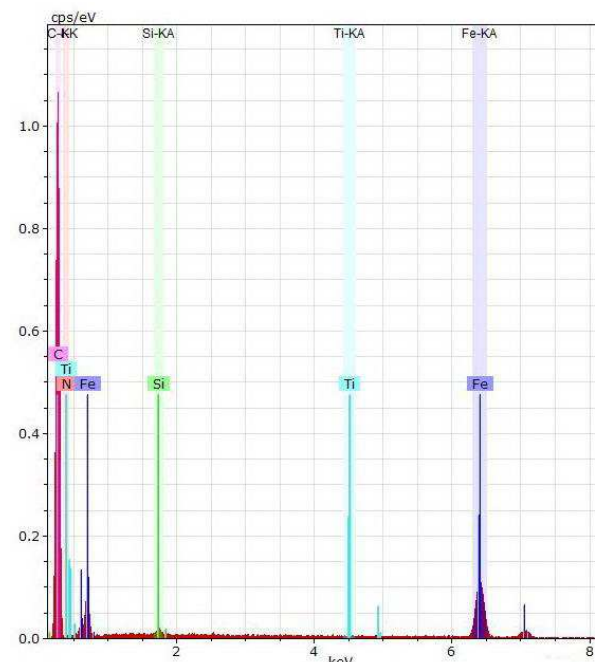


Figure 6. EDX analysis of the graphite phase of spheroidal graphite cast irons with nanoadditives of TiCN+TiN (sample 2)

Studied in this work spheroidal graphite cast iron with or without nanosized particles have an equilibrium ferrite-pearlite structure of the substrate and inclusions of graphite spheres [9].

The results of the quantitative metallographic analysis show that the nanosized additives without changing the graphite shape, increase its volume and decrease the average diameter of the graphite spheres (Figures 1 and 2), which leads to a reduction of the average distance between the graphite grains. Wear resistance of the cast iron with nanoadditives increase by 55 ÷ 88% compared to this one of the cast iron without nanoparticles (Figure 7).

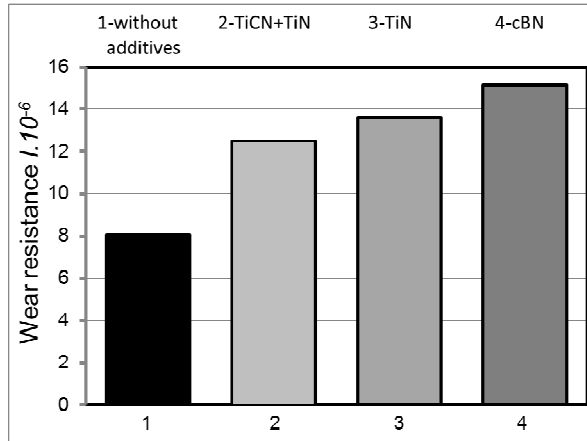


Figure 7. Wear resistance I of spheroidal graphite cast irons: 1,2, 3, 4 – sample number

The spheroidal graphite cast irons without and with nanoparticles are undergone to austempering with the aim to receive a bainitic structure of the metal substrate. The austempering mode includes austenitization at 900°C, 1 h followed by austempering at 280 °C, 2 h and at 380°C, 2 h. As a result of this thermal treatment cast iron structure obtained lower bainitic (Fig. 8) or upper bainitic structure (Fig. 9).

Bainite is an oriented structure consisting of needles α - phase (bainitic ferrite), carbides and unconverted austenite. α -phase is formed by martensitic mechanism in austenitic areas with low carbon content [1,2,10]. Upon cooling on the temperature of isotherm to ambient temperature, the part of the unconverted austenite undergoes martensitic transformation, and another part thereof remains in the structure as retained austenite A. The austenite bainitic transformation begins with the formation of individual needles α -phase (bainitic ferrite) and is developed with the formation of new oriented needles located close to each other and forming a package of alternating plates α -phase and the unconverted austenite enriched with carbon A (c) [1,2,10].

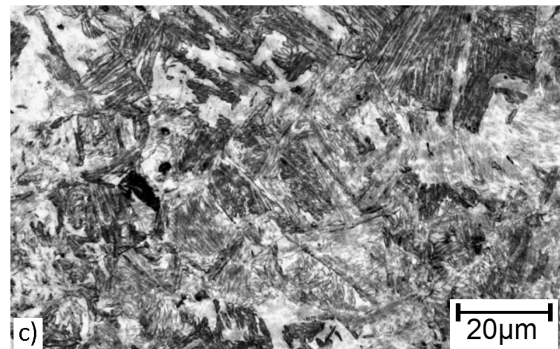
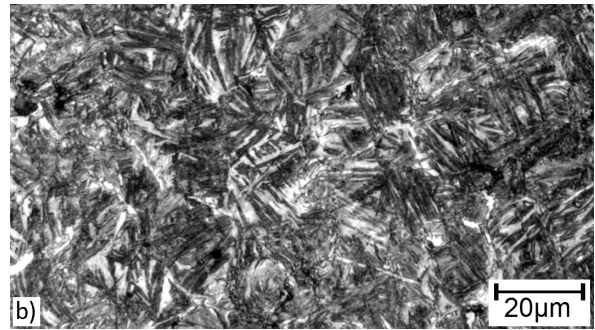
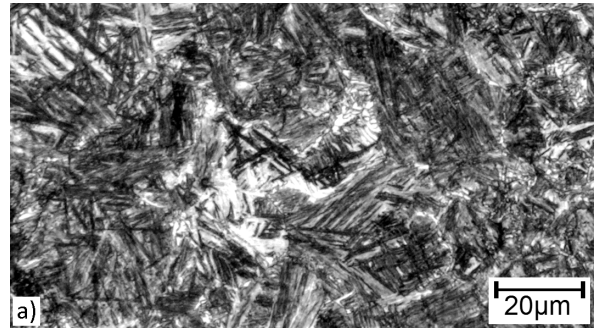


Figure 8. Lower bainite in austempered spheroidal graphite cast irons: a -sample 5; b- sample 6; c- sample 8

TABLE 1.

Nanoadditives, graphite characteristics, graphite, pearlite and ferrite quantity and mechanical properties of spheroidal graphite

№ of sample	Nanosized additive	D _{mid} μm	Roundness	Volume part of: [%]			Hardness HB	Impact strength KC MJ/m ²	Wear resistance I
				graphite	pearlite	ferrite			
1	-	11,00	1,59	8,44	32,12	59,44	185	0,81	8,06.10 ⁶
2	TiCN+TiN	10,52	1,28	16,36	25,36	58,28	180	0,93	12,5.10 ⁶
3	TiN	10,64	1,49	11,36	34,28	54,36	165	1,11	13,6.10 ⁶
4	cBN	10,34	1,23	16,34	35,74	47,92	170	1,0	15,15.10 ⁶

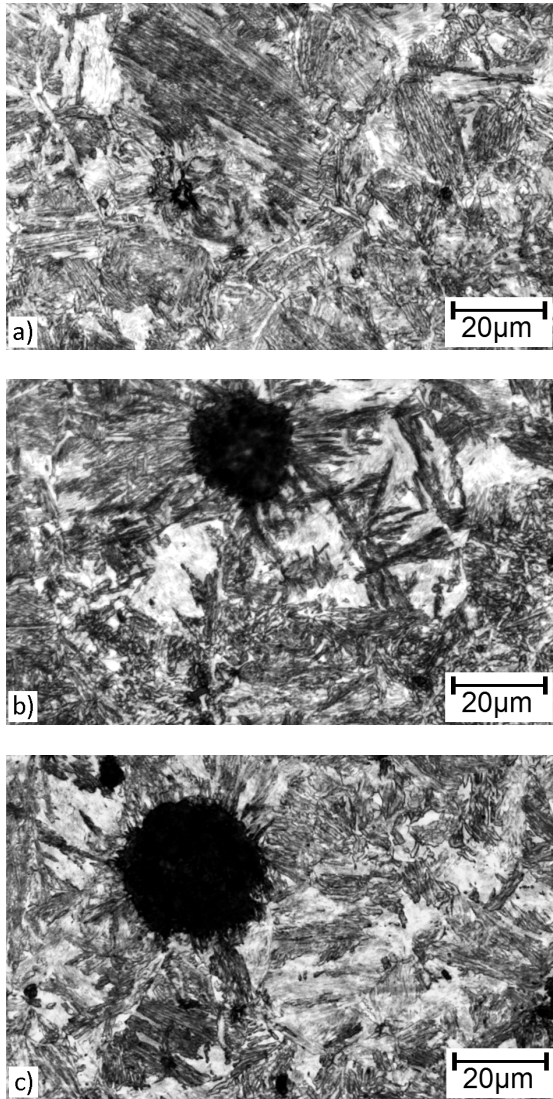


Figure 9. Upper bainite in austempered spheroidal graphite cast irons: a- sample 9; b- sample 10; c- sample 11

Optical metallographic analysis shows this package as individual needle in the lower bainitic structure. Carbide phase is formed as a result of self-tempering of the α -phase or directly from A(c). Silicon in the spheroidal graphite irons (2-3%) hinders process of the carbide formation. Bainitic ferrite and enriched with carbon unconverted austenite A(c) structures with high mechanical characteristics are realized at austempering 2-4 hours. An austempering mode over 6 hours could lead to a decomposition of the enriched with carbon austenite to a composite of ferrite and carbide (α +carbide), which decreases the iron mechanical properties and in practice not be carried out.

The lower bainitic structure hardness HV10 is in the range of 388 - 422 HV10, whereas this one of the upper bainite is – 312 - 319 HV10 (Table2, Figure 10). The higher upper bainitic hardness is correlated to the higher carbon saturation of the α -phase and to the higher degree of the austenite transformation in

the lower temperature range of the bainitic area.

The quantity of the retained austenite in the samples with upper bainitic structure is higher than this one in the samples with the lower bainitic structure. This correlates with the characteristics of the bainitic transformation mechanism in the upper and lower range of the bainitic area (Figure 11). The higher quantity of the retained austenite in the samples with upper bainitic structure defines their higher impact strength compared to this one of the samples with lower bainitic structure (Figure 12).

The wear resistance of the samples with nanosized additives of TiCN+TiN and structure of lower bainite is 73 % higher compared to this one of the samples without nanoadditives. The increase of the wear resistance of the samples with the same additives and an upper bainitic structure is 27% higher (Figure 13). The quantity of the retained austenite in the austempered samples before and after tribological testing is defined by X-Ray analysis (Table 2). It is found that the retained austenite quantity decreases in all of the samples after tribological testing (Figure 11).

The reduction of the retained austenite quantity is in the greatest extent in the samples with nanoadditives of TiCN+TiN. They possess highest wear resistance (Figure 13). The tribological properties of the metal materials largely depend on the structural condition forming on the contact surface in the friction process. The retained austenite in the austempered ductile irons' structure is a metastable structure and by friction impact could be undergone strain inducing $\gamma \rightarrow \alpha$ martensitic transformation. Friction partially transforms retained austenite in strain induced martensite consisting the same quantity carbon as well as high carbon austenite and appears untampered martensite with high hardness and possibility for intensive strengthening wear [10]. The formation of the strain induced martensite from the metastable retained austenite in the area of the friction contact probably is one of the reasons for the wear resistance increase of these irons.

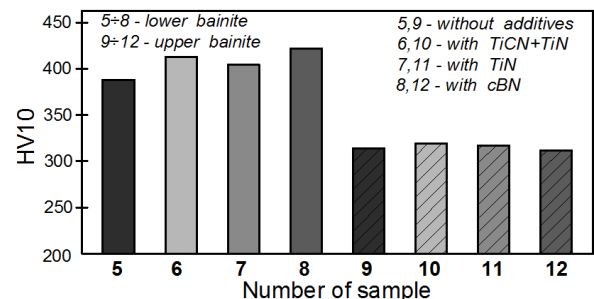


Figure 10. Hardness HV10 of austempered spheroidal graphite cast irons with lower bainitic structure (samples 5,6,7,8) and upper bainitic structure (samples 9,10,11,12)

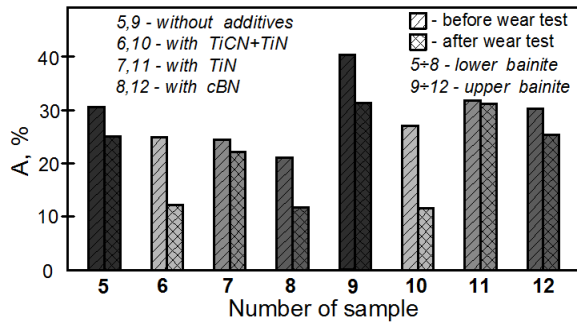


Figure 11. Retained austenite quantity A in austempered spheroidal graphite cast irons with lower bainitic structure (samples 5,6,7,8) and upper bainitic structure (samples 9,10,11,12) before and after tribological testing

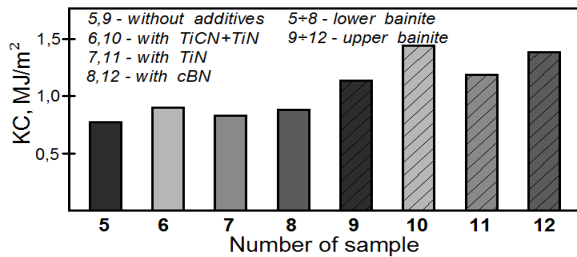


Figure 12. Impact strength KC of austempered spheroidal graphite cast irons with lower bainitic structure (samples 5,6,7,8) and upper bainitic structure (samples 9,10,11,12)

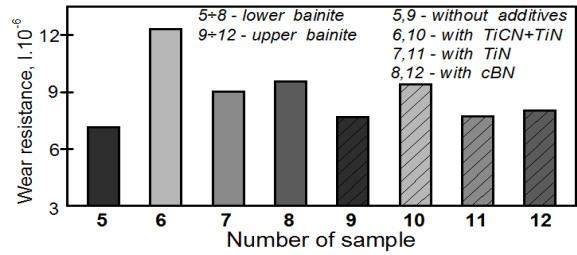


Figure 13. Wear resistance I of austempered spheroidal graphite cast irons with lower bainitic structure (samples 5,6,7,8) and upper bainitic structure (samples 9,10,11,12)

Table 2.

Nanoadditives, hardness, impact strength, wear resistance and retained austenite of austempered ductile iron (ADI)

№ of sample	Structure	Nanosized additive	Hardness HV10	Impact strength KC MJ/m²	Wear resistance I	Retained austenite A, %	
						before wear test	after wear test
5	lower bainite	-	388	0,771	7,13.10 ⁶	30,6	25,0
6		TiCN+TiN	413	0,901	12,3.10 ⁶	24,9	12,2
7		TiN	405	0,828	9,03.10 ⁶	24,4	22,1
8		cBN	422	0,884	9,56.10 ⁶	21,0	11,8
9	upper bainite	-	314	1,137	7,67.10 ⁶	40,4	31,3
10		TiCN+TiN	319	1,442	9,42.10 ⁶	27,1	11,6
11		TiN	317	1,190	7,72.10 ⁶	31,8	31,2
12		cBN	312	1,387	8,03.10 ⁶	30,2	25,3

IV. CONCLUSION

The microstructure, hardness, impact strength and wear resistance of the spheroidal graphite cast irons and austempered ductile irons without and with nanosized additives of titanium carbonitride and titanium nitride (TiCN+TiN), titanium nitride TiN and cubic boron nitride cBN are investigated.

Nanosized additives in the spheroidal graphite cast irons have a modifying effect on the graphite phase. They don't change the graphite shape, but decrease the graphite spheres size and increase the graphite quantity in the irons' structure. Spheroidal graphite cast irons with nanosized additives have a higher abrasion resistance and higher impact strength

compared to the irons without nanoparticles.

Nanosized additives in the austempered ductile irons change the bainitic transformation kinetic and accelerate the austenite transformation to bainite. The austempered ductile irons with nanoadditives have higher impact strength and higher abrasion resistance compared to the samples without nanoadditives. The partially transformation of the metastable retained austenite to strain induced martensite by friction impact in the greatest extent occurs in the irons with nanoadditives of TiCN+TiN, which influence on their wear resistance.

REFERENCES

- [1] Dorasil E. High-strength Bainitic Nodular Cast Iron. Prague, Academia, 1985, 170 p.
- [2] Bhadeshia H.K.D.H. Bainite in Steels, 2nd ed., Inst. of Materials, Cambridge, London, 2001, 460p.
- [3] A.S.M.A. Haseeb, Md.A. Islam, Md.M.A. Bepari, Tribological behavior of quenched and tempered, and austempered ductile iron at the same hardness level, *Wear* 244 (2000) 15–19.
- [4] Y. Sahin, M. Erdogan, V. Kilicli, Wear behavior of austempered ductile irons with dual matrix structures, *Mater. Sci. Eng. A* 444 (2007) 31–38.
- [5] W. Xu, M. Ferry, Y. Wang, Influence of alloying elements on as cast microstructure and strength of gray iron, *Mater. Sci. Eng. A* 390 (2005) 326–333.
- [6] K. Hirasata, K. Hayashi, Y. Inamoto, Friction and wear of several kinds of cast irons under severe sliding conditions, *Wear* 263 (2007) 790–800.
- [7] J. Li, M. Chen, H. Gao, Y. Zhao, Structures and Properties of Cast Irons Reinforced by Trace Addition of Modified SiC Nanopowders. *Chinese Journal of Chemical Physics*, Vol.20, No 6 (2007) 625 – 631.
- [8] Y. Wang, Z. Pan, Z. Wang, X. Sun, L. Wang, Sliding wear behavior of Cr–Mo–Cu alloy cast irons with and without nanoadditives, *Wear* 271 (2011) 2953–2962.
- [9] Kaleicheva J., M. Kandeve, V. Mishev, Z. Karaguiozova. Wear Behavior of Ductile Cast Irons with Nanoparticle Additives. *J. Chem. Chem. Eng.*, Vol. 7, No 11, (2013), p. 1044–1049.
- [10] Kaleicheva J., V. Mishev, G. Avdeev, Z. Karaguiozova, B. Dineva. Influence of Nanoadditives on the Structure and Properties of Austempered Ductile Irons. European Conference on Heat Treatment and 21st IFHTSE Congress, 12-15 May 2014, Munich, Germany, 2014, p. 537-543.
- [11] Gavrilo G., C. Nicolov. Electroless Nickel and Composite Coatings, Tehnika, Sofia, 1985.
- [12] BIRKENSTOCK, J., FISCHER, R.X., MESSNER, T. (2003): BRASS 2003: The Bremen Rietveld Analysis and Structure Suite. *Ber. DMG, Beih. z. Eur. J. Mineral.* 15(1), 21

On Mathematical Modelling of the 2-D Filtration Problem in Porous axial symmetrical cylinder

Imārs Kangro¹, Harijs Kalis², Ērika Teirumnieka¹, Edmunds Teirumnieks¹

1 - Rezekne Academy of Technologies, Faculty of Engineering, Atbrīvošanas aleja 115, LV – 4601, Rēzekne, Latvia, Tel. +371 4625150, Fax +371 4625901;

e-mail: Erika.Teirumnieka@ru.lv, ilmars.kangro@ru.lv, Edmunds.Teirumnieks@ru.lv

2 - Institute of Mathematics, Latvian Academy of Sciences and University of Latvia, Zelļu 8, Rīga LV – 1002, Latvia, Tel. +371 67033721, Fax +371 67820113; e-mail: kalis@lu.lv

Abstract. In this paper we study diffusion and convection filtration problem of one substance through the pores of a porous material which may absorb and immobilize some of the diffusing substances. As an example we consider round cylinder with filtration process in the axial direction. The cylinder is filled with sorbent i.e. absorbent material that passed through dirty water or liquid solutions. We can derive the system of two partial differential equations (PDEs). One equation is expressing the rate of change of concentration of water in the pores of the sorbent and the other - the rate of change of concentration in the sorbent or kinetically equation for absorption. The approximation of corresponding initial boundary value problem of the system of PDEs is based on the conservative averaging method (CAM). This procedure allows reducing the 2-D axis-symmetrical mass transfer problem described by a system of PDEs to initial value problem for a system of ordinary differential equations (ODEs) of the first order.

Keywords: absorption, analytical and numerical solution. diffusion problem, filtration, sorbents, special splines.

I. INTRODUCTION

The task of sufficient accuracy numerical simulation of quickly solution 3-D problems for mathematical physics in multilayered media is important in known areas of the applied sciences – heat transfer in multilayered media, for example, calculation of the concentration of metals in peat layers [16], the heat and moisture transfer processes in the porous multilayered media layer, for example, mathematical modelling of moistening and drying process in the wood-block [1].

For this purpose we consider two methods: special finite difference schemes and conservative averaging method (CAM) by using integral parabolic and exponential splines.

Therefore, the CAM is considered in the present article; too, the finite-difference method is used for solving the 1-D initial value problem for system of ODEs due to obtain the solution of the 3-D initial value problem.

A. Buikis was developed different assumptions for CAM along the vertical coordinate in the Cartesian coordinates using parabolic splines [3], [11]. We are expanding the usage of splines method with integral parabolic and exponential splines [16], [2] in addition, not only in Cartesian coordinates, but also in cylindrical coordinates too [1], [10], if it requires the model under consideration.

The study of hydrodynamic flow and heat transfer through a porous media becomes much more interesting due to its vast applications [8], [2] and [10]. Many mathematical models are developed for the analysis of such processes, for example, mathematical models of moisture movement in wood, when the wood is considered as porous media [1], [10].

II. MATERIALS AND METHODS

1. A mathematical model

Filtration is the separation process of removing solid particles, microorganisms or droplets from a liquid or a gas by depositing them on a filter medium [15]. This paper deals with filtration processes of solid-liquid mixtures (suspensions, slurries, sledges) [12]. For adsorption kinetics we use linear Henry [9] and nonlinear Langmuir [3], [13], [14] sorption isotherms.

In [3] a contaminant transport model with Langmuir sorption under non-equilibrium conditions which is described by two coupled equations – advective-dispersion equation and non-equilibrium sorption equations is considered. In this paper we study the filtration process with diffusion and convection in the domain

$$\Omega = \{(r, z, \phi): 0 \leq r \leq R, 0 \leq z \leq L, 0 \leq \phi \leq 2\pi\}.$$

This domain Ω consists of porous material, where through the pores of filter moves incompressible

ISSN 1691-5402

© Rezekne Academy of Technologies, Rezekne 2017
<http://dx.doi.org/10.17770/etr2017vol3.2566>

liquid - pollutants in z -direction. This problem has practical meaning and also theoretical interest in mathematical physics problems in which several small parameters appear. These parameters are connected with some geometrical dimensions in the problem and also with the relations between the coefficients of the equations. We will consider the nonstationary axis-symmetrical problem of the linear filtration theory.

We can derive two equations; one is the adsorbed phase of concentration $a(r, z, t)$ for the pollutants which are absorbed per unit volume and per unit time. The other equation is the aqueous phase of pollutants concentration $u(r, z, t)$ in sorbent pores. Then convection and diffusion PDEs in the cylindrical coordinates are in the following form [17], [5]:

$$\begin{cases} \left(\frac{1}{r} \frac{\partial}{\partial r} \left(D_r r \frac{\partial u}{\partial r} \right) + D_z \frac{\partial^2 u}{\partial z^2} \right) + V_0 \frac{\partial C u}{\partial z} = m \frac{\partial u}{\partial t} + \frac{\partial a}{\partial t}, \\ \frac{\partial u}{\partial t} = \beta(u - \tilde{u}), r \in [0, R], z \in [0, L], t > 0, \end{cases}$$

where $a = \tilde{u} / \gamma$ is the expression for linear isotherm of Henry, D_r, D_z are the transversal un tangential diffusion coefficients or the dispersion coefficients, $V_0 = const$ is the pore water velocity in z -direction, m is the fraction of the total volume of the material occupied by pores, \tilde{u} is concentration of pollutants, which is in local equilibrium conditions $\partial a / \partial t = 0$ with the amount of liquid sorbet, t is the time, β is the kinetically coefficient or the sorption rate constant, $1/\gamma$ is the Henry coefficient for the sorbent characteristic.

We assume that all coefficients in the PDEs are assumed constant and independent of concentration. For nonlinear sorption we have $a = \tilde{u} / (\lambda(1 + p\tilde{u}))$, which is referred to as Langmuir isotherm, where p is positive parameter (for $p=0$ we have Henry isotherm). For the initial condition for $t=0$ we give $u(r, z, 0) = 0, a(r, z, 0) = 0$. We use following boundary conditions:

$$\begin{cases} \frac{\partial u(0, z, t)}{\partial r} = \frac{\partial u(R, z, t)}{\partial r} = 0, u(R, z, t) = a(R, z, t) = 0, \\ u(r, L, t) = u_0(t) = U_0(1 - \tanh(\alpha t)), \frac{\partial u(r, 0, t)}{\partial z} = 0, \\ \frac{\partial a(r, 0, t)}{\partial z} = 0, \end{cases} \quad (1)$$

where $\alpha = const, U_0 = const$. The concentration u on the inlet is depending on t .

For predetermined parameters $u_1 = u/U_0, a_1 = a\gamma/U_0, \tilde{u}_1 = \tilde{u}/U_0, t_1 = t\gamma\beta$ we have following system (3):

$$\begin{cases} \left(\frac{1}{r} \frac{\partial}{\partial r} \left(D_r r \frac{\partial u_1}{\partial r} \right) + D_z \frac{\partial^2 u_1}{\partial z^2} \right) + V_0 \frac{\partial u_1}{\partial z} = m\gamma\beta \frac{\partial u_1}{\partial t_1} + \beta \frac{\partial a_1}{\partial t_1}, \\ \frac{\partial a_1}{\partial t_1} = u_1 - f(a_1), r \in [0, R], z \in [0, L], t > 0, \end{cases}$$

where $f(a_1) = a_1 / (1 - \tilde{p}a_1), \tilde{p} = pU_0,$

$u_1(r, L, t_1) = u_{0z}(t_1) = 1 - \tanh(\alpha t_1), \alpha_1 = \alpha / \gamma\beta.$

For $\tilde{p} = 0$ we have a linear Henry isotherm.

2. The conservative averaged method in z -direction

We consider conservative averaging method (CAM) of the special integral splines with hyperbolic trigonometrically functions for solving the initial-boundary-value problem in z -direction [6]. This procedure allows reducing the 2-D problem in r, z -directions to a 1D problem in r direction. Using CAM in z -direction with parameter a_z we have

$$\begin{aligned} u_1(r, z, t_1) &= u_v(r, t_1) + m_z(r, t_1) \frac{0.5L \sinh(a_z(z - 0.5L))}{\sinh(0.5a_z L)} + \\ e_z(r, t_1) &\left(\frac{\cosh(a_z(z - 0.5L)) - A_z}{8 \sinh^2(a_z L / 4)} \right), \end{aligned}$$

where, $u_v(r, t_1) = L^{-1} \int_0^L u_1(r, z, t_1) dz,$

$$A_z = \frac{\sinh(a_z L / 2)}{a_z L / 2}.$$

The parameter a_z can be choosing for minimizing the maximal error. If the parameter $a_z > 0$ tends to zero then the limit is the integral parabolic spline (A. Buikis [4]), because of $A_z \rightarrow 1$:

$$u_1(r, z, t_1) = u_v + m_z(z - 0.5L) + e_z \left(\frac{(z - 0.5L)^2}{L^2} - \frac{1}{12} \right)$$

The unknown functions $m_z = m_z(r, t_1), e_z = e_z(r, t_1)$ can be determined from conditions:

1) for $z = 0, m_z d_z - e_z k = 0, m_z = e_z p_1,$

$p_1 = k/d, u_1(r, 0, t_1) = u_v - m_z L/2 + e_z b,$

2) for $z = L, u_{0z} = u_v + m_z L/2 + e_z b,$

$e_z = (u_{0z} - u_v) / g_0,$ where $d = 0.5L a_z \coth(0.5 a_z L),$

$k = 0.25 a_z \coth(0.25 a_z L),$

$b = (\cosh(a_z L / 2) - A_z) / (8 \sinh^2(a_z L / 4)),$

$g_0 = b + 0.5L p_1.$

Now the 1-D initial-value problem (3) is in the following form

$$\left\{ \begin{aligned} m\gamma\beta \frac{\partial u_v}{\partial t_1} + \beta \frac{\partial a_v}{\partial t_1} &= \frac{1}{r} \left(\frac{\partial}{\partial r} \left(D_r r \frac{\partial u_v}{\partial r} \right) \right) + \\ &a0^2(u_{0z} - u_v), \\ \frac{\partial a_v}{\partial t_1} &= u_v - f(a_v), r \in [0, R], L, t > 0, \\ \frac{\partial u_v(0, t_1)}{\partial r} &= 0, \frac{\partial a_v(0, t_1)}{\partial r} = 0, u_v(R, t_1) = \\ a_v(R, t_1) &= 0, u_v(r, 0) = a_v(r, 0) = 0, \end{aligned} \right. \quad (4)$$

Where $a_v(r, t_1) = L^{-1} \int_0^L a_1(r, z, t_1) dz$,

$$a0^2 = \left(2D_z \frac{k}{L} + V_0 p_1 \right) / g_0, f(a_v) = a_v / (1 - \tilde{p} a_v) -$$

here we assume that the averaging of the nonlinear term $f(a_v)$ does not change its form.

3. The conservative averaged method in r-direction

Using averaged method in r-direction with parameters a_r we have

$$u_v(r, t_1) = u_{vv}(t_1) + m_r(t_1) f_m(r) + e_r(t_1) f_e(r),$$

where

$$f_m(r) = \frac{0.25R^2(a_r)^2 \sinh(a_r(r - 0.5R))}{\sinh(0.5a_r R)(d_1 - 1)} - 1,$$

$$f_e(r) = \frac{\cosh(a_r(r - 0.5R)) - A_r}{8 \sinh^2(a_r R/4)},$$

$$\frac{2}{R^2} \int_0^R r f_m(r) dr = -\frac{2}{R^2} \int_0^R r f_e(r) dr = 0,$$

$$A_r = \frac{\sinh(a_r R/2)}{a_r R/2}, d_1 = 0.5R a_r \coth(0.5a_r R).$$

We can use following values of parameters

$$a_r = a0 \sqrt{1/D_r}.$$

If the parameter $a_r > 0$ tends to zero then the limit is the integral parabolic spline:

$$u_v(r, t_1) = u_{vv} + m_r \left(\frac{6}{R} (r - 0.5R) - 1 \right) + e_r \left(\frac{(r - 0.5R)^2}{R^2} - \frac{1}{12} \right).$$

From boundary conditions (4) follows the unknown coefficients-functions:

$$1) \text{ for } r = 0 \quad m_r dr - e_r k_r = 0 \text{ or } m_r = e_r p_r$$

$$2) \text{ for } r = R, \quad 0 = u_{vv} + m_r b_m + e_r b_e \text{ or}$$

$$e_r = -u_{vv} / g_r, \text{ where } d_r = \frac{0.5d_1 R (a_r)^2}{d_1 - 1},$$

$$k_r = 0.25a_r \coth(0.25a_r R), \quad p_r = k_r / d_r,$$

$$b_e = (\cosh(a_r R/2) - A_r) / (8 \sinh^2(a_r R/4)),$$

$$b_m = \frac{0.25R^2(a_r)^2}{d_1 - 1} - 1, \quad g_r = b_e + p_r b_m.$$

Now the 1-D initial-value problem (4) is in the form of following ODEs system:

$$\left\{ \begin{aligned} m\gamma\beta \frac{\partial u_{vv}}{\partial t_1} + \beta \frac{\partial a_{vv}}{\partial t_1} &= -b0^2 u_{vv}(t_1) + \\ &a0^2(u_{0z}(t_1) - u_{vv}(t_1)), \\ \frac{\partial a_{vv}}{\partial t_1} &= u_{vv}(t_1) - f(a_{vv}), t_1 > 0, \\ u_{vv}(0) &= a_{vv}(0) = 0, \end{aligned} \right. \quad (5)$$

where $f(a_{vv}) = a_{vv}(t_1) / (1 - \tilde{p} a_{vv}(t_1))$,

$$a_{vv}(t_1) = \frac{2}{R^2} \int_0^R r a_v(r, t_1) dr, \quad b0^2 = \frac{4D_r k_r}{R g_r}.$$

We rewrite the 1-D initial-value problem for system ODEs (5) in following normal form:

$$\left\{ \begin{aligned} \dot{u}_{vv}(t_1) &= b_{11} u_{vv}(t_1) + b_{12} f(a_{vv}) + f_1 u_{0z}(t_1), \\ \dot{a}_{vv}(t_1) &= b_{21} u_{vv}(t_1) + b_{22} f(a_{vv}), t_1 > 0, \\ u_{vv}(0) &= 0, a_{vv}(0) = 0, \end{aligned} \right. \quad (6)$$

where $b_{11} = -\frac{\beta + b0^2 + a0^2}{m\gamma\beta}, b_{12} = \frac{1}{m\gamma}, b_{21} = 1,$

$$b_{22} = -1, f_1 = -\frac{a0^2}{m\gamma\beta}.$$

If $\tilde{p} = 0$ then we have the following vector form of linear ODEs system:

$$\dot{W}(t_1) = AW(t_1) + F, W(0) = 0, \quad (7)$$

where $W(t_1), F(t_1)$ are the 2-order vector-column with elements $(u_{vv}(t_1), a_{vv}(t_1)), (f_1 u_{0z}(t_1), 0)$.

$$A \text{ is the 2-order matrix } A = \begin{pmatrix} b_{11} & b_{12} \\ b_{21} & b_{22} \end{pmatrix}.$$

The averaged linear and nonlinear ($\tilde{p} \neq 0$) solution we can obtain with Matlab solver "ode15s".

4. Backward orientation for CAM

For estimation the parameters a_z, a_r we use also backward orientation for CAM – first of all, we do CAM in r-direction and then in the in z-direction.

Then in r-direction we have

$$u_1(r, z, t_1) = u_v(z, t_1) + m_r(z, t_1) f_m(r) + e_r(z, t_1) f_e(r).$$

From boundary conditions we have $e_r = -u_v / g_r, m_r = e_r p_r$ and the problem (3) is in following form (8):

$$\begin{cases} m\gamma\beta \frac{\partial u_v}{\partial t_1} + \beta \frac{\partial a_v}{\partial t_1} = D_z \frac{\partial^2 u_v}{\partial z^2} + V_0 \frac{\partial u_v}{\partial z} - b0^2 u_v, \\ \frac{\partial a_v}{\partial t_1} = u_v - f(a_v), z \in [0, L], z \in [0, L], t > 0, \\ \frac{\partial u_v(0, t_1)}{\partial z} = 0, \frac{\partial a_v(0, t_1)}{\partial z} = 0, u_v(L, t_1) = u_{0z} \\ a_v(L, t_1) = 0, u_v(z, 0) = a_v(z, 0) = 0 \end{cases}$$

where

$$a_v(z, t_1) = \frac{2}{R^2} \int_0^R r a_1(r, z, t_1) dr, b0^2 = \frac{4D_r k_r}{R g_r},$$

$$f(a_v) = a_v / (1 - \tilde{p} a_v).$$

Using CAM in z-direction we have

$$a_v(z, t_1) = u_{vv}(t_1) + m_z(t_1) \frac{0.5L \sinh(a_z(z - 0.5L))}{\sinh(0.5a_z L)} +$$

$$e_z(t_1) \left(\frac{\cosh(a_z(z - 0.5L)) - A_z}{8 \sinh^2(a_z L / 4)} \right),$$

where

$$u_{vv}(t_1) = L^{-1} \int_0^L u_v(z, t_1) dz, a_z = b0 \sqrt{1/D_z}.$$

From boundary conditions we have

$e_z = (u_{0z} - u_{vv})/g_0$, $m_z = e_z p_1$ and the problem (8) is in the form of (5), where

$$a_{vv}(t_1) = L^{-1} \int_0^L a_v(z, t_1) dz,$$

$$a0^2 = \left(2D_z \frac{k}{L} + V_0 p_1 \right) / g_0.$$

Therefore we have in every CAM orientation obtained two algebraic equations for determine the spline parameters in following form

$$a_r = f_1(a_r) = a0 \sqrt{1/D_r}$$

$$a_z = f_2(a_z) = b0 \sqrt{1/D_z}.$$

The optimal parameters we can obtained by solution these equations with method of simple iteration. For $V_0 \neq 0$ it is possible usage of exponential type spline for equations (8) in method CAM [7].

5. CAM for model equations

For approbation CAM in r-direction and estimated the parameter a_r we consider model stationary 1-D boundary-value problem in following form:

$$\begin{cases} Dr^{-1}(ru'(r))' - a0^2 u(r) = F_0, r \in [0, R], \\ u'(0) = 0, u(R) = u_0, \end{cases} \quad (9)$$

where $u_0, F_0, a0 > 0, D > 0$ are given constants. The analytical solution is $u(r) = C_1 I_0(a_1 r) - f_1$,

$$C_1 = \frac{u_0 + f_1}{I_0(a_1 R)}, \text{ where } I_0'(0) = I_1(0) = 0, I_0', I_1 \text{ are}$$

the modified Bessel functions, $f_1 = F_0/a0^2$, $a_1 = a0/\sqrt{D}$.

Using averaged method in r-direction with parameter a_r we have $u(r) = u_v + m f_m(r) + e f_e(r)$, where

$$m = \frac{(u_0 - u_v) p_r}{g_r}, e = \frac{u_0 - u_v}{g_r},$$

$$u_v = \frac{4Du_0 k_r - F_0 g_r R}{4Dk_r + a0^2 g_r R}.$$

For

$D_1 = 1, F_0 = -10, a0 = 2, a_r = 2, u_0 = 1, R = 5$ we have following maximal error:

- 1) 1.278 for parabolic spline ($a_r = 10^{-4}$),
- 2) 0.0021 for hyperbolic spline.

III. RESULTS AND DISCUSSION

6. Some numerical results

Experimental data have been obtained studying the filtration process through hemp shives using the adsorption column "Adsorption CE 583" [12] at the Chemistry, biology and biotechnology research centre laboratory of Faculty of Engineering of RTA.

The results of calculations are obtained by MATLAB. We use the discrete grid value

$$t_n = n \frac{t_f}{N_t}, n = \overline{0, N_t}, z_i = i \frac{L}{N_z}, i = \overline{0, N_z},$$

$$r_j = j \frac{R}{N_r},$$

$$j = \overline{0, N_r}, N_z = 10, N_t = 50, N_r = 30, t_f = 5; 50,$$

$$R = 0.15[m], L = 1[m], \text{ and parameters } U_0 = 25 \left[\frac{g}{l} \right],$$

$$\beta = 1; 3, \quad \gamma = 1; 2, \quad m = 0.4, D_r = 10^{-4} \left[\frac{m^2}{\text{min}} \right],$$

$$D_z = 5 \cdot 10^{-4} \left[\frac{m^2}{\text{min}} \right], \quad V_0 = 0.1 \left[\frac{m}{\text{min}} \right], \quad \alpha_1 = 0.2,$$

$\tilde{p} = 0; 0.1; 1; 5; 10, t_1 \in [0, t_f]$. For $\beta = 3, \gamma = 1, a_z = 10.00, t_f = 50, \tilde{p} = 0$ (dimensional final time

is $\frac{t_f}{\beta\gamma} = 50/3[\text{min}]$) we obtain with direct CAM

orientation $a_r = 34.155$ (the results of calculations are represented in Figs.1-4 with backward CAM orientation $a_z = 11.53$, with direct CAM orientation $a_r = 34.0312$, with backward CAM orientation $a_z = 11.5176$ (Figs. 5, 6) and with direct CAM orientation $a_r = 34.0312$ (we have quickly convergent iteration process).

The maximal values of $u(r, z, t_f) = 0.0198$, $u_{vv}(t) = 0.0706$, $a_{vv}(t) = 0.0698$ and $u_{vv}(t_f) = 0.013$ are equal for both CAM orientation.

The maximal calculated dimensional value of liquid concentration in the final time ($0.50 [g/l]$) is good (acceptable for practical problems) comparing with experimentally obtained concentration ($0.54 [g/l]$).

The matrix A has following eigenvalues: $\lambda_1 = -3.61$, $\lambda_2 = -0.042$. It was obtained, that in outlet of the domain $0.5L \leq z \leq L$ the concentration u is small and:

1) The averaging concentration of u_v for $r = 0$ is decrising in the time with maximal value by $t_1 = 5$ (Fig. 1),

2) The concentration u for $t_1 = 50$ is maximal by $r = 0$ and is incrising in z -direction (Fig. 2, Fig. 3),

3) The averaging concentrations of u_{vv} and a_{vv} are equal for both CAM orientation and different depending on the time, $a_{vv} > u_{vv}$ only for $t_1 > 10$,

4) The averaging concentration for CAM in r -direction of $u_v(z, t_f)$ is maximal by $z = 0$ and is decreasing in z -direction (Fig. 6).

The maximal values of $u_v(r, t_f)$, $u_v(0, t)$, $u(r, z, t_f)$, $u_{vv}(t)$, $a_{vv}(t)$ and $u_{vv}(t_f)$ for different \tilde{p} are represented in Table 1.

Table 1: The maximal values of $u_v(r, t_f)$, $u_v(0, t)$, $u(r, z, t_f)$, $u_{vv}(t)$, $a_{vv}(t)$ and $u_{vv}(t_f)$ depending on \tilde{p}

\tilde{p}	$u_v(r, t_f)$	$u_v(0, t)$	$u(r, z, t_f)$	$u_{vv}(t)$	$a_{vv}(t)$	$u_{vv}(t_f)$
0	.0180	.1025	.0200	.0711	.0702	.013
0.1	.0179	.1029	.0199	.0714	.0700	.013
1.0	.0172	.1067	.0191	.0740	.0683	.012
5.0	.0144	.1249	.0160	.0865	.0603	.010
10	.0118	.1474	.0131	.1022	.0505	.008
1.0*	.0214	.0863	.0237	.0598	.0561	.015
1.0*	.0012	.2400	.0013	.1604	.1405	.0008

We can see, that with increasing \tilde{p} the filtration process is faster (see $u_v(r, t_f)$, $u_{vv}(t)$, $a_{vv}(t)$, $u_{vv}(t_f)$), but the maximum of concentration is increasing (see $u_v(0, t)$, $u_{vv}(t)$). In the present table by $\tilde{p} = 1.0^*$ there are maximal values for $\beta = 3, \gamma = 2$ ($\lambda_1 = -2.29$, $\lambda_2 = -0.033$).

We can see that the filtration process is slow.

For $\tilde{p} = 1.0^*$ and $\beta = 1, \gamma = 1$ ($\lambda_1 = -3.84$, $\lambda_2 = -0.119$) the filtration process is faster.

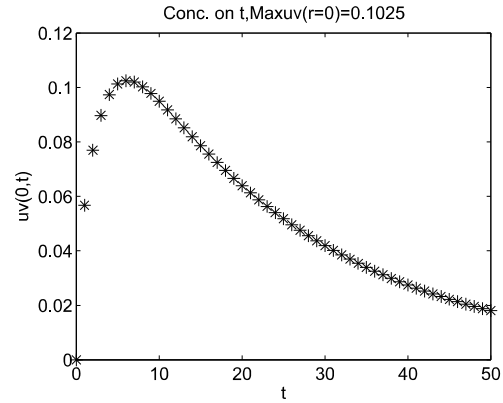


Fig. 1. Averaging concentration u_v depending on t_1 for $r = 0$

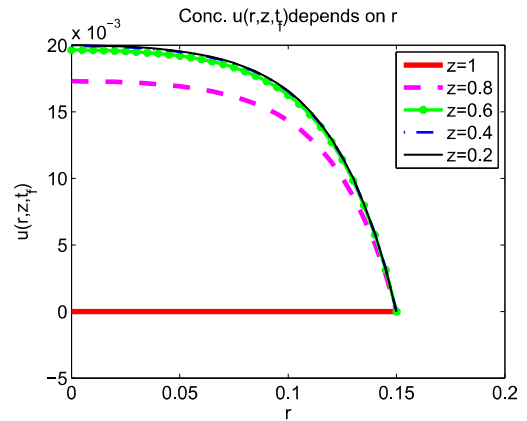


Fig. 2. Concentration $u(r, z, t_f)$ profile depending on z for $t_f = 50$

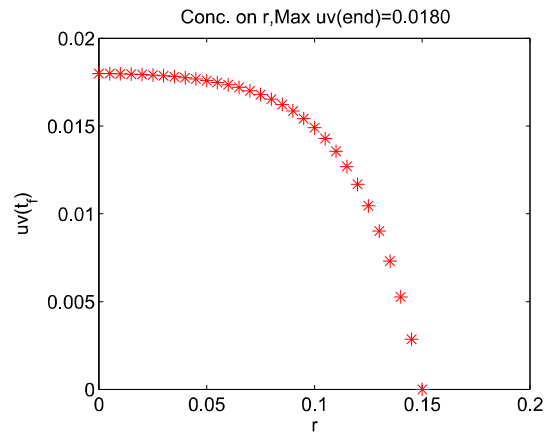


Fig. 3. Averaging concentration $u_v(r, t_f)$ depending on r for $t_f = 50$

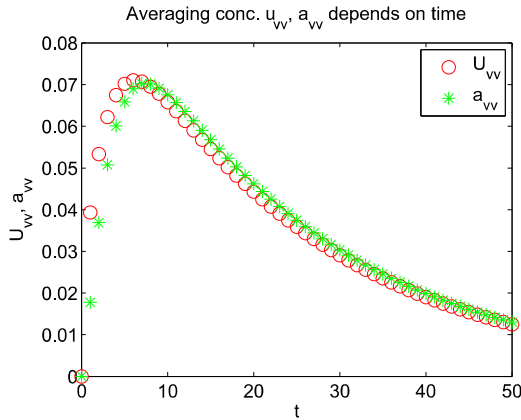


Fig. 4. Averaging concentration $u_{vv}(t_1)$ and $a_{vv}(t_1)$ depending on t_1

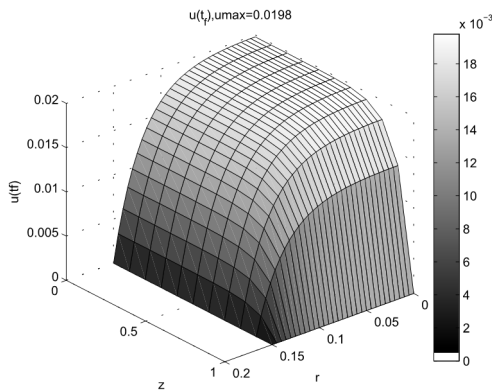


Fig. 5. Concentration $u(r, z, t_f)$ for $t_f = 50$

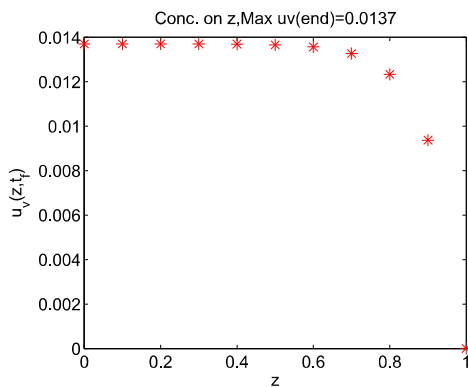


Fig. 6. Averaging concentration $u_v(z, t_f)$ depending on z for $t_f = 50$

IV. CONCLUSIONS

The approximation of corresponding initial boundary value problem of the system of PDEs is based on the conservative averaging method (CAM), where the new hyperbolic type splines are used.

For these splines the best parameter for minimal error is calculated using the direct and backward orientation for CAM. Numerical experiments

confirmed the correctness of the best parameter calculation using a convergent iteration process.

The problem of the system of 3D PDEs with constant coefficients is approximated on the initial value problem of a system of ODEs of the first order. The 1-D differential and discrete problems are solved analytically.

The maximal calculated dimensional value of liquid concentration in the final time was compared with experimentally obtained concentration. It was observed in the results of good agreement that is acceptable practice.

Such a mathematical model allows us to obtain analytical solution with a simple engineering algorithm for mass transfer equations for modelling the filtration process.

The mathematical model can be used under consideration filtration process modelling - to determine the impurity concentration in the solution of filtration depending on the time.

More generally, it allows you to calculate the saturation of the filtering material, depending on the time.

REFERENCES

- [1] Aivars Āboltiņš, Harijs Kalis and Ilmārs Kangro, *On Mathematical Modelling of Heat and Moisture Distribution in the Porous Multilayer Media: 15-th International Scientific Conference "ENGINEERING FOR RURAL DEVELOPMENT"*, Jelgava, May 25-27, 2016.
- [2] A. Aboltins, *Theoretical study of thin layer material, concentration depending drying coefficient: 13 Int. conf. "Engineering for rural developmen"*, Jelgava May 29-30, 2013, Jelgava. Latvia University of Agriculture: Proc. of 13 Int. Conf., pp.1-7., 2013.
- [3] A.R. Appadu, *Comparative Study of Three Numerical Schemes for Contaminant Transport with Kinetic Langmuir Sorption. International Conference of Numerical Analysis and Applied Mathematics 2015 (ICNAAM 2015)*, AIP Conf. Proc., doi: 10.1063/1.4951777, AIP Publishing.
- [4] M. Buikis and A. Buikis. "Modelling 3-D transport processes in anisotropic layered stratum by conservative averaging method," *WSEAS Transactions on Heat and Mass Transfer*, vol.1, No. 4, pp. 430-437, 2006.
- [5] A. Buikis, E.J. Titushkina. "Applied Makkormak's method for calculation the filtration of liquid solutions in soil," *Mathematical Modelling, applied problems in mathematical physics*, No.2, Riga, University of Latvia, pp.71-80, 1991.
- [6] A. Buikis, H. Kalis and I. Kangro, *Special Hyperbolic type spline for mass transfer problems in multi-layer 3-D domains: 3-rd Int. Conf. on Applied, Numerical and Computational Mathematics (ICANCM'15)*, Sliema, Malta, August 17-19, 2015, Sliema, Proc. of 3-rd Int. Conf., pp. 25-34., 2015.
- [7] A. Buikis, H. Kalis and I. Kangro. "Special splines of exponential type for the solutions of mass transfer problems in multilayer domains," *Mathematical Modelling and Analysis*, vol. 21, No. 4, pp. 450-465, 2016.
- [8] J. Crank. *The mathematics of diffusion*. Oxford: Clarendon Press, 1956.
- [9] William Henry. "Experiments on the quantity of gases absorbed by water," *Philosophical Trans. of the Royal Soc.*, 93, pp. 29-274, 1803.
- [10] Harijs Kalis, Andris Buikis, Ilmārs Kangro and Aivars Aboltins. "Special splines of hyperbolic type for the solutions of heat and mass transfer 3-D problems in porous multi-layered axial symmetry domain", journal: *Mathematical Modelling and Analysis*, Taylor & Francis, "submitted for publication"

- (manuscript ID: TMMA-2016_0394.R2, manuscript type: review).
- [11] H. Kalis, I. Kangro. "Calculation of heat and moisture distribution in the porous media layer," *Mathematical Modelling and Analysis*, vol. 12, No. 1, pp. 91-100, 2007.
- [12] M. Kellow. *Energy and Environment, Experiment instructions*, CE 583, Adsorption, 2011.
- [13] Irvin Langmuir. "The adsorption of gases on plane surfaces of glass, mica and platinum," *J. Am. Chem. Soc.*, 40, pp.1361-1403, 1918.
- [14] G. Limousin, J.P. Gaudet, L. Charlet, S. Szenknect, V. Barthes, M. Krinissa. "Sorptions isotherms: a review on physical bases, modeling and measurement," *Applied Geochemistry*, 22, pp. 249-275, 2007.
- [15] S. Ripperger, W. Gosele, C. Alt. *Ullman's Encyclopedia of industrial chemistry, Filtration, 1. Fundaments*, vol.14. Germany, 2012.
- [16] Teirumnieka, Ē., Kangro, I., Teirumnieks, E. and Kalis, H., *The analytical solution of the 3D model with Robin's boundary conditions for 2 peat layers: 10-th Int. Scientific and Practical Conference "Environment. Technology. Resources"*, Rezekne June 18-20, 2015, Rezekne. Rezekne Higher Education institution: Proc. of 10-th Int. Conf., Volume III, pp.186-192, 2015.
- [17] A.N. Tihonov, A.A. Samarsky, *Equations of Mathematical Physics*. Moskow, Press: Nauka, 1966, pp.163-173 (in Russian).

Investigations of Electric Power Quality in Autonomous Low Power Plant

Andrei Khitrov, Alexander Khitrov, Evgeny Veselkov, Vyacheslav Tikhonov
Pskov State University, Computer Science and Electric Power Engineering Faculty. Address: Russian Federation, Pskov, Lenin square, 2.

Abstract. Autonomous low power electric power plants working with variable speed energy sources or electric subsystems of cogeneration plants of some type need to increase the low speed or the low voltage of the system. In this paper the investigations and the results of the experiments conducted using different structures are given.

Keywords: autonomous power supply system, permanent magnet synchronous machine, DC/DC converter, starter-generator set.

I. INTRODUCTION

The problem of increasing autonomous energy sector efficiency is settled in such legislative acts of the Russian Federation as Energy Strategy of Russia till both 2020 and 2030, government programs, etc. [1, 2, 3, 4]. Agency for Strategic Initiatives (Skolkovo) published a list of new professions in 2015. The following titles were introduced among them: «microgeneration systems developer», «recuperation systems projector», «local energy systems specialist», «energy storage developer».

Autonomous low power plants and generating sets will be high-demand in energy supply systems in remote areas, in emergency situations in case of power supply loss. It can be used as a system of backup for mobile power plants, for agriculture and housing and utilities infrastructure.

At the present time the most common and universal decentralized autonomous power supply systems (APSS) are diesel power stations (DPS) and gas-fired generation plants (GFGP). It usually has the power more than 50 kW and has a number of disadvantages which include the output power control problems. The promising alternative is APSS (cogeneration plants in particular) based on the external combustion engine (EC engine). The specific construction of the EC engine and the processes of thermal-to-mechanical energy conversion impose a number of issues for development of such power plant [5].

The aspects of structure designing the starter-generator set for autonomous cogeneration power plant based on the EC engine having rotary-vane construction (as well as the features and advantages of this type of engines) were considered in [6, 7].

Figure 1 shows the designed structure of the starter-generator set which has become the result of

the first phase research. The simulation results using MATLAB program were considered in [6].

The second phase of research was devoted to the development of the experimental stand for live experiments. The issues of creating the experimental model as well as the investigations of starting mode of the rotary-vane EC engine (RVE) were considered in [8].

This article focuses on the continuation of the mentioned researches including the results of experiments conducted on the test stand.

II. THE STRUCTURE

Autonomous low power plant based on RVE requires increasing the output shaft speed (mechanical output of RVE) or increasing the output generator voltage. With fluctuations of speed it makes such system similar to so-called variable-speed systems.

The proposed structure, shown in fig. 1, is based on using the 3-phase permanent magnet synchronous motor (PMSM); this decision is a prospective for such systems [9].

Besides PMSM the diagram comprises three electric power converters: bidirectional active front end converter 1 (AFE/IN₁), DC link 2 including DC/DC converter (power factor corrector) and inverter 3 (IN₂), and also corresponding control systems (CS AFE, CS DC/DC and CS IN) 4, 5, 6 for them.

DC link control is made in accordance with both fluctuations of the PMSM driving engine and fluctuations in the electric load by monitoring DC link voltage or current levels or the voltages or currents of the electric load at the output.

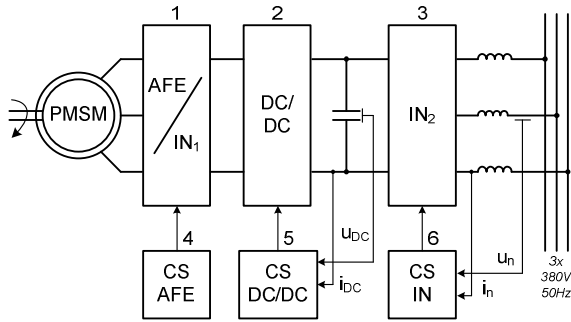


Fig. 1. The diagram of the autonomous generator plant with PMSM

To confirm the efficiency of the system proposed the experiments of monitoring the quality of autonomous plant generated power were conducted. The system had to meet (or partly meet) the quality indicators of current regulations. Monitoring the quality was conducted using power quality meter «Resource-UF2» and its proprietary software.

It is worth noting that there are no quality standards for the autonomous power plants in the Russian Federation. So monitoring the quality was performed with feeding the data standards from the general purpose power supply networks regulations of the Russian Federation (all-Union State Standard 32144-2013 [10]).

Fig. 2 shows the basic circuit diagrams of a series of experiments monitoring the quality of electric energy:

a – preliminary experiment monitoring the quality of energy feeding the test stand, just the industrial network and the electric load;

b – the industrial network works into the load via the rectifier and the inverter;

c – the experiment with RVE work imitation and using PMSM and the transformer (T), the output generator voltage is boosted with the transformer;

d – the experiment with RVE work imitation and using PMSM, the DC/DC converter and the structure proposed, the output generator voltage is boosted with the DC/DC.

Active and active-inductive load (including asynchronous motor) were connected and switched on and off during the experiment (load-on/load-off). The output inverter in circuit diagrams b, c, d (Fig. 2) was the same.

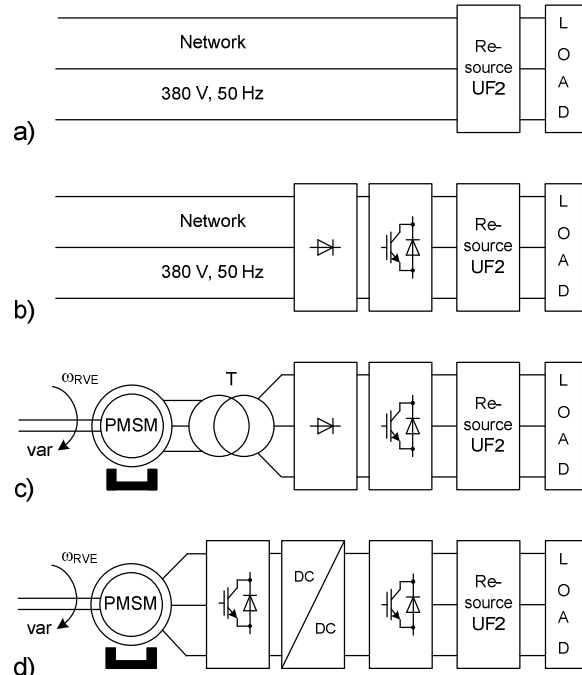


Fig. 2. Experiment circuit diagrams

III. RESULTS AND DISCUSSION

The measurements of power quality were produced for three-phase four-wire circuit. The following quality indicators were registered:

- Steady state voltage deviation.
- Voltage unbalance factor for negative phase sequence and zero phase sequence.
- Voltage nonsinusoidality ratio.
- Single harmonic distortion.
- Frequency deviation.
- Voltage dip duration.
- Voltage surge duration.
- Voltage dip depth.
- Temporary voltage surge ratio.
- Peak-to-peak voltage fluctuations.
- Power-line flicker.

The usual parameters such as voltages, currents, phase angles, active and reactive power, active and reactive energy were also registered.

The frequency deviation from the rated value of 50 Hz for all of the above-mentioned circuits (Fig. 2) didn't exceed the value of 0.2 Hz. Beyond that the frequency value can be adjusted accurately with inverter in case of parameter drift. Positive and negative rapid voltage changes didn't exceed the indicator of 5% from the rated value during the experiments (in the case of autonomous power plant the indicator values are values from the standard for low-voltage network). Fig. 3 shows the example of time diagrams of the output 3-phase voltage of the system for the structure Fig. 2, d. The y-axis is voltage value (V), the x-axis is current experiment time (hh:mm format, hereinafter the same designation for the x-axis). Voltage dip in Fig. 3 is caused by load

switching on and is not above the voltage deviation limit.

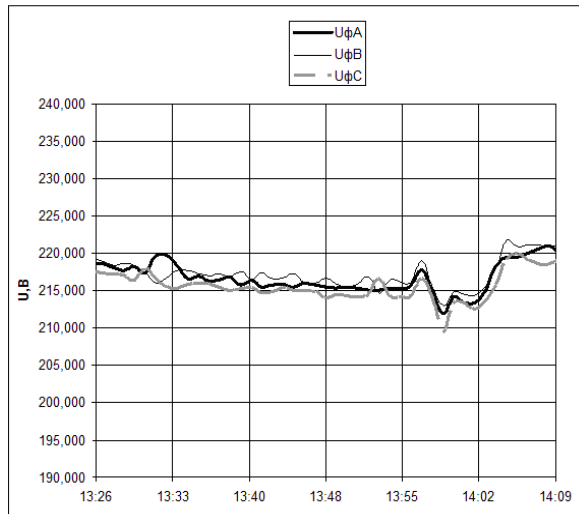


Fig. 3. Voltage time diagram

The values of voltage unbalance factor for negative phase sequence and zero phase sequence didn't exceed indicator value of 2% during the experiments.

Fig. 4 shows the time diagrams of the voltage nonsinusoidality ratio during the experiments conducted corresponding to different circuits (Fig. 2).

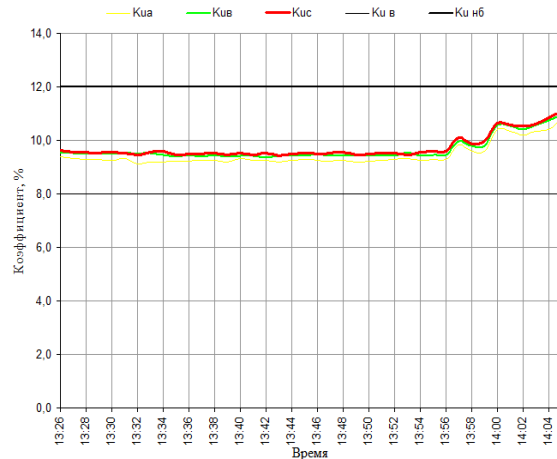
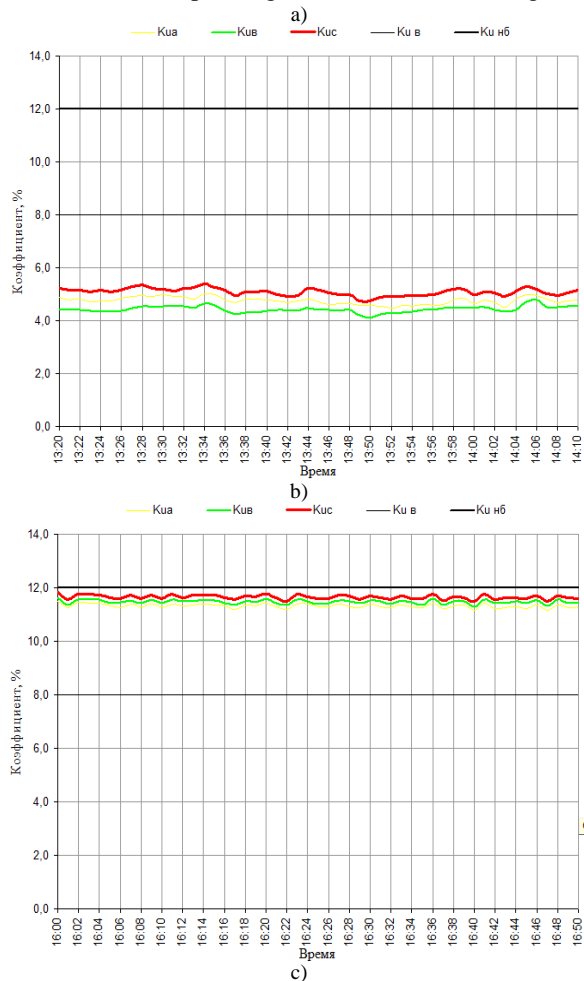


Fig. 4. Voltage nonsinusoidality ratio time diagrams corresponding to the experiments diagrams: a) Fig. 2, a, b) Fig. 2, b, c) Fig. 2, d

The value of voltage nonsinusoidality ratio has exceeded the permissible by the standard indicator value during the experiments corresponding to the structures containing the inverter at the output: the structures b, c, d in Fig. 2. The permissible indicator value for this ratio is 8% during 95% of time. At the same time the second indicator value (12% during 100% of time) wasn't exceeded.

The value of voltage nonsinusoidality ratio during the experiment corresponding to the diagram Fig. 2, d (DC/DC + inverter) was lower (Fig. 4, c) than during the experiment corresponding to the diagram Fig. 2, b (network + inverter, Fig. 4, b corresponds to the circuit Fig. 2, b). In this two experiments the work of low-speed motor with variable speed was simulated. Fig. 4, a shows the value of voltage nonsinusoidality ratio of the industrial network (4-6%) and corresponds to the diagram Fig. 2, a.

Hence, it can be concluded that the use of DC/DC converter in autonomous power supply system in order increase the voltage doesn't increase such quality indicator as voltage nonsinusoidality ratio (moreover, some decrease was registered).

Notations for the Fig.4: K_{UA} , K_{UB} , K_{UC} – voltage nonsinusoidality ratio values in phases A, B, C, respectively, K_{UB} – upper limit, the value should not be exceeded during 95% of time, K_{UHB} – maximum limit, the value should not be exceeded during 100% of time.

When powered from the industrial network (Fig. 2, a) the value of any single harmonic component didn't exceed the permissible indicator values. The value of the 3-rd harmonic component was about 4%, 5-th – 3.5%, 7-th and 9-th – about 1%, and the rest components were less than 0.5%.

When powered from the structure containing inverter (Fig. 2, b) the values of any even harmonic component, except 2-nd and 4-th, exceeded the permissible single harmonic values. Also the appearance of higher harmonics should be stated: 1-2% from the 8-th and up to 40-th.

When powered from the structure containing DC/DC converter (Fig. 2, d) the output voltage has the same distortions as that in experiment corresponding to the diagram Fig. 2, b. Also all the even harmonic components appeared (at the same time the appearance of even harmonics doesn't cause a general increase in the voltage nonsinusoidality ratio). Even harmonic components also appear during the experiment corresponding to the structure Fig. 2, c (containing transformer). The appearance of even harmonics during the experiment corresponding to the structures containing PMSM can be explained by the peculiarities of DVU2M series synchronous motor application as a generator.

Voltage surges and voltage dips caused by switching various loads on and off didn't exceed the permissible indicator value of 1 minute.

IV. CONCLUSION

Output voltage distortions observed when the load is powered from the structure containing DC/DC and inverter are similar to the distortions observed when there is no intermediate multiplier DC-link. It allows to conclude about the necessity of completing such autonomous low-power plant with the inverter having high quality output voltage and the capability to be connected to DC-link (the output of the DC/DC converter).

The experiments conducted on the test stand have confirmed the efficiency of the low-power plant (electric part of cogeneration plant) based on RVE. The quality of electric power generated by the electric part of the plant meets all the indicator parameters of all-Union State Standard 32144-2013 except the voltage nonsinusoidality ratio.

V. ACKNOWLEDGMENTS

This study is supported by Foundation for Assistance to Small Businesses in Science and Technology (the program «UMNIK» in Pskov Region in particular) [11]. The contract number is 11003GU2/2016.

REFERENCES

- [1] Об энергосбережении и о повышении энергетической эффективности и о внесении изменений в отдельные законодательные акты Российской Федерации / Федеральный закон № 261 от 23.11.2009.
- [2] Энергетическая стратегия России до 2030 г. / утверждена Распоряжением Правительства России от 13 ноября 2009 года № 1715-р.
- [3] Об Энергетической стратегии России на период до 2020 года / Распоряжение Правительства РФ от 28.08.2003 N 1234-р (ред. от 15.06.2009).
- [4] Энергоэффективность и развитие энергетики / Государственная программа РФ, утверждена постановлением правительства РФ от 15 апреля 2014 г. № 321.
- [5] Плохов И.В., Донченко М.А., Лукьянов Ю.Н. Энергоэффективная автономная энергоустановка нового поколения. Доклад на международной конференции «Инновационные технологии 2009». М.:Интотехэкспо, 2009.
- [6] Khitrov A.I., Khitrov A.A. Electrical subsystem of the low power cogeneration plant with low-speed vehicle. *Environment. Technology. Resources. Proceeding of the 9th International Scientific and Practical Conference*, 2013. Volume II. Rezekne. pp.119-123.
- [7] Перминов А. Л., Хитров А. А., Хитров А. И. Мехатронная система «магнитоэлектрический синхронный двигатель - активный выпрямитель» для автономной системы электроснабжения на базе роторно-лопастной машины с внешним подводом тепла. Труды VII Международной (VIII Всероссийской) конференции по автоматизированному электроприводу АЭП-2012: ФГБОУВПО "Ивановский государственный энергетический университет им. Ленина". - Иваново, 2012. с. 330-335
- [8] Khitrov A.A. Khitrov A.I. Investigation of permanent magnet synchronous machine with recuperation block». *Proceedings of the 10-th International Scientific and Practical Conference «Environment. Technology. Resources. Volume I. Rezekne, Latvia*, 2015. pp. 53-56.
- [9] Харитонов С. А. Электромагнитные процессы в системах генерирования электрической энергии для автономных объектов. – Новосибирск: Изд-во НГТУ, 2011. – 536 р.
- [10] ГОСТ 32144-2013. Нормы качества электрической энергии в системах электроснабжения общего назначения. – Москва, Стандартфинорм, 2014. – 16 р.
- [11] Foundation for Assistance to Small Businesses in Science and Technology: <http://umnik.fasie.ru/o-fonde/>

Non-linear Transformation of Signals in Software Design of Digital Control Systems Complex

Vladimir Konevtsov, Lilia Motaylenko

Pskov State University

Faculty of Computer Science and Electrical Power Engineering.

Address: Leo Tolstoi Street 4, Pskov, Russia

Abstract. Dependencies between signals and dependence of signals on time are strictly non-linear. Non-linear elements, commonly used in the synthesis of automatic control systems, include: a two-point link, a two-point link with hysteresis, a three-point link, a three-point link with hysteresis, a module, saturation with insensitivity.

Keywords: three-position controller, three-position controller with hysteresis, two-position controller, two-position controller with hysteresis.

I. INTRODUCTION

Currently, link-off, three-position with or without hysteresis, saturation types of nonlinear links are widely used in the automatic control systems of technological processes [1-3].

International standard IEC 61131-3 does not contain a single integrated means for developing complex systems of automatic control of technological processes with nonlinear links in the control device. Such a tool was created by SIEMENS. However, it is intended exclusively for its specialists working with the equipment of this firm [4].

The software-hardware SDSDC complex provides the possibility of software implementation of nonlinearities in the tasks of developing, modeling and creating complex systems for automatic control of technological processes with nonlinear links [5].

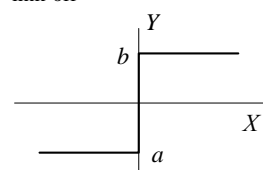
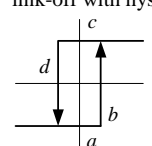
II. POSITION CONTROLLER

Let us consider the mathematical description and software implementation of typical nonlinearities.

Dependencies between signals and the dependence of signals on time are strictly non-linear. In general, a distinction is made between single-valued and multi-valued non-linear dependences, as well as between non-linear dependences with memory and without memory, analytically described and piecewise linearly approximated.

To non-linear links, commonly used in the synthesis of automatic control systems (ACS) refer nonlinearities [1-3] shown in a summary form in Table. 1.

Table I
 Non-Linear Links

Graphic symbol	Dependence
link-off 	$Y = \begin{cases} b & \text{by } X \geq 0 \\ -a & \text{by } X < 0 \end{cases}$
link-off with hysteresis 	$Y = \begin{cases} \left. \begin{matrix} c & \text{at } X \geq b \\ -a & \text{at } X < b \end{matrix} \right\} & \text{at } X(k) - X(k-1) \geq 0 \\ \left. \begin{matrix} c & \text{at } X \geq -d \\ -a & \text{at } X < -d \end{matrix} \right\} & \text{at } X(k) - X(k-1) < 0 \end{cases}$

Graphic symbol	Dependence
	$Y = \begin{cases} c & \text{at } X \geq b \\ 0 & \text{at } (X < b) \& (X \geq -d) \\ -a & \text{at } X < -d \end{cases}$
	$Y = \begin{cases} -a & \text{at } X \leq e \\ 0 & \text{at } e < X < c \\ d & \text{at } X \geq c \end{cases} \text{ at } X(k) - X(k-1) \geq 0$ $Y = \begin{cases} d & \text{at } X \geq b \\ 0 & \text{at } f < X < b \\ -a & \text{at } X \leq -f \end{cases} \text{ at } X(k) - X(k-1) < 0$
	$Y = \begin{cases} -a & \text{at } X < -d \\ c & \text{at } X > b \\ kX & \text{at } (X \geq -d) \& (X \leq b) \end{cases}$ $k = \text{tg}(\alpha)$
	$Y = \begin{cases} 0 & \text{at } (X \geq -b) \& (X \leq a) \\ kX & \text{at } (X > a) \vee (X < -b) \end{cases}$ $k = \text{tg}(\alpha)$
	$Y = \begin{cases} kX & \text{at } X \geq 0 \\ -kX & \text{at } X < 0 \end{cases}$ $k = \text{tg}(\alpha)$
	$Y = \begin{cases} -a & \text{at } X < -f \\ -kX & \text{at } (X \geq -f) \& (X < -e) \\ 0 & \text{at } (X \geq -e) \& (X < b) \\ kX & \text{at } (X \geq b) \& (X \leq c) \\ d & \text{at } X > c \end{cases}$ $k = \text{tg}(\alpha)$

A. A two-position controller

A variety of a two-position controller is a relationship [6-9]

$$u(k) = \begin{cases} U1 & \text{at } (w(k) - \Delta w) > y(k) \\ U2 & \text{at } (w(k) + \Delta w) < y(k) \\ u(k-1) & \text{at } (w(k) - \Delta w) \leq y(k) \leq (w(k) + \Delta w), \end{cases} \quad (1)$$

where $u(k)$ – the value of the manipulated variable;

$w(k)$ – the value of the reference variable;

$y(k)$ – the value of the controlled variable;

Δw – dead zone;

$U1, U2$ – the value of the manipulated variable outside the dead zone;

$u(k-1)$ – the value of the manipulated variable in the preceding control cycle.

If we assume $\Delta w = 0$ then the manipulated variable can be displayed through a two-position actuator. In this case, $U1$ and $U2$ are the inverse values of the logic signal. A two-position unit of general form is used as a two-position controller (Table 1), at $a \cong \langle 0 \rangle$, $b \cong \langle 1 \rangle$; here \cong symbol indicates

correspondence of parameters a and b to the inverse values of the logic signal:

$$u = \begin{cases} 1 & \text{at } e \geq 0 \\ 0 & \text{at } e < 0 \end{cases}, \quad (2)$$

$$e = w - y$$

where u – the value of the manipulated variable;

w – the value of the reference variable;

y – the value of the controlled variable;

e – control error.

The block diagram and the program of a two-position controller are shown in Fig. 1 and 2.

The block diagram of a two-position controller

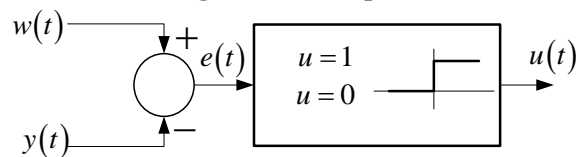


Fig.1

The program of a two-position controller

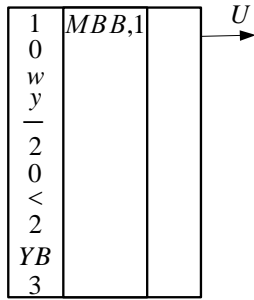


Fig.2

B. A two-position controller with hysteresis

A two-point link with hysteresis of general form is used as a two-position controller with hysteresis (Table 1), [9-14]: at $a \cong \ll 0$, $c \cong \ll 1$, $d + b = H$

$$u = \begin{cases} \left. \begin{matrix} 1 & \text{at } e(k) \geq H/2 \\ 0 & \text{at } e(k) < H/2 \end{matrix} \right\} & \text{at } e(k) - e(k-1) \geq 0 \\ \left. \begin{matrix} 1 & \text{at } e(k) \geq -H/2 \\ 0 & \text{at } e(k) < -H/2 \end{matrix} \right\} & \text{at } e(k) - e(k-1) < 0 \end{cases} \quad (3)$$

$e(k) = w(k) - y(k)$,

where u – the value of the manipulated variable;
 w – the value of the reference variable;
 y – the value of the controlled variable;
 e – control error;
 H – the value of hysteresis.

The block diagram and the program of a two-position controller with hysteresis are shown in Fig. 3 and 4.

The block diagram of a two-position controller with hysteresis

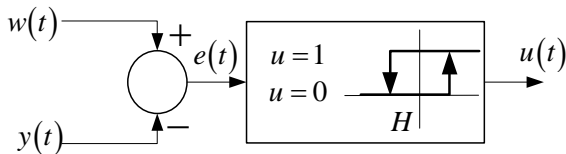


Fig.3

The program of a two-position controller with hysteresis

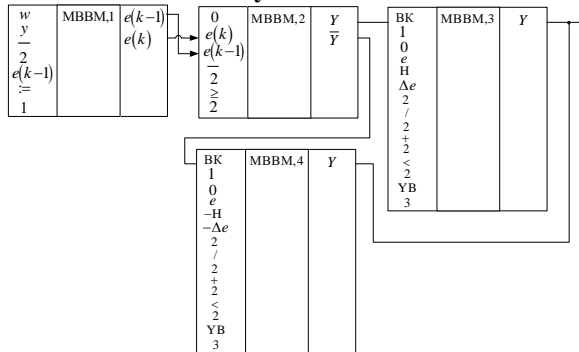


Fig.4

C. A three-position controller

A three-point link of general form is used as a three-position controller (Table 1) [5, 15-21],

$a \cong u_2, c \cong u_1, |d + b| = \Delta e$:

$$u_1 = \begin{cases} 1 & \text{at } e(k) \geq \Delta e/2 \\ 0 & \text{at } e(k) < \Delta e/2 \end{cases}$$

$$u_2 = \begin{cases} 1 & \text{at } e(k) \geq -\Delta e/2 \\ 0 & \text{at } e(k) < -\Delta e/2 \end{cases} \quad (4)$$

$e = w - y$,

where u_1, u_2 – the value of the manipulated variable;

w – the value of the reference variable;
 y – the value of the controlled variable;
 e – control error;
 Δe – dead zone.

The block diagram and the program of a three-position controller are shown in Fig. 5 and 6.

The block diagram of a three-position controller

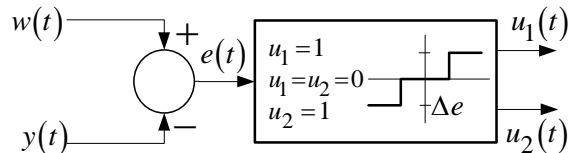


Fig.5

The program of a three-position controller

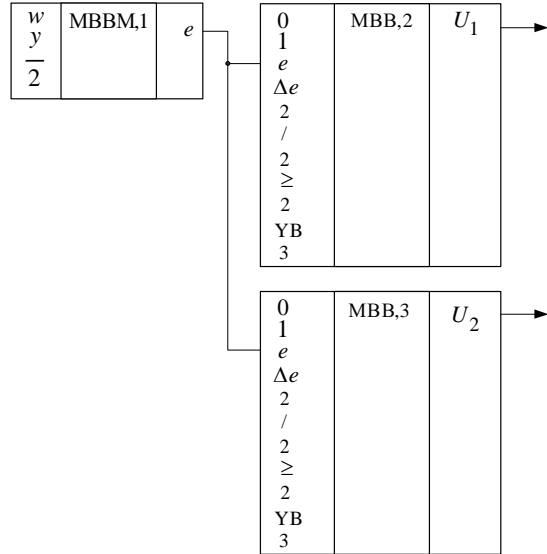


Fig.6

D. A three-position controller with hysteresis

A three-point link with hysteresis of general form is used as a three-position controller with hysteresis (Table. 1),

$a \cong u_2, c \cong u_1, |f + e| = |c - b| = H, |e| + |b| = \Delta e$:

$$u_1 = \begin{cases} 1 & \text{at } e(k) \geq \Delta e/2 \\ 0 & \text{at } e(k) < H + \Delta e/2 \end{cases} \text{at } e(k) - e(k-1) \geq 0$$

$$u_2 = \begin{cases} 0 & \text{at } e(k) \geq -H - \Delta e/2 \\ 1 & \text{at } e(k) < -\Delta e/2 \end{cases} \text{at } e(k) - e(k-1) < 0$$

$e(k) = w(k) - y(k)$,

(5)

where u – the value of the manipulated variable;
 w – the value of the reference variable;
 y – the value of the controlled variable;
 e – control error;
 H – the value of hysteresis;
 Δe – dead zone.

The block diagram and the program of a three-position controller with hysteresis are shown in Fig. 7 and 8.

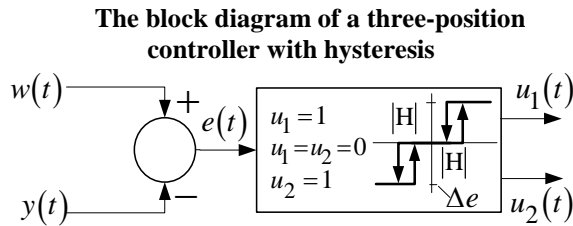


Fig.7

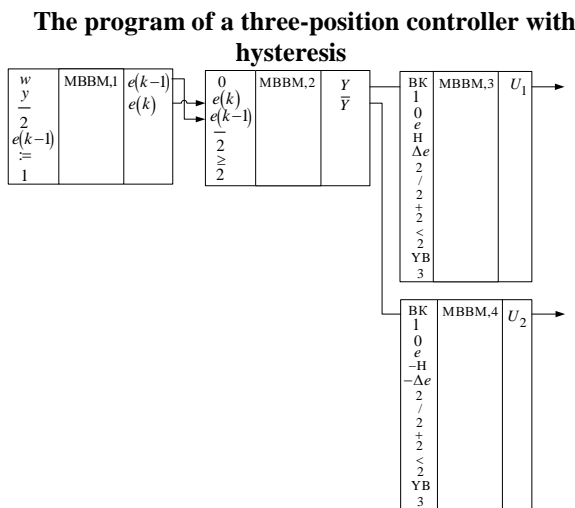


Fig.8

Thus, the software and hardware SDSDC complex provides the possibility of a unified approach for the synthesis of automatic control systems for technological processes with linear and nonlinear links in the control device based on their software implementation.

III. CONCLUSION

A comparative evaluation of the standardized properties of the nonlinearities of the SDSDC complex (a two-position link with and without hysteresis, a three-position link with and without hysteresis) makes it possible to expand the composition of the nonlinearities of the SDSDC complex without any significant expenditure. This is especially easy to implement due to the application of the abovementioned expression evaluation modules.

IV. ACKNOWLEDGEMENTS

The authors wish to express their sincere thanks to Tatyana Klets, Deputy Dean of Engineering and

Construction Technologies Faculty of Pskov State University, for her invaluable foreign language assistance and supportive comments.

REFERENCES

- [1] Попов Е.П. Теория нелинейных систем автоматического регулирования и управления. – М.: Наука 1979, 256 с.
- [2] Юревич Е.И. Теория автоматического управления.- СП БХВ Петербург, 2007. с.456.
- [3] Goldner K., Kubik S. Nichtlineare Systeme der Regelungstechnik.- VEB Verlag Technik Berlin, 1978, 232.
- [4] Wellenreuter G., Zastrow D. Automatisierung mit SPS. Theorie und Praxis.- Vieweg + Teubner, 5. Auflage, 2011, s.870.
- [5] Конецов В.А. САПР цифровых САУ. Концепция: Монография. Псков: Издательство ППИ, 2011. – 256 с.
- [6] Куприянов, Михаил Степанович. Цифровая обработка сигналов : Процессоры. Алгоритмы. Средства проектирования .— 2-е изд., перераб. и доп. — Санкт-Петербург : Политехника, 2002 .— 592 с. : ил. — ISBN 5-7325-0546-6.
- [7] Сергиенко, Александр Борисович. Цифровая обработка сигналов : учебное пособие для вузов / А. Б. Сергиенко .— 2-е изд. — Санкт-Петербург : Питер, 2006 .— 750 с. : ил. — (Учебник для вузов) .— ISBN 5-469-00816-9.
- [8] Дорф, Ричард. Современные системы управления / Р. Дорф, Р. Бишоп ; пер. с англ. Б. И. Копылова .— Москва : Лаб. Базовых Знаний, 2002 .— 831 с. : ил. — ISBN 0-201-30864-9 .— ISBN 5-93208-119-8.
- [9] Бесекерский Виктор Антонович. Теория систем автоматического управления : учеб. для вузов .— 4-е изд., перераб. и доп. — Санкт-Петербург : Профессия, 2003 .— 747 с. : ил. — ISBN 5-93913-035-6.
- [10] Абрамов, Валерий Михайлович. Электронные элементы устройств автоматического управления : Схемы. Расчет. Справочные данные / В. М. Абрамов .— Москва : ИКЦ "Академкнига", 2006 .— 680 с. : ил. — ISBN 5-94628-222-0.
- [11] Ерофеев Анатолий Александрович. Теория автоматического управления : учеб. для вузов .— 2-е изд., перераб. и доп. — Санкт-Петербург : Политехника, 2005 .— 302 с. : ил. — ISBN 5-7325-0529-6.
- [12] Александров, Альберт Георгиевич. Методы построения систем автоматического управления / А. Г. Александров ; Ин-т проблем упр. РАН .— Москва : Физматлит, 2008 .— 230 с. : ил. — Научное .— ISBN 9785-94052-174-7.
- [13] Белик А.Г., Цыганенко В.Н. Анализ эффективности применения прикладного функционального моделирования информативных сигналов в автоматическом регулировании// Системы управления и информационные технологии: Научно-технический журнал, №4(62), 2015, С. 56-60
- [14] Unbehauen H., Böttiger F. Regelalgorithmen für Prozessrechner.- PDV-Berichte, 1974, №26, s. 108.
- [15] Chiu K.C., Corripio A.B., Smith C.L. Digital Control Algorithms: Part I Dahlin-Algorithm; Part II Kalman-Algorithm; Part III Tuning of PI- and PID-Controllers.- Instruments Controlsystems, 1973, №10, p. 57-59; №11, p. 55-59; №12, p. 41-43.
- [16] Бабаянц А.В, Конецов В.А. Идентификация динамических характеристик процессов микробиологического синтеза с помощью УВК.- Автоматика и телемеханика, 1982, №3, с. 79-86.
- [17] Takahashi Y., Chan C.S., Auslander M.D. Parametereinstellung bei linearer DDC-Algorithmen .- Regelungstechnik und Prozessdatenverarbeitung, 1971, №6, s.237-244.
- [18] Конецов В.А. САПР цифровых САУ. Концепция: монография. – Изд-е второе, дополн. и испр. – Псков: Издательство ПсковГУ, 2012. – 307 с.
- [19] Конецов В.А., Казаченко А.П., Литвинова Л.М., Бунин А.Б. Модифицированные средства цифрового управления.- М.: Информприбор, Каталог

- Государственной Системы Приборов СССР, 1987, том 4, вып. 10, 11, 12, с. 112.
- [20] Konevtsov V.A., Verteshev S.M., Poletaev I.A. Eigenschaften von Complex SDSDC // European Science and Technology: 7th International scientific conference. Germany, Munich 2014, Vol.I, p. 493-497.
- [21] Verteshev S.M., Konevtsov V.A., Poletaev I.A. Softwaremittel der Projektierung von Systemen der digitalen Steuerung // European Science and Technology: 5th International scientific conference. Germany, Munich 2013, Vol. I, p. 501-504.

Aerated Concrete Microwave Reflection and Transmission Properties in a Wet Environment

Tarmo Koppel¹, Inese Vilcane², Viktor Mironov², Andrei Shiskin²,
Sanita Rubene², Piia Tint¹

¹ Department of Work Environment and Safety, Tallinn University of Technology, Ehitajate tee 5,
19086 Tallinn, Estonia

² Riga Technical University,

Send correspondence to tarmo.koppel@ttu.ee

Abstract. Excess water content within the building material could greatly alter the interaction of the microwave with the material. In this study aerated concrete (AEROC) block walls (60x60cm) were investigated for their microwave (2.4 GHz) properties under wetting conditions. The spray wetting of the wall was conducted to simulate the environmental processes such as raining or water damage. 50ml/m² water dosage was applied on the surface of the concrete 21 times in 1 min intervals. The results show a noticeable decrease in microwave penetration power through the material after the sample gets enriched with water. As the water content on the surface of the material rises, so does the transmission loss. During the different water content of the aerated concrete, the reflection loss varied from -15.04 dB (dry wall) to -5.03 dB (wet wall's surface). The transmission loss continues to rise during the entire length of the experiment, from -4.5 dB as a dry sample to -8.3 dB after 441 ml (1035 ml/m² during 23 min) of sprayed water. The variation of reflected microwave power was approximately ten times, which is quite a significant indicator of alteration of microwave propagation. The results demonstrate wetting process as an considerable factor in assessing microwave propagation in near the sources, such as mobile phone base station antennas, industrial microwave heaters and ovens etc.

Keywords: electromagnetic fields, microwaves, reflection, transmission, aerated concrete, water, wetting.

I. INTRODUCTION

Microwaves attenuate inside the buildings and building materials. Microwave permeability of the construction materials varies to a large degree. A portion of the microwaves is also absorbed and reflected by the materials. Microwave transparent materials include wood, drywall and other lightweight dielectric materials. Reflections within the construction materials or from neighboring surfaces can also account for attenuation of the microwaves as waves may cancel each other out.

Excess water content within the building material could greatly alter the interaction of the microwave with the material. Both reflective and absorptive properties of the materials could be emphasized, resulting in a new electromagnetic wave scenario in the vicinity of the building material. Such cases may become relevant where high power mobile communications or broadcasting antennas are located. While assessing the safety of workers and other people nearby these antennas, the risk assessment is likely to be carried out under conditions without water interaction with the material. In unforeseen cases, where water would affect the reflection properties of the walls surrounding the high power

transmission antenna, the microwave exposure levels may be significantly elevated and endanger the nearby people. In such examples, the risk assessment should be always carried out under worst case scenario examples, including the reflective properties of the materials surrounding the antenna.

Water related changes within the material would not only affect the behavior of the electromagnetic fields. Such water related processes could occur and subject building materials to physical reconditioning, likely altering the thermal isolative, structural strength and other properties of the materials. In extreme cases such water damage could even endanger the physical integrity of the building.

In planning shielding characteristics against microwaves, specific construction materials are accounted for their attenuation or transmission effect. Nowadays, a variety of building materials exist with either high transmission or reflection characteristics. Dependent on the chemical composition and the structure of the material, this may greatly affect the microwave propagation. In the literature, almost no attention is paid on the change in the microwave characteristics of the materials under various weather conditions. Cold and rain or the combination of two

could significantly affect the microwave transmission and reflection properties of construction materials. In this study the focus is on aerated concrete blocks - a popular contemporary building material.

In observing microwave propagation and interaction with materials, three types of behavior can be observed: transmission, reflection and absorption. Microwave transparent materials have low dielectric loss and microwaves pass through it with little or no attenuation. Microwaves reflect back from opaque materials and no transmission occurs. In case of absorbing materials, high dielectric loss causes absorption within the material, and the level of absorption is dependent on the dielectric loss factor. Absorption is in relation with transmission and reflection, where both are reduced and the microwave energy is absorbed within the material and turned into heat [1-4].

The conductive surfaces cause the reflection, where the microwave is reflected from the surface and/or from the inside layers of the material. The capacitive and conductive components of the dielectric response of the material is determined by the dielectric constant and the dielectric loss factor [2].

Determining concrete moisture content (w/c ratio) by means of radar has been undertaken by Sbartai et al., where testing showed that an increase in the degree of water saturation lead to significant decrease in the amplitude of direct and reflected wave, determined by a good correlation. Sbartai et al. concluded it to be directly related to the increase of complex permittivity related to the polarization and conduction mechanisms occurring in the concrete [5].

Also Laurens et al. reported the concrete relative humidity to greatly affect the direct wave signal amplitude of the radar measurements. The frequency of the radar they used was of 1.5 GHz, complemented by moisture sensors [6].

Dielectric constant of concrete varies in between 5 to 12, depending mainly on the moisture content and signal frequency [7]. The variation of water volume in the concrete pores results in great change in the complex permittivity and therefore in the attenuation of the propagation velocity of microwaves from radar [8]. The loss factor is greatly dependent on the concrete moisture state (0-2 for dry concrete; 14-16 for saturated concrete) [9-11].

II. METHOD

In this study aerated concrete (AEROC) block walls were investigated for their microwave properties under wetting conditions. The selected microwave frequency was 2.4 GHz, which is a widely used frequency for mobile communications and networking, but also for home microwave cooking or industrial microwave heating. Considering the frequencies of the civilian mobile communications, 2.4 GHz lies approximately at the center of the

microwave spectrum utilized for the that purpose. 2.4 GHz is also the frequency of the microwave oven, since it has good absorption characteristics within the water content in the food.



Fig. 1. One of the three aerated concrete sample walls constructed of three blocks.

Three sample walls of the same type of aerated concrete blocks were investigated. The sample surface size was 60x60 cm. Single blocks were of size 60x30x20 cm. For each sample wall, three blocks were piled on top of each other, without the use of blending material (figure 1). Careful attention was paid so to avoid any cracks or gaps within the sample wall, from where the microwaves could leak through.

The moisture content of sample aerated concrete blocks was measured by electrical impedance method. The blocks were determined to be dry. The blocks had been indoors for 2 months with the average room temperature of 20°C and average relative humidity (RH) 35%.

The wetting of the wall was conducted to simulate the environmental processes such as raining or water damage (figures 2, 3). Wetting was conducted by a hand spray. The wall was subjected to repetitive spraying treatments, each of which delivered 21 ml of room temperature tap water evenly on the 0.6x0.6m surface of the sample wall i.e. 50ml/m². There was total of 21 spraying treatments, with the accumulating dosage of sprayed water 441ml. The spraying treatments were separated by 1 minute period, during which the water was allowed to be absorbed into the material. By such dosing, there was no dripping of the water and the only water lost from the sample was due to normal drying in the room temperature (21 degrees Celsius, RH 36 %). By the end of the last spraying treatment, the top layers of the block were absorbed with water. The measurements of transmission and reflection properties were done after

each spraying treatment, i.e. 21 times, plus an initial dry sample measurement.



Fig. 2. Aerated concrete sample blocks: above dry and below surface wetted 441 ml during 23 min.

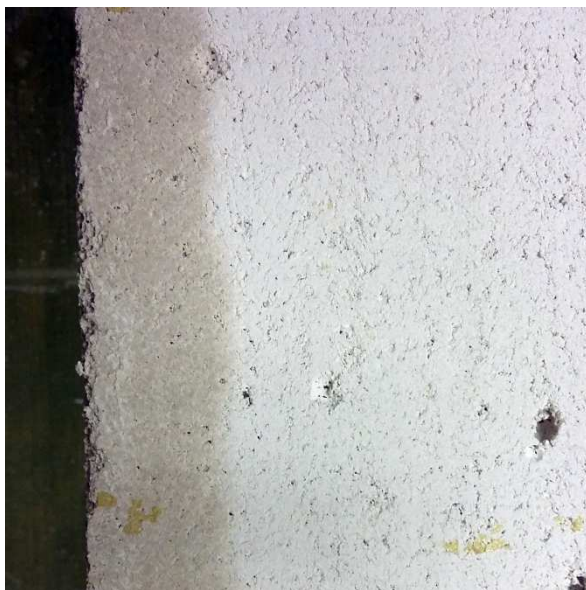


Fig. 3. Intersection view of aerated concrete wetted sample block after dosage of 441 ml sprayed water during 23 min– the penetration of water into the deeper surface areas is visible up to ~4 cm.

The measurement setup consisted of standard gain horn antennas as presented in figure 4. The antennas were positioned in a manner to place the sample to the far field region (10 wavelengths) while the microwave was hitting the material.

From the transmitting horn antenna, the microwave propagates from the horn antenna in a parallel beam, which is called the near-field or also Fresnel zone. Field divergence takes place in the so-called far-field or Fraunhofer zone and the wave intensity decreasing by the inverse square law - the

amplitude decreases in inverse proportion to distance from the aperture of the horn [22].

The distance of the near field zone (l) in case of rectangular horn opening is to be determined by the formula by Botsco [23] (Formula 1), where A is the dimension of the largest side of the rectangle and λ the wavelength. The wavelength of 2.4 GHz electromagnetic field is 0.125 m.

$$l = \frac{A^2}{2\lambda} \quad (1)$$

A 2.4 GHz signal generator was used with an output power of 20 dBm. The microwave reflecting back from the material and transmitting through the material was measured by a spectrum analyzer Aaronia Spectran HF6080 (Euscheid, Germany), which was controlled and monitored by a PC. In order to register a reflection/transmission incident, ten sequential measurements were monitored, of which the highest reading was automatically recorded.

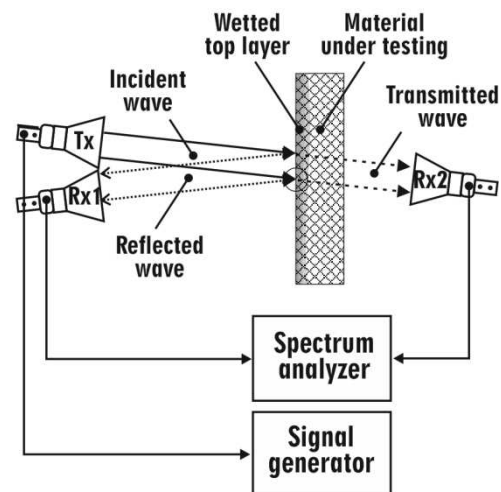


Fig. 4. Measurement setup included irradiator horn antenna Tx and two receiving horn antennas: Rx1 for reflected wave and Rx2 for transmitted wave measurement.

Prior and after measuring samples a calibration procedure was done including measuring full and zero reflection/transmission microwave levels. Full reflection was determined by placing a sample size aluminum plate to the sample and measuring full reflection by antenna Rx1, whereas full transmission was determined by leaving the sample tray empty and measuring the fully transmitted wave at antenna Rx2. Reflection loss (RL) and transmission loss (TL) were calculated to each tested sample as a logarithmic ratio of powers in decibels (dB), as a ratio of the transmitted (P_t) or reflected (P_r) wave to the full transmission or full reflection (P_i). The measurements were registered in unit of measure powers decibel milliwatts (dBm). Ratio in decibels (dB) is a representation of gain or loss of the material under

testing (MUT). Subtracting two powers (dBm) is resulting in their ratio (dB); reflection loss (RL) in formula 2 and transmission loss (TL) in formula 3.

$$RL(\text{dB}) = 10 \cdot \log_{10} \left(\frac{P_r}{P_i} \right) \text{dB} = P_r | \text{dBm} - P_i | \text{dBm} \quad (2)$$

$$TL(\text{dB}) = 10 \cdot \log_{10} \left(\frac{P_t}{P_i} \right) \text{dB} = P_t | \text{dBm} - P_i | \text{dBm} \quad (3)$$

The testing was carried out in a laboratory conditions under the controlled microwave levels. In order to have high reliability of the test results, the reflections were minimized by using specialized forms/materials in the immediate surroundings.

III. RESULTS

The results averaged across the samples, show a noticeable decrease in microwave penetration power through the material after the sample gets enriched with water. As the water content on the surface of the material rises, so does the transmission loss. On the other hand, with the rise of the water content, the reflective properties of the material increase as expressed in the decrease of the reflection loss.

The extremities of the transmission and reflection loss were determined by 1) removing the sample and 2) replacing the sample with a fully reflective Aluminum sheet. The maximum transmission loss was registered -31.8 dB and the maximum reflection loss -32.1 dB.

The transmission loss and reflection loss dependency on the amount of accumulated sprayed water is shown on graph 5.

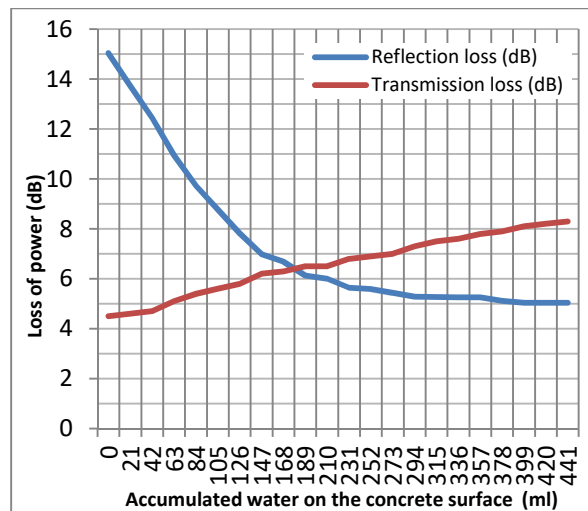


Fig. 5. The transmission loss and reflection loss dependency on the amount of accumulated sprayed water. Vertical bars also constitute of 1 min intervals.

The change in the reflection loss is most evident with the first 210 ml (493 ml/m² during 12 min) of accumulated sprayed water, after that the reflection loss doesn't change as rapidly. After about 400 ml (937 ml/m² during 21 min) of sprayed water the

reflection loss remains at the same level of approximately -5 dB. Contrarily, the transmission loss continues to rise during the entire length of the experiment, ending at -8.3 dB after 441 ml (1035 ml/m² during 23 min) of sprayed water.

During the different water content of the aerated concrete, the reflection loss varied from -15.04 dB (dry wall) to -5.03 dB (wet wall's surface after 23 min of experiment) which is a variation of 10.01 dB. The results from three samples showed little variability, indicating a good repeatability of the test. The average Delta for the reflection was 0.6 dB and transmission 0.4 dB across the corresponding water amount.

IV. CONCLUSIONS AND DISCUSSION

Although the total reflection (reflection loss of 0 dB) was not achieved, the variation of reflected microwave power was approximately ten times, which is quite a significant indicator of alteration of microwave propagation.

The results demonstrate wetting process as a considerable factor in assessing microwave propagation in near the sources, such as mobile phone base station antennas, industrial microwave heaters and ovens etc. The safety of the people including the workers near such installation and devices should be assessed also accounting for the nearby building materials and their potential being wetted as this may significantly raise the exposure level and put people at risk or inhibit the work of electrical apparatuses.

The results have also pointed out the perspective usage of electromagnetic radiation in assessment of surface water, absorbed into the pours of the concrete. Both registering transmitted and reflected signal has shown a functional dependence on the amount of water absorbed by the concrete sample. Further studies should investigate the attenuation factor dependency on the temperature and humidity conditions in the respective environment, since in a warm and dry environment the natural water evaporation from the concrete surface would be faster and hence the absorbance of water lower.

REFERENCES

- [1] Sutton, W.H., Microwave processing of ceramic materials. Am. Ceram. Soc. Bull. 1989, 68, 376-386.
- [2] Thostenson, E.T., Chou, T.-W., Microwave processing: fundamentals and applications. Compos. Part A Appl. Sci. Manuf. 1999, 30, 1055-1071.
- [3] Clark, D.E., Folz, D.C., West, J.K., Processing materials with microwave energy. Mater. Sci. Eng. A 2000, 287, 153-158.
- [4] Das, S., Mukhopadhyay, A., Datta, S., Basu, D., Prospects of microwave processing: An overview. Bull. Mater. Sci. 2009, 32, 1-13.
- [5] Sbartaï ZM, Laurens S, Balaýssac JP, Ballivy G, Arliguie G. Effect of concrete moisture on radar signal amplitude. ACI materials journal. 2006 Nov 1;103(6):419
- [6] Laurens, S.; Balaýssac, J.-P.; Rhazi, J.; and Arliguie, G., "Influence of Concrete Moisture Upon Radar Waveform," Materials and Structures, V. 35, No. 248, May 2002, pp. 198-203.

- [7] Bungey, J. H., "Sub-Surface Radar Testing of Concrete: A Review," *Construction and Building Materials*, V. 18, 2004, pp. 1-8.
- [8] Halabe, U. B.; Bhandarkar, V.; Chen, H.-L.; and Sami, Z., "Detection of Sub-Surface Anomalies in Concrete Bridge Decks Using Ground Penetrating Radar," *ACI Materials Journal*, V. 94, No. 5, Sept.-Oct. 1997, pp. 396-408.
- [9] Soutsos, M. N.; Bungey, J. H.; Millard, S. G.; Shaw, M. R.; and Patterson, A., "Dielectric Properties of Concrete and their Influence on Radar Testing," *NDT&E International*, V. 34, 2001, pp. 419-425.
- [10] Rhim, H. C., and Büyüköztürk, O., "Electromagnetic Properties of Concrete at Microwave Frequency Range," *ACI Materials Journal*, V. 95, No. 3, May-June 1998, pp. 262-271.
- [11] Robert, A., "Dielectric Permittivity of Concrete Between 50 MHz and 1 GHz and GPR Measurements for Building Materials Evaluation," *Journal of Applied Geophysics*, V. 40, 1998, pp. 89-94.

Experimental Investigations of Effect of LC-circuits on Sparking and Thermal State of Sliding Electric Contact Unit

Oksana Kozyreva, Igor Plokhov, Nikita Kotkov, Igor Savraev, Alexander Ilyin

Pskov State University, Computer Science and Electric Power Engineering Faculty.

Address: Russian Federation, Pskov, Lenin square, 2.

Abstract. such processes in electric machines having sliding contacts as sparking and overheating can be the reason of the deep electroerosive wear. Searching effective ways to reduce sparking has an obvious practical significance since it extends the service life of the sliding contact in particular and service life of the electro-mechanic units in whole.

This article contains information about physical processes in the electrical sliding contact. The method of spark suppression related to LC filters introduced to the electromagnetic brush circuits is considered, the device for spark reducing is suggested. The calculations of the impact of the device for spark reducing on sparking and thermal processes in the contact pairs are described.

Keywords: electrical machines, turbogenerator, thermal processes, sparking, brush contacts.

I. INTRODUCTION

Electric sliding contact (SC) is widely used in electric machines and apparatus for such purpose as current transfer (both direct and alternating) from the fixed contact points to the parts in motion.

When sliding contacts are applied in electric machines, such processes as sparking and overheating the contacts can be the reason of deep electroerosive wear. These processes can be caused by several factors. The main factors are the mechanic SC contacting instability and the processes occurring in the electromagnetic circuits of the SC, which cause high-frequency overcurrents and overvoltages.

Searching effective ways to reduce sparking has an obvious practical significance since it extends the service life of the SC in particular and service life of the electro-mechanic units in whole. One of the effective methods of spark suppression (electromagnetic interference, thermal stress reducing) in the SC is the method related to the development of LC filters introduced to the electromagnetic brush circuits. For example in the works of I.V. Plokhov [1] the capacitance was connected between one isolated brush on the slip ring and the group of working brushes. The device was developed for reducing sparking in sliding electric contact units having slip rings and for applying in turbo generators.

In the works of F.Veselka [2], [3] it was suggested to use supplementary capacitance and inductance couplings for the spark suppression by applying electrically conductive film coatings to the surfaces of each brush and brush holder (for the DC

commutator motor). Furthermore at the Electric Drive and Automation Systems Department of Pskov State University the modification of the construction of SC unit was proposed. The modification includes adding the inductive and capacitive elements to the electromagnetic circuit of the SC. The device for spark reducing (DSR) in the sliding electric contact unit was patented [4].

II. MATERIALS AND METHODS

Investigations of electric contacts thermal design were began by R. Holm and continued by a number of researches [5]-[8], these investigations consider the particular cases of the SC thermal conductivity boundary value problems. In the 70-s – 90-s a number of scientific researches were devoted to in-depth investigations of the physical dependences of the electro-frictional interaction [8]-[11]. In these investigations the attempts of mathematical formulation of the nonstationary dynamic modes of the electro-frictional interaction is given for the first time.

The modern explanation of the physical processes in the sliding electric contact is summarized to the following. In the contact of two rough bodies the total interface (sliding surface) is split into a number of spots (α -spots). Therefore when the flow of energy passes through this surface it has to overcome an additional resistance caused by the violation of the flow lines homogeneousness – it is called constriction resistance. This resistance is summed with the resistance of oxide films in general case. In addition to this resistances there are some films consisted of

wear products on the contact surfaces, and this wear products do not react chemically with the contact material.

In the area of direct surface-to-surface mechanical contact (transition layer) commutating occurs in high-temperature thermal spikes caused by the flow of the electric current through the conductive α -spots (areas of constriction of the electric current and of the heat flow). Bad commutating can occur in an electric arc, and then the areas of conductivity can be melted, if the action is prolonged, it causes the significant increase in the overall transition layer and brush temperature. Thus it can be seen that there is more significant heat release in the contact area in the sparking brush in comparison with the brush without sparking (Fig. 1).

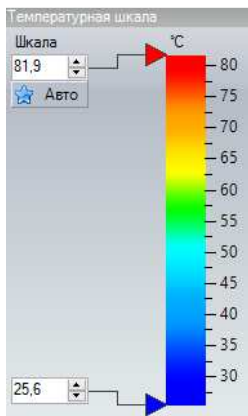
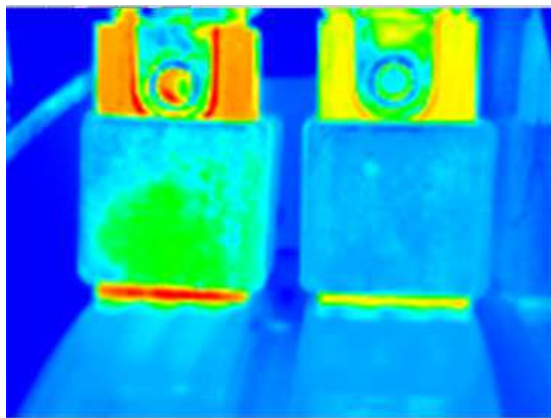


Fig.1. Thermograms during the experiment: a) for sparking brush b) brush without sparking during the process. Thermograms testify to a higher heating the contact area of the brush working with the increased sparking

Due to the process of electric current passing the constriction resistance, the Joule heat is released; in addition to this heat there is a thermal power caused by the friction between the bush and the slip ring. Arcing has a significant impact on the heating processes in the contact area.

In cases when the temperature of the contact surface exceeds the softening point of the brush material, the mechanical and electrical characteristics

of the contact deteriorate and the brush wear becomes accelerated.

In the work of V.N. Zaboin [6] the solution of the problem of the steady-state thermal balance was proposed with a set of assumptions. Based on the Kohlrausch-Holm equations for determining the maximum temperature value in the homogeneous linear conductor or fixed electric contact and the Jaeger equation for calculating the maximum temperature value on the surface of the heat source moving along the semi-infinite surface [6], [7], the expression for calculating the maximum temperature inside the element having a lower thermal conductivity in any contact pair was obtained. Having used the calculation formula [6], one can obtain the table of temperature and losses distributions for the elements of different contact pairs. The values of the maximum temperatures in the contacts of the different brushes are given in the Table 1.

Table 1.

Type of brush	ЭГ2АФ (EG2AF) (electro-graphite)	ЭГ2АФ (EG2AF) (electro-graphite)	МГСО (MGSO) (copper-graphite)	МГСО (MGSO) (copper-graphite)
Slip ring	Steel	Copper	Steel	Copper
$Q_{max}, °C$	513	122	300	72

As can be seen from the table, for example, the maximum temperature in the SC in the contact pair of the brushes of ЭГ2АФ type and the steel slip rings can reach 500 °C, which is close to the temperature of the recrystallization of the contact pairs.

According to the Table 1, it is possible to determine approximately the temperature ranges in the contact area during the experiments.

III. RESULTS AND DISCUSSION

A number of experiments at the Electric Drive and Automation Systems Department of Pskov State University were conducted. The investigations included the calculate of impact the device for spark reducing (DSR) on sparking and thermal processes in the contact pairs.

The experimental setup of turbogenerator commutator having the contact pair: electro-graphite brushes of ЭГ2АФ type – slip rings made of stainless steel was used for the investigations mentioned above. The device (Fig. 2) is basically the electric capacitance 5 introduced between the electrically connected in parallel brush groups 1 of one slip ring of the sliding contact unit 3. Along with that, the first brush group is connected with the power bus 4 and the second brush group 2 is disconnected from the power bus. Moreover the electrical capacitance consists of two groups of the capacitors connected in parallel, polar 7 and non-polar 6; the non-polar group of the capacitors is connected directly to the circuit, and the second capacitor group is connected via the inductance 8. The diode 9 is connected between the

terminals of the polar capacitors group, and its anode should be connected to the positive terminal of the polar capacitors.

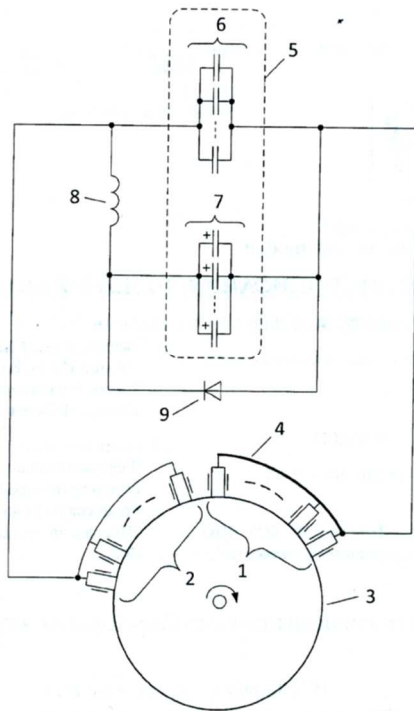


Fig.2. The device for spark reducing in the sliding electric contact unit [4].

Fig. 3 shows the curves of brushes heating obtained from the experiments while working at the sparking mode with or without using the DSR. The visual observation showed that applying the DSR allows to reduce sparking from 2 to 1 ¼ points.

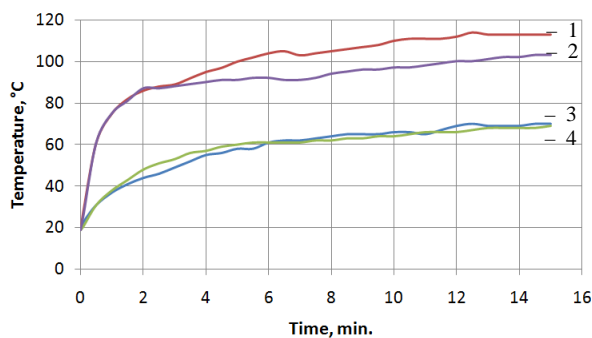


Fig.3. Anode brush and sparking cathode brush temperature dependence on time with or without applying the DSR: 1 – cathode brush, the DSR is turned off; 2 – cathode brush, the DSR is turned on; 3 – anode brush, the DSR is not connected; 4 – anode brush, the DSR is connected.

As can be seen from the graph, the sparking brush heats up much slower and reaches the lower steady state temperature when the device is turned on. As the dependences were obtained at some distance from the contact surface (at the slight distance value), the values of the temperatures after recalculating it for

the area of the direct contact would be close to the values in table. However it should be taken into account that temperature of the short-term thermal spikes occurring in the transition layer can be several times higher than the average temperatures of the working contact pair. It causes melting and evaporating the brush material but there is not enough time (because of the very short duration of the single high-temperature spike) for heat transfer to the brush body. It is also necessary to take into consideration that the proportion of the heat losses removed from the lateral brush surface is about a half of the total losses in the contact [6].

In any case it can be concluded that if the temperature gradients in the brushes are equal, the contact surface of the brush having the worst commutation reaches the steady state temperature value, which is lower when the device for spark reducing is connected.

In parallel with the experiments of temperature dependences registering, the experiments of registering the voltages between the working group of brushes and the isolated brush for each temperature point were conducted (Fig. 4).

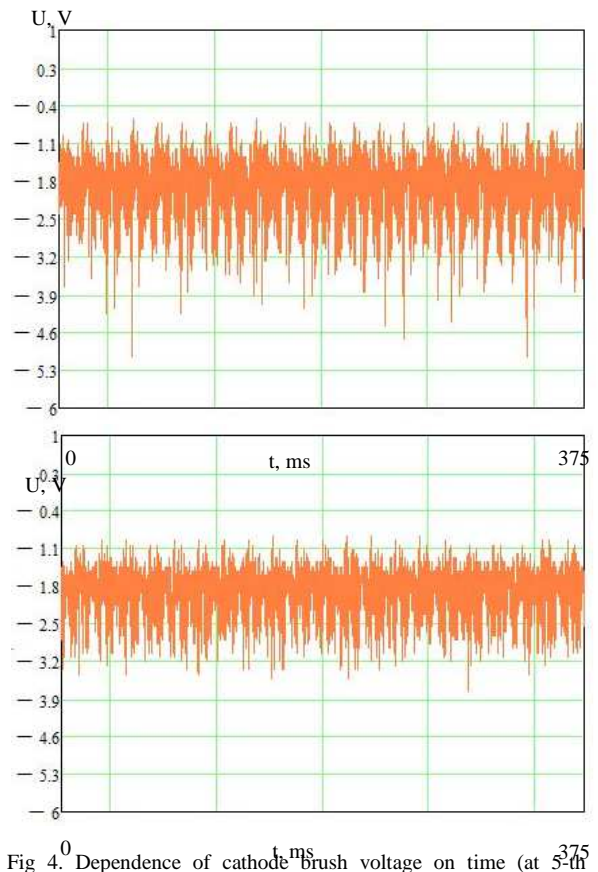


Fig 4. Dependence of cathode brush voltage on time (at 5th minute) with or without applying the DSR: the DSR is turned on (top graph), the DSR is turned off (bottom graph)

Analyzing the obtained dependencies it can be concluded that the magnitude of the transition voltage drop and the number of voltage spikes decrease due

to the effect of the DSR on the thermal and electromagnetic process.

Basically, the main interest is in obtaining high quality dependence of the brush heating process near the transition layer for the brush working in the sliding electric contact unit of the turbogenerator (when the current comparable to the rated turbo generator current passes through the brush). The temperature dependence clearly shows the significant effect of the connected device for spark reducing on the contact pair temperature state and on the electromagnetic processes in the brush circuit consequently.

It is worth emphasizing that the small modification in the construction of the commutator electromagnetic circuit results in reducing brush sparking, decreasing the temperature of the sparking brush contact surface and, consequently, in increasing the service life of the brushes and the service life of the electric machine commutator in general.

IV. CONCLUSION

The positive effect of the device for spark reducing in the sliding electric contact unit on the thermal and electromagnetic processes in the commutator is confirmed by the experimental investigations. Connecting the device results in reducing brush sparking and decreasing the temperature of the sliding contact.

Such modification of brush contacts as adding the devices for spark reducing to the each sliding contact allows to:

- reduce the overall level of the electromagnetic oscillations,
- reduce the intensity of the sparking process in the sliding contact and the rate of its mechanical wear the as a consequence,
- extend the overall service life of the electric machine commutator.

V. ACKNOWLEDGMENTS

This study was carried out within the one-year phase of the research work № 173 of the basic part of the Ministry of Education and Science of the Russian Federation state task №2014/700.

REFERENCES

- [1] Плохов И. В. Комплексная диагностика и прогнозирование технического состояния узлов скользящего токосъёма турбогенераторов. Диссертация доктора технических наук. СПбГПУ. 2001.
- [2] Забоин В.Н., Веселка Ф. Способы уменьшения искрения и износа щёток в коллекторных электрических машинах. Механика и физика процессов на поверхности и в контакте твёрдых тел, деталей технологического и энергетического оборудования. 2009, сс. 124-129.
- [3] Chmelík, K. Kluzný kontakt v elektrických strojích. K. Chmelík, F. Veselka. Ostrava. KEY Publishings.r.o. 2007, c. 256.
- [4] Плохов И.В., Ильин А.В., Исаков А.Н., Козырева О.И. Устройство для уменьшения искрообразования в узле скользящего токосъёма. Патент на полезную модель RU132630. 2013.09.20.
- [5] Мерл В. Электрический контакт. Госэнергоиздат. 1962, с. 80.
- [6] Забоин В.Н. Оценка тепловой напряжённости элементов неоднородного скользящего электрического контакта. Механика и физика фрикционного контакта и граничных слоёв. 2004, сс.129-133.
- [7] Ragnar Holm, Electric Contacts Handbook, 3rd ed., Berlin, Springer-Verlag. 1958.
- [8] Реутт Е.К., Саксонов И.Н. Электрические контакты. М.: Воениздат. 1971, с.126.
- [9] Омельченко В.Т. Теория процессов на контактах. Харьков: ХГУ, Вища школа. Издательство при Харьковском ун-те. 1979, с. 126.
- [10] Ким Е.И., Омельченко В.Т., Харин С.Н. Математические модели тепловых процессов в электрических контактах. Алма-Ата. Изд-во Наука. 1977, с. 236.
- [11] Кончиц В.В., Мешков В.В., Мышкин В.В. Триботехника электрических контактов. Минск, Наука и техника. 1986.
- [12] Забоин В.Н. Определение сопротивления стягивания неоднородного скользящего электрического контакта. Scientific proceedings of Riga technical university. Power and electrical engineering. 2002, сс. 77-82.
- [13] Kohlrausch F. Statioarer Temperaturzustand. Ann. Phys. Lpz. № 1. 1990, сс. 134-158.
- [14] Carslaw, H. S., Jaeger, J. C. Conduction of heat in solids. Second edition, Oxford. 1959.

Capacitance Reduction Using Ripple Suppression Control of Single Phase Energy Stored Quasi-Z-source inverter

Kaspars Kroics^{1,2}, Janis Zakis², Oleksander Husev^{2,3}

Institute of Physical Energetics¹, Riga Technical University², Chernihiv National University of Technology³

Abstract. The energy stored Quasi-Z-source Inverter (qZSI) allows integrate energy storage in addition to the other energy source mainly for output power smoothening. Single phase inverter suffers from double-frequency power ripple in the input side and also in the energy storage that is transferred there from the ac-side. In qZSI must be used large electrolytic dc capacitors in the impedance network to suppress this 100 Hz ripple. Also to suppress this ripple can be applied two types of power decoupling: passive power decoupling and active power decoupling. In this paper is analyzed passive power decoupling that is realized by means of the modified control strategy that produces the time-varying shoot-through duty cycle to mitigate power ripple without deteriorating of the output power quality. The validity of proposed control strategy was confirmed by simulation results that were obtained in PSIM software.

Keywords: passive decoupling, single-phase inverter, PR controller, double-frequency ripple, energy stored quasi-Z source.

I. INTRODUCTION

The cost of electricity produced by renewable energy sources and probabilistic nature of the generation are major concerns that limits its wider usage. Storage technologies have big potential for smoothing out the electricity supply from these sources and ensuring that the supply of generation matches the demand. Typical solution for energy storage integration in renewable energy system is to use additional dc-dc or even dc-ac converter that increases costs [1], [2]. More and more popular are becoming multiport dc-dc converters that can be used for integration of energy source and battery or different types of storages into the grid. Usually, a multiport converter is used in combination with traditional dc-ac converter. Further possible reduction of size, costs and losses can be obtained with the development of novel multiport dc-ac single stage converters having less semiconductor switches and passive elements [3]. Such type of the converter can be designed with reduced number of components and smaller size. One of the possible topology that allows integration is quasi-Z-source inverter with integrated storage in parallel to one of the Z-source capacitor. In [4], [5], [6], [7] is compared qZSI topologies to the traditional voltage source inverter with additional boost converter. The results show that the power losses of the semiconductors of the Z-source inverter are higher but the volume of passive elements in some applications and modes can be reduced. Also the number of switches is less that makes practical design of the converter easier. Additional advantages

of ZSI is wide-range input voltage regulation possibility along with enhanced reliability.

The benefits of the qZSI can be extended with integration of energy storage into the converter structure without additional passive and semiconductor elements. Scientific papers about this topology are summarized in [8]. Mainly in the literature is analyzed three phase qZSI. In single phase application the bulky capacitors and inductors are needed to limit 100 Hz pulsations [9], [10] therefore it makes the application of this topology in practical applications unattractive.

In the literature are proposed a few strategies to reduce the double frequency ripple [11], [12]. Passive decoupling is analyzed in [13], [14]. There is no paper that analysis application of this methods to the energy stored qZSI. As the energy storage is connected in parallel to the one of the capacitors the ripple reduction influences input power ripple therefore there must be find some compromise. This paper is dedicated to investigate the passive power decoupling in energy stored qZSI. In this paper approach based on proportional resonant controller will be analyzed.

II. ENERGY STORED QZSI

Fig. 1. shows schematics of qZSI with integrated battery The battery is connected in parallel to the upper capacitor of the quasi-Z-source inverter, it is possible to control output power, and state of charge (SOC) of the battery at the same time by controlling

the shoot-through (ST) duty ratio and modulation index [15].

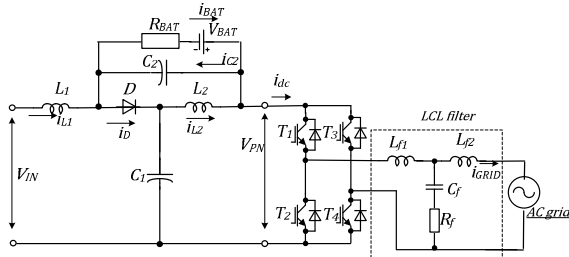


Fig. 1. Quasi-Z source inverter with integrated battery

If the battery is connected in parallel to the upper capacitor C_2 then low voltage battery can be used. The converter is controlled by means of full bridge inverter transistors and only one additional diode or transistor is needed to provide operation of the converter. Two inductors and capacitors form quasi Z source network and by means of shoot through state duty cycle (D) output voltage can be controlled.

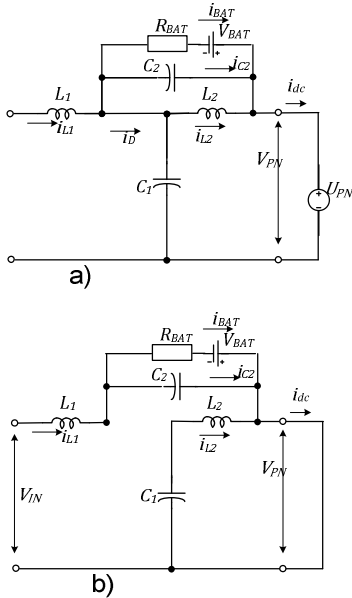


Fig. 2. Equivalent circuits of the converter: (a) - during non shoot-through state; (b) - during shoot-through state

Operation modes of the converter also are shown in Fig. 2. From the equivalent circuit can be derived expressions that describes voltages and currents in particular state. The relation between variables of the converter can be described mathematically by solving equations that describes both states of the converter and taking into account that average voltage of an inductor over one switching period is zero and also average current of a capacitor over one switching period is zero. Expressions are relatively simple and was solved analytically. Must be taking into account that in equations is not taking into account parasitic resistances of all elements, the deeper analysis is provided in [16] and [17]. The final equations for steady-state conditions are as follows:

$$V_{C1} = \frac{1-D}{1-2D} V_{IN}. \quad (1)$$

$$V_{C2} = \frac{D}{1-2D} V_{IN}. \quad (2)$$

$$V_{PNmax} = \frac{1}{1-2D} V_{IN}. \quad (3)$$

If the battery is connected in parallel to the capacitor C_2 and considering that V_{BAT} is approximately equal to the V_{C2} , the following expression can be derived:

$$V_{PN} = 2V_{BAT} + V_{IN}. \quad (4)$$

The output power of the inverter can be controlled by manipulating of output voltage, as the output peak phase voltage of the inverter is:

$$V_{line max} = V_{PNmax} \cdot \frac{M}{2}, \quad (5)$$

where M is a modulation index.

Also for the connection of the battery in parallel to C_2 exists battery discharge power limitations [18] that also must be taken into account. The calculation of the parameters of passive components of the quasi Z-source inverter without energy storage is analyzed in many papers for example in [19]–[22]. The difference from traditional qZSI in parameter calculation is that voltage ripple on the capacitors must be lower to limit battery power pulsations it means that passive component values must be higher than in traditional qZSI.

In the single phase system, the power injected in the ac grid can be expressed as follows:

$$P = \frac{V_{max} I_{max}}{2} - \frac{V_{max} I_{max}}{2} \cos(2\omega t). \quad (6)$$

The second term in the equation above causes ripples at the dc side. Therefore, the input power also oscillates with the ac power at 120Hz. Such oscillating currents and voltages will reduce the photovoltaic array or generator lifetime and will cause degradation of capacitor and increase switching stresses. The ripple can be removed in case if bulky electrolytic capacitors are used but this will result in decrease in power density of the converter.

III. CONTROL SYSTEM

The basic principle of the capacitance reduction method can be explained by fact that energy is distributed between capacitors C_1 and C_2 according to the voltage variation:

$$\Delta E_1 = \frac{C_1 (V_{C1_max}^2 - V_{C1_min}^2)}{2} = C_1 \cdot V_{C1} \cdot \Delta V_{C1}, \quad (7)$$

$$\Delta E_2 = \frac{C_2 (V_{C2_max}^2 - V_{C2_min}^2)}{2} = C_2 \cdot V_{C2} \cdot \Delta V_{C2}, \quad (8)$$

where ΔE is the ripple energy that is stored in the capacitor and V_{Cmax} and V_{Cmin} are the maximum and minimum voltages across the capacitor. According to (7) and (8) there are two ways to increase ΔE in

traditional qZSI. One is to increase the capacitance or use unsymmetrical passive components [23] and the other way is to increase the voltage fluctuation across the capacitors [24], [14] by implementing advanced control system or by using active filter [25]. In the energy stored qZSI the voltage ripple of upper capacitor C_2 causes battery current ripple that shortens lifetime of the battery. Instead of increasing the capacitance, the control system can be used that will increase the voltage fluctuation across the input to remove double-frequency ripple from the capacitors. By using this method it is not possible full reduction of voltage ripple but partly the value of capacitance can be reduced improving power density of the converter.

The control structure used in simulations of energy stored qZSI is shown in Fig. 3. As there are three power flows: from PV panel or other energy source, from or to battery and from or to ac grid then by controlling two of them the third one of them is determined [26]. In particular case battery power or input power is controlled by shoot trough duty cycle D which is controlled by PI algorithm and inverter output power is controlled by modulation index M .

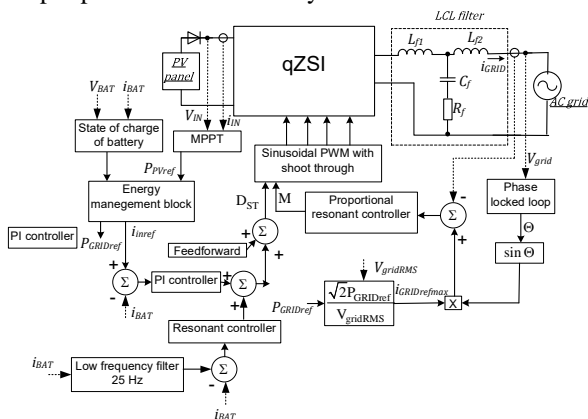


Fig. 3. General control structure of energy stored qZSI

To speed up response and improve stability the feedforward control is used, the average duty cycle can be calculated by equation expressed from previous equations (1) - (5). If the battery is connected in parallel to the upper capacitor C_2 the equation for average duty cycle can be calculated as follows:

$$D_{STaverage} = \frac{V_{BAT}}{V_{IN} + 2V_{BAT}}, \quad (9)$$

The inverter side of the converter is controlled by using proportional resonant controller that controls modulation index M . The accurate extraction of the grid voltage phase angle and frequency is very important to ensure stable operation of grid-connected power converter. Comparison of PLL is done in [27]–[29] and as most promising are carried out Second-Order Generalized Integrator (SOGI) PLL and Park, the Park PLL is more difficult to

implement therefore hybrid SOGI and Park based PLL is used.

For the inverter control is used sinusoidal PWM with added ST states via logic "OR" element [14]. Signal from the PR controller is compared with triangular modulation signal and traditional sinusoidal PWM is formed. The PI controller regulates shoot through duty cycle D to maintain desired input or battery power. Duty cycle D is added to the sinusoidal PWM and shoot through states is formed in which all of the transistors of the inverter are in on state

IV. SIMULATION RESULTS

The results of the simulation study are shown in this section. The main goal of simulation is to shown pulse reduction possibility by using additional resonant controller as can be seen in Fig. 3. The PSIM model was used for simulation. The calculation of passive components of qZSI have been studied in [23]–[26]. In the simulation examples various values of passive components is used to show it influence to the current ripple. Switching frequency of the converter is 50 kHz, $R_{BAT}=0,5 \Omega$, parasitic resistance of the inductors are equal to $0,1 \Omega$.

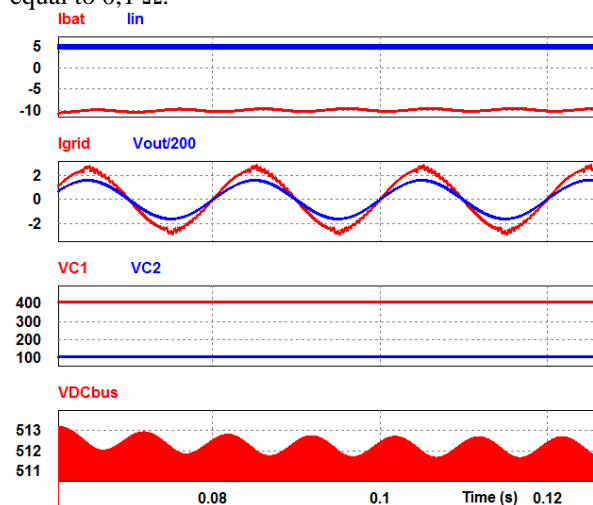


Fig. 4. Waveforms of energy stored qZSI in charge mode $L_1=L_2=1000 \mu H$, $C_1=C_2=4000 \mu F$, $V_{IN}=200 V$, $V_{BAT}=50 V$ without current ripple compensation

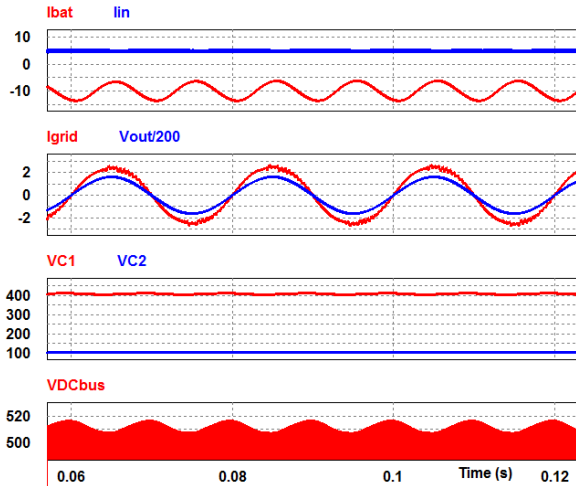


Fig. 5. Waveforms of energy stored qZSI in charge mode $L_1=L_2=1000 \mu\text{H}$, $C_1=C_2=1000 \mu\text{F}$, $V_{\text{IN}}=200 \text{ V}$, $V_{\text{BAT}}=50 \text{ V}$ without current ripple compensation

Figures 4. and 5. shows simulation results that shows waveforms of the qZSI with large capacitance and in case if value of capacitance is 4 times reduced. The input current have low ripples as the regulator regulates duty cycle to maintain this current constant. Whereas the battery current ripple is determined by capacitor value. If the capacitance is reduced the battery current ripple increases.

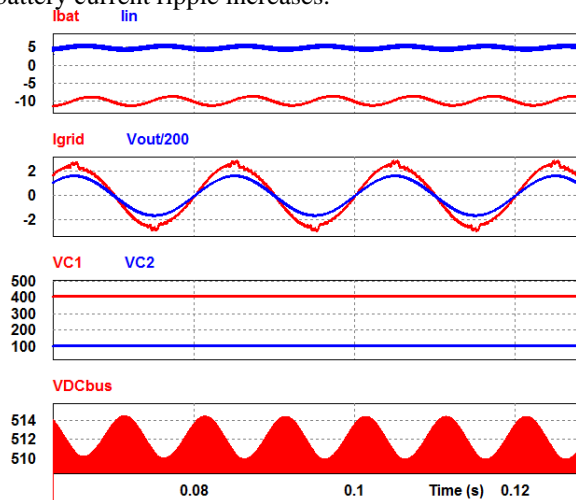


Fig. 6. Waveforms of energy stored qZSI in charge mode $L_1=L_2=1000 \mu\text{H}$, $C_1=C_2=1000 \mu\text{F}$, $V_{\text{IN}}=200 \text{ V}$, $V_{\text{BAT}}=50 \text{ V}$ with battery current ripple compensation

Fig. 6 shows simulation results in case if resonant current ripple suppression controller is used. As can be seen the current ripples can be reduced to the nearly as in case if both of the capacitors are with 4 times larger capacitance. The input current ripples is only a little bit bigger. The battery current ripples can be reduced even more if the coefficient of resonant control is bigger but then the input current ripple is significant and PI controller can become unstable.

V. CONCLUSIONS

In the energy stored qZSI the size of the capacitors can be reduced by using 100 Hz ripple suppression control method. The control is realized

by means of the resonant control of battery current ripple. The ripple suppression have limitations as by reducing battery power ripples the input power ripples becomes higher. This method does not need any additional costs only algorithm by means of digital control must be implemented therefore even minor current ripple reduction gives benefit. Active power decoupling method for ripple reduction must be analyzed as alternative, it is obvious disadvantage that additional passive and active elements will be needed.

VI. ACKNOWLEDGEMENT

This research work has been supported by Latvian Council of Science (Grant 673/2014).

REFERENCES

- [1] B. Singh, B. N. Singh, A. Chandra, K. Al-Haddad, A. Pandey, and D. P. Kothari, "A review of single-phase improved power quality AC-DC converters," *IEEE Transactions on Industrial Electronics*, vol. 50, no. 5, pp. 962–981, Oct. 2003.
- [2] W. Li, Y. Gu, H. Luo, W. Cui, X. He, and C. Xia, "Topology Review and Derivation Methodology of Single-Phase Transformerless Photovoltaic Inverters for Leakage Current Suppression," *IEEE Transactions on Industrial Electronics*, vol. 62, no. 7, pp. 4537–4551, Jul. 2015.
- [3] N. Zhang, D. Sutanto, and K. M. Muttaqi, "A review of topologies of three-port DC-DC converters for the integration of renewable energy and energy storage system," *Renewable and Sustainable Energy Reviews*, vol. 56, pp. 388–401, Apr. 2016.
- [4] O. Husev et al., "Comparison of Impedance-Source Networks for Two and Multilevel Buck-Boost Inverter Applications," *IEEE Transactions on Power Electronics*, vol. 31, no. 11, pp. 7564–7579, Nov. 2016.
- [5] A. Battiston, J. P. Martin, E. H. Miliani, B. Nahid-Mobarkeh, S. Pierfederici, and F. Meibody-Tabar, "Comparison Criteria for Electric Traction System Using Z-Source/Quasi Z-Source Inverter and Conventional Architectures," *IEEE Journal of Emerging and Selected Topics in Power Electronics*, vol. 2, no. 3, pp. 467–476, Sep. 2014.
- [6] M. Shen, A. Joseph, J. Wang, F. Z. Peng, and D. J. Adams, "Comparison of Traditional Inverters and Z-Source Inverter for Fuel Cell Vehicles," *IEEE Transactions on Power Electronics*, vol. 22, no. 4, pp. 1453–1463, Jul. 2007.
- [7] W. T. Franke, M. Mohr, and F. W. Fuchs, "Comparison of a Z-source inverter and a voltage-source inverter linked with a DC/DC-boost-converter for wind turbines concerning their efficiency and installed semiconductor power," in *2008 IEEE Power Electronics Specialists Conference*, 2008, pp. 1814–1820.
- [8] J. Zeng, W. Qiao, C. Wei, and L. Qu, "A soft-switched three-port single-stage inverter for photovoltaic-battery systems," in *2015 IEEE Energy Conversion Congress and Exposition (ECCE)*, 2015, pp. 4568–4573.
- [9] D. Sun, B. Ge, X. Yan, H. Abu-Rub, D. Bi, and F. Z. Peng, "Impedance design of quasi-Z source network to limit double fundamental frequency voltage and current ripples in single-phase quasi-Z source inverter," in *2013 IEEE Energy Conversion Congress and Exposition*, 2013, pp. 2745–2750.
- [10] Y. Liu, H. Abu-Rub, B. Ge, F. Blaabjerg, O. Ellabban, and P. C. Loh, "Design of Z-Source and Quasi-Z-Source Inverters," in *Impedance Source Power Electronic Converters*, Wiley-IEEE Press, 2016, p. 424.
- [11] Y. Liu, B. Ge, H. Abu-Rub, and D. Sun, "Comprehensive Modeling of Single-Phase Quasi-Z-Source Photovoltaic Inverter to Investigate Low-Frequency Voltage and Current

- Ripple," *IEEE Transactions on Industrial Electronics*, vol. 62, no. 7, pp. 4194–4202, Jul. 2015.
- [12] Z. Qin, Y. Tang, P. C. Loh, and F. Blaabjerg, "Benchmark of AC and DC Active Power Decoupling Circuits for Second-Order Harmonic Mitigation in Kilowatt-Scale Single-Phase Inverters," *IEEE Journal of Emerging and Selected Topics in Power Electronics*, vol. 4, no. 1, pp. 15–25, Mar. 2016.
- [13] Y. Zhou, H. Li, and H. Li, "A Single-Phase PV Quasi-Z-Source Inverter With Reduced Capacitance Using Modified Modulation and Double-Frequency Ripple Suppression Control," *IEEE Transactions on Power Electronics*, vol. 31, no. 3, pp. 2166–2173, Mar. 2016.
- [14] Y. Li, W. Gao, J. Li, R. Zhang, and F. Fang, "Double line frequency ripple cancelling for single-phase quasi-Z-source inverter," in *2016 IEEE Energy Conversion Congress and Exposition (ECCE)*, 2016, pp. 1–6.
- [15] L. Liivik, A. Chub, D. Vinnikov, and J. Zakis, "Experimental study of high step-up quasi-Z-source DC-DC converter with synchronous rectification," in *2015 9th International Conference on Compatibility and Power Electronics (CPE)*, 2015, pp. 409–414.
- [16] J. Khajesalehi, M. Hamzeh, K. Sheshyekani, and E. Afjei, "Modeling and control of quasi Z-source inverters for parallel operation of battery energy storage systems: Application to microgrids," *Electric Power Systems Research*, vol. 125, pp. 164–173, Aug. 2015.
- [17] Y. Liu, B. Ge, H. Abu-Rub, and F. Z. Peng, "Control System Design of Battery-Assisted Quasi-Z-Source Inverter for Grid-Tie Photovoltaic Power Generation," *IEEE Transactions on Sustainable Energy*, vol. 4, no. 4, pp. 994–1001, Oct. 2013.
- [18] B. Ge *et al.*, "An Energy-Stored Quasi-Z-Source Inverter for Application to Photovoltaic Power System," *IEEE Transactions on Industrial Electronics*, vol. 60, no. 10, pp. 4468–4481, Oct. 2013.
- [19] J. Anderson and F. Z. Peng, "Four quasi-Z-Source inverters," in *2008 IEEE Power Electronics Specialists Conference*, 2008, pp. 2743–2749.
- [20] Y. P. Siwakoti, F. Z. Peng, F. Blaabjerg, P. C. Loh, G. E. Town, and S. Yang, "Impedance-Source Networks for Electric Power Conversion Part II: Review of Control and Modulation Techniques," *IEEE Transactions on Power Electronics*, vol. 30, no. 4, pp. 1887–1906, Apr. 2015.
- [21] I. Roasto, D. Vinnikov, J. Zakis, and O. Husev, "New Shoot-Through Control Methods for qZSI-Based DC/DC Converters," *IEEE Transactions on Industrial Informatics*, vol. 9, no. 2, pp. 640–647, May 2013.
- [22] Y. Li, J. Anderson, F. Z. Peng, and D. Liu, "Quasi-Z-Source Inverter for Photovoltaic Power Generation Systems," in *Twenty-Fourth Annual IEEE Applied Power Electronics Conference and Exposition, 2009. APEC 2009*, 2009, pp. 918–924.
- [23] W. Liang, B. Ge, Y. Liu, H. Abu-Rub, R. S. Balog, and Y. Xue, "Modeling, analysis, and impedance design of battery energy stored single-phase quasi-Z source photovoltaic inverter system," in *2016 IEEE Energy Conversion Congress and Exposition (ECCE)*, 2016, pp. 1–6.
- [24] Y. Zhou, H. Li, and H. Li, "A Single-Phase PV Quasi-Z-Source Inverter With Reduced Capacitance Using Modified Modulation and Double-Frequency Ripple Suppression Control," *IEEE Transactions on Power Electronics*, vol. 31, no. 3, pp. 2166–2173, Mar. 2016.
- [25] S. A. Singh, N. A. Azeez, and S. S. Williamson, "Capacitance reduction in a single phase Quasi Z-Source Inverter using a hysteresis current controlled active power filter," in *2016 IEEE 25th International Symposium on Industrial Electronics (ISIE)*, 2016, pp. 805–810.
- [26] Y. Liu, B. Ge, H. Abu-Rub, and F. Z. Peng, "Control System Design of Battery-Assisted Quasi-Z-Source Inverter for Grid-Tie Photovoltaic Power Generation," *IEEE Transactions on Sustainable Energy*, vol. 4, no. 4, pp. 994–1001, Oct. 2013.
- [27] I. Galkin and M. Vorobyov, "Optimizing of sampling in a low-cost single-phase instantaneous AC-grid synchronization unit with discrete calculation of derivative function," in *IECON 2015 - 41st Annual Conference of the IEEE Industrial Electronics Society*, 2015, pp. 004538–004543.
- [28] I. Roasto, T. Jalakas, and O. Husev, "Modeling of grid-connected quasi-Z-source series resonant topology based microinverter," in *2016 10th International Conference on Compatibility, Power Electronics and Power Engineering (CPE-POWERENG)*, 2016, pp. 192–195.
- [29] Y. Han, M. Luo, X. Zhao, J. M. Guerrero, and L. Xu, "Comparative Performance Evaluation of Orthogonal-Signal-Generators-Based Single-Phase PLL Algorithms #x2014;A Survey," *IEEE Transactions on Power Electronics*, vol. 31, no. 5, pp. 3932–3944, May 2016.
- [30] Y. Han, M. Luo, X. Zhao, J. M. Guerrero, and L. Xu, "Comparative Performance Evaluation of Orthogonal-Signal-Generators-Based Single-Phase PLL Algorithms #x2014;A Survey," *IEEE Transactions on Power Electronics*, vol. 31, no. 5, pp. 3932–3944, May 2016.

Study of Auxiliary Gas Pressure on Laser Cutting Technology

Lyubomir Lazov, Hristina Deneva, Erika Teirumnieka

Rezekne Academy of Technologies, Faculty of Engineering
Address: Atbrivosanas aleja 115, Rezekne, LV-4601, Latvia

Abstract. Two types of electrical sheet steel M250-35A and M530-50A were used to cut by melting with a TruLaser 1030 technological system. It was observed that pressure of auxiliary gas had a major effect on kerf width b and cut angle deviation α . Nitrogen as an assisted gas has been taken. The basic parameters as laser power, cutting speed, focus position were constantly supported and the pressure was changed from 4 bar to 20 bar by step 2 bar. As well as the experimental results of gas pressure on entrance and exit kerf widths, have been analyzed and discussed in this study.

Keywords: laser cutting by melting, electrical steel, auxiliary gas pressure, kerf width.

I. INTRODUCTION

Automobile industry is constantly developing. The automotive market can be divided into two main parts, automobile manufacturers and the so-called independent segment, primarily charged with creating modules, replacement parts, and accessories intended both for installation in new vehicles and for aftermarket sales. As a result, the manufacturers of replacement parts and vehicles (occupying top positions in terms of total value of production, export volume, investments, and employment), look for new technology to make them rapidly, flexible, easily and with higher quality [1]. For example, American manufacturer of Tesla Motors reported that he has the best quarterly results in his history and in the first quarter of 2015, 10 030 cars have been made. Over the same quarter of the last year this represents an increase of 55 % [2]. Development of electrical vehicles production in this trend will increasingly strengthen. Basic module in this type car is an electric motor.

Over the past decade laser cutting has become into state-of-the-art automotive technology. As a new technology about rapidly designing, developing and testing of new constructions motors, is appeared laser technology. It offers a higher quality and flexibility when solving new constructive ideas. Laser cutting is an energetically and economically advantageous solution when cutting electrical steels for rotor and stator packages (figure 1) to electric cars.

In practice there are three methods of laser cutting: oxygen, through melting, sublimation (figure 2). They are happening at different temperatures, as well as they differed with their technological parameters and characteristics (figure 3).



Fig. 1. Rotor and stator lamellae and packages [3]

Criteria defined quality of the process are [4]:

- deviation from the required profile and dimensional tolerances;
- perpendicularity and angularity deviations of cuts (DIN EN ISO 9013:2003-7);
- widening of kerf;
- kerf roughness;
- lack of slag.

They are dependent on some factors. The main of them are: material properties; characteristics of a laser source; cutting speed; passing of an auxiliary gas, focus position, etc. (figure 3) [5, 6].

To realize a qualitative laser cutting technological process it has to choose a suitable laser source, as well as the auxiliary gas, gas nozzle and gas pressure [7].

For cutting of thin metal sheets in the industry have been mostly used disc Nd:YAG and Yb:YAG lasers, providing power densities from 10^7 W/cm² to 10^8 W/cm², sufficient to implement laser cutting process through melting.

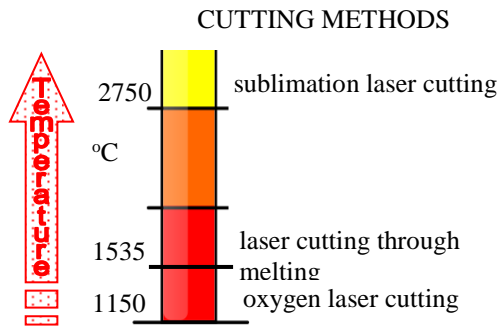


Fig. 2. Temperatures for electrical steel with which are realized the three methods of laser cutting

An almost parallel laser beam, which is usually invisible, is generated in the laser source and directed to the cutting head by mirrors, where it is focused by a lens on a small spot. In a treatment zone material is melted and ejected under the influence of inert gas flow which is directed to cutting area (figure 4). Simultaneously the gas puts pressure onto melts as well as hinders oxidation process and cools the processing area as helping to avoid forming a large heat affected zone around cut edge.

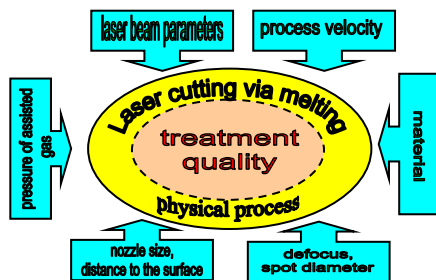


Fig. 3. Factors influencing on treatment quality of laser cutting process

The choice of optimum operating mode to submission of the auxiliary gas during the technological process is crucial for the quality in laser cutting process through melting. Two factors influence on forming of gas flow. From the one side are nozzle type and form, as the other one is distance between nozzle and working surface (figure 4). In modern technological system this distance is controlled by special sensor with aim to keep up optimum mode of treatment although possible defects on metal surface sheet.

Nozzle type for laser cutting through melting is different by these for technological operations as welding and hardening. In this kind of operation is important the nozzle diameter to be elected so that it is correspond with cutting width in the material. Only a certain portion of gas flow entering through nozzle is directed and came into the groove of cutting area. The distance from the nozzle end to the working surface is chosen depending on the design of the nozzle itself (its diameter). In the most general case it must be less than diameter of the nozzle itself, in order to avoid advent of turbulence and decreases of

the pressure. For smaller distances itself slit is appeared as additional small nozzle, that has a favorable influence on the processing quality.

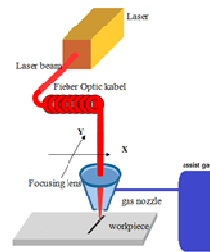


Fig. 4. Laser cutting by melting with assist gas

When cutting of thin sheet material having a thickness up to 1 mm with a good approximation, it may be considered that the parameters of gas stream are remained constant. In this case, a pressure gradient $\frac{\partial p}{\partial z}$ along the channel cut in realization of an isentropic process is given by the equation

$$\frac{\partial p}{\partial z} = \frac{p_{in} - p_a}{h} \quad (1)$$

where p_{in} is gas pressure on the enter, p_a – atmospheric pressure, h – thickness of the sheet.

When it comes to work with larger distance between the nozzle and working surface it is necessary the nozzle to be special designed for this purpose. Particularly this concern about the cases of gas pressures higher than 2 – 3 bar. Standard nozzles are with a diameter of 0,8 – 3,0 mm, as working distance is kept in the range of 0,5 – 1,5 mm.

II. EXPERIMENTS

Some series of experiments were done to investigate the influence of auxiliary gas pressure (nitrogen) on the geometry and cutting quality. The pressure was changed in the range from 4 bar to 20 bar by step 2 bar. Experiments were performed of prior prepared samples of electrical steel M250-35A and M530-50A. As a laser source was used TruDisk 2001. Technological parameters which in the course of studying remain constant are given in table 1.

Table 1
Technological parameters that were constant during experiments

Parameter	Value
Power of laser radiation P	2 000 W
Cutting speed v	50 m/min
Impulses frequency ν	20 000 Hz
Nozzle diameter	1,7 mm
Defocus position Δf (0,35 mm)	- 1,85 mm
Defocus position Δf (0,50 mm)	- 2,00 mm

The laser cut quality was monitored by measuring kerf width on the surface of electrical steel. The kerf width was measured with Neophot 2 CARLZEISS

JENA magnified 10 – 2 000 times. Both the entrance and exit surfaces kerf width (b_{entr} , b_{exit}) were measured.

When the cutting process by melting has been performed, in the processing area was observed a cut angle deviation (figure 5). To studied this effect we used a developed by us methodic based on Standards DIN EN ISO 9013:2003-7 and DIN EN ISO 12584 [8]. The deviation of perpendicularity is defined by line segment $u = AB$ or with that of cut angle α ($\text{tg}\alpha = AB/BC$),

$$\text{where } u = AB = (b_{entr} - b_{exit}) / 2,$$

$$BC = z - \text{lamella thickness}$$

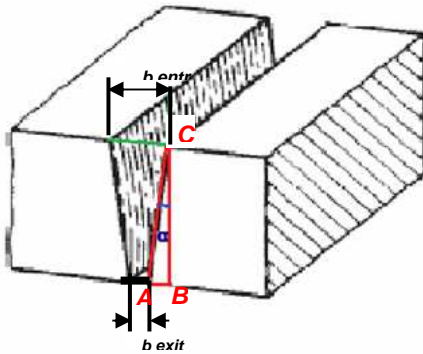


Fig. 5. Deviation from parallelism of the walls of cut

III. RESULTS OF STUDY

Dependence $b = b(p)$

Intervals of measured values cutting widths b_{entr} and b_{exit} in research range of gas pressure are shown in table 2.

Table 2
Alterations of kerf widths in studied pressure range

material thickness, mm	b_{entr} , μm	b_{exit} , μm
0,35	273÷283	182÷192
0,50	278÷288	180÷190

The results obtained for functional dependences of entrance width b_{entr} and exit width b_{exit} by pressure of inert gas p about samples of two blade steels (with thickness 0,35 mm and 0,50 mm), are shown respectively in figure 6 (a) and figure 6 (b).

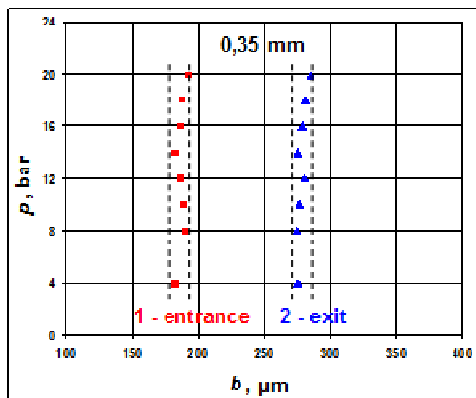


Fig. 6 (a)

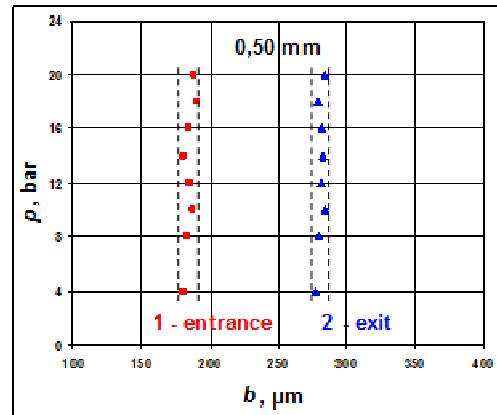


Fig. 6 (b)

Fig. 6. (a), (b) Experimental dependences of $b_{entrance}$ and b_{exit} as a function to technological gas

Dependence $\alpha = \alpha(p)$

When is carried out the experimental series (auxiliary gas pressure p - angle of inclination α) the pressure is increased in specified above interval, as the values given in table 1 were kept constant, too.

The results obtained for functional dependences $\alpha = \alpha(p)$ for two type sheet materials, are shown in figure 7.

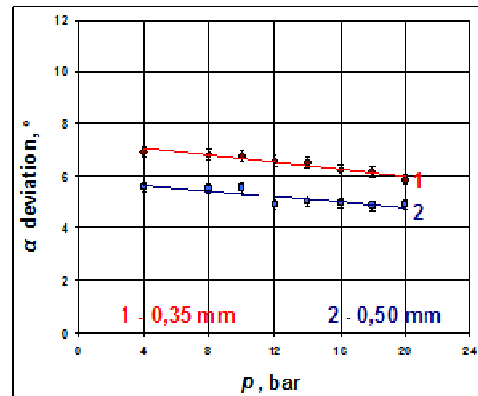


Fig. 7. Influence of pressure p of the auxiliary gas nitrogen on the angle of deviation from parallelism of the walls of cut $\alpha = \alpha(p)$

IV. DISCUSSION

Experiments that were conducted in studied ranges allow doing the following conclusions:

- ✓ Cutting widths b was kept constant during the studied interval of pressure p of the auxiliary gas. The alteration of the pressure in the interval 4 ÷ 20 bar is connected only with changes in cutting widths $\Delta b_{entr} = \Delta b_{exit} \approx \pm 5 \mu\text{m}$ about the samples of two steel grades. Maximum deviation of Δb is on the order of accuracy measurement.
- ✓ About both samples of plates with thicknesses respectively 0,35 mm and 0,50 mm, rapidity with which varies the cutting width Δb by gas pressure p , has minimum values, as:
 - cutting width on the entrance

- $\frac{\Delta b_{entr}}{\Delta p} = 0,56 \frac{\mu m}{bar}$ for samples with 0,35 mm;
- $\frac{\Delta b_{entr}}{\Delta p} = 0,50 \frac{\mu m}{bar}$ for samples
- cutting width on the exit
- $\frac{\Delta b_{exit}}{\Delta p} = 0,38 \frac{\mu m}{bar}$ for samples with 0,35 mm,;
- $\frac{\Delta b_{exit}}{\Delta p} = 0,31 \frac{\mu m}{bar}$ for samples with 0,50 mm.

Larger values of the ratio $\frac{\Delta b_{entr}}{\Delta p}$, than those of $\frac{\Delta b_{exit}}{\Delta p}$ are due to the fact that the processing were realized from surface heat source and absorbed laser radiation has a Gaussian intensity distribution.

- ✓ The angle α decreases with increasing pressure p of the auxiliary gas nitrogen. Changing the pressure from 4 bar to 20 bar generated minimal changes in the angle $\Delta\alpha \approx 10$.
- ✓ Optical analyses of the processing area showed that at values of the pressure p less than 8 bar cutting quality are getting worse. Below this gas pressure at the set out experimental technological parameters it is impossible to be disposed entirely and molten material from the processing area. The molten material is postponed on the output kerf as thus forming drops and other imperfections (figure 8).

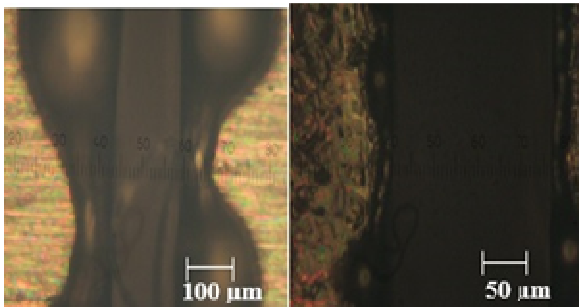


Fig. 8. Sections on cutting parts of samples with 0,35 mm (left photo) and 0,50 mm (right photo)

- ✓ The indicated interval $p = (10 \div 14)$ bar during laser cutting by melting with technological system TruLaser 1030 for samples with thickness 0,35 mm and 0,50 mm is proved optimal for achieving qualitative indicators about cut.

V. CONCLUSION

Actually, in the scientific literature there are a limited number of studies and analyzes for the processes as well as the efficiency to removing of melt from channel zone and formation of slag.

The complexity of the physical picture and also the practical needs required to maintain a high activity of research in the field of study of parameters related to gas supply.

It is interesting to investigate in addition to the role of the pressure of the auxiliary gas and that the distance from the edge of the nozzle to the work surface, and the change in diameter of the nozzle. This is planned in a future series of experiments. Such research will complement and enrich the picture of the interaction of laser radiation with matter and will eventually optimize the entire process more widely.

REFERENCES

- [1] Traczyk W., L. Hohmann, Poland: Spare parts – the strong point of Polish automotive industry, *Maschinen Markt*, 2016. <http://www.maschinenmarkt.international/english/eastern-europe/articles/528946/?cmp=nl-339&uuid=01EF1734-9490-4370-863B6D17432007A5>
- [2] Giovanni Tani, Luca Tonissani, Giampaolo Campana, Prediction of melt geometry in laser cutting, *Applied surface science* V 208-209 (2003), pp. 142-147.
- [3] <http://pearlengineeringco.com/>
- [4] Wolfgang Schulz, Vadim Kostykin, Markus Nieben, Jan Michel, Dirk Petring, Ernst W Kreutz and Reinhart Poprawe, Dynamics of ripple formation and melt flow in laser beam cutting, *J. Phys. D: Appl. Phys.* 32 (1999) pp. 1219–1228.
- [5] Schuöker, D. Dynamic Phenomena in Laser Cutting and Cut Quality. *Applied Physics*, 1986, B 40, pp. 9 -14.
- [6] Veiko, V. P., *Tehnologicheskie lasera i lasernoe izluchenie*, St. Petersburg, ITMO, 2007, 52c (Russian).
- [7] <http://www.din.de/cmd?level=tpl-home&contextid=din&languageid=en>
- [8] Steen W. M., *Laser Material Processing*// Third Edition, L.: Springer, 2003.

Influence of Defocus Position on Laser Cutting Process in Sheet Steel

Lyubomir Lazov, Hristina Deneva, Erika Teirumnieka

Rezekne Academy of Technologies, Faculty of Engineering
 Address: Atbrivosanas aleja 115, Rezekne, LV-4601, Latvia

Abstract. Some researches about influence of defocus position to carry out laser cutting technological process through melting when producing lamellae for electric motors are presented here. Experimental series at defocus position Δf in the range $-3,5$ mm to $+3,5$ mm with two grade electrical steels M250-35A and M530-50A are described, too. The experiments are performed with a technological laser system TruLaser 1030. Functional dependencies of cutting width from defocus position $b = b(\Delta f)$ have been shown. Theoretical relationships connected to the change of impact on a unit of area working spot over power density q_s of the laser radiation and interaction time t_{proz} (respectively cutting speed v), are examined too

Keywords: laser cutting, sheet steel, laser focusing.

I. INTRODUCTION

Production forecasts of electric vehicles show that over the next 10 – 15 years it will dominate over that of petrol and diesel cars [1]. Therefore for contemporary design new challenges are appeared to development and testing on new constructions of this type of cars. They impose demand for a new innovative technology when producing lamellae for stator and rotor packages of electric motors. Given the present punching technology for each new engine model it is necessary to make a special tool for production of new design lamella. This from technological and economic character is unprofitable. In general, the production of punching tool is connected with high costs and long time for its elaboration which are justified only in serial production. An innovative technological solution for cutting of lamellae by Si-sheet metal for the stator and rotor packages provides the laser technology for contour cutting.

For adopting of specific laser technology with given technological system for cutting of lamellae to production electric motors it is necessary to make thorough particular pilot studies. To achieve the desired quality during technological process it is important to test a number of parameters (figure 1) that are directly related to technology of the laser cutting such as: cutting speed v ; power density q_s of laser radiation in the treatment area; repetition rate ν ; pulse width τ ; defocus position Δf , etc.

In this paper the influence of defocus position as factor that is very important in processing of large size (3 000 mm x 1 500 mm) steel sheets will be examined. When processing such areas it is crucial to

keep the optimum operating mode throughout the treatment zone

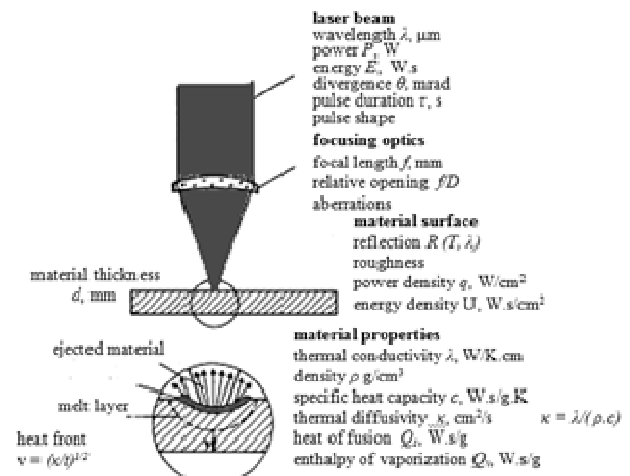


Fig. 1. Parameters which influence in the process of laser cutting [6]

The defocus position realized by the optical system provides the optimal diameter of spot d which in its turn is connected with two important technological parameters: power density q_s and impact time t_{proz} . [1,2,3,4,5].

II. THEORETICAL ASPECTS

In order to obtain a good quality in the process of laser cutting through melting, it is necessary the power density q_s of laser radiation and the interaction time t_{proz} to be at their optimum operating range providing the absorption of sufficiently energy with which could be melt material in the treatment zone

(fig. 2). Both technological parameters q_s and t_{proz} are connected with each other and with the diameter of the working spot d . Role of the working radius spot $r = d/2$ and its relationship with average power P and interaction time during the process are clearly seen from the dependence

$$t_{proz} = \frac{\pi^3 k^2 r^4 (T - T_0)^2}{4aA^2 P^2}, \quad (1)$$

where k – thermal conductivity;
 P - average power;
 A – absorption coefficient;
 a – thermal diffusivity;
 T – process temperature;
 T_0 – ambient temperature.

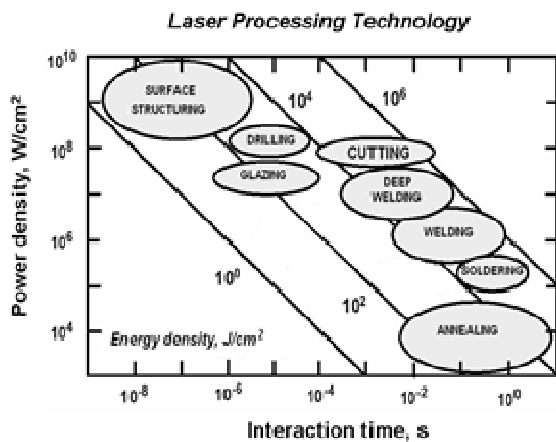


Fig. 2. Operational regimes for various processes of laser treatment

On the other hand power density in the area of working spot is given by

$$q_s = P / S, \quad (2)$$

where S is a unit of area on the working spot,
 P – power of the falling laser radiation on the surface.

Considering that

$$S = \pi d^2/4$$

where d is the diameter of working spot and substituting in (2) is obtained

$$q_s = 4P / \pi d^2. \quad (3)$$

Diameter of the working spot d is a complex magnitude and it is connected with parameters for quality of the laser radiation (figure 3) and with these of the optical system as you can be seen from the following dependence

$$d = 2r = M^2, \quad (4)$$

where f is a focal distance,

D - beam diameter,
 λ – wavelength of laser radiation,

M^2 – a parameter (a number to the diffraction – it describes an approximation of the actual laser beam with the Gaussian beam).

In the scientific literature M^2 is also described as K -factor – another measure of quality. It varies between $0 < K < 1$. In the basic Gaussian mode TEM₀₀ it is equal on 1. K – factor is related with wavelength λ , beam divergence θ and Gaussian beam waist r_0 as you can be see from the dependence

$$K = \frac{\lambda}{\pi r_0 \theta}, \quad (5)$$

where the divergence θ is defined with a limit of the relationship (fig. 4):

$$\theta = \lim \frac{r(z)}{z} = \frac{\lambda}{\pi r_0}, \quad (6)$$

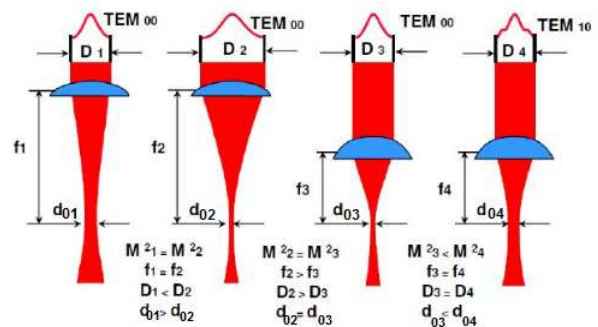


Fig. 3. Role and meaning of M^2 , D and f on the size of working spot d [7]

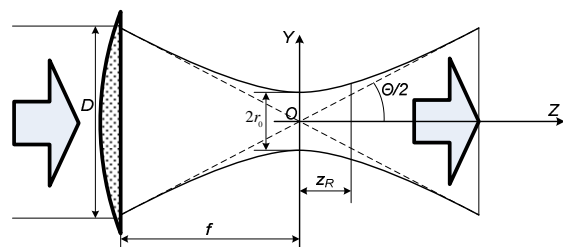


Fig. 4. A spatial distribution of the beam after its exit to the focusing system

A major parameter for the practice is the Rayleigh length z_R . It is defined as a distance from the beam waist (fig. 4) for which the cross sectional area of the laser beam is increased twice

$$z_R = \frac{\pi r_0^2}{\lambda} K = \frac{r_0}{\theta} \quad (7)$$

To realize desired qualitative technological result unto laser cutting, diameter of the working spot or its position to the working surface often is required to

change by the optical system. Laser beam can be placed with three positions: inside the sample (fig. 5a), on the target surface (fig. 5b) and above the sample surface (fig. 5c). In cases (a) and (c) is operated at defocus position Δf . When the focus is above the sample surface, Δf has positive values, and when it is under the surface – negative values.

When defocus position Δf is above or under the surface, the power density q_s reduces very quickly in comparison the operating mode - $\Delta f = 0$. When Δf is larger than Rayleigh length (fig. 4), the diameter d of the working spot is given by equation

$$d = \frac{D(z' + \Delta f)}{f + z'} \quad (8)$$

where D is the diameter of laser beam that incident on the lens, f – focal distance of the lens, and the parameter z' is defined by expression

$$z' = \frac{d_f f}{D - d_f} \quad (9)$$

where d_f is diameter of working spot in focus.

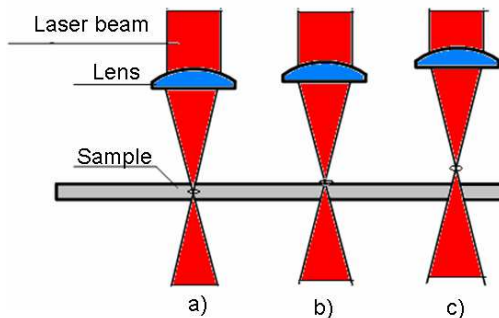


Fig. 5. Location of the working spot to the sample surface: a) inside the sample ($\Delta f < 0$); b) on the surface ($\Delta f = 0$); c) above the surface ($\Delta f > 0$)

When condition $\Delta f < z_R$ is satisfied, the diameter of working spot almost does not change and therefore the power density of laser radiation reduces very small at compared to that in $\Delta f = 0$.

By the equation (8) we can see that if $\Delta f > z_R$ the increasing of defocus position Δf the diameter d of working spot is increased too, as the dependence is linear. The power density q_s is inversely proportional to the second degree of diameter d (3). It follows that the power density decreases very quickly with increasing of defocus position Δf , as well as optimal technological cutting regime is interrupted and required quality of cut is impossible to obtain.

III. RESULTS

To study the influence of defocus position Δf on kerf width b and quality, some experiments were carried out in conditions close to industrial system TruLaser 1030 [8]. Samples of electrical steel M250-35A and M530-50A suitable for lamellae of rotor and stator packages with thickness respectively 0,35 mm and 0,50 mm, are used. As a laser source in the system is Disk Yb:YAG laser emitting a radiation with wavelength $\lambda = 1,03 \mu\text{m}$.

On based our studies and methodic published in previous papers [9, 10, 11], to current report, the parameters systemized in table 1 are selected as constants. The study influence of defocus position Δf is realized in the range from $-3,5 \text{ mm}$ to $+3,5 \text{ mm}$ i.e. as well as with immersed focus and with taking out above the surface (see fig. 5).

There are studies on the effect of defocus position to the width input and output of the cut i.e. dependencies $b_{in} = b_{in}(\Delta f)$ and $b_{out} = b_{out}(\Delta f)$, are studied too. Concerning the quality of treatment zones and areas around them were carried out optical observations with microscope Neophot2 CARLZEISS JENA [12] at a magnification of 10 to 2 000 times.

Table 1
 Technological input parameters for laser system trulaser 1030

Parameter	Value
power P , W	2 000
cutting speed v , m/min	50
repetition rate ν , Hz	20 000
nozzle diameter ϕ , mm	1,7
pressure of N_2 p , bar	14
focus distance f , mm	200

Obtained results for functional dependencies of input width b_{in} and output width b_{out} to the defocus position Δf for both grade steels are given respectively in fig. 6 and fig. 7.

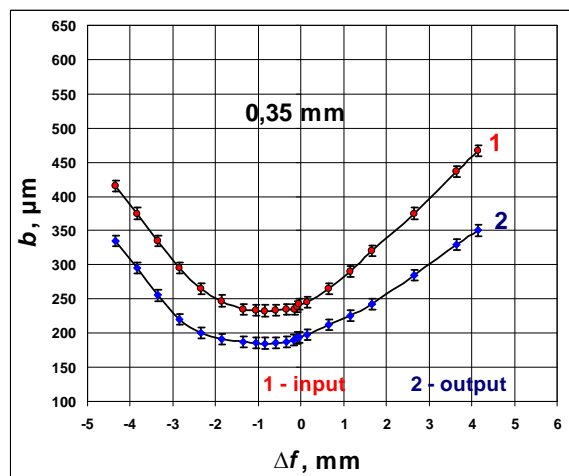


Fig. 6. Graphics of experimental dependencies $b_{in} = b_{in}(\Delta f)$ and $b_{out} = b_{out}(\Delta f)$ for samples M25-35A

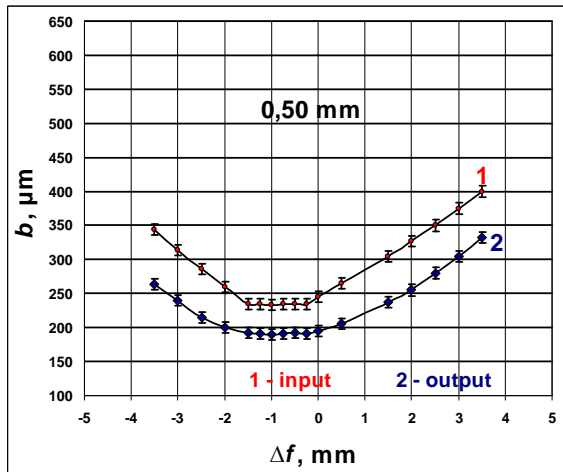


Fig. 7. Graphics of experimental dependencies $b_{in} = b_{in}(\Delta f)$ and $b_{out} = b_{out}(\Delta f)$ for samples M530-50A

Accumulated molten drops on the cutting edge are noted too on the samples with thickness 0,35 mm when defocus position is $\Delta f > +2,65$ mm (fig. 8a) and $\Delta f > -3,5$ mm (fig. 8b).

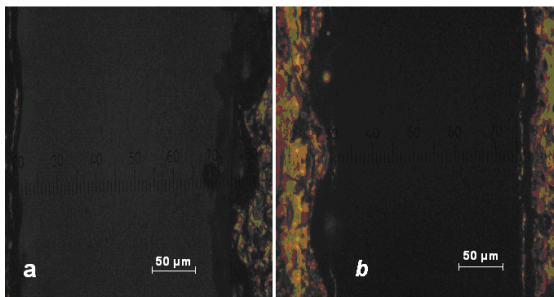


Fig. 8. Photographs of samples with thickness 0,50 mm and 0,35 mm at defocus margin Δf greater than +2,5 mm and -3,5 mm

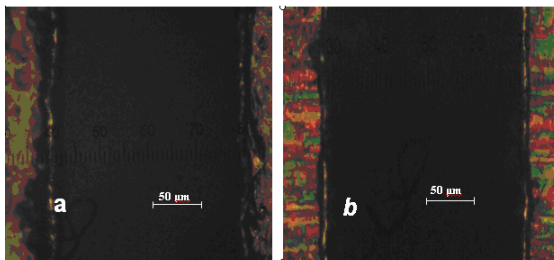


Fig. 9. Photographs of samples M250-35A at defocus position $\Delta f = -0,85$ mm and $\Delta f = -1,0$ mm for samples of M530-50A

Optical observations of cutting zone shown some good quality results at values of $\Delta f = -0,85$ mm (fig. 9) и $\Delta f = +0,65$ mm.

IV. DISCUSSIONS

From the analysis of experimental results it can be made following conclusions:

- With increasing of defocus position Δf in a plus direction up to + 3,5 mm input cutting width b_{in} is increased nearly linear $\Delta b \sim 170 \mu\text{m}$. But in minus direction $-\Delta b \sim 110 \mu\text{m}$, i.e. there is a slight change of cutting width b at immersed focus in the material.

Such trend is observed and for the output cutting width bout.

- Left parts of graphics are little steep i.e. cutting width is changed faster in minus direction. This dependence is more strongly expressed for samples with less thickness: 0,35 mm. The rate at which input cutting width increases in the interval to variation of defocus position $\Delta f = (0,65 \div 4,15)$ mm for M250-35A, was $\Delta b_{in} / \Delta f = 48,55 \mu\text{m} / \text{mm}$; and $\Delta b_{in} / \Delta f = 62,5 \mu\text{m} / \text{mm}$ in the range $\Delta f = (-4,35 \div -1,85)$ mm.

- Significant change of the cutting width Δb in the range of defocus position $\Delta f = (-0,15 \div -1,35)$ mm for the samples of steel M250-35A and $\Delta f = (-0,25 \div -1,5)$ mm - at samples of M530-50A, is not observed. This is explained by the fact that in the indicated interval are and the values of beam waist (Rayleigh length z_R). Cutting width is changed by $\Delta b = \pm 5 \mu\text{m}$ in the above ranges of defocus position Δf .

- Microscopic observations and analyzes are shown a good cutting quality on the input as well as on the output when defocus position were in the range $\Delta f > +1,0$ mm and $\Delta f > 2,0$ mm for both samples. This is due to the fact that at these technological regimes obtained melt was removed well from the N_2 gas supplied in the treatment zone with pressure of 14 bar.

- Minimum input cutting width $b_{in} = 230 \mu\text{m}$ was observed at $\Delta f = -0,15$ mm for samples of steel M250-35A, and $\Delta f = -0,25$ mm - for samples of M530-50A.

V. CONCLUSION

Studies have shown that the magnitudes q_s and t_{proz} influencing on the laser cutting process through melting of sheet steel material for lamellae of electric motors, are in complex dependencies with the diameter of working spot d and conditions of focusing as well as with a number variables connected with the beam quality. Knowledge of the relationships between them helps to shortening the path for optimization of the technological process - it enables to evaluate the effect on each of these parameters over the studying process. Experimental and theoretical analyzes are shown that the defocus position Δf is an important factor having a significant influence on the technological mode and on the quality of the processing. If you must use mixed units, clearly state the units for each quantity that you use in an equation.

REFERENCES

- [1] Grigoryants, A. G., Osnovy lazernoy obrabotki materialov. M., Mashinostroyeniye, ISBN: 5-217-00432-0, 1989, 301s.
- [2] Grigoryants A., I. Shiganov, A. Misyurov Tekhnologicheskkiye protsessy lazernoy obrabotki, izd. MG TU im. N. Baumana, Moskva, ISBN 5-7038-2701-9, 2006.
- [3] Schuöcker, D. Dynamic Phenomena in Laser Cutting and Cut Quality. Applied Physics, 1986, B 40, pp. 9 -14.
- [4] Schuöcker, D. Handbook of the EuroLaser Academy, Chapman&Hall, London, 1998, ISBN 0412819201.
- [5] Veyko, V. P. Tekhnologicheskkiye lazery i lazernoye izlucheniye. Sankt-Peterburg, ITMO, 2007, 52 s.

- [6] VDI-Technologiezentrum Physikalische Technologien: „Präzise Optische Behandlung von Festkörpern - Oberflächenbearbeitung“ (Handbuchreihe: Laser in der Materialbearbeitung, Bd. 5) VDI-Verlag GmbH, Düsseldorf, 1996
- [7] Florian Scherm Lasermaterialbearbeitung, VL_Lasermaterialbearbeitung_WS0910.pdf, powerpoint presentation- Folie 35 (35 pp); http://www.metalle.uni-bayreuth.de/de/download/teaching_downloads/Vorl_Fuegetechnik/VL_Lasermaterialbearbeitung_WS0910.pdf
- [8] <http://www.us.trumpf.com/en/products/machine-tools/products/2d-laser-cutting/laser-cutting-machines/trulaser-1030-fiber.html>
- [9] Deneva, H., Izsledvane na procesa lazerno rjazane na lameli za rotorni I statorni paketi. Dissertation, TU – Gabrovo, 2014.
- [10] Lazov, L., H. Deneva. Investigation of Cutting Width from Laser Power and Velocity. IJETCAS, Issue 4, Vol 1, 2 & 3, March - May, 2013, ISSN 2279-0047.
- [11] Lazov, L., H. Deneva. Investigation on the Influence of the Process Parameters Power and Velocity to Laser Cutting of Lamellae. Journal of the Technical University - Sofia, Plovdiv branch, Bulgaria, Fundamental Sciences and Applications, Vol. 21, Book 2, 2015, ISSN 1310-8271.
- [12] http://microscopy.zeiss.com/microscopy/en_de/products.html L. Bass, P. Clements, and R. Kazman. *Software Architecture in Practice*, 2nd ed. Reading, MA: Addison Wesley, 2003. [E-book] Available: Safari e-book.

Optimization of CO₂ Laser Parameters for Wood Cutting

Lyubomir Lazov, Pavels Narica, Janis Valiniks, Antons Pacejs, Hristina Deneva,
Dainis Klavins

Rezekne Academy of Technologies
Faculty of Engineering
Rezekne, Latvia
Lyubomir.Lazov@rta.lv

Abstract. By taking advantage of the best characteristics of wood, modern production methods can offer hard wearing and ecological solutions in industrial construction, house building, machinery construction, furniture manufacturing, transport and many other industries. Laser cutting process is an alternative choice to prepare the final shape of wood parts. Materials like wood have good laser light absorption of wavelength 10600 nm. In this paper a CO₂ laser system with a maximum continuous-wave output power of 150 W is described and used in studying laser cutting process of wood materials. Cut depth is evaluated with variation of values of laser power and cutting speed. Additionally, optimal values of parameters for laser cutting of different wood plate thicknesses are determined and graphs are created showing the results.

Keywords: CO₂ laser, laser cutting, laser parameters optimization, wood.

I. INTRODUCTION

Lasers become more widespread by the day and are used by the industry more often. It can be observed that lasers replace other industrial machines and systems that people are accustomed to. Lasers are commonly used to weld, cut, mark, engrave different types of materials. There are a lot of reasons and evidence about laser materials processing advantages, and in this paper particular case of laser wood cutting is described in more detail. In general, the development of modern laser cutting technology occupies one of the leading positions compared with other materials processing methods [7].

Due to high power densities lasers can produce it is possible to achieve different kinds of macro-, micro-, and even nano- processing of materials. Mainly, laser is used for processing of such materials as metals, semiconductors, leather, different alloys, plastics, rubber, ceramics, wood etc. Laser cutting technology has quite a lot of advantages in comparison with other cutting equipment, i.e., clean cut, cutting of extremely fine contour and various thicknesses of materials as well as combinations thereof using only a single operation. Contactless treatment results in insignificant deformation of the material and high accuracy [1].

The aim of this paper was to determine relationship between the cut depth and laser parameters by performing analysis of obtained measurements during preliminary experimental investigation. As a result, options for optimization of

laser parameters for wood cutting using CO₂ laser were considered.

II. METHODOLOGY

A. Materials

Material which was studied is spruce cross laminated timber (CLT) panel. Fig. 1 shows a schematic view of a CLT panel configuration. A cross-section of a CLT element has at least three glued layers of boards that are finger-jointed using structural adhesive and placed in orthogonally alternating orientation to the neighboring layers. Lumber is visually-graded or machine stress-rated and is kiln dried. [4].

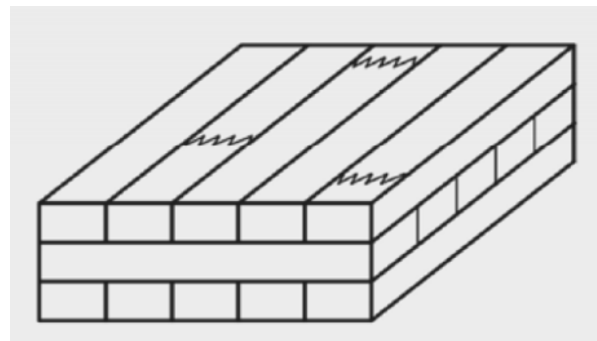


Fig. 1. CLT panel configuration [8]

Humidity of 13% +/-3% for boards of cross laminated timber (X-Lam) was set in the factory before packaging the panels. The humidity was

estimated by electrical resistance method as it is shown in Fig. 2.

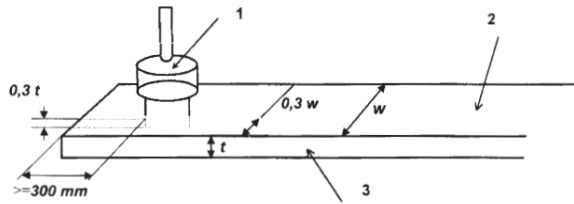


Fig. 2. Method of measuring humidity of board by electrical resistance, where 1 – hammer electrode, 2 – face, 3 – edge, t – thickness, w – width [9]

In panel production process timber sample was planed and subjected to pressure of 8 bar for 100 minutes. 60 mm thick panel was used for samples, consisting of three layers of crosswise compound, with board thickness of 20 mm. After all, CLT panel was cut into samples with 160 mm x 160 mm x 30 mm size as it is shown in Fig. 3.

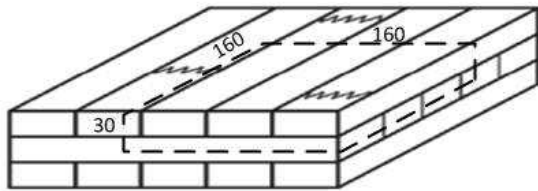


Fig. 3. Cut samples from CLT panel

B. Experimental set-up

In this study CHANXAN CW-1325 CO2 continuous-wave laser system with wavelength of 10060 nm was used. Schematic view of experimental set-up is shown in Fig. 4.

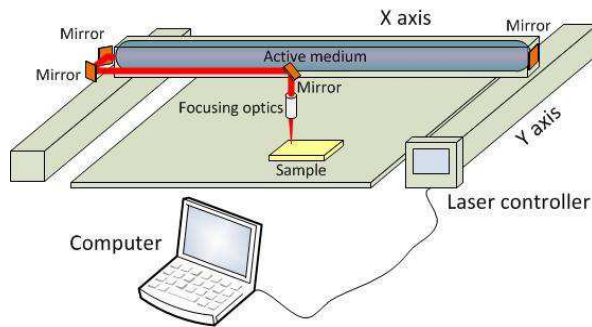


Fig. 4. Schematic view of experimental set-up

Laser system characteristics are shown in Table I.

Table I.
CHANXAN CW-1325 characteristics

Laser type	CO2 glass tube
Wavelength λ [nm]	10600
Laser power P [W]	0 - 150
Cutting area [mm]	2500 x 1300
Scanning speed [mm/s]	1 - 400
Cooling type	Water Colling
Assisted gas	Air
Focal lens diameter [mm]	19
Focus distance [mm]	63.5
Focal spot diameter [μ m]	~60

There are two main modes of laser scanning provided by the laser system - raster mode and vector mode (Fig. 2). Raster mode (Fig. 5 - A) traces the laser beam across the surface in a back-and-forth motion and is good for engraving. Vector mode (Fig. 5 - P) follows the path of the outline of the shape and is good for cutting [2].

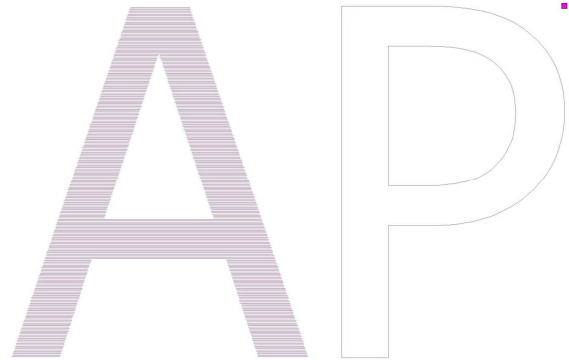


Fig. 5. Sample comparison of two modes of laser scanning provided by CHANXAN CW-1325

Fig. 6 shows that samples were cut by the CO2 laser in a form of a 10 x 10 matrix with each cell having different combination of laser parameters values. The variable parameters were power regulation coefficient k_P for columns and scanning speed v for rows. Values of former varied from 10% to 100% with step being 10%, while values of latter varied from 10 mm/s to 100 mm/s with step being 10 mm/s.

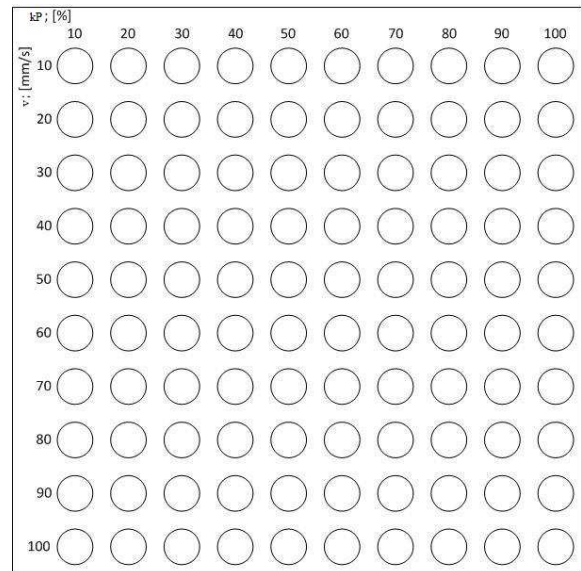


Fig. 6. Matrix of 100 cells with different combinations of values of laser parameters

Thickness of CLT panel was selected so that during experiments the material is not cut through and the depth of cut d can be measured for all combinations of values of laser parameters used during experiment.

Cross-sections of CLT panels were studied to determine the depth d of laser cuts as it is shown in Fig. 7.

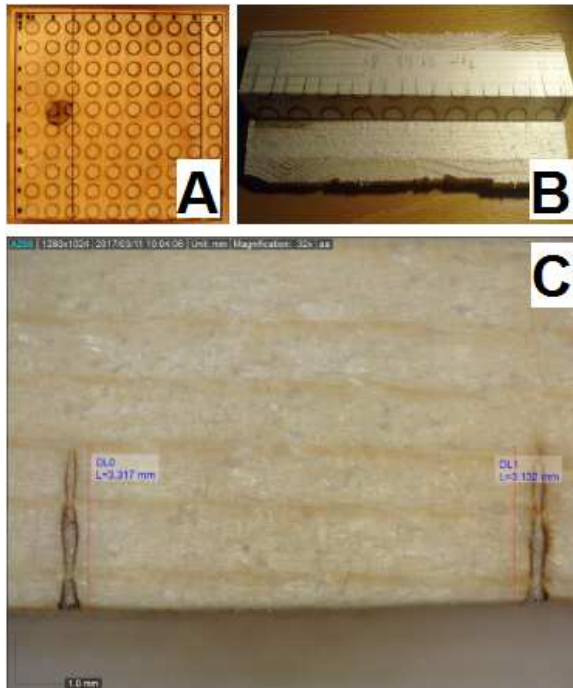


Fig. 7. A – sample with cut cells, B – overview of cross-section of CLT panel, C - cuts measurements under microscope

Samples were cut in such a way as to obtain 4 measurements for one cut (Fig. 8).

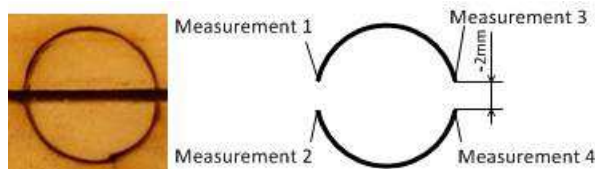


Fig. 8. Place of measurements and width of a circular saw cut

In total from 800 measurements, but 109 were excluded due to errors (wrongly entered parameters, cuts located in lamella gluing place).

C. Additional equipment

For cut depth measurements multi-purpose zoom microscope Dino-Lite Edge AM7115MZT (Fig. 9) was used, technical specifications of which are shown in Table II.

Resolution	5M pixels (2592x1944)
Magnification	20x~220x
Lighting	8 white LEDs
Unit Dimension	10.5cm (H) x 3.2cm (D)

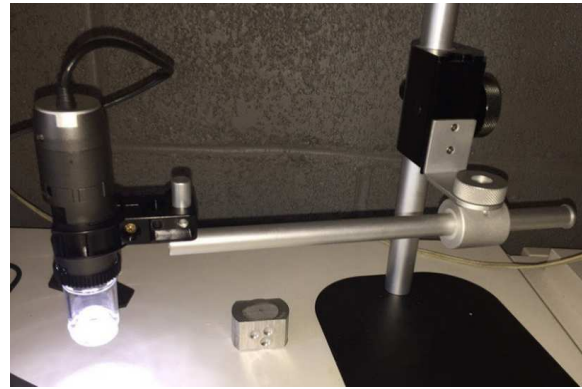


Fig. 9. Multi-purpose zoom microscope Dino-Lite Edge AM7115MZT

Power measurement sensor OPHIR F150A-BB-26 used during measurements of laser power is shown in Fig. 10. Its specifications are summed up in Table III.

Absorber Type	Broadband
Spectral Range [μm]	0.19 - 20
Aperture diameter [mm]	26
Power Range [W]	0,05 - 150
Power Noise Level [mW]	3
Max Average Power Density [kW/cm^2]	12
Max Energy Density [J/cm^2]	10
Power Accuracy [+/- %]	3
Cooling	fan



Fig. 10. Power measurement sensor OPHIR F150A-BB-26

III. RESULTS AND DISCUSSION

In this work a power measurement of a CO₂ laser was carried out. This way values of power regulation coefficient k_P were mapped to measured laser power P . The measured data was studied and plotted in form of a graph shown in Fig. 11.

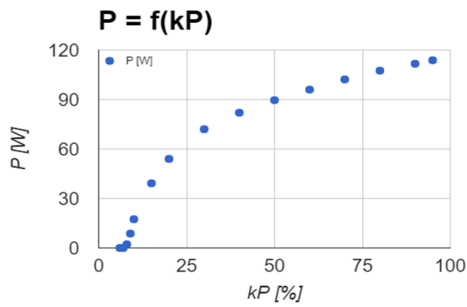


Fig. 11. Mapping of values of power regulation coefficient k_P to laser power P

During preliminary examination of experimental data, it was determined that there exists an alternative way of approaching measurements. Two main laser parameters used during experiments were laser power P and scanning speed v , but from these two parameters an additional parameter can be derived called linear energy density L . Basically, it describes how much energy per unit length material receives from laser beam. To calculate the linear energy density L formula (1) is used.

$$L = \frac{P}{v} \left[\frac{J}{mm} \right] \quad (1)$$

In Fig. 12 one can see, that for specific laser power P there is a certain relationship between cut depth d and scanning speed v . Lower values of scanning speed v result in higher values of linear energy density L , given laser power P is constant. Thus, higher values of linear energy density L correspond to deeper cuts. Nevertheless, the graph in Fig. 12 is hard to interpret, as relationship can only be observed if laser power P is constant. Here it may be easy to choose a necessary scanning speed v for accomplishing laser cutting of wood with specified thickness d , but to determine the scanning speed v for another laser power P a new similar graph would be required.

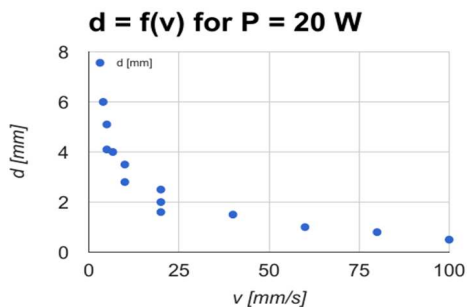


Fig. 12. Mapping of cut depth d value with constant power P and changing scanning speed v

In Fig. 13 one can see the same problem once again. For specific scanning speed v there is a certain relationship between cut depth d and laser power P . Higher values of laser power P result in higher values of linear energy density L , given scanning speed v is

constant. As in the previous case, higher values of linear energy density L correspond to deeper cuts. Nevertheless, the graph in Fig. 13 is also hard to interpret, as relationship can only be observed if scanning speed v is constant. Here it may be easy to choose a necessary laser power P for accomplishing laser cutting of wood with specified thickness d , but to determine the laser power P for another scanning speed v a new similar graph would be required.

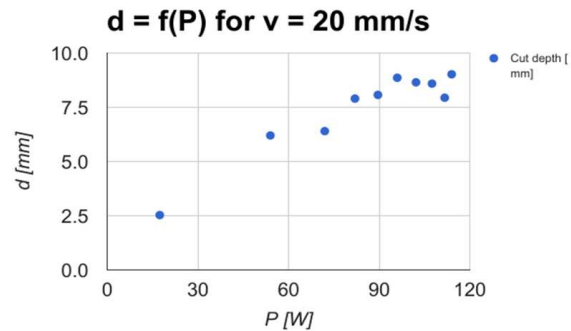


Fig. 13. Mapping of cut depth d value with constant scanning speed v and changing power P

The solution for both problems described above is to plot cut depth d against linear energy density L (Fig. 14). Linear energy density L is calculated using formula (1) and thus is a function of laser power P and scanning speed v both of which do affect cut depth d .

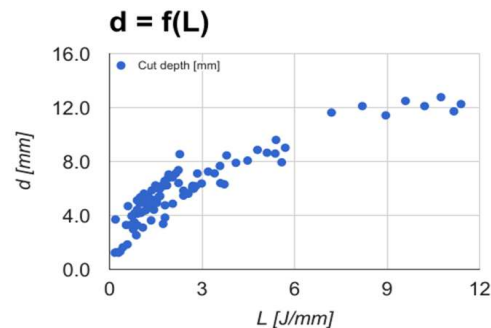


Fig. 14. Mapping the values of cut depth d against linear energy density L

In Fig. 14 one can see a clear relationship between linear energy density L and cut depth d . Interestingly enough, the relationship $d = f(L)$ seems valid no matter what actual values of both laser power P and scanning speed v were used during preliminary experiment. To test it, additional two experiments were carried out, where for specific values of linear energy density L values of laser power P and then values of scanning speed v were varied (Fig. 15).

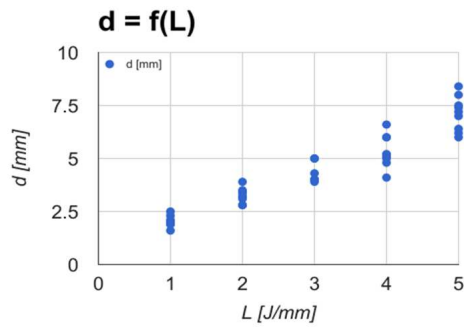


Fig. 15. Cut depth d as function of linear energy density L

Both Fig. 14 and Fig. 15 display that, given one knows the value of linear energy density L , then it is possible to foresee approximate possible cut depth d for specific material, i.e., wood. One can also observe that it is possible to make deeper laser cuts, while minimizing value of linear energy density L . Based on Fig. 14 it may look that linear energy density L is directly proportional to the square of laser cut depth d . This means, one requires more and more energy per unit length to cut through thicker plates. This seems true, as the diameter of laser beam spot increases with further distance from lens focus, resulting in weaker intensities.

Interestingly enough, the optimization of values of laser parameters is possible, but further study on effects of linear energy density L is required. Basically, there are two ways one could optimize the wood cutting process if only the cut depth d is important: either by reducing the amount of time T or by reducing the amount of energy E required to do the cutting. Ideally, for certain length and depth of cut both time and energy must be minimized (Fig. 16).

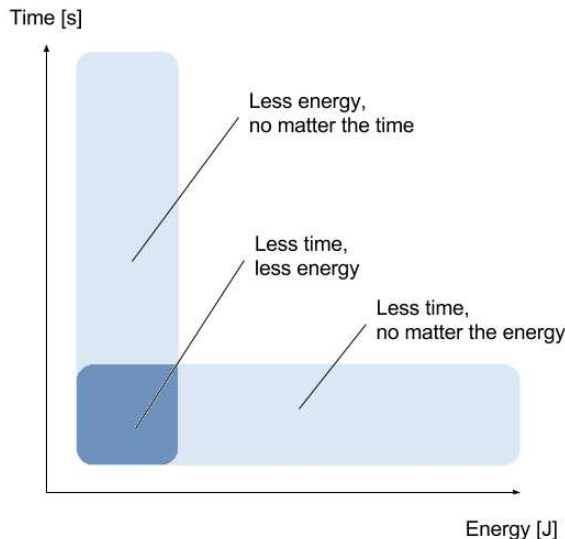


Fig. 16. Optimization of laser cutting by minimization of time and energy necessary for the process

Formula (2) is used to calculate time required to do the laser cutting for certain $length$. One can immediately see that cutting time T can only be

minimized by increasing the value of scanning speed v , given $length$ stays constant.

$$T = \frac{length}{v} [s] \quad (2)$$

Formula (3) is used to calculate energy required to do the laser cutting for certain $length$. Here one can observe that energy E can be minimized by decreasing the value of linear energy density L , given $length$ stays constant.

$$E = P \cdot T = \frac{P \cdot length}{v} = L \cdot length [J] \quad (3)$$

It can be seen in formula (1) that linear energy density L itself can be minimized either by decreasing laser power P or by increasing scanning speed v .

To be able to optimize laser wood cutting process, i.e., find best values for laser power P and scanning speed v , an algorithm is required. First, linear energy density L must be determined for specific cut depth d . Next, either lowest possible laser power P or highest possible scanning speed v must be determined, while keeping linear energy density L constant.

Thus, supposing the cut $length$ is given and is constant, one must minimize linear energy density L in order to minimize total energy E required for cutting at the same time maximizing scanning speed v in order to minimize total time T required for cutting. In the end, necessary minimal laser power P required for cutting some plate of given thickness d can be calculated as the product of linear energy density L and scanning speed v .

IV. CONCLUSION

Preliminary investigation resulted in understanding the usefulness of linear energy density L parameter and its relationship with cut depth d . On the one hand in Fig. 14 one can observe a clear functional relationship between linear energy density L and cut depth d , while on the other hand in Fig. 15 one can see that for specific value of linear energy density L cut depth d can deviate from expectations.

For this specific reason additional experiment was carried out for PMMA acrylic material. Here, linear energy density L , no matter the actual values of laser power P and scanning speed v , always corresponded to some specific cut depth d . PMMA acrylic compared to wood has more uniform and homogeneous structure, which thus results in more precise results and measurements. After all, the unique structure of wood materials results in less precise cut depths d for specific values of linear energy density L .

Given, one knows necessary amount of linear energy density L necessary for cutting specific cut depth d , one has to determine which approach is better to take – cutting fast while wearing and tearing

CO2 laser tube and mechanical parts of X/Y coordinate system or cutting slow and wasting time.

All in all, there is a clear need for further thorough studies on effects of linear energy density L in context of laser cutting process so as to establish a database that will serve as a useful reference for laser cutting of different materials. It is still important to know and understand how specific values of linear energy density L , when applied to some material, will behave for extremely low and high values of laser power.

In conclusion, this study is the first one in the coming series of future articles where further features of CO2 laser will be studied such as “dot mode”, i.e., laser radiation can be time controlled and higher values of linear energy density L can be set, as wells as raster mode where effects of planar energy density on the depth of engraving are to be studied.

REFERENCES

- [1] Wairimu G., Ikua B.W., Kioni P.N. CO2 laser machining of wood, perspex and glass with and without use of assist gas. International Journal of Scientific Research and Innovative Technology, 12, 2015, pp. 128-133.
- [2] Shaikh A.A., Varsi A.M. Investigation on depth of cut by varying cutting parameters for single pass cutting on CO2 laser. International Journal of Innovative Research in Science, Engineering and Technology. Vol.3, Issue 9. 2014, pp. 15917-15925.
- [3] Radovanovic M., Madic M. Nonconventional Technologies Review, 4, 2001, pp. 34-42.
- [4] Mohamed M., Sylvain Gagnon Eng., Bradford Douglas K., Podesto Lisa P.E. Introduction to Cross Laminated Timber. Wood Design Focus V.22, N.2. 2002, pp. 3-12.
- [5] Moisture content of piece of sawn timber- Estimation by electrical resistance method. .British Standard. 2002, pp. 1-10.
- [6] Rongrong Li., Xiaolei G., Pingxiang C. Optimization of laser cutting parameters for recombinant bamboo based on response surface methodology. Nanjing Forestry University, Faculty of Material Science and Engineering.. 2016, pp. 275-286.
- [7] Design for Manufacturability: Maximizing the Advantages of Laser Cutting http://cdn2.hubspot.net/hub/327041/file-2067602000-pdf/Design_for_Manufacturability.pdf . Laserage. 2014, pp.7.
- [8] Timber structures- Cross laminated timber- Requirements. EN 16351 2012 01 01 EN, pp.7.

Minimizing the Detent Force in Permanent Magnet Linear Synchronous Motor for driving of 2D Laser Marking Table

Lyubomir Lazov¹, Peter Uzunov²

Latvia Academy of Technologies, Rezekne, Latvia¹
Electricity System Operator, Sofia, Bulgaria²

Abstract. In this paper the research results for reducing the detent force in one innovative permanent magnet linear synchronous motor for 2D laser marking system was published. There two methods are used. The first of these methods features the usage of two additional end teeth with chamfers in the magnetic circuit of the movable part. In the second method, the teeth of the ferromagnetic core are with different lengths. As a result of the change of the air gap permeance in both cases substantial reduction of detent force is achieved, in multiples at times. The results obtained are based on modeling and analyzing the linear motor magnetic field by the Finite Element Method (FEM). Provided experimental research of the linear motor prototype proves the correctness of the simulations results.

Keywords: Laser Marking, Permanent Magnet Linear Synchronous Motors, Detent force, Finite Element Analysis.

I. INTRODUCTION

Nowadays, linear motors are meant to replace a system using a rotating motor and a transmission to realize a linear movement. With linear motors the performances increase considerably since the mechanical limitations are removed. This leads to a better precision, a higher acceleration and a higher speed of the moving part. Therefore, direct drives with linear motors are increasingly used in industrial applications although these solutions need often more investment costs.

In [1] the design of PMLSM drive table for laser marking system of small details has been described. This is one flat type iron core Permanent Magnet Linear Synchronous Motor (PMLSM).

Its dynamics and control are hindered by the presence of detent force.

Due to permanent magnets (PM), a high force of attraction between the supply part and the magnetic way appears. For the same propulsion force, the ratio between the attractive force and the propulsion force is about 5 times without additional cooling. Furthermore, due to the teeth in the mover core, this type of motor can have a higher cogging force.

The force of attraction between the iron-core of the primary and the PM of the secondary is known as the cogging force and it occurs in both the rotational and linear machines. In linear machines, there is an additional force due to the finite length of the mover, which is called the end-effect force [2].

The end-effect force is caused only by the interaction of the end teeth with magnets, whereas the

cogging force is produced by all teeth along the iron core.

Both the cogging force and the end-effect force combine to produce the net detent force of a PMLSM. Mathematically,

$$F_{\text{detent}} = F_{\text{cogging}} + F_{\text{endeffect}} \quad (1)$$

Detent force generates pulsations in propulsion force and causes disturbances in the control of PMLSM. Therefore, measures must be taken for its reduction.

For this reason, special techniques for minimizing this detent force are used. One of them is the usage of additional teeth end on both sides of the ferromagnetic core [3]. Another way for minimizing the cogging force is the usage of teeth of ferromagnetic core with unequal length [4].

In this paper the both techniques for the minimizing the detent force are analyzed. The analysis of the detent force in both cases is very difficult to perform with an analytical method and therefore FEM is used to show their impact on the detent force. Detent force was calculated on the base of the results from FEA of the motor magnetic field. As this magnetic field in both cases is flat parallel, 2D FEM was used for the simulations.

The 3D CAD model of PMLSM under study in this paper is shown in Fig.1 [1].

The main technical specifications of the linear servomotor are given in Table I.

In this article, the research results are published for decreasing the detent force of this PMLSM which

ISSN 1691-5402

© Rezekne Academy of Technologies, Rezekne 2017
<http://dx.doi.org/10.17770/etr2017vol3.2651>

drives the two-coordinate table to which details for laser marking are affixed.

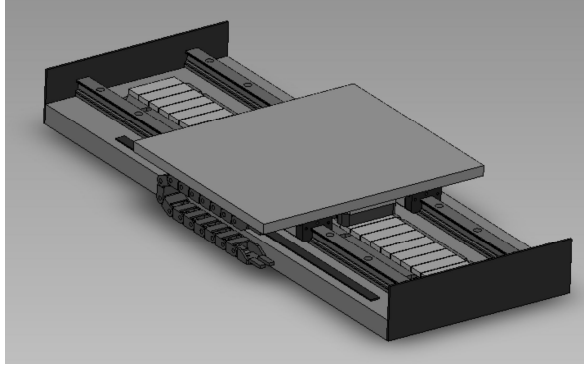


Fig. 1. 3D CAD model of PMLSM

II. FEM MODELING

The motor magnetic field modeling has for basics the Maxwell's laws. Here the static magnetic field exited only from PMs in 2D case is modeled.

The general differential form of the Maxwell's equations is:

$$\vec{\nabla} \times \vec{H} = \vec{J} \quad (1)$$

$$\vec{B} = \mu \vec{H} \quad (2)$$

$$\vec{\nabla} \cdot \vec{B} = 0 \quad (3)$$

where: \vec{H} is the vector of magnetic field; \vec{B} is the vector of magnetic flux density.

Table I
Specifications of the test bench

N	Quantity	Value
1	Number of phases	3
2	Number of poles	10
3	Slot number	12
4	Rated phase voltage (V)	50
5	Magnetic flux density in teeth and core yoke (T)	1.6
6	Sizes of permanent magnets (mm)	76.2/12.7/6.35
7	Air gap (mm)	1
8	Pole pitch (mm)	15
9	Tooth pitch (mm)	12.5
10	Rated phase current (A)	9.0
11	Propulsion force (N)	180
12	Speed (m/s)	3
13	Mover mass (kg)	2.0
14	Efficiency	0.85
15	Power factor	0.9

Furthermore, from (3) by applying one particular property of vector calculation the magnetic potential vector \vec{A} is defined as:

$$\vec{B} = \text{rot } \vec{A} \quad (4)$$

If a material is nonlinear, the permeability μ , is actually a function of \vec{B} :

$$\mu = \frac{\vec{B}}{\vec{H}(\vec{B})} \quad (5)$$

Then, (1) can be rewritten as [5]:

$$\vec{\nabla} \times \left(\frac{1}{\mu(\vec{B})} \vec{\nabla} \times \vec{A} \right) = \vec{J} \quad (6)$$

For a linear isotropic material (and assuming the Coulomb gauge, $\vec{\nabla} \cdot \vec{A} = 0$), (6) reduces to:

$$-\frac{1}{\mu} \vec{\nabla}^2 \vec{A} = \vec{J} \quad (7)$$

In the general 3-D case, \vec{A} is a vector with three components. However, in the 2-D planar and axis-symmetric cases, two of these three components are zero, leaving just the component in the "out of the page" direction.

The advantage of using the vector potential formulation is that all the conditions to be satisfied have been combined into a single equation. If \vec{A} is found, \vec{B} and \vec{H} can then be deduced by differentiating \vec{A} . The form of (6), an elliptic partial differential equation, arises in the study of many different types of engineering phenomena.

The distribution of linear motor static magnetic field can be found by solving the equation (7) with the program FEMM [5].

FEMM retains the form of (6), so that magnetostatic problems with a nonlinear $B-H$ relationship can be solved.

The problem was solved in area, shown on Fig. 2.

The problem was solved under Dirichlet boundary conditions applied to outside border of the model – the circle around the geometry of the linear motor, as was shown in Fig. 2.

$$\vec{A} \Big|_K = 0 \quad (8)$$

These boundary conditions allow the simulation of the linear motor motion. For this purpose, in the program written in GUI Octave software [6], a loop over the position of the motor mover within the limits of two pole pitches $2\tau_p$ has been used. The position step x_{step} used in simulation was calculated as follows

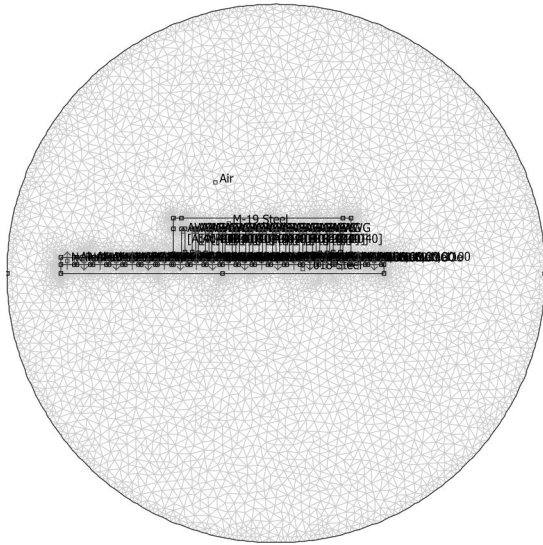


Fig. 2. The solution area for FEA

$$x_{step} = \frac{\tau_p}{n}, \quad (9)$$

where n is the number of steps.

The problem domain was discretized on the FEM mesh with 30727 nodes and 61092 triangle finite elements (Fig.2).

For each mover position, Finite Element Analysis (FEA) of the motor magnetic field at no-load (Fig. 3) were performed and on the base of results obtained by Maxwell tensor, force components over the motor moving part along both axes Ox and Oy were calculated.

The force component along axis Ox really represents the detent force that opposes the motor thrust.

The detent force versus mover position for the PMLSM designed in [1] without any measures for its reduction is shown in graphical form in Fig.6 for $b_z = 0$ mm.

III. DETENT FORCE MINIMIZING

A. Using additional two end teeth with chamfer

This method is described in many references [7]. In accordance with it, in the ferromagnetic core two additional teeth 1 and 2 are formed as shown in Fig.4. Furthermore, these teeth have chamfers 3 and 4.

With this ferromagnetic core geometry new FEM model was made. On the base of the magnetic field analysis results the detent force of the linear motor was calculated. The calculation results show a decreasing of the detent force.

This is due to the fact that the permeance of the magnetic flux changes in this manner at the end regions of the mover core, thus improving the magnetic field distribution (Fig. 5).

To establish the optimal width of the end teeth and the chamfer angle, field analyses are made for models wherein tooth width changes with specific steps for certain chamfer angles. When the optimal width of

the teeth at the ends of the core is established, the angle of the chamfer starts varying until its optimal value is set. The criterion is the minimum value of the detent force.

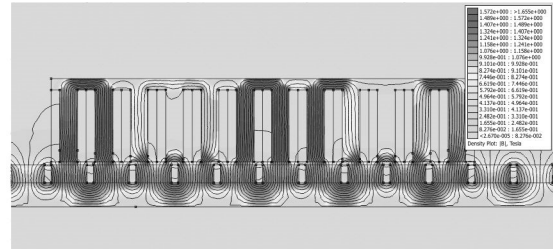


Fig. 3. The motor magnetic field distribution in final loop step

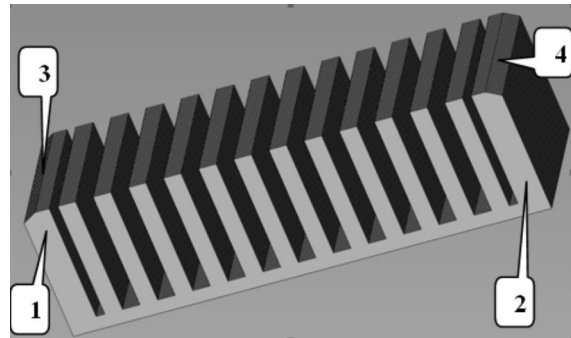


Fig.4. 3D CAD model of mover core

The results from the optimization of the width b_z of the additional teeth are shown in graphical form in Fig.6.

Calculations shows that for a mover core having thickness of additional teeth $b_z = 10$ mm, a good reduction of the detent force is obtained. But then, attraction force increases from 3431 N per 3968 N. This effect leads to unnecessary load on the linear guide of the mover and shortens the service life of the linear motor as a whole.

This method of reducing the detent force is characterized by the fact that the additional teeth lead to greater weight of the movable part. Furthermore, increase of strength of attraction between the permanent magnets and the ferromagnetic core of the movable part is obtained.

B. Using different length of the teeth of mover core

In [4] an alternative method to reduce the detent force was presented. For this purpose, ferromagnetic core of the movable part is used wherein the teeth are with different length - progressively decreasing in the direction of travel and symmetrically in the opposite direction, as shown in Fig. 7.

The determination of the step which reduces the length of the teeth is the task of FEA of the motor magnetic field.

For this purpose, a new FEM model was made, shown in Fig. 8.

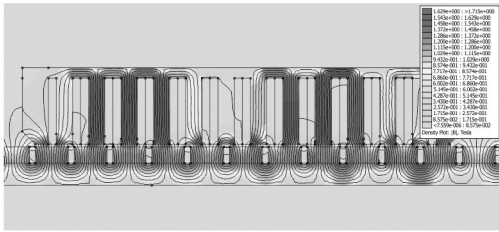


Fig. 5. Magnetic flux density distribution in the case of mover core with two additional end teeth

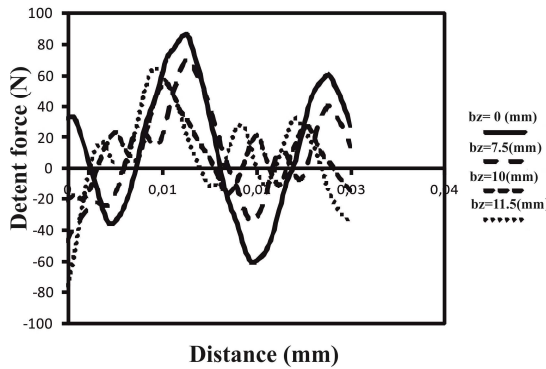


Fig. 6. Detent force in relation to the additional teeth width

The analysis of the motor magnetic field at different mover positions to the PMs was performed and the detent force in each step was calculated. Fig. 9 shows the field distribution for the mover displacement $x = 30$ mm.

It is important to clarify the question for the size of step for reducing the teeth length. The results from the detent force calculations for two-step reduction of the teeth length - 0.5 and 1 mm - are shown in Fig. 10.

The research shows that in the case of reducing the final four teeth of mover core near its two ends with step size 1 mm, significant reduction of the detent force is achieved.

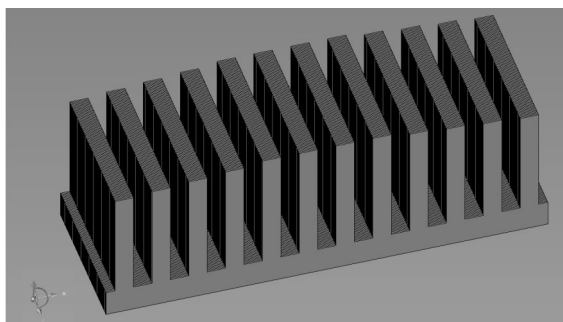


Fig. 7. Mover ferromagnetic core with teeth with progressively decrease

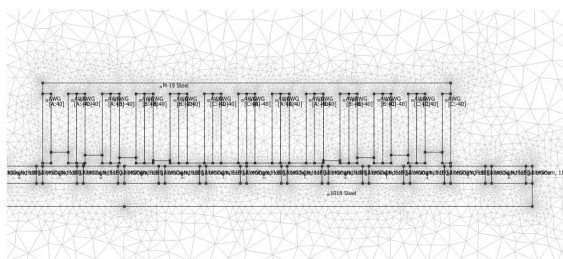


Fig. 8. FEM model of the linear motor with a mover ferromagnetic core with teeth of different lengths

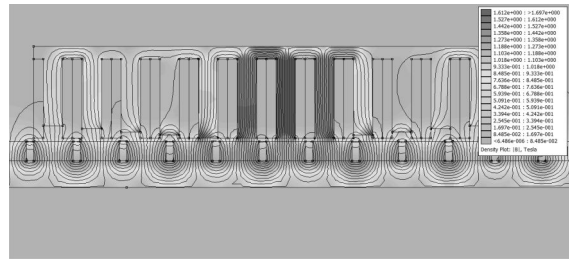


Fig. 9. Distribution of the magnetic field density at the mover position $x = 30$ mm

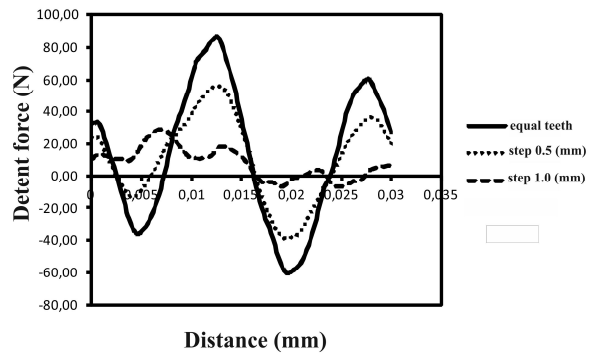


Fig. 10. Detent force relation to step size 0.5 and 1 mm, for decreasing the teeth length

IV. CONCLUSIONS

From FEM simulations of the PMLSM drive laser marking table in this paper it was found out that the reduction of the detent force can be achieved by using two additional teeth at both ends of the mover ferromagnetic core formed with a chamfer and by using teeth of the mover core with different lengths. The greater weight of the movable part in the case with two additional teeth and the bigger force of attraction between PMs and the mover core are respectively a reason for worsening the dynamic performance of the linear motor. For these reasons, this method for detent force reduction will be not used in final prototype of researched linear synchronous servomotor. Hence, a second way - ferromagnetic mover core with decreasing length of its teeth - was used. Thus the permeance of motor air gap was changed and in result pulsations and amplitude of the detent force was reduced. The absence of additional final two teeth and reducing the weight of ferromagnetic core in this case improved the motor dynamics.

REFERENCES

- [1] P. Uzunov, L. Lazov, "Design of Permanent Magnet Linear Synchronous Motor driving 2D Table for Laser Marking", Presented of 11th International Scientific and Practical Conference. Environment. Technology. Resources. Rezekne Academy of Technologies, Rezekne, Latvia, 2017.
- [2] Chevailler S., "Comparative study and selection criteria of linear motors", Ph.D. Thesis, EPFL, Suisse, 2006.

- [3] Remy, G., G.Krebs, A. Tounzi, P.Barre, "Finite Element Analysis of a PMLSM (part 1) – Meshing techniques and thrust computations", LDIA 2007, Lille, France, Sept. 2007.
- [4] A. Jenny, "Iron core linear motor having low detent force with high power density", US Patent 7,687,942 B2, March 30, 2010.
- [5] D. Meeker, "FEMM reference manual", 2015. [Online]. Available: <http://www.femm.info/Archives/doc/manual42.pdf>
- [6] J. Varandas,"GUI Octave",2011. [Online]. Available: http://download.cnet.com/windows/joaquim-varandas/3260-20_4-10128082-1.html
- [7] Gomand G.,Remy J., A. Tounzi, Pierre-Jean Barre, "Impact of currents on the detent force of a PMSLM", Proceedings of EPNC 2008, Lille, France, July 2-4, 2008.

Computer Control the Accuracy of the Parts Processed on CNC Machine Tools Based on Statistical Process Control

Angel Lengerov¹, Galina Nikolcheva², Julieta Kaleycheva², Lyubomir Lazov³

¹Department of Machine Tools and Mechanical Engineering, Technical University, Plovdiv, Bulgaria,
²Department of Machine Tools and Mechanical Engineering, Technical University, Sofia, Bulgaria, ³Rezekne Academy of Technologies, Latvia

Abstract. Statistical process control (SPC) can help manufacturers improve the quality of their products. This paper describes a relatively simple and effective method and algorithm to adjust the accuracy of parts produced on CNC machine tools using the methods of statistical process control. Examined the possibilities of the proposed method by computer simulation of the process. By using the proposed algorithm scattering of size is placed in the middle of the tolerance zone. Various variants carrying out the method are proposed adequate on the machining time during processing details in the sample. This can optimize the total time for processing of the batch.

Keywords: machining, CNC machine tools, computer control, statistical control.

I. INTRODUCTION

CNC machine tools are used in modern engineering production has increased radically over the last few decades. Manufacturing requirements along with quality requirements have become progressively more stringent for achieving high-quality products [3]. One way to improve accuracy in the production of machine parts is to use methods of statistical process control. These methods allow to apply in process control systems. Statistical Process Control (SPC) has traditionally been used in manufacturing systems to analyse and interpret measurement results and to provide compensation parameters [8]. SPC can help manufacturers improve the quality of their products. It is effective in controlling the fluctuations of the manufacturing process. SPC utilizes statistical methods to monitor manufacturing processes with an aim to maintain and improve the product quality while decreasing the variance [4].

Many researchers as Falsone [5], Nani [6] and Ramamoorthy and Radhakrishnan [7], develop and implement schemes for statistical control of production quality improvement and productivity. SPC helps define the capability of the stable process to judge whether it is operating at an acceptable level. Although in modern information technology is accumulated a huge amount of databases from prior production experience, any new device is required to provide initial information for carrying out the process and control the quality. Automated data collection, low cost calculation, and demands for higher quality, lower cost, and greater reliability are the cause of using SPC [4]. The statistical analysis of

the measurement results provides information about the technological process stability [6]. The aim of this article is to create a method and algorithm to adjust the accuracy of parts produced on CNC machine tools using the methods of statistical process control.

II. METHODOLOGY

In the process of making a series of identical parts are controlled the dimensional accuracy, the location of the surfaces and material properties. These are indicators for the accuracy of the products. For each is given norms of accuracy and limits deviations. These characteristics are controlled by their statistical evaluations [1].

Before the processing of each batch is carried out dimensional setting. This is done in order to get as close to the working adjusting size A_{hp} . Where the rate of tool wear has a great influence, the size is determined by the expression:

$$A_{hp} = A + EM \mp (0,5T - \omega_{uzm} - 0,5\omega), \quad (1)$$

where: A is the nominal size of surface; T is the tolerance size; EM is the average deviation of the tolerance zone; ω_{uzm} is error of the measurement at setup; ω is field of scattering. The “-“ refers to the processing of shafts; the sign “+” refers to the processing of holes.

From equation (1) that to determine A_{hp} need to know the field of scattering of the upcoming manufacturing process. Unlike mass and large series

ISSN 1691-5402

© Rezekne Academy of Technologies, Rezekne 2017
<http://dx.doi.org/10.17770/etr2017vol3.2623>

production in small batch production and small amount of batch thus information is not available. For determination of A_{hp} , apply different solutions.

Classical approach is the use of small sample test details. The method of small sample apply to processes that are scheduled rarer setups. It successfully applied in large series and mass production. Then the statistical characteristics of the process are known, including the dispersion caused by random factors. It is used primarily to assess the accuracy of the initial static dimensional setting-up.

When using CNC machine tools, the method of the small samples has a different implementation [9]. Carry out initial dimensional setting trial chips to size $A'_{hp} = A + EM$. The scattering of the size at the finish machining is considerably less than the tolerance size, so the initial setting has to ensure the production of workable parts. But the initial setting is not optimal in terms of the process to the first setting-up. The test sample contains a small number of parts sufficient to an indicative evaluate the dispersions and the working adjusting size. After making the adjustment to the initial setting are controlled the size of each of the following processed details and the accumulating information with appropriate statistical analysis allows for more precise dimensional setting. A different approach for dimensional setting used in [2]. The initial setting is static. Each workpiece is measured and is corrected the dimensional size to stabilize the process. For dimensional control is applied original method by touching the tool with the workpiece.

The experience accumulated for initial dimensional setting warrants the conclusion that at CNC machine tools is appropriate after the initial static setting to exercise ongoing control of all processed parts. The obtained information is processed at real-time statistically. As a result of the analysis is precise dimensional adjustment.

For the realization of this idea was developed following algorithm that has a simple software implementation of the discussed above solutions.

The algorithm is given below.

- Step 1. Static or trial chips is carried out initial dimensional setting of average size:

$$A_{hp} = A + EM ;$$

- Step 2. Starts batch processing, as measured after processing every detail and fills a database of information: $A_1; A_2; A_3 \dots ;$

- Step 3. After processing the small sample with size n (at least pieces) started statistical information processing in parallel with the implementation of the manufacturing process.

Calculate at real-time the average sample size and corrections of the dimensional setting to maintain the size-adjusting $A_{hp} = A + EM = const$:

After the first n details:

$$\bar{A}_1 = \frac{1}{n} \sum_{i=1}^n A_i; \quad \Delta_{n,1} = A_{hp} - \bar{A}_1;$$

- Step 4. If $|\Delta_{n,1}| > 0,1T$,

Then made a correction on to the initial setting with $\Delta A_{hp} = \Delta_{n,1}$

Otherwise, the process continues without correction.

Processing new sample with size n the workpiece, and are carried out the same actions as described above.

Whatever is the process, at the implementation of the proposed algorithm is achieved scattering of the sizes of processed details around the average size. It is the most favorable location at the accuracy diagram in the tolerance zone.

To study the effect of the proposed algorithm is carried out computer simulation of processes with and without dominant systematic factor. The factors which influence on the accuracy of machining of parts are tool wear, thermal deformation, changing the cutting conditions and setting the technological system.

III. RESULTS AND DISCUSSION

Table 1 shows a part of the numerical results obtained from the testing of the algorithm with dominant systematic factor at turning of a shaft with size $D = 35_{-0,04}$.

$$(A_{hp} = 34,98 \text{ mm}; \quad 0,1T = 0,004 \text{ mm})$$

Table 1

№	A	A+Δ _n	A _{cp}	Δ _n
1	34,998	34,998		
2	35,001	35,001		
3	35,006	35,006		
4	34,998	34,998		
5	34,997	34,997	35	-0,02
6	35,008	34,988		
7	34,991	34,971		
8	35,005	34,985		
9	35,002	34,982		
10	34,99	34,970	34,979	0,001
11	35,006	34,986		
12	34,99	34,972		
13	35,007	34,987		
14	34,997	34,977		
15	34,998	34,978	34,98	0,000
16	35,002	34,982		

In figure 1 shows the diagrams of the process without dominant systematic factor. Above located diagram is computer-generated Gaussian distribution with standard deviation $\sigma = 3,5 \mu\text{m}$ compared to the nominal size $D=35 \text{ mm}$. The second diagram located

below the first one presents the results after applying the algorithm for dimensional setup.

dominant systematic factor at turning of a shaft with size $D = 35_{-0,04}$.

$$(A_{np} = 34,98 \text{ mm}; 0,1T = 0,004 \text{ mm})$$

Table 2

№	A	A+Δ _н	A _{ср}	Δ _н	ΣΔ _н
1	34,998	34,998			
2	35,003	35,003			
3	35,01	35,01			
4	35,004	35,004			
5	35,005	35,005	35,004	-0,024	-0,024
6	35,018	34,994			
7	35,003	34,979			
8	35,019	34,995			
9	35,018	34,994			
10	35,008	34,984	34,989	-0,009	-0,033
11	35,026	34,992			
12	35,014	34,981			
13	35,031	34,998			
14	35,023	34,99			
15	35,026	34,993	34,991	-0,011	-0,044
16	35,032	34,988			

In figure 2 shows the diagrams of the process with dominant systematic factor. Above located diagram is computer-generated Gaussian distribution with standard deviation $\sigma = 3,5 \mu\text{m}$ compared to the nominal size $D=35 \text{ mm}$. The second diagram located below the first one presents the results after applying the algorithm for dimensional setup.

The figures 1 and 2 shows that and when there is a systematically increase in the dimensions of the machined parts caused by the tool wear, the algorithm successfully maintains the dimensional setting on the average value of size. Moreover, the accuracy of the process is increased considerably. For the specific example, at tendency to increase in size up to 0,002 mm/pcs and field of scattering around the center line $\omega = 23 \mu\text{m}$; without applying of the algorithm the size scatter is $\omega = 100 \mu\text{m}$. When used the algorithm, the size scatter is $\omega = 26 \mu\text{m}$.

Table 2 shows a part of the numerical results obtained from the testing of the algorithm with

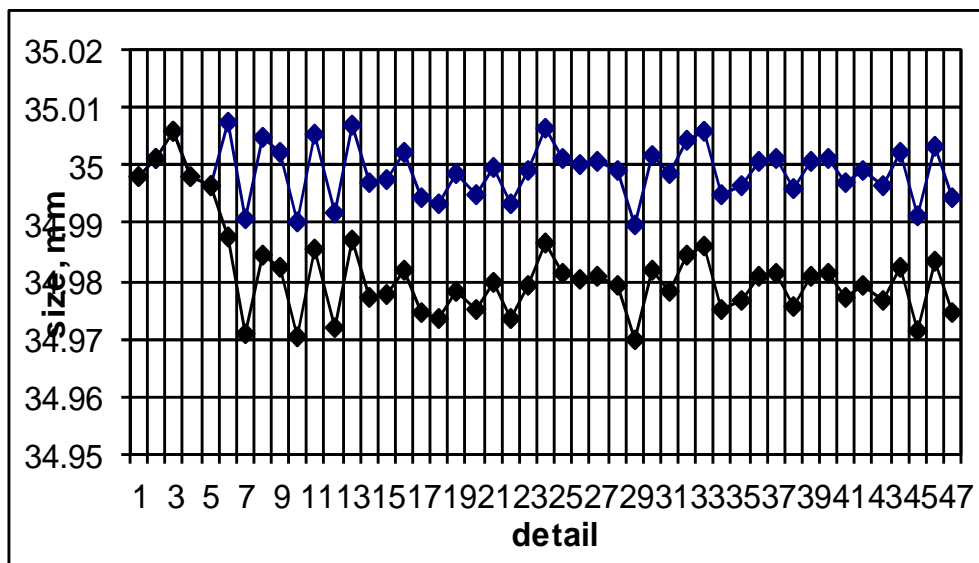


Fig.1. Diagrams of the process without dominant systematic factor

When the processing detail of the algorithm, the sample sizes comply with manufacture time during processing of the workpiece. As already mentioned, the minimum sample size is 3 details. When manufacture time is less and dimensional wear does not occur dynamically during the process, the average

size is verified through a larger time interval (number details). It is possible be made for time interval in algorithm, during which the sequence of n workpiece to be measured. So the principle of small current samples will be used. This will shorten the total time for the control of parts that are processed.

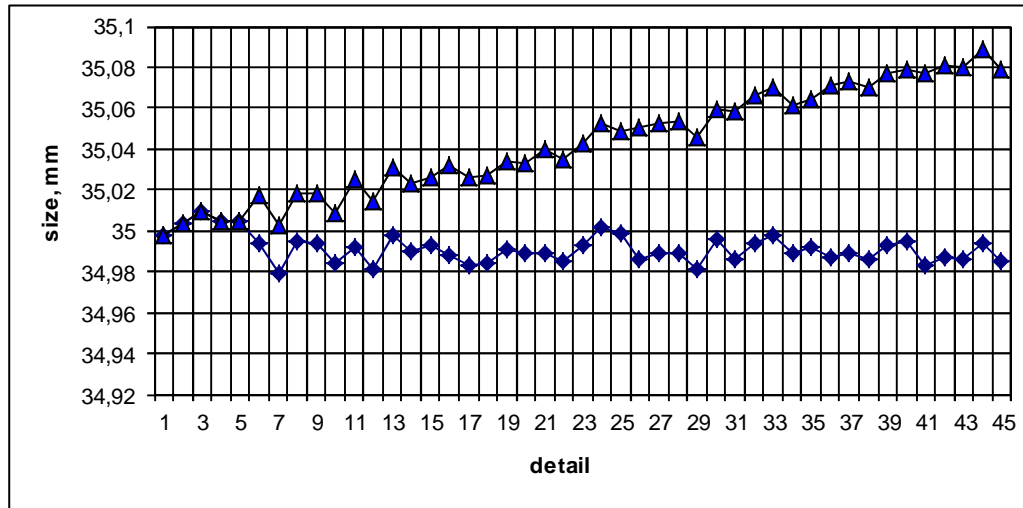


Fig. 2. Diagrams of the process with dominant systematic factor

IV. CONCLUSION

Statistical process control (SPC) can help manufacturers improve the quality of their products. Proposed is a relatively simple and effective method and algorithm for computer control accuracy in turning CNC machine tools using the methods of statistical process control. Examined the possibilities of the proposed method by computer simulation of the process. It shows good performance as in processes without systematic dominant factor and expressed systematically varying the dimensions of tool wear. By using the proposed algorithm scattering of size is placed in the middle of the tolerance zone. It is optimal to obtaining of minimal probability of rejects, both the upper and the lower limit of the tolerance zone. Various variants carrying out the method are proposed adequate on the machining time during processing details in the sample. This can optimize the total time for processing of the batch.

REFERENCES

[1] W. Cochran, *Sampling Techniques*. Third ed. Wiley, 1977.
 [2] M. Enchev and S. Koleva, Transitional process in initial dimensional setting with setup of details. X International

Congress "Machines, technologies, materials», September, 18-20, Varna, Bulgaria, 2013.

- [3] P. Hadjiski and C. Kaldashev, *Programming of CNC machine tools with CAM systems*. Technical University-Sofia, 2017.
 [4] A.R Fazeli and E. Sharifi, *Statistical Control and Investigation of Capability of Process and Machine in Wire Cut . EDM Process of Gas Turbine Blade Airfoil Tip*. Engineering. 2011; 3: 260-265. <http://www.SciRP.org/journal/eng> [Accessed 2011].
 [5] G.Falsone and D. Settineri, On the application of the probability transformation method for the analysis of discretized structures with uncertain proprieties. *Probabilistic Engineering Mechanics*, 35, 2014 pp.44-51, doi: 10.1016 /j. probengmech. 2013.10.001
 [6] V.M. Nani, Statistical control of processing prismatic pieces on grinding machines, *Measurement*, 47, 2017, pp 516 – 520, (doi: 10.1016/ j.measurement. 2013.09.033
 [7] B. Ramamoorthy, V. Radhakrishnan, A.Weckenmann, M. Knauer and D.A. Geus, Improvement of machining accuracy on a CNC lathe through error prediction and compensation. in: XV IMEKO World Congress, June 13–18, Osaka, Japan (1999)
 [8] S. Kumar and S. T. Newman, Standardised Process Control System for CNC Manufacturing in: *Advanced Design and Manufacturing Based on STEP*, 2009, pp. 233-259.
 [9] S. Salapatieva, *Technology research for active control Turning CNC*. PhD Thesis. TU-Sofia, branch Plovdiv, 2005.

Statistical Control of Accuracy at Machining

Angel Lengerov¹, Galina Nikolcheva², Lyubomir Lazov³

¹Department of Machine Tools and Mechanical Engineering, Technical University, Plovdiv, Bulgaria,

²Department of Machine Tools and Mechanical Engineering, Technical University, Sofia, Bulgaria, ³Rezekne Academy of Technologies, Latvia

Abstract. This research examines the statistical method for quality control. The accuracy of parts is controlled statistical evaluation - an average and a dispersion of the indicator for accuracy. This paper reports a method for quality control of parts of average indicators and algorithm for quality control of the average and dispersion of samples of small size. It proposes a criterion of applicability of statistical adjustment of accuracy by sampling for control of the average data of the quality indicator. It proves the influence of the dispersion of the quality indicator for impairing the quality of the process.

Keywords: dispersion, Statistical Process Control, quality indicator, sample.

I. INTRODUCTION

In today's computer-aided manufacturing environment, one of the main objectives of quality control is to achieve higher accuracy of machined workpieces. One way to improve the workpiece accuracy is to utilize concept of deterministic metrology by focusing on the machine tool and the cutting process to control the cutting tool position accurately in the workspace of the machine tool. Another way to improve accuracy in the production of machines parts is to use methods of statistical process control. These methods allow to apply in process control systems. By implementing statistical process control (SPC), which involves the gathering and analysis of data to determine which machining process is most suitable for a workpiece, we can ultimately improve quality and reliability, and reduce operating costs.

SPC is a commonly used control method of manufacturing processes which is effective in controlling the fluctuations of the manufacturing process. Statistical Process Control (SPC) techniques, when applied to measurement data, can be used to highlight areas that would benefit from further investigation. These techniques enable the user to identify variation within their process. SPC utilizes statistical methods to monitor manufacturing processes with an aim to maintain and improve the product quality while decreasing the variance. Understanding this variation is the first step towards quality improvement. SPC techniques are tools for highlighting this unusual behavior. Automated data collection, low cost calculation, and demands for higher quality, lower cost, and greater reliability are the cause of using SPC [4].

Past 30 years, many researchers as Georgiev and Kuzmanov [3], Woodall and Montgomery [9], and Stoumbos et al. [7] develop and implement schemes for statistical control of production quality improvement and productivity. SPC helps define the capability of the stable process to judge whether it is operating at an acceptable [2, 5].

This research examines the statistical method for quality control. The aim of this article is to create a method and algorithm to control the quality of parts by the average data of indicators and dispersion of samples of small size. The machined parts accuracy affects to quality of the machine tools. The two terms often used with quality are error and accuracy. Error represents deviations of the cutting tool point from the theoretical position on the part in order to machine part dimensions to specified tolerance. Accuracy is defined as the part's conformance to the specifications in the manufacturing drawing or CAD MODEL [8]

Section 2 describes statistical control methods of the accuracy of machining, section 3 describes the developed methodology and algorithm for control accuracy in the manufacture of machine parts by controlling the average data and by dispersion of samples of small size.

II. METHODS FOR STATISTICAL CONTROL

There are various sources of errors, which result in inaccurate details. Main indicators of the quality of the parts are geometric shape, dimensional accuracy, relative position of their surfaces and material properties. These indicators are measurable physical quantities. For each of them a nominal size and the size of the deviation are referred. These quality

characteristics are controlled by statistical evaluation of the processing of the series of identical parts. The control is carried out with different sample size - small and big samples [4]. The method of small samples applies to processes that are scheduled rarer setups. The information necessary for the analysis need to be collected in a long time [3,7]. Samples are up to 10 and they are taken at regular intervals of 30 to 60 minutes.

The method of the big sample is applied to processes with high intensity of the dominant systemic factors. The method of the big sample is applied to processes with high intensity of the dominant systemic factors. They require more frequent setups or presetting of the technological system. Controls all parts in the sequence of their execution [3,7]. The sample size is 50 to 200.

At small samples - to control the nominal value using the evaluation on the average of the controlled indicator, at big samples - the regression equation for the average data.

Reasons for deviation of the quality

The types of deviation of the quality are shown graphically in Fig. 1. In the case of Fig. 1a, as a result of the systematic increase in the average \bar{A} the field of scattering has reached the upper limit of the tolerance zone. If the process continued after time τ_{kp} there is probability to produce poor quality parts.

In the case of Fig. 1b, with continued work increased the average \bar{A} and the dispersion. Both factors together lead to problems in the process.

In the case of Fig. 1c, the initial setting process is of poor quality. It reduces operating time until the next presetting. The purpose is through the control to establish the moment that should be stopped setup process.

Where production has a big series, with accumulated statistical data on the process and the process is stable then the control can be limited to statistical evaluation, which reflects the change of the center of grouping of quality indicator as a function of time. The dispersion is a constant and with a certain size.

When there is no a priori statistical data about the characteristics of the process, then is required at real-time to identify the regression equation and the probable field of scattering. Parallel is implemented and specific algorithm for process control. This approach applies to the frequent change of the manufactured products and relatively small batches.

For the control of process is necessary to determine the criterion by which to evaluate the probability of deviations of the quality. The diagrams in Fig. 1 show that this is the time, that this criterion is the time τ_{kp} at which the field a scattering of the indicator for quality passes limit of the tolerance zone. The problem is that the field a scattering is determined by the theoretical law distribution and the

dispersion of quality indicator as a random variable. For a normal distribution is accepted the limits of scattering to be $\omega = \pm 3\sigma = 6\sigma$. The dispersion $D(x)$ and the standard deviation σ are characteristics of the overall population - the number of parts $n \rightarrow \infty$. In practice, the process is monitored with limited sample size of the overall population. Therefore as a criterion not used the limits of the tolerance zone and control limits within the tolerance zone. The position of these limits are determined by what statistical evaluations of mathematical expectation $M(x)$ and the dispersion $D(x)$ are used for ongoing quality control.

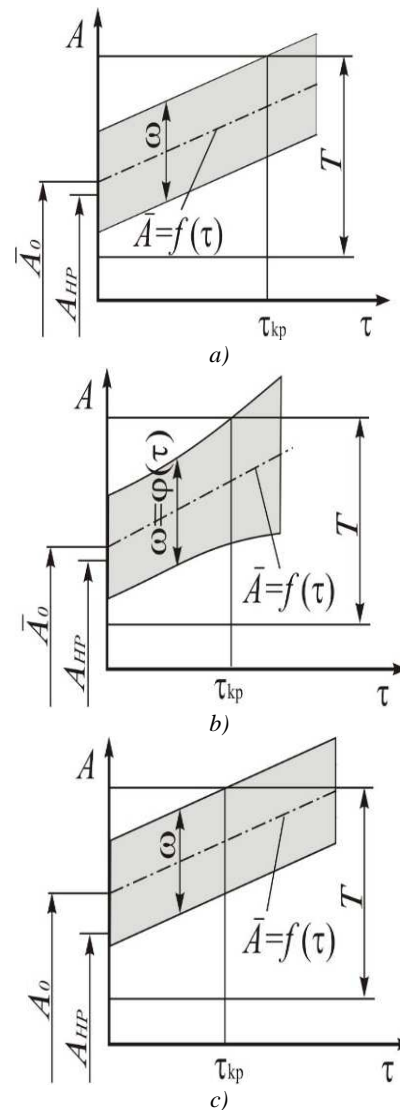


Fig. 1. Reasons for the deviation of quality

Control according to the average indicator for quality

The change in the average data is caused under the influence of factors such as tool wear, thermal deformation, changing the cutting conditions and setting the technological system. Probability of

obtaining a reject occurs when average value approached the limits of the tolerance zone. The limit positions of the average \bar{A} of the sample are shown in Fig. 2, where the distribution of the overall population is indicated by the dotted line, and the sample - a continuous line.

As statistical evaluation, the average \bar{A} scattering around the mathematical expectation M of the overall population within the limits is

$$\bar{A} = M \pm \frac{3\sigma}{\sqrt{n}}, \quad (1)$$

where σ is the standard deviation of overall population; n - the number of parts in a sample. The smallest permissible value of \bar{A} is shown in Fig. 2a. Then the overall population in probability may be located on the border of reject, taking into account measuring error ω_{u3M} at control. Probability of reject is obtained when:

$$\bar{A} < A + EI + \omega_{u3M} + \frac{\omega}{2} + \frac{3\sigma}{\sqrt{n}}$$

Therefore, the lower control limit K_{min} is

$$\begin{aligned} K_{min} &= A + EI + \omega_{u3M} + \frac{\omega}{2} + \frac{3\sigma}{\sqrt{n}} = \\ &= A + EI + \omega_{u3M} + 3\sigma \left(1 + \frac{1}{\sqrt{n}}\right) \end{aligned} \quad (2)$$

Similarly of Fig. 2b is defined upper control limit K_{max}

$$K_{max} = A + ES - \omega_{u3M} - 3\sigma \left(1 + \frac{1}{\sqrt{n}}\right) \quad (3)$$

When the average \bar{A} reaches one of the control limits with tend to pass, then having to make setup. The condition for stopping the process to make a setup is:

$$K_{min} \geq \bar{A} \geq K_{max} \quad (4)$$

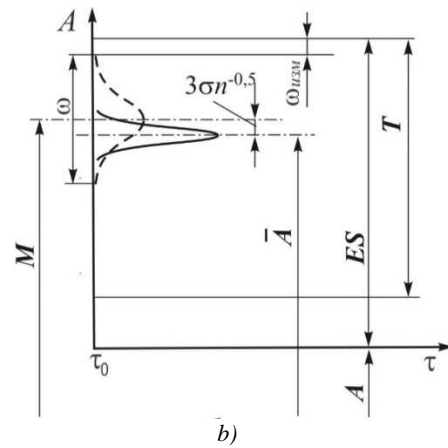
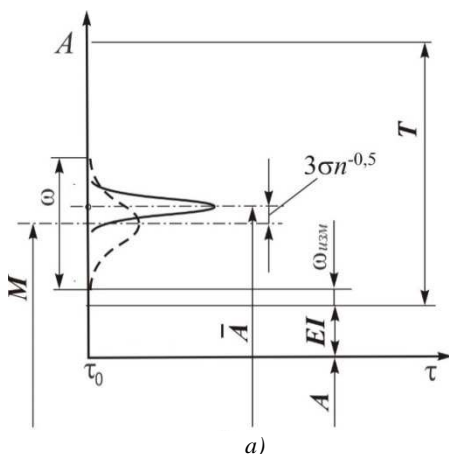


Fig. 2. Limit positions of the scattering on the overall population

From (2) and (3) that to determine the control limits is necessary to know the dispersion of the overall population. For this purpose, it is the statistical evaluation of the dispersion S . The relationship between S and the standard deviation σ is the formula for the probable field scattering of the overall population:

$$\omega = 2sk_{\gamma,P,n} = 6\sigma$$

Therefore:

$$\sigma = \frac{k_{\gamma,P,n}}{3} s \quad (5)$$

The bigger is the number of parts of which is determined S , the closer will be up to standard deviation σ . It follows that at statistical control with small current sampling to determine the dispersion of the overall population do not use the average dispersion sample. Each sample dispersions is determined by a small number of parts and unjustified will underreport the probable field of the overall population, and hence will narrow and the zone between the control limits. This creates abnormal conditions of control process, and in certain cases impossible. Therefore the dispersion should be determined from all measured products during the observation. For example, if it is 10 samples, each of which has 5 products, the dispersion will be determined by a total of 50 articles instead of 5. The evaluation of the dispersion of statistical data for small current sample equals to:

$$s^2 = \frac{\sum_{j=1}^{N_j} \sum_{i=1}^{n_j} (A_{j,i} - \bar{A}_j)^2}{\left(\sum_{j=1}^{N_j} n_j \right) - 1} = \frac{\sum_{j=1}^{N_j} s_j^2 (n_j - 1)}{\left(\sum_{j=1}^{N_j} n_j \right) - 1}, \quad (6)$$

where: N_j is the number of samples, n_j is the size of the sample with a number j , s_j^2 is the sampling dispersion with number j .

$$s^2 = \frac{n-1}{nN_j-1} \sum_{j=1}^{N_j} s_j^2 \quad (7)$$

The range, which varies the average of the samples so that the process to ensures the quality equals to

$$\Delta \bar{A} = K_{max} - K_{min} = T - 2\omega_{uzm} - 6\sigma \left(1 - \frac{1}{\sqrt{n}} \right), \quad (8)$$

where $T - 2\omega_{uzm} = T_{mex}$ is called tolerance for machining and is accepted to be $0,8T$. To be able to controlled the process is necessary $\Delta \bar{A} > 0$.

Then from equation 8 is obtained condition:

$$\sigma < \frac{0,8T}{6 \left(1 + \frac{1}{\sqrt{n}} \right)}; \quad \omega < \frac{0,8T}{1 + \frac{1}{\sqrt{n}}} \quad (9)$$

For example, If $n = 5$, then are calculated $\omega < 0,55T$. At $\omega = 0,4T$, the range of adjustment is calculated $\Delta \bar{A} = 0,22T$, which is a relatively narrow range when the process has a dominant systematic factor.

Control algorithm on average \bar{A}

The algorithm is given below.

- Step 1. Input data: part, operation, surface, dimensions A, T, EM, the method of small samples, size of the samples, time between samples τ , process characteristics $\sigma, \omega, \omega_{uzm}$.
- Step 2. Verification of applicability of the method: inequality (9). If satisfying, the algorithm continues. Otherwise go to step 1 and change an input.
- Step 3. Calculation of the control limits by the formulas (2), (3).
- Step 4. Input number of first sample j .

- Step 5. Entering the dimensions $n_{j,i}$ parts of the sample.
- Step 6. Calculation of \bar{A}_j, s_j^2, s .
- Step 7. If $K_{min} \geq \bar{A} \geq K_{max}$, then the process stops. Otherwise, the algorithm continues.
- Step 8. Input number of next sample $j = j + 1$.
- Step 9. Repeat steps 2 to 8 to satisfy the inequality (4), wherein the process is interrupted for setup.

Is another new cycle for many small current samples.

It is possible that the algorithm can be extended to determine the regression equation and the dispersion of the set of processed samples. This information can be displayed graphically and be entered into the database for use in future developments.

Control by dispersion of the indicator for quality

In cases where the dispersion is a key indicator of the quality of production, it is used to control the quality process. Most often the control on dispersion is combined with the control on average data. In this variant both indicators have a shared role in the quality of products. Both methods of control are based on a sample control for the dispersion of quality indicator.

The main purpose of monitoring is to establish whether the dispersion is statistically constant, whether occurs systemic change or is there an abrupt change of dispersion.

The check for the constancy of the dispersion is limited to verifying the hypothesis of equality of the dispersions. For samples of the same size are applied the criteria of Cochran [1] wherein is verified the equality of the series of dispersions, when the samples have different size are applied the criteria of Bartlett [3].

During the process, the inspection begins after the third sample and is done after each subsequent sample. For the application of this method computing resources for a quick statistical analysis, such as modern computer systems are needed.

At the moment at which the null hypothesis $H_0 : s_1^2 = s_2^2 = s_3^2 = \dots = s_m^2 = s^2$ is not confirmed, this is a signal for an abrupt or for systemic change of the dispersion. If not passed limits for a quality produce, then are checked another 2-3 samples in short time. After checking on homogeneity, the sample with significantly different values of dispersion is excluded from the analysis. If the null hypothesis is confirmed, it implies that the abrupt change of dispersion is momentary phenomena and the process can continue (do not lose accuracy). If the next samples don't confirm the null hypothesis, it is signals for deviation accuracy of the process.

At processes where control is performed only by dispersion of the quality indicator, then the dispersion of all samples is determined by (6) or (7). The obtained dispersion is compared with the permissible for the process in order to evaluate the need to setup. When the dispersion is used together with the average indicator of quality, should be monitored change of S by (6) and respectively of σ . With the new values after each sample are recalculated the control limits (K_{max}, K_{min}). With the increase in the dispersion is narrowed the range between the control limits and is increased the probability the average \bar{A} of the qualitative indicator of the sample reach the limits. Thus, the change of the dispersion reflects the moment when the process is interrupted for a setup or a new setting.

III. CONCLUSIONS

Statistical Process Control (SPC) techniques enable the user to identify variation within their process. The accuracy of parts is controlled statistical evaluation - an average and a dispersion of the indicator for accuracy. Method for quality control of parts by average indicators is created. A criterion of applicability of statistical adjustment of accuracy by sampling for control of the average \bar{A} of the quality indicator is proposed. The influence of the dispersion of the quality indicator for impairing the quality of the process is proven.

The proposed algorithm for control accuracy in the manufacture of machine parts is based of the average data and dispersion of samples of small size. It takes into account the influence of the dispersion during the process. Using SPC technique helps us to easily understand when the permanent improvement occurs in the processes.

REFERENCES

- [1] Cochran W. Sampling Techniques. Third ed. Wiley, 1977.
- [2] Danov T. Statistical methods for quality control. Technika. Sofia.Bulgaria. 1987.
- [3] Georgiev B, Kuzmanov T. Statistical methods for analysis and quality of technological processes in mechanical engineering. EXP-PRES. Gabrovo. Bulgaria. 2006.
- [4] Fazeli AR, Sharifi E. Statistical Control and Investigation of Capability of Process and Machine in Wire Cut EDM Process of Gas Turbine Blade Airfoil Tip. Engineering. 2011; 3: 260-265. <http://www.SciRP.org/journal/eng>
- [5] Montgomery DC. Introduction to Statistical Quality. John Wiley&Sons. Hoboken.1996.
- [6] Rachev R, Lengerov A, Levicharov G. Providing manufacturability of engineering products. Plovdiv. Bulgaria.2016.
- [7] Stoumbos ZG, Reynolds MR, Ryan TP and Woodall WH.. "The State of Statistical Process Control as We Proceed into the 21st Century," Journal of the American Statistical Association.2000; Vol. 95. No. 451: 992-998.
- [8] Stephenson DA, Agapiou JS. Metal Cutting Theory and Practice. Third ed. Marcel Dekker.2016.
- [9] Woodall WH, Montgomery DC. Research Issues and Ideas in Statistical Process Control, Journal of Quality Technology.1999; Vol. 31. No. 4: 376-386.

Adaptive Control of the 1-DOF Active Magnetic Bearing

Sergei Loginov, Yuri Zhuravlyov, Yulia Domracheva, Dmitriy Fedorov

Pskov State University, Department of Electric Drive and Automation Systems.

Address: Lenin Square 2, Pskov, 180000, Russian Federation.

Abstract. active magnetic bearing is the electromechanical device allowing to suspend the rotor of the electric machine. Friction is eliminated and high speed of rotation can be achieved. However, the parameters of the electromechanical system may change during operation. Adaptive control system allows to maintain stability under varying parameters.

Keywords: active magnate bearing, adaptive control system.

I. INTRODUCTION

Active magnetic bearings (AMB) are increasingly used in various fields of industry [1],[2]. The absence of mechanical contact makes it possible to use them in ultra-high-speed electric drives (now it is much in demand) [3], [4]. The main trend of AMB development is the improvement of the control system: application of the modern elemental base of electronic components and improvement of control algorithms [5], [6]. The use of a traditional AMB control system with a PID controller is limited in some areas. For example, there are systems where the parameters can change during operation, while for the PID controller it is necessary to know exactly the parameters of the control object. In addition, the general trend of modern management systems is their intellectuality. In AMB, it is design engineering of self-tuning systems. One type of such systems is the adaptive control system [7]-[9].

II. MATERIALS AND METHODS

Let's consider the control system of 1 degree of freedom (1-DOF) active magnetic bearing. It includes rotor position sensor, a regulator, power amplifiers and electromagnets. (Fig. 1).

There are various AMB control systems, one of the most simple is a system based on a PD controller with current control. Let's assume that we want the free motion of a suspended body, described by the known equation [2]

$$m\ddot{y} - k_y y = k_i i \quad (1)$$

under identical initial conditions exactly coincided with free motion of a mechanical linear oscillator with viscous friction described by the equation $m\ddot{y} + b\dot{y} + cy = 0$ or

$$\ddot{y} + 2\zeta\omega_0\dot{y} + \omega_0^2 y = 0. \quad (2)$$

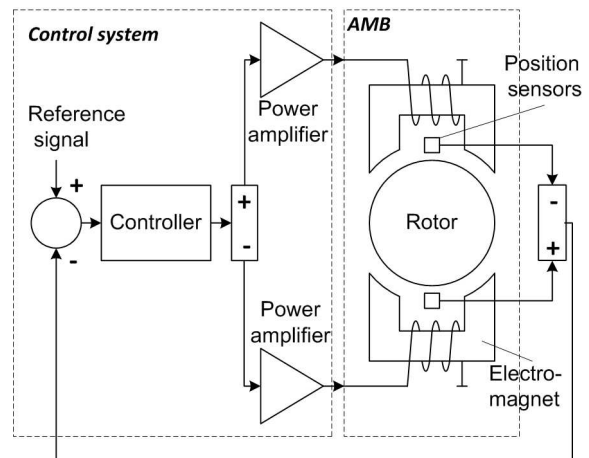


Fig. 1. Principle of operation of active magnetic bearing

Here m - is the rotor mass, y - is the position coordinate, k_y - is the coefficient "force-current", k_i - is the coefficient "force-displacement", b - is the coefficient of damper viscous friction, c - is the spring stiffness, $\zeta = b/(2m\omega_0)$ - is the dimensionless damping parameter, $\omega_0 = \sqrt{c/m}$ - is the frequency of the undamped free vibration. Obviously, for the identical systems' motions under identical initial conditions, it is necessary and sufficient that the current values of the accelerations of both systems to be identical. Expressing acceleration \ddot{y} out of (2) and substituting it in (1), we obtain the current control action:

$$i = -(k_p y + k_d \dot{y}), \quad (3)$$

where $k_p = (m\omega_0^2 + k_y)/k_i$ - is the feedback gain factor for the displacement and $k_d = 2 \cdot \zeta \cdot m \cdot \omega_0 / k_i$ - for the speed.

As it is known, the controller that implements the control action (3) is called the PD controller. The block diagram of the 1-DOF AMB control system is shown in Fig. 2 [10].

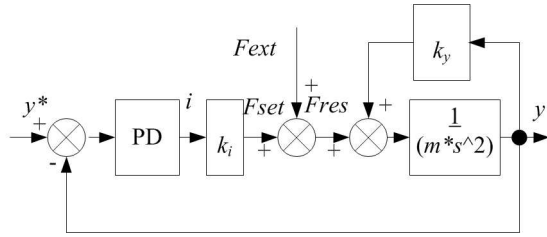


Fig. 2. Block diagram of the 1-DOF AMB with PD controller

Where y^* is the reference position signal, i is the reference current, F_{set} is the reference force, F_{ext} - the external disturbance. $F_{res} = F_{set} + F_{ext}$.

Let us set the following real values for the parameters: $m = 10$ kg, $k_i = 500$ N/A, $k_y = 2,5 \cdot 10^6$ N/m, the frequency of undamped oscillation $\omega_0 = 350$ rad/s and the dimensionless damping parameter $\zeta = 0,5$. Then $k_p = 7450$ A/m, $k_d = 7$ Ac/m.

The Simulink model is shown in Figure 3.

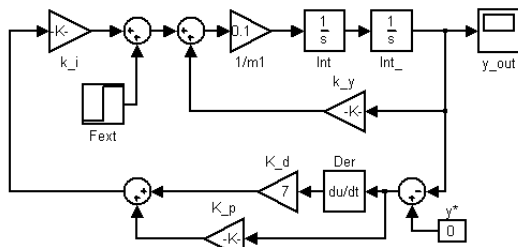


Fig. 3. Simplified Simulink model of the 1-DOF AMB with PD controller

As a result, with an external stepped action of the force $F_{ext} = 200$ N at time point 0,01 s, we obtain the transient process shown in Fig. 4.

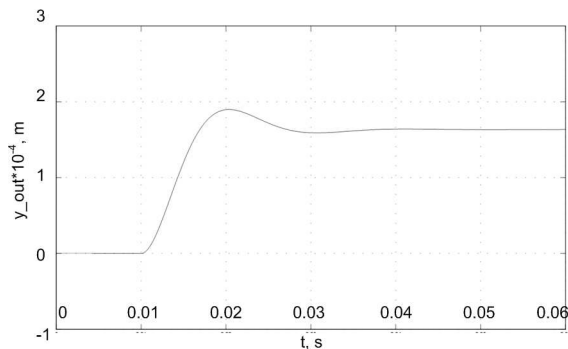


Fig. 4. Transient process under the influence of an $F_{ext} = 200$ N

However, if the “negative” stiffness increases, $k_y = 4 \cdot 10^6$ N/m, the system becomes unstable (Fig.5).

It is possible to recalculate the values of the coefficients for the new regulator parameters, then the view of the transient process will become again as in Fig. 4. However, the problem is that the “negative” stiffness parameter can change during operation. For example, when the electric motor is turn on, the

“negative” stiffness of the suspension is added to the “negative” stiffness of the electric motor, caused by the radial magnetic forces of stator, which will depend on the currents in the motor windings. In addition, the rotor parameters can change, for example, change of the spindle mass in the process of filament winding. In these cases, adaptive control is needed (maintenance of the stability of the suspension dynamic qualities in a wide range of changes in its parameters).

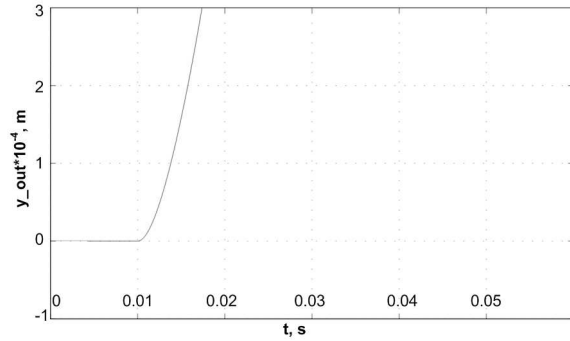


Fig. 5. Transient process under the influence of an external force 200 N ($k_y = 4 \cdot 10^6$ N/m)

III. RESULTS AND DISCUSSION

Let's consider a system with adaptive control.

The current-controlled suspension equation can be written as:

$$\ddot{y} = f(y, \dot{y}, i). \quad (4)$$

Condition of incompleteness of information about the control object: for all possible values of the arguments of the function (4), the partial derivative with respect to the control current is positive $\partial f / \partial i > 0$.

Let there be given a program function $f = f^0$ that implements the required action of motion of the body. Given a differential program of the form $\ddot{y} + 2\zeta\omega_0\dot{y} + \omega_0^2 y = 0$, we have

$$f^0(y, \dot{y}) = -(2\zeta\omega_0\dot{y} + \omega_0^2 y) \quad (5)$$

Now the problem arises: for each time moment t and its corresponding state $y(t), \dot{y}(t)$ it is required to find a value $i^0(t)$ for which

$$f(y, \dot{y}, i^0) = f^0(y, \dot{y}) \quad (6)$$

If there were complete information about the suspension, i.e. for a known function $f(y, \dot{y}, i)$, the required value i^0 could be found on the basis of an analytical solution of equation (6). In the case under consideration, equation (6) can only be solved algorithmically:

$$di/dt = \rho_1 \cdot \Delta f, \Delta f = f^0(y, \dot{y}) - f(y, \dot{y}, i). \quad (7)$$

Indeed, with the assumption made about the function $f(y, \dot{y}, i)$ for each instant of time, the following limit is valid:

$$\lim_{\tau \rightarrow \infty} i(\tau) = i^0(t), \quad f(y, \dot{y}, i^0) = f^0(y, \dot{y}), \quad (8)$$

where τ - is fast time.

This is a consequence of the fact that the tracking system (7) is stable.

Substituting the expressions from (6) and (4) into (7), we obtain

$$di/dt = \rho_1 \cdot \Delta f, \Delta f = -(\ddot{y} + 2\zeta\omega_0\dot{y} + \omega_0^2 y). \quad (9)$$

The block diagram of the control loop is shown in Figure 6.

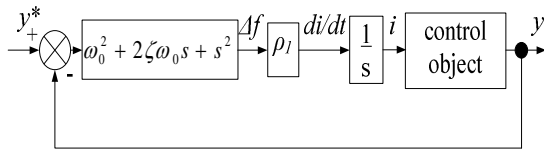


Fig. 6. Block diagram of the control loop with adaptive control

The peculiarity of the algorithm (9) is that it is not necessary to know the explicit functional dependence.

This functional dependence may be unknown. The structure of the control algorithm does not explicitly contain the parameters of the control object. Therefore the algorithm (9) is in the full sense adaptive. The practical implementation of the algorithm is based on the measurement of acceleration.

Tracking accuracy is substantially determined by the value of ρ_1 . For a finite value of ρ_1 , the required action of body motion will be approximate. The degree of approximation increases with increasing ρ_1 . The value of ρ_1 should be selected according to the following condition: the current values must be processed substantially faster than in the program system (2).

The Simulink model of the 1-DOF active magnetic bearing control system is presented in Figure 7

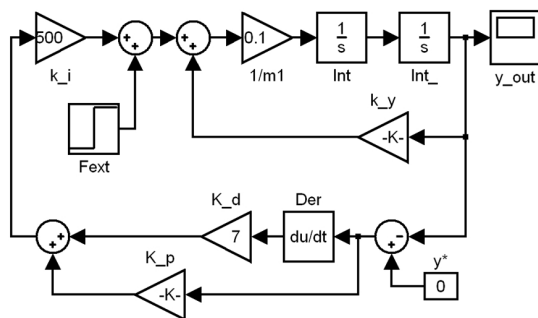


Fig. 7. Simplified Simulink model of the 1-DOF AMB with adaptive control

The parameters of the adaptive PD controller are adjusted to create a control law (2) ($\omega_0 = 350$ rad/s and $\zeta = 0,5$.)

Figures 8 and 9 show the transient processes in the system with the adaptive regulator under the external action of a force of 200 N with coefficients of “negative” stiffness $k_y = 2,5 \cdot 10^6$ N/m and $k_y = 4 \cdot 10^6$ N/m.

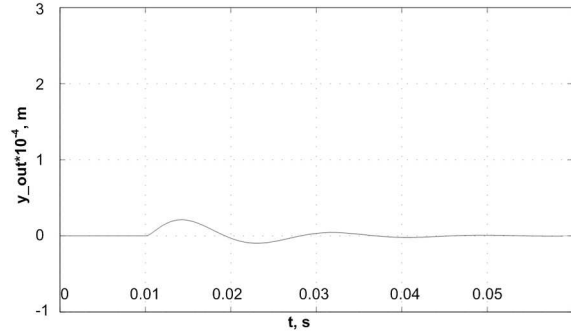


Fig. 8 Transient process in the adaptive control system at $k_y = 2,5 \cdot 10^6$ N/m

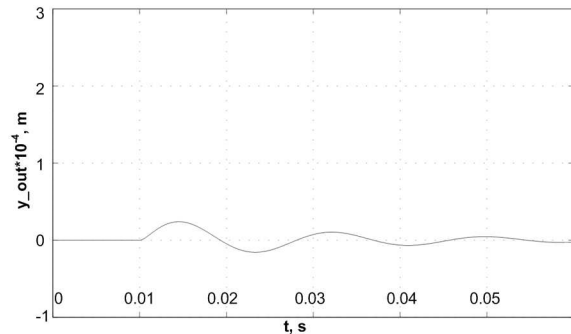


Fig. 9 Transient process in the adaptive control system at $k_y = 4 \cdot 10^6$ N/m

As the graphs show, the transient processes are almost identical. The results are similar when the rotor mass is changed.

IV. CONCLUSION

The article deals with the synthesis of the adaptive regulator system for a 1-DOF active magnetic bearing.

The method of constructing a regulator based on the desired parameters of the system transient processes is presented. Unlike other papers, the results of computer Simulink simulation 1-DOF active magnetic bearing are presented. A quantitative comparison of the transient processes in the active magnetic bearing with a PID controller and with an adaptive control system is given. The advantage of the adaptive control system is shown. The system remains stable even with significantly varying of “negative” stiffness coefficients.

It should be noted that the adaptive controller can be applied not only to a system in which the parameters of a control object are changed over time, but also in systems in which the parameters of the control object are unknown. Application of such

systems for AMB enables to considerably simplify system design engineering and setting.

V.ACKNOWLEDGMENTS

This study was partly supported by the Ministry of Education and Science of the Russian Federation. Project "Development of the Bearingless Synchronous Electrical Machine Theory Foundations" No. 2014/700

REFERENCES

- [1] G. Schweitzer, H. Bleuler, and A. Traxler, *Active Magnetic Bearings*. Zurich, VDF Hochschulverlag AG, pp. 31-77 1994
- [2] Y. Zhuravlyov *Active Magnetic Bearings: Theort, Design, Aplication*. St. Petersburg: Politechnica, 2003, pp. 12-25
- [3] G. Schweitzer, and E. Maslen, *Magnetic Bearings - Theory, Design and Application to Rotating Machinery*. Springer-Verlag Berlin Heidelberg , pp. 33-78 2009.
- [4] A.Chiba, T.Fykao, O.Ichikawa, M.Oshima, M.Takemoto and D.G.Dorrell, *Magnetic Bearings and Bearingsless Drives*. ELSEVIER, pp. 127-135.
- [5] V.S. Polamraju, G.V. Sobhan, K. Nagesh, J. Amarnath and M. Subbarao. "Stabilization of active magnetic bearing system using single neuron PID controller", *ARN Journal of Engineering and Applied Sciences* vol. 9, no. 7, july 2014
- [6] Ming-Mao Hsu, Seng-Chi Chen, Van-Sum Nguyen and Ta-Hsiang Hu "Fuzzy and online trained adaptive neural network controller for an AMB system", *Journal of Applied Science and Engineering*, vol. 18, No. 1, pp. 47 -58. 2015
- [7] T.A.Izosimova and Yu. K. Evdokimov "Adaptive control of the dynamic behavior of the rotor in active magnetic bearings", *Dynamics of complex systems - XXI century* No. 3, pp. 37-42, 2014.
- [8] Silu You "Adaptive backstepping control of active magnetic bearings", *Bachelor of Electrical Engineering Huazhong University of Science and Technology* July, 2007.
- [9] Kai-Yew Lum, Vincent T.Coppola and Dennis S. Bernstein "Adaptive autocentering control for an active magnetic bearing supporting a rotor with unknown mass imbalance", *IEEE transactions on control systems technology*, vol.4, No.5, september 1996.
- [10] S. Loginov "Suspension control in a bearingless reluctance motor without current feedback", *Electrotechnical complexes and control systems* No.4, 2010 pp. 33-37.

Evaluation of Heavy Metals Around the Mining of Decorative Stone Ore in Susong County Liaohe River

SiHeng Lu, Chang Pan, YuJuan Jin, Xiang Wang, Xinlai Wei, ZhiMin Yu

Department of Biology and Environment Engineering, Hefei University, Hefei 230601, P. R. China.

Address: No. 99, Jinxiu Road, Hefei 230601, P. R. China. * Corresponding author. e-mail: 1035319332@qq.com

Abstract. In order to study the pollution of heavy metals around Liaohe Fender stone mine in Susong County, the soils at six points and the sediment at four points were selected. The effects of heavy metals Cu, Zn, Pb, Cd, Cr, Ni, Hg and As were measured, the single factor index and the Nemero index method were used to evaluate the heavy metal elements in soil and sediment. The results showed that the values of heavy metal elements in the soil and sediment were less than 1 and the $P_{integrated}$ values were less than 0.85, the mine area was not polluted by heavy metals and belonged to the clean area within the grade I.

Keywords:- ore rock, heavy metal; soil sediment, the single factor index, the nemero index.

I RESEARCH AREA

In this paper, the mining area is the open pit mining and main mining marble, the amount of ore 110.7729 million m³, the range of 1.4064 square kilometers. The mining area is located in the north of Susong County, and the geographical coordinates of the center of the mining area are E 115 ° 55'25 " and N 30 ° 21'37". The mining area is 71 km from the Changjiang Fuxing Town Pier, by the revival of the town pier along the Yangtze River golden waterway east to Shanghai.

II THE PURPOSE AND SIGNIFICANCE OF THE STUDY

Long-term mining of the mine not only caused soil erosion, but also led to the long-term enrichment of heavy metals during the mining process, and caused a serious threat to the surrounding soil environment.

Heavy metal generally refer to metals with a density greater than or equal to 5.0 [1], which is non-degradable persistent toxic pollutants, that dissolve, adsorb, precipitate, complex and so on in a series of migration and enrichment process in the soil [2], not only caused serious harm to the soil environment and water environment, But also through the food chain

into the human body and accumulated, leading to health problems. In this paper, multi-method has been used to evaluate the heavy metal elements in the mining area, it is of great significance to provide the basis for the content of heavy metals in the mining area and to better manage the mining environment.

III EXPERIMENT AND DATA PROCESSING

A. Sample collection

In the sampling area using a checkerboard sampling points, collecting the thickness of the soil in the 0-20cm deep 6 points of the soil, where each point of soil samples were equely mixed with quartiles [3], the collected samples into the polyethylene plastic bag, and take back to the laboratory. The collection of its sediment along the river to the direction, a sample of 4 points was collected from the sediment layer using a sediment sampler, each sample was taken at a rate of 10 cm for one time [4], then mixed into a sealed bag and numbered back to the laboratory. The sampling points for soil and sediment are shown in Table 2.1 and Table 2.2 below:

Table 2.1
Soil Point Arrangement

Point number	Sampling point	Location	Detection Indicator
S1	Farmland on the south side of the mining area 20cm	N : 30°19'29" E : 115°57'26"	pH, Cd, Hg, As , Cu, Pb, Cr, Zn , Ni
S2	Farmland on the south side of the mining area 50cm		
S3	Farmland on the south side of the mining area 100cm		
S4	Forest on the north side of the mining area 20cm	N : 30°19'29" E : 115°57'16"	
S5	Forest on the north side of the mining area 50cm		
S6	Forest on the north side of the mining area 100cm		

Table 2.2
Placement of The Sediment

Point number	Sampling point	Detection Indicator
1#	Changxi River downstream of the sewage outfall 5000m	pH, Cd, Hg, As, Cu , Pb, Cr, Zn, Ni
2#	Changxi River downstream of the sewage outfall 2000m	
3#	Changxi River downstream of the sewage outfall 500m	
4#	Changxi River sewage outfall upstream 500m	

B. Pretreatment of the sample

Take 500g of soil samples and sediment on the tray in the natural air-dried, polished in the glass, filter with 100 mesh nylon screen [5].

(1) Method for digestion of Cu - Zn - Cd - Cr Ni heavy metal hydrochloric acid - nitric acid - hydrofluoric acid - perchloric acid [6].

Weigh the soil and sediment (0.2 ~ 0.5g) into the digestion cup, wet with water and add 10 mL of hydrochloric acid to heat up to 3 mL on a hot plate at 80 ° C, the addition of nitric acid and hydrofluoric acid 5mL and 3mL of high chloric acid, then heated until the contents of the digestion cup were viscous, and the digestion cup was washed with deionized water and transfer the contents to a 50 mL volumetric flask.

(2) Determination of As Sulfuric Acid - Nitric Acid - Perchloric Acid [7].

Weigh 0.20 ~ 0.5g sieve and sample into the 150mL Erlenmeyer flask, add 7mL sulfuric acid,

10mL nitric acid and 2mL perchloric acid, heating on the hot plate until the liquid was white residue, adding distilled water to 50mL.

(3) Digestion of Hg sulfuric acid - nitric acid - potassium permanganate [8].

Weigh 0.2 ~ 0.5g sieve soil samples and sediment into 150mL Erlenmeyer flask, add sulfuric acid, nitric acid mixture 5 ~ 1mL and 10mL potassium permanganate, in the hot plate for 30 ~ 60min. Remove the cooling, add hydroxylamine hydrochloride solution until brown, add distilled water to 100mL.

C. Standard curve preparation

According to the approximate range of the detection limit of each heavy metal Cu1mg / Kg, Zn0.5mg / Kg, Pb and Cd 0.2mg / Kg, Cr and Ni0.5mg / Kg [9], preparation of the standard curve, the final transfer to 50mL capacity bottle, the marking gradient is shown in Table 2.3:

Table 2.3
Concentration Gradient of Each Element

Mixed standard volume /mL	0.00	0.50	1.00	2.00	3.00	5.00
Cu (mg/L)	0.00	0.20	0.40	0.80	1.20	2.00
Zn (mg/L)	0.00	0.10	0.20	0.40	0.60	1.00
Pb (mg/L)	0.00	0.50	1.00	2.00	3.00	5.00
Cd (mg/L)	0.00	0.025	0.005	0.10	0.15	0.25
Cr (mg/L)	0.00	0.50	1.00	2.00	3.00	4.00
Ni (mg/L)	0.00	0.20	0.50	1.00	2.00	3.00
Hg (mg/L)	0.00	0.50	1.00	2.00	3.00	4.00
As (mg/L)	0.00	0.50	1.00	1.50	2.00	3.00

D. Sample test results

(1) Instrument type and related parameters

The Cu,Zn,Cd,Cr and Ni heavy metals were characterized by flame atomic absorption spectrophotometry(Model AA900),for Hg cold atomic using absorption spectrometer (F732-VJ), As

using UV-Vis spectrophotometer (Uvmini1240), The parameters of the relevant elements of flame atomic absorption are shown in Table 2.4 [10], The determination method and the minimum detection limit for each heavy metal are shown in Table 2.5:

Table 2.4
Parameters of Flame Atomic Absorption Related Elements

copper parameter	Wavelength (nm)	Slit width(nm)	Lamp current(mA)	Acetylene: air
Cu	324.8	0.8	2.0	1:5-1:6
Zn	213.9	0.2	2.0	1:4
Pb	283.3	0.8	2.0	1:4
Cd	228.8	0.8	2.0	1:5-1:6
Cr	357.9	0.2	4.0	1:2-1:3
Ni	232.0	0.2	3.0	1:4

Table 2.5
Determination of Heavy Metals and Minimum Detection Limit

Detection Indicator	Detection method	testing base	Detection limit or minimum detection concentration
pH	Potential method	NY/T 1377-2007	--
Cd	KI-MIBK Extraction Flame Atomic Absorption Spectrophotometry	GB/T 17140-1997	0.05
Hg	Cold atomic absorption spectrophotometry	GB/T 17136-1997	0.005
As	Silver dimethyldithiocarbamate spectrophotometric method	GB/T 17134-1997	0.5
Cu	Flame Atomic Absorption Spectrophotometry	GB/T 17138-1997	1.0
Pb	KI-MIBK Extraction Flame Atomic Absorption Spectrophotometry	GB/T 17140-1997	0.2
Cr	Flame Atomic Absorption Spectrophotometry	HJ 491-2009	5
Zn	Flame Atomic Absorption Spectrophotometry	GB/T 17138-1997	0.5
Ni	Flame Atomic Absorption Spectrophotometry	GB/T 17139-1997	5

(2) Heavy metal elements Soil and sediment measurements Data Table 2.6 and Table 2.7:

Table 2.6
Soil Element Measurement Data

Detection Indicator	S1	S2	S3	S4	S5	S6	unit
pH	6.87	7.21	7.38	7.46	7.04	7.33	Dimensionless
Cd	0.021	0.020	0.032	0.07	0.07	0.07	mg/kg
Hg	0.012	0.015	0.017	0.008	0.011	0.012	mg/kg
As	4.35	5.15	4.58	8.51	6.31	5.89	mg/kg
Cu	16.1	12.3	15.0	15.1	10.3	10.2	mg/kg
Pb	4.18	4.10	4.57	15.6	15.5	12.0	mg/kg
Cr	32.8	32.9	31.9	44.3	42.5	37.2	mg/kg
Zn	1.52	1.59	1.46	5.95	5.63	6.03	mg/kg
Ni	12.7	14.8	12.3	36.1	30.7	18.3	mg/kg

Table 2.7
Sediment Element Measurement Data

Detection Indicator	1#	2#	3#	4#	unit
pH	7.34	7.81	7.22	7.63	Dimensionless
Cd	0.035	0.022	0.029	0.035	mg/kg
Hg	0.012	0.009	0.010	0.015	mg/kg
As	0.32	0.26	0.28	0.19	mg/kg
Cu	5.1	0.8	1.36	9.96	mg/kg
Pb	4.18	0.16	2.01	9.93	mg/kg
Cr	25.3	4.2	4.6	27.9	mg/kg
Zn	7.47	0.23	0.10	28.1	mg/kg
Ni	13.2	2.3	3.4	11.6	mg/kg

IV EVALUATION AND ANALYSIS OF RESULTS

Evaluation of soil environmental quality is generally based on the standard limits of «Soil Environmental Quality Standard» (GB15618-1995) [11]. In this paper, we mainly use the single factor and Nemer index to evaluate the content of various metal elements in the soil.

A. Soil pH grade and soil metal element background values

For the pH in the soil, the soil scientist uses it to represent the hydrogen ion concentration in the soil sample [12]. We usually use the pH value to represent the relative pH, through the determination of pH, you can generally understand the evaluation of soil quality in the region, but also for the background of the various elements of the soil to provide a corresponding reference basis [13], The soil pH grades are as follows: Table 3.1:

Table 3.1
Classification of Soil pH

pH	<4.5	4.5~5.5	5.5~6.0	6.0~6.5	6.5~7.0	7.0~7.5	7.5~8.5	8.5~9.5	>9.5
rank	Very strong acidity	Strong acidity	acidity	Weak acidity	neutral	Weakly alkaline	alkaline	Strong alkaline	Very strong alkaline

Soil background value refers to the composition and content of chemical elements in the soil which are not affected by human activities [14]. Soil background value is not only the standard of

environmental quality, but also the basis of various soil pollution evaluation methods [15]. The soil environmental quality standards (GB15618-1955) mg / kg as shown in Table 3.2:

Table 3.2
 Soil Environmental Quality Standard (GB15618-1955)

Soil pH	Level one	Level two			Levelthree	
	Natural background	<6.5	6.5~7.5	>7.5	>7.5	
Cd≤	0.2	0.3	0.3	0.6	1.0	
Hg≤	0.15	0.3	0.5	1.0	1.5	
As	Paddy fields≤	15	30	25	20	30
	dry land≤	15	40	30	25	40
Cu	Farmland n≤	35	50	30	100	400
	orchard≤	--	150	100	100	400
Cr	Pb≤	35	250	300	350	500
	Paddy fields≤	90	250	300	350	400
	dry land≤	90	150	200	250	300
	Zn≤	100	200	250	300	500
Ni≤	40	40	50	60	200	

B. Single Factor Index and Nemer Index

The so-called single factor evaluation is the evaluation of the degree of influence on an element or compound in the soil [16]. The evaluation is based on the individual accumulation index Pi of the material. The advantage of this method is that these transformations are linear, and the value of the attribute before and after the change is proportional [17], only need to calculate the individual indicators of soil elements and the calculation is relatively simple [18]. The single factor pollution index

environmental quality evaluation criteria in Table 3.3 [19]:

Single factor index formula [20]:

$$P_i = \frac{C_i}{S_i} \quad (1)$$

Where Pi - soil i pollutant environmental index;
 Ci - Measured concentration of soil i contaminants (mg / kg);
 Si - soil i pollutants evaluation criteria (mg / kg) (generally take II types of standards);

Table 3.3
 Single Factor Pollution Index Environmental Quality Evaluation Standards in Table

rank	P _i value	Comparison of measured and background values	Pollution assessment
I	P _i ≤1	similar	No pollution
II	1<P _i ≤2	Higher than the background value below the pollution start value	Slight contamination
III	2<P _i ≤3	Higher than the pollution start value	Mild contamination
IV	3<P _i ≤5	More than 1 times the initial value of pollution	Moderately polluted
V	P _i >5	More than 2 times the initial value of pollution	Severe pollution

The comprehensive evaluation method for a region can be used to evaluate the multi - factor, including the Nemeru comprehensive index method and the overlap index method with weights. In this paper, the evaluation of the heavy metal elements in the soil is mainly based on the Nemeru comprehensive index method. The advantage is not only to consider the average accumulation of various chemical elements of the material level, but also reflects the accumulation of the most serious chemical substances to the extent of the harm to the environment [21]. The evaluation criteria for the

environmental quality of the Nemeru pollen index are shown in Table 3.4 [22]:

Nemeru comprehensive index method formula [23]:

$$P_{integrated} = \sqrt{\frac{(C_i / S_i)^2_{max} + (C_i / S_i)^2_{av}}{2}} \quad (2)$$

Where Pintegrated - a comprehensive pollution index in a region;
 (Ci / Si) max - the maximum pollution index in soil contaminants;
 (Ci / Si) av - the average pollution index in soil contaminants;

Table 3.4
Nemero Pollutants Environmental Quality Assessment Criteria

rank	Pintegrated value	Comparison of measured and background values	Pollution assessment
I	Pintegrated ≤ 0.85	A variety of metals are at the background level	Clean (safe)
II	$0.85 < \text{Pintegrated} \leq 1.75$	One or more of the background values	Mild contamination
III	$1.75 < \text{Pintegrated} \leq 2.56$	One or more of which has clearly exceeded the background value	Moderately polluted
IV	Pintegrated > 2.56	One or more has far exceeded the background value	Severe pollution

C. Soil and Sediment Single Factor Index and Nemerot Pollution Index

According to the range of pH, to determine the environmental quality standard selected soil background value of the evaluation level, and then through the single factor index and Nemerot pollution

index evaluation formula calculated data, the Nemerot pollution index are shown in Table 3.5, single factor sediment soil data are shown in Table 3.6, Integrated Pollutant Soil Index are shown in Table 3.7 and Integrated Pollution Index Sediment Index are shown in Table 3.8.

Table 3.5
Single Factor Soil Data

Detection Indicator	S1	S2	S3	S4	S5	S6
Cd	0.070	0.067	0.107	0.233	0.233	0.233
Hg	0.024	0.030	0.034	0.016	0.022	0.024
As	0.145	0.172	0.153	0.284	0.210	0.196
Cu	0.537	0.410	0.500	0.503	0.343	0.340
Pb	0.014	0.014	0.015	0.052	0.052	0.040
Cr	0.164	0.165	0.160	0.222	0.213	0.186
Zn	0.006	0.006	0.006	0.024	0.023	0.024
Ni	0.254	0.296	0.246	0.722	0.614	0.366

Table 3.6
Single Factor Sediment Data

Detection Indicator	1#	2#	3#	4#
Cd	0.117	0.073	0.097	0.117
Hg	0.024	0.018	0.020	0.030
As	0.013	0.010	0.011	0.008
Cu	0.170	0.027	0.045	0.332
Pb	0.014	0.001	0.007	0.033
Cr	0.084	0.014	0.015	0.093
Zn	0.030	0.001	0.000	0.112
Ni	0.264	0.046	0.068	0.232

Table 3.7
Integrated Pollutant Soil Index

Point	S1	S2	S3	S4	S5	S6
Pintegrated value	0.395	0.308	0.370	0.542	0.459	0.286

Table 3.8
 Integrated Pollution Index Sediment Index

point	1#	2#	3#	4#
Pintegrated value	0.197	0.055	0.071	0.243

In order to visually and clearly compare the pollution of each point, The Pintegrated value of the each soil and sediment points are shown in a histogram shown in Figure 3.1 and 3.2:

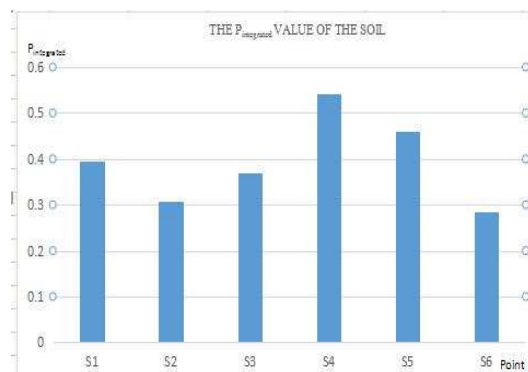


Figure 3.1 Soil Pintegrated Value

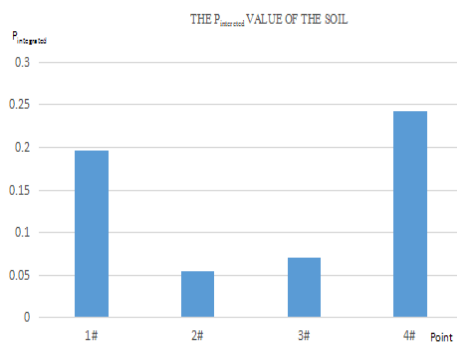


Figure 3.2 Sediment Pintegrated Value

D. Results analysis and summary

The results of the evaluation of soil and sediment according to single factor index and Nemerot pollution index method are as follows:

single factor index evaluation

The results of six points and four sediment points calculation of soil using single factor index formula show that show that the Pi value of Cu in soil 1 ~ 4 is the highest and the pollution of Cu is the most serious. Point Pi and S6 Ni Pi value of the largest, Ni pollution is most serious. The Pi values of S1, S2, S3 and S6 Zn are the smallest and the pollution of Zn is the smallest. The Pi value of 1 # and 4 # Ni in the sediment is the highest, the Ni pollution is the most serious, the Pi value of 2 # and 3 # Cd is the largest, the Cd pollution is the most serious, the Pi value of 1 # As is the smallest, the As pollution is the lightest, and Pi value of 3 # Zn is the smallest, Zn pollution is the lightest, the Pi value of 4 # Hg is the smallest, and the pollution of Hg is the lightest.

The results of single factor index show that the Pi values of soil and sediment are less than 1, belong to

grade I, and there is no heavy metal pollution compared with soil environmental quality standard (GB15618-1955).

(2) The Calculation Results of Soil and Sediment at the Point of Nemerot Pollutant Index

The results show that the Pintegrated value of S4 is the largest and the pollution is the most serious, and the Pintegrated value of S6 is the smallest and the pollution is the lightest. Sediment 4 #Pintegrated maximum value of the most serious pollution,3 # Pintegrated minimum value of the smallest, the smallest pollution.

The calculation of the pollution index from Nemerot indicated that the Pintegrated value of soil and sediment was less than 0.85 and belonged to grade I, and there was no pollution compared with soil environmental quality standard (GB15618-1955).

The results of the evaluation of soil and sediment by single factor index and Nemerot pollen index show that the contents of Cu, Ni and Cd in heavy metals around Liaohe facade stone mining are relatively high. Zn, Hg content is relatively low, but according to the soil environmental quality standards (GB15618-1955) to evaluate, are within the level of I, and no heavy metal pollution. From the two evaluation criteria of the mining area of heavy metal control is better, the environment did not bring a greater threat.

REFERENCES

- [1] Chen Chen. a typical area of heavy metal pollution status and evaluation in Anhui Province[D]. Hefei University of Technology, 2013. (in Chinese)
- [2] Shao Li, Xiao Huayun, Wu pity, Tang Congguo.Advances in Heavy Metal Pollution of Traffic Sources [J]. Earth and Environment, 2012, (03): 445-459. (in Chinese)
- [3] Zhang Qing. Soil heavy metal spectroscopy detection method [J]. Jiangxi Building Materials, 2016, (08): 291-292. (in Chinese)
- [4] Wang Mei, Li Shutian. Fertilizer Heavy Metal Content and Effects of Fertilization on Heavy Metal Accumulation in Soil and Crops [J]. Journal of Plant Nutrition and Fertilizer Science, 2014, (02): 466-480. (in Chinese)
- [5] Feng Yanhong, Wang Guoqing, Ying Rongrong, Zhao Xin, Zheng Liping, Zhou Yan, Zhu Xin, Lin Yu lock. Study on Pretreatment Method for Determination of Total Mercury in Soil [J]. Environmental Science and Technology, 2014, (09): 87-91. (in Chinese)
- [6] Qi Wenqi, Cao Jishan, Lu Minghuai.Comparison of Dissolution of Pb, Cr, Ni, Cd, Mn, Cu and Zn in Typical Soil Samples by Several Dissolution Methods [J]. Drought Environmental Monitoring, 1990, (04): 179-183. (in Chinese)
- [7] XIAO Ming, YANG Wen-jun, SUN Xiao-feng, LV Xin.Effects of Soil As Dynamic on the Quality Evaluation and Environmental Risk Prediction [J].Agricultural Resources and Environment, 2014, (03): 273-278. (in Chinese)
- [8] Xie Tao, Luo Yan. Determination of Total Mercury in Soils by Direct Mercury [J]. Spectroscopy Laboratory. 2012 (03) (in Chinese)

- [9] Wang Lina, Si Hongyan, Fu Huafeng. Determination of Cu, Zn, Pb, Cd, Cr and Ni in Sewage Sludge by Flame Atomic Absorption Spectrometry [J]. Journal of Xuchang University, 2010, (02): 91-95. (in Chinese)
- [10] Qi Wenqi, Cao Jishan, Dai Wenhong. Comparison of Pb, Cr, Ni, Cd, Mn, Cu and Zn in Three Kinds of Soil by Different Acidic Methods [J]. China Environmental Monitoring, 1991, (03): 47-50. (in Chinese)
- [11] Zhang Xiaolei, Kong Linghui, He Kuan, Fu Yan. Henan University campus soil heavy metal status and its evaluation [J]. Journal of Luoyang Normal University, 2006, (05): 145-148. (in Chinese)
- [12] Feng Guoming. Determination of soil pH [J]. Friends of the rich farmers, 2000, (10): 14. (in Chinese)
- [13] Wu Lingzhen. Study on urban soil environmental quality evaluation based on soil heavy metal [D]. Southwest University, 2013. (in Chinese)
- [14] MA Hui-ying. Research on soil background value of Ebinur Lake Basin [D]. Xinjiang University, 2010.
- [15] Wei Fusheng, Chen Jingsheng, Wu Yanyu, Zheng Chunjiang. Study on Soil Environmental Background Value in China [J]. Environmental Science, 1991, (04): 12-19. (in Chinese)
- [16] YANG Xu, ZENG Xiang-liang. Evaluation of water quality of Meiyu Lake in Zhengzhou University based on single factor evaluation method and pollution index method [J]. Jiangsu Science and Technology Information, 2014, (05): 51-53. (in Chinese)
- [17] Luo Fang, Wu Guorong, Wang Chong, Zhang Lin. Nemeró pollution index method and single factor evaluation method in water quality evaluation [J]. Environment and Sustainable Development, 2016, (05): 87-89. (in Chinese)
- [18] Spatial distribution and contamination assessment of heavy metals in surface soils of Hassi Messaoud, Algeria [J]. Mohammed L. Benhaddya, Mohammed Hadjel. Environmental Earth Sciences . 2014 (3)
- [19] Li Xiaolong. Evaluation of soil heavy metal pollution in a smelter in Tongguan County, Shaanxi Province [D]. Northwest A & F University, 2014. (in Chinese)
- [20] Li Renzhe. A rare metal plant environmental pollution assessment of the status quo and its impact on the quality of the plant [D]. Northwestern Polytechnical University, 2006. (in Chinese)
- [21] Liang Bao. Yong Bridge area high risk area river coastal soil heavy metal pollution and ecological risk assessment [D]. Anhui Medical University, 2016. (in Chinese)
- [22] KONG Fan-bin, LIU Yang. Comparison of single factor index method and Nemeró index method in soil environmental quality evaluation [J]. Gansu Science and Technology, 2014, (03): 21-22. (in Chinese)
- [23] Zhang Yulian, Yan Tianzeng. Application of Nemeró Index Method in Soil Heavy Metal Pollution Evaluation [J]. Journal of Henan Institute of Education (Natural Science Edition), 2012, (02): 35-39. (in Chinese)

Effect of Heat Treatment on Electrical and Mechanical Properties of the Solid Sapropel

Andris Martinovs¹, Rasma Tretjakova¹, Rene Castro³, Vladimir Solovyev⁴,
Josef Timmerberg², Alexander Cvetkov⁴, Sergey Gango⁴, Angelika Borkenstein²,
Paul Beckmann², Helmut Schütte², Nikolai Puchkov⁴, Sergey Trifonov⁴

¹ Rezekne Academy of Technologies, LV-4601 Rezekne, Latvia

² Jade University of Applied Sciences, 26389 Wilhelmshaven, Germany

³ Herzen State Pedagogical University of Russia, 191186 St. Petersburg, Russia

⁴ Pskov State Universities, 180000 Pskov, Russia

Abstract. In this work changes of electrical and mechanical properties (hardness) of the solid sapropel after its heat treatment were researched. Changes of real and imaginary parts of dielectric permittivity, dielectric losses and specific electrical resistance depending on electrical field frequency in the range 0.01Hz- 1MHz were observed. Temperature dependences of AC (at 1 kHz) and DC electrical conductivity were studied. Chemical sample composition, IR spectra and structure of the solid sapropel were investigated. Heat treatment has a noticeable effect on the electrical characteristics of solid sapropel due to the strong influence of water on the charge transfer in this complex material. Charge transfer occurs predominantly due to ion migration and demonstrates strong dependence upon hydration - dehydration processes. After the heat treatment of the solid sapropel at the temperature of 100°C its hardness doesn't change. If the sample of the solid sapropel is subjected to 20 min heat treatment at the temperature of 150°C, its hardness decreases by 5.4%, the number of C=C bonds decreases by 6.3±0.1%, the number of C=N bonds decreases by 2.2±0.1%, the number of C-C bonds decreases by 1,7±0.1%, the number of C-H bonds increases by 18.5±0.3%. It shows that in the temperature range 100-150°C destructive processes of the solid sapropel start, although visually (with optical microscope and with SEM) changes of structure are impossible to observe yet.

Keywords: solid sapropel, dielectric permittivity, specific electrical resistance, hardness, IR spectra, chemical composition.

I. INTRODUCTION

Latvia, Russia's Pskov region, Lithuania, Belarus are rich with lake sediments - sapropel. For example, in Russian Federation the total sapropel reserves exceed 200 billion m³ [15], in Latvia they are approximately 2 billion m³ [11]. Sapropel is renewable resource; its layer in lakes enlarges by 1-2 mm per year [11]. At present usage of sapropel in production volumes is insignificant; it is used mostly for enrichment of soil, in balneology and cosmetology. Sapropel can be used as binding substance in production of fuel briquettes [12], as adsorbent [12], [13], [14], [21], as biologically active substance [16], [17], [18], as binding substance in the production of thermal and acoustic insulation building materials [24], [25]. Possibly, this resource can have also other usages, which enable to develop products with high added value. Therefore, complex research of mechanical, physical, chemical and biological properties of sapropel is the necessary purpose. Elaboration foreruns in research of mechanical and electrical properties of the solid sapropel were made in work [6], thermal properties are researched in [20]; biological [23], [26], chemical [11], [21], [22], [23], and magnetic [19] properties

were also investigated. In order to change properties of material, it is modified. Modification methods of various materials are viewed in work [10].

The purpose of this work is to research changes of electrical and mechanical properties of the solid sapropel after its heat treatment.

II. MATERIALS AND METHODS

Samples of sapropel were taken from the depth 0.5m in the gulf of Diunoklis of the lake Rušons in Latvia and dried in stationary air space with temperature 20°C and relative humidity 60- 70% until the solid sapropel was obtained. Material was sawn to 3mm thick plane-parallel plates (with Struers Secotom-15 saw), their surfaces were grinded (Struers LaboPol-5 grinding machine; disk MD-Allegro, 200mm, diamond spray in grain sizes from 15- 3µm). All samples of the solid sapropel were placed into the thermostat Memmert UNE 400 with temperatures of 20, 50, 75, 100, 125 and 150°C for 20 minutes. After cooling at the temperature 20°C Shore D hardness was measured, structure of the material was researched (optical microscope, SEM), chemical composition was determined (SEM), IR spectra were captured and electrical properties were determined.

ISSN 1691-5402

© Rezekne Academy of Technologies, Rezekne 2017
<http://dx.doi.org/10.17770/etr2017vol3.2611>

Dielectric spectra of the samples under study were investigated within wide frequency range 0.01Hz-1MHz by dielectric spectrometer “Novocontrol” with high-resolution automatic frequency analyser ALPHA-ANB.

The temperature dependences of all the electrical characteristics of the samples with graphite electrodes were obtained upon continuous heating or cooling with a rate of 1 to 2 degrees per minute. Alternating-current (AC) conductivity and dielectric permittivity were measured by an E7-13 impedance meter at the frequency of 1kHz. Direct current (DC) measurements were carried out by micro ammeters F195 or M95.

III. RESULTS AND DISCUSSION

Figure 1 demonstrates frequency dependences of dielectric characteristics (real ϵ' and imaginary ϵ'' parts of dielectric permittivity, as well as dielectric losses $\tan\delta$) measured at room temperature for solid sapropel samples annealed at 20°C (curves 1-3) and 100°C (curves 4-6). The most striking observation is the pronounced dielectric loss relaxation maximum which can be seen in the low-frequency region: $\tan\delta_{\max} \approx 0.4$ near $f \approx 70\text{Hz}$ after the heat treatment at 20°C (curve 3) and $\tan\delta_{\max} \approx 0.5$ near $f \approx 20\text{Hz}$ after the heat treatment at 100°C (curve 6). Similar dielectric losses at low frequencies ($10^{-3} - 10^2 \text{ Hz}$) are usually referred to migration polarisation which occurs due to charge migration to the grain boundaries or other types of structure inhomogeneity [1].

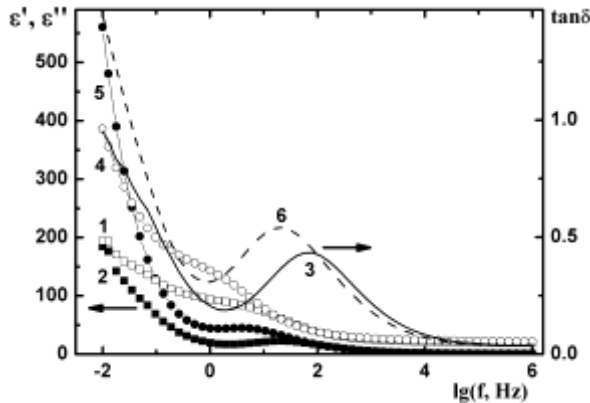


Fig.1. Frequency dependences of the dielectric characteristics measured at room temperature for the sapropel samples after heat treatment at $t=20^\circ\text{C}$ (curves 1-3) and $t=100^\circ\text{C}$ (curves 4-6): real part ϵ' of dielectric permittivity (1 - open quadrates, 4 - open circles), imaginary part ϵ'' of dielectric permittivity (2 - closed quadrates, 5 - closed circles), dielectric losses $\tan\delta$ (3 - solid line, 6 - dashed line).

One can also analyse dependence $\epsilon''=F(\epsilon')$, i.e. Cole-Cole plot [2], approximated by [3], [4].

$$\epsilon' = \epsilon_\infty + \frac{(\epsilon_c - \epsilon_\infty) \left[1 + (\omega\tau)^{1-\alpha} \sin \frac{\pi\alpha}{2} \right]}{1 + 2(\omega\tau)^{1-\alpha} \sin \frac{\pi\alpha}{2} + (\omega\tau)^{2(1-\alpha)}}, \quad (1)$$

$$\epsilon'' = \frac{\sigma}{\epsilon_0 \omega} + \frac{(\epsilon_c - \epsilon_\infty) (\omega\tau)^{1-\alpha} \cos \frac{\pi\alpha}{2}}{1 + 2(\omega\tau)^{1-\alpha} \sin \frac{\pi\alpha}{2} + (\omega\tau)^{2(1-\alpha)}}, \quad (2)$$

where ϵ_c and ϵ_∞ are the values of dielectric permittivity at low ($\omega\tau \ll 1$) and high ($\omega\tau \gg 1$) frequencies, respectively, σ represents DC electric conductivity, $\epsilon_0=8.85 \cdot 10^{-12} \text{ F/m}$, and parameter α characterises distribution of relaxation time τ values ($0 \leq \alpha < 1$).

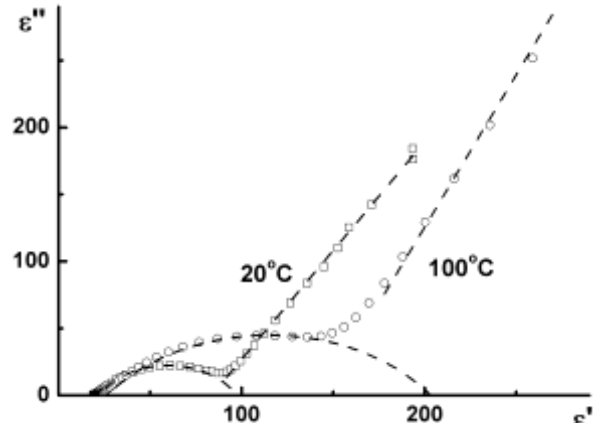


Fig. 2. Cole-Cole plots obtained from room temperature data for the sapropel samples after heat treatment at $t=20^\circ\text{C}$ and $t=100^\circ\text{C}$.

If $\alpha=1$, formulae (1) and (2) reduce to the well-known Debye expressions, and $\epsilon''=F(\epsilon')$ graph transforms to the semicircle, its centre lying in the ϵ' -axis. As could be seen from Fig. 2, it does not take place for the sapropel samples under study: the centres of their Cole-Cole semicircles are down shifted along the ϵ'' -axis. The estimated values of distribution parameter are $\alpha_{20} \approx 0.3$, $\alpha_{100} \approx 0.4$ for the sapropel samples annealed at 20°C and 100°C, respectively.

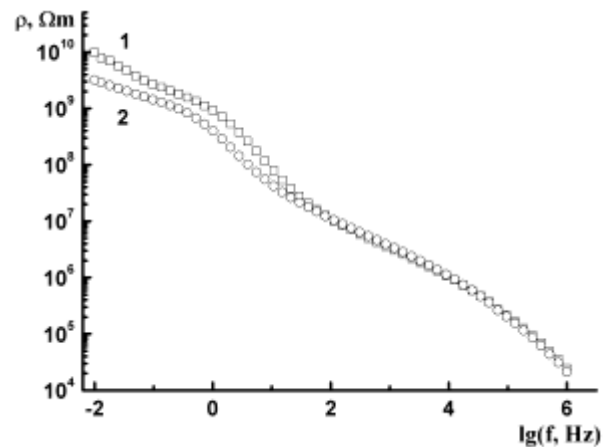


Fig. 3. Frequency dependences of the specific electrical resistance measured at room temperature for the sapropel samples after heat treatment at $t=20^\circ\text{C}$ (curve 1) and $t=100^\circ\text{C}$ (curve 2)

At low frequencies ($f < 3\text{Hz}$ and $f < 1\text{Hz}$ for the sapropel samples annealed at 20°C and 100°C , respectively) Cole-Cole plots demonstrate linear dependences $\varepsilon'' = k \cdot \varepsilon' + b$ (straight lines in Fig. 2). This effect can be interpreted as the manifestation of the universal relaxation power law proposed by Jonscher [5], as well as the predominance of DC conductivity contribution in formula (2) at low frequencies.

Figure 3 demonstrates frequency dependences of the specific electrical resistance of the sapropel samples measured at room temperature and gives one more confirmation of this universal relaxation power law: one can see few linear parts in this double-logarithmic plot. Similar result was published earlier in [6].

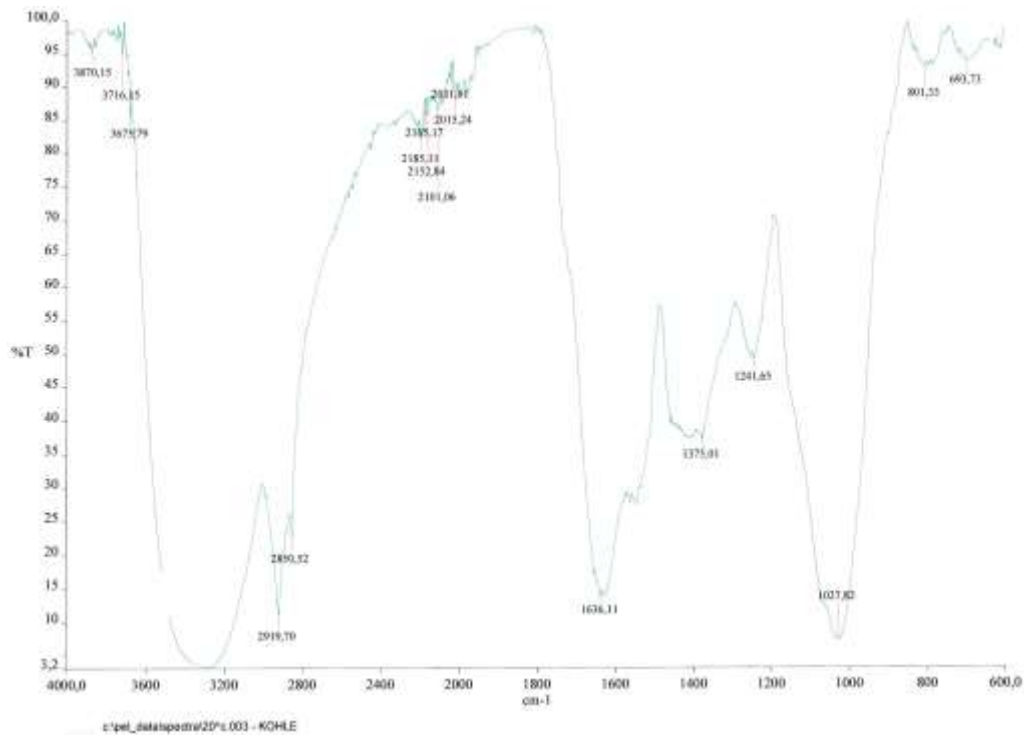


Fig. 4. Infrared spectra of the sapropel sample after heat treatment at $t=20^{\circ}\text{C}$

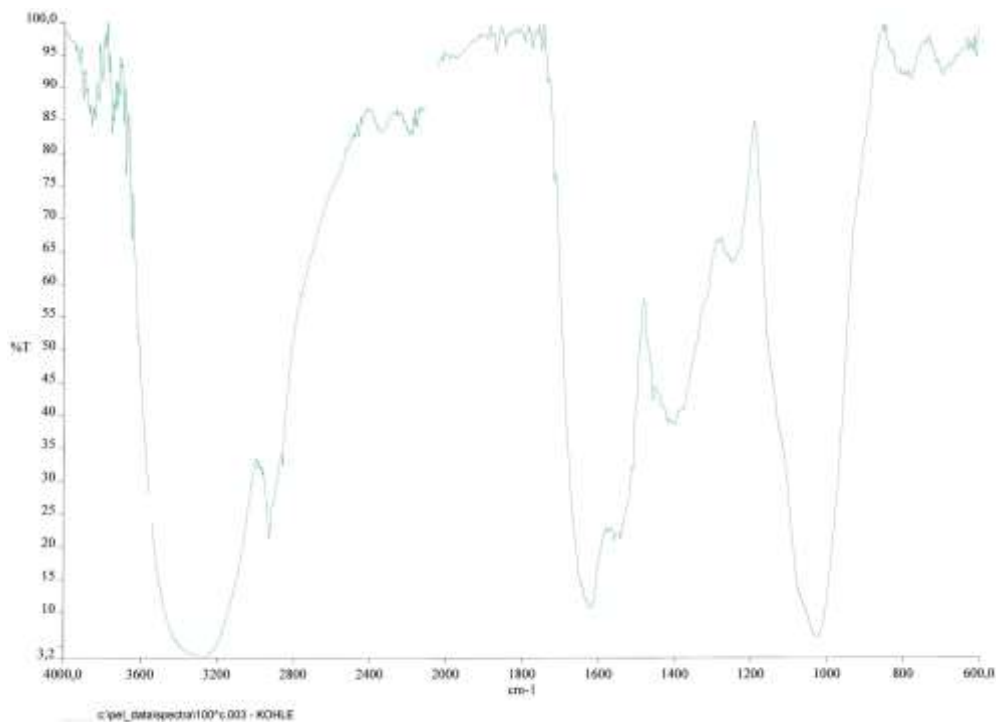


Fig. 5. Infrared spectra of the sapropel sample after heat treatment at $t=100^{\circ}\text{C}$

It should be emphasized that after the heat treatment at $t=100^{\circ}\text{C}$ specific electrical resistance of the sapropel sample at low frequencies decreases (see curves 1 and 2 in Fig. 3). We suppose that this effect may be due to the sample dehydration during annealing at high temperature. Indeed, the spectral position of the strongest absorption band in the infrared spectra of the initial sapropel sample (3400cm^{-1}) corresponds to the vibrations of the OH^- groups (Fig. 4-5)

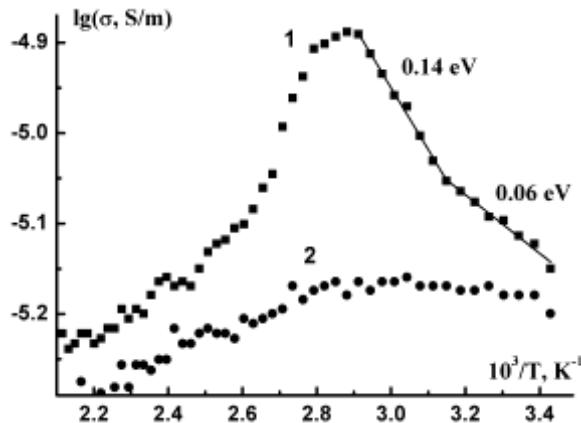


Fig. 6. Arrhenius temperature dependences of the AC electrical conductivity measured twice (curve 1 – first heating, curve 2 – second heating) at $f = 1 \text{ kHz}$ for the sapropel sample after annealing at $t=20^{\circ}\text{C}$

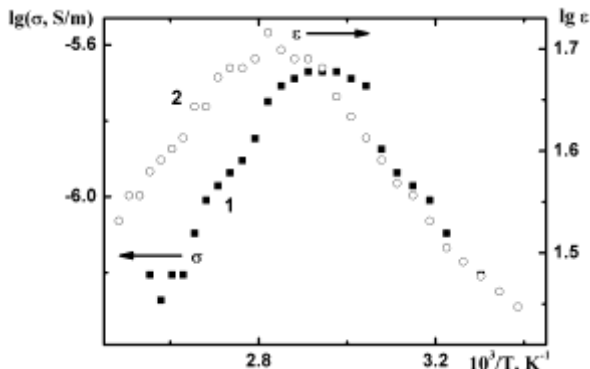


Fig. 7. Arrhenius temperature dependences of the AC electrical conductivity (curve 1) and dielectric permittivity (curve 2) measured at $f = 1 \text{ kHz}$ for the sapropel sample after annealing at $t=100^{\circ}\text{C}$

Temperature dependences of the AC electrical conductivity σ of sapropel samples (Fig. 6-7) also agree with this assumption. During the first heating of the sapropel sample annealed at $t=20^{\circ}\text{C}$ Arrhenius dependence $\sigma = \sigma_0 \cdot \exp(-E/(k \cdot T))$ occurs up to the temperature $T_0 \approx (345-355)\text{K}$; activation energy E values for two observed regions (curve 1, Fig. 6) are 0.06 eV and 0.14 eV , respectively. Further heating of the sample (when $T > T_0$) results in the conductivity decrease, probably, due to removal of water molecules from the sample. During subsequent cooling of the sample only Arrhenius decrease of conductivity σ with activation energy $E = 0.06 \text{ eV}$ can be observed. Dehydration of the sapropel sample seems to be irreversible: the second heating (after 4

days storage under the ambient conditions) does not reproduce the initial result (curve 2 in Fig. 6 demonstrates much lower conductivity value and much weaker maximum at $T \approx T_0$ as compared with characteristic features of curve 1). Analogous phenomena (when sapropel electrical characteristics “remember” sample prehistory) were previously observed in [6] and were treated as “memory” effect.

AC electric conductivity and dielectric permittivity values of the sapropel sample annealed at $t=100^{\circ}\text{C}$ demonstrate similar behaviour (Fig. 7), but corresponding values are smaller than those of the sapropel sample annealed at $t=20^{\circ}\text{C}$ (see Fig. 6-7).

Similar results were obtained when the temperature dependence of DC electric conductivity was measured (Fig. 8), but the activation energy value during sample cooling was found to be much larger (about 1.5 eV). Remarkably, the sample mass value after heating during electrical conductivity measurements decreases probably due to water removal from the pores of this natural adsorbent.

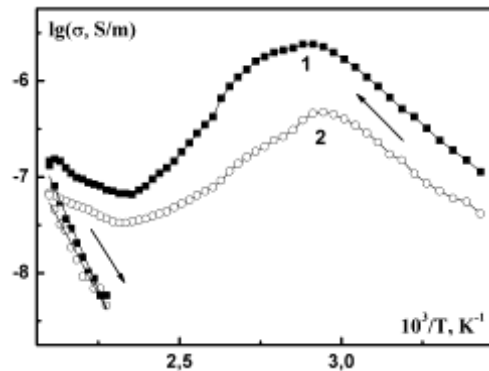


Fig. 8. Arrhenius temperature dependences of the DC electrical conductivity for the sapropel samples after annealing at the temperatures $t_1=50^{\circ}\text{C}$ (curve 1) and $t_2=150^{\circ}\text{C}$ (curve 2). Arrows indicate heating and cooling of the samples.

Thus, observed effect of humidity on the electrical properties of sapropel samples allows concluding noticeable ionic contribution into charge transport processes in these substances at low frequencies. It should be noted that our attempts to measure thermal electromotive force of sapropel samples were not successful: no evidence for electronic conduction in these solid dielectrics has been observed.

Mechanical properties of solid sapropel (ultimate compression strength, ultimate strain, Young’s modulus) were explored in work [6]. In this paper hardness from Shore D (after heat treatment) dependent on heat treatment temperature was studied – see results in Fig. 9. At temperatures below 100°C hardness practically doesn’t change, while in the temperature range $100-150^{\circ}\text{C}$ the observed hardness decreases by 5.4% – probably due to the destruction of C-C, C=C molecular bonds and the starting of the sapropel destruction process at high temperatures.

IR spectra of the samples (see Figs. 4-5), show that the main chemical bonds of sapropel are O-H, C-C, C-H, C=N, C=C with valence oscillations and -CH₃ with deformation oscillations [9]. Figure 10 demonstrates IR transparency T dependence on the heat treatment temperature. Supposing, that the number of bonds is proportional to (1-T) value, then at temperature range 100-150°C the number of C=C bonds decreases by 6.3±0.1%, the number of C=N bonds decreases by 2.2±0.1%, the number of C-C bonds decreases by 1,7±0.1%, the number of C-H bonds increases by 18.5±0.3%; however the number of O-H bonds doesn't change. It means that the humidity of the material during IR spectra capturing is constant.

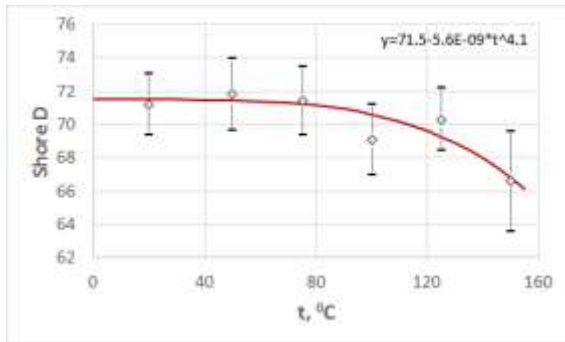


Fig. 9. Shore D hardness dependent on heat treatment (20 min) temperature (after heat treatment)

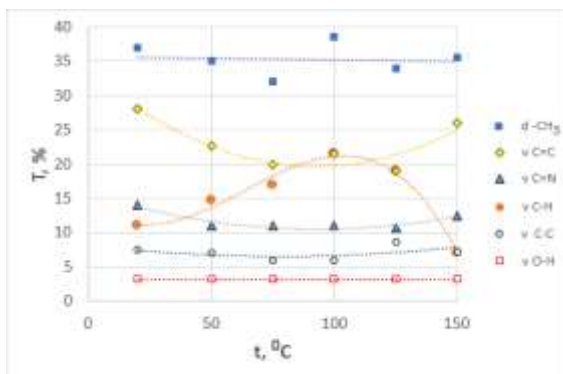


Fig.10. IR transparency T dependent on heat treatment (20 min) temperature (after heat treatment); v- valence oscillations, d- deformation oscillations; measurement error $\Delta T=0,5\%$



Fig.11. Sapropel structure (polished surface) after heat treatment at $t=20^{\circ}\text{C}$

Structure of sapropel is highly inhomogeneous with different compositions, many cracks are observed (see Figs.11-12). Different diameter spherical imprints that left by Shore D indenter, reveal about highly different composition. At temperature range 20-150°C visual changes of structure were not detected. If indenter gets in crack, then hardness measurer shows lower value. This explains significantly large scatter of results (measurement error) in hardness measuring (Fig.9).



Fig.12. Sapropel structure after 20 min heat treatment at $t=150^{\circ}\text{C}$

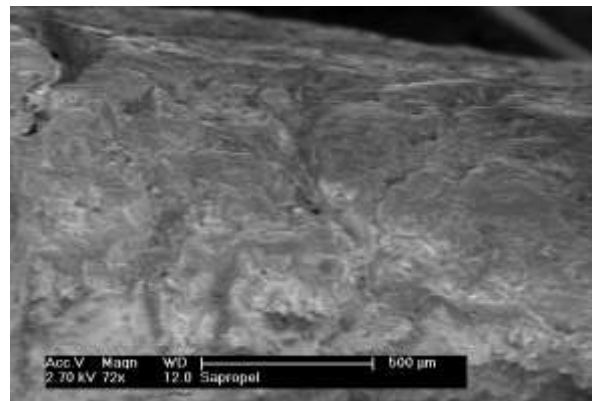


Fig.13. Surface of solid sapropel after heat treatment at $t=20^{\circ}\text{C}$

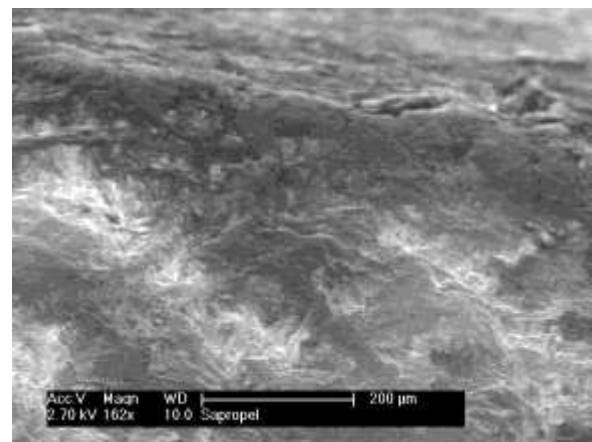


Fig.14. Surface of solid sapropel after 20 min heat treatment at $t=150^{\circ}\text{C}$

Comparing SEM images of sapropel surface (Figs. 13 and 14) it is obvious that structure doesn't

change at the temperature range 20-150°C. Ascertained, that high porosity presents in the solid sapropel. This is shown by SEM tests, for example, in order to create corresponding SEM vacuum for 1cm³ sample, period of 2.5h is necessary. Considering also that in this material microorganisms develop very well [26], the solid sapropel can be used as biological container for transportation of microorganisms.

We did not detect any changes of chemical composition after heat treatment of the solid sapropel at the temperature of 150°C – see chemical composition of given solid sapropel in table 1.

Table 1.
Chemical composition of solid sapropel

Chemical elements	T=20°C	T=150°C
	% by weight	% by weight
O	45,43±14,2	44,40±14,0
C	41,41±13,2	40,16±12,9
N	7,47±2,9	8,19±3,3
Si	2,02±0,1	1,97±0,1
Ca	1,25±0,1	1,17±0,1
Fe	1,18±0,1	2,77±0,2
S	0,45±0,0	0,51±0,0
Al	0,38±0,0	0,29±0,0
K	0,21±0,0	0,20±0,0
Mg	0,14±0,0	0,17±0,0
Na	0,06±0,0	0,17±0,0

IV. CONCLUSION

In summary, heat treatment has a noticeable effect on the electrical characteristics of solid sapropel due to the strong influence of water on the charge transfer in this complex material. We suppose that electrical properties of sapropel natural sorbents are to some extent similar to those of zeolites (porous dielectric aluminosilicates [7, 8]): in both cases charge transfer occurs predominantly due to ion migration and demonstrates strong dependence upon hydration - dehydration processes.

After heat treatment of the solid sapropel at temperatures below 100°C, its hardness doesn't change. If sample of the solid sapropel is subjected to 20 min heat treatment at temperature 150°C, then its hardness decreases by 5.4%, the number of C=C bonds decreases by 6.3±0.1%, the number of C=N bonds decreases by 2.2±0.1%, the number of C-C bonds decreases by 1,7±0.1%, the number of C-H bonds increases by 18.5±0.3%. It shows that in temperature range 100- 150°C destructive processes of the solid sapropel start, although visually (with optical microscope and with SEM) changes of structure are impossible to observe yet.

REFERENCES

- [1] Поплавко Ю.М., Переверзева Л.П., Раевский И.П. Физика активных диэлектриков (Physics of active dielectrics). Ростов н/Д: Изд-во ЮФУ, 2009. 480 с.
- [2] Cole K.S., Cole R.H. Dispersion and absorption in dielectrics// J. Chem. Phys. 1941. V. 9. P. 341-351.
- [3] Богородицкий Н.П., Волокобинский Ю.М., Воробьев А.А., Тареев Б.М. Теория диэлектриков (Theory of dielectrics). М.-Л.: Энергия, 1965. 344 с.
- [4] Богатин А.С. Релаксационная поляризация в диэлектриках с большой сквозной электропроводностью (Relaxation polarization in dielectrics with large through conductivity). Автореферат дисс. на соискание ученой степени доктора физ.-мат. наук. Ростов-на-Дону, 2011. 42 с.
- [5] Jonscher A.K. Universal relaxation law. London: Chelsea Dielectric Press, 1996. 415 p.
- [6] Martinovs A., Timmerberg J., Tretjakova R., Beckmann P., Popa V., Wagner R. Mechanical and electrical properties of the solid sapropel // Environment. Technology. Resources: Proceedings of the 10th International Scientific and Practical Conference. Rezekne, Latvia, 2015, Vol. 1, pp. 139-146.
- [7] Breck D.W. Zeolite Molecular Sieves. Wiley: New York, 1974. 782 p.
- [8] Solovyev V.G., Ivanova M.S., Pan'kova S.V., Trifonov S.V., Veisman V.L. Preparation and physical properties of zeolite, zeolite-like single crystals and zeolite-based nanocomposite materials // Handbook of Zeolites: Structure, Properties and Applications / Editor T.W. Wong. New York: Nova Science Publishers, 2009. Chapter 5. P. 77–99.
- [9] Demuth R., Kober F. Grundlagen der Spektroskopie (Gebundene Ausgabe). Verlag: Diesterweg Salle Sauerländer, 1977, 159 Seiten.
- [10] P. M. Sivakumar, V.I. Kodolov, G.E. Zaikov, A. K. Haghi. Nanostructure, Nanosystems, and Nanostructured Materials: Theory, Production and Development. Apple Academic Press, Toronto, New Jersey, 2013, pp.580.
- [11] Stankevica K., Kļavins M. Sapropel un tā izmantošanas iespējas (Sapropel and Its Application Possibilities)// Material Science and Applied Chemistry. 2013 / 29, p.109-126. (in Latvian)
- [12] Nikolaeva L. A., Latyshev V. G., Burenina O. N. Fuel Briquettes from Brown Coals of Yakutia. ISSN 0361-5219, Solid Fuel Chemistry, 2009, Vol. 43, No. 2, pp. 109–112.
- [13] Kovalenko G. A., Perminova L. V., Terent'eva T. G., Sapunova L. I., Lobanok A. G., Chuenko T. V., Rudina N. A., Chernyak E. I. Glucose Isomerase Activity in Suspensions of *Arthrobacter nicotianae* Cells and Adsorption Immobilization of the Microorganisms on Inorganic Carriers. Applied Biochemistry and Microbiology, 2008, Vol. 44, No. 2, pp. 174–181
- [14] Kovalenko G.A., Perminova L.V., Rudina N.A., Maksimova Yu.G., Maksimov A. Yu. Sapropel-based supports as novel macroporous carbon-mineral adsorbents for enzymatic active substances. Resource-Efficient Technologies, Vol. 2, 2016, pp. 159-167.
- [15] Smetanin V. I., Sogin A. V. Use of hydraulic excavation for cleaning and construction of water bodies. Power Technology and Engineering, Vol. 45, No. 4, November, 2011, pp. 254-257.
- [16] Перк А. А. Использование сапропелей криолитозоны в качестве источника получения биологически активных веществ гуминового ряда// Перспективы фитобиотехнологии для улучшения качества жизни на Севере: материалы Междунар. конф. с элементами научной школы для молодежи, г. Якутск, Россия, 11-16 окт. 2010 г.- Якутск, 2010. - С. 154-158. (in Russian)
- [17] Ядрихинский В. Ф., Перк А. А., Егорова М. С. Применение препарата из сапропеля для лечения демодекоза собак// Актуальные вопросы ветеринарной медицины. - Новосибирск, 2003. - С. 71-72. (in Russian)
- [18] Павлова П. А., Перк А. А., Егорова М. С. Влияние биостимулятора из сапропеля на рост и развитие интродуцентов в условиях многолетней мерзлоты// Фундаментальные и прикладные проблемы ботаники в начале XXI века: материалы Всерос. конф. (Петрозаводск, 22-27 сент. 2008 г.). - Петрозаводск, 2008. - Ч. 6: Экологическая физиология и биохимия растений. Интродукция растений. - С. 291-294. (in Russian)
- [19] Juan C. Larrasoana, Andrew P. Roberts, Joseph S. Stoner, Carl Richter, Rolf Wehausen. A new proxy for bottom-water ventilation in the eastern Mediterranean based on diagenetically controlled magnetic properties of sapropel-

- bearing sediments. *Palaeogeography, Palaeoclimatology, Palaeoecology*. Vol. 190, 2003, pp. 221-242.
- [20] Petrunin G. I., Popov V. G., Soskov A. V. Thermal Properties of the Bottom Sediments of the Black Sea// *Moscow University Physics Bulletin*, 2008, Vol. 63, No. 1, pp. 61–66.
- [21] Adeeva L. N., Kovalenko T. A. Removal of Organic Substances and Metal Ions from Water Using a Carbon-Mineral Sapropel Sorbent. *Russian Journal of Applied Chemistry*, 2012, Vol. 85, No. 4, pp. 557–563.
- [22] Platonov V. V., Nikolaev D. S., Sakharovskii V. G., Proskuryakov V. A., Nikolaev S. G. High-Resolution ¹H NMR Spectroscopy of Organic Matter of Carbonate-Chara Sapropel. *Russian Journal of Applied Chemistry*, Vol. 75, No. 12, 2002, pp. 2021-2026
- [23] Vysokogorskii V. E., Nozdrunova A. A., Plaksin G. V., Krivonos O. I., Mkrchan O. Z., Petrosyan L. Yu. Antioxidant activity of liquid products of heat-treated sapropels. *Pharmaceutical Chemistry Journal*, Vol. 43, No. 4, 2009, pp. 191-194.
- [24] Giedrius Balčiūnas, Jadvyga Žvironaitė, Sigitas Vejelis, Aleksandras Jagniatinskis, Sergejus Gaidučis. Ecological, thermal and acoustical insulating composite from hempshives and sapropel binder. *Industrial Crops and Products*, Vol. 91, 2016, pp. 286–294.
- [25] Arūnas Kremensas, Rūta Stapulionienė, Saulius Vaitkus, Agnė Kairyte. Investigations on physical-mechanical properties of effective thermal insulation materials from fibrous hemp. *Procedia Engineering*, Vol. 172, 2017, pp. 586-594.
- [26] Tretjakova R., Grebeža J., Martinovs A. Research into biological characteristics of dried sapropel// *Environment. Technology. Resources: proceedings of the 10th International Scientific and Practical Conference, Rezekne, 2015, Vol. 1, pp. 223-227.*

LED Lamp for Application in Medical Centers – Design and Thermal Management

Petko Mashkov, Hristo Beloev, Berkant Gyoch, Tamara Pencheva
University of Ruse, Bulgaria

Abstract. The goal of this work is research and development of light sources suitable for use in hospitals, nursing homes, hospices and other similar institutions. During the day spectral power distribution (SPD) of this type luminaire needs to simulate natural day light that affects the natural circadian rhythm of humans. Maintaining the natural circadian rhythm impacts positive on human health, improves mood, prevents the development of depression and helps to overcome them. In the late afternoon increase light in the red-orange part. Light of this kind of spectral composition doesn't inhibit melatonin production and the human body naturally prepares for rest and sleep. At night artificial lighting should be in the red - orange area to enable patients to sleep and staff to fulfill their obligations. Theoretical analysis and selection of suitable LEDs for the realization of the luminaire with the desired characteristics are made. Performed experimental studies make possible achieving the desired characteristics of light and appropriate LEDs' modes of operation.

Keywords: Healthy illumination, LEDs' thermal management, Power LEDs.

I. INTRODUCTION

The influence of illumination on the hormonal balance in the human body is well known [1 - 8]. The rapid development of lighting technology based on LEDs allows the light flux of artificial lighting to resemble sunshine. This is particularly relevant in developing lighting systems for hospitals, nursing homes, hospices and others, as lighting of this type maintains the natural circadian rhythm in humans. It positively affects the health and mood of the people and prevents falling into depression.

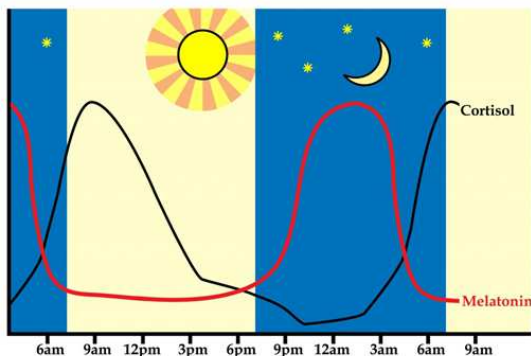


Fig.1. Circadian rhythm [1]. During the day the blue light suppresses melatonin and increases cortisol levels, so human body is prepared to day job. In the late afternoon, with lack of blue light, hormone levels are shifted and the body is preparing for restful sleep.

In the morning the spectral composition of the light should be more intensive in the blue-violet part

of the spectrum (correlated color temperature CCT = 5500 ÷ 6500 K). It is known that the radiation in that part of the spectrum (with maximum close to 440 nm – 480 nm) stimulates the production of cortisol and improves the cognitive abilities, work productivity, concentration, focus, and has positive effect on the mood – fig. 1. On the other hand light in this part of the spectrum inhibits production of melatonin. In the late afternoon the blue light should decrease and increase light in the red-orange part. Light of this kind of spectral composition doesn't inhibit melatonin production and the human body naturally prepares for rest and sleep.

Night in the hospital must be maintained lighting, which is sufficient for movement of people and to enable staff to perform their duties. In the same time the light should not interfere with restful sleep to patients, i.e. its spectral composition should be in orange - red area.

II. MATERIALS AND METHODS

A. Desirable characteristics of light in hospitals, nursing homes, hospices and other similar institutions

The characteristics of human vision are heavily dependent on age - for example the children's eyes are more transparent than those of adults [7]. Therefore light in the blue - violet region (where light quanta are more energy) is harmful to children's eyes and its intensity should be limited in rooms inhabited by children. For such premises maximum color

temperature of light output should be limited to around 4000 – 4500 K. In rooms for accommodating elderly maximum color temperature of the luminous flux is normal to reach 6000 – 6500 K. For rooms in nursing homes color temperature of lighting can be increased above 7500 K as well as to increase the illumination of the premises - this reflects positively on mood and prevents depression in older people.

The above mentioned features set these requirements to the designed luminaire:

- Depending on the time automatically should be changed the spectral composition of light output, so as to mimic the characteristics of sunshine;

- Depending on the type of the patients the maximum color temperature of the light flux should be limited to three grades - up to about 4000 – 4500 K; to about 6000 - 6500 K and to about 7500 - 8000 K.

- Ranging from 5 p.m. to 7 a.m. color temperature of white light output of the luminaire should be around 3000 K.

- The luminous flux of the lamp can be adjusted over a wide range - for example from 20% to 100%.

- At night when the patients sleep luminous flux should be in the orange - red spectral region and its intensity can be remotely controlled from 0 to 100%.

B. Choice of LEDs with proper spectral and power characteristics

Using the procedure described in [2] theoretical analysis and selection of appropriate combinations of LEDs and LED modules for lighting fixture with features suitable for the lighting of hospitals, nursing homes, hospices and others are made.

$$X=x*(Y/y); Y=Y; Z=(Y/y)*(1-x-y) \quad (1)$$

$$X_{mix}=X1+X2+X3; Y_{mix}=Y1+Y2+Y3;$$

$$Z_{mix}=Z1+Z2+Z3 \quad (2)$$

$$x_{mix} = X_{mix}/(X_{mix} + Y_{mix}+Z_{mix}) \quad (3)$$

$$y_{mix} = Y_{mix}/(X_{mix}+Y_{mix}+Z_{mix}) \quad (4)$$

$$\Phi_{mix} = Y1+Y2+Y3 \quad (5)$$

Where:

X, Y, Z; X_{mix}, Y_{mix}, Z_{mix} are color coordinates;
 x, y, x_{mix}, y_{mix} are chromaticity coordinates according to 1931 CIE Chromaticity Diagram.

Experimental model of lamp which allows to investigate the possibilities for realization of the desired characteristics of the luminous flux, options for their management and to meet the stated above requirements is made. For the manufacture of the experimental model the following LEDs are used: one warm white CXA 2520 LED module (CCT 3500 K), five blue XPE LEDs (Xlamp – CREE Inc.) and eight red XPE LEDs (Xlamp – CREE Inc.).

Lamp's spectral characteristics using 1m integrating sphere and UV-VIS Spectrometer from Stellar Net. are obtained experimentally.

Thermal loading of LEDs is tested in a thermal chamber. Solder points' temperatures distributions are obtained experimentally using IR camera ThermaCam E300 – FLIR Systems and verified by conventional measurements by thermocouples.

III. RESULTS AND DISCUSSION

A. Thermal management and power consumption

Thermal resistance model for evaluation LEDs' temperature load described in [2] is used.

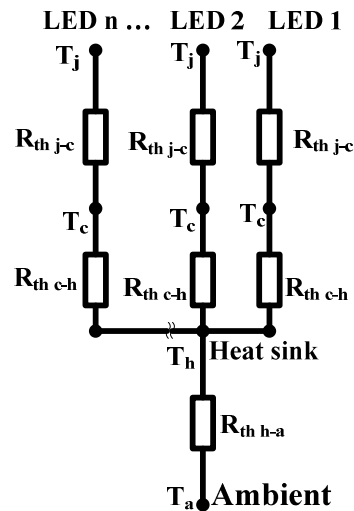


Fig. 2. Thermal resistance model [2]. $R_{th\ j-c}$ - thermal resistances from junction to case; $R_{th\ c-h}$ - thermal resistance from case to heat sink; $R_{th\ h-a}$ - thermal resistance from heat sink to ambient; T_j and T_c are junction and case temperatures correspondingly.

The maximal junction temperature (T_{jMAX}) depends on the ambient temperature (T_{a-max}), LEDs' power and all the thermal resistances in the model:

$$T_{jMAX}=T_{a-max}+(R_{th\ j-c}+R_{th\ c-h})*P_{LED}+R_{th\ h-a}*P_{tot} \quad (6)$$

The forward current (I_F) and voltage (U_F) of LEDs allow to calculate the consumed electrical power: $P_{LED} = I_F * U_F$;

The nominal power of CREE CXA 2520 LED module is: $P_{WHITE} = I_F * U_F = 0.55 * 35 = 19.25$ W and varies from about 10 W at $I_F = 300$ mA to about 34 W at $I_F = 800$ mA.

The power of blue LEDs varies from about 0.7 W at $I_F = 200$ mA to about 2.8 W at $I_F = 800$ mA.

Maximal total power (at $I_F = 800$ mA through CXA 2520 LED module and blue LEDs):

$$P_{tot} = P_{WHITE} + 5 * P_{BLUE} = 48$$
 W; (7)

The thermal resistances are as follows: CREE CXA 2520 LED module - $R_{th\ j-c} = 0.8$ K/W; blue LED $R_{th\ j-c} = 9$ K/W [2];

Using equation (6) heat sink with thermal resistance from heat sink to ambient about $R_{th\ sp-h} = 0.5\text{ K/W}$ is chosen.

B. Spectral characteristics and CCT

Measured spectral characteristics of CXA 2520 at nominal operating regime (forward current $I_{CXA}=550\text{ mA}$) are shown in fig. 3.

The luminous flux' spectrum of the CXA 2520 is typical warm-white with correlated color temperature (CCT) about 3500K. The relatively small maximum in the blue region (440 – 480 nm) does not suppress melatonin synthesis and is good for illumination in the late afternoon or evening.

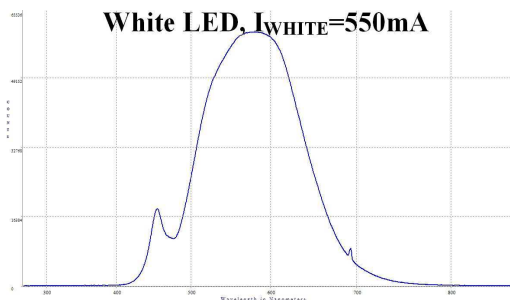


Fig. 3. Relative SPD of CXA 2520 LED module. The current's value is the nominal $I_{CXA}=550\text{mA}$.

By control of the forward current's value I_{CXA} from 300 mA up to 800 mA the luminous flux of the LED module can be set to the desired value in the range of 900 to 2400 lumens. Changes in color temperature are negligible i.e. the luminous flux is suitable for lighting evening in hospitals.

When white LED module and blue LEDs are used in combined mode of operation, options for achieving the desired spectral composition and luminous flux are much larger:

- $I_{CXA}=300\text{mA}$; the current's value through blue LEDs is changed from $I_{BLUE} = 200\text{ mA}$ up to $I_{BLUE} = 500\text{ mA}$. CCT of the luminous flux changes from about 4000 K to about 14000 K – fig. 4.

The total luminous flux varies from 1000 lm to 1200 lm.

- $I_{CXA}=400\text{mA}$; the current's value through blue LEDs is changed from $I_{BLUE} = 200\text{ mA}$ up to $I_{BLUE} = 800\text{ mA}$. CCT of the luminous flux changes from about 4500 K to about 13500 K – fig. 5.

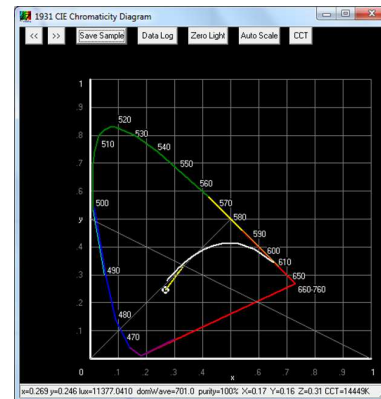
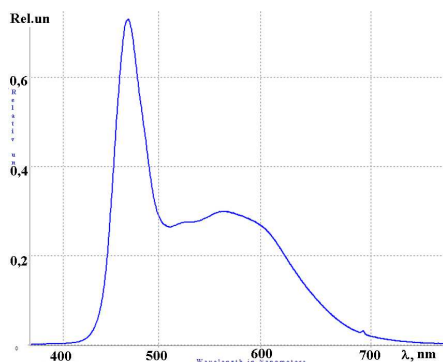


Fig. 4. Relative SPD of the lamp. The current's values: $I_{CXA}=300\text{ mA}$, $I_{BLUE} = 500\text{ mA}$. CCT $\approx 14000\text{ K}$.

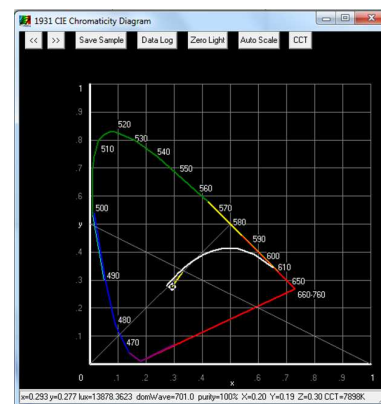
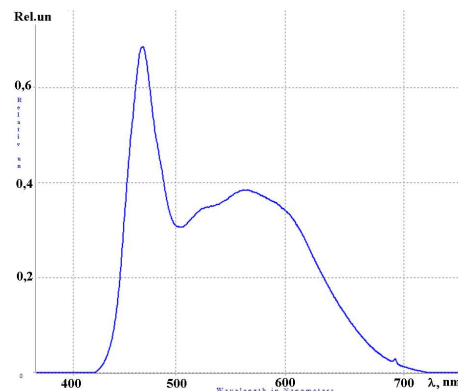


Fig. 5. Relative SPD of the lamp. The current's values: $I_{CXA}=400\text{mA}$, $I_{BLUE} = 450\text{ mA}$. CCT $\approx 7900\text{K}$.

The total luminous flux varies from 1500 lm to about 1600 lm.

- $I_{CXA}=500\text{mA}$; the current's value through blue LEDs is changed from $I_{BLUE} = 200\text{ mA}$ up to $I_{BLUE} = 800\text{ mA}$. CCT of the luminous flux changes from about 4500 K to about 9500 K – fig. 6.

The total luminous flux varies from 1700 lm to about 1900 lm.

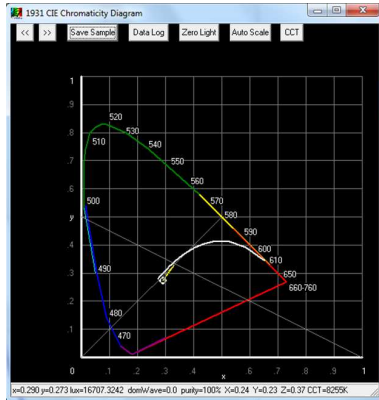


Fig. 6. Relative SPD of the lamp. The current's values: $I_{CXA}=500$ mA, $I_{BLUE}=600$ mA. CCT ≈ 8200 K.

- $I_{CXA}=600$ mA; the current's value through blue LEDs is changed from $I_{BLUE}=200$ mA up to $I_{BLUE}=800$ mA. CCT of the luminous flux changes from about 4500 K to about 7900 K – fig. 7.

The total luminous flux varies from 1900 lm to about 2100 lm.

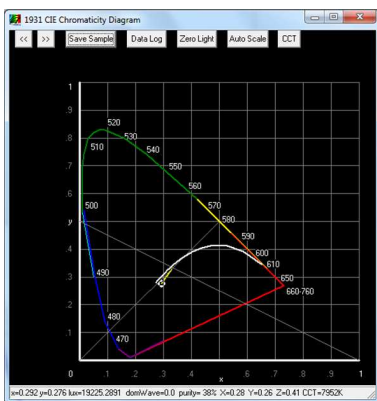


Fig. 7. Relative SPD of the lamp. The current's values: $I_{CXA}=600$ mA, $I_{BLUE}=800$ mA. CCT ≈ 7900 K.

- $I_{CXA}=700$ mA; the current's value through blue LEDs is changed from $I_{BLUE}=200$ mA up to $I_{BLUE}=800$ mA. CCT of the luminous flux changes from about 4200 K to about 7000 K – fig. 8.

The total luminous flux varies from 2200 lm to about 2400 lm.

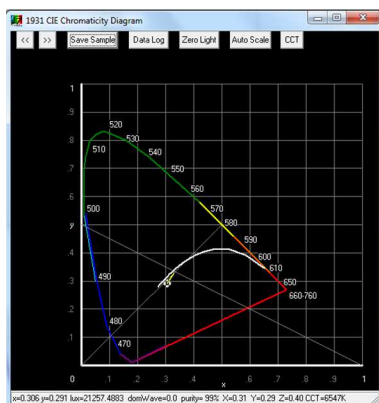


Fig. 8. Relative SPD of the lamp. The current's values: $I_{CXA}=700$ mA, $I_{BLUE}=600$ mA. CCT ≈ 6500 K.

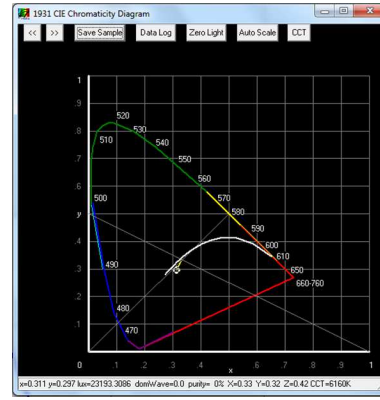


Fig. 9. Relative SPD of the lamp. The current's values: $I_{CXA}=800$ mA, $I_{BLUE}=600$ mA. CCT ≈ 6150 K.

- $I_{CXA}=800$ mA; the current's value through blue LEDs is changed from $I_{BLUE}=200$ mA up to $I_{BLUE}=800$ mA. CCT of the luminous flux changes from about 4200 K to about 6500 K – fig. 9.

The total luminous flux varies from 2400 lm to about 2600 lm.

So, it can be seen from figures 3 ÷ 9, that as a larger part of the blue LEDs' radiant flux in total luminous flux, as its light is colder, i.e. the CCT is higher.

C. Night lighting

As it is noted above, the night lighting in hospitals, nursing homes and others should be in orange - red region not to interfere with sleep of the patients. At the same time there must be sufficient visibility for safe movement and to enable staff to perform their duties. Experimental investigations using red, red - orange and amber XPE LEDs – Xlamp – CREE Inc. were carried out. Spectral power distribution (SPD) of combination of 6 red and 2 amber XPE LEDs is shown in fig. 10.

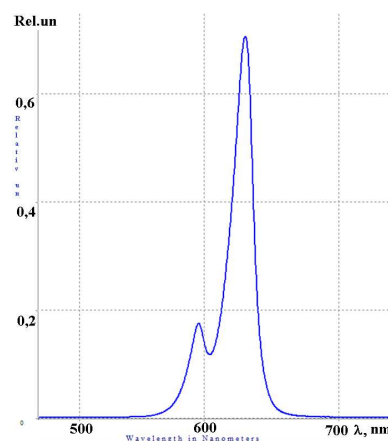


Fig. 10. Measured SPD of the 6 red and 2 amber XPE LEDs – CREE Inc.; current is 350 mA.

Despite the desire to expand the spectral characteristics of the luminous flux, finally we gave up using of amber LEDs as their light output strongly depends on the junction temperature - at 85°C it

decreased to below 30% of the light output at 25°C. The experimental lamp is realized using eight red XPE LEDs.

D. Junction temperatures and LEDs' thermal load experimental investigations

The LED module is tested in a thermal chamber. The ambient temperature is changed from 20°C to 40°C. When it reaches desired value, the temperature is kept constant. The solder points and case temperatures are measured using IR camera Therma Cam E300 – FLIR Systems and verified by thermocouples – fig. 11.

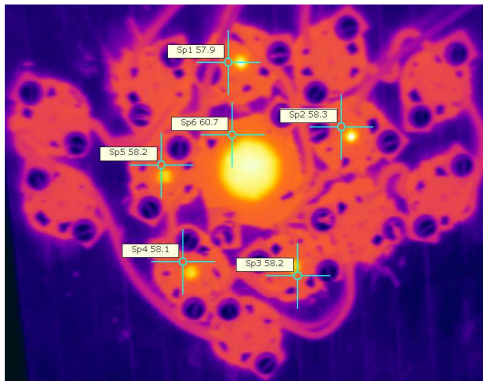


Fig. 11 Thermal load in daylight/noon LEDs regime. Ambient temperature is $T_a=40^\circ\text{C}$. Blue LEDs solder points are around $T_{sp}\approx 58^\circ\text{C}$. The CXA corpus temperature is $T_c\approx 61^\circ\text{C}$.

The corresponding junction temperatures are then calculated using the equation:

$$T_j = T_{sp} + (I_f \cdot U_f \cdot R_j - sp) \quad (8)$$

for the blue LEDs and equation:

$$T_j = T_c + (I_f \cdot U_f \cdot R_j - c) \quad (9)$$

for the white module (CXA2520).

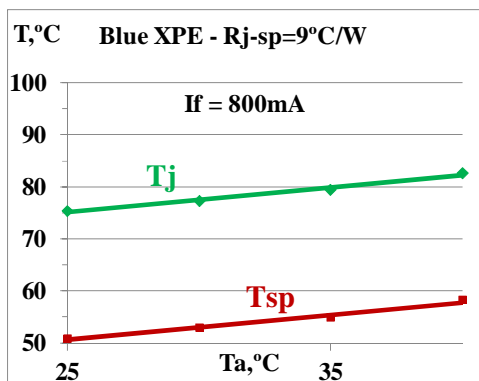


Fig. 12. Junction (T_j) and solder point (T_{sp}) temperatures in various ambient conditions: The temperature of the thermal chamber (T_a) is gradually increased.

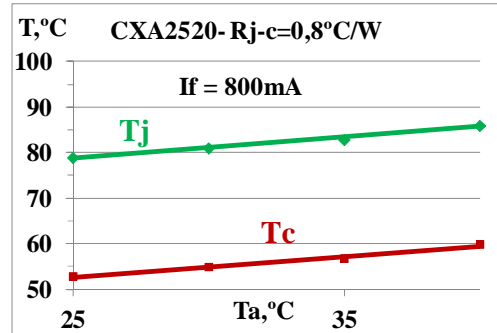


Fig. 13. Junction (T_j) and case (T_c) temperatures in various ambient conditions: The temperature of the thermal chamber (T_a) is gradually increased.

The worst LEDs' heat load is at daily mode of operation at maximum values of the currents through the white LED module and the blue LEDs. The experiments show that even then for all LEDs junction temperatures (figures 12, 13) do not exceed 90°C even at severe ambient conditions ($T_a=40^\circ\text{C}$).

IV. CONCLUSIONS

Appropriate combinations of LEDs and LED modules for luminaire with features suitable for the lighting of hospitals, nursing homes, hospices and others are made. During the day spectral power distribution (SPD) of this type luminaire can simulate natural day light that affects the natural circadian rhythm of humans. Depending on the type of the patients the maximum color temperature of the light flux can be limited to three grades – for children ($\text{CCT} \leq 4000 \text{ K}$), adults (CCT varies to $6000 \div 6500 \text{ K}$) and the elderly (CCT varies to $7500 \div 8000 \text{ K}$). At night when the patients sleep luminous flux can be in the orange - red spectral region and its intensity can be remotely controlled from 0 to 100% to enable patients to sleep and staff to fulfill their obligations.

Performed experimental studies make possible achieving the desired characteristics of light and appropriate LEDs' modes of operation.

Thermal management of the module shows stable LED operation even at tough ambient conditions.

V. ACKNOWLEDGMENTS

The National Science Fund, Ministry of Education and Science of Bulgaria, is gratefully acknowledged for the financial support of research project DFNI – B02/2 2014 .

REFERENCES

- [1] <https://www.thepaleomom.com/regulating-circadian-rhythm/>
- [2] LED_color_mixing; <http://www.cree.com>
- [3] Bellia L., A. Pedace, G. Barbato, Lighting in educational environments: An example of a complete analysis of the effects of daylight and electric light on occupants, Building and Environment, 68 (2013), pp. 50-65.
- [4] Cajochen C., Alerting effects of light, Sleep Medicine Reviews (2007)11, pp.453-464.
- [5] Chellappa L. S., R. Steiner, P. Blattner, P. Oelhafen, T. Gotz, C. Cajochen, Non-Visual Effects of Light on Melatonin,

- Alertness and Cognitive Performance: Can Blue-Enriched Light Keep Us Alert?, Blue-Enriched Light, Alertness and Performance, January 2011, Volume 6, Issue 1, e16429, pp.1-12.
- [6] Edwards L. and P. Torcellini, A Literature Review of the Effects of Natural Light on Building Occupants, U.S. Department of Energy Laboratory, 2002, p.58.
- [7] Ellis E. V., E. W. Gonzalez, D. A. Kratzer, D. L. McEachron, G. Yeutter, Auto-tuning Daylight with LEDs: Sustainable Lighting for Health and Wellbeing, ARCC 2013, The Visibility of Research Sustainability: Visualization Sustainability and Performance, pp.465-473.
- [8] Gabel V., M. Maire, C. F. Reichert, S. L. Chellappa, C. Schmidt, V. Hommes, A. U. Viola and C. Cajochen, Effects of Artificial Dawn and Morning Blue Light on Daytime Cognitive Performance, Well-being, Cortisol and Melatonin Levels, Chronobiology International, Informa Healthcare USA, Inc (2013), pp.1–10.

Partial Purification and Characterization of Bacteriocin-like Peptide Produced by *Staphylococcus xylosus*

Veslava Matikevičienė^{1,2}, Saulius Grigiškis¹, Erika Lubytė¹, Gervydas Dienys²

¹JSC Biocentras. Address: Graičiūno g. 10, Vilnius, LT-02241, Lithuania.

²Vilnius University, Institute of Biotechnology, Sector of Applied Biocatalysis. Address: Saulėtekis al. 7, Vilnius, LT-10257, Lithuania.

Abstract. The extensive use of antibiotics leads to an increasing number of antibiotic-resistant pathogenic microorganisms. The development of new antimicrobials is needed for clinical, veterinary, and food applications. Bacteriocins are small peptides with antimicrobial activity ribosomally synthesized by bacteria and could be applied as an alternative to classical antibiotics. In this study, the bacteriocin-like (BLIS) peptide, produced by *Staphylococcus xylosus* was partially purified and main characteristics (pH, thermal stability, resistance to some protease enzymes and molecular weight) were evaluated. Ammonium sulfate precipitation, acetone extraction and ion-exchange chromatography methods were applied for purification of bacteriocin. The activity of bacteriocin was detected using a well diffusion assay method and the amount of protein concentration was estimated by Lowry method. Molecular weight (~ 6 kDa) of purified bacteriocin was determined by sodium dodecyl sulphate polyacrylamide gel electrophoresis (SDS PAGE) method. The highest purification yield (80 %) was obtained using ion-exchange chromatography and SP-sepharose as sorbent. The purified bacteriocin remained stable at pH values between 2.0 and 12.0 for 4 h. No decrease in antibacterial activity was estimated after 30 min at 121° C temperature. The purified bacteriocin was resistant to papain, pepsin and trypsin action. The BLIS inhibits a growth of *Listeria monocytogenes* (93 ± 3.0 %), *Bacillus subtilis* (85 ± 4.0 %), *Pediococcus pentosaceus* (79 ± 4.0 %), *Staphylococcus aureus* (51 ± 5.0 %) and *Propionibacterium acnes* (70 ± 5 %) up to 24 hours. Such bacteriocin preparation could be applied as antimicrobial agent in medical and food industry.

Keywords: antimicrobial agent, bacteriocin, purification, *Staphylococcus xylosus*.

I. INTRODUCTION

An extensive use of broad-spectrum antibiotics in a treatment of human and animal diseases promotes the growing of antibiotic resistant pathogenic bacteria. In recent years the development of new antimicrobial agents has become of increasing importance for medicine, veterinary and food industry [1].

Bacteriocins are natural peptides or small proteins ribosomally synthesized and secreted in the living environment by many varieties of bacteria and some archae for the purpose of killing other bacteria [2], [3]. These antimicrobial peptides are usually characterized by a narrow spectrum of activity targeting only close related species. However, some of them (mostly synthesized by gram-positive bacteria) show very broad inhibitory spectra and even inhibit spore germination [3], [4].

Bacteriocins are divided into different groups based on their variable structural, physicochemical and molecular characteristics [5]. A number of different bacteriocins classification principles are described in the literature; however, most authors distinguish bacteriocins into three main classes: Class I (lantibiotics) - after the broadcast modified peptides;

Class II (non-lantibiotics) - heat-resistant, minimally modified peptides; Class III - heat-labile and large molecular mass bacteriocins [6].

A considerable number of bacteriocin-like substances have been reported in the literature but only a few of them have been isolated and thoroughly characterized. The bacteriocin purification procedure often involves a few steps which are quite long and time-consuming. The precipitation, ion exchange chromatography and reversed-phase chromatography are the main techniques used by different authors.

In this study the bacteriocin-like peptide (BLIS), produced by *Staphylococcus xylosus* was partially purified and same characteristics were determined.

II. MATERIALS AND METHODS

Microorganisms and Media

Staphylococcus xylosus strain was obtained from JSC "Biocentras" microorganisms' collection and was used for production of bacteriocin-like peptide. *Listeria monocytogenes* strain was used for evaluation of bacteriocin activity as an indicator strain. Oxoid mineral medium was used for cultivation of *L. monocytogenes*. Solid medium was produced by supplementing 1.5 % of agar to the

ISSN 1691-5402

© Rezekne Academy of Technologies, Rezekne 2017
<http://dx.doi.org/10.17770/etr2017vol3.2586>

broth. Bacteriocin production was investigated in basal medium composed of meat extract, triptone, glucose, K_2HPO_4 and NaCl in 500 mL Erlenmeyer flasks for 18 h at 30 °C and 200 rpm.

Experimental procedure

Cell-free *S. xylosus* culture supernatant was collected by centrifugation at 10,000×g for 20 min at 4 °C temperature. The pH of the supernatant was adjusted to 6.0 ± 0.5 with 0.1 M NaOH or 0.1 M H_3PO_4 . The supernatant was filtered through a 0.20 µm pore size cellulose acetate syringe filter. Ammonium sulphate precipitation, acetone extraction and ion-exchange chromatography methods were applied for purification procedure.

Purification of bacteriocin

Partial purification of the sample was done by adding $(NH_4)_2SO_4$ at 80 % of saturation level, followed by dialysis for 12 h. The pellet was collected after centrifugation at 10,000×g at 4 °C for 30 min. The pellet was dissolved in phosphate buffer (0.1 M, pH 7.0) and stored at 4 °C for further use.

Acetone extraction. Four times the sample volume of cold (-20°C) acetone was added to the cooled sterile supernatant sample (4 °C), mixed for 15 min and incubated 60 min at 4 °C. The pellet was collected by further centrifugation. The bacteriocin pellet was dissolved in phosphate buffer (0.1 M, pH 7.0) and stored at 4 °C for further use.

Ion exchange chromatography. Prepared supernatant sample was applied on SP sepharose column (1.6/20 cm) equilibrated with 0.02 mol/L sodium phosphate buffer (pH 5.0) and eluted with same buffer using linear salt gradient of NaCl (0-1 mol/L). The active fractions were pooled together.

Bactericidal activity. The inhibition of indicator strains was detected using agar well diffusion assay [7]. The solid MRS agar medium pre-inoculated with the indicator microorganism was prepared and wells of 9 mm diameters were cut. The prepared supernatant was placed in wells and plates were incubated at 37 °C for 24 h. Positive results, the inhibitory of grow of indicator microorganisms, were assessed by measuring a clear zone around the well in the vertical and horizontal direction by using a calliper. Measurements were done in duplicate and an average was calculated.

Soluble proteins. The amount of soluble bacteriocins was evaluated using modified Lowry method [8].

Characterisation of bacteriocin

SDS-PAGE was run to check the purity of the sample as well as to determine molecular mass of the sample. The gel used for the separation was 16.0 % tris-tricine SDS-PAGE and the ladder used was PageRuler Unstained Low Range protein ladder (Thermo Scientific). The gel was subjected to 25 mA for 120 min and then stained with Coomassie brilliant blue R 250 (Merck).

The effect of pH on bacteriocin activity was evaluated by adjusting the pH between 2.0 and 12.0 with sterile 1 mol/L NaOH or 1 mol/L H_3PO_4 and by further incubating for 4 h at 30 °C. The temperature effect on activity of the purified bacteriocin was tested by incubating at various temperatures (30, 40, 50, 60, 70, 80, 100 °C) and the residual activity was determined after 60 min and after 30 min at 121 °C. Samples were also stored for 28 days at -20, 4, and 40 °C and were assayed for antimicrobial activity at 1-week intervals.

Samples of the purified bacteriocin were treated with the following enzymes (2 mg/mL) and incubated for 2 h at 37 °C: papain, trypsin and pepsin. Antimicrobial activity was monitored by using the agar well diffusion assay.

III. RESULTS AND DISCUSSION

Staphylococcus xylosus secretes to the growing media bacteriocin-like peptide, that inhibits the grow of many Gram positive bacteria. Three methods of protein purification were applied during the study. Yields of purification processes are presented in Table I.

Table I
Summary of the purification processes of bacteriocin from culture supernatant of *S. xylosus*

Sample	Total activity, (U)	Total protein, (mg)	Specific activity, (U/mg)	Purification (Fold)	Yield, %
Culture supernatant	38500	3570	10.8	1	100
$(NH_4)_2SO_4$ precipitate	4801	318	15.1	1.4	10.6
Acetone extract	20290	719.5	28.2	2.6	52.7
SP sepharose	30916	203.0	152.3	14.1	80.3

The obtained results showed, that the ammonium sulphate fractionation provided low yield with low specific activity and fold purification. The high purification yield with low specific activity was obtained during the cold-acetone precipitation. But sufficiently pure preparation of bacteriocin, with high specific activity and fold purification, was determined using ion exchange chromatography and SP-sepharose as sorbent. The purified preparation yielded a single protein band on SDS-PAGE with a molecular weight about 6.0 kDa (Fig. 1).

The different purification techniques are described in the literature. Mesentericin Y105, produced by *Leuconosto mesenteroides* Y105, was purified using three-step method (carboxy-methyl-cellulose-filled column (2.5 by 18 cm), followed by a C₁₈ cartridge and C₈ Kromasil analytical HPLC column) and the 60 % yield of recovery activity was obtained [9]. Bacteriocin, leucocin A-UAL 187 has been purified by ammonium sulfate or acid (pH 2.5) precipitation, hydrophobic interaction chromatography, gel filtration, and reversed-phase high-performance

liquid chromatography with a yield of 58% of the original activity [10].

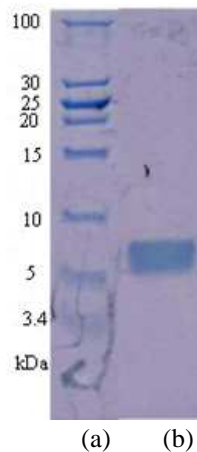


Fig. 1. SDS-PAGE of purified bacteriocin from *S. xylosus*. (a) – molecular mass marker; (b) – purified bacteriocin.

During the study the purified bacteriocin from *S. xylosus* was characterized. BLIS remained stable at pH values between 2.0 and 12.0 for 4 h (Fig. 2.). It retained more than 70 % of its original activity at the investigated range. The maximum residual activity was obtained at pH 6-8.

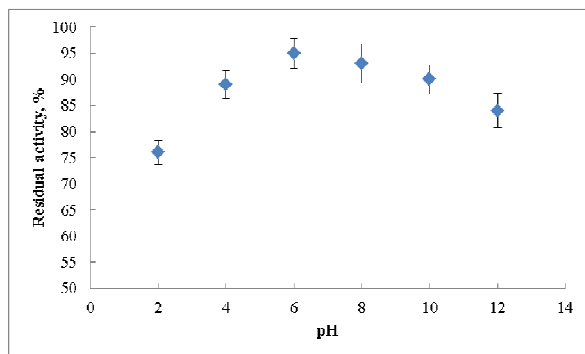


Fig. 2. The effect of pH on the bacteriocin activity.

The heat stability of bacteriocin is presented at Figure 3. The purified bacteriocin was stable over a broad temperature range between 30-100 °C. It retained more than 70 % of its activity even at 80 °C for 60 min. The purified bacteriocin showed inhibitory activity after exposing to 121°C for 30 minutes.

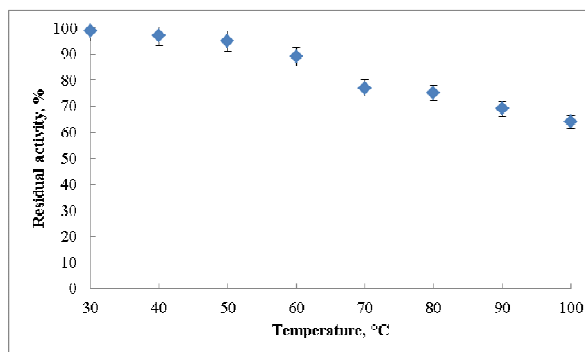


Fig. 3. The effect of temperature on the bacteriocin activity.

The long term (28 days) bacteriocin stability studies shown (Table 2), that the solution of purified bacteriocin was stable at -20 °C and 4 °C temperature and maintained about 100 % of its activity. More than 80 % of activity was retained at 40 °C after 28 days.

The purified bacteriocin preparation was resistant to papain, pepsin and trypsin action. No significant effect on residual activity of bacteriocin was evaluated.

Table II
The stability of bacteriocin solution

Time, days	Residual bacteriocin activity (%) at different temperatures (°C)		
	-20 ± 2	4 ± 1	40 ± 2
0	100	100	100
3	98,4 ± 1,4	98,3 ± 1,5	77,0 ± 6,7
7	97,6 ± 2,8	96,6 ± 3,1	54,6 ± 3,3
14	98,7 ± 2,5	98,2 ± 2,0	28,1 ± 1,4
21	98,9 ± 3,1	90,3 ± 3,7	17,9 ± 1,8
28	99,3 ± 1,1	88,9 ± 3,5	7,3 ± 1,5

Some studies of characterization of bacteriocins show the similar results. The bacteriocins ST28MS and ST26MS produced by *Lactobacillus plantarum* isolated from molasses remained stable after incubation for 2h at pH values between 2.0 and 12.0. No decrease in antibacterial activity was recorded after 90 min at 100°C or 20 min at 121° C [11]. Weissellin A, produced by *Weissella paramesenteroides* DX, retained its activity after exposure to 121 °C for 60 min or to -20 °C for 6 months, and to pH 2.0–10.0. It was not sensitive to trypsin, a-chymotrypsin, pepsin and papain [12]. Acidocin, produced by *L. acidophilus* DSM 20079, has been characterized as a one-component peptide of low molecular weight (6.6 kDa), extremely heat-stable and active over a wide pH range, although with a narrow inhibitory activity spectrum [1].

Bacteriocins are usually only active against bacteria related to the producer although some may affect a wide range of other Gram-positive organisms and even inhibit spore germination.

TABLE III
Antibacterial activity of purified bacteriocin against various bacteria

Microorganism	Inhibition, after 24 h
<i>Listeria monocytogenes</i>	93 ± 3,0
<i>Bacillus subtilis</i>	85 ± 4,0
<i>Pediococcus pentosaceus</i>	79 ± 4,0
<i>Staphylococcus aureus</i>	51 ± 5,0
<i>Propionibacterium acnes</i>	70 ± 5,0

In this study the inhibitory spectrum of purified bacteriocin from *S. xylosus* was determined. It effectively inhibits a growth of many Gram positive bacteria up to 24 hours (Table III). The highest inhibitory activity against *Listeria monocytogenes* and lowest against *S. aureus* was evaluated.

The bacteriocin isolated from *Weissella confusa* A3 was shown the inhibitory activity towards *Bacillus cereus*, *Escherichia coli*, *Pseudomonas aeruginosa* and *Micrococcus luteus*[13]. The purified bacteriocin of *L. murinus* AU06 was shown to have the significant antibacterial activity against *Micrococcus* sp., *Staphylococcus aureus*, *Pseudomonas aeruginosa* and *Escherichia coli* whereas lower inhibition found with *Enterococcus faecalis*, *Bacillus licheniformis* and *Listeria monocytogenes* [5].

IV. CONCLUSION

The bacteriocin isolated from *Staphylococcus xylosus* cell-free supernatant was purified using ion exchange chromatography with a yield of 80 % of the specific activity and characterized. The purified bacteriocin was shown to be heat stable and active at broad pH range. The purified bacteriocin exhibited various levels of activity against all gram-positive bacteria tested. The properties of bacteriocin and the ability in inhibiting a wide-range of pathogenic bacteria make it a potentially suitable agent for food and medical industry.

REFERENCES

- [1] J. L. Parada, C. R. Caron, A. P. Medeiros and C. R. Soccol, "Bacteriocins from Lactic Acid Bacteria: Purification, Properties and use as Biopreservatives", Brazilian Archives of Biology and Technology, vol.50, n. 3, pp.521-542, May 2007.
- [2] Alvarez-Sieiro, P., Montalbán-López, M., Mu, D., & Kuipers, O. P. (2016). Bacteriocins of lactic acid bacteria: extending the family. Appl. Microbiol. Biotechnol., 100 (7), pp. 2939-2951.
- [3] Martínez, B., Rodríguez, A., & Suárez, E. (2016). Antimicrobial Peptides Produced by Bacteria: The Bacteriocins. In *New Weapons to Control Bacterial Growth* (pp. 15-38). Springer International Publishing.
- [4] H. Holo, T. Fayec, D. Bredehaug, T. Nilsena, I. Ødegård, Th. Langsrud, J. Brendehaug, I. F. Nes, Bacteriocins of propionic acid bacteria. Lait 82 (2002) 59-68, Oral communication at the 3rd International Symposium on Propionibacteria, Zurich, Switzerland, July 8–11, 2001.
- [5] S. Elayaraja, N. Annamalai, P. Mayavu, T. Balasubramanian, "Production, purification and characterization of bacteriocin from *Lactobacillus murinus* AU06 and its broad antibacterial spectrum", Asian Pac J Trop Biomed, vol. 4(Suppl 1), pp. S305-S311, 2014.
- [6] V. Kaškonienė, M. Stankevičius, K. Bimbiraitė-Survilienė, G. Naujokaitytė, L. Šernienė, K. Mulkytė, M. Malakauskas, A. Maruška, "Current state of purification, isolation and analysis of bacteriocins produced by lactic acid bacteria", Appl Microbiol Biotechnol, vol. 101, pp. 1323–1335, 2017.
- [7] D. Cizeikiene, G. Juodeikiene, A. Paskevicius, E. Bartkiene, "Antimicrobial activity of lactic acid bacteria against pathogenic and spoilage microorganism isolated from food and their control in wheat bread", Food Control, vol. 31(2), pp. 539-545, 2013.
- [8] J. H. Waterborg, *The Lowry Method for Protein Quantitation*. The Protein Protocols Handbook, 2nd Edition. Humana Press, 2002, pp. 7-9.
- [9] Guyonnet, D.; Fremaux, C.; Cenatiempo, Y. and Berjeaud, J. M., "Method for rapid purification of class IIa bacteriocins and comparison of their activities. Appl. Environ. Microbiol., vol. 66, pp. 1744-1748, 2000.
- [10] J. W. Hastings, M. Sailer, K. Johnson, K. L. Roy, J. C. Vederas, and M. E. Stiles, "Characterization of leucocin A-UAL 187 and cloning of the bacteriocin gene from *Leuconostoc gelidum*", J. Bacteriol., 173, pp. 7491-7500, 1991.
- [11] S. D. Torodov, L. M. T. Dicks, "Lactobacillus plantarum isolated from molasses produces bacteriocins active against Gram-negative bacteria". Enzyme and Microbial. Technol., vol. 36, pp. 318-326, 2005.
- [12] M. Papagianni, E. M. Papamichael, "Purification, amino acid sequence and characterization of the class IIa bacteriocin weissellin A, produced by *Weissella paramesenteroides* DX", Bioresource Technology, vol. 102, pp. 6730–6734, 2011.
- [13] H. F. Goh, K. Philip, "Purification and Characterization of Bacteriocin Produced by *Weissella confusa* A3 of Dairy Origin", PLoS ONE 10(10): e0140434. doi:10.1371/journal.pone.0140434

The Impact of Harvester Calibration on the Accuracy of Birch Veneer Logs Measurements by Measuring Diameter in Short Intervals Using Electronic 3d Systems

Ziedonis Miklašēvičs

Rezekne Academy of Technologies, Faculty of Engineering, Environmental Technology Transfer Contactpoint.
Address: Atbrivosanas aleja 76, Rezekne, LV-4601, Latvia.

Abstract. Accurate calibration of the harvester head relies on accurate manual log measurements. According to the recommended calibration procedures as proposed by the harvester manufacturer the differences between the volume measurements from harvester measurement system and the caliper-and-tape system must be within $\pm 3\%$ and harvester diameter measurements within $\pm 6\text{mm}$ of manual measurements in 80% cases.

Requirements in Latvia stipulate that total volume measurement accuracy levels must be within $\pm 5\%$ of actual volume if veneer or birch logs are being harvested, $\pm 3\%$ if saw logs are being harvested and $\pm 10\%$ if pulp wood or fire wood are being harvested.

The purpose of this study is to assess the impact of harvester calibration on the accuracy of birch veneer logs measurements by Measuring Diameter in Short Intervals using electronic 3D systems when different double bark volume determination algorithm are used in harvester and stacionar measurement system. The research was carried out in December 2016 in the region Latgale in Latvia. The wood felling area was chosen - *Mercurialis mel.* For volume estimation the sequent measurement equipment were applied: harvester Ponsse ERGO 8W, harvester information system Opti 4G and electronic 3D scanner system Elmes 3600.

The research is a continuation to the work done in the project „Harmonisation of piece-by-piece measurement methods of roundwood approved by Standard LVS 82:2003 „Apaļo kokmateriālu uzmērīšana” [6], the project “Harmonization of piece-by-piece measurement methods in all stages of roundwood manufacturing processes” [7] and the project "Investigation and evaluation of the methodology of determination of solid volume according to the stacked volume on roadside and in forwarder loads for logistics purposes in LATVIA" [8].

Keywords: Harvesters; calibration; measurement accuracy, veneer logs, volume.

I. INTRODUCTION

Sawmills orders for roundwood assortments from the woods are being made by increasingly tight specifications. A log that has been harvested in a specified length and diameter in the wood felling place often ends up in a different diameter class at the sawmill. Thus the quantities of logs in the specified classes delivered to the mill often fail to meet the specification. The main reasons are sequential:

1. *Harvester measuring system doesn't work correctly.*

In order to ensure that the harvester systems for measuring roundwood length, diameter are accurate, the harvester control and calibration procedures are applied making random control measurements of a number of stems and comparing the results with the machine data. In Latvian forest industry the methodology of harvester calibration is based on StanFord standard [10]. According to the standard, the analysis of harvester measuring system accuracy

has been made using harvester calibration and control measurement Ktr-file.

An independent auditor monitors the results continually and visits every harvester a number of times a year to verify that the specified procedures are being followed.

In Finland data from these measurement systems are used as a basis for optimising machine yield and assortment mix, payment of contractors, payment of timber growers and the monitoring of operators [5].

What does it mean “well calibrated harvester measurement system”?

In Ireland volume accuracy levels of 6.7% for a clearfell site and 5.3% for a thinning site are determined [9].

Harvester calibration requirements in Latvia stipulate that volume estimates of control roundwood assortments must be within $\pm 3\%$ of the true volume and at least 80% of all diameter measurements shouldn't exceed $\pm 6\text{mm}$ deviation.

2. Measurement requirements used by the harvesters differ from those used by the mills.

The analyses of roundwood measurement requirements used in harvester measuring systems [1;2;3; 4;11;12;13] are given (Table 1).

Table 1
The Measurement Requirements Used in Harvester Measuring Systems

Variables B2:O55	Criteria	Countries									
		Swe _{sub}	Swe _{to}	Fin _{sub}	Nor _{mid}	Ger _{mid}	Ger _{top}	Dan _{mid}	Est _{mid}	Fra _{sub}	Latvia* _{sub}
Diameters in Diameter Classes (price matrix)	1=Top 2= Midpoint	1	1	1	1	2	1	2	1	1	1
Diameter Class Adjust	1=diameter class smaller or equal to log diameter 2=closest diameter class, normal rounding	1	1	1	1	1	1	1	1	1	1
Diameter Classes under bark	True/False	TRUE	TRUE	FALSE	TRUE	TRUE	TRUE	FALSE	TRUE	TRUE	TRUE
Position from top end of log where top diameter is measured	Cm	10	10	0	10	0	0	0	0	0	10
Lenght Class Adjust	1=lenght class smaller or equal to log diameter 2= closest lenght class, normal rounding	1	1	1	1	1	1	1	1	1	1
Diameters in log price volume calculation	1=measured diameter 2=measured diameter rounded down to cm	1	1	1	1	1	1	1	1	1	1
Diameters used in log price volume calculation	1=Solid volume 2=Top 3=Mid 4=Calculated Norwegian mid 5=Calculated Estonian mid	1	2	1	4	3	3	3	5	1	1
Lenghts used in price volume calculation	1=Physical lenght 2=Lenght as defined in Lenght Classes 3= Rounded downwards to nearest dm-module 4=Rounded to nearest dm-module	1	2	1	3	2	2	1	1	1	2
Price volume under bark	True/False	TRUE	TRUE	FALSE	TRUE	TRUE	TRUE	FALSE	TRUE	TRUE	TRUE
Position from top end of log where top diameter for log volume calculation is measured	Cm	10	10	0	10	0	0	0	0	0	10
Bark Function Category	1=None 2=Swedish Zacco B=f(diam o.b.) 3=German B=f(diam o.b.) GermanDistanceBased B=f(dbh, h) 4=Skogforsk 2004, Scots pine B=f(dbh, h, lat) 5=Skogforsk 2004, Norway spruce B=f(dbh, diam o.b.) 6= Joint Stock company's "Latvijas valsts meži "Apt-file, pine B=f(diam o.b.) 7= Joint Stock company's "Latvijas valsts meži "Apt-file, spruce B=f(diam o.b.) 8= Joint Stock company's "Latvijas valsts meži "Apt-file, birch B=f(diam o.b.) 9= Joint Stock company's "Latvijas valsts meži "Apt-file, aspen B=f(diam o.b.)	2; 4; 5	2; 4; 5	1	2; 4; 5	3	3	1	2; 4; 5	2; 4; 5	0; 6; 7; 8; 9

3. Diameter (under bark) measuring technique used in the mills is not the same as that used by the harvesters.

Inspite of calibration of the harvester measuring system using individual logs is very accurate, the volume measurement results are unsatisfactory when comparing the volume calculation results obtained in harvester and stacionar measurement equipment in sawmill. The differences between the harvester measurements and the stacionar measurement equipment measurements fluctuate, varying from positive to negative volume values. These differences could be explained with the methodical procedure based on different and variet criteria.

One of the criteria is bark thickness estimation methodology. Harvester measurement system calculate double bark thickness from diameter over bark and use the results to estimate roundwood assortment diameter and volume under bark (u.b.).

For birch logs and veneer logs the double bark thickness at the point of measuring is determined in Apt-file by using the sequential formula (1).

$$B=3,45+0,0404xD \quad (1)$$

where: D – diameter of roundwood assortment over bark (o.b.), mm.

In veneer mill each veneer log is appreciated according to bark amount (%) and diameter (mm) coherence (Table 2.) and bark's presence on log surface. If the bark presence on log is less than 50%, the log is measured without bark.

The corresponding variables related to the investigation are defined below:

Apt-file Bucking(cross-cutting) instructions
DBH (d_{1,2}) The first measuring point done by harvester measuring system for butt diameter prediction

Ktr-file	Harvester calibration and control measurement file. Sent from digital callipers to (on-board) merchandising (bucking) computer, and from merchandising computer to the office computer
Mercurialiosa mel.	Woodlands on drained mineral
Prd-file	Production of the harvester (measurement certificate)
Pri-file	Production-individual. Data of each log made from the site

Table 2.
Bark Amount (%) and Diameter (mm) Coherence

Bark amount,%	Diameter min. (mm)	Diameter max. (mm)
12	0	190
11	190.1	230
10	230.1	390
9	390.1	999

II. MATERIALS AND METHODS

The wood felling area (Fig. 1.) was chosen - *Mercurialiosa mel.* The study was carried out in december 2016 in the region Latgale in Latvia. The wood falling time was chosen because of the minimal risk of debarking in the process of harvesting.

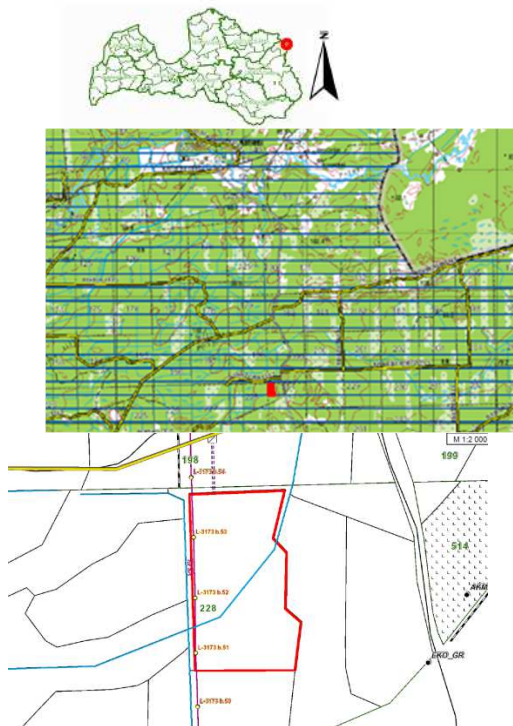


Fig. 1. Wood felling area and the technological scheme of harvesting, where species of a trees: 10% pine, 20% spruce, 70% birch

The following procedures were used to achieve the required objective:

To control the measurement accuracy of harvester Ponsse ERGO 8W measuring systems and electronic 3D scanner system Elmes 3600.

1. To identify the birch stems before harvesting and all veneer logs after harvesting. To measure the identified veneer logs by measuring diameter in short intervals using electronic 3D systems.
2. To collect and analyse the harvester measurement Pri-file data in connection with automatically measured parameters of veneer logs.
3. To analyse the measurement results.

The following measurement methods were applied in the investigation:

1. Individual measurement method by measuring diameter in short intervals using harvester measurement system.
2. Individual measurement method by measuring diameter in short intervals using electronic 3D system.

The following equipment were applied in the experimental investigation:

manual measuring equipment; harvester *Ponsse ERGO 8W*, harvester information system *Opti 4G* and electronic 3D scanner system *Elmes 3600*.

The object of the investigation were assortments harvested according to the specification (Table 3.).

Table 3
Specification of Birch Veneer Logs

Assortment, mm	Identification of the top diameter, mm	Top diameter (min/max), mm	Nominal length, m	Max. diameter, mm
120x139	120-139	130/139	4.8	700
140x159	140-159	140/159	4.8	700
160x179	160-179	160/179	4.8	700
180x209	180-209	180/209	4.8	700
210x249	210-249	210/249	4.8	700
250-299	250-299	250/299	4.8	700
300-399	300-399	300/399	4.8	700
400<	400	400/700	4.8	700

III. RESULTS AND DISCUSSION

Harvester measurement accuracy were assessed through comparison with manual log measurements and volume calculation according to the schemes (Fig.2.,3.,4.)

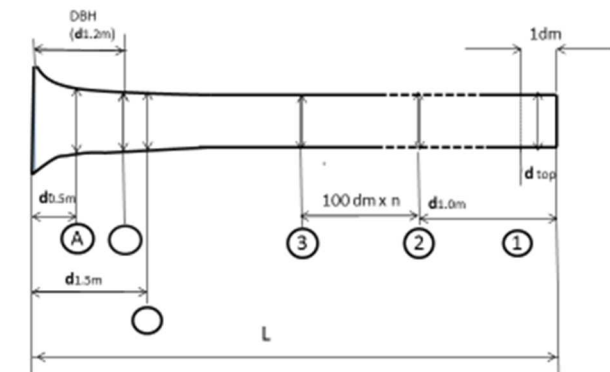


Fig. 2. The scheme of measuring points for logs from neiloid zone of stem in the process of harvester Ponsse ERGO 8W measurement system controlling, where:

DBH ($d_{1.2m}$)- the first measuring point done by harvester measuring system for butt diameter prediction; A - the last manual control measuring point ($A=50$ dm)

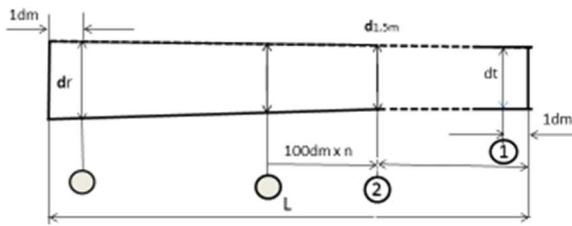


Fig. 3. The scheme of measuring points for logs from paraboloid zone of stem in the process of harvester Ponsse ERGO 8W measurement system controlling



Fig. 4. The control of the harvester Ponsse ERGO 8W measuring system by independent auditor, where:

volume of the control assortments measured by harvester measurement system 5.430m³; volume of the control assortments measured by caliper 5.426m³; volume deviation 0.1%; 49% of all diameter include in ±2mm deviation; 79% of all diameter include in ±4mm deviation; 93% of all diameter include in ±6mm deviation

All veneer logs were identified in the process of harvesting (Fig.5.), collected in the load (Fig.6.) and measured by measuring diameter in short intervals using electronic 3D systems (Fig.7).



Fig. 5. The example of identified veneer logs N° 22; 23; 24



Fig. 6. The load of identified veneer logs



Fig. 7. The example of measuring process and measurement results of identified veneer log N° 24 using 3D scanner system Elmes 3600, where: actual length (cm) 493; nominal length (cm) 480; top diam.u.b.(mm) 232.9; actual volume u.b.(m³) 0.236; nominal volume u.b.(m³) 0.230

All harvester measurement results were collected using Pri-file data (Fig.8.) and analyzed (Table 3) in connection with automatically measured parameters of veneer logs.

The measurement results of the investigation are given (Table 4.)

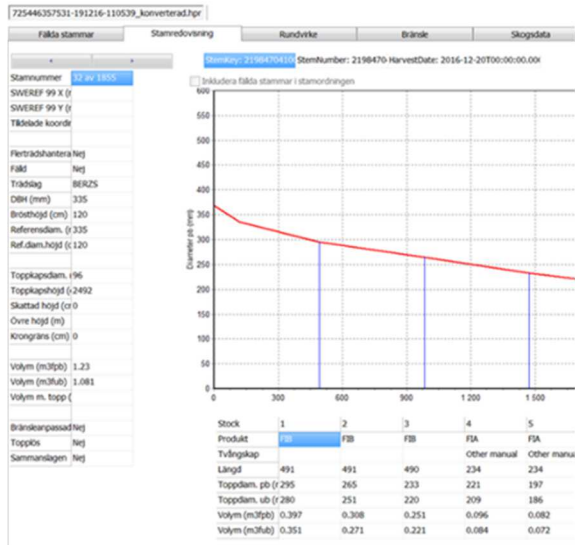


Fig. 8. The example of the measurement results of the stem and identified veneer logs Nr.22; 23; 24 in Pri- file, where:
 birch stem DBH (mm) 335; birch stem volume (m³ fub) 1.081; veneer log Nr.22 - length 491(cm); top diam.u.b.(mm) 280; volume u.b.(m³) 0.351; veneer log Nr.23- length 491(cm); top diam.u.b.(mm) 251; volume u.b.(m³) 0.271; veneer log Nr.24- length 490(cm); top diam.u.b.(mm) 209; volume u.b.(m³) 0.221

Table 4.
 The Measurement Results

Variable	Measurements
Number of veneer logs	50
Amount of butt assortments, %	36
Neto volume by harvester, m³ (u.b.)	13.397
Actual volume by 3D scanner, m³ (u.b.)	13.819
Neto volume by 3D scanner, m³ (u.b.)	13.484
DBH (1.2m), mm	
Average	309.8
Median	316.5
Length, cm	
Average	491
Median	491
Standard deviation	2.08
Standard error	0.29
Diameter, mm	
Average	245.3
Median	246.5
Standard deviation	6.1
Standard error	0.86
Volume, m³	
Average	0.267
Median	0.253
Standard deviation, %	3.6
Standard error, %	0.5

IV. CUNCLUSION

1. No clear effect of calibration can be detected on diameter measurements due to different approach of double bark thickness calculation. Diameter standard deviation reaches 6.1mm if the harvester measuring system calculates diameters (u.b.)

using double bark function (1), but electronic 3D scanner system uses bark amount (%) and diameter (mm) coherence (Table 2).

- Standard deviation reaches 3.6% if volume of veneer logs (u.b.) are calculated using different double bark calculation methods.
- Standard deviation reaches 2.08 cm in length measurements.

REFERENCES

- [1] *Apažo kokmateriālu uzmērīšana*. LVS 82:2003.
- [2] Anon 2000. Kompendium i virkesmätning. Virkesmätningrådet, SDC, Sundvall.
- [3] Arlinger, J. and Moller, I. J. Kvalitetssäkring av skördarnas mätning. Skogforsk Results No.20.2006. *Skogforsk* <http://www.skogforsk.se/contentassets/3a3c190011e241d5a92e22ee8c26a598/resultat20-06-lowres.pdf>
- [4] European Forest Sector Outlook Study 1960-2000-2020: Main Report (UNECE/FAO). 2005. <http://www.unece.org/timber/efsos/data/conversion-factors.pdf>.
- [5] Gingras, J-F. *Recent Developments in Chip Cleaning and Cut-To-Length Harvesting Technologies in Finland*. Forest Engineering Research Institute of Canada (FERI) Eastern Division, Internal Report IR-1995-06-01.
- [6] Miklasevics, Z. Harmonization of piece-by-piece measurement methods of roundwood approved by Latvian standard LVS 82:2003 "Apažo kokmateriālu uzmērīšana". ISSN 1691-5402. Environment. Technology. Resources. Proceedings of the 9th international conference reports, Rezekne. 2013, pp. 154-163
- [7] Miklasevics, Z. Harmonization of piece-by-piece measurement methods in all stages of roundwood manufacturing processes". ISSN 1691-5402. Environment. Technology. Resources. Proceedings of the 10th international conference reports, Rezekne, 2015, pp. 207-218.
- [8] Miklasevics, Z. Investigation and evaluation of the methodology of determination of solid volume according to the stacked volume on roadside, in forwader and in truck loads for logistics purposes in Latvia./The 49th FORMEC Symposium, Warsaw, Poland 2016, pp. 89-98
- [9] Nieuwenhuis, M. and Dooley, T. 2006. The effect of Calibration on the Accuracy of Harvester Measurements. *International Journal of Forest Engineering*. 17(2). 2006, pp. 25-33.
- [10] Räsänen, T., Poikela, A., Arlinger, J. 2010. Spp-file in StanForD. <http://www.skogforsk.se/en/About-skogforsk/Collaboration-groups/StanForD/Standard-Documents/>
- [11] Standard procedures for checking timber measurement and timber reporting. 2015. SDC's instructions for timber measurement. <http://www.sdc.se/default.asp?id=3005>
- [12] Timber measurement manual. Standard procedures for the measurement of round timber for sale purposes in Ireland. 1999. <http://www.coford.ie/media/coford/content/publications/proj ectreports/TimberMeasurementManual.pdf>
- [13] Sondell, J., Moller, I. J. and Arlinger, J. *Third-generation merchantiSing computers*. Skogforsk Results No.2. 2002.

Thermal Conductivity and Frost Resistance of Foamed Concrete with Porous Aggregate

Eva Namsone, Genadijs Sahmenko, Elvija Namsone, Aleksandrs Korjakins

Riga Technical University, Faculty of Civil Engineering, Institute of Materials and Structures Address: Kipsalas street 6a, Riga, LV-1048, Latvia

Abstract. *The paper reports a study, which was carried out to examine thermal and frost resistance properties of foamed concrete (FC) with porous aggregate (expanded glass (EG) granules and cenospheres). By adding lightweight and porous aggregate to the FC mixture, it is possible to improve important physical, mechanical, and thermal properties of the prepared FC specimens. In the framework of this study the coefficient of thermal conductivity and frost resistance of hardened FC samples were determined. The structure of FC matrix and used aggregates were characterised by using a method of optical microscopy.*

Keywords: *porous aggregate, microstructure, foamed concrete, expanded glass, thermal conductivity.*

I. INTRODUCTION

Construction industry in the total energy consumption is composed of forty per cent [1]. Growing costs of energy demand energy-efficient construction [2]. Engineering scientists are developing production of environmentally friendly building materials, such as foamed concrete (FC) [3].

Currently FC is regarded as very modern and widespread building material. It belongs to the group of lightweight concrete and is suitable for using in precast building elements as well as in monolithic structures [4].

The presence of considerable shrinkage is one of the main drawbacks of FC. This can be prevented by using a porous aggregate [5]. Physical properties of lightweight aggregates depend on the effect of moisture during the life cycle of a building material. Moisture influences characteristics of the respective building material, especially its durability properties. In porous materials drying rate is closely linked to their drying conditions [6]. For increasing durability it is necessary to obtain high water resistance.

The aim of this study is to analyse thermal and frost resistance properties of FC with porous aggregate.

II. MATERIALS AND METHODS

Used materials

All FC mixes were obtained experimentally in a laboratory setting. Intensive mixer (having a turbulence effect), foaming and pump functions was used. The following main components were used for preparation of FC mixes:

- Main binding agent – normal type Portland cement CEM I 42.5 N. Compressive strength after 28 days is at least 42.5 MPa and the specific surface is 3500-3900 cm²/g

(information provided by the producer, CEMEX, Ltd.).

- Filling component – natural, washed sand with fraction size 0/0.3 mm. Sand also helps to promote the formation of foam. During the mixing the synthetic foaming agent was added.
- Pozzolanic additives – silica fume or microsilica (MS) and metakaolin (MK). MS usually has fine particles (1 µm – 15 nm) and it is useful as supplementary cementing material [7]. MK is a technogenic waste material, obtained from the manufacturing of expanded glass granules. It helps to improve workability and durability of concrete [8-9]. By using pozzolanic additives in the concrete mixture, the potential risk of alkali-silica reactions is reduced [10-13].
- Porous aggregate – expanded glass (EG) granules and cenospheres (CS). In this study cream-coloured EG granules (fraction size 4 to 8 mm) were used. The pore structure with closed pores ensures low water absorption ability of EG granules (information provided by producer, JSC Stiklaporas). CS are obtained as a by-product from coal processing at the thermal power plants and have small diameters (30 – 350 µm) but high strength (20 – 100 MPa) [10].

In this study six experimental mixes of FC were produced. All of them were obtained with an average density class D800. EG granules were added in the mixes IP, IIP, IIIP. CS were used to obtain the mixes II, IIP, III, IIIP. Superplasticizing admixture ('Stachema'), based on polycarboxylate was added in the mixes III and IIIP. Data and designations of all prepared FC mixes are summarized in Table 1.

ISSN 1691-5402

© Rezekne Academy of Technologies, Rezekne 2017
<http://dx.doi.org/10.17770/etr2017vol3.2625>

Table 1.
Compositions of Prepared Fc Mixes

	I	IP	II	IIP	III	IIP
Portland cement CEM I 42.5 N	+	+	+	+	+	+
Sand 0/0.3 mm	+	+	-	-	-	-
Water	+	+	+	+	+	+
Foaming agent	+	+	+	+	+	+
Cenospheres	-	-	+	+	+	+
Metakaolin	+	+	+	+	+	+
Microsilica	+	+	+	+	+	+
EG granules, 4 to 8 mm	-	+	-	+	-	+
PVA fibres	+	+	+	+	+	+
Superplasticizer	-	-	-	-	+	+

Experimental procedure

The coefficient of thermal conductivity was determined by using heat flow measurement device 'Laser Comp's heat flow meter instrument FOX 600' (see Fig.1). Thermal conductivity test was performed according to EN 12667.



Fig. 1. Heat flow meter instrument 'Laser Comp FOX 600' used in the test of thermal conductivity

The operating principle of measuring equipment is based on the Bio – Fourier law, where the heat flow, the coefficient of thermal conductivity and temperature gradient are connected by the following Formula 1:

$$q = -\lambda \left(\frac{dT}{dx} \right), \text{ where:} \quad (1)$$

q - heat flow that passes through the sample (W/m²);
 λ - coefficient of thermal conductivity (W/mK);
 $\left(\frac{dT}{dx} \right)$ – temperature gradient of flat surface (K/m) [11].

The tested specimens were placed in this device between two metal plates with temperature difference

20°C (the bottom plate was the warm part (+20°C) and the upper plate was the cold part (0°C)).

Frost resistance was tested according to LVS CEN/TS 12390-9. The tested specimens (cubes with dimensions 100 x 100 x 100 mm, sawn in half) were partly immersed in water and then subjected to several freeze-thaw cycles. The samples were immersed in water at a depth of about 5 mm, placing them face down in the containers. Under the tested surface of FC specimens (5 mm ± 0.1 mm) spacers were placed, thereby ensuring uniform water layer beneath the concrete specimens.

If previously the same FC specimens have been used in the capillary water absorption test, the containers in this case must be sealed to prevent evaporation. Totally 14 cycles were applied to the tested specimens.

Freeze-thaw cycles were carried out in a climatic chamber 'Sunrise' by freezing to -20°C and thawing at +20°C (according to LVS CEN/TS 12390-9). After a certain number of cycles the specimens were visually inspected and additional frost resistance was determined by the quantity of crumbled particles in certain surface area (g/m²). The freeze-thaw cycle interval (accordingly to the above mentioned regulation) is presented in Fig. 2.

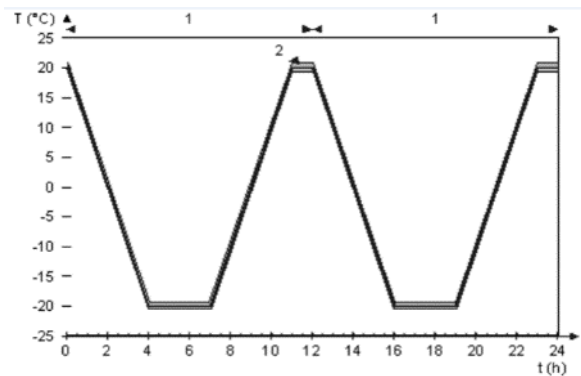


Fig. 2. Illustration of freezing-thawing cycles

Microstructure of the prepared FC mixes was investigated with the optical microscope VHX-2000 'Keyence Corporation'. The obtained images were used to determine the pore size (both of FC matrix and porous aggregate) with the computer software 'VHX-2000 Analyzer'.

The test of compressive strength was performed according to LVS EN 12390-3. The specimens with standard dimensions (100x100x100 mm) were stored at the temperature 15°-20°C and relative humidity level more than 90%, and were tested at the age of 7 and 28 days.

III. RESULTS AND DISCUSSION

Thermal conductivity

FC specimens – plates with dimensions of 350 x 350 mm (the thickness of slabs was determined by heat flow meter with an accuracy 0.01 mm) were used for

the thermal conductivity test. The results of the thermal test are summarized in Table 2.

Data about the thermal conductivity depending on the drying time (in days) are presented in a diagram (see Fig. 3). Till the age of 28 days, the prepared specimens were stored at the temperature 22°C and relative humidity >90%, but later the relative humidity was reduced to 50%. According to the diagram, it can be seen that the coefficient of thermal conductivity tends to decrease over time. For example, the plate made from the FC composition II had about 18% lower thermal coefficient value (comparing measurements taken after 28 and 124 days of drying). The coefficient of thermal conductivity had lower values when all observed plates were in dryer condition than at the beginning of the test. This can be explained with the fact that the material with larger amount of water in its pores has higher thermal transmittance [12], so it resulted in higher values of thermal conductivity coefficient.

Table 2.
 Results of Thermal Conductivity Test

FC composition	Drying time (days)	The coefficient of thermal conductivity λ (x 1000)		Average value of λ (W/mK)
		Upper	Lower	
I	2	7	8	9
I	28	133.91	138.86	0.136
	124	138.40	132.50	0.135
I P	28	122.90	121.09	0.122
	124	111.80	111.90	0.112
II	28	204.92	202.81	0.204
	124	172.86	173.09	0.173
II P	28	122.90	122.67	0.123
	124	108.41	108.29	0.108
III	28	254.64	246.93	0.251
	124	242.82	203.12	0.223
III P	28	151.46	151.78	0.152
	124	149.15	127.44	0.138

The higher values of thermal conductivity coefficient after 124 days of hardening in in the laboratory setting (with the relative humidity level about 50%) were obtained from plates prepared from I, II and III compositions (0.135 W/mK, 0.173 W/mK and 0.223 W/mK respectively). About 20.5%, 60.2% and 62% lower values of coefficient of thermal conductivity were gained from the plates made of IP, IIP and IIIP mixes (0.112 W/mK, 0.108 W/mK and 0.138 W/mK respectively) (see data of Fig. 3 and Table 2). This observation can be explained by the porosity of obtained FC specimens. Homogenous, porous composite concrete structure was obtained in compositions with EG granules and CS. By contrast, porosity of samples without porous aggregate was not so high. As it is known, the materials with high porosity level possess lower thermal conductivity coefficient values, because the heat in the material

flows through both the pore walls and the pores of enclosed air.

The highest coefficient of thermal conductivity (0.223 W/mK) after 124 days of curing was determined for the plate prepared from the composition III. During the mixing process, the superplasticizer was added in this composition. It created denser and less porous structure of the material. Comparing the specimens with porous aggregates, it can be seen that the higher value of thermal conductivity coefficient (0.138 W/mK) is for the composition IIIP, it also has added chemical additive (superplasticiser).

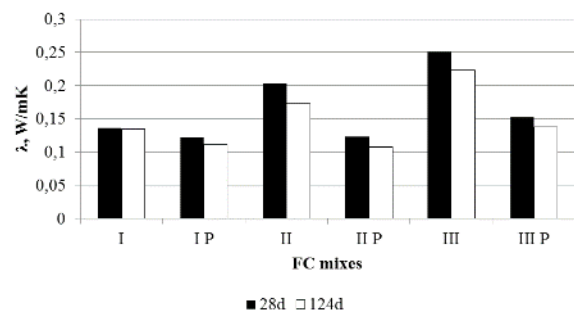


Fig. 3. Coefficient of thermal conductivity depending on the drying time (24 and 124 days)

Interaction of thermal conductivity and density

Thermal properties of concrete are closely connected with the moisture content in the structure of concrete; air has about 25 times lower thermal conductivity than water [17-18]. The thermal conductivity of concrete also depends on its density, cement content, mineralogy of the used aggregate, mineral admixture and temperature of concrete [19-22].

In summarizing the data about FC specimen coefficient of thermal conductivity and density, a graphic relationship is created (see Fig. 4, function in blue colour). It is clearly defined that thermal conductivity is a function of density [15]. Following the obtained graph, it can be seen that plates with lower density have lower thermal conductivity values and with higher density – higher values. Specimens with higher values of density (without light and porous aggregate) are less porous, but samples with lower density values (with granules of EG and CS) contain more cells or pores with enclosed air. Consequently, together with the reduced density and increased porosity of prepared specimens, the thermal properties of FC samples with lightweight and porous aggregate are improved.

There is a recommendation (see Formula 2) from ACI Committee 213R-03 (Guide for Structural Lightweight-Aggregate Concrete) [16] how to estimate the coefficient of thermal conductivity for the lightweight concrete:

$$\lambda = 0.0864 \cdot e^{0.00125 \cdot \gamma} \quad (2)$$

where:

λ - the coefficient of thermal conductivity (W/mK);

γ - the density of lightweight concrete (kg/m³). The result of ACI formula is seen in Fig. 4 (function in red colour).

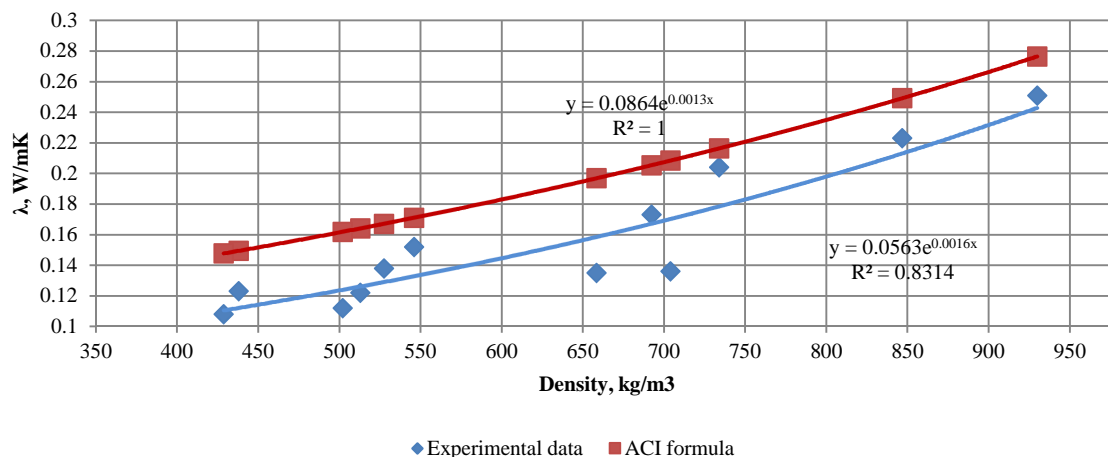


Fig. 4. Interaction of thermal conductivity and density of FC

As can be seen in Fig. 4 and Formula (2), there is a strong relationship between the coefficient of thermal conductivity and the density of FC specimens ($R^2 = 0.831$ and $R^2 = 1$). Analysing the results obtained experimentally and using a formula provided by ACI, it can be seen that both function graph have exponential tendency and the obtained functions are almost parallel. The values of thermal conductivity gained from the suggested equation are higher than experimentally obtained. The difference can be explained by the specifics of the formula provided by ACI; it is only relying on the density of concrete and does not take into account the volume of added aggregates (EG granules and CS). The comparison of experimental data and ACI formula data is included in Table 3.

Table 3. Comparison of DATA: obtained experimentally VS using formula provided by aci

FC composition	Time (days)	Exp. obtained value of λ (W/mK)	ACI formula proposed value of λ (W/mK)
I	28	0,136	0,208
I	124	0,135	0,197
IP	28	0,122	0,164
IP	124	0,112	0,162
II	28	0,204	0,216
II	124	0,173	0,205
IIP	28	0,123	0,149
IIP	124	0,108	0,148
III	28	0,251	0,277
III	124	0,223	0,249
IIIP	28	0,152	0,171
IIIP	124	0,138	0,167

Frost resistance

The results of frost resistance test are presented in Table 4. The main parameter is an average weight loss of tested samples or quantity of crumbled particles during the freeze-thaw cycles.

Table 4. Summary of obtained results – I

FC mix	Density (kg/m ³)	Compressive strength, age of 28 days (MPa)	Average weight loss (g)	Weight loss (g/m ²)
1	2	3	4	5
I	736	2.5	0.6	60
IP	565	1.4	1.3	130
II	769	6.3	0.5	50
IIP	445	2.5	1.1	110
III	952	14.4	0.3	30
IIIP	589	5.7	0.4	40

From the obtained results it can be seen that specimens with higher density values have better frost resistance properties; the average weight loss is small (see Table 4). The samples prepared from mixes I, II and III showed the following values of weight loss: 60 g/m², 50 g/m² and 30 g/m². The specimens from FC compositions IP, IIP and IIIP have more porous structure comparing to compositions I, II and III. Performance of these specimens in the tests was better as there was less pores and consequently water frozen inside the material damaged it less. Therefore, the values of weight loss from the FC compositions IP, IIP and IIIP were about 54 %, 55 % and 33 % higher than I, II and III mixes. It can be explained by the use of light and porous aggregate (EG granules and CS) that made the structure less dense and more porous.

The specimens made from compositions III and IIIP had the lowest amount of damages; after 14 freeze-thaw cycles these specimens had almost none crumbled particle while in other specimens the process of scaling could be observed already after 14 cycles (see Fig. 5).



Fig. 5. FC (IP) after 14 cycles of freezing-thawing

The use of superplastifying additive in the FC mixes III and IIIP contributed to higher resistance of these specimens to freeze-thaw test. The structures of these specimens were denser compared to others and their pore size was smaller. It is very important to avoid capillary-sized pores because it decreases durability of the material.

Analysing the obtained data, it can be seen that higher values of compressive strength (at the age of 7 and 28 days) were for FC specimens, where porous aggregate were not included. Comparing the FC compositions I to II, it can be concluded that replacing the traditional quartz sand with CS gives a significant strength increase (up to 53.5% at the age of 7 days and up to 59.6% at the age of 28 days). The highest values of compressive strength 11 MPa (at the age of 7 days) and 14.4 MPa (at the age of 28 days) were obtained testing the specimens prepared from the FC mix IIIP, which contained CS and superplasticizer contributing to a denser and less porous structure of the material. Among the compositions, where porous aggregate was used, the best results of compressive strength showed specimens from the FC mix IIIP (4.7 MPa at the age of 7 days and 5.7 MPa at the age of 28 days).

Porosity and structure

Microstructure of FC was studied in the cross-sectional view of the material after sawing it with a diamond disc.

Analysing FC mixes with EG it can be concluded that lightweight aggregates are distributed uniformly over the cross-section without any processes of segregation. Examination of the FC mix IIIP showed that structure of pores of EG and matrix of FC cement is similar (see Fig. 6.). In the digital picture of microstructure can be seen that both (granules of EG and matrix of FC) have closed structure of pores, filled with air. This composition has homogeneous structure

of pores that is ensure good thermal properties and capillary water absorption properties.

There is a risk of alkali-silica reactions on the contact area between matrix of FC cement and EG aggregate, when using amorphous silicates. Namely, use of the EG granules in cement-based composites can cause the reaction between amorphous silicon oxide and the alkali of cement. Consequently the volume of alkali silicate hydrogel can increase causing internal osmotic pressure, which results in the processes of concrete expansion and destroying of concrete structure. It may cause the deterioration of physico-mechanical properties and have negative impact on the longevity of concrete [4]. Therefore, special attention should be paid to this contact area. As shown in Fig. 6, contact area is relatively dense and there are no signs of deterioration.

Correlation between thermal conductivity and diameter of pores is presented in Fig. 7 and Table 5. Compositions of FC (IP, IIP, IIIP) with lightweight aggregate had lower value of thermal conductivity.

Table 5.
 Summary of obtained results - II

FC mix	Total porosity, %	Average diameter of pores, mm	Average value of λ (W/mK)
1	2	3	4
I	74.3	525.98	0.136
			0.135
IP	80.2	521.02	0.122
			0.112
II	73.1	552.16	0.204
			0.173
IIP	84.4	500.42	0.123
			0.108
III	66.7	382.18	0.251
			0.223
IIIP	79.4	560.88	0.152
			0.138

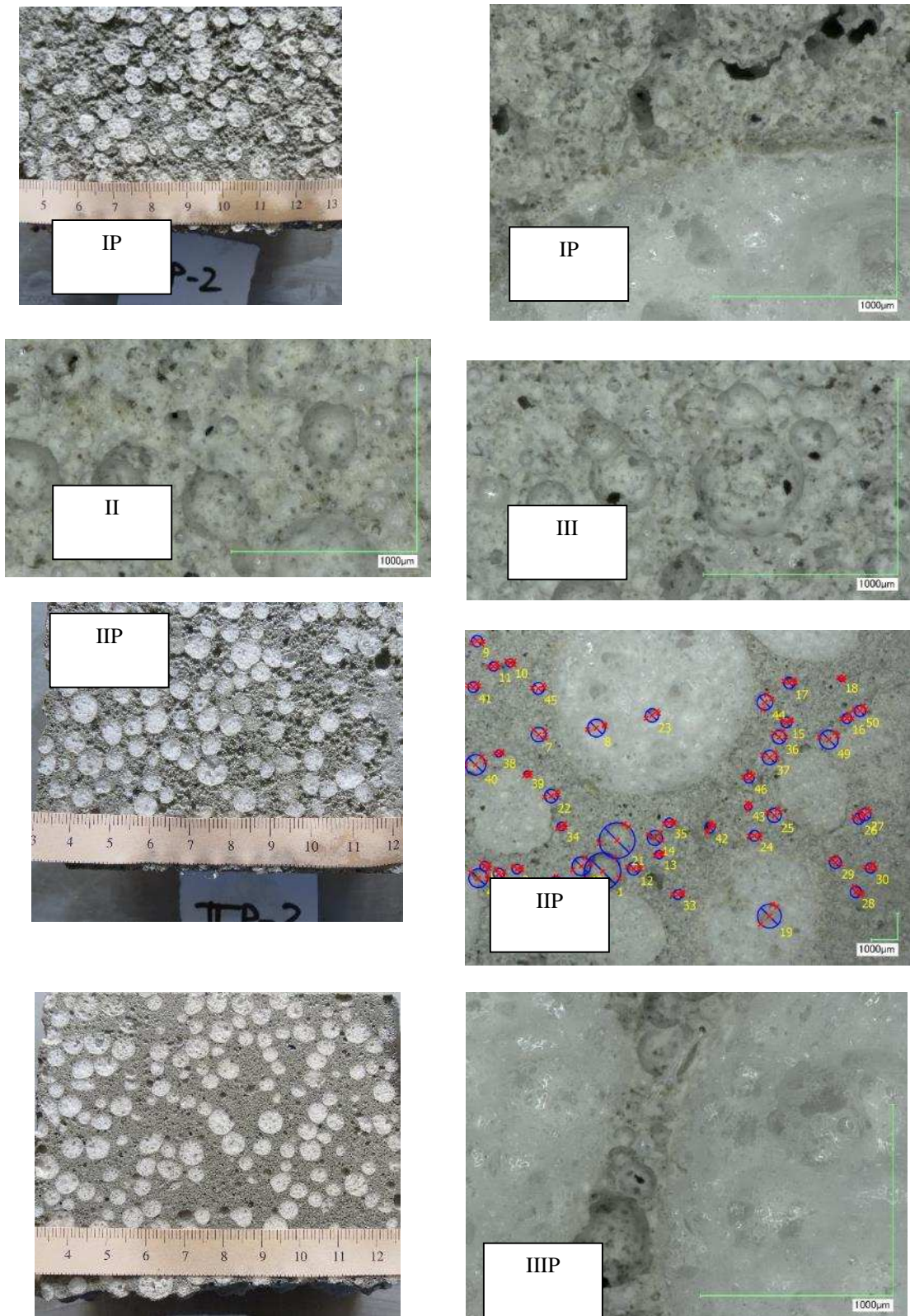


Fig. 6. Macro- and micro- structures of cross-section of FC.

Total porosity of FC mixes increases by adding porous aggregate up to 7.9% in the IP mix and up to 19% in the IIP mix. Increase of total porosity for the

IIP FC composition can be explained by adding superplasticizer. As it can be seen in Table 5, the diameter of pores reduces by adding porous

aggregates, except of composition of FC mix with IIIIP. This phenomenon can be explained by the use of superplasticizer.

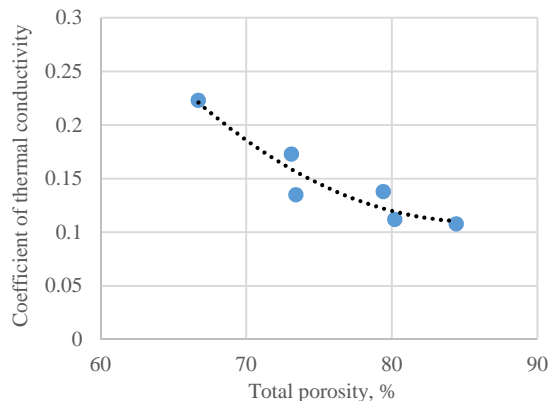


Fig. 7. Correlation between total porosity and thermal conductivity.

IV. CONCLUSIONS

FC is widely used in the construction industry; the porous structure of FC can be obtained without heat treatment which is required for production of autoclaved aerated concrete.

Value of thermal conductivity can be reduced up to 0.108 W/mK by using porous and lightweight aggregates in the production of FC.

Values of compressive strength increased using a superplasticiser. Also the use of cenospheres increased the compressive strength about 60 % and 44 %.. Thereby for the FC with similar density the properties of mechanical strength were improved.

Reference compositions (I, II, and III) had lower values of weight loss (g/m^2) after freeze-thaw test comparing to compositions with porous aggregate.

In the future studies it would be necessary to obtain more complete correlation between density and thermal conductivity of the FC. Therefore more detailed study of the pore size distribution and their impact on thermal conductivity of FC would be necessary.

V. ACKNOWLEDGMENTS

The financial support of European Regional Development Fund project Nr.1.1.1.1/16/A/007 "A New Concept for Sustainable and Nearly Zero-Energy Buildings" is acknowledged.

REFERENCES

- [1] P. Chastas, T. Theodosiou, and D. Bikas, "Embodied energy in residential buildings-towards the nearly zero energy building : A literature review," *Build. Environ.*, vol. 105, pp. 267–282, 2016.
- [2] M. A. O. Mydin, "Effective thermal conductivity of foamcrete of different densities," *Concr. Res. Lett.*, vol. 2, no. March, pp. 181–189, 2011.
- [3] D. Bajare, G. Bumanis, and A. Korjakins, "New Porous Material Made from Industrial and Municipal Waste for Building Application," vol. 20, no. 3, pp. 3–8, 2014.
- [4] V. Vaganov, M. Popov, A. Korjakins, and G. Šahmenko, "Effect of CNT on Microstructure and Mineralogical Composition of Lightweight Concrete with Granulated Foam Glass," *Procedia Eng.*, vol. 172, pp. 1204–1211, 2017.
- [5] E. Namsone, G. Sahmenko, and A. Korjakins, "Durability Properties of High Performance Foamed Concrete," *Procedia Eng.*, vol. 172, pp. 760–767, 2017.
- [6] N. Karagiannis, M. Karoglou, A. Bakolas, M. Krokida, and A. Moropoulou, "Drying kinetics of building materials capillary moisture," *Constr. Build. Mater.*, vol. 137, pp. 441–449, 2017.
- [7] U. Sharma, A. Khatri, and A. Kanoungo, "Use of micro-silica as additive to concrete-state of art," *Res. India Publ.*, vol. 5, no. 1, pp. 9–12, 2014.
- [8] J. T. Ding and Z. Li, "Effects of metakaolin and silica fume on properties of concrete," *ACI Mater. J.*, vol. 99, no. 4, pp. 393–398, 2002.
- [9] B. Sabir, S. Wild, and J. Bai, "Metakaolin and calcined clays as pozzolans for concrete: A review," *Cem. Concr. Compos.*, vol. 23, no. 6, pp. 441–454, 2001.
- [10] S. Sen, "Physical Properties of CENOSPHERE," 2014.
- [11] "FOX 600 and FOX 800 Series Instruments Manual. - Laser Comp, Inc." p. 32, 2001.
- [12] M. . Khan, "Factors affecting the thermal properties of concrete and applicability of its prediction models," *Build. Environ.*, vol. 37, no. 6, pp. 607–614, 2002.
- [13] U. Schneider, *Behavior of concrete at high temperatures*. 1982.
- [14] I. Örtüing, "A research on usage possibilities of ground lightweight aggregate in agricultural buildings," no. Turkey 26, pp. 90–111, 1996.
- [15] J. Setina, A. Gabrene, and I. Juhnevica, "Effect of pozzolanic additives on structure and chemical durability of concrete," *Procedia Eng.*, vol. 57, pp. 1005–1012, 2013.
- [16] 213R-03, *Guide for Structural Lightweight-Aggregate Concrete*, American Concrete Institute. ACI, 2003.

Study of Laser Source Output Characteristics

Pavels Narica, Jurijs Komkova

Rezekne Academy of Technologies
Faculty of Engineering
Rezekne, Latvia
Pavels.Narica@rta.lv

Abstract. Laser source is one of the most important components of a laser marking system, others being its scanner and control unit. Laser source is characterized by its output parameters, i.e., factors that define the source and determine its limits. In this study average laser power, pulse repetition frequency, pulse duration, pulse peak power, and, most importantly, pulse energy are analyzed in order to better determine capabilities of a system.

Keywords: average laser power, laser source, pulse duration, pulse energy, pulse peak power, pulse repetition frequency.

I. INTRODUCTION

In this work the output characteristics of laser sources of Rofin PowerLine F-20 Varia and Chanxan CX-20G are studied. To accomplish that, laser light output was studied for different values of laser source input parameters. Laser light output is characterized by laser source output parameters and adjusted by laser source input parameters. Both Rofin PowerLine F-20 Varia and Chanxan CX-20G (further in text, Rofin and Chanxan) generate laser light in form of a pulse wave that is periodic in both time and space (Fig. 1).

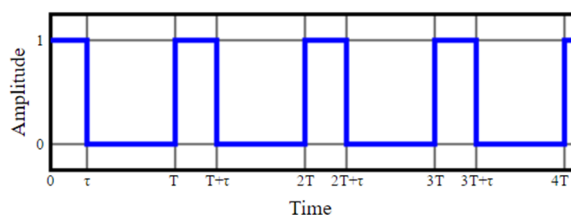


Fig. 1. Schematic representation of pulse wave as a function of time with pulse wave period T and pulse duration τ

Pulsed laser systems do not generate energy in a form of continuous stream of coherent photons, but instead output photons grouped in form of laser pulses and pulse repetition frequency f relates to the amount of such pulses generated by the laser source in one second [1].

To understand laser source output one needs to study laser light in terms of both laser pulse wave and individual laser pulse. Laser pulse wave can be characterized in terms of both space (and its dimensions) and time. Pulse wave length l (in terms of space) is directly proportional to pulse wave period

T (in terms of time), and speed of light c is the constant of this proportionality as shown in formula (1).

$$l = c \cdot T, \text{ [m]} \quad (1)$$

Laser pulse wave period T (temporal pulse spacing, pulse repetition period) represents the amount of time passing between two consecutive laser pulses. Laser pulse wave period T is controlled by pulse repetition frequency f input parameter for both laser marking systems and there is inversely proportional relationship between them as shown in formula (2).

$$f = \frac{1}{T}, \text{ [Hz]} \quad (2)$$

Pulse repetition frequency f is measured in inverse seconds (s^{-1} , Hz). Thus, pulse repetition frequency f must be interpreted not as the amount of pulses generated in one second, but instead as the amount of similar events that took place during one second. In case of a pulsed laser, these similar events refer to laser pulses [2].

Laser pulses from the same pulse wave refer to individual pulse that is similar to all other pulses within this pulse wave. This pulse can be described in terms of its energy as having energy E_P equal to that of one laser pulse. Thus, the amount of pulses generated in one second can be described in terms of the total amount of energy generated by a pulsed laser in one second also known as average laser power P as shown in formula (3).

$$P = E_p \cdot f = \frac{E_p}{T}, \text{ [W]} \quad (3)$$

As shown in formula (3) laser pulse wave period T also represents the amount of time, in which there is energy E_p equal to that of one laser pulse. Because laser pulse wave is periodic, in each such laser pulse wave period T there is energy E_p equal to that of one laser pulse [3].

By itself the laser pulse is a collection of coherent photons of some central frequency. In one particular instant of time, the laser pulse is localized in space [4].

In any straight line forming a plane which is perpendicular to direction of laser pulse propagation and which cross-sections laser pulse (Fig. 2), the distribution of energy (photons) can be characterized by a normal (Gaussian) distribution. Thus, within a laser pulse there is more energy closer to the axis representing direction of laser pulse propagation.



Fig. 2. Normal (Gaussian) distribution of energy within cross-section perpendicular to direction of laser pulse propagation

Laser pulse can be interpreted as a wave packet that has distinct temporal duration τ and thus a directly proportional spatial length l , with speed of light c being the constant of this proportionality as shown in formula (4).

$$l = c \cdot \tau, \text{ [m]} \quad (4)$$

This way pulse energy E_p , which is moving at the speed of light c in certain direction, can cross imaginary plane that is perpendicular to this direction in the amount of time equal to pulse duration τ . In other words, total amount of laser pulse energy E_p that can be delivered in continuous way to a plane perpendicular to direction of its propagation in the amount of time equal to pulse duration τ defines pulse peak power P_p as shown in formula (5).

$$P_p = \frac{E_p}{\tau} = \frac{P}{f \cdot \tau} = \frac{P \cdot T}{\tau}, \text{ [W]} \quad (5)$$

Both average laser power P and pulse peak power P_p characterize the flow of energy in form of laser pulses and/or photons that constitute the laser pulses.

II. METHODOLOGY

A. Laser systems

Laser systems being studied are commonly used for laser marking. They provide several adjustable laser input parameters that can be categorized in three main groups:

- laser source – power regulation coefficient, pulse repetition frequency, pulse duration (only Rofin);
- scanner – scanning speed, line step;
- control unit – repeat count.

Only two parameters are available for adjusting the properties of laser light generated by the laser source of Chanxan – power regulation coefficient k_p and pulse repetition frequency f . Rofin provides additional parameter for adjusting pulse duration τ .

Power regulation coefficient k_p allows laser operator to indirectly set the amount of average power P generated by the laser source. Initially, it was not known how power regulation coefficient k_p affects laser power P , so power measurements for different values of power regulation coefficient k_p were necessary. Before experimental investigation it was assumed that the value of power regulation coefficient k_p is directly proportional to the value of average laser power P on the output and that maximum possible average power $P_{\max} = 20 \text{ W}$ specified in technical characteristics of both laser systems is a constant of this proportionality as shown in formula (6).

$$P = P_{\max} \cdot k_p, \text{ [W]} \quad (6)$$

Nevertheless, formula (6) does not account for the effect pulse repetition frequency f and pulse duration τ can have on output laser power P . Therefore average laser power P measurements are necessary for different input values of all available laser source input parameters for both laser systems.

The three laser source input parameters under study (power regulation coefficient k_p , pulse repetition frequency f , and pulse duration τ) should provide enough information for calculating average laser power P , pulse energy E_p , and peak power P_p . When values of all these output parameters are determined, interpretation of laser materials processing results becomes considerably easier. Moreover, if values of these laser source output parameters can be repeated on other laser marking systems, then the result of laser marking (color) can also be repeated under similar ambient conditions and for similar material. In other words, these laser source output parameters form a universal system with the help of which it becomes possible to achieve similar processing results using different marking systems.

B. Additional equipment

For taking measurements three different devices were used:

- Power measurement sensor Ophir F150A-BB-26 and Ophir Nova II laser power meter,
- Multi-purpose zoom microscope Dino-Lite Edge AM7115MZT,
- Angle grinder AEG WS 6-125.

C. Measurements

The problem with the laser source is that one can set the laser power P indirectly by adjusting power regulation coefficient k_P . Eventhough it is stated in technical specification of both systems that laser can generate up to $P_{max} = 20\text{ W}$ of laser power, the mapping between values of power regulation coefficient k_P and actual average laser power P is not known and has to be measured using power meter.

Measurements were taken for both systems and for different values of all available laser source input parameters. For Rofin, all three laser source parameters affected the output laser power P , while for Chanxan, only power regulation coefficient k_P had an effect similar to that shown in formula (6) (Fig. 3).

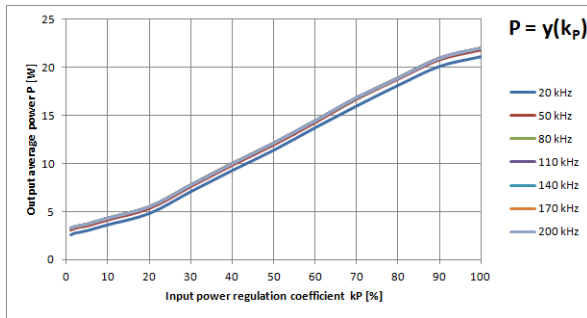


Fig. 3. Chanxan output power P as a function of power regulation coefficient k_P for different values of pulse repetition frequency f

For maximum value of power regulation coefficient k_P , low values of pulse repetition frequency f and each value of pulse duration τ Rofin showed lower average power P output. The value of measured average power P was directly proportional to a value of pulse repetition frequency f up to a certain point f_{limit} , after which average power P reached $P_{max} = 20\text{ W}$ and stayed constant for all higher possible values of pulse repetition frequency f (Table I).

While the input and output values of pulse repetition frequency f for Rofin were consistent, on Chanxan additional mapping was necessary. The mapping of input pulse repetition frequency f_i to output pulse repetition frequency f_o was carried out by scanning photosensitive inked paper at high scanning speed $v_{max} = 10\text{ m/s}$. Scanned lines were then analyzed using microscope to measure distance Δy between two consecutive laser pulses as shown in formula (7).

$$\Delta y = \frac{v}{f}, \text{ [m]} \quad (7)$$

Table I
Limit Pulse Repetition Frequency and Maximum Possible Pulse Energy for Every Available Pulse Duration of Rofin

τ , [ns]	f_{limit} , [kHz]	E_{Pmax} , [μJ]
4	500	40
8	200	100
14	125	160
20	111	180
30	83	240
50	63	320
100	40	500
200	20	1000

Because input scanning speed v_i was consistent with output scanning speed v_o , output pulse repetition frequency f_o was determined using formula (7) and mapped as shown in Fig. 4.

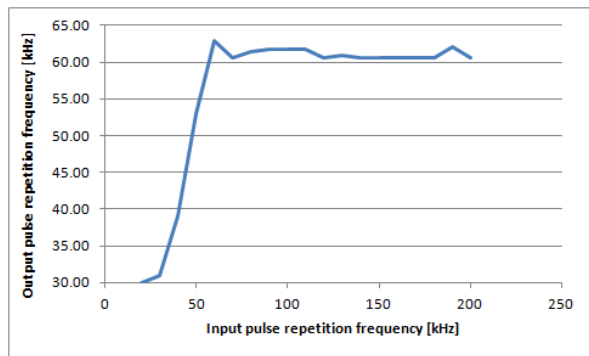


Fig. 4. Mapping of input pulse repetition frequency f_i to output pulse repetition frequency f_o on Chanxan

Based on newly gathered information pulse energy E_P for different possible values of output pulse repetition frequency f_o were determined and graphed in Fig. 5.

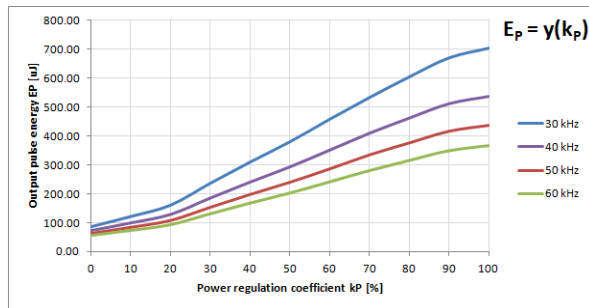


Fig. 5. Chanxan pulse energy E_P as a function of power regulation coefficient k_P for different values of output pulse repetition frequency f_o

To measure pulse duration τ , an angle grinder was used. It allowed to produce scanning speed greater to that of a laser system by a factor of 10. In specifications of angle grinder it was mentioned that it can produce 167 rotations per second or $w = 167\text{ Hz}$. Photosensitive inked paper was cut in form of a circle with diameter $d = 170\text{ mm}$ and attached to the angle grinder. Thus, the speed on the edge of a circle could be reached amounting to $v_c = 90\text{ m/s}$ as shown in formula (8).

$$v_c = \pi \cdot d \cdot w, \text{ [m/s]} \quad (8)$$

The angular speed w of an angle grinder was tested by lasing a rotating photosensitive inked paper for specific short amount of time $t = 5$ ms and then measuring the angle θ (specified in turns or full rotations) of a mark left on a paper as shown in formula (9).

$$w = \frac{\theta}{t}, \text{ [Hz]} \quad (9)$$

Angular speed of an angle grinder was consistent, therefore pulse duration τ could be measured. For this, a line of length $a = 50$ mm was marked at scanning speed $v_{\max} = 10$ m/s and pulse repetition frequency $f = 30$ kHz on a rotating photosensitive inked paper. Thus, a scanned surface with respect to a laser beam was moving at total speed of $v_t = 100$ m/s as shown in formula (10) (Fig. 6).

$$v_t = v_c + v_{\max}, \text{ [m/s]} \quad (10)$$

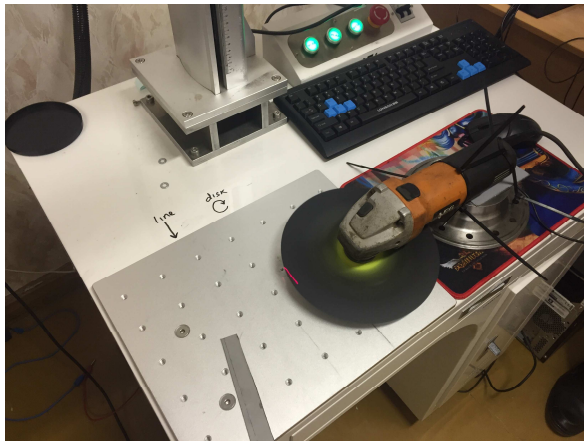


Fig. 6. Measuring pulse duration τ using angle grinder

It was assumed that in certain amount of time τ (pulse duration) the laser beam would scan some certain amount of distance s as shown in formula (11) (Fig. 7).

$$s = v_t \cdot \tau, \text{ [m]} \quad (11)$$

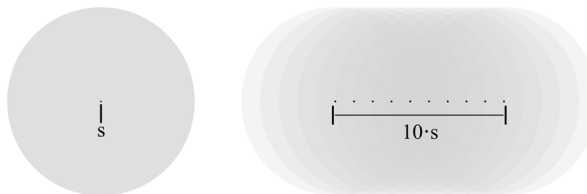


Fig. 7. Distribution of pulse energy on scanned distance s for scanning speed $v_{\max} = 10$ m/s (left) and increased scanning speed $v_t = 100$ m/s

Because individual laser pulses could leave a mark on photosensitive inked paper, it was possible to measure the scanned distance s using microscope

and then calculate the amount of time τ (pulse duration) by using formula (11). Nevertheless, laser pulses left similar round marks for both maximum possible laser scanning speed $v_{\max} = 10$ m/s (Fig. 8) and increased scanning speed $v_t = 100$ m/s (Fig. 9).

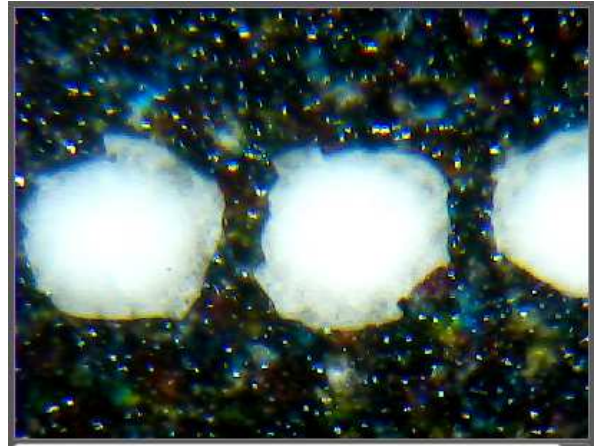


Fig. 8. Mark left by pulses scanned at maximum possible laser scanning speed $v_{\max} = 10$ m/s

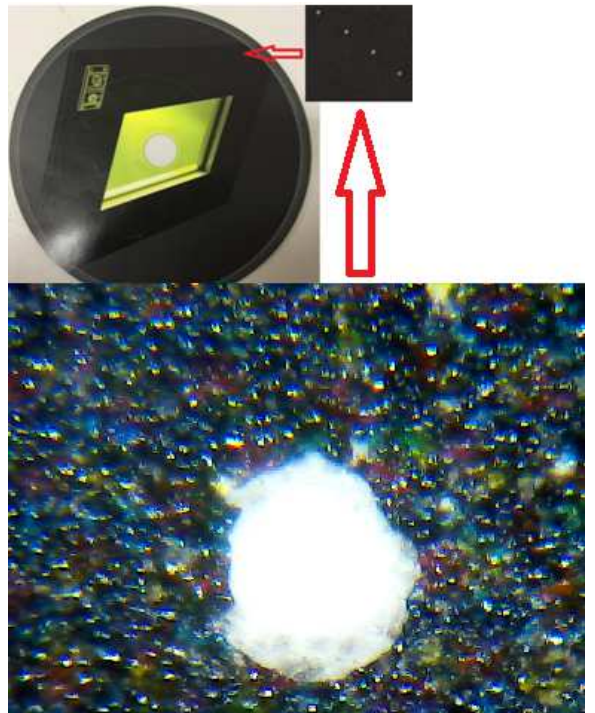


Fig. 9. Mark left by pulse scanned at increased scanning speed $v_t = 100$ m/s

Thus, energy of a single pulse was distributed over a very small scanned distance s even at increased scanning speed $v_t = 100$ m/s. Therefore additional mathematical simulation was carried out for distributing energy E_p of a single laser pulse over some scanned distance s (Fig. 10) [5].

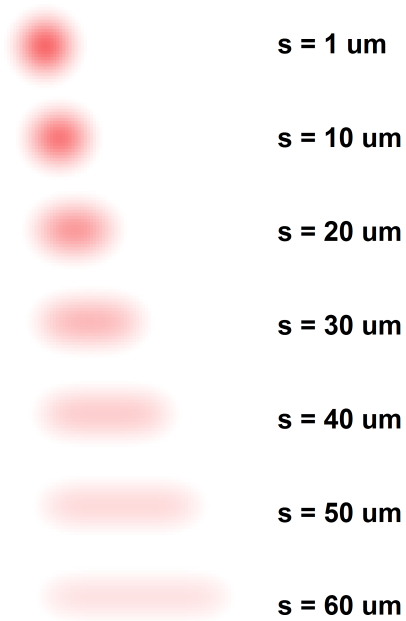


Fig. 10. Simulation of distributing laser pulse energy E_p over some scanned distance s

Based on the results of a simulation it can be seen that pulse was scanned over a distance $s \leq 20 \mu\text{m}$, which corresponds to pulse duration $\tau \leq 200 \text{ ns}$.

ACKNOWLEDGEMENT

This study was supported by laser system equipment from Rofin-Sinar Laser GmbH.

REFERENCES

- [1] F. K. Kneubuhl, "Laser", Vieweg+Teubner, pp. 443, 2008.
- [2] J. Bliedtner, H. Muller, A. Barz, "Lasermaterialbearbeitung" Fachbuchverlag Leipzig im Carl Hanser Verlag, pp. 530, 2013.
- [3] M. Eichhorn, "Laser physics", Springer, pp. 171, 2014.
- [4] C. Breck Hitz, "Introduction to laser technology", Wiley-IEEE Press, pp. 298, 2012.
- [5] P. Narica, A. Teilans, L. Lazov, P. Cacivkins, E. Teirumnieks, "Mathematical model of distribution of laser pulse energy"

Enhancing the Technological Capabilities of Universal Grinding Equipment

Igor Nikiforov¹, Pavel Maltsev¹, Loginov Sergey²

Pskov state university, Faculty of Mechanical and machine building, Department of Technology of machinebuilding. Address: Lenin square 2, Pskov, 180000, Russian Federation¹, Pskov state university, Faculty of Electro-mechanical, Department of Electric and automation systems. Address: Lenin square 2, Pskov, 180000, Russian Federation²

Abstract. *A method to enhance the technological capabilities of universal grinding equipment and improve the durability of grinding wheels is proposed. A device that allows to implement this method by using of continuously variable grinding speed is proposed. This reduces the cost of manufacturing products of various structural materials.*

Keywords: *grinding, rotation frequency, durability of grinding wheels, variable grinding speed, frequency converter.*

I. INTRODUCTION

In a world tendencies towards an increase in the degree of convergence with the manufacture of machine tools are planned. Including [1]:

- expand the range of metal cutting equipment to provide multipurpose treatment on a single machine complex parts, through a series of combined or sequential operations;
- more widely used multi-functional machines and machining centers that allow to combine milling, grinding, chemical and electrochemical machining, heat treatment;
- different types of abrasive handle combine on the machine, for example, internal and external grinding;
- increase the possibility of treatment different materials on the same equipment, such as the grinding of ceramics and hardened steels.

Difficulties of grinding at single machine tool for various materials with different physical and mechanical properties are caused mainly by the need of select and install the appropriate grinding wheel and device for its truing. Thus, for example, hardened steel more efficiently handle by wheels of cubic boron nitride (CBN), and ceramics – diamond wheels. This requires an appropriate adjustment of the cutting conditions. The problem with using the same grinding wheel in the processing of various materials occurs due very low (in some cases) of the cutting ability, which define the abrasive tool life.

One reason for the loss of cutting ability is clogging of the grinding wheel. GOST 21445-84 (RU) determines the «clogging» as the transfer on the working surface of an abrasive tool of sludge particles. As a result, the operation of grinding some viscous materials with high adhesion properties is irrational and replaced by the edge cutting. Such

materials include a of nonferrous alloys, some complex alloyed steels and alloys, metallic and non-metallic composites.

In this regard, the expansion of technological capabilities of grinding equipment, which allows to increase the range of different materials to be processed using the same tools and equipment is important for the tool, engineering and machine tool industries.

A significant amount of researches devoted to increase the efficiency of the grinding. However, many of the obtained positive results are not implemented in the real production sectors. This is due, inter alia, to the fact that industrial companies are reluctant to modernize the standard equipment, the use of non-standard technologies and special cutting tools. This important fact to consider when selecting a vector of scientific researches and the routes of rationalization.

II. MATERIALS AND METHODS

In [2] the authors proposed and justified the method to eliminate the clogging of grinding wheels due by using comprising variable (continuous variable) cutting speed of grinding. On the basis of this idea developed practical methods that can be implemented by modernization of machine tools. As part of the research received a patent for utility model «Device for abrasive machining with a variable cutting speed» (RU 129444), and the patent for the invention «Method of abrasive machining of flat surfaces with a variable cutting speed» (RU 2608867).

The present paper describes an improved and more universal method of varying the cutting speed of the grinding process, which «complements» the existing universal equipment. Wherein processing is

held by conventional grinding wheels using conventional cutting conditions.

The method is based on the use of the frequency converter, allowing continuously variation of the frequency of rotation of the output shaft of the three-phase asynchronous motor. Overall scheme of control shown at Fig. 1.

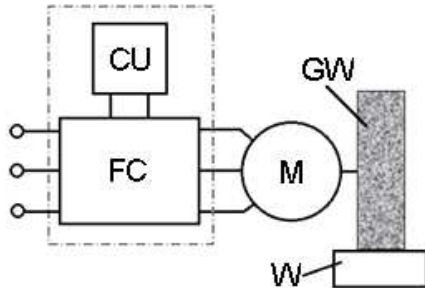


Fig. 1. Scheme of control of the rotation frequency of the grinding wheel: M – asynchronous motor; GW – the grinding wheel; W – workpiece; FC – frequency converter; CU – control unit

The frequency converter (FC) and the control unit (CU) (Fig. 2) is further connected to the electric circuit of the machine tool.

CU sends a signal to the analog input of FC and actually control it, that allows you to varying grinding conditions. A feature of the device is the possibility of varying the output shaft speed by a certain law, for

example, sinusoidal. And CU allows you to change the period, the amplitude and the nominal value of the rotational speed of the grinding wheel.

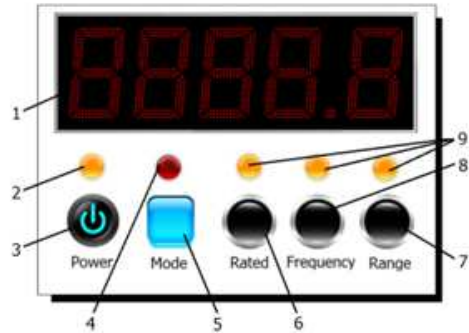


Fig. 2. The control unit: 1 – digital display; 2 – the network indicator; 3 – power button; 4 – overload indicator; 5 – mode button; 6 – switch selection of rated speed; 7 – switch selection of the oscillation amplitude; 8 – switch selection of the oscillation period; 9 – mode indicators

The frequency converter is connected to the electric circuit of the machine tool after branching to engines «1M» and «2M», in order to control the main drive «M» and do not affect the operation of other drives (hydraulic drive «4M», drive of accelerated movement of the wheelhead «6M», the electric pump of cooling «1M» and magnetic separator «2M») (Fig. 3).

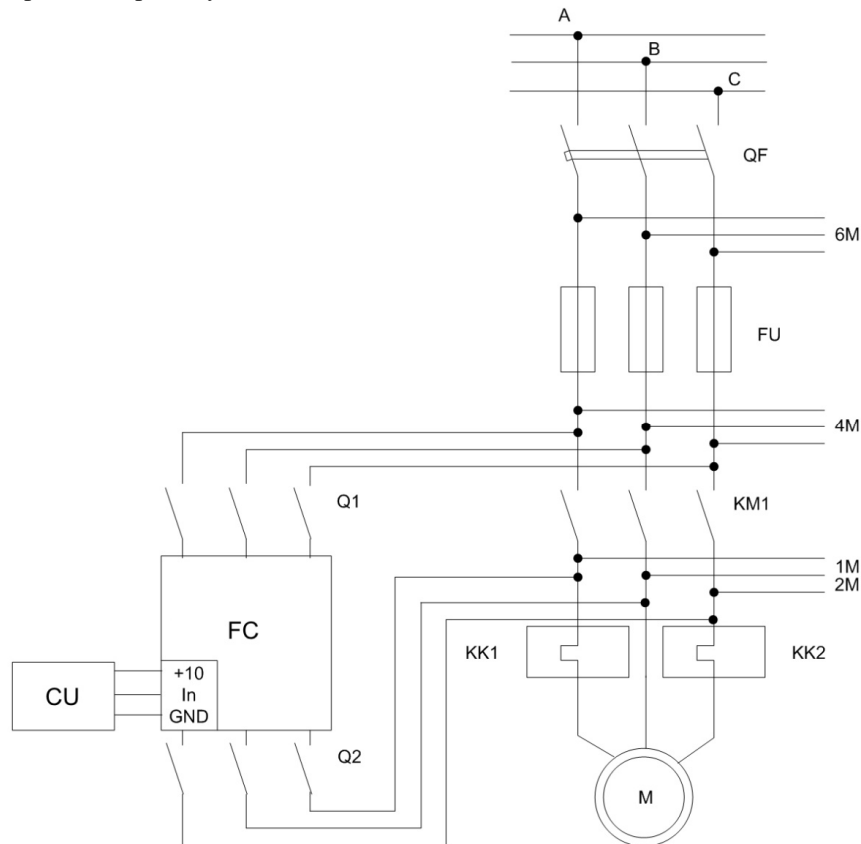


Fig. 3. The scheme of connection of the frequency converter

The frequency converter connected to the computer in debug mode and mode of adjustment for grinding operations of a variety of structural materials. Monitoring of major control parameters was carried out on the basis of a special program «Scope movitools» (Fig. 4).

These settings include: Y1 – the current speed (rev/min); Y2 – setting speed (rev/min); Y3 – converter frequency (Hz); Y4 – motor current (in % of the nominal value), etc. The interface of the program allows you to visually track the changes in these parameters over time.

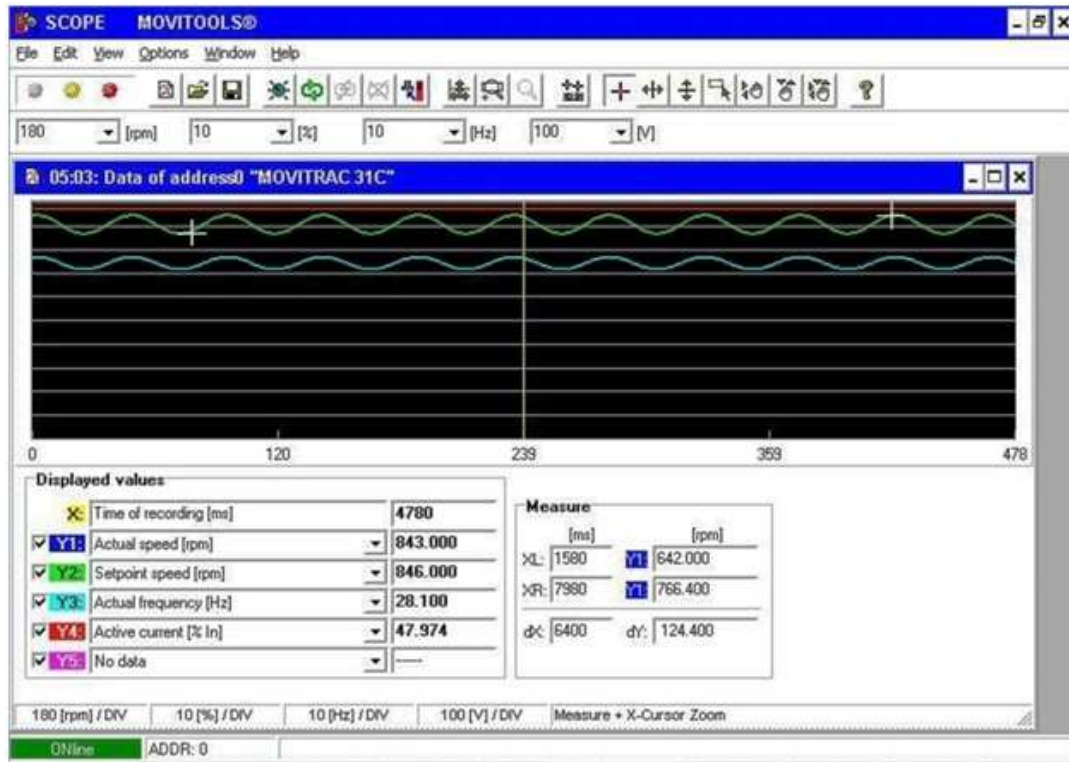


Fig. 4. «Scope movitools» interface

The experimental studies have been conducted in order to test the proposed method and technology. The aim of the research is to define the effect of continuously variation the cutting speed on the

durability of the grinding wheel by white synthetic aluminum oxide. Data of the used equipment are summarized in Table 1.

Table 1
 Equipment Characteristics

No	Name	Type	Model
1	Machine tool	Surface-grinding	3G71
2	Grinding wheel	White synthetic aluminum oxide	1-250x20x76WAF30L6V50-2
3	Frequency converter (FC)	Flux vector control without sensor	ATV32HU75N4
4	Control unit (CU)	Original	—
5	Power	3 phases, 380 V	—

III. RESULTS AND DISCUSSION

In the course of the experiment processed the following materials: carbon structural steel 1045, chromium steel 5140 (hardening) and high-speed steel

T1 (hardening). Cooling was absent, dressing of grinding wheel by diamond-point dresser made before each experiment. Other conditions of the experiment and the obtained results are presented in Table 2.

Table 2
 Conditions of the Experiment and the Obtained Results

Workpiece material	Hardness	S, μm /double m.p.	Parameter (v=var)		Wheel durability, s		Durability increase, %
			A, %	T, s	v=const	v=var	
Steel 1045	150 HB	5	±2,5	3,9	990	1250	26,3
Steel 5140	220 HB	10	±2,5	3,9	302	393	30,1
	280 HB	10	±2,5	3,9	91	137	50,5
Steel T1	57 HRC	5	±2	5,7	137	194	41,6

Note: Wheel rated speed range – 2760 rev/min; nominal cutting speed – 35 m/s; longitudinal feed – 12 m/min; S – wheel vertical feed per double manufacturing pass; A – amplitude of oscillation wheel rotation speed; T – oscillation period (sinusoid).

The table shows that the use of a grinding technology continuously varying cutting speeds improves wheels durability of 1.25 ... 1.5, depending on the material, heat treatment, grinding modes and control parameters.

Durability of grinding wheels was determined by the time of the intensive appearance of visible burn marks on the work surface. The machined surface was also seen under the microscope model Axiovert

40 MAT. Figure 5 shows a 3-D image of the machined surfaces (fragments with the largest area of burns). Workpiece material – steel 1045, grinding time – 990 s (corresponding to the durability range for grinding by the traditional technology, $v = \text{const}$). It can be seen that the number of burns is noticeably reduced at grinding with continuously variable cutting speed.



Fig. 5 The 3-D microphotography of the machined surfaces: a – the traditional technology ($v = \text{const}$); b – the proposed grinding technology with variable cutting speed ($v = \text{var}$)

IV. CONCLUSION

Besides the main advantages of the proposed grinding technology with continuously variation of cutting speed – increase durability of wheel, to the advantages of proposed method can be attributed:

- flexibility, i.e. the ability to install additional equipment on the different types of machines: surface grinding, cylindrical grinding, internal grinding etc., without their physical upgrading;
- varying the frequency of spindle rotation in the range, the limited strength of the grinding wheel, power of machine and dynamic overload of control system;
- varying the amplitude and period of oscillation in a wide range of values;
- quick adjustment to the recommended settings for individual grade of processed materials;
- the ability to quickly disconnect additional equipment to work in normal conditions (for example, dressing of wheel).

Research on the use of new technologies continues. The next goal are: 1) the optimization of the control parameters with considering equipment and materials of wheel and workpiece; 2) improvement of the management system, bringing device to the industrial embodiment; 3) introduction of new technologies into production.

REFERENCES

- [1] Modernization of Russia: conditions, premises, chances. Collection of articles and materials / Ed. V.L. Inozemtsev. – Vol. 1. – M.: Center for studies of post-industrial community, 2009. – 240 p.
- [2] I.P. Nikiforov, «Justification hypothesis effective grinding with variable cutting speed» / I.P. Nikiforov, D.A. Vasilyev, E.N. Ivanov, P.N. Maltsev // High intelligent technology and innovation in education and science. Proceedings of the XVII International Scientific and Methodological conference, February 11-12, 2010, St. Petersburg. – SPb.: Publishing House of SPbSTU. – 2010. – V 2. – P. 106-108.

Smart Socks System as an Equipment to Analyze Temporal Parameters of Human Gait and Running

Aleksandr Oks¹, Aleksey Katashev², Edgars Bernans³, Valters Abolins³

¹ Riga Technical University, Institute of Textile and Technology, Riga, Latvia.

² Riga Technical University, Institute of Biomedical Engineering and Nanotechnology, Riga, Latvia.

³ Latvian Academy of Sport Education, Laboratory of Physical Capacity, Brivibas street 333, Riga, Latvia
E-mail: aleksandrs.okss@rtu.lv

Abstract. The aim of present study was to demonstrate usability of the recently developed “Smart Socks” System for analysis of locomotion temporal parameters. Smart socks system exploits pressure sensors which can be knitted directly in the garment, thus providing minimal discomfort for user. Two types of locomotion were analysed: walking and running. Experienced athletes took part in the experiment to perform movements in the controlled conditions in laboratory. The research demonstrated that temporal accuracy of Smart Sock system is acceptable for practical purposes. Data, provided by the system could distinguish heel strike and non-heel strike run and walk modes. More data is required for deeper analysis and interpretation of obtained temporal parameters and for development of recommendations for athletes and coaches.

Keywords: smart socks, running, walking, biomechanics.

I. INTRODUCTION

Development of useful wearable motion capture tool for sport purposes is a complicated task. Athletes are moving with a continuously changing velocity and direction, therefore, adaptive instrument which provides on-line locomotion monitoring is required.

Recently developed wearable “Smart socks” system [16] provides potential solution for acquisition of human locomotion spatio-temporal parameters at walking, running, jogging and other activities, that involve movements of the feet. The wearability of the system allows record data during physical activity in natural conditions both indoor and outdoor. Another important feature, that distinguish the proposed system from commercially available accelerometric devices is an ability to monitor the contact between feet sole and ground. The system consists of a pair of specially designed socks with integrated knitted pressure sensors and conductive lines and a data acquisition block, that communicates via bluetooth with computer or other kind of electronic gadgets. The socks are easy to wear and causes minimal discomfort for athlete.

Each sock has five sensors which can be arranged and knitted in different parts of the sock according to the specific demands of locomotion monitoring. Sensors can be used to determine different spatio-temporal parameters of running and walking, including cadence and strike pattern [16].

There is three types of strike pattern at running: heel strike, midfoot and forefoot strike [4]. Heel strike is a

pattern when rear part of the foot makes contact with ground surface first (it has also been called as rear foot strike) [15]. In midfoot strike it's the middle part of foot which touches the running surface first and the front of the foot land first in forefoot strike [11]. Each of them has it's own advantages and disadvantages [7]. Runners most often are choosing their favourite strike pattern by a natural way or study which one suits them best of all [5, 9].

Study of the most appropriate strike pattern has great interest from the scientific point of view. Number of research has been done to find the most efficient running technique that helps to avoid athlete's injuries [3]. Typically these patterns have been analysed by measuring ground reaction forces (GRF) in running. In that case it is possible to determine the pattern of foot strike and analyse the volume and parameters of different GRF components [1, 14].

Smart sock system does not allow to analyse GRF directly, but strike patterns still may be determined using temporary signals from five foot plantar pressure sensors, for example, by analysis of the sensor's activation timing.

The strike timing information, obtained by a trained person in real time could be immediately used for instant movement pattern correction in the training process or even in competitions [2].

In walking, different patterns of foot strike are

ISSN 1691-5402

not defined in detail, as compared with running [10, 13]. In gait analysis, a stride is generally subdivided into a stance and a swing phase. More attention is paid for measurements of such parameters as step time and frequency, or cadence, foot - ground contact time as well as to analysis of different gait phases [12].

Measurements of the step time allows to analyse and compare differences in these variables between both legs. It's also important to define movement asymmetry [6]. Step frequency can be defined as the count of steps, performed over the certain period of time [17, 18]. Contact time of foot is defined as a period of time from the moment when foot makes first contact with ground surface until the moment when it takes off [8].

The purpose of the present work is to evaluate usability of the developed "Smart socks" for the evaluation of athletes' locomotions at race walking and running.

II. MATERIALS AND METHODS

Volunteer participants performed walking and running on treadmill and also on casual surface indoor. Running was performed by an experienced distance runner. The running velocity was 6 km/h. Walking velocity was 3 km/h. Participants had to wear the smart socks system, size of socks was adapted individually.

The placement of foot sensors is shown in Fig. 1. Sensors A and B are placed in front, C and D -in the middle, and sensor E is placed in the rear part of the foot.

Increase of the plantar pressure on the sensors lead to the decrease in the electric resistance of the sensors. The resistance of the sensors was measured by custom-made data acquisition system with the sampling rate of 15Hz. The resistance reciprocal value was calculated and normalised to form arbitrary sensor pressure signal.



Fig.1. Placement of the sensors [16]

Procedure for determination of spatio-temporal parameters

In order to determine the foot strike phases, each step should be "recorded" by all of the sensors. When the output signal values of all five sensors are summed together, ground contact phase may be detected. Fig. 5

demonstrates 4 s long running pattern fragment, 5 strides and 5 contact phases are clearly visible..

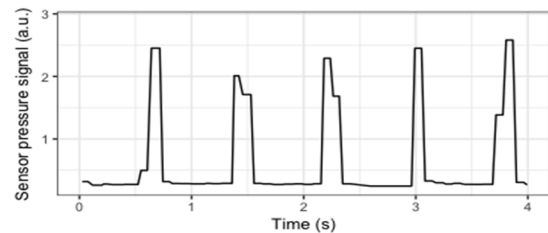


Fig.2. Signals of all sensors in running locomotion.

When running or walking with heel strike pattern, heel hits the ground first, The rest of the foot follows afterward, so the sensor E activates earlier than rest of the sensors. Sensor E also reaches the maximum value earlier than sensors A and B, placed in front of the foot. Sensors C and D, that are placed in the middle of the foot, could perform differently in dependence of the foot landing patterns. These sensors are not affect heel strike pattern detection.

When running with other strike pattern, the sequence of sensors activation will be different: if sensor E reaches its maximum value at the same time as other sensors or later, then it is not a heel strike pattern.

Based on these observations algorithm to determine if the person is running or walking with heel strike pattern was created.

III. RESULTS AND DISCUSSION

When running with heel strike, sensor E (or the heel sensor) reaches the highest value before sensors A and B (or their sum). It is demonstrated at the Fig.3 and Fig.4.

At Fig.3, heel sensor reaches its highest value in 0.03s from the beginning of the cadence, but A and B (or the forefoot sensors) reaches the highest value in 0.12s.

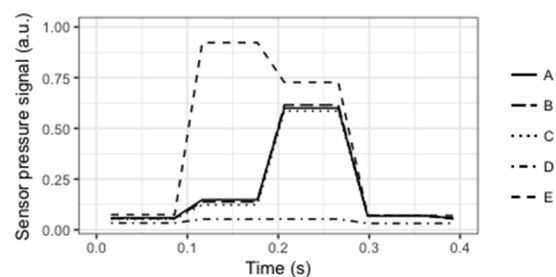


Fig.3. Heel strike running

At Fig.4, heel sensor reaches its highest value in 0.03s but sum of forefoot sensors reaches the highest value in 0.12s. Its clearly visible, that heel sensor reaches the highest value before forefoot sensors in Fig.4. and Fig.5.

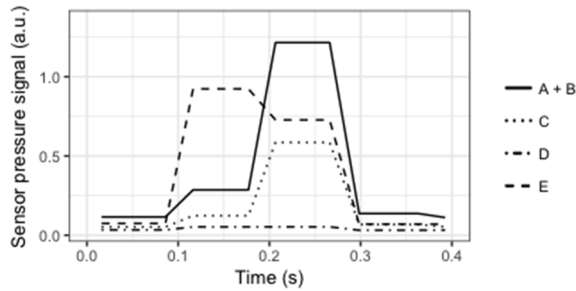


Fig.4. Heel strike running

This means that running was done with a heel strike. When running with full feet striking the ground the forefoot sensors and heel sensor got the highest value at the same time (Fig.5. and Fig.6).

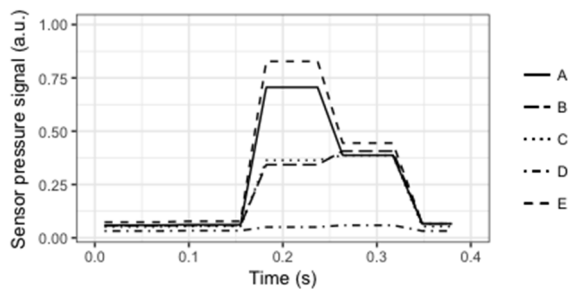


Fig.5. Running non heel strike pattern

In this case it's not clear, if running was done with a midfoot strike or forefoot strike. Despite this fact it's clear that running wasn't done with heel strike.

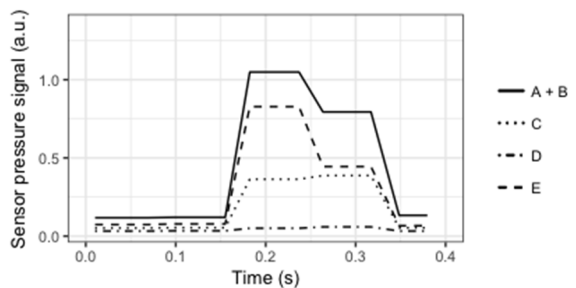


Fig.6. Running non heel strike pattern

When walking (Fig.7.) the sensors get their highest values similar to heel strike running - heel sensor gets the highest value faster than forefoot sensors or their sum (Fig.8.). At Fig.7, heel sensor reaches its highest value in 0.21s but forefoot sensors in 0.29s and 0.45s, A and B respectively.

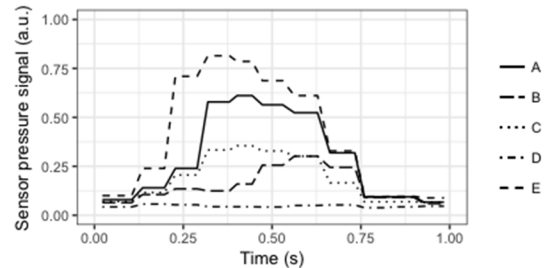


Fig.7. Walking pattern

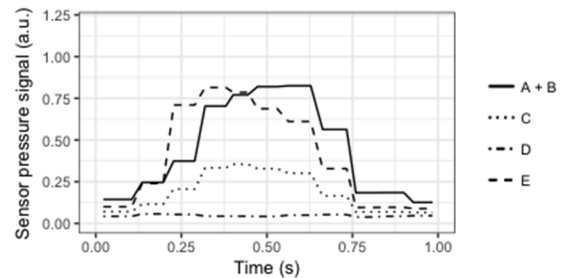


Fig.8. Walking pattern

IV CONCLUSION

Smart socks system is an applicable tool to identify several spatio-temporal parameters of human gait and running.

System works accurate with relatively slow running and walking velocity, moving in higher velocity need to be researched.

The temporal resolution of the of Smart Sock System is acceptable for strike pattern analysis purposes. The system could be used for determination of gait/run temporal parameters and differentiation of the mode of locomotion.

More detailed research is required for elaboration, analysis and interpretation of other biomechanical parameters as well as for development of the recommendations to athletes and coaches.

V ACKNOWLEDGEMENT

The work was supported by the European Regional Development Fund project "Synthesis of textile surface coating modified in nano-level and energetically independent measurement system integration in smart clothing with functions of medical monitoring", agreement 1.1.1.1/16/A/020

REFERENCES

- [1] Cavanagh, P. R., & LaFortune, M. A. Ground reaction forces in distance running. *Journal of biomechanics*, 13(5), 1980, pp 397-406.
- [2] Crowell, H. P., Milner, C. E., Hamill, J., & Davis, I. S. Reducing impact loading during running with the use of real-time visual feedback. *journal of orthopaedic & sports physical therapy*, 40(4), 2010, 206-213.
- [3] Daoud, A. I., Geissler, G. J., Wang, F., Saretsky, J., Daoud, Y. A., & Lieberman, D. E.. Foot strike and injury rates in endurance runners: a retrospective study. *Med Sci Sports Exerc*, 44(7), 2012, 1325-1334.
- [4] Fellin, R. E., Rose, W. C., Royer, T. D., & Davis, I. S. Comparison of methods for kinematic identification of footstrike and toe-off during overground and treadmill

- running. *Journal of Science and Medicine in Sport*, 13(6), 2010, 646-650.
- [5] Giandolini, M., Poupard, T., Gimenez, P., Horvais, N., Millet, G. Y., Morin, J. B., & Samozino, P. A simple field method to identify foot strike pattern during running. *Journal of biomechanics*, 47(7), 2014, pp 1588-1593. ISO 690.
- [6] Gregg, R. D., Dhaher, Y. Y., Degani, A., & Lynch, K. On the mechanics of functional asymmetry in bipedal walking. *IEEE Transactions on Biomedical Engineering*, 59(5), 2012
- [7] Horvais, N., & Samozino, P. Effect of midsole geometry on foot-strike pattern and running kinematics. *Footwear Science*, 5(2), 2013, 81-89.
- [8] Hreljac, A., & Marshall, R. N. Algorithms to determine event timing during normal walking using kinematic data. *Journal of biomechanics*, 33(6), 2000, 783-786.
- [9] Kasmer, M. E., Liu, X. C., Roberts, K. G., & Valadao, J. M. Foot-strike pattern and performance in a marathon. *International journal of sports physiology and performance*, 8(3), 2013, 286-292.
- [10] Keller, T. S., Weisberger, A. M., Ray, J. L., Hasan, S. S., Shiavi, R. G., & Spengler, D. M. Relationship between vertical ground reaction force and speed during walking, slow jogging, and running. *Clinical Biomechanics*, 11(5), 1996, 253-259.
- [11] Larson, P., Higgins, E., Kaminski, J., Decker, T., Preble, J., Lyons, D., ... & Normile, A. Foot strike patterns of recreational and sub-elite runners in a long-distance road race. *Journal of sports sciences*, 29(15), 2011, 1665-1673.
- [12] Lohman, E. B., Sackiriyas, K. S. B., & Swen, R. W. (2011). A comparison of the spatiotemporal parameters, kinematics, and biomechanics between shod, unshod, and minimally supported running as compared to walking. *Physical Therapy in Sport*, 12(4), 2011, 151-163.
- [13] Masani, K., Kouzaki, M., & Fukunaga, T. Variability of ground reaction forces during treadmill walking. *Journal of Applied Physiology*, 92(5), 2002, 1885-1890.
- [14] Nilsson, J., & Thorstensson, A. Ground reaction forces at different speeds of human walking and running. *Acta Physiologica*, 136(2), 1989. pp 217-227.
- [15] Ogueta-Alday, A., Rodríguez-Marroyo, J. A., & García-López, J. Rearfoot striking runners are more economical than midfoot strikers. *Med Sci Sports Exerc*, 46(3), 2014, 580-5.
- [16] Oks A., Katashev A et al. Development of Smart Sock System for Gait Analysis and Foot Pressure Control. IFMBE Proceedings, 57, 2016, pp. 466-469.
- [17] Rowlands, A., Stone, M. R., & Eston, R. G. Influence of speed and step frequency during walking and running on motion sensor output. *Medicine and science in sports and exercise*, 39(4), 2007, 716.
- [18] Zatsiorsky, V. M., Werner, S. L., & Kaimin, M. A.. Basic kinematics of walking. Step length and step frequency. A review. *The Journal of sports medicine and physical fitness*, 34(2), 1994, 109.

Study and Optimization of Electric Heating for Oil and Petroleum Products Pipeline

Alexander Pavlov, Igor Plohov, Sergey Drozdov, Vadim Smirnov

Pskov State University, Faculty of Electric drive and automation systems, Address: Lenin Square 2,
Pskov, 180000, Russia

Abstract. The objectives of the study are to analyze the transients in heated pipelines using the finite element method and the achievement of reduction of energy losses during transportation of liquids in pipelines with electric heating systems by determining the optimal operating conditions and design parameters of the pipeline and electric heating system.

Keywords: polymer pipes, electric heating, experiment planning theory, finite element method (FEM), exponential regression model, the minimum energy criterion.

I. INTRODUCTION

During transportation of oil and petroleum products (hereinafter oil) through pipelines, a problem with cooling of the transported fluid by environment arises. Cooling fluid increases its viscosity, which causes an increase in hydraulic losses and adversely affect the pump stations. Besides, temperature decrease can lead to deposition of paraffin on the walls of the pipeline. Therefore, different types of heaters are widely used [1, 2]. Obvious advantages of electric heating systems (EHS) prior to similar water and steam systems are: small material consumption, easy installation, no corrosion processes and resistance to large temperature variations [3].

Flexible polymer pipes were developed at the beginning of the 80s of the 20 century to prevent corrosion of pipeline transport. The basis of the flexible pipe engineering solutions were established by Russian and French oil experts, working in a joint project to create a method of drilling deep wells with a continuous process of tripping. This particular design of flexible drill pipes, which had been being tested for 5 years while drilling an experimental deep borehole, were put behind the foundation of pipe designs for the pipeline transport [4].

II. MATERIALS AND METHODS

The design of the polymer pipe

One of the disadvantages of flexible polymeric pipe designs with electric heating is uneven heating of the transported product inside the pipe and the difficulty of controlling the heating process in case of transient state (non-stationary behavior) [5]. Authors developed the design of polymer pipe, which provides uniform heating of the inner tube space filled by any agent.

Self-regulated heating elements (HE) provide even heating due to polymer allow with a positive temperature factor of resistance. HE consists of two longitudinal electrical conductors separated by a polymer alloy. The polymer alloy is uniformly distributed over the inner layer of the cylindrical tube. Longitudinal and transverse projections developed umbilical shown in Figure 1.

Our design consists of flexible polymer working tube over which there is a layer of a polymer alloy 2 within which longitudinally has two symmetrical diametrically opposed electrical conductors 3 and 4. A layer of a polymer alloy 2 is covered with the shielding layer 5. On top of the shield layer 5 is laid insulating layer 6 (e.g., polyethylene foam), the surface of which formed the outer shell 7.

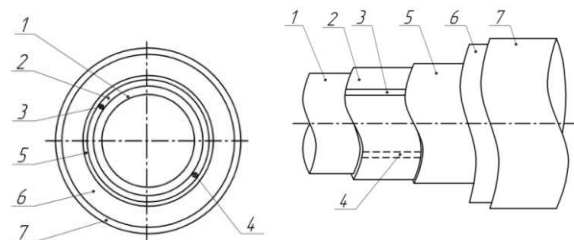


Fig. 1 – The design of the polymer tube with electrical heating

A layer of a polymer alloy 2 is a conductor of electric current, therefore currents appear over the entire length of a self-regulating cable between the electrical conductors 3 and 4 through a layer of a polymer alloy 2. While the current flow the polymer alloy is heated, transferring the heat of fluid flowing in the pipeline, thus increasing the electrical resistance of a polymer alloy. At various sections of self-regulating heating layer, the heating capacity can be different depending on the temperature of the

polymer alloy. Thus, we achieve self-regulation of the heating power. As a result of the uniform distribution of the polymer alloy layer around the inner tube space, and due to the symmetric diametrically opposite location of conductors, we achieve uniform heat power output around the inner tube space and uniform input of heat in the forgoing space. Also due to the uniformly distributed heat resistance on the way of the heat flow from the polymer alloy layer to the inner tube space.

Selection of important factors

For the transitional process approximation, we analyzed pipelines design parameters, environmental conditions and characteristics of the ground. As a result, we highlighted factors that have an impact on the pipeline system operation of the electric heating

Table 1.
Factors and Ranges of Variation

№	Factor	Ranges of variation		Dimension
		Lower level	Upper level	
1	Heat capacity of crude oil	1.7	2.1	kJ/(kg·s)
2	Density of oil	0.8	1	t/m ³
3	Heat capacity of insulation	1.5	2.4	kJ/(kg·s)
4	Thermal conductivity of insulation	0.02	0.05	W/m ² ·s
5	Density of insulation	40	100	kg / m ³
6	Heat capacity of the soil	1.1	3.3	kJ/(kg·s)
7	Thermal conductivity of soil	0.4	2.1	W/m ² ·s
8	Density of the soil	1.6	2.2	t/m ³
9	Environment temperature	-50	50	°C
10	Coefficient A	0	0.002	relative units
11	Coefficient B	0.3	1	relative units
12	Radius of the inner tube	20	200	mm
14	Thermal conductivity of crude oil	0.1	0.2	W/m ² ·s
15	Temperature of crude oil	-50	50	°C
16	Volumetric flow of crude oil	30	250	m ³ /day
17	Initial pipe temperature	-50	50	°C
18	Length of pipe	50	250	m

List factors and their variation ranges are shown in Table 1. Factors change range based on the tabular ranges of values of the materials, and soil environments, which may be used in the manufacture and operation of the pipelines. Justification of the choice of values of the coefficients A and B will be presented below. To test the effect of changing the value of each factor to the target amount (power consumption system) computer experiment was conducted in which each of the factors was varied on several levels. As the importance criterion, we assumed influence on the level of the target function, not exceeding 5%. The magnitude of effect was evaluated by the value δ_F relative system response factor for individual variation from the average value to the upper (lower) in percentage by the following expression:

$$\delta_F = \frac{P_k^i - P_k^A}{P_k^A} \cdot 100, \quad (1)$$

where: P_k^i – the amount of power in the i -th experiment in k -th point in time; P_k^A – the amount of power in the central experimental experience in k -th time.

Of above factors the system response higher than 5% was recorded for 7 out of 18 factors (Table 2).

Table 2.
Significant Factors

№	Factor	Symbol	Ranges of variation		Dimension	δ_{Φ} , %
			Lower level	Upper level		
1	Environment temperature	T_E	-60	20	°C	28,5
2	Coefficient A	A	-0,6	-0,3	rel. units	6,8
3	Coefficient B	B	10	60	rel. units	39,6
4	Radius of the inner tube	R	10	70	mm	25
5	Temperature of crude oil	T_O	2	38	°C	18,7
6	Volumetric flow of crude oil	Q	5	95	m ³ /day	16,2
7	Length of pipe	L	50	250	m	41,8

A and B coefficients are calculated using the heating power variation graphs $P(T)$. These relationships are included by manufacturers of self-regulating materials and confirmed by company "SST" through the testing (Figure 2). [6]

Dependence of power density on the EHS temperature represented a linear function with the coefficients A and B:

$$P(T) = A \cdot T + B. \quad (2)$$

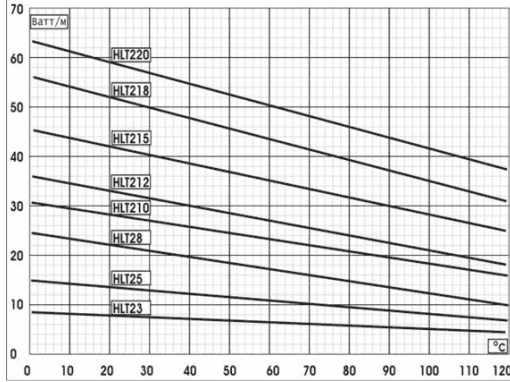


Fig. 2 - Heating power variation graphs P(T)

According to preliminary computational and natural experiments, we found nonlinearity in the dependence of power consumption on certain factors and justified the exponential nature of transients in EHS.

Selecting dynamic model

A dynamic model of power consumption, describing the time behavior of the system for fixed values of the factors is

$$P(C_0, C_1, C_2, t) = C_0 \cdot e^{(C_1 \cdot t)} + C_2, \quad (3)$$

where coefficients C_0, C_1, C_2 are functions of the form

$$C_m(X_0, X_1, \dots, X_j, \dots, X_K), \quad (4)$$

where: X_j – the value of the j -th factor; $m = 0, 1, 2$ – number of the coefficient C ; K – number of important factors.

In this regard, as the static mathematical model chosen incomplete quadratic regression

$$C_m(X_0 \dots X_K) = b_0^{C_m} + \sum_{j=1}^K b_j^{C_m} X_j + \sum_{j=1}^K b_{jj}^{C_m} X_j^2 \quad (5)$$

where: $b_0^{C_m}, b_j^{C_m}, b_{jj}^{C_m}$ – calculated coefficients of a mathematical model.

Orthogonal central composite plan

Orthogonal central composite plan (OCCP) was selected as an experiment plan. Parameter values of OCCP:

- number of factors – $N = 7$;
- fractionality – $p = 4$;
- number of tests in core plan – $N_{\text{core}} = 2^{(N-p)} = 8$;
- number of star points – $N_a = 2N = 14$;

- number of experiments in the middle of the plan – $N_0 = 1$;
- total number of tests – $N = N_A + N_a + N_0 = 23$;
- star shoulder – $\alpha = \sqrt{2^{\frac{N-p}{2}-1} \left(\sqrt{N-2} - 2^{\frac{N-p}{2}} \right)} = 1,668$.

Modeling the pipeline heating process with electric heating was performed in COMSOL Multiphysics 4.4 [7, 8]. We modeled the transition process in the heated pipeline, namely, the inclusion of an EHS simultaneously with the start of the transport of the product through the pipe. Construction of the model is made in the module for the calculation of non-isothermal flow of liquids in pipelines (Non-isothermal Pipe Flow interface) [9]. Machining simulation results produced in MathCad 15.

Exponential transients obtained at different combinations of factors and approximated by the formula (5). The approximation was carried out by the method of least squares. We minimize the objective function. The objective function is the sum of squared residuals of the experimental $(h^{(i)})_k$ and theoretical exponent $C_0 \cdot e^{(C_1 \cdot t_k)} + C_2$ for each combination of the plan of factors:

$$Q(C_0, C_1, C_2) = \sum_{k=0}^{N_i} \left[C_0 \cdot e^{(C_1 \cdot t_k)} + C_2 - (h^{(i)})_k \right]^2 \rightarrow \min, \quad (6)$$

where $N_i = 100$ – number of control points in each of the experiments; $(h^{(i)})_k$ – experimental value of magnitude in the k -th point in time i -th experiment.

The accuracy of selection coefficients estimated by relative approximation mistake

$$\varepsilon = \frac{100}{N_r} \sum_{k=0}^{N_i} \frac{\left| C_0 \cdot e^{(C_1 \cdot t)} + C_2 - (h^{(i)})_k \right|}{(h^{(i)})_k}, \quad (7)$$

where: N_r – number of experiments.

Verification received mathematical model adequacy revealed that high precision (less than 5%) is achieved in the combinations of factors to those shown in close OCCP, otherwise the relative approximation mistake (7) may extend beyond the accepted limits of 15%.

Using OCCP was obtained by approximating an additional function of the form

$$T_K = b_0^{T_K} + \sum_{i=1}^K b_i^{T_K} X_i + \sum_{i=1}^K b_{ii}^{T_K} X_i^2, \quad (8)$$

where: T_K – the average temperature of the oil in the final section of the pipeline.

The relative mistake of approximation ε (7) was 3.27%.

Heuristic plan

We developed a new unsaturated heuristic plan, including pairwise interactions between factors, to improve the accuracy of approximation. The objective function over time has previous form (3). To determine the level of influence of individual factors on the values of the coefficients of the regression C_0, C_1, C_2 used equation of the form

$$C_m(X_1..X_K) = b_0^{C_m} + \sum_{j=1}^K X_j \cdot b_{1,j}^{C_m} + \sum_{j=1}^K X_j^2 \cdot b_{2,j}^{C_m} + \sum_{j=1}^K X_j^3 \cdot b_{3,j}^{C_m} \quad (9)$$

where: $m = 0, 1, 2$ – number of coefficient C ; j – number of factor (1..7); $C_m(X_1..X_K)$ – value of m -th coefficient to a combination of factors ($X_1..X_K$); K – number of factors; $b_0^{C_m}, b_{1,j}^{C_m}, b_{2,j}^{C_m}, b_{3,j}^{C_m}$ – the calculated coefficients of the factors X first, second and third order, respectively. After a series of trial calculations to improve the accuracy of the regression equations were added to the terms describing the pair interaction of factors:

$$C_m(X_1..X_K) = b_0^{C_m} + \sum_{j=1}^K X_j \cdot b_{1,j}^{C_m} + \sum_{j=1}^K X_j^2 \cdot b_{2,j}^{C_m} + \sum_{j=1}^K X_j^3 \cdot b_{3,j}^{C_m} + \sum_{q \neq p}^K b_{q,p}^{C_m} \cdot X_q \cdot X_p \quad (10)$$

$$P(C_0, C_1, C_2, t) = C_0 \cdot e^{(C_1 \cdot t)} + C_2, \quad (11)$$

where $b_{q,p}^{C_m}$ – coefficients of pair interactions of factors.

The objective function, which is subjected to minimize in order to determine the optimal values of coefficients has the form:

$$Q_{C_m}(b_0^{C_m}, b_{1,j}^{C_m}, b_{2,j}^{C_m}, b_{3,j}^{C_m}, b_{q,p}^{C_m}) = \sum_{i=0}^{Nm} \left[C_m(X_{1,i}..X_{K,i}) - \hat{C}_m \left(\hat{X}_{1,i}.. \hat{X}_{K,i} \right) \right]^2 \rightarrow \min \quad (12)$$

where: Nm – number of heuristic plan tests; i – number of test; $C_m(X_{1,i}..X_{K,i})$ – m -th coefficient, obtained by the regression formula for the combination of factors ($X_{1,i}..X_{K,i}$); $\hat{C}_m \left(\hat{X}_{1,i}.. \hat{X}_{K,i} \right)$ – m -th coefficient obtained by the distributed model in Consol Multiphysics for combination of factors

$$\left(\hat{X}_{1,i}.. \hat{X}_{K,i} \right).$$

We define a mathematical expression for the relative mean mistake of approximation of experimental data by a polynomial regression. Residual function is quasi random variable

$$O_i = \left| C_m(X_{1,i}..X_{K,i}) - \hat{C}_m \left(\hat{X}_{1,i}.. \hat{X}_{K,i} \right) \right|. \quad (13)$$

To determine the relative mistake, we need to find the middle line graphs of two functions:

$$L_{AVi} = \frac{1}{2} \left| C_m(X_{1,i}..X_{K,i}) + \hat{C}_m \left(\hat{X}_{1,i}.. \hat{X}_{K,i} \right) \right|. \quad (14)$$

The relative mistake for the i -th experience and averaged mistake experimentation through Nm respectively:

$$\delta O_j = \frac{O_j}{L_{AVj}}, \quad (15)$$

$$\delta_{AV} = \frac{\sum_{j=0}^{Nm} \delta O_j}{Nm} = \frac{2}{Nm} \sum_{i=0}^{Nm} \frac{\left| C_m(X_{1,i}..X_{K,i}) - \hat{C}_m \left(\hat{X}_{1,i}.. \hat{X}_{K,i} \right) \right|}{\left| C_m(X_{1,i}..X_{K,i}) + \hat{C}_m \left(\hat{X}_{1,i}.. \hat{X}_{K,i} \right) \right|} \quad (16)$$

Results of calculating residual values and mistakes of functions are shown in Table 3. In order to smooth the results of C_1 introduced logarithm. For the C_0 and C_2 , the average error is less than 5%. The accuracy of C_1 does not exceed 15% of that for the multivariate approximation is acceptable.

Table 3. Approximation Mistakes of the Mathematical Model

№	Parameter	C_0	$\ln(C_1)$	C_2
1	Arithmetic average of the residual functions	0.12	0.0064	0.1
2	Average mistake, %	4.81	14.394	4.8

To assess the adequacy of the obtained expressions, authors conducted computational experiments with arbitrary values of a combination of factors (the variation within the test range) by substituting the values of the coefficients b , and calculate the average approximation mistake. According to results of computational experiments, standard mistake does not exceed the permissible values (Table 3).

The energy consumption of EHS is determined by integrating (11) over a time period τ :

$$W_H = \int_0^{\tau} P(C_0, C_1, C_2, t) dt = \int_0^{\tau} (C_0 \cdot e^{(C_1 \cdot t)} + C_2) dt = \frac{C_0 \cdot (e^{(C_1 \cdot \tau)} - 1)}{C_1} + C_2 \tau \quad (17)$$

Exponentially-regression model

Thus, the final appearance of the combined exponentially regression model represented by expressions (9), (10) and (17) with the calculated coefficients $b_0^{C_m}, b_{1,j}^{C_m}, b_{2,j}^{C_m}, b_{3,j}^{C_m}, b_{q,p}^{C_m}$.

A study of the properties of the pipe with a self-regulating EHS using the constructed model and the

technique of optimization by the criterion of minimum power consumption, taking into account transients.

Optimization of the parameters of the mathematical model

Optimization of the parameters is carried out by the criterion of minimum energy costs for transportation and heating oil. Energy costs for heating is counted as passing heating costs and costs for preheating, if it is technically necessary. For example, in the case of high-viscosity oil transported that require additional measures to prevent paraffin precipitation and other forms of precipitation. Furthermore, the use of preheating in some cases, allows the use of heating pipeline system associated only to stabilize the temperature of the transported fluid. The criterion of minimum total cost of transportation and heating is:

$$W_M + W_H + W_T \rightarrow \min ,$$

where: W_M – energy [J], spent on the work of pumping equipment; W_H – energy spent on passing an electric heating oil in the pipeline; W_T – energy spent on preheating the oil.

Optimization of the pipeline parameters is carried out under specified conditions: a certain temperature, the soil, the specified bandwidth, the known properties of the oil, etc. During operating, many pipeline conditions are changing. Thermal operation mode of the pipelines is unsteady for many reasons [10]: seasonal changes in soil temperature, variations pipeline capacity, emergency stop pumping. With increasing heating temperature, energy consumption of the pre-heating system increases; energy consumption of associated heating system, oil viscosity, the pressure loss in the pipe and the cost of pumping oil reduced (Figure 3).

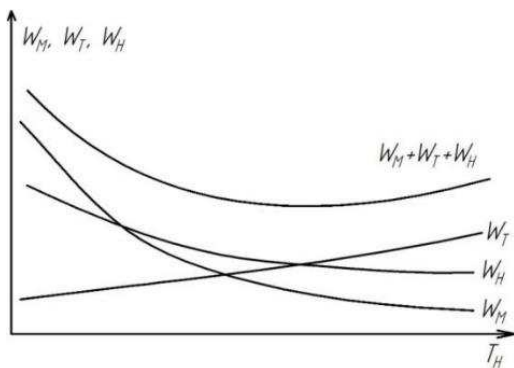


Fig. 3 - The dependence of the energy consumption on the oil temperature

Oil temperature T_H are accepted in view of technological limitations. In particular, for high-viscosity oils in the oil temperature of the end portion should be at least 3-5 degrees higher than its solidification temperature.

Power consumed by the pump per unit in time:

$$P_M = \frac{QH\rho_H g}{\eta_M}, \quad (18)$$

where: Q – volumetric oil flow rate, m^3/s ;

$$H = \frac{\lambda L V^2}{2d_{BH} g},$$

H – head loss in the pipeline, m ;

$\rho_H = \rho_{293} - (1.825 - 0.001315\rho_{293}) \cdot (T_H - 293)$ – density of oil, kg/m^3 ; ρ_{293} – density of oil at $20^\circ C$,

kg/m^3 ; η_M – coefficient of efficiency of the pump, λ – kinematic coefficient of friction; L – pipeline length, m ; V – oil flow rate, m/s ; d_{BH} – inner diameter of pipeline, m .

The energy consumed by the pump for a period in time τ

$$W_M = P_M \tau . \quad (19)$$

The power consumed by the pre-heating system of oil:

$$P_T = \frac{Q\rho_H c_P (T_S - T_{S.CO})}{\eta_T}, \quad (20)$$

where: c_P – specific heat of crude oil, $J/(kg \cdot K)$; $T_{S.CO}$ – crude oil temperature coming from the borehole, K ; η_T – coefficient of efficiency of pre-heat system.

The energy consumed by the pre-heating system in time τ

$$W_T = P_T \tau . \quad (21)$$

We integrate the mathematical expression for the power of associated heating system $P(t, Q, R, A, B, T_O, T_E, L)$ in time and get an expression that describes the amount of energy consumed electric heating system associated for the period τ

$$W_T(Q, R, A, B, T_O, T_E, L) = \int_0^\tau P(t, Q, R, A, B, T_O, T_E, L) dt \quad (22)$$

The total energy consumption described by systems $W = W_M + W_H + W_T$, taking into account important factors in the expressions for the individual energy subsystems

$$W(Q, R, A, B, T_O, T_E, L) = W_M(Q, R, T_O, L) + W_T(Q, T_O) + W_H(Q, R, A, B, T_O, T_E, L) \quad (23)$$

III. RESULTS AND DISCUSSION

With (23), we assess the value of consumed energy and the optimization of the parameters (important factors) in order to minimize energy consumption.

We analyzed influence of factors on the value of the total consumed energy. These curves were obtained for the following combinations of values of factors corresponding to the central test heuristic unsaturated plan using hybrid-exponential regression mathematical model.

- Volumetric flow of crude oil: $Q = 50, \text{ m}^3/\text{day}$;
- Inner radius of the pipeline: $R = 0.04, \text{ m}$;
- Coefficient $A = - 0.45$;
- Coefficient $B = 35$;
- Temperature of the crude oil, flowing into the pipeline $T_O = 20, \text{ }^\circ\text{C}$;
- Environment temperature $T_E = - 20, \text{ }^\circ\text{C}$;
- Pipeline length $L = 150, \text{ m}$.

Graphic dependences for volumetric flow of oil and oil temperature are shown in Figure 4.

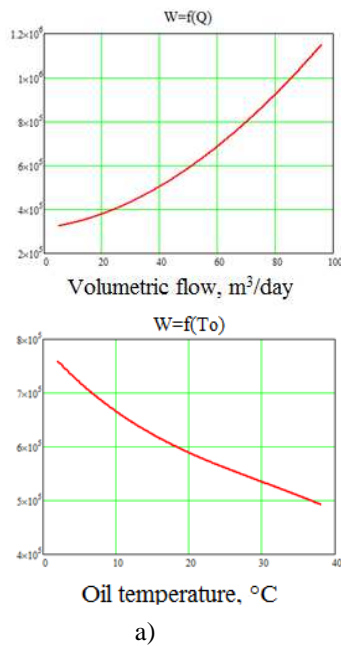


Fig. 4 - Dependences of the of consumed energy by factors: a) changing the crude oil flow rate in the pipeline; b) changing the inlet crude oil temperature at the pipeline.

Subsystems energy costs individually and generally are reflected in Figure 5.

With increasing the crude oil temperature, coming into the pipeline after the pre-heating system, there is a decrease of amount of energy consumed by pre-heating subsystem, and decrease of costs for pumping oil. Growth of energy consumption is observed only for preheating subsystem. These results correspond to the theoretical dependencies. Based on the graph (Figure 5) that the heating oil temperature rise in the pipeline, leads to a decrease of the total energy consumed by system.

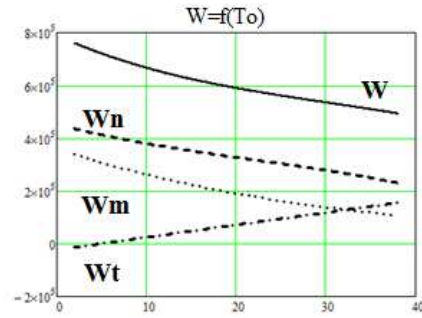


Fig. 5 - Energy costs

Determination of the oil temperature at the end of the pipeline

The oil temperature in the final section of the pipeline:

$$T_K \geq b_0^{T_k} + \sum_{i=1}^n b_i^{T_k} X_i + \sum_{i=1}^n b_{ii}^{T_k} X_i^2 . \tag{24}$$

T_K set as the desired value (a number) or in the form of expression $T_K = T_{HEAT} + \Delta T$, where ΔT – excess oil temperature in the final section of the pipeline to the temperature of the oil at the inlet of pipeline, $^\circ\text{C}$.

As environmental temperature, T_E chosen average temperature in the ground for the operation period of the pipeline.

Algorithm of optimization by the criterion of a minimum energy consumption

1. To identify the number of fixed, unchanging parameters and duration of the process (the upper limit of time integration).
2. To select the range of variation of the values of the factors are optimized. These ranges are based on a previously selected for the mathematical model ranges (within the ranges of the mathematical model is adequate) and based on the technological and constructive restrictions;
3. To identify boundary conditions and to determine minimum acceptable final oil temperature T_K .
4. To conduct minimization of the objective function;
5. To substitute these optimized factors values in expression (23). If necessary, compare optimized energy consumed with the original value.

IV. CONCLUSIONS

1. We developed three-dimensional computer simulation distributed mathematical model of polymer pipeline with a self-regulating EHS. The model is created in Comsol Multiphysics using the FEM. We selected a list of parameters that have a significant influence on the course of the transition process. With the application of the experiment planning theory authors constructed

an orthogonal central composite plan, calculated by the constant coefficients of the regression model for the power transition process. The regression model for the temperature in the final section of pipeline with EHS also developed.

2. Authors developed experimental plan, taking into account the pairwise interactions between significant factors of the mathematical expression of the power transition process and hybrid heuristic mathematical model (exponential regression) of the transition process, describing the dynamics of self-regulated pipeline with electric heating.
3. Authors obtained expression of the total energy consumed by the pump and heating subsystems, in view of relevant factors included in the expression for the energy of the individual subsystems, and power graphics for electric heating systems and pump energy consumption and guidelines for choosing the optimal oil heating temperature.
4. We developed method for optimization of pipeline construction parameters of the self-regulatory system with electric heating according to criterion of minimum energy.

REFERENCES

- [1] Strupinskiy M.L. «Classification and main characteristics of the low temperature electrical heating system for the large area objects», Вестник МЭИ. – 2010. – № 3. С. 90-99.
- [2] Farago, P.S. «An Introduction to Linear Network», The English Universities Press Ltd. – 1961. PP. 117-121.
- [3] Быков, И.Ю. «Композиционно - волокнистые трубы в нефтегазовом комплексе», под редакцией доктора технических наук, профессора И.Ю. Быкова - М: Изд. ЦентрЛитНефтеГаз. – 2008. – 271 с.
- [4] Реммаш-сервис: Гибкие трубы, режим доступа [Online]. Available: <http://remmash63.ru/2.html>. (Accessed: 12.05.2014).
- [5] «Саморегулируемый кабель для выкидных трубопроводов», utility patent № RU 142154 U1, Authors: Плохов И.В., Павлов А.Б. Patent owner: ООО НИП «Дельта-Т». Published. 26.06.2014.
- [6] Хренков, Н.Н. «Расчет режимов остывания и разогрева трубопроводов с учетом замерзания и плавления». Промышленный электрообогрев и электроотопление. – 2011. – №3. – С. 18-22.
- [7] The COMSOL Multiphysics User's Guide [Online]. Available: <https://www.comsol.com/>.
- [8] S.E. Haaland, «Simple and Explicit Formulas for the Friction Factor in Turbulent Flow», J. Fluids Engineering (ASME). – 1983. – vol. 103. – №5. – PP. 89-90.
- [9] Heat Transfer Module User's Guide [Online]. Available: <https://www.comsol.com/>.
- [10] Гаррис, Н.А. «Расчет эксплуатационных режимов магистральных неизолированных нефтепродуктопроводов с применением динамических характеристик», Нефтегазовое дело. – 2003. – №2. – 8 с.

Processing Possibilities of Birch Outer Bark into Green Bio-composites

Aigars Paze, Janis Rizhikovs, Prans Brazdausks, Maris Puke, Juris Grinins,
Ramunas Tupciauskas, Ance Plavniece

Latvian State Institute of Wood Chemistry, 27 Dzerbenes street, Riga, LV-1004, Latvia

Abstract. The main objective of the study was to obtain bio-composites from grey alder sawdust using a mixture of birch outer bark suberinic acids as a binder, and to test their mechanical properties. Ethanol-extracted birch outer bark was used as a raw material for the investigation. Characteristics (suberinic acids content, epoxy acids content and acid number) of the hydrolytically depolymerized birch outer bark binder were also determined. The initial filler/binder ratio and molding parameters (temperature and pressure) were established by the full factorial design. Preliminary data showed that the increase of the pressing temperature from 160 to 200 °C at a pressure of 3.5 MPa resulted in a minor growth of the boards' density (up to 1.0 g/cm³) and bending strength (up to 17.1 MPa).

Our investigation has shown that it is possible to use one of the plywood production residues – outer birch bark – as a raw material for obtaining particleboards, which have mechanical properties beyond the standard limits. The used method is also environmentally friendly, easy realizable in practice and has a potential to be cost-effective.

Keywords: Bio-composites, birch outer bark, suberinic acids.

I. INTRODUCTION

Processing of birch bark has a high potential in both Latvia and Europe. Besides the veneer industry, there are other important industries, such as the furniture or cellulose industry in Europe, which has a large amount of residual birch bark combusted for energy needs. Therefore, an industrial research was started to develop the knowledge basis and gain a better understanding of the possibilities of birch bark processing in the scope of circular bio-economy.

A common method for producing composites is to use synthetic thermo-reactive binders: phenol-formaldehyde, carbamide-formaldehyde or isocyanide based resins. These composite materials are toxic to humans during the production and exploitation of the products because of the formaldehyde emission. If the concentration of formaldehyde is above 0.1 ppm in the air, it begins to irritate the eyes, throat and nasal mucosa, as well as to cause difficulty in breathing. In 2004, the International Agency for Research on Cancer of the World Health Organization found formaldehyde to be a carcinogenic compound [1].

To reduce formaldehyde emissions, adhesive additives such as boric acid or calcium metasilicate can be used, but it solves the problem only partially (emission reductions of 15-30 %) [2]. From synthetic binders, less toxic and without harmful emissions are isocyanate-based adhesives. However, these binders are significantly more expensive than phenol-formaldehyde and urea-formaldehyde binders.

From natural products, plant protein-based adhesives are widely used as binders. However, there is a problem that the moisture resistance of such particleboards is low [3]. It is well described in the scientific literature that many natural binders have a common drawback – food products such as soy flour or starch are used as the main component. In some cases, toxic and carcinogenic α -epichlorohydrin is used, for example, to improve the water resistance of soy protein-based adhesives [4].

Silver birch (*Betula pendula* Roth.) is widely used in the Latvian plywood industry, whose one of the processing by-products – birch outer bark – has a high content of valuable extractives (up to 35 % from oven dry (o.d.) birch outer bark). These extractives have a very wide range of different types of applications (pharmacy, cosmetology etc.); therefore, there is a high commercialization potential. It can be expected that, in the near future, the production capacity of such extractives will increase significantly [5]. Thus, the amount of birch outer bark extraction residues will also increase, which could be efficiently processed into a green binder for production of wood particle bio-composites.

A beneficial, accessible and ecological binder produced from birch outer bark is hydrophobic suberin. It consists of 40-45 % from o.d. birch outer bark and is usually isolated as suberinic acids or partly depolymerized suberin [6], [7]. Russian scientists have already tried to obtain bio-composites, as a binder using isolated suberinic acids of birch outer bark [8]. However, at the Latvian State Institute

of Wood Chemistry, a relatively simpler and hence more efficient method for processing of extracted birch outer bark into a particleboard binder has been invented and patented. Following this methodology, a mixture of birch outer bark suberinic acids and a complex of insoluble bark processing residue is obtained together as a binder, which is mixed with the filler (wood particles), and bio-composites are prepared by hot pressing [9].

Grey alder used to be a less desirable raw material because of its low quality; as a result, its utilization was mainly limited to household heating and low-value products, such as packaging and pallets. Today, the situation has changed, and sufficient amounts of high-quality grey alder lumber as well as processing by-products – sawdust – are available in the market. Therefore, the main objective of the study was to obtain medium density bio-composites from grey alder (*Alnus incana* (L.) Moench) sawdust using a mixture of birch outer bark suberinic acids and a complex of insoluble bark processing residue as a binder, and to test their mechanical properties.

II. MATERIALS AND METHODS

A. Preparation of Feedstock

The birch bark (*Betula pendula* Roth.) from a plywood factory in Latvia was used as a feedstock to obtain a binder. At first, the collected birch bark was dried at room temperature to 7-10 % moisture content and then ground to chips by a hammer cutting mill (Retsch SM 100) to pass a 2.0 mm sieve. The outer bark was separated from the inner bark by the floating method, wherein milled birch bark was soaked by mixing from time to time in deionized water for 24 h. Finally, outer bark (the floating part of the mixture) was collected and dried to 2-4 % moisture content in a convection-type oven at 50 °C.

B. Chemical Composition Analysis of Birch Outer Bark

Extractives of birch outer bark were analyzed by a Soxhlet extraction apparatus. Samples (size of particles 0.4-2.0 mm) were extracted with ethanol (95 % v/v) for 11 h to be sure that all the extractives were removed. The optimal extraction time has been determined in our previous experiments [10]. To remove alkali-soluble compounds, the extracted birch outer bark was treated for 1 h with 1 % KOH-water solution (weight ratio – 1:10), intensively stirring under reflux. The obtained solution was filtered through a previously dried sintered glass crucible. After that, the same volume of fresh 1 % KOH-water solution was added to the liquid fraction and the boiling process was continued for another 20 min under reflux. The solid residue was filtered, washed to pH 7 and dried to a constant weight. The content of cellulose and acid-insoluble lignin in this solid material was determined by the Kürschner–Hoffer nitration method [11] and the TAPPI 222 standard method [12], accordingly. The liquid fraction was

acidified to pH 4-5 by concentrated nitric acid (65 % v/v). During the reaction, suberinic acids potassium salts were precipitated. After that these sediments were filtered, washed with deionized water and dried to the constant weight at 105 ± 3 °C. The content of ash in the untreated birch outer bark was determined according to the standard EN 14775 [13]. All the above-mentioned analyses were performed in triplicate.

C. Obtaining of Suberinic Acids Containing Binder

For hydrolytic depolymerization in a basic water medium, the patented method was chosen [9]. Optimized suberin depolymerization conditions like alkali concentration in water, processing time and temperature were used from the previous studies of obtaining suberinic acids [14]. To obtain a suberinic acids containing binder, extracted outer birch bark was hydrolytically depolymerized in the solution of 3 % KOH (processing time – 1 h, temperature – 80-90 °C). Outer birch bark and KOH solution weight ratio was 1:10. The depolymerization process was carried out in a reactor, where the material was intensively stirred; the reactor was immersed in a water bath. At the end of the depolymerization process, the obtained suspension of the solution of suberinic acids potassium salts and other soluble compounds (potassium hydroxide, carbohydrates, etc.) and the insoluble residue (lignin, cellulose, etc.) was cooled down to a temperature of 15-20 °C and then acidified with 65 % nitric acid solution to pH 2. In the next step, the resulting mass was centrifuged for 1 h in the sedimentation centrifuge at 2000 min⁻¹ rpm. The precipitate was further washed twice with distilled water and centrifuged until the solution reached pH 3. At the end, the obtained paste could be easily mixed with wood sawdust. The suberinic acids containing binder was obtained in two replications.

D. Determination of Binder's Acid Value

A sample containing 0.12-0.15 g of dry suberinic acids was dissolved in 25 mL dimethyl sulfoxide for 20 h and then potentiometrically titrated with 0.1 M KOH aqueous solution using a titration workstation (Titralab 980). The result was expressed as mg KOH/g suberinic acids.

E. Determination of Binder's Epoxy Groups

The sample containing 0.12-0.15 g of dry suberinic acids was treated with 5 mL of non-aqueous HCl solution in dimethylsulfoxide (composition of the reagent – 100 mL dimethyl sulfoxide + 0.7 g hydroxylamine hydrochloride + 2 mL acetone) for 20 h. Then the excess of HCl was potentiometrically titrated with 0.1 M KOH aqueous solution using a titration workstation (Titralab 980). The blank sample, i.e. 5 mL of non-aqueous HCl solution in dimethylsulfoxide, was also titrated. The amount of epoxy groups was equivalent to the loss of hydrochloric acid estimated in the titration of the analysis and blank samples. The amount of the main

suberinic epoxy acid (9,10-epoxy-18-hydroxy-octadecanoic acid) was calculated using a molecular weight of 313 g/mol. The result was expressed as % from the o.d. suberinic acids containing binder.

F. Particle Board's Preparation

For the production of wood plate bio-composites, grey alder (*Alnus incana* (L.) Moench) sawdust with a fraction of 0.6-2.0 mm and a moisture content of 8.2 ± 0.1 % was used. The mixture of the binder (moisture content 78.9 ± 0.2 %) prepared by alkaline-water hydrolytic depolymerization was mixed with a wood filler at the ratio of 20:80, 30:70 and 40:60. Then the produced raw material was dried in a drying chamber to a moisture content of 0.5-1.0 %. The dry mass (free-flowing material) was pressed on a laboratory press LAP-40 (Gotfried Joos Maschinefabrik GmbH & Co) for 10 min. The amount of the binder $X_1=30\pm 10$ % on o.d. mass, temperature $X_2=180\pm 20$ °C, and pressing pressure $X_3=3\pm 0.5$ MPa were chosen as the 3 main parameters for realizing the full factorial design (Table II), wherein the first value was the zero level for each parameter. Plates (dimensions of the plates 150×150×10-12 mm), after pressing, were removed from the press without cooling. Pressed samples were conditioned in a climatic chamber at 55 % humidity and a temperature of 20 °C for 48 h. The quality of the obtained particle boards was characterized by density (EN 323) and bending strength (EN 310), which was determined on a testing machine Zwick/Roell Z010 (Ulm, Germany) [15], [16]. The test results are given as the average of the four parallel bending strength measurements.

III. RESULTS AND DISCUSSION

The chemical component analysis was performed in order to characterize industrial raw birch outer bark, and the results are summarized in Table I. Analysis series was started by extractive separation in a Soxhlet apparatus using ethanol as a solvent. Extracted birch outer bark was treated with 1 % KOH solution to determine alkali soluble substances. The main soluble substance of birch outer bark was suberinic acids, which represented hydrolytic depolymerization products of bio-polyester suberin. As shown by the results, with these two treatments, on average, 88.3 % of the o.d. birch outer bark mass was separated. With the alkali treatment, not only suberinic acids were separated, but also other compounds (phenolic compounds, carbohydrates, etc.) with an amount of 14.9 % from the o.d. birch outer bark mass. In contrast, insoluble cellulose, lignin and other components made only up to 9.6 % from the o.d. bark mass.

In order to obtain the suberinic acids containing binder for production of bio-composites from wood particles, the method from a novel concept was used [9]. This technique is unique compared to similar methods of obtaining because the hydrolytically depolymerized salt solution of suberinic acids and the

insoluble residual suspension are acidified before filtration [8]. In this way, not only acidified suberinic acids and other compounds are separated, but also the alkali insoluble solid residue.

To obtain the suberinic acids containing binder, 300.0 g (relative moisture content 5.2 %) of extracted birch outer bark was processed. At first, birch outer bark was hydrolytically depolymerized in alkaline conditions and then the obtained suspension, after cooling, was neutralized and acidified to pH 2 to obtain the maximal amount of the binder in the chemical exchange reaction. The resulting suspension was centrifuged and washed twice to pH 3, thus removing most of the residual acid, potassium nitrate salts and other soluble compounds. As a result, 1227.8 ± 36.8 g of the suberinic acids containing paste was obtained with the dry matter content of 21.1 ± 0.6 % (259.1 ± 0.5 g). The yield was 91.1 ± 0.2 % from the o.d. extracted birch outer bark mass.

Table I
Content of Basic Components of Industrial Birch Outer Bark

No	Components	% from the o.d. raw material
1.	Extractives of ethanol	34.7 ± 0.9
2.	Substances soluble in 1 % KOH solution* from which:	53.6 ± 1.1
	Suberinic acids	38.7 ± 1.3
	Other (condensed tannins, etc.)	14.9
3.	Cellulose**	3.6 ± 0.3
4.	Lignin**	2.2 ± 0.2
5.	Other**	3.8
6.	Ash	2.1 ± 0.1

* a group of compounds, identified after extraction with ethanol

** components, identified after the isolation of extractives and separation of substances, soluble in 1 % KOH solution

The main adhesive component of the binder paste is represented by suberinic acids, which react at elevated temperature and as a result of the polycondensation reaction, generate a linear polymer structure. Later, a three-dimensional elastomer is formed, which is insoluble in organic solvents [17].

Taking into account the untreated birch outer bark chemical composition (Table I), the amount of the separated suberinic acids can reach, on average, up to 59.3 % of the o.d. extracted bark mass. The content of suberinic acids in the obtained paste can reach, on average, up to 65.1 % of the o.d. paste mass.

The suberinic acids containing binder was obtained in two parallel experiments to be further characterized with an acid number (carboxyl- groups) and the amount of epoxy groups.

After the depolymerization, the monomer composition of suberin mostly consists of fatty acids, ω -hydroxyfatty acids, α -, ω -dicarboxylic acids, aliphatic alcohols and aromatic acids, depending on the plant material. ω -hydroxyfatty acids are generally the most abundant group of suberin monomers in the outer bark of silver birch, and the main compounds in

the suberic acid mixture are epoxy and hydroxyl groups containing derivatives [18]. Thus, the hydroxyl and epoxy group content can be used for the characterization of the chemical composition

repeatability of the used binder obtaining methodology. As demonstrated by the results, the obtained binder's acid number was 84.8 ± 2.3 mg

Table II
Full Factorial Design for Plates obtained from Sawdust of Grey Alder using Suberic Acids containing Binder

Experiment No.	1	2	3	4	5	6	7	8	9
X₁ - Binder (%)	20	20	20	20	40	40	40	40	30
X₂ - Temperature (°C)	160	200	160	200	160	200	160	200	180
X₃ - Pressure (MPa)	2.5	2.5	3.5	3.5	2.5	2.5	3.5	3.5	3.0
Y₁ - Density* (g/cm³)	0.673 ± 0.006	0.682 ± 0.007	0.764 ± 0.007	0.856 ± 0.005	0.874 ± 0.006	0.916 ± 0.003	0.931 ± 0.004	1.056 ± 0.006	0.867 ± 0.008
Y₂ - Bending strength** (MPa)	4.07 ± 0.34	5.27 ± 0.41	7.57 ± 0.39	12.50 ± 0.29	12.10 ± 0.35	13.30 ± 0.86	15.00 ± 0.83	17.10 ± 0.67	14.20 ± 0.48

Non load-bearing boards for use in humid conditions (P3) – Requirements for specified mechanical and swelling properties. * EN 312 requirements – 0.85 g/cm³. ** EN 312 requirements – 15 MPa

KOH/g and epoxy group content was 1.6 ± 0.1 %. The low standard deviation values indicate that the resulting binder's chemical composition is uniform and therefore will affect the particle board properties insignificantly. Both binder samples, after their characterization, were used in the preparation of medium density particle boards.

The advantages of the binder preparation technology patented by the Latvian State Institute of Wood Chemistry are as follows: 1) the extracted bark raw material is processed completely and a potassium nitrate aqueous solution is formed as a by-product, which can be used as a plant fertilizer; 2) the raw material, product and processing methodology are environmentally friendly. According to the patented methodology, the product is washed only to pH 3, and it results in less waste water compared to the case of similar extraction methods (more water is used for washing out to pH 7 [8]).

To investigate the preliminary technological parameters of the green bio-composites obtained from depolymerized birch outer bark, the amount of the binder (X₁), pressing temperature (X₂) and pressure (X₃) were chosen as 3 main parameters for realizing the full factorial design. Response variables for the preliminary parameters of the pressing of bio-composites were chosen by the density and bending strength of the obtained plate materials. The results obtained according to this method are shown in Table II.

$$Y_1 = 0.84 + 0.10X_1 + 0.03X_2 + 0.06X_3 \quad (1)$$

Equation (1), where the response variable is density, Y₁ (g/cm³), indicating that the higher densities are reached if the chosen parameters are above the zero level because all the coefficients are positive. More significant influence on the plate material density is demonstrated by the amount of the binder (+0.10) and pressure (+0.06), but the pressing temperature has less significance (+0.03).

$$Y_2 = 10.86 + 3.51X_1 + 1.18X_2 + 2.18X_3 \quad (2)$$

Equation (2), where the response variable is bending strength, Y₂ (MPa), indicating that the same tendency that the higher values are reached if the chosen parameters are above the zero level. More significant influence on the plate material bending strength is shown by the amount of the binder (+3.51) and pressure (+2.18), but the pressing temperature has less significance (+1.18).

This means that the amount of the binder must be taken as high as possible to obtain a higher bending strength of the obtained plate materials. If we look at the properties of the plate samples obtained at the zero level parameters (experiment 9) and compare them with the calculated average values of the experimental plan in the respective equations, we can conclude that density is close to that obtained experimentally (0.84 and 0.86 g/cm³). In the case of bending strength, there is a significant difference in both values (10.86 and 14.2 MPa), which means that, for better bending strength, all parameters must be higher. The realization of such a task could increase the sample density. Therefore, it will be a great challenge to obtain bio-composites from depolymerized birch outer bark, which would conform to EN 312 requirements by choosing the appropriate filler or by changing the binder preparation conditions [19].

The obtained data show that the increase of the pressing temperature from 160 to 200 °C at a pressure of 3.5 MPa and the amount of the binder 40 % results in a minor growth of the boards' density (up to 1.0 g/cm³) and bending strength (up to 17.1 MPa), but their density exceeds the standard limits specified in particle board standards. In this respect, for better results, our next initial parameter range will be as follows: 20 and 30 % of the binder should be pressed at 200-220 °C and at lower pressure to obtain medium density (up to 0.85 g/cm³) bio-composites with appropriate bending strength properties (below 15 MPa). A higher temperature was chosen based on the fact that it has less significance on the plate density (Equation 1).

When pressing at high temperature, obviously, there occurs the formation of grid-type structures due to the generation of new chemical bonds between suberin and the wood filler; hence, the physico-mechanical characteristics of bio-composites are improved without the potential emission of formaldehyde [20].

IV. CONCLUSIONS

To obtain the suberinic acids containing binder for production of bio-composites from wood particles, a method from a novel concept was used. The content of suberinic acids in the obtained binder reached 65.1 % of the o.d. mass. The hydroxyl and epoxy group content was used for the characterization of the chemical composition.

More significant influence on the plate material density and bending strength was demonstrated by the amount of the binder and pressure, but the pressing temperature had less significance. Therefore, elevation of temperature was chosen for future investigations to obtain better mechanical properties of bio-composites.

Preliminary data showed that the increase of the pressing temperature from 160 to 200 °C at a pressure of 3.5 MPa resulted in a minor growth of the boards' density (up to 1.0 g/cm³) and bending strength (up to 17.1 MPa).

Our investigation has shown that it is possible to use one of the plywood production residues – outer birch bark – as a raw material for obtaining particleboards, which have good mechanical properties. The used methods are also environmentally friendly, realizable in practice and have a potential to be cost-effective. The obtained bio-composites do not have any harmful effects on human health.

V. ACKNOWLEDGMENTS

This study was supported by the European Regional Development Fund (ERDF) project No. 1.1.1.1/16/A/042.

NATIONAL
DEVELOPMENT
PLAN 2020



EUROPEAN UNION
European Regional
Development Fund

INVESTING IN YOUR FUTURE

REFERENCES

- [1] "Update on the formaldehyde release from wood-based panels // MDF Yearbook" Sept. 2008. [Online]. Available: [http://chimarhellas.com/wp-](http://chimarhellas.com/wp-content/uploads/2008/07/FA_2008.pdf)

- [content/uploads/2008/07/FA_2008.pdf](http://chimarhellas.com/wp-content/uploads/2008/07/FA_2008.pdf) [Accessed Febr. 27, 2017].
- [2] S. Wawzonek, "Formaldehyde depressed particle board," U. S. Patent 4457978A, July 3, 1984.
- [3] S. Khosravi, F. Khabbaz, P. Nordqvist and M. Johansson, "Protein-based adhesives for particleboards," *Ind. Crops Prod.*, vol. 32, pp. 275-283, 2010.
- [4] N. S. Sulaiman, R. Hashim, M. H. M. Amini, O. Sulaiman and S. Hiziroglu, "Evaluation of the properties of particleboard made using oil palm starch modified with epichlorohydrin," *BioResources*, vol. 8, pp. 283-301, 2012.
- [5] "Final Report Summary – FORESTSPECS, Wood Bark and Peat Based Bioactive Compounds, Speciality Chemicals, and Remediation Materials: from Innovations to Applications", [Online]. Available: http://cordis.europa.eu/result/rcn/149969_en.html [Accessed Febr. 27, 2017].
- [6] P. A. Krasutsky, "Birch bark research and development," *Natural Product Reports*, vol. 23, pp. 919-942, 2006.
- [7] A. N. Kislitsyn, "Outer birch bark extractives: isolation, composition, properties and application," *Khimiya drevesiny (Wood Chemistry)*, vol. 3, pp. 3-28, 1994.
- [8] I. G. Sudakova, N. V. Garyntseva and B. N. Kuznetsov, "Obtaining of wood plate materials using binders based on suberin of birch outer bark," *Himija rastitel'nogo syr'ja (Chemistry of Plant Raw Material)*, vol. 3, pp. 65-68, 2011 (source is in Russian).
- [9] J. Zandersons, J. Rižikovs, A. Pāže, A. Tardenaka and B. Spince, "Method for making formaldehyde-free particle boards," *LV Patent 15031 (A)*, July 20, 2015.
- [10] J. Rižikovs, J. Zandersons, G. Dobeļe and A. Pāže, "Isolation of triterpene-rich extracts from outer birch bark by hot water and alkaline pre-treatment or the appropriate choice of solvents," *Ind. Crops Prod.*, vol. 76, pp. 209-214, 2015.
- [11] A. V. Obolenskaya, Z. P. Elnitskaya and A. A. Leonovich, *Laboratory Works in the Chemistry of Wood and Cellulose*. Moscow: Ecologia, pp. 75-76, 1991 (source is in Russian).
- [12] TAPPI 222 om-02:2006. Acid-insoluble lignin in wood and pulp.
- [13] BS EN 1477:2009. Solid biofuels. Determination of ash content.
- [14] I. G. Sudakova, B. N. Kuznetsov and N. V. Garyntseva, "A study of the isolation process of the suberinic substances from birch outer bark," *Himija rastitel'nogo syr'ja (Chemistry of Plant Raw Material)*, vol. 1, pp. 41-44, 2008 (source is in Russian).
- [15] BS EN 323:1993. Wood-based panels. Determination of density.
- [16] BS EN 310:1993. Wood-based panels. Determination of modulus of elasticity in bending and of bending strength.
- [17] V. A. Levandansky and S. A. Kuznetsova, *Chemical Products of Wood Bark*. Krasnoyarsk: Siberian State Technological University, 2012, pp. 146-162 (source is in Russian).
- [18] J. Rižikovs, J. Zandersons, A. Pāže, A. Tardenaka and B. Spince, "Isolation of suberinic acids from extracted outer birch bark depending on the application purposes," *Baltic Forestry*, vol. 20, pp. 98-105, 2014.
- [19] DIN EN 312:2010. Particleboards. Specifications.
- [20] I. G. Sudakova, B. N. Kuznetsov, N. V. Garyntseva, N. I. Pavlenko and N. M. Ivanchenko, "Functional and thermal analysis of suberin isolated from birch bark," *Journal of Siberian Federal University. Chemistry*, vol. 4, pp. 355-362, 2008.

Basic Algorithm for Induction Motors Rotor Faults Pre-Determination

A. Petrov^{1,2}, A. Rassõlkin², T. Vaimann², A. Belahcen^{2,3}, A. Kallaste², I. Plokhov¹

¹Department of Electrical Drives and Automation Systems, Pskov State University, RUSSIA, Address: Lenin Square, 2, 180000, Pskov, Russia

²Department of Electrical Power Engineering and Mechatronics, Tallinn University of Technology, ESTONIA Address: Ehitajate tee 5, 19086 Tallinn, Estonia

³Department of Electrical Engineering and Automation, Aalto University, FINLAND, Address: P.O. Box 11000, FI-00076 Aalto, Espoo, Finland

Abstract. Due to importance of squirrel cage induction motor in today's industry, the fault detection on that type of motors has become a highly developed area of interest for researchers. The electrical machine is designed for stable operations with minimum noise and vibrations under the normal conditions. When the fault emerges, some additional distortions appear. The necessity to detect the fault in an early stage, to prevent further damage of the equipment due to fault propagation, is one of the most important features of any condition monitoring or diagnostic techniques for electrical machines nowadays. In this paper possible induction motors faults classified and basic algorithm for rotor faults pre-determination is presented.

Keywords: Electric machines, modeling, equivalent circuits, fault diagnosis.

I. INTRODUCTION

The relatively mature ac induction motors (IMs) technology has advanced fast with the progress of power electronics in the last 40 years. A squirrel cage IM has a very simple rotor construction, which increases the reliability and performance of the motor. The IM has been named the workhorse of the industry due to many advantages over other electrical machines. Those advantages include low cost, rugged configuration, versatility, rather small size and capability to reasonably comply with different power grids supply. Moreover, vector control of the IM can allow the motor to behave in the same manner as a separately excited dc motor, which means straight torque-speed characteristics and flexible control. There is no doubt that wide application of the IM is related with failures of the machines.

Because of large number of different faults that can occur in IM, there are several ways of fault classification. Fault classification based on criteria of IM fault sources is given in Table 1.

Most rotating machine failures occur due to bearing faults and winding faults. Estimated probabilities of occurrence of faults are [1], [2]:

- 1) Bearing faults – 40%;
- 2) Stator winding faults – 38%;
- 3) Rotor faults – 10%;
- 4) Complex of other faults – 12%.

The next weak spot of the electrical machine is the rotor, the only rotating part in the IM. Main rotor faults are rotor eccentricity; breakage of rotor bars;

breakage of end-rings; rotor bow; others failures after rotor damage.

Table 1.
IM fault classification

Sources of IM Faults	Fault Type	Faults
Internal	Mechanical	- Eccentricity; - Rotor strikes; - Bearing faults; - Coil and lamination movement.
	Electrical	- Dielectric failures; - Magnetic circle faults; - Rotor bars cracks.
External	Mechanical	- Pulsation of load; - Overload; - Poor mounting.
	Electrical	- Voltage fluctuation; - Unbalanced voltage; - Transient voltage.
	Environmental	- Temperature; - Humidity; - Cleanness

By employing condition monitoring and fault identification methods the electrical machine failure can be detected at an early stage, which in hand, will prevent the unexpected downtime as a result of accidents, reduce repair costs and increase motor lifespan [3].

II. IM ROTOR CONDITION MONITORING TECHNIQUES

Condition monitoring techniques for rotor fault detection can broadly be classified as follows [4], [5]:

ISSN 1691-5402

© Rezekne Academy of Technologies, Rezekne 2017
<http://dx.doi.org/10.17770/etr2017vol3.2526>

- Motor circuit analysis;
- Electromagnetic field monitoring;
- Air-gap torque;
- Stator current;
- Induced voltage;
- Surge testing;
- Instantaneous power;
- Instantaneous angular speed;
- Vibration;
- Acoustic emission.

Some of the methods, like motor circuit analysis require the machine to be taken off-line, which causes additional service and interrupts the manufacturing process.

Methods that use voltage and current measurements offer several advantages over off-line test procedures or techniques that require special sensors to be mounted on the motor [6], [7]. At the same time, the stator current methods are sensitive to motor electrical faults [8].

A lot of research work has been published on diagnosis of vibration of the electrical machines [1], [9]–[12]. Studies show that the vibration method is most sensitive in case of detection of bearing faults [8].

Several studies [6], [1], [13]–[16] have been conducted to acoustic studies and noise generated by the vibration of machine parts. It should be mentioned that audible noise measurements are more complex compared to vibration measurements [14].

The main sources of the noise in IM could be classified in three parts [17], [18] mechanical, aerodynamic and electromagnetic. The main source of mechanical noise generation is the same as vibration source - bearings [9], [10] and rotor unbalance (eccentricity) [16]. The sources of aerodynamic noise in IM are the fans, rotor wings or cooling ducts [17]. The magnetic stress wave acts in radial directions on the stator and rotor active surfaces causing the electromagnetic noise [17]. Several acoustic monitoring methods are presented nowadays: frequency analysis [19]; partial discharge acoustic measurements [15], speckle noise reduction [11].

III. BASIC ALGORITHM FOR FAULTS PRE-DETERMINATION

For a large number of diagnostic methods dismantling and disconnection of IM or installation of sensors around the IM perimeter or inside the IM itself is needed. In such case, preliminary examination of IM must be performed. Detection of basic fault signs during preliminary examination is a sufficient reason for continuing with complex and detailed fault determination procedure.

Serious problems in IM rotor can be determined without the use of special equipment and techniques. For example, a bending of rotor bar, which might progress with the bar intruding the air-gap, will cause

sharp decreasing of machine speed, or even a jamming of the rotor. Other signs of major problems in IM rotor are excessive heating of the machine and extraneous sounds such as hammering, crackling or gritting.

Rotor faults lead to appearance of higher harmonics of currents and magnetomotive force (MMF), which in hand causes the unbalance of radial force, appearance of additional vibration components and acoustic noise. Thus, increased motor noise and vibration can be considered as signs of IM fault.

Since any fault in electric motor leads to the reducing of its performance, deterioration of static and dynamic characteristics and parameters comparing to rated ones can be a reliable indication of failure occurred in the motor [20]. For the mentioned parameters could be for instance, increased duration of transient processes of induction motor, decreased motor's efficiency and motor power factor, increased values of currents in the motor windings etc.

Motor Current Signature Analysis (MCSA) can also be used for IM fault pre-determination. In the stage of motor preliminary examination, the determination of frequencies present in current spectrum, that are characteristic for cases of squirrel cage faults and rotor eccentricity, would be sufficient. These frequencies can be obtained as:

$$f_{cbrf} = f_s \left[n \frac{(1-s)}{P} \pm s \right]; \quad (1)$$

$$f_{ce} = f_s \left[(nR_s \pm O_{re}) \frac{(1-s)}{P} \pm O_{smh} \right], \quad (2)$$

where f_{cbrf} – components generated by broken rotor faults; f_s – supply frequency, s – per-unit slip; $n = 1, 2, 3, \dots$ – integral values, P – number of pole pairs; f_{ce} – components associated with eccentricity; R_s – number of rotor slots; O_{re} – rotating eccentricity order; O_{smh} – stator MMF harmonic order.

It should be noticed, that these frequency components cannot be treated as exact signs of occurrence of motor faults as these frequencies can be detected in the spectrum of even healthy motors due to unavoidable manufacturing symmetries and misalignment etc. Therefore, this sign should be considered only in complex with the others [2].

Based on foregoing, basic pre-determination algorithm is:

- 1) Motor examination for the presence of obvious signs of IM rotor faults;
- 2) Motor examination for increased motor noise and vibration;
- 3) Comparing static and dynamic IM parameters and characteristics with rated ones, identification of differences;
- 4) Basic current spectrum analysis for the presence of broken rotor faults and eccentricity frequency components.

After identification of one of these signs, one of the complex and detailed methods of faults determination can be used.

IV. SMARTPHONES

In present day smartphones have changed our habits and demeanor. Variety of available models and extensions of mobile phones have been used in different ways. Smartphone apps estrange the use of a mobile phone only for calls and bring many different applications, like information collecting and exchange, web services, remote control of devices, locating and traction of objects, etc. Some studies [21], [22] show opportunities for teaching and learning contexts. Special attention is put to use smartphone sensors in different applications [22]–[24]. Moreover, some of the smartphone based applications [25], [26] are used for medical purposes.

Studies shows [8] that most bearing fault related components could be easily identified in acoustic spectra. That means that it can be easily applied in portable solution as smartphone application for mechanical noise detection [27]. Nowadays, the acoustic analysis is more attractive in bearing fault detection, but there are ongoing investigations to use the smartphones for detection of other machine faults.

Noise measurements are more complex compared to vibration measurements. The advantage of noise monitoring over vibration monitoring is that the former can detect the growth of subsurface cracks, whereas the latter can detect defects only when they appear on the surface [10]. Condition based monitoring technique of the electrical machines is very attractive in bearing faults detection. It has been applied for rotor faults detection by researchers [4], [28] and is used by industries [11], [29] for avoiding sudden machine failure. Some researchers [16], [17] studied the effects of rotor eccentricity on the acoustic emission spectrum from an induction machine.

Broken rotor bars of squirrel-cage induction machines have been the subject of interest in numerous scientific studies. As the given fault is one of the more usual types of failures, condition monitoring to predict the possible fault and detection of broken bars can be considered an important issue in the field of induction machine diagnostics.

Noise produced by an electrical machine can provide the information about the electromagnetic forces as well as. The human ear is most sensitive to sound in the frequency range from 1 kHz to 5 kHz, while the sensitivity drops at higher and lower frequencies [14]. Experimental results show that noise produced by the electrical machine is mostly low frequency noise. Analysis of experimental data [28] shows that bearing faults are found in the frequency range from 50 Hz to 200 Hz in acoustic signature. It is also important to note that the energy released by neighboring components in the

vibrational frequency range (up to 50 kHz), which often masks the vibrational energy released from a defective rolling element bearing, do not affect the acoustic emission signal released in the very high frequency range [10]. That means the microphone, that records the noise, picks up all the sound signals in its sound field, which means measurement location should be carefully chosen to provide full range of the noise frequencies.

The distribution of the sound power versus frequency is needed for identifying the noise-generation mechanism. Studies show that noise spectrum depends on the position where the noise has been measured. There are three imaginary measuring surfaces recommended by ISO 3744:2010: hemispherical measurement surface, rectangular parallelepiped surface and conformal surface [14]. Other factors that may influence the noise measurements are size of source [15], source operating conditions [28], surroundings [27], etc.

Microphones in today's smartphones are capable of recording audio signals with frequencies up to 48 kHz [30]. Thereby, there is an opportunity of spectrum audio analysis of faults in the IM, which audible noise is recorded on smartphone from different directions. Due to the advantages of such fault diagnostic method, which are the mobility of recording device and simplicity of organization, it is possible to use this method for IM fault pre-determination, along with MCSA diagnostic method.

V. CONCLUSION

It is important to detect the electrical machine fault in an early stage, to prevent further damage of the equipment due to fault propagation, is one of the main features of any condition monitoring or diagnostic techniques.

The proposed algorithm of detection the basic symptoms of IM rotor faults can be used as algorithm for IM rotor faults pre-determination. The results of such pre-determination procedure can be a sufficient reason for the dismantling of IM and faults determination using desired diagnostic method.

The proposed method of using smartphone for spectrum audio analysis can be used for IM fault pre-determination. In future, the research of correctness of the method and the possibility of its implementation will be carried out.

Moreover, our research [31] shows the necessity of posing and solving inverse problems in the diagnostic procedures of electric machines. This is essential in order to achieve better and more precise results in the condition monitoring of the machines due to the growing complexity of the machine setups, which challenges the traditional electric machine diagnosis methods.

ACKNOWLEDGMENT

This research has been supported by the Estonian Research Council grants PUT (PUT1260) and PUTJD (PUTJD134), also by European Regional Development Fund under Mobilitas Plus program returning researcher grant (MOBTP13).

REFERENCES

- [1] M. A. A. Elmaleeh, N. Saad, N. Ahmed, and M. Awan, "On-line fault detection & diagnosis of rotating machines using acoustic emission monitoring techniques," in *2007 International Conference on Intelligent and Advanced Systems*, 2007, pp. 897–900.
- [2] P. S. Bhowmik, P. S. Bhowmik, S. Pradhan, and M. Prakash, "Fault Diagnostic and Monitoring Methods of Induction Motor: A Review."
- [3] L. G. Sidel'nikov and D. O. Afanas'ev, "Control Methods Review of Induction Motors Technical State During Operation", Perm National Research Polytechnic University Gazette," *Jpurnal Perm Natl. Res. Polytech. Univ. (In Russ., no. 7*, pp. 127–137, 2013.
- [4] M. R. Mehriou, N. Marioun, M. Hamiruce Marhaban, and N. Misron, "Rotor fault condition monitoring techniques for squirrel-cage induction machine—A review," *Mech. Syst. Signal Process.*, vol. 25, no. 8, pp. 2827–2848, Nov. 2011.
- [5] S. Nandi, H. A. Toliyat, and X. Li, "Condition Monitoring and Fault Diagnosis of Electrical Motors—A Review," *IEEE Trans. Energy Convers.*, vol. 20, no. 4, pp. 719–729, Dec. 2005.
- [6] J. Sottile, F. C. Trutt, and J. L. Kohler, "Experimental investigation of on-line methods for incipient fault detection [in induction motors]," in *Conference Record of the 2000 IEEE Industry Applications Conference. Thirty-Fifth IAS Annual Meeting and World Conference on Industrial Applications of Electrical Energy (Cat. No.00CH37129)*, 2000, vol. 4, pp. 2682–2687.
- [7] A. Kallaste, A. Belahcen, A. Kilk, and T. Vaimann, "Analysis of the eccentricity in a low-speed slotless permanent-magnet wind generator," in *2012 Electric Power Quality and Supply Reliability*, 2012, pp. 1–6.
- [8] W. Li, "Detection of Induction Motor Faults: A Comparison of Stator Current, Vibration and Acoustic Methods," *J. Vib. Control*, vol. 12, no. 2, pp. 165–188, Feb. 2006.
- [9] D. S. Shah and V. N. Patel, "A Review of Dynamic Modeling and Fault Identifications Methods for Rolling Element Bearing," *Procedia Technol.*, vol. 14, pp. 447–456, 2014.
- [10] N. Tandon and A. Choudhury, "A review of vibration and acoustic measurement methods for the detection of defects in rolling element bearings," *Tribol. Int.*, vol. 32, no. 8, pp. 469–480, Aug. 1999.
- [11] B. Torcianti, C. Cristalli, and J. Vass, "Non-Contact Measurement for Mechanical Fault detection in Production Line," in *2007 IEEE International Symposium on Diagnostics for Electric Machines, Power Electronics and Drives*, 2007, pp. 297–301.
- [12] J. Sobra, T. Vaimann, and A. Belahcen, "Mechanical vibration analysis of induction machine under dynamic rotor eccentricity," in *2016 17th International Scientific Conference on Electric Power Engineering (EPE)*, 2016, pp. 1–4.
- [13] A. Gaylard, "Acoustic evaluation of faults in electrical machines," in *Seventh International Conference on Electrical Machines and Drives*, 1995, vol. 1995, pp. 147–150.
- [14] S. P. Verma and W. Li, "Measurement of Vibrations and Radiated Acoustic Noise of Electrical Machines," *Electrical Machines and Systems, 2003. ICEMS 2003. Sixth International Conference on*, vol. 2, pp. 861–866 vol.2, 2003.
- [15] Xiaoqin Ma, Weisheng Lu, Xiangtian Chun, and Hengkun Xie, "Acoustical technology applications in large high voltage motors," in *Proceedings of 2001 International Symposium on Electrical Insulating Materials (ISEIM 2001). 2001 Asian Conference on Electrical Insulating Diagnosis (ACEID 2001). 33rd Symposium on Electrical and Electronic Insulating Materials and Applications in System*, 2001, pp. 737–740.
- [16] A. J. Ellison and S. J. Yang, "Effects of rotor eccentricity on acoustic noise from induction machines," *Proc. Inst. Electr. Eng.*, vol. 118, no. 1, p. 174, 1971.
- [17] M. Janda, O. Vitek, and M. Skalka, "Noise diagnostic of induction machine," in *The XIX International Conference on Electrical Machines - ICEM 2010*, 2010, pp. 1–4.
- [18] S. P. Verma, "Noise and vibrations of electrical machines and drives; their production and means of reduction," in *Proceedings of International Conference on Power Electronics, Drives and Energy Systems for Industrial Growth*, 1996, vol. 2, pp. 1031–1037.
- [19] W. Doorsamy and W. A. Cronje, "A study on Bayesian spectrum estimation based diagnostics in electrical rotating machines," in *2014 IEEE International Conference on Industrial Technology (ICIT)*, 2014, pp. 636–640.
- [20] A. Rassolkin et al., "Adjusted electrical equivalent circuit model of induction motor with broken rotor bars," in *2016 Electric Power Quality and Supply Reliability (PQ)*, 2016, pp. 213–218.
- [21] D. May and P. Ossenberg, "Fit for science a course for teaching to organize, perform and present scientific work in engineering with mobile devices," in *2015 IEEE Global Engineering Education Conference (EDUCON)*, 2015, pp. 176–183.
- [22] M. A. Bochicchio, M. Zappatore, and A. Longo, "Using Mobile Crowd Sensing to teach technology and entrepreneurship in high schools: An experience from Southern Italy," in *2015 IEEE Global Engineering Education Conference (EDUCON)*, 2015, pp. 948–953.
- [23] J. Lim, S. J. Lee, G. Tewolde, and J. Kwon, "Ultrasonic-sensor deployment strategies and use of smartphone sensors for mobile robot navigation in indoor environment," in *IEEE International Conference on Electro/Information Technology*, 2014, pp. 593–598.
- [24] A. Anjum and M. U. Ilyas, "Activity recognition using smartphone sensors," in *2013 IEEE 10th Consumer Communications and Networking Conference (CCNC)*, 2013, pp. 914–919.
- [25] X. Xu et al., "Advances in Smartphone-Based Point-of-Care Diagnostics," *Proc. IEEE*, vol. 103, no. 2, pp. 236–247, Feb. 2015.
- [26] J. Lee, J. Jung, J. Lee, and Y. T. Kim, "Acute myocardial infarction detection system using ECG signal and cardiac marker detection," in *IEEE SENSORS 2014 Proceedings*, 2014, pp. 2255–2257.
- [27] N. K. Verma, S. Sarkar, S. Dixit, R. K. Sevakula, and A. Salour, "Android app for intelligent CBM," in *2013 IEEE International Symposium on Industrial Electronics*, 2013, pp. 1–6.
- [28] W. Li, "Detection of Induction Motor Faults: A Comparison of Stator Current, Vibration and Acoustic Methods," *J. Vib. Control*, vol. 12, no. 2, pp. 165–188, Feb. 2006.
- [29] M. A. A. Elmaleeh, N. Saad, and M. Awan, "Condition monitoring of industrial process plant using acoustic emission techniques," in *2010 International Conference on Intelligent and Advanced Systems*, 2010, pp. 1–6.
- [30] P. Rzeszucinski, M. Orman, C. T. Pinto, A. Tkaczyk, and M. Sulowicz, "A signal processing approach to bearing fault detection with the use of a mobile phone," in *2015 IEEE 10th International Symposium on Diagnostics for Electrical Machines, Power Electronics and Drives (SDEMPED)*, 2015, pp. 310–315.
- [31] T. Vaimann, A. Belahcen, and A. Kallaste, "Necessity for implementation of inverse problem theory in electric machine fault diagnosis," in *2015 IEEE 10th International Symposium on Diagnostics for Electrical Machines, Power Electronics and Drives (SDEMPED)*, 2015, pp. 380–385.

Industrial Tests of Current Distribution Dynamics in the Brush-contact Apparatus of the Turbo-generator

Igor Plokhov, Igor Savraev, Alexander Markov, Alexander Ilyin,
Oksana Kozyreva, Nikita Kotkov

Pskov State University, Department of Electric Drive and Automation Systems.
Address: Lenina 8, Pskov, 180000, Russia.

Abstract. The article is devoted to analysis of the results of industrial tests of current distribution dynamics in the brush-contact apparatus of the turbo-generator TVV-800 (800 MW) using a microprocessor based monitoring system. New methods of assessing the quality of current-collecting devices functioning is developed, allowing to assess current transfer in dynamics and to determine their quality characteristics. New trends of current distribution dynamics between the parallel brushes that allow on the basis of statistical and variance analysis to develop practical recommendations for maintenance of these devices are revealed. The results of the research in the form of scientific articles are published for the first time.

Keywords: industrial tests, turbo-generator, brush-contact, current distribution between the parallel brushes.

I. INTRODUCTION

The electrical sliding contact is one of the main technical devices intended to transfer current between stationary and moving parts of electrical machinery and apparatus. The transmission of electrical current through sliding contact is accompanied by heating of the contacting parts, sparking and arcing [1, 2]. Mechanical vibration of parallel sliding contacts and the wear lead to the unbalanced distribution of current between the contacts (brushes), overcurrents and thermal overloads and result to decreasing the reliability of the brush-contact device (BCD). The electromagnetic instability of BCD leading to "ring fire" on the contact rings can occur [3, 4]. Methods and devices for monitoring physical characteristics of BCD [5-8] and for measurement of currents of the individual brushes are known [9, 10].

Powerful turbo-generators have BCD for supplying current to the rotor windings. Individual brushes and brush groups established in removable cassettes pressure on the slip ring is necessary to regulate in operation of BCD. Otherwise after a while there is a significant overload of some brushes and no-load condition of the others. It leads to increased wear of the brushes, overheating and damage of the contact pairs and entire cassette. Now current measurement of the separate brushes and brush groups is performed using portable operative diagnostics devices that enable to measure currents brushes separately, but they are not able to show instantaneous distribution of the currents in all brushes [9, 10]. It should noted that BCD of the

turbo-generator TVV-800 has 100 brushes, so tuning the device for even current load is very labour and time consuming task.

New method of current distribution monitoring in BCD of the electric machine and the device for its implementation as a microprocessor system have been applied and patented by the team of the authors [11].

II. MATERIALS AND METHODS

The next indicators were used to determine the quality of the current distribution in turbo-generator BCD – representing the time dependence of the average deviation currents brush cassettes q_j , % and the standard deviation of currents brush cassettes Q_j , % from the average current of brush cassette I_{avj} for a given period of time:

$$q_j = 100 \cdot \frac{\sum_{i=1}^N |I_{ij} - I_{avj}|}{N \cdot I_{avj}}, \quad (1)$$

$$Q_j = \frac{100}{I_{avj}} \cdot \sqrt{\frac{\sum_{i=1}^N (I_{ij} - I_{avj})^2}{N}}, \quad (2)$$

$$I_{avj} = \frac{1}{N} \sum_{i=1}^N I_{ij}, \quad (3)$$

where I_{ij} - the current of the cassette № j in the measurement № i, $j = 1 \dots k$; I_{avj} - average current of all cassettes for a given period of time, N is the number of measurements.

Then $q_j, \%$ are the time dependences of the average deviation of the currents of the brush cassettes from the average current of the cassettes for a given period of time and $Q_j, \%$ - time dependences of the standard deviation of the cassette currents from the average current of the cassettes for a given period of time.

We using a microprocessor monitoring system recorded digitally the current distribution on the brush cassettes (in each cassette there are 5 brushes) and the on-line setting of BCD for even current load of the brush cassettes. In the operation of the system at the Nizhnevartovsk State District Power Stations a significant amount of experimental data have been accumulated and processed by means of which the dynamics of current distribution of cassette of brushes has been analyzed and a number of previously unknown physical laws of functioning of the current device with sliding contacts of large turbo-generator have been revealed. New methods of analysis of the obtained results was developed. Program for statistical processing of measurements and for creation of graphs which allows to build the schedule was created:

- 1) graphs of the current of cassette № i I_i for the measurement time;
- 2) graphs of the current of pole of BCD for a specified period of time

$$I_g = \sum_{i=N_g+1}^{N_g} I_i, \quad (4)$$

$$I_c = \sum_{i=N_g+1}^{N_e} I_i, \quad (5)$$

where $N_g, -$ the number of cassettes of poles of BCD (G – side «Generator») on a ring with positive polarity, $N_e -$ the number of cassettes of poles of BCD (side «Exciter») on a ring with negative polarity; 3) indicators of the quality of the current distribution q_j and Q_j in time.

The program also allows to display the new dynamic characteristics, developed by the authors:

- the locus diagram of a unbalance of current load of the sides of the pole of BCD

$$f_{gg}(I_{ga}, I_{g\delta}, t), f_{ge}(I_{ea}, I_{e\delta}, t); \quad (6)$$

where I_{ga} is the current of the pole from the side «Generator» (side «A»), I_{gb} is the current of the pole from the side «Generator» (side «B»), I_{ea} is the current of the pole from the side «Exciter» (side «A»), I_{eb} is the current of the pole from the side «Exciter» (side «B»); T - time;

- the dependence of the relative systematic measurement error from time ($\varepsilon -$ for excitation current of BCD, $\varepsilon_j -$ for the current j cassettes), where N is the number of cassettes of one pole, $N_g -$ the maximum number of cassettes of the pole "Generator"; $N_e -$ the maximum number of cassettes of the pole "Exciter"

$$E_j = 100 \cdot \frac{\sum_{i=1}^{N_g} I_{ij} - \sum_{i=N_g+1}^{N_e} I_{ij}}{\sum_{i=1}^{N_g} I_{ij} + \sum_{i=N_g+1}^{N_e} I_{ij}}, \quad (7)$$

$$\varepsilon_j = \left(\sum_{i=1}^{N_g} I_{ij} - \sum_{i=N_g+1}^{N_e} I_{ij} \right) / I_j / N \quad (8)$$

- a time dependence of the imbalance of the measured values of the total currents of poles.
- the locus diagram of a equilibrium of the currents system of the pole of BCD

$$f_{eg}(x_{og}, y_{og}, t), f_{ee}(x_{oe}, y_{oe}, t); \quad (9)$$

For getting generalized information about the dynamics of the current transfer in group sliding contact of a separate pole will introduce the concept of a hodograph of an equilibrium of current system as a function of the center mass coordinates of a regular polygon with weight coefficients of the vertices equal to the brush cassette currents. The axial projection of the BCD pole is shown schematically for the explanation in Fig. 1.

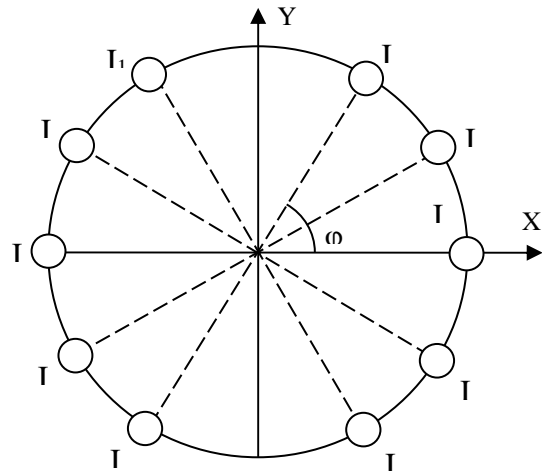


Fig. 1. To the construction of the hodograph of the equilibrium of the currents.

Each pole has two groups of brushes "series A" and "series B" placed on different sides of BCD. Redistribution of the currents there are between rows and between individual brackets ($I_A \neq I_B$) given that $I_{exc} = I_A + I_B$. An excessive current of the load affects the quality of functioning of BCD causing overheating of brushes, increasing the sparking and the wear. We define the numeric indicators determining the deviation of the excitation current of the nominal value and the degree of uneven loading of the row of brushes.

The instantaneous position of the point of the equilibrium defined as:

$$X_0(t) = \frac{\sum_{i=1}^N I_i(t) \cdot \cos(\varphi_i)}{\sum_{i=1}^N I_i(t)}, \quad (10)$$

$$Y_0(t) = \frac{\sum_{i=1}^N I_i(t) \cdot \sin(\varphi_i)}{\sum_{i=1}^N I_i(t)} \quad (11)$$

and the statistically average equilibrium coordinates as the integral estimation of the mathematical expectation:

$$X_0 = \frac{1}{T} \cdot \int_0^T X_0(t) dt, \quad (12)$$

$$Y_0 = \frac{1}{T} \cdot \int_0^T Y_0(t) dt, \quad (13)$$

where T – total measurement time.

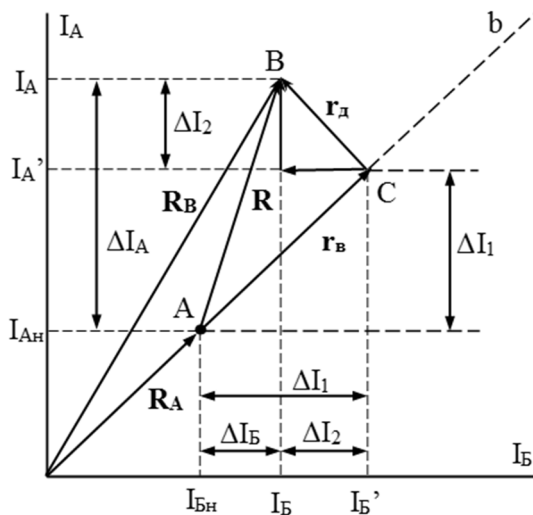


Fig. 2. To the definition the indicator of imbalance of series.

The point of the nominal mode in the absence of non-uniform loading of the rows – point A=(I_{An}, I_{Bn}) with I_{An}=I_{Bn} and a point corresponding to the non-ideal operation mode of BCD (I_A≠I_B) shows in the vector diagram (Fig. 2). The position of the operating points is characterized by the vectors R_A and R_B. The deviation of the operating point from the nominal position specifies the vector R, which is represented by the sum of the vectors r_a and r_b, defining the deviation of the excitation current of the nominal value and the uneven loading of series (vector of imbalance).

From the vector diagram it follows:

$$\Delta I_1 = \Delta I_B + \Delta I_2, \quad \Delta I_2 = (\Delta I_A - \Delta I_B) / 2, \quad (14)$$

$$\Delta I_1 = (\Delta I_A + \Delta I_B) / 2, \quad (15)$$

where ΔI₁ is the scalar index of the deviation of the excitation current from the nominal value; ΔI₁ is the indicator of the imbalance of series. Moreover ΔI_A ΔI_B are determined using the known values currents of series I_A and I_B and using the nominal value currents:

$$I_{An} = I_{Bn} = I_{exc} / 2. \quad (16)$$

That is

$$\Delta I_B = I_B - I_{Bn}, \quad \Delta I_A = I_A - I_{An}. \quad (17)$$

BCD of the turbo-generator TVV-800 contains 100 brushes placed in 20 removable brush cassettes: 10 cassettes for each pole. The numeration of the cassettes starts from the pole “Generator” which located closer to the turbo-generator and continues to the pole “Exciter” which located closer to the exciter. Cassette of pole are divided into the series of “A” and into the series of “B” located on different sides of BCD under protective covers. Every series has 5 cassette on the pole (Fig.3).

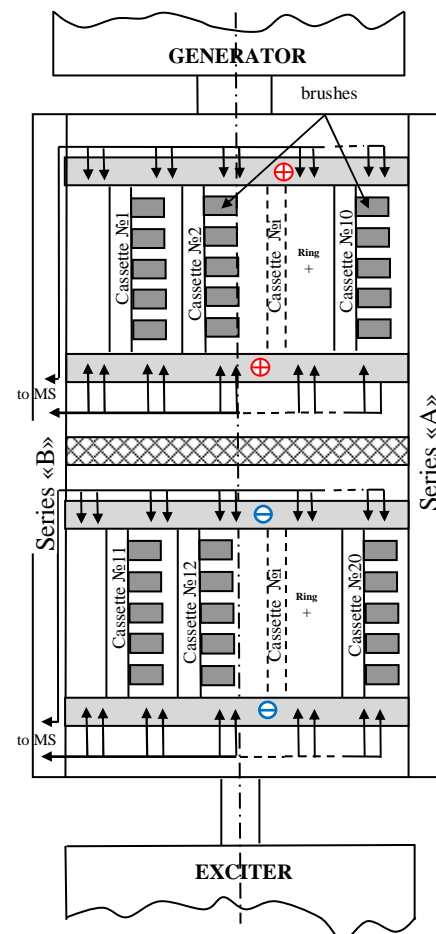


Fig.3. The brush-contact device of the turbo-generator.

The main blocks of the monitoring system MS and the placement on the case of BCD shown in Fig.

4. The operation principle of the system is to measure the voltage drops on the current-carrying portions of the brush traverses with the following calculation by derived formulas the currents of the brush cassette (Fig.5) [11, 12]:

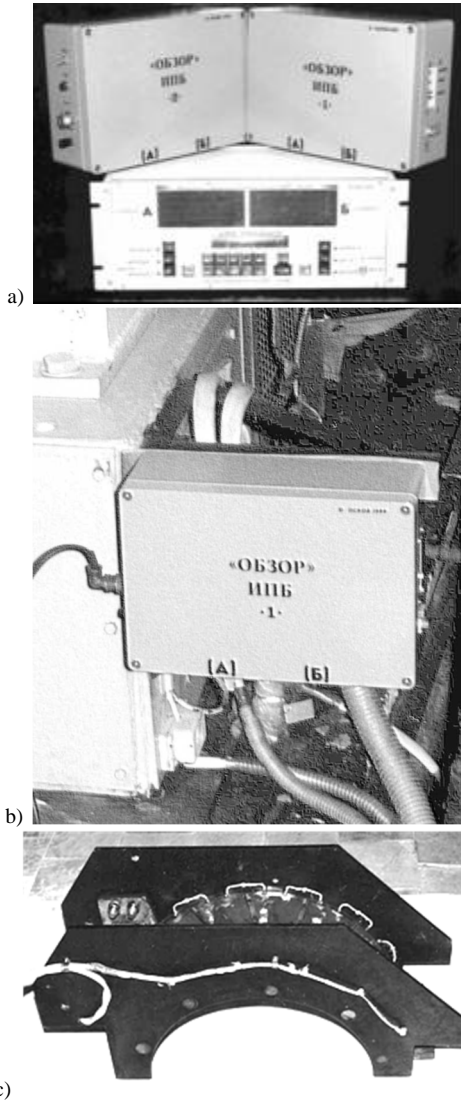


Fig. 4. Blocks of the monitoring system (including a block of visual output of information about the measured currents of the cassettes) (a); measuring-transducer block in the case of BCD (b); section of the case of BCD TVV-800 with signal cables of diagnostic system (c).

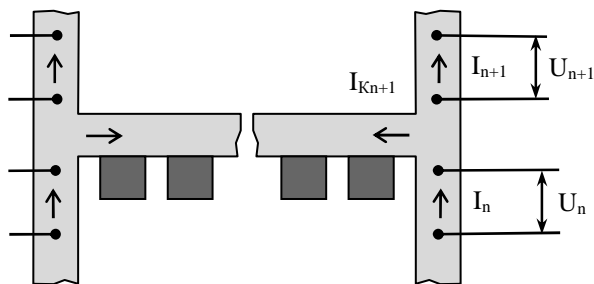


Fig.5. To determine the current of the cassette.

The current of the cassette is determined by the formula:

$$I_{Kn+1} = I_{n+1} - I_n = (U_{n+1} - U_n) \times G, \quad (18)$$

where U_{n+1} and U_n are measured drops in voltage in the same part of the current bus of the pole;

G – the conductivity of the relevant part.

The calculated values of the cassette currents can be displayed visually in relative units, or calculated in absolute units according to the current consumption of the current bus.

III. RESULTS AND DISCUSSION

Graphs of the some cassettes currents of BCD measured by the system over a period of 900 hours and with an interval of 0.5 hours with the placed over linear approximation are shown in Fig. 6 and Fig. 7. Cassettes with the most unstable current distribution in time were selected.

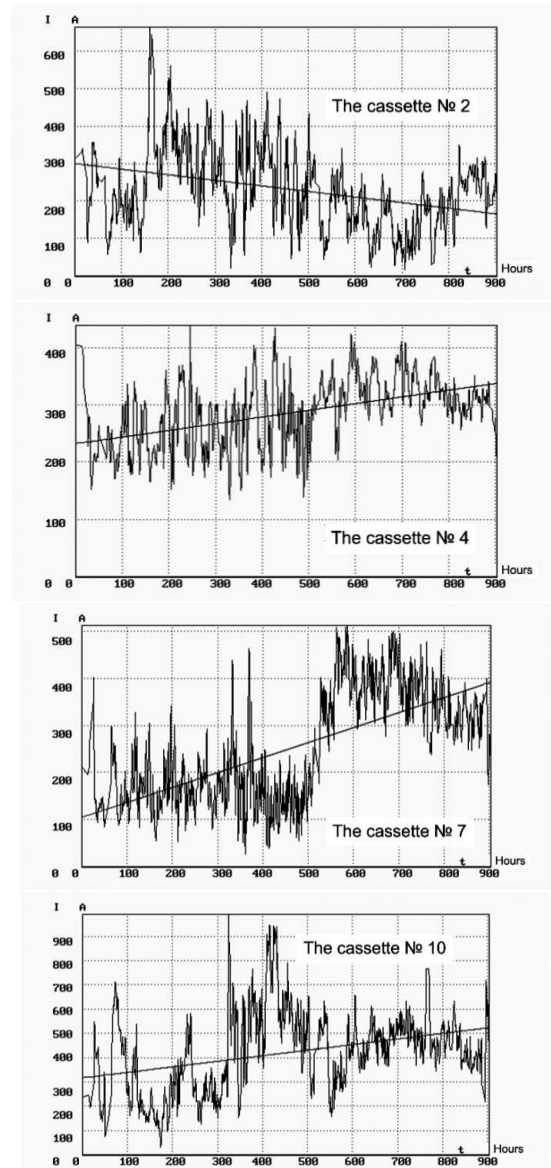


Fig. 6. The currents of the brush cassette of the pole "Generator" (straight line is linear approximation of the obtained graph).

The assessment of presented graphs allows us to make the preliminary estimations and conclusions:

- the process of a drift of load current of the brush of the cassettes are stochastic in nature;
- most of the graphs contains the 0.5–2 hours intervals during which the current exceeds the average value more than two times;
- there are periods during which the separate cassette are practically deenergized.

The graphs of the pole “Generator” cassettes currents are more chaotic. It can be explained by the fact that in the test period the ring had the higher level of the wear and vibration.

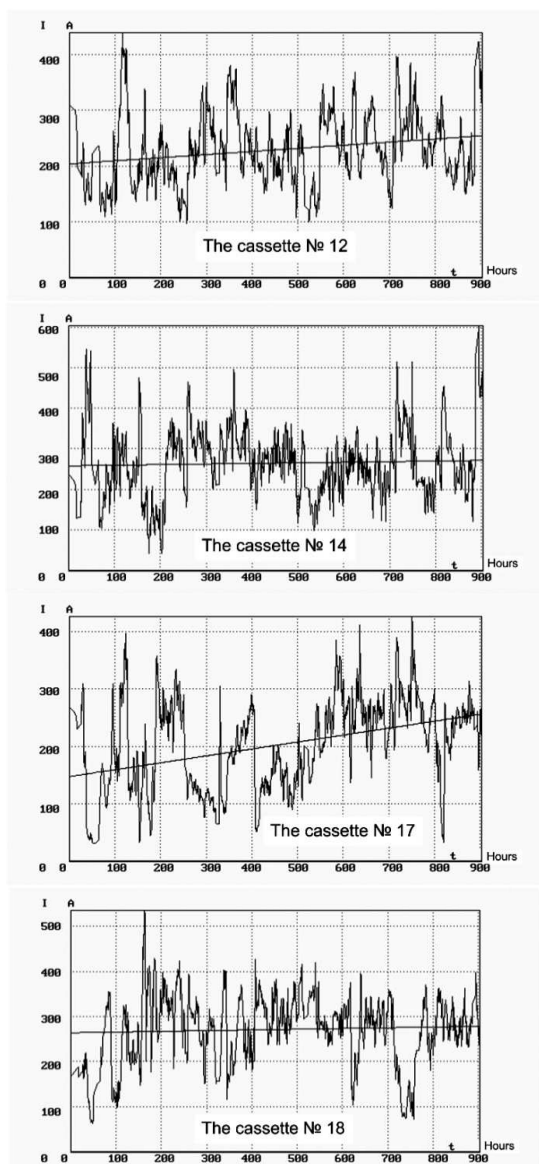


Fig. 7. The currents of the brush cassette of the pole “Exciter” (straight line is linear approximation of the obtained graph).

The linear approximation of the graphs allows to conclude that the average currents of the cassettes are in the range 200–300 A (40–60 A for one brush, in this case the nominal current of the brush is 80 A).

Comparison of the integral indicators of individual brushes cassette and pole of BCD their current load for the study period and the stability of current transfer is given in Table 1.

Table 1.

№ CASSETTE	SIZE SAMPLE	RATING MATHEMATICAL EXPECTATIONS	UNBIASED RATING DISPERSION	STANDARD DEVIATION (%)	SECONDARY DEVIATION (%)
1	1726	292	16199	43.4	33.2
2	1726	230	15082	53.2	41.5
3	1726	324	15941	38.8	29.8
4	1726	286	5962	26.9	21.3
5	1726	284	9345	34.0	25.3
6	1726	342	12436	32.5	24.7
7	1726	252	17924	52.9	45.5
8	1726	219	7390	39.2	30.0
9	1726	249	15233	49.4	39.3
10	1726	423	33972	43.5	34.3
11	1726	238	6227	33.1	26.4
12	1726	229	4849	30.3	24.1
13	1726	190	3986	33.2	24.9
14	1726	264	9274	36.4	28.1
15	1726	311	17118	42.0	36.9
16	1726	166	7305	51.4	41.6
17	1726	203	6954	40.9	33.9
18	1726	270	7303	31.5	24.7
19	1726	201	9836	49.3	40.3
20	1726	285	4470	23.3	17.8

The average values indicators for the poles are:

- the dispersion: 14948 – pole “G”, 7732 – pole “E”;
- the standard deviation: 41.4 – pole “G”, 36.1 – pole “E”;
- the average deviation: 36.1 – pole “G”, 29.8 – pole “E”.

Used assessment leads to the conclusion, that the pole “Generator” works almost twice less stable than the pole “Exciter”.

Let’s plot the currents of brush cassettes in a form of histograms, where each column corresponds to the current of a certain cassette in a given time. The histograms of currents during four hours work of BCD captured at intervals of 1 hour from $t = 300$ hours and up to the beginning of continuous measurements are shown in Fig. 8.

The numbers of cassettes is on the x-axis and the value of current consumed in a given moment of time is on the y-axis.

The currents of the pole “E” change noticeably slower than the currents of the pole “G”, that is also confirmed by study of the graphs of the first derivative of current in dynamic processes that are represented selectively in Fig. 9.

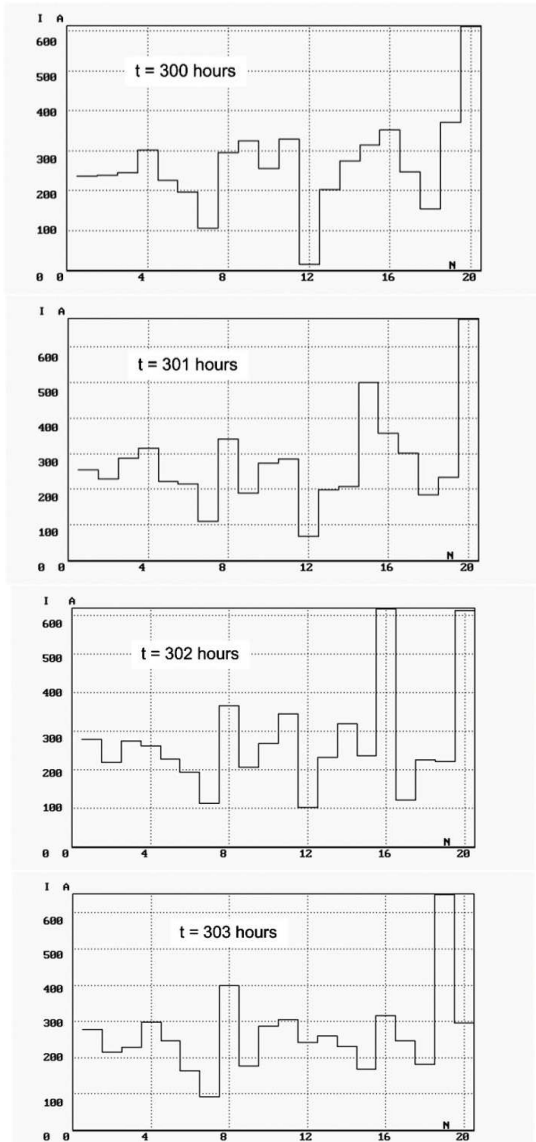


Fig. 8. The histogram of the current distribution in the cassettes of BCD in fixed moments of time t (N is the number of the cassette).

For cassettes № 1, № 2 of the pole “G” the rate of current change is 100–150 A/hour, and for cassettes № 11, 12 of the pole “E” – no more than 30–50 A/hour, that allows to conclude about more high-quality work of the pole “E” of BCD. A polishing of the ring contact surface located on the generator side is recommended to agree the described research results.

Let’s consider the graphs of changing poles currents calculated as the sum of the individual cassettes currents (Fig. 10). The currents are in the range of 2000–3000 A. There are daily deviations of the excitation current that do not exceed 20% and there are also daily deviations of the shorter duration that do not exceed 10%.

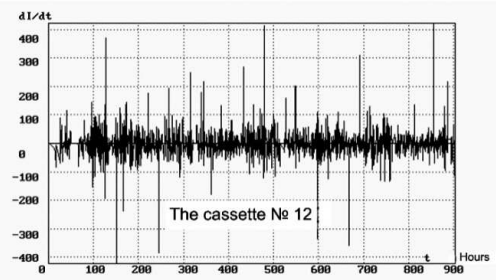
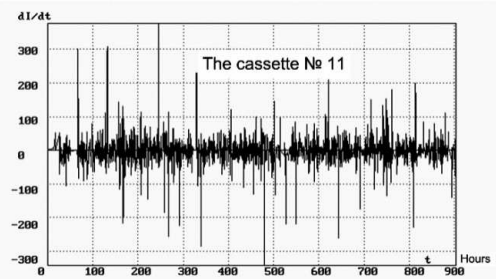
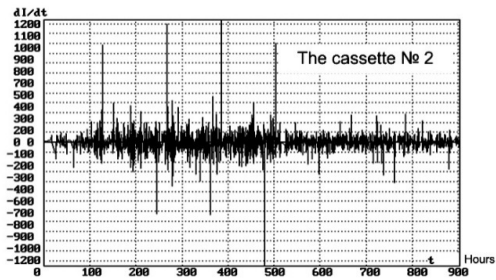
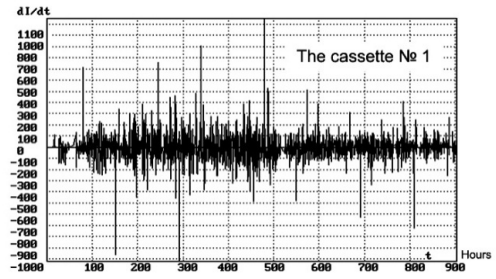


Fig. 9. The rate of a change of the current some cassettes of the different poles BCD.

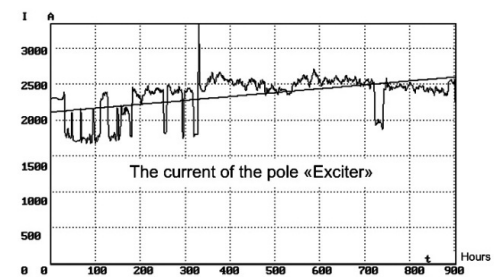
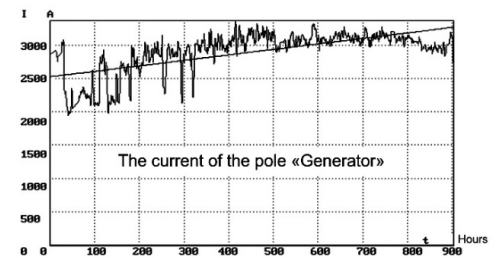


Fig. 10. Graphs of the change of currents of the poles of BCD for 900 hours of work (straight line is linear approximation of the obtained graph).

The graphs of the first derivative of the currents of the poles (Fig. 11) allow to make conclusion about the stability of the current transfer through total sliding contact brush cassettes of the corresponding BCD poles.

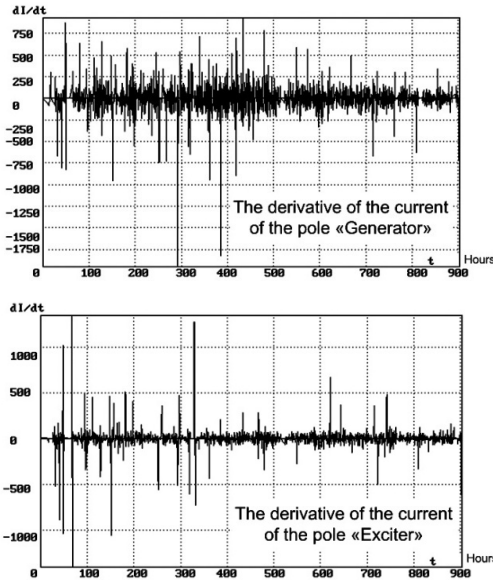


Fig. 11. The rate of BCD poles currents change of the turbo-generator TVV-800.

The assessment of dynamic asymmetries of the series of brushes load for the pole BCD is presented in a form of a phase trajectories (Fig. 12). The value of the total brushes current of the series A is postponed on the ordinate axis and of the series B – on the abscissa axis.

Each phase contains two stochastic trajectories of the attractor, extending perpendicular to the bisector of the first quadrant. Therefore, a main displacement of the imaging point in the phase plane is caused by the processes of a redistribution of the current between the series. The number of attractors indicates two quasistatic modes with different values of the total load current. Moving along the bisectors are determined by fluctuations of the excitation current of the turbo-generator. The smaller current load of BCD at night can explain the existence of the small attractor.

Define the statistical distribution of the density of a realizations of a random process in the region of possible values of $p(y \in [y_s, y_{(s+1)}])$. To build this graph we find the relative frequency of a random variable fall in the given intervals of values as a percentage of the total number of realizations. An example of probability density function for graphs of the cassettes currents and poles of BCD is shown in Fig. 13. The presence of two or more peaks indicate a long work in several quasi-stationary modes. The third part of the total number of cassettes relates to the latter category.

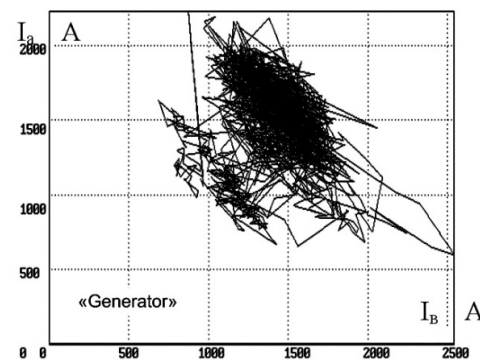
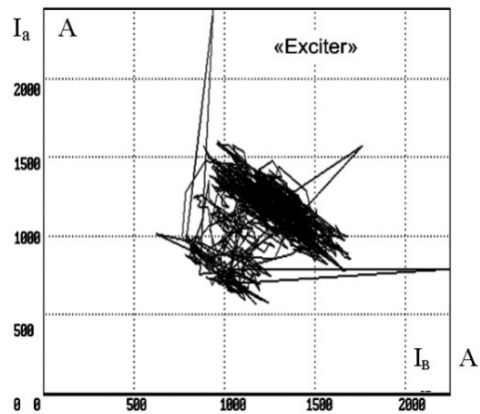
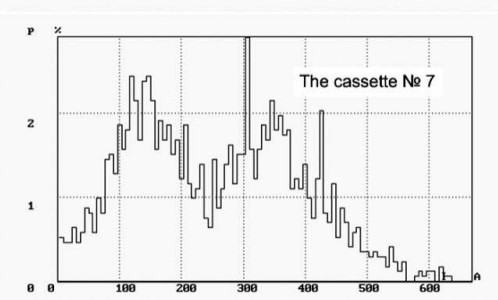
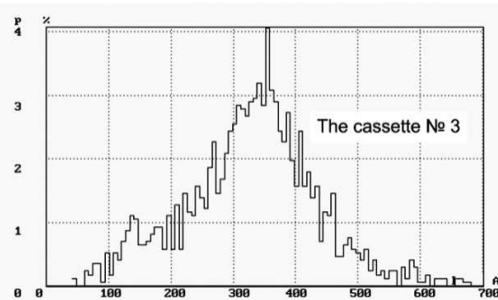


Fig. 12. The phase trajectory of current download of the series of brushes.

Let's show that for the monitoring system of current distribution of BCD main technical effect is to improve the quality of the current's distribution and the associated increasing of operation reliability of BCD.



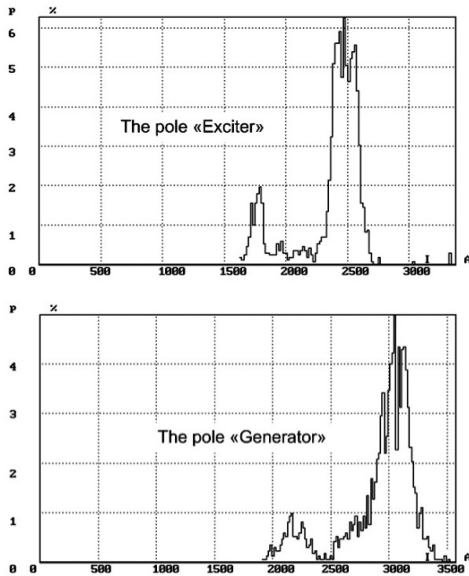


Fig. 13. The probability distribution of the currents of the cassettes and poles.

Let's show how the quality indicator of the current distribution Q (2) was changed in the search period. Its dependence on time for the poles is shown in Fig. 14. In the absence of the continuous monitoring and control of the technical condition of the indicator usually deteriorates as evidenced by the earlier experiments on the measurement of currents by the devices of on-line diagnostics.

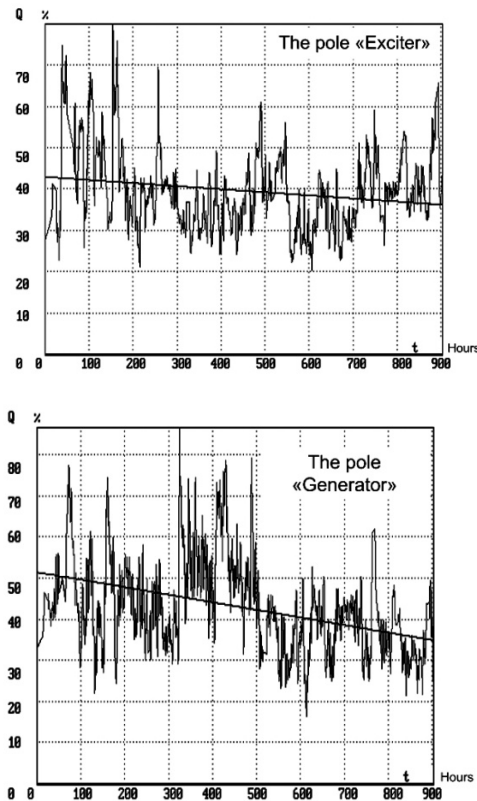


Fig. 14. The change of the indicator of the quality of current distribution during the study period (straight line - linear approximation of the obtained graph).

The diagrams show that the quality indicator of current distribution has improved in the process of the system working. Such conclusion allows to make an approximation by linearization of the graphs by the least square method. Moreover Q for pole "E" dropped from 44 to 35% and was on average 9%, and for the pole of "G" – from 52 to 35% and was 17%. The relative drop reached 20% and 33% respectively. The steady-state value of the indicator in both cases reaches 35% although the initial levels differed significantly ($Q=35\%$ corresponds to an excellent effect evaluation for the even current distribution).

The positive effect after the tuning of the BCD current distribution on the readings of the monitoring system is resulted in the reduction of the dispersion of current series, poles and dispersion quality indicator (Fig. 15–17). The estimate of the variance was produced by calculating the standard deviation W by scanning processes with an interval of 5% of the analyzed time period. The decrease of the root-mean-square scattering is tens of percent in all cases.

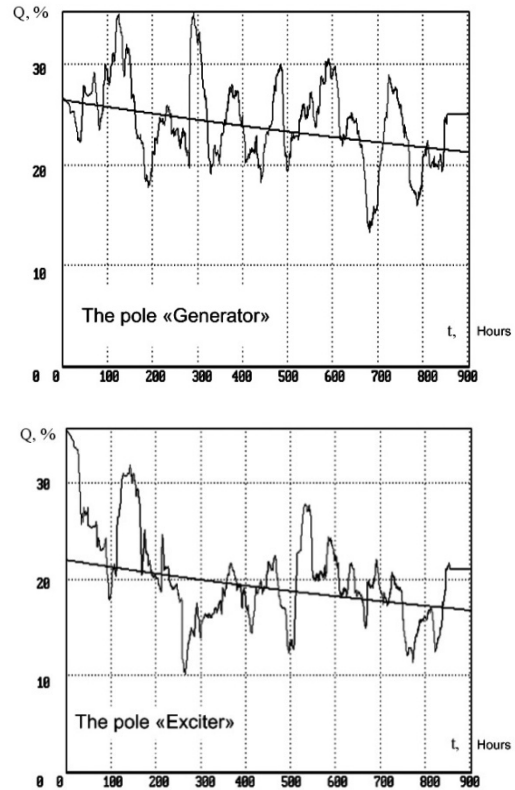


Fig. 15. The change of standard deviation of indicator of the quality of current distribution (straight line - linear approximation of the obtained graph).

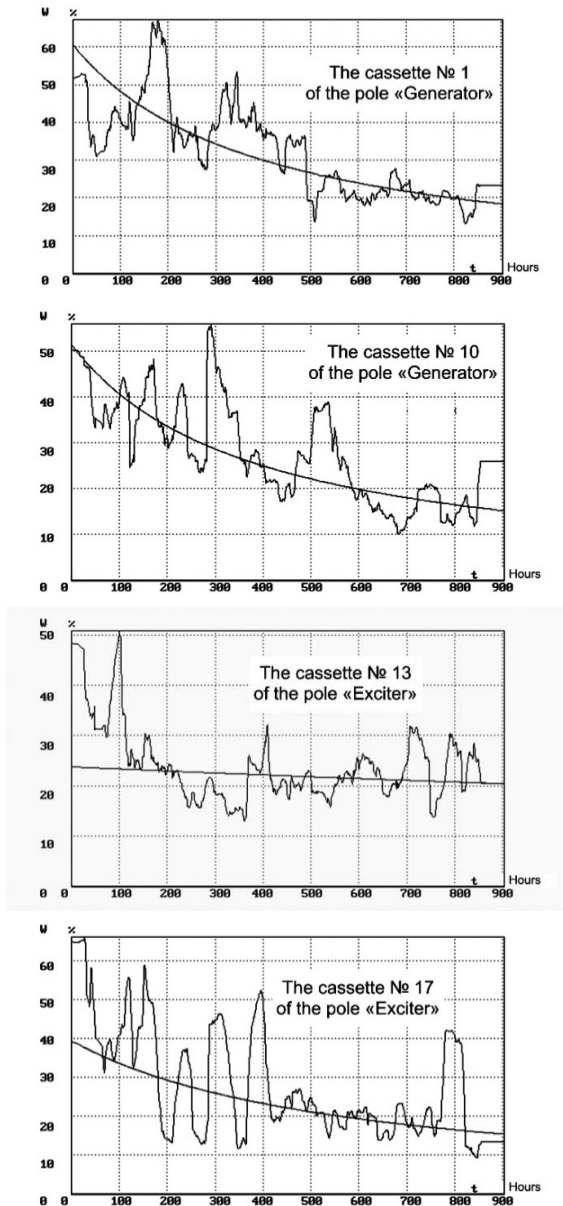


Fig. 16. The change of the standard deviation of the currents of the cassettes during the test period (drooping characteristic is nonlinear approximation of the obtained graph)/

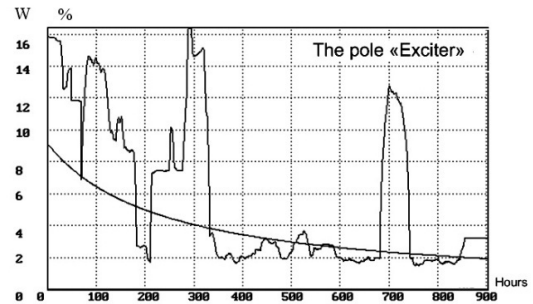
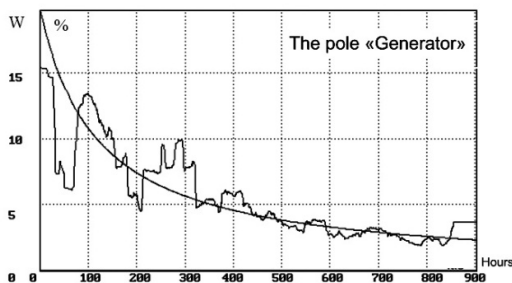


Fig. 17. The change of the standard deviation of the currents of the poles during the test period (drooping characteristic is nonlinear approximation of the obtained graph).

The data of the phase trajectory in the analyzed period of the work of BCD are shown in Fig. 18.

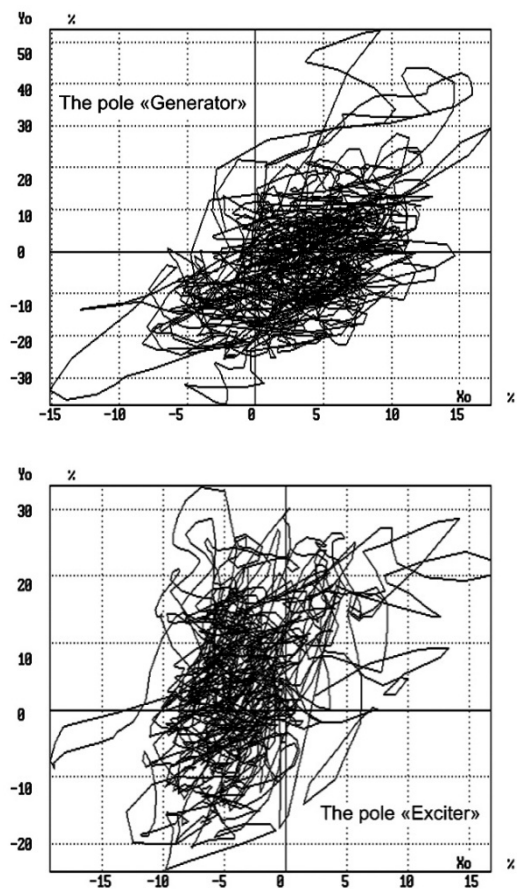


Fig. 18. Hodographs of the equilibrium of the currents of the poles of BCD of TVV-800.

The statistical average, the variance and the characteristic features of the configuration of the attractors are estimated from the given characteristics:

- 1) the statistically average coordinates of the points of the equilibrium: $X_{0G} = -3.3\%$, $Y_{0G} = 4.6\%$ (pole "G") and $X_{0E} = 3.5\%$, $Y_{0E} = -1.5\%$ (pole "E");
- 2) the process of moving the point of the equilibrium has a stochastic nature;
- 3) the fluctuations of a given point along the y-axis is about two times larger than along the x-axis therefore the current is distributed less evenly in the

vertical section of BCD due to the uneven influence of the gravity force on the different cassettes;

4) the attractor of the pole “G” is stretched along the bisectrix of the 1–3 quadrants suggesting more active redistribution of the current between the cassettes 1–3 and 6–8, it allows to make a conclusion about the high instability of the current transfer through this cassettes;

5) the variance of the attractor pole “G” is almost two times higher than the variance of the attractor “E”, indicating a more stable process current transfer on the pole “E”.

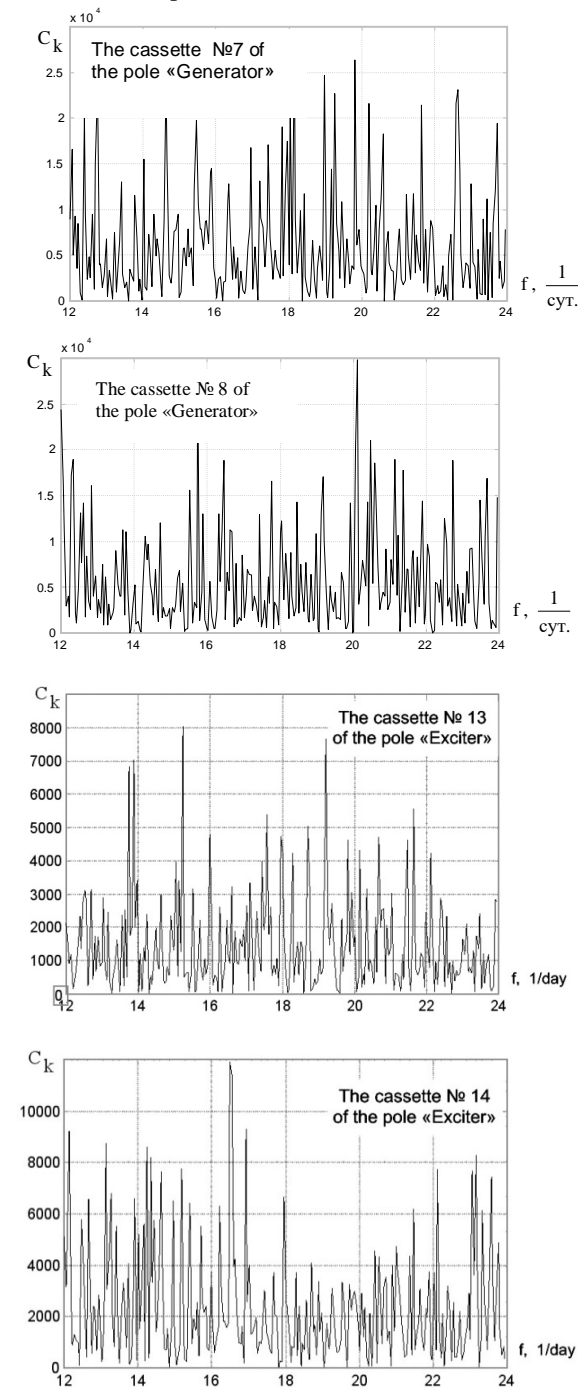


Fig. 19. Spectra of dynamic processes of transfer current through brush cassette (selective)

Let's consider the spectra of the analyzed processes obtained with a fast algorithm for the discrete Fourier transform in MATLAB (Fig. 19). We introduce for the spectral functions a marking of the frequency in units of $[\text{Hz}^*] = [\text{day}^{-1}]$.

A noticeable increase of amplitude is observed with the decrease of frequency especially in the region below 12 Hz*. The daily fluctuations of the currents have the highest levels. Additionally, the amplitude of the spectral components is much higher for pole “G”, that indicates its unstable operation.

IV. CONCLUSION

The presented new diagnostic system underwent industrial tests and proved its effectiveness in determining parameters of the current distribution in the BCD of the turbo-generator of Nizhnevartovsk State District Power Stations.

The developed new ways of assessing the quality of the BCD operation allowed us to evaluate the current transfer processes in static and dynamic modes and determine their qualitative characteristics.

During the operation of the diagnostic system new regularities of the current distribution in dynamic between brush cassette were discovered, which based on statistical and dispersion analysis allowed to develop practical recommendations for the maintenance of these units (replacement of brush cassettes, grinding of the rings, adjusting the force of pressing the brushes to the ring and etc.).

The new dynamic characteristics of the current distribution in the BCD developed by the authors include:

- vector diagram allowing to determine the unevenness of loading rows of brushes (vector of unbalance of series);
- the locus diagram of a equilibrium of the currents system of the pole of BCD.
- the locus diagram of a unbalance of current load of the sides of the pole of BCD

Upon review of the characteristics of the dynamic processes of the current transfer can make the following conclusions about the effectiveness of monitoring the current distribution of BCD of turbo-generator:

- 1) the monitoring system of the current distribution introduce a fairly strong negative feedback on the quality of functioning of man-machine systems of “BCD-technical staff”;
- 2) the operation of diagnostic system improves the quality of the current distribution and reduces the dispersion processes of current transfer;
- 3) application of monitoring system the current distribution system simplifies the adjustment procedures, render possible promptly and reasonably to respond to adverse changes in the modes (for example sparking of individual brushes) and take targeted measures for maintenance, increases

operating reliability of the current collector of the turbo-generator.

V.ACKNOWLEDGMENTS

This research was undertaken with the support of the management and staff of the electrical Department of the Nizhnevartovsk State District Power Stations.

Senior lecturer of Department of electric drive and automation systems PskovSU A. Andrusich have done extensive work on the development of a monitoring system.

The authors of the article congratulate prof. of Pskov State University I.V.Plokhov with the medal "For merits in the development of engineering education in Russia".

REFERENCES

- [1] Хольм Р., *Электрические контакты*, М.: Иностранная литература, 1961.
- [2] Кончиц В.В., Мешков В.В., Мышкин В.В. *Триботехника электрических контактов*, Минск: Наука и техника, 1986.
- [3] O. I. Kozyreva, I. V. Plokhov, Y. N. Guraviev, I. E. Savraev, A. V. Ilyin, The regions of parametric instability of brush-contact device electromagnetic circuit in unstable working conditions *Environment. Technology. Resources. Proceedings of the International Scientific and Practical Conference / Rezekne, REZEKNE HIGHER EDUCATION INSTITUTION*. 2015 – Volume 1. P. 84-88.
- [4] Method of Decreasing Arcing in Brush-Slip Ring Unit of Turbo-generators / Kozyreva O. I., Plokhov I.V., Ilyin A. V., // Proceedings of Tula State University. Engineering Sciences. 2012 #12-2. P. 342-348.
- [5] Henaо H., Capolino G.A., Fernandez-Cabanас M., Filippetti F., Bruzzese C., Strangas E., Pucsa R., Riera-Guasp M., Hedayati-Kia S., Trends in Fault Diagnosis for Electrical Machines: A review of Diagnostic Techniques, *IEEE industrial electronics magazine*, vol. 8, No.2, June 2014. pp. 31–42.
- [6] Toliyat, A., Nandi S., Choi S., Meshgin-Kelm H. *Electric machines. Modeling, condition monitoring and fault diagnosis*. CRC Press and Taylor & Francis Group, edition 2012, 272 p.
- [7] Juergen Klaar. *Apparatus for monitoring a sliding contact element in an electrical rotating machine*, US 20030011388 A1. 16.01.2003.
- [8] Харламов В. В., *Методы и средства диагностирования технического состояния коллекторно-щеточного узла тяговых электродвигателей и других коллекторных машин постоянного тока: монография* / В. В. Харламов. – Омск: ОмГУПС, 2002. – 233 с.
- [9] Попов И.Н., Попов И.И., Попов Н.И., *Способ измерения тока щеток щеточно-контактного аппарата синхронных генераторов*, Патент на изобретение RU 2383029, опубликовано: 27.02.2010, бюл. № 6.
- [10] Попов И.Н., Зражевский С.М., Калмыков А.В., *Устройство для контроля токораспределения щеточно-контактного аппарата электрической машины*, Патент на изобретение 2157033, опубликовано: 27.09.2000, бюл. № 27.
- [11] Плохов И.В., Савраев И.Е., Андрусич А.В., *Способ контроля токораспределения по комплектam щеток узла токосъема электрической машины и устройство для его осуществления*, Патент на изобретение №2178609, опубликовано 20.01.2002.
- [12] Плохов И.В., Савраев И.Е., Андрусич А.В., *Диагностическая система для узлов токосъема турбогенераторов*, *Электросила* № 40, 2001.

Aging, Fatigue and Durability of Rubber Vibration Isolation Elements

Svetlana Polukoshko¹, Andris Martinovs², Svetlana Sokolova³

¹Ventspils University College, Engineering Research Institute "VSRC", Latvia, ²Rezekne Academy of Technologies, Latvia, ³Riga Technical University, Institute of mechanics, Latvia

Abstract. This paper deal with shock and vibration insulators, which usually are performed from the elastomeric (rubber-like) materials. Elastomeric materials give many engineering advantages due to their capability of absorbing input energy much better than engineering materials, high elasticity, good dynamic properties, low volume compressibility, a linear relationship between stress and strain up to strain of 15% ÷ 20%, resistance to aggressive environmental factors. Elastomeric materials are widely used in machine building, shipbuilding, civil engineering, aviation and aerospace as compensation devices, vibration dampers, shock absorbers. Laminated elastomers, consisting of interleaved thin layers of elastomer and rigid reinforcing layers are also successfully used as bearing, joints, dampers, compensating devices, shock-absorbers. Such structures have many advantages: ability to endure high stress (>200 MPa), ease of maintenance, non- necessity for lubrication, vibration and noise reduction, ability to work in a very dirty, dusty, abrasive environment. The disadvantage of elastomeric material are aging, i.e. changing its properties over time. In this paper the influence of aging of elastomeric materials on the damping properties of shock absorbers is considered based on the mechanical models of elastomers - Maxwell and Burgers modes. Fatigue endurance, i.e. the ability to withstand mechanical actions for a long time is studied based on experiments on dynamic shear with laminated rubber-metal structures. The experiments show that such structures have a very high fatigue life - up to 100 million cycles.

Keywords: elastomers, shock and vibration protection, aging, Burgers model, Maxwell model, fatigue.

I. INTRODUCTION

At the present time the questions of preventing the harmful effects of vibration and impacts on machines and construction elements require particular attention. In most cases it is necessary to provide of shock and vibration protection devices at the design stage. Elastomers, i. e. rubber and rubber-like materials, are most suitable material for shock absorbers and anti-vibration devices due to their capability of absorbing input energy much better than engineering materials. These materials have a specific properties: high elasticity, resistance to aggressive environmental factors, good dynamic properties, low volume compressibility, a linear relationship between stress and strain up to strain of 15% ÷ 20%. They are widely used in machine building, shipbuilding, civil engineering, aviation and aerospace as compensation devices, vibration dampers, shock absorbers [1] - [4].

Reinforced elastomers consist of alternating thin layers of elastomer and reinforcing layers of much more rigid material (usually metal), connected by means of vulcanization or gluing; number of elastomeric layers may be different, at least three. Reinforced elastomeric structures are able to endure high stress (>200 MPa) and they have many evident advantages: ease of maintenance, no necessity for lubrication, vibration and noise reduction, ability to work in a very dirty, dusty, abrasive environment, improving the dynamics of machines which provide

the properties of rubber and lack of clearances, as well as compensation of various skew distortions and inaccuracies in joint connection; smaller size, weight and cost [5] - [7]. Packages of thin-layered rubber-metal elements (further TRME) are successfully used as bearing, joints, dampers, compensating devices, shock-absorbers etc. Examples of elastomeric shock absorbers and TRME packages are presented in Fig. 1.

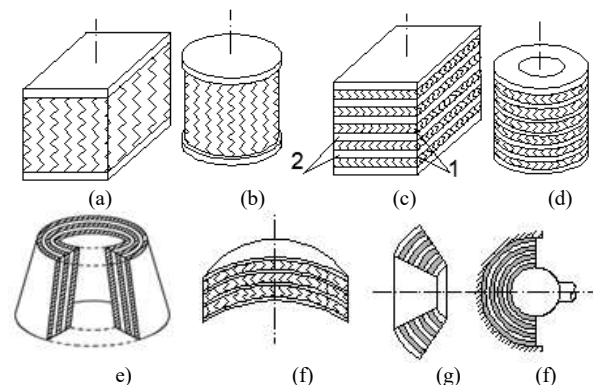


Fig. 1. Construction of typical elastomeric shock absorbers: (a) – rectangular prism, (b) – straight circular cylinder; blocks of TRME elements: (c) – rectangular, (d) – cylindrical form, (e) – conical form, (f) – spherical pad, (g) – spherical nozzle, (f) spherical hinge; 1 – rubber layer, 2 – metal layer.

Since many elastomeric and rubber-metal products, serving as elastic links, take up the impulsive load,

alternating-sign load, periodical and non-periodical high-frequency load, it is necessary to study the behaviour and the mechanical properties of rubber under dynamic loads. The most important characteristic of the service performance of rubber devices operating under conditions of repeated cyclic loading (alternate stress) in couplings, hinges, etc., is the ability to withstand mechanical actions for a long time, that is, fatigue endurance. The simplest and most reliable comparison of the service life with alternating stresses is the evaluation of the self-heating temperature, i.e. each specific temperature of self-heating corresponds to a concise lifetime.

It is also necessary to take into account the aging of material - changing its properties with time. When considering aging, it is assumed that the parameters of the model slowly change their properties. In this paper, it is proposed to account for the aging of rubber by multiplying the constants of material in Maxwell and Buzgers models by special functions and time. To determine slow processes (creep and relaxation), the best is considered the four-element Burgers model.

II. MATEARIALSS AND METHODS

A. Aging treatment of rubber-metal elements

Aging of the material is its properties ochanging in time under the influence of air or aggressive media. The duration of this process is very large even in comparison with the relaxation time. Therefore, accounting of aging is usually performed by a substitution of the empirically determined functions of time instead of material constants. To determine the slow processes (creep and relaxation), the differential relationships are used, which provide coincidence with the experiment. The four-elements model of Burgers is considered the best (Fig.2) [8] - [11].

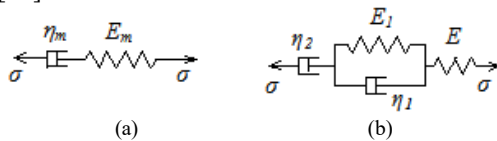


Fig. 2. Scheme of mechanical models of elastomers: (a) Maxwell model, (b) four-element Burgers model

For this model the relationship between stress and strain is expressed by the equation:

$$\frac{1}{E} \ddot{\sigma} + \left(\frac{1}{\eta_1} + \frac{1}{\eta_2} + \frac{E_1}{E\eta_1} \right) \dot{\sigma} + \frac{E_1}{\eta_1\eta_2} \sigma = \ddot{\varepsilon} + \frac{E_1}{\eta_1} \dot{\varepsilon}. \quad (1)$$

In the particular case if $\eta_1 = \infty$ Burgers model is transforming into Maxwell model, which quite well describes the creep before destruction.

$$\frac{\dot{\sigma}}{E_m} + \frac{\sigma}{\eta_m} = \dot{\varepsilon}. \quad (2)$$

When aging is taken into account in accordance with equations (1) or (2) it is assumed that the

parameters E, E_1, η_1, η_2 change their properties very slowly. To generalize the results, taking into account the temperature changing, the dependencies are at once given in the reduced time.

$$\begin{aligned} E(t_n) &= E\varphi_1(t_n), & E_1(t_n) &= E_1\varphi_2(t_n), \\ \eta_1(t_n) &= \eta_1\varphi_3(t_n), & \eta_2(t_n) &= \eta_2\varphi_4(t_n) \end{aligned} \quad (3)$$

The experiment confirms the possibility of taking an approximation:

$$\varphi_i(t_n) = 1 + A_i t_n. \quad (4)$$

For Maxwell model the relationships are

$$\begin{aligned} \frac{E_m(t_n)}{E} &= \varphi_{1m}(t_n) = 1 + A_m t_n \\ \frac{\eta_m(t_n)}{\eta} &= \varphi_{2m}(t_n) = 1 + B_m t_n. \end{aligned} \quad (5)$$

The value of Burgers model constants E, E_1, η_1, η_2 and corresponding them A_1, A_2, A_3, A_4 are estimated and tabularized for some kinds of rubbers, as well as value E_m, η_m, A_m, B_m for Maxwell model [7].

To obtain creep under the condition $\sigma = \sigma_0 = \text{const}$ assuming Maxwell model of rubber, if the stress is applied at time τ , the strain at time t is equal to:

$$\begin{aligned} \varepsilon(t, \tau) &= \sigma_0 \left[\int_{\tau}^t \frac{d\tau}{R_m(\tau)} + \frac{1}{E_m(\tau)} \right] = \\ &= \sigma_0 \left[\frac{1}{R_m B_m} \ln \left| \frac{1 + B_m t}{1 + B_m \tau} \right| + \frac{1}{E_m (1 + A_m \tau)} \right]. \end{aligned} \quad (6)$$

A1. Thin-layered rubber-metal vibration isolator

In order to trace how the age of rubber effect on the service properties of elastomeric devices we consider the damping properties of rubber shock absorber. This device serves occasionally for a short period of time, so the fatigue is not taken into account, for example, it may be seismic protector. In [12] the formulas are derived for the damping properties of vibroisolator under unilateral harmonic excitation (Fig.2).

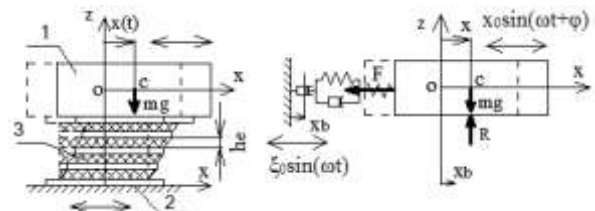


Fig. 3. Scheme of the object vibration with elastomeric shock absorber 1 – protected object, 2 – vibration base, 3 – vibroisolator

Damping properties are expressed by the ratio of amplitude of the driving vibration to the amplitude of the forced oscillations of object.

For Maxwell model of the elastomer we have [12]:

$$\frac{x_0}{\xi_0}(\omega) = \frac{\eta_m \omega_0^2}{\sqrt{E_m^2 \omega^2 + \eta_m^2 (\omega^2 - \omega_0^2)^2}}, \quad (7)$$

In case of aging taking into account equations (5):

$$\frac{x_{a0}}{\xi_0}(\omega) = \frac{\omega_{a0}^2}{\sqrt{\frac{E_m^2 (1 + A_m t_n)^2}{\eta_m^2 (1 + B_m t_n)^2} \omega^2 + (\omega^2 - \omega_{a0}^2)^2}}$$

$$\omega_{a0} = \omega_0 \sqrt{1 + A_m t_n} \quad (8)$$

For the case of resonance, i.e. $\omega = \omega_0$ without aging and with aging $\omega = \omega_{a0}$ from (7) and (8) it is obtained:

$$\frac{x_0}{\xi_0}(\omega) = \frac{\eta_m}{E_m} \omega, \quad \frac{x_{a0}}{\xi_0}(\omega) = \frac{\eta_m (1 + B_m t_n)}{E_m (1 + A_m t_n)} \omega. \quad (9)$$

For Burgers model of elastomer x_0/ξ_0 ratio received in [12] is equal:

$$\frac{x_0}{\xi_0}(\omega) = \frac{\omega_0^2}{\omega \eta_1} \sqrt{E_1^2 + \eta_1^2 \omega^2} \cdot \left[\left[(\omega^2 - \omega_0^2) - \frac{E_1 E}{\eta_1 \eta_2} \right]^2 + \left[\omega^2 \left[\frac{E_1 \omega_0^2}{\eta_1 \omega^2} - \left(\frac{E}{\eta_2} + \frac{E + E_1}{\eta_1} \right) \right]^2 \right]^{\frac{1}{2}} \right. \quad (10)$$

For the case of resonance if $\omega = \omega_0$ from (10) it is received:

$$\frac{x_0}{\xi_0}(\omega) = \frac{\omega \eta_2 \sqrt{E_1^2 + \eta_1^2 \omega^2}}{E \sqrt{E_1^2 + (\eta_1 + \eta_2)^2 \omega^2}}. \quad (11)$$

In order to take into account aging it is necessary to substitute into the equations (10) and (11) instead of constants E, E_1, η_1, η_2 expressions $E(t), E_1(t), \eta_1(t), \eta_2(t)$ in accordance with (3) and (4) and ω_{a0} instead of ω_0 . Since E is considered as initial modulus in Burgers model natural frequencies ω_0 and ω_{a0} are assumed:

$$\omega_0 = \sqrt{AE/mh}, \quad \omega_{a0} = \omega_0 \sqrt{1 + A_1 t_n}.$$

A2. Impact rigid body with rubber shock absorber

In this part the influence of aging on the restitution coefficient of rubber shock absorber is studied in case of direct central impact (Fig.4).

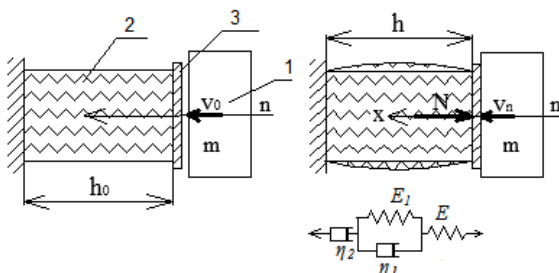


Fig. 4. Scheme of rubber shock absorber: 1 – impact body, 2 – rubber cylinder, 3 – reinforcing plate

After collision of body and rubber shock absorber they move together in x -direction till the velocity reaches zero value and then move in opposite direction till disconnection. Mass and deformation of reinforcing plate 3 are not taken into account. The equation of body motion during impact:

$$m\ddot{x} = -N = -\sigma A, \quad x = \varepsilon h = \varepsilon(h_0 - x), \quad (12)$$

where A – cross-section area of absorber.

Substituting equations (12) and corresponding derivatives from (12) into equation (1) it is obtained:

$$\ddot{x} + \left(\frac{E}{\eta_2} + \frac{E + E_1}{\eta_1} \right) \dot{x} + \left(\frac{E_1 E}{\eta_1 \eta_2} + \frac{EA}{m(h_0 - x)} \right) x + \frac{E_1}{\eta_1} \frac{EA}{m(h_0 - x)} x = 0 \quad (13)$$

Equation (13) is solved numerically under initial conditions: if $t=0, x=0, v=v_0, w_0=0$.

B. Fatigue and durability of TRME elements

The most important characteristic of TRME performance qualities, operating under conditions of repeated cyclic shear loading with simultaneous permanent action of the static load in the constructions of couplings, hinges, etc. is the ability to withstand mechanical influences for a long time, i.e. fatigue life.

Analysis of numerous experimental data shows that the frequency of dynamic loading for rubber, which varies in a not too wide range of practically realizable frequencies (10-100 Hz), does not (or has very little effect) on fatigue life at a constant temperature.

The testing of TRME was carried out at Moscow Scientific Research Institute VNIINMASH; when carrying out tests of TPME for fatigue life, only mechanical parameters were taken into account as variable parameters, all other test conditions (temperature, environmental composition) were considered as unchanged. TRME with flat layers (dimensions are given in Table I) were tested during the operation of the compensating coupling, the construction of which is shown in Fig. 5 [13].

The coupling consists of two half-couplings 1 and 2 and a cross slide block 3 with thin-layered rubber-metal elements 4 fixed on it (two identical elements were attached to each side of the slide block). The width of the groove formed by the outstanding cams 5 and 6 of the half couplings is less than the thickness of the slide block, and the cam 6 is divided by a slot 7 into an elastic 8 with a threaded hole 11 and a rigid 9 part with a cylindrical hole 10.

In these coaxial holes, a bolt 12 is installed during assembly, which, pressing the head into the rigid part

of the cam, presses the elastic part and the cross slide block freely enters the groove.

After removing the bolt 12, the elastic part of the cam compresses the rubber-metal elements. Then the

screws are inserted into the threaded elements, which, through the cam 6 and the gaskets, evenly increase the compression load of the TPME.

Table I
Testing elements dimension

Number of elements No	Thickness of one layer of rubber 8871, mm	Number of rubber layers, n items	Total thickness of rubber layers, mm	Thickness of one metal layer, mm
1	0.16	24	3.84	0.05
2	0.33	13	4.29	0.05
3	0.39	12	4.68	0.05
4	0.25	8	2.00	0.05
5	0.10	17	1.70	0.10
6	0.28	13	3.64	0.10
7	0.44	9	3.96	0.10

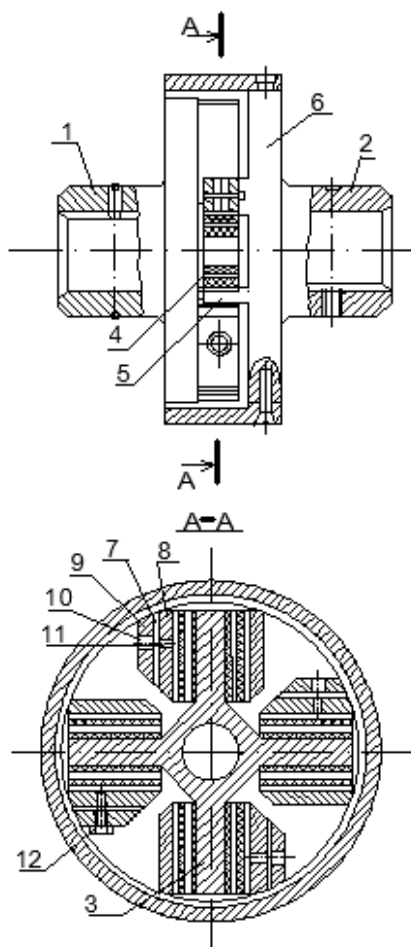


Fig. 5. Cross-rocker coupling: 1, 2 – half-coupling

The compression deformation was determined on an instrumental microscope after the final assembly of the coupling. The test showed that after the testing a strain remained unchanged in the range of 5-10%. The compression force P_z was determined according to the compression deformation by the previously obtained calibration curves (for all elements the compression force is equal 9-10 kN). For an equal area of all elements $A = 1.8 \text{ cm}^2$, the specific pressure p on the clutch cams is 50-55 MPa.

The coupling connected the drive shaft with the electric motor AO-42-4 ($N = 2.8 \text{ kW}$, $n = 1440 \text{ rpm}$) with a brake shaft that worked idly. Because of the radial misalignment between the two shafts e , artificially created with calibrated plates, placed under the feet of the electric motor, a shift of each rubber-metal element was created twice in one revolution or at a frequency of 50 Hz. The observed decrease of shear modulus by 8-10% compared to the initial one was the criterion of fatigue life of TRME; this decreasing is explained by the fact that under the action of intensive variable stresses in the rubber, the action of chemical and physical-mechanical processes slowly destroying the rubber structure and fatigue failure of rubber can occur in TRME.

Stresses reduction (relaxation) is the most obvious manifestation of the process of fatigue. This process is related to relaxation under static deformation and creep under static loading. After each stage of testing (a certain number of cycles N and the misalignment value e), the coupling was disassembled and the shear stiffness of the TRME was measured.

When the shear rigidity was reduced by not less than 8-10%, the relative deformation of the cyclic shear γ corresponding to a given number of cycles N was noted (Fig. 5). In the next stage new elements, in all respects identical, participated. The sequence and conditions of the experiment fulfilling may be seen from Table II. Analysis of the dependence of the relative shear strain γ on the number of cycles N shows that the number of cycles characterizing the working capacity of the TRME decreases with increasing of relative shear deformation (Fig. 5). Throughout all experiments the destruction of TRME was not observed. Experimental curve may be approximated by exponential curve or by logarithmical curve, the best coincidence gives logarithmical approximation, presented in Fig. 3, where approximate function is:

$$\gamma_a(N) = 0.966 - 0.128 \ln(N - 1.411) \quad (14)$$

where N - number of millions of cycles, γ - relative shear deformation.

Using dependence (14) it is possible to calculate the allowed relative share strain for laminated bearing.

When carrying out the second stage of fatigue life tests, one previously destroyed (when cutting) element No. 6 with partially peeled rubber was installed in the coupling. However, this element

worked normally during 20 mln of cycles with a relative shear deformation $\gamma = 0.274$ and $p = 55$ MPa, which proves the possibility of maintaining TRME operating capacity even under conditions of partial failure.

In whole, the experiment proved that TRMEs have a very high fatigue life (to 100 million cycles), which may be further improved when the manufacturing process will be improved.

Table II
 Relative shear deformation under different CONDITIONS

Number of elements No	Relative shear deformation γ under different value of misalignment e and number of cycles N					
	$e=0.5\text{mm}$ $N=20$ mln.	$e=1\text{mm}$ $N=20$ mln.	$e=2\text{mm}$ $N=1.1$ mln.	$e=2\text{mm}$ $N=1.4$ mln.	$e=2.5\text{mm}$ $N= 12$ mln.	$e=0.4\text{ mm}$ $N= 12$ mln.
1	0.13	0.26	0.52	-	-	-
2	-	-	-	0.47	0.58	0.435
3	-	-	-	0.43	0.535	0.835
4	0.25	0.5	1.0	-	-	1.1
5	0.294	0.59	1.17	-	-	-
6	0.137	0.274	0.55	0.55	0.686	1.1
7	-	-	-	0.505	0.63	1.01

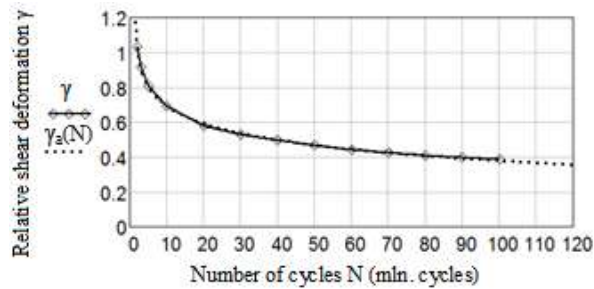


Fig. 5. Plot of dependence of the relative shear γ deformation on the number of cycles N : \diamond - experimental curve, - approximated curve.

B 1. Definition of fatigue life

The simplest and at the same time fairly reliable comparison of the service life with alternating stresses is the evaluation of the self-heating temperature. It means that each specific temperature of self-heating corresponds to a specific service life. For some grades of rubber these dependencies are tabulated [7].

The following dependence was experimentally established for the number of cycles N^* before failure:

$$N^* = N(W, T) = \left(\frac{W_p}{W} \right)^n, \quad (5)$$

where W_p - a specific work of material destruction; W - a specific potential energy; n - coefficient.

Specific work of material destruction is defined as

$$W_p = W_1 e^{-W_2 T}, \quad (6)$$

where T is the operating temperature, °C, W_1 and W_2 are tabular data.

For the rubber 8871 the values of coefficients in accordance with [7] are next: $W_1 = 46.4$ MPa·m³, $W_2 = 0.0261$ deg⁻¹, $n=2.94$. Assuming the operating temperature $T=80$ °C, from (6) specific work of material failure is received $W_p = 5.751$ MNm.

$$W = \frac{W_p}{\sqrt[n]{N^*}},$$

Plot of dependence the specific potential energy on critical number of cycles is presented in Fig. 6.

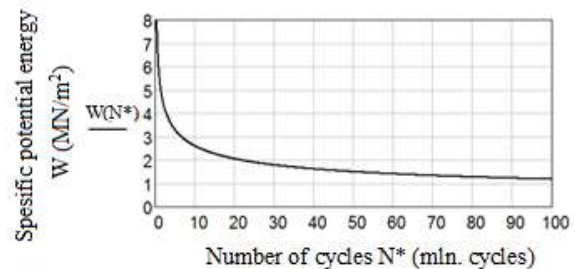


Fig. 6. Plot of dependence of specific potential energy on number of cycles before failure for rubber 8871.

III. RESULTS AND DISCUSSION

For numerical examples the rubber of grade 8871 was chosen, necessary data were taken from [7]. The constants and the aging coefficients for Maxwell model have the values: $E_m=1.23$ MPa, $\eta_m=1.16$ MPa, $A_m=0.65 \cdot 10^{-4}$ day⁻¹, $B_m=3.16 \cdot 10^{-4}$ day⁻¹. The constants of four-elements Burgers model are: $E = 1.63$ MPa, $E_1 = 5.09$ MPa, $\eta_1 = 36.3$ MPa, $\eta_2 = 1.16$ MPa, the aging coefficients: $A_1 = 0.81 \cdot 10^{-4}$ day⁻¹, $A_2 = 0.33 \cdot 10^{-4}$ day⁻¹, $A_3 = -0.24 \cdot 10^{-4}$ day⁻¹, $A_4 = 3.16 \cdot 10^{-4}$ day⁻¹.

The results of investigation of aging influence on damping properties of multilayered rubber-metal vibroisolator, shown in Fig.3, are presented in Fig.7-8. In Fig.7 the dependence of amplitude x_0/ξ_0 ratio on excitation frequency ω is given in accordance with Maxwell model, in Fig. 8 - in accordance with Burgers model. Time of aging is assumed three years.

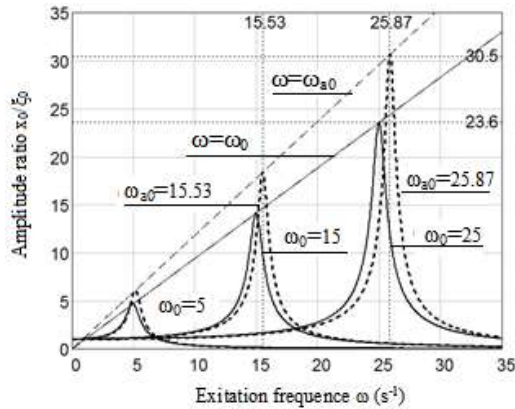
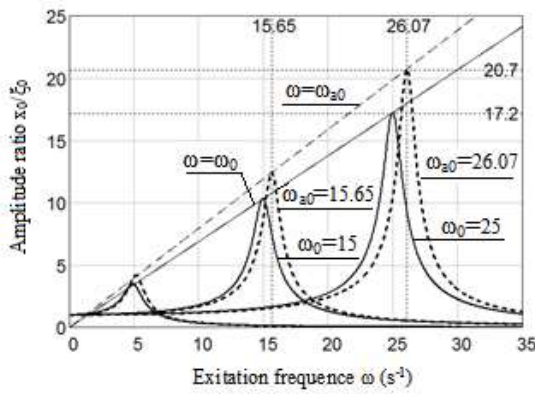
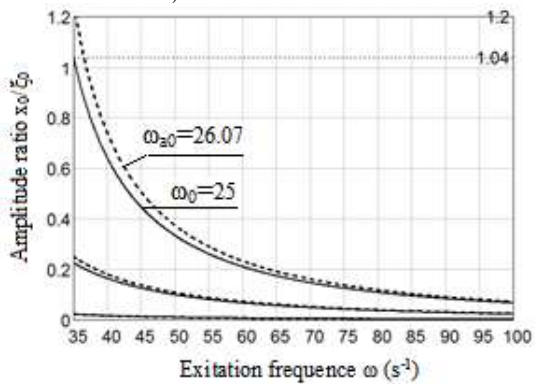


Fig. 7. Plots of dependence of the amplitude ratio x_0/ξ_0 on the excitation frequency ω for Maxwell model: — without aging, - - - taking into account aging 3 years.



a) from $\omega=0s^{-1}$ to $\omega=35s^{-1}$



b) from $\omega=35s^{-1}$ to $\omega=100s^{-1}$

Fig. 8. Plots of dependence of the amplitude ratio x_0/ξ_0 on excitation frequency ω for Burgers model: — without aging, - - - taking into account aging 3 years.

For both models three natural frequencies is examined: $\omega_0 = 5, 15, 25 s^{-1}$ without aging, which increase natural frequency. Burgers model shows better damping properties in comparison with Maxwell; the difference appear near resonance zone, in post-resonance zone (hear $\omega > 35 s^{-1}$) the results of both model are coincided.

For definition the aging influence on restitution coefficient (Fig. 4) body with mass $m=20kg$, colliding rubber 8871 cylinder $d=0.06 m$ $h=0.06 m$ with initial velocity $v_0=1 m/s$, is considered. Post-impact velocity for this size of shock absorbers is shown in Fig. 9, 10.

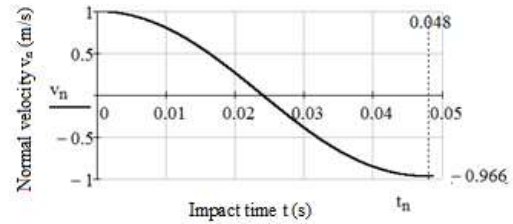


Fig. 9. Plot of dependence of impact velocity on time without aging

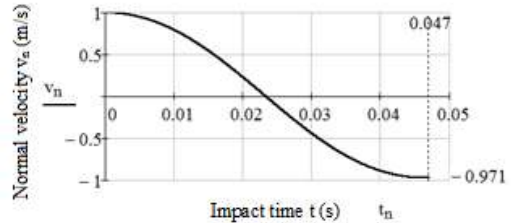


Fig. 6. Plot of dependence of impact velocity on time taking into account aging 3 years.

IV. CONCLUSIONS

In this paper the influence of aging on the working properties of rubber-metal shock absorbers is discussed. The changing of damping properties depending on aging for two mechanical model of elastomeric material is studied. The aging influence on restitution coefficient during impact was defined using Burgers model of elastomer. Fatigue life definition in under shear stress was performed by series of experiments. These experiments proved that TRMEs have a very high fatigue life.

REFERENCES

- [1] A. N. Gent, *Engineering with Rubber: How to Design Rubber Components*. Munich, Carl Hanser Verlag, 2011.
- [2] W. L. Hinks, Randolph Research Co. (RRC). *Laminated-rubber bearings: heavy duty composites for aerospace and undersea*. Presentation at the Spring 2013 183rd Technical Meeting of the Rubber Division of the American Chemical Society. [Online]. Available on: http://randolphresearch.com/LAMINATED%20Rubber%20Bearings%20Rubber%20Div%20paper_2_trim.htm
- [3] J. T. Bauman, *Fatigue, Stress and Strain of Rubber Components: Guide for Design Engineers*. Munich, Carl Hanser Verlag, 2008.
- [4] J. M. Kelly and D. A. Konstantinidis, *Mechanics of Rubber Bearings for Seismic and Vibration Isolation*. UK: John Wiley & Sons, 2011.
- [5] D. A. Konstantinidis and J. M. Kelly, *Advances in Low-Cost Seismic Isolation with Rubber. Proceedings of the 10th U.S. National Conference in Earthquake Engineering*, July 21-25, 2014, Earthquake Engineering Research Institute, Anchorage, Alaska, [Online]. Available on: <https://www.nees.org/resources/11388/download/10NCEE-000422.pdf>
- [6] V. A. Lepetov, *Rubber Technical Products. (Резинотехнические изделия)*. Moscow, Chemistry, 1972. (In Russian)
- [7] V. T. Lyapunov, E. E. Lavendel and S. A. Shlyapochnikov, *Rubber vibration isolators: Handbook. (Резиновые виброизоляторы: Справочник)* Leningrad: Sudostrojenie, 1988. (In Russian).
- [8] A. R. Bhuiyan; A. F. M. S. Amin; T. Hossain; and Y. Okui "Nonlinear viscosity law for rate-dependent response of high damping rubber: FE implementation and verification", in *Constitutive Models for Rubber V* – Boukamel,

- Laiarinandrasana, Meo & Verron (eds), Taylor & Francis Group, London, 2008, pp. 279 - 284.
- [9] V.N. Poturaev and V.I. Dyrda, *Rubber Machine Elements*. (Резиновые детали машин), Mashinostrojenie, Moscow, 1977. (in Russian)
- [10] A. R. Bhuiyan Y. Okui , H. Mitamura and T. A. Imaic, Rheology Model of High Damping Rubber Bearings for Seismic Analysis: Identification of nonlinear viscosity, *International Journal of Solids and Structures*. 46 (2009), 1778–1792, [Online]. Available on: <http://www.sciencedirect.com/science/article/pii/S0020768309000298>
- [11] A. A. Iljushin and B. E. Pobedrja, *Fundamentals of mathematical theory thermo-viscoelasticity*, (Основы математической теории термовязко-упругости), Nauka, Moscow, 1970.
- [12] S. Polukoshko, “Estimation of damping capacity of rubber vibration izolators under harmonic exitation.”, in “Vibroengineering Procedia”, Ortober 2016, Volume 8.,pp. 50-56.
- [13] N. S Gusyatinskaya, *Application of Thin Layered Rubber-Metal Elements(TRME) in Machine-Tools and Other Engines* (Применение тонкослойных резиноталлических элементов (ТРМЭ) в станках и других машинах). Mashinostroenie, Moscow, 1978. (In Russian).

Steam Explosion as a Pre-treatment Method for Bio-refined Hybrid Aspen Lignocellulose

Sanita Reinerte, Martins Andzs, Ramunas Tupciauskas, Andris Veveris, Janis Gravitis

Latvian State Institute of Wood Chemistry, Laboratory of Bio-refinery. Address: 27 Dzerbenes str., Riga, LV-1006, Latvia.

Abstract. Steam explosion (SE) is a well renowned pre-treatment method used for bio-refined material synthesis due to its simplicity in machinery and efficiency in resource and energy use in creation of high-value products. Used for separation of lignocellulose originated from wood and other sources, current research in wood-based lignocellulose has mainly focused in separation of wood fractions from commonly grown tree species. Scientific studies are needed for better understanding of common tree species to generate new possible products, e.g., bio-based composite materials.

Commercially grown hybrid aspen (*Populus tremuloides* x *Populus tremula*) was pre-treated by SE to obtain a nano-level structured cellulose and lignin for bio-based composite materials.

The results present a yield of extracted cellulose and lignin depending on SE conditions (severity factor) and subsequent water/alkaline extraction. Extractions have been executed with and without heat treatment. The research reveals a positive correlation between the yield of extracted lignin and SE severity factor, and a negative correlation for SE cellulose. The study concludes that SE hybrid aspen is proving to be a promising source for extraction of cellulose and lignin for bio-based composite materials.

Keywords: Bio-refinery, Green production, Hybrid aspen, Lignocellulose separation, Steam explosion.

I. INTRODUCTION

Bio-refinery as a process is a group of technologies where energy (heat, electricity, fuel), chemicals and materials (biodegradable polymers, composites and nanomaterials) are solely made from biomass [1]. Likewise, a biorefinery is a facility that integrates biomass conversion processes and equipment to produce fuels, power, and chemicals from biomass [2]. The main technologies to produce chemicals from biomass are [3]:

- biomass refining or pre-treatment;
- thermo-chemical conversion (gasification, pyrolysis, hydrothermal upgrading);
- fermentation and bioconversion;
- product separation and upgrading.

Steam explosion (SE) as a method belongs in the biomass refining or pre-treatment category, since it is used primarily for treatment of the material before any other physicochemical or chemical modifications. The lack of additional chemicals needed for wood fractionizing process – the wood is treated under pressurized high-temperature steam – makes SE a good addition to Green production technologies.

Today we have learned to efficiently use almost all of commercially grown tree species. However, new species introduced through either selection or genetic modification processes in industry give

opportunities for scientists to evaluate these species from multiple perspectives: environmental, ecological, use for energy purposes, new material synthesis etc. In this study a type of aspen hybrid named *Populus tremuloides* x *P. tremula* has been studied from biorefinery perspective through the use of SE pre-treatment process to evaluate if this aspen hybrid would be a good source for biorefined cellulose and lignin.

Hybrid aspen

Previous studies exclusively on *Populus tremuloides* x *P. tremula* in Latvia [4], Estonia [5] and Finland [6] reveal both industrial benefits in wood-based product creation and maintenance of balance in existing ecosystem if this aspen hybrid is introduced in environment as tree plantations, since it is well-suited for both climate conditions and neighboring tree species in these territories. However, being relatively new tree species, hybrid aspen for successful growing and harvesting still requires a development of suitable low-cost technologies for promoting thinning and mitigation options. Moreover, technology will have to be developed for making effective use of small wood, including thinned timber, in forest products and markets [7]. Thankfully, thinning and tree pruning for fuelwood and fodder are regularly conducted in many

developing countries as part of local integrated forest management strategies, therefore a plan of effective hybrid aspen use can be based on biologically similar tree species cultivation.

Hybrid aspen (*Populus tremuloides* × *P. tremula*) is suitable for short-rotation management in Northern Europe. It exceeds growth of both of its parent species (respectively, *Populus tremuloides* “Quaking aspen” and *Populus tremula* “European aspen”), as well as other forest tree species in the region, and in 20–25 year rotations in fertile sites, it has a mean annual increment of 20 m³ ha⁻¹ y⁻¹ [8], which is similar or slightly lower to that of other *Populus* hybrids [9]. In addition, modelling of climate-growth relationships has revealed a potentially beneficial effect of predicted climatic changes on the productivity of hybrid aspen [4] which is a promising aspect for balanced ecosystem creation while maintaining wood industry a profitable one. Therefore, on the basis of the evaluation of environmental interactions the potential risk of the influence of hybrid aspen plantations on the local environment is considered to be low [5].

The fast growth of *P. tremula* × *tremuloides* does not last more than ca. twenty years. During this period, the trees attain their final cutting size, whereas *P. tremula* appears to require 40–50 years of growth to reach the same dimensions. Therefore, the timings of different silvicultural management practices, such as cleaning of young stands, thinnings and final cutting, differ clearly between the two aspen species [6].

Steam explosion

Steam explosion auto-hydrolysis SE (also referred as steam explosion, steam explosion pulping, flash auto-hydrolysis or steam cracking) is principally a simple technique [10]. The first experimental SE device along with its working method for wood fiber defibrillation was invented by Mason in 1927 [11]. The biomass (wood or non-wood forest material, agricultural waste and fiber materials, waste from forestry, municipal and plantation management) in reactor is treated with saturated water steam in temperatures from 230°C to 260°C at pressures from 20 to 40 atmospheres followed by split second decompression to one atmosphere, causing the defibrillation of wood fibers [12]. The treatment time varies from seconds to minutes depending on the desirable products.

The aforementioned factors – temperature and exposure time – are the main variables for severity parameter or the reaction ordinate R_o . It can be expressed as [13]:

$$R_o = t * \exp [(T- 100)/ 14.75]$$

where: duration of treatment (t, min) and temperature (T, °C) express the set SE severity against the base temperature T_{base} or reference = 100°C. R_o dimension

is expressed in minutes, however, in practice $\log R_o$ is used.

II. MATERIALS AND METHODS

Hybrid aspen used in this study was collected from the Forest Tree breeding area in Latvian State Forest Research Institute “Silava”. The log (dimensions: length 17.5 cm x diameter 19.1 cm; total weight 1134.85 g; average moisture content (MC) 6.62 %; average dry weight (m_d) 1059.72 g) was rossed and chipped (chip dimensions: 2-3 cm x 0.5-1 cm). Before SE the MC of chips was increased to 20.0±1.0 % to facilitate the fractioning process of fibres during the treatment procedure in the reactor of SE machinery.

Working temperature of SE pre-treatment was chosen to be 235°C since the process literature [14] states that 234°C is an optimum temperature for achieving desirable properties such as SE lignin solubilization and enzyme accessibility of the cellulose.

Each batch of wood chips was measured by volume in 0.5 L cup before dispersed in SE reactor and pre-treated with settings shown in Table I.

Table I
Steam explosion process parameters

Sample label	Time, min	Temperature, °C	Pressure, bar	$\log R_o$
SE1	1	235	32	3.97
SE2	2	235	32	4.28
SE3	3	235	32	4.45
SE4	4	235	32	4.58
SE5	5	235	32	4.67

The extracted material was collected and dried until moisture levels were constant. The MC of pre-treated fractions was determined with a Moisture Analyzer Precisa 330 XM 120-HR (capacity 124g; readability 0.1mg/0.001%). For water and alkaline extractions samples from each batch of steam exploded mass were prepared by weighting 20.00 g of dry weight SE mass (Table II).

Table II
Weighted se samples for extractions

Sample label	m_d , g	MC, %	m, g
SE1	20.00	4.10	20.86
SE2	20.00	3.69	20.77
SE3	20.00	3.11	20.64
SE4	20.00	2.57	20.53
SE5	20.00	2.09	20.43

Among the various chemical pre-treatments, alkali pre-treatment is the most widely used method to enhance the enzymatic hydrolysis of various lignocellulosic biomasses. Sodium, potassium, calcium and ammonium hydroxides are the frequently used reagents for the alkaline pre-treatment. Among

these, sodium hydroxide (NaOH) has received the greatest attention due to its out-standing delignification capacity which is essential to achieve high biomass digestibility [15].

For water extraction the SE mass was suspended in 0.5 L of distilled water for water-soluble component extraction – suspension was left to sit for 24 h, filtered using vacuum filtration (pore size 388 µm) and collected – steps repeated in total of 4 times. For the experimental heat treatment suspensions were heated for 1 h in 98±2°C – before heating solution was left to sit for 24 h – filtered (pore size 388 µm) and collected. The treated mass was filtered using vacuum filtration (pore size 388 µm) and dried until moisture levels were constant.

For alkaline extraction the collected lignocellulose mass was suspended in 0.5 L of 0.4 %/ 1 M NaOH solution for alkaline-soluble component extraction. Extraction and filtering processes were done the same as water extraction for both heat treated and non-heated suspensions.

For SE lignin collection the alkaline extract was neutralized with 0.01 L 37 % hydrochloric acid HCl and left to sit for 24 h for lignin sedimentation [16]. The SE lignin was filtered using vacuum filtration (pore size 90 µm), washed with equal amount of distilled water to that used in lignin sedimentation and dried until moisture levels were constant.

III. RESULTS AND DISCUSSION

The results shown in Table III and Table IV illustrate how the various severity factors (Table I) of SE biorefinery process affected the original hybrid aspen sample and how much difference it caused to subsequent water and alkaline extractions for lignocellulose separation from water-soluble components and further cellulose and lignin separation.

Table III
Hybrid aspen mass changes after se pre-treatment

Sample label	Raw material		Pre-treated material			
	m, g	MC, %	m _d , g	m, g	MC, %	m _d , g
SE1	191.16		154.00	155.10	4.28	148.46
SE2	186.12		150.55	106.88	2.77	103.92
SE3	192.74	19.44	155.90	122.22	3.21	118.29
SE4	193.62		155.98	110.37	2.64	107.45
SE5	190.24		153.26	107.62	2.13	105.33

Figure 1 shows visual comparison of untreated and SE samples.



Fig. 1. Visual comparison of untreated and SE samples

Figures 2, 3 and 4 show how the experimental application of heat during both water and alkaline extractions affected the final outcome of water-soluble component extraction from SE mass for lignocellulose obtainment as well as extracted cellulose and lignin mass compared to the respective severity factor of the sample.

SE increases the calorific value of biomass due to removal of moisture and volatile components and the thermal degradation of hemicelluloses [1] – this results in a loss of hybrid aspen mass introduced in SE reactor (Table II). The carbon content of the biomass increases, oxygen and hydrogen are removed from the biomass – the visual effect visible in Figure 1 – resulting in SE biomass to appear and develop more “coal-like” characteristics.

It appears that heating SE mass solution during water extraction has produced more refined lignocellulose (Fig. 2), since, compared to non-heated samples, the dry weight lignocellulose masses on the same starting weight (20.00 g) are smaller – extracted solutions must have contained more water-soluble components than those in non-heated extracts. Further analyses are needed to confirm the hypothesis.

As the SE mass collection and extractions require a large input from human work – accuracy in sample measurement, extracted mass collection – in perfect conditions the coefficient of determination R² would be close to 1, but the tiny amounts of sample masses lost during product collection from SE reactor and extractions gradually accumulate, resulting in uneven values in graphs, but still showing a visible trend in said values.

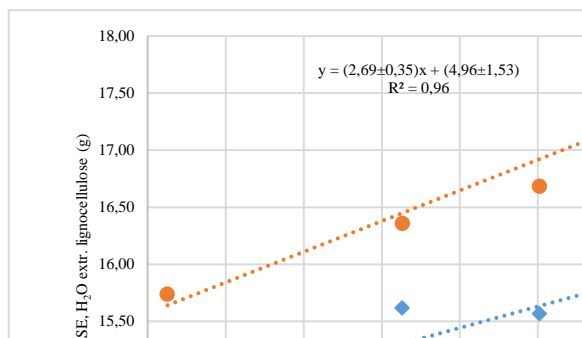


Fig. 2. SE lignocellulose mass change dependence on severity factor

The graphs for cellulose (Fig. 3) and lignin (Fig. 4), however, reveal a very interesting aspect of solution heating during alkaline extraction. The start amount of lignocellulose is roughly the same, but the extracted cellulose and lignin masses reveal a trend of

difference between cellulose and lignin separated masses in case of heat application.

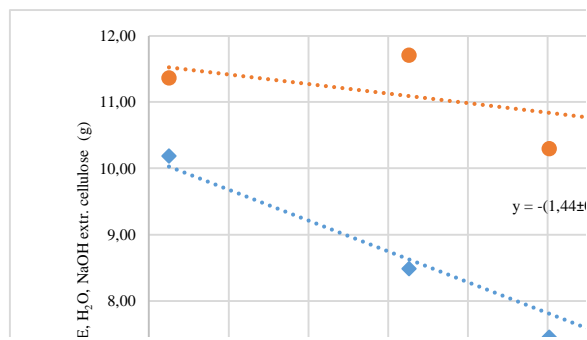


Fig. 3. SE cellulose mass change dependence on severity factor

Table IV
Lignocellulose, cellulose and lignin masses after water, alkaline extractions

Lignocellulose m, g	MC (LC), %	Lignocellulose m _d , g	Cellulose m, g	MC (C), %	Cellulose m _d , g	Lignin m, g	MC (L), %	Lignin m _d , g
With heat treatment								
15.36	5.20	14.56	11.15	8.62	10.19	3.35	4.89	3.18
16.53	5.52	15.62	9.23	8.00	8.49	4.25	4.91	4.04
16.41	5.14	15.57	8.14	8.49	7.45	5.69	5.04	5.40
16.83	4.78	16.02	8.14	7.66	7.51	6.45	4.90	6.13
16.59	4.59	15.82	7.40	7.47	6.85	7.30	4.95	6.94
Without heat treatment								
16.53	4.79	15.74	11.93	4.75	11.36	3.16	4.69	3.01
17.19	4.84	16.36	12.29	4.73	11.71	3.42	4.98	3.25
17.45	4.38	16.69	10.77	4.42	10.29	4.88	5.08	4.63
18.07	3.44	17.45	11.01	3.86	10.58	4.96	4.92	4.72
18.23	3.72	17.55	11.15	4.04	10.70	5.36	4.87	5.10

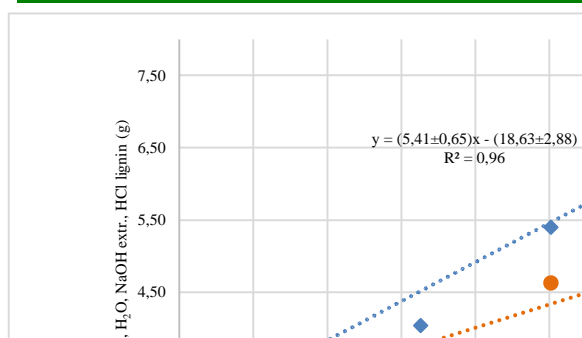


Fig. 4. SE lignin mass change dependence on severity factor

In non-heated separation cellulose in every SE setting has little differences in mass changes – less than 6% of mass difference between SE 1 min and SE 5 min cellulose. Non-heated lignin mass appears to increase as severity factor increases (positive change in nearly 70% of mass difference between SE 1 min and SE 5 min).

Compared with non-heated cellulose and lignin, cellulose and lignin from heated alkaline solutions show a more distinguished patterns in separation – a negative correlation for cellulose (more than 30% of

mass difference between SE 1 min and SE 5 min) and a positive one for lignin (nearly 120% of mass difference between SE 1 min and SE 5 min). The confirmation of a more purified cellulose from heat treatment must be proven with further testing – an evaluation of residual lignin content in SE cellulose for both heated and non-heated samples.

It is possible that mimicking the conditions from steam explosion process, in which the lignocellulosic mass is originally separated to micro- and nano-size fiber particles, helps the removal of water-soluble components from SE lignocellulose mass and creates better conditions for separation of SE cellulose and SE lignin during extractions. An explanation of this phenomena could be both higher solubility of caramelized hemicelluloses and other hardly water-soluble components at room temperature (22.0±0.5°C) from SE mass during water extraction and the structural changes of lignin when subjected to SE treatment – smaller molecular weights, narrow polydispersity, less phenolic -OH groups, lower syringyl/guaiacyl ratios and lower amounts of substructures – making SE lignin an entirely different substance than milled wood lignin [17]. Therefore, a

recreation of these conditions, even small-scale like heating of suspension, stimulates SE cellulose and SE lignin to be more inclined to separate in extraction processes.

In literature there is not a lot information about the chemical content of hybrid aspen. For purposes of evaluating SE effectiveness in biomass separation a comparison between SE hybrid aspen and milled hybrid aspen wood was created (Table V). Data for milled hybrid aspen wood were taken from Latvian State Institute of Wood Chemistry.

TABLE V
COMPARISON OF HYBRID ASPEN CHEMICAL CONTENT

Poly.	Lit. (av.)	Std. Dev.	SE (av.)	Diff. f. lit. (max)	SE (av.), +T	Diff. f. lit. (max)
C, %	51.9124	±1.5393	54.65	+1.20	40.49	-9.89
L, %	19.263	±1.176	20.71	+0.27	25.70	+5.25

The comparison of cellulose and lignin in Table V is a rough one because milled wood cellulose and lignin differs in physical characteristics and chemical properties when compared with SE cellulose and SE lignin. The separation processes of cellulose and lignin for milled wood is also different, thus further compromising an objective comparison. However, some observations can be explained with evidence from SE biomass studies.

The non-heated SE cellulose and SE lignin results are very similar to milled wood cellulose and lignin, both having slightly larger amount of extracted mass. Yet previously analyzed heat-treated SE cellulose and SE lignin results, based on hypothesis about similar-to-SE-extraction-conditions argue that the actual amount of obtained SE cellulose must be smaller than extracted from non-SE wood. A study for steam-exploded and alkaline delignified sugarcane bagasse confirms a loss of cellulose can occur during SE and extraction processes up to 22% due to degradation of carbohydrates and washout during washing of the solid fractions [18] which is the most reasonable explanation for smaller final SE cellulose mass compared to milled wood cellulose. The residual lignin content in SE cellulose can be determined by purifying SE cellulose to chemically clean cellulose and calculate the difference in mass.

The 5% greater heat-treated SE lignin value, being average over SE1 to SE5 lignin values, is concerning, since normal lignin values for deciduous trees stem wood grown in temperate-zones are between 20-25%, though it is unknown how old was the hybrid aspen tree from which milled wood sample was made, since lignin content in wood varies based on the age of tree. The other explanation for this would be the mass of "heat-treated SE lignin" contains additional products from SE and water/alkaline extractions, which are insoluble in solutions with pH<6. Further analysis is needed for confirmation, a possible method being use of known

lignin-selective solvents (e.g., acetone/water or acetone/ethyl acetate) to dissolve extracted SE lignin until the hypothetical insoluble fraction remains that ideally would be the same mass as the difference between extracted SE lignin and maximum milled hybrid aspen wood lignin mass. Spectroscopical methods would be used for initial qualitative analysis of SE insoluble lignin fraction, followed by analytical quantitative chemical analysis.

IV. CONCLUSION

The study concludes Hybrid aspen tree can be a good source for cellulose and lignin production from wood lignocellulose.

Comparison of dry mass of extracted SE cellulose and SE lignin reveals a positive correlation between extracted steam-exploded lignin and severity factor increase, and a negative correlation for steam-exploded cellulose.

Heat treatment has been beneficial in both water and alkaline extractions – the yield of SE lignin is higher compared to non-heated SE lignin while SE cellulose in appearance is lighter colour (less residual lignin) than non-heated SE cellulose.

Imitation of SE conditions – the aforementioned heat application during extractions – alleviates the separation of SE cellulose and SE lignin.

Further analyses are needed for determining residual lignin content in SE cellulose to confirm the effectiveness of heat application in lignin extraction process. Likewise, an evaluation of water-soluble component content in water extracts are needed to confirm the effectiveness of heat application in hemicellulose and other water-soluble component extraction process.

ACKNOWLEDGMENTS

This study was supported by Latvian State Institute of Wood Chemistry under the National Research Programme "Forest and earth entrails resources: research and sustainable utilization – new products and technologies" (ResProd)" Project Nr.3 "Biomaterials and products from forest resources with versatile applicability". As well the study was supported by the ERIFORE project of HORIZON 2020, ref. 654371.

REFERENCES

- [1] W. Stelte, "Steam explosion for biomass pre-treatment," Danish Technological institute, Taastrup, Denmark, 2013.
- [2] J. Gravitis, "Zero techniques and systems – ZETS strength and weakness," J. of Clean. Prod., vol. 15, pp. A1190-A1197, 2007.
- [3] A. Demirbas, "Biorefineries: Current activities and future developments," Energy Conv. & Manag., vol. 50, pp. A2782-A2801, 2009.
- [4] J. Smilga, "Profitability of hybrid aspen breeding in Latvia," Agro. Res., vol. 13, pp. A430-A435, 2015.
- [5] H. Tullus, "Hybrid aspen plantations: a new tree for energy and pulp in boreal Estonia," presented at European Forest Network meeting, Reykjavík, Iceland, 2009.

- [6] H. Heräjärvi and R. Junkkonen, "Wood Density and Growth Rate of European and Hybrid Aspen in Southern Finland," *Baltic Forestry*, vol. 12, pp. A2–A8, 2006.
- [7] S. Kellomäki and A. Kilpeläinen, Eds., *Forest BioEnergy Production: Management, Carbon sequestration and Adaptation*. New York: Springer Sc. & Business Media, 2013, p. 268
- [8] L. Rytter, and L.G. Stener, "Productivity and thinning effects in hybrid aspen (*Populus tremula* L × *P. tremuloides* Michx.) stands in southern Sweden," *Forestry*, vol. 78, pp. A285–A295, 2005.
- [9] A. Jansons, "Productivity of poplar hybrid (*Populus balsamifera* × *P. laurifolia*) in Latvia," *Agro. Res.*, vol. 12, pp. A469–A478, 2014.
- [10] J. Abolins, "Energy from biomass for conversion of biomass," *Latvian J. of Phys. & Tech. Sc.*, vol. 5, pp. A16–A23, 2009.
- [11] W.H. Mason, "Pulp and board from steam exploded wood," *Paper Trade J.*, vol. 84, pp. A131–A136, 1927.
- [12] G. Zakis, *Basics of Wood Chemistry (latv. Koksnes ķīmijas pamati)*. Rīga: Latvian State Institute of Wood Chemistry Press, 2008, p. 199
- [13] R.P. Overend, "Fractionation of Lignocellulosics by steam aqueous pretreatments,"; *Phil. Trans. of The Royal Society A*, vol. 321, pp. A523–A536, 1987.
- [14] R.H. Marchessault, "Characterization of aspen exploded wood lignin," *Can. J. Chem.*, vol. 60, A2372–A2382, 1982.
- [15] J. Singh, "Augmented digestion of lignocellulose by steam explosion, acid and alkaline pretreatment methods: A review," *Carbohydr. Poly.*, vol. 117, pp. A624–A631, 2015.
- [16] V. Perelmans, *A Short Handbook for a Chemist (in Latvian: Ķīmika īsa rokasgrāmata)*. Rīga: Liesma, 1965, p. 550
- [17] M. Zhu, "Structural changes in lignin during integrated process of steam explosion followed by alkaline hydrogen peroxide of "Eucommia ulmoides" Oliver and its effect on enzymatic hydrolysis," *Appl. Energy*, vol. 158, pp. A233–A242, 2015.
- [18] G. J. M. Rocha, "Mass balance of pilot-scale pretreatment of sugarcane bagasse by steam explosion followed by alkaline delignification," *Biores. Tech.*, vol. 111, pp. A447–A452, 2012.

A Novel Method for Birch Outer Bark Quality Control Using Higher Heating Value

Janis Rizhikovs¹, Aigars Paze¹, Ance Plavniece¹, Kristaps Stankus², Inguss Virsis²

Latvian State Institute of Wood Chemistry, 27 Dzerbenes street, Riga, LV-1006, Latvia¹

Latvijas Finieris AS, 59 Bauskas street, Riga, LV-1004, Latvia²

Abstract. In plywood plants, the bark of a birch tree is a readily accessible and already concentrated feedstock for further processing. It consists of two distinct layers: outer bark and inner bark. Up to 25.7 % of biologically active compounds (betulin, lupeol, betulinic acid) are concentrated in outer bark, with a broad spectrum of applications in the chemical, pharmaceutical, cosmetic and food industries. The inner bark must be separated from outer bark as well as possible because it causes a decrease in the yield and purity of the prepared ethanol extractives. Therefore, it is very important to predict the content of inner bark in the feedstock taken for the extraction process.

A novel method for the characterization of feedstock was developed using the higher heating value (HHV) as a reference. The developed method for birch outer bark quality control is very useful in birch outer bark extraction plants. Thus, it would be possible to control the purity of the feedstock and to predict the potential yield of extractives as well as the amount of the solvent to be taken for the extraction process. Pure enough (≥ 90 % of outer bark) feedstock for biologically active extractives production can be obtained by the floating method after 5 h if the HHV is more than 32-33 MJ/kg.

Keywords: Birch bark, feedstock quality, polysaccharides, higher heating value.

I. INTRODUCTION

Birch wood in the Northern hemisphere is widely used in the furniture, pulp and plywood manufacture. 2 % of veneer blocks' mass is made up of birch outer bark (BOB) [1]. It is readily accessible and already concentrated for further processing. In the concept of the circular bio-economy, it is necessary to upgrade the by-products generated in the processing of forest products. In this context, birch plywood, furniture or pulp plants are well established industrial enterprises that generate known amounts of birch bark residues, which could have considerable value as a feedstock for the production of higher added value products, for example, triterpene rich extractives [2], [3]. Pentacyclic lupane type triterpenes (betulin, lupeol, betulinic acid) are promising starting materials for the synthesis of biologically active compounds with a broad spectrum of medical applications [4]. Additionally, after triterpene extraction, the remaining biomass can still be used for the production of other products from suberin – individual suberinic acids for macromolecular materials [5] or as a hydrophobic binder for particleboards [6]. It is known that valuable triterpenes and suberin are concentrated in BOB, up to 27 % [3] and 45 % [2], respectively. Birch inner bark (BIB) has a completely different chemical composition (Table I), especially regarding the

content of carbohydrates and hot water extractives [7], [8].

Table I
Chemical Composition of Birch Bark Constituents Calculated on the Oven-dry Mass

Value	BOB	BIB	Ref.
Carbohydrates (%)	4.4-10.4	45.2-55.0	[2,7-9]
Ash (%)	0.3-1.0	1.5-2.4	[2,8,9]
Organic solvent extractives (%)	29.1-40.0	9.0-15.8	[2,8,9]
Hot water extractives (%)	0.9	19.3	[8]
Suberin - NaOH soluble extractives (%)	34.5-45.0	25.2-25.5	[2,8,9]
Lignin (%)	2.2-9.0	9.1-18.1	[2,8,9]
HHV (MJ/kg)	34.1	21.1	Table II

The above-mentioned substances may cause a decrease in the yield and triterpenes content in the obtained extractives if BIB and woody admixtures are present in the feedstock. Therefore, it is very important to predict the content of BIB in the feedstock taken for the extraction process.

The main aim of the study was to develop an appropriate and precise BOB quality controlling method. Therefore, two different BIB and BOB analysis methods were used, which could serve on an industrial scale:

1) Easily- and hardly hydrolysable polysaccharides (EHP and HHP) due to the difference of BIB and BOB in carbohydrates;

2) Higher heating value (HHV) because that for BOB is 1.5 times higher and HHV for BIB is similar to that of wood.

II. MATERIALS AND METHODS

A. Feedstock

Birch bark, left over at a plywood factory in Latvia, was selected as a representative industrial waste with the relative moisture content 35-40 %. The collected feedstock was dried at room temperature to a moisture content of 4-7 % and milled in a cutting mill SM 100 (Retsch GmbH & Co) to pass the sieve with holes of diameter 2.00 mm.

Milled dry birch bark samples were soaked in deionized water for 48 h by occasional mixing. Birch outer bark, floated to the top of the water surface (BOBF), was collected and used as a reference raw material for the pure BOB sample. To determine the optimal floating time and suitability of the above-mentioned BOB control method based on HHV, a flotation experiment was carried out, in which dry birch bark (200 g) was soaked from 15 min to 48 h by occasional mixing (bark/water hydro modulus 1/5). After flotation, BOBF was dried to a moisture content of 4 % for further operations. The BIB, which sank to the bottom, was collected and dried to a moisture content of 7 % for further operations. For elemental and HHV analysis needs, the samples were additionally ground to the particle size below 0.5 mm directly prior to analyzing.

For EHP and HHP analysis, the collected birch bark was separated from the BIB by hand to prevent the leaching of polysaccharides during the flotation.

B. Analytical Methods

Moisture and ash content was determined according to EN 14774 and EN 14775 standards, respectively.

Elemental analysis was performed according to EN 15104 on an Elementar Analysensysteme GmbH – vario MACRO CHNS Element Analyzer – an analyzer used for the determination of C, H and N in solid and liquid samples, using a thermal conductivity detector.

The content of EHP was determined by mild hydrolysis of approximately 5.0 g of the sample with 2 % HCl for 3 h. The hydrolyzed sample, after EHP analysis, was further hydrolyzed by 80 % H₂SO₄ for 5 h and the content of HHP was determined [10].

HHV was determined according to the EN 14918 standard. Measurements were performed on a “Parr” Oxygen Bomb Calorimeter, in which approximately 1.0 g of an oven-dried birch bark sample was completely combusted under a pressurized (3000 kPa) oxygen atmosphere. The rise in temperature of the cylinder allows the calculation of the calorific value when the exact weight of the sample is known.

The net calorific value was calculated on a dry basis (MJ/kg) to compare the samples.

All analyses were performed in triplicate, and their average values did not exceed a 1.0 % variation.

C. Experimental Procedure

At first separated by hand, milled dry birch outer (BOBH) and inner (BIBH) bark samples were mixed together in five proportions (0, 30, 50, 70 and 100 % of the BIB admixture calculated on the oven-dry mass) for EHP and HHP analysis, and for creation of a calibration curve. When the more precise HHV method was chosen, additional points in the curve were added (10, 20, 40, 60, 80 and 90 % of the BIB admixture), the prepared barks’ mixture samples were analyzed and a calibration curve was created.

III. RESULTS AND DISCUSSION

A. Easily- and Hardly-hydrolyzable Polysaccharides

As mentioned in the introduction, valuable triterpenes are concentrated in BOB. The purity of BOB depends on the separation methodology, as well as the starting feedstock’s composition (admixture of BIB, woody particles). Therefore, it is very important to predict the content of BIB in the feedstock taken for the extraction process.

Because BOB has a very low content (4-10 %) of total sugars (carbohydrates) [2], [8], [9], but BIB has a relatively high content (45-55 %) of carbohydrates [7], [8], our first idea was to use this difference between these two representative parts of birch bark for determining its purity.

Mixed BIBH/BOBH samples in five proportions, as described in the experimental section, were prepared. The content of EHP and HHP was determined. The obtained results are shown in Fig. 1. Both EHP and HHP content logically increases with increasing BIBF proportion in the sample.

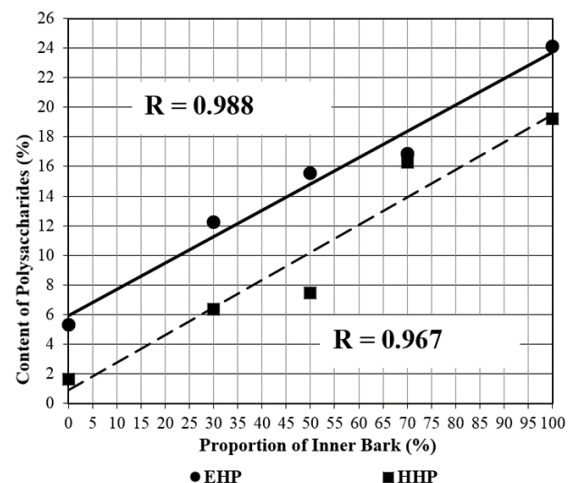


Fig. 1. Calibration curves for the content of easily- and hardly-hydrolyzable polysaccharides in the prepared birch bark mixtures.

It can be concluded that the EHP content shows better correlation (R=0.988) than the content of HHP (R=0.967), and the method for determining the EHP

content is less time-consuming. Still, the method has some disadvantages, which were observed during the research.

It is very difficult to obtain 100 % pure BOB if separated mechanically – by hand or by winnowing. Fig. 1 shows that the total content of EHP and HHP in pure BOBH is already 6.9 % (5.3 % + 1.6 %), and it is reported in the available literature that the content of carbohydrates can vary in the range of 4.4-10.4 % (Table I), which means that there are some BIB admixtures left after mechanical separation.

It is possible to obtain pure BOB by the floating method, but then it is difficult to calibrate EHP because, during the floating in a water environment, about a half of EHP could be leached off from BIB. Besides, there are also woody particles in the BOB and as we know, the EHP content in the birch wood (up to 28 % [11]) is higher than that in BIB (24.1 %). Of course, it is possible to make some assumptions but it will not improve the obtained results, and the controlling process of the BOB quality will not be precise enough.

B. Higher Heating Value and Elemental Composition

The above-mentioned obstacles (leaching of polysaccharides from BIB, non-homogeneous admixture composition) enabled us to find some properties which would not have so many variables depending on the BOB separating methodology. During the routine BOB and BIB analysis, a parameter – HHV – was revealed. It can be seen from Table II that HHV for pure BOB was more than 1.5 times higher than that for BIB calculated on the oven-dry mass. In addition, HHV for birch wood was close to that for BIB. This gave a hope that it would be possible to obtain a more precise calibration curve for controlling the BOB purity.

There are some differences between BOB samples depending on the separation method. The highest HHV was for BOBF – 34.1 MJ/kg; therefore, this was chosen as a reference feedstock for pure BOB in the calibration experiments. BIBH was chosen as a representative of the 100 % admixture because its HHV (21.1 MJ/kg) was almost the same as for birch wood (21.2 MJ/kg). This means that the origin of the admixture – BIB or wood particles – will not affect the HHV.

Table II
 Higher Heating Value and Ash Content of Birch Log Components
 Calculated on the Oven-dry Mass

Sample	HHV (MJ/kg)	Ash content (%)
Birch wood (BW)	21.2 ± 0.0	0.4 ± 0.0
Birch bark (BB)	26.0 ± 0.1	1.0 ± 0.0
Inner bark (floating) (BIBF)	21.5 ± 0.0	2.4 ± 0.1
Inner bark (by hand) (BIBH)	21.1 ± 0.1	2.4 ± 0.1
Outer bark (floating) (BOBF)	34.1 ± 0.0	0.5 ± 0.0
Outer bark (by hand) (BOBH)	32.2 ± 0.1	1.0 ± 0.0
Outer bark from log (BOBL)	33.3 ± 0.0	0.3 ± 0.0

Table III
 Elemental Composition of Birch Log Components

Sample*	C (%)	N (%)	H (%)	O (%)**
BW	48.9 ± 0.1	0.2 ± 0.0	5.0 ± 0.1	46.0 ± 0.2
BB	67.5 ± 0.1	0.5 ± 0.0	6.0 ± 0.1	26.0 ± 0.1
IBF	52.7 ± 0.1	0.5 ± 0.0	5.3 ± 0.3	41.5 ± 0.2
IBH	52.4 ± 0.3	0.5 ± 0.0	5.2 ± 0.2	41.9 ± 0.2
BOBF	71.3 ± 0.1	0.4 ± 0.0	8.5 ± 0.1	19.7 ± 0.1
BOBH	70.4 ± 0.2	0.5 ± 0.0	6.3 ± 0.1	22.9 ± 0.1
BOBL	70.9 ± 0.1	0.4 ± 0.0	7.4 ± 0.1	21.3 ± 0.1

* Abbreviations are explained in Table II

** By difference

The BIBF obtained after floating has a close enough HHV (21.5 %), but still somewhat higher because of some BOB particles sediment together with the BIB fraction.

BOBL was collected from a birch log before the soaking operation in a plywood factory. This sample showed that, after soaking and floating operations, small amounts of EHP were extracted, which led to an increase in HHV.

The elemental composition shown in Table III testifies the above-mentioned facts. The HHV of BOB is higher than that of BIB because it has a higher content of carbon and hydrogen, as well as a lower content of oxygen due to a lower amount of carbohydrates in the structure.

After the decrease of oxygen, also HHV can be prognosticated because that for BIB samples is approximately 1.5 times higher than for BOB samples.

C. Calibration Curve of HHV

In the light of known facts, the calibration curve for the characterization of the feedstock was developed using HHV as a reference to determine the content of the pure BOB (Fig. 2).

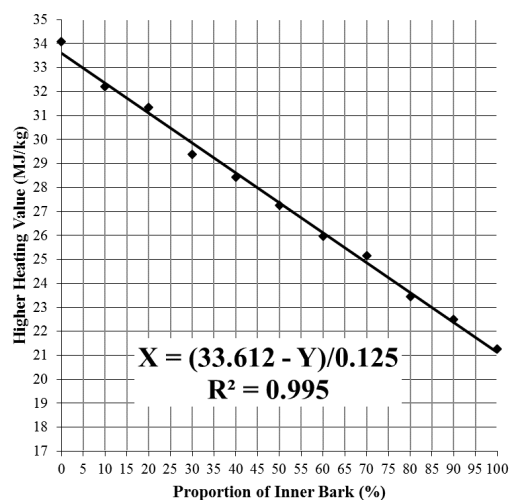


Fig. 2. Calibration curves for the HHV in the prepared birch bark mixtures.

HHV increases with the increase of the BOB proportion in the sample. Such a method turned out to be more accurate ($R=0.995$) and faster (45 min). Obtained equation of the calibration curve allow

calculating the amount of impurities, depending on the calorific values determined experimentally.

D. Impact of the Floating Time on HHV

To determine the optimal floating time, an experiment was carried out, in which equal dry birch bark samples were soaked in distilled water and the HHVs were determined as a reference for pure BOBF. Experimental results are shown in Table IV.

Table IV
Impact of the Floating Time on the Yield and Higher Heating Value of Birch Outer Bark

Floating time (h)	Floating yield (% dry mass)	HHV (MJ/kg)
0 (BB)	100	26.0 ± 0.1
0.25	52.3 ± 0.1	29.4 ± 0.1
1	48.0 ± 0.1	30.8 ± 0.0
3	43.2 ± 0.0	31.3 ± 0.1
5	39.5 ± 0.1	32.2 ± 0.0
12	38.7 ± 0.1	32.5 ± 0.1
24	36.9 ± 0.1	33.5 ± 0.0
48 (BOBF)	35.4 ± 0.1	34.1 ± 0.0

It is obvious that, with increasing floating time, the yield of BOBF decreases while the HHV increases due to the increase of the BOB proportion in the obtained sample. To obtain a sufficiently pure BOBF, the flotation time must be at least 5 h, in which the yield of the floated BOBF is 39.5 % from the dry birch bark. The BOBF obtained by the floating method can be regarded as qualitatively and sufficiently purified from birch inner bark if its combustion heat is above 32-33 MJ/kg (BIB content would be below 10 %).

Therefore, the developed method for the BOB quality control is very useful in BOB extraction plants. Thus, it would be possible to control the purity of the feedstock and to predict the potential yield of extractives as well as the amount of the solvent to be taken for the extraction process.

IV. CONCLUSION

If we compare EHP and HHP, then the EHP content shows better correlations ($R=0.988$) than the content of HHP ($R=0.967$), and the method for determination of the EHP content is less time-consuming. Still, the method has some disadvantages – it is very difficult to obtain 100 % pure BOB if separated mechanically – by hand or by winnowing.

The HHV for pure BOB was more than 1.5 times higher than that for BIB. Therefore, the calibration

curve for the characterization of the feedstock was developed using HHV as a reference to determine the content of pure BOB, which was more accurate ($R=0.9955$) and faster (45 min).

Pure enough (≥ 90 % of BOB) feedstock for triterpene production can be accepted if the HHV is more than 32-33 MJ/kg.

V. ACKNOWLEDGMENTS

The study was funded in accordance with the contract No. 1.2.1.1/16/A/009 between "Forest Sector Competence Centre" Ltd. and the Central Finance and Contracting Agency, concluded on 13 October 2016.

This study was partly supported by the European Regional Development Fund (ERDF). Project No. 1.1.1.1/16/A/042.



INVESTING IN YOUR FUTURE

REFERENCES

- [1] E. Bergelin and B. Holmbom, "Reactions and distribution of birch extractives in kraft pulp oxygen delignification," *J. Wood Chem. Technol.*, vol. 28, pp. 261-269, 2008.
- [2] P. C. R. O. Pinto, A. F. Sousa, A. J. D. Silvestre, C. P. Neto, A. Gandini, Ch. Eckerman and B. Holmbom, "*Quercus suber* and *Betula pendula* outer barks as renewable sources of oleochemicals: A comparative study," *Ind. Crops Prod.*, vol. 29, pp. 126-132, 2009.
- [3] J. Rizhikovs, J. Zandersons, G. Dobeles and A. Paze, "Isolation of triterpene-rich extracts from outer birch bark by hot water and alkaline pre-treatment or the appropriate choice of solvents," *Ind. Crops Prod.*, vol. 76, pp. 209-214, 2015.
- [4] S. Alakurtti, T. Mäkelä, S. Koskimies and J. Yli-Kauhaluoma, "Pharmacological properties of the ubiquitous natural product betulin," *Eur. J. Pharm. Sci.*, vol. 29, pp. 1-13, 2006.
- [5] A. Gandini, C. P. Neto and A. J. D. Silvestre, "Suberin: a promising renewable resource for novel macromolecular materials," *Prog. Polym. Sci.*, vol. 31, pp. 878-892, 2006.
- [6] J. Rizhikovs, J. Zandersons, A. Paze, A. Tardenaka and B. Spince, "Isolation of suberinic acids from extracted outer birch bark depending on the application purposes," *Baltic Forestry*, vol. 20, pp. 98-105, 2014.
- [7] A. J. Mian and T. E. Timell, "Isolation and characterization of a cellulose from the inner bark of white birch (*Betula Papyrifera*)," *Can. J. Chem.*, vol. 38, pp. 1191-1198, 1960.
- [8] D. N. Vedernikov, N. Yu. Shabanova and V. I. Roshchin, "Change in the chemical composition of the crust and inner bark of the *Betula pendula* Roth. birch (Betulaceae) with tree height," *Russ. J. Bioorganic Chem.*, vol. 37, pp. 877-882, 2011.
- [9] A. Karnaouri, U. Rova and P. Christakopoulos, "Effect of different pretreatment methods on birch outer bark: New biorefinery routes," *Molecules*, vol. 21, pp. 427-443, 2016.
- [10] A. V. Obolenskaya, Z. P. Elnitskaya and A. A. Leonovich, *Laboratory Works in the Chemistry of Wood and Cellulose* (source is in Russian). Moscow: Ecologya, 1991.
- [11] A. Bredihhin, U. Mäeorg and L. Vares, "Evaluation of carbohydrates and lignocellulosic biomass from different wood species as raw material for the synthesis of 5-bromomethylfurfural," *Carbohydr. Res.*, vol. 375, pp. 63-67, 2013.

Experience of Application High Performance Cement Composites for Creating Durable Sculptural Elements

Genadijs Sahmenko, Sandis Aispurs, Aleksandrs Korjakins

*Riga Technical University, Faculty of Civil Engineering, Institute of Materials and Structures,
Kipsalas street 6a, Riga, LV-1048, Latvia*

Abstract. Traditionally, sculptural and decorative elements of building facades are created from mortar mixes based on lime, gypsum or Portland cement. Generally these materials have porous and permeable structure, which determines their accelerated degradation, especially in the aggressive environment of modern cities. High performance cement composites (HPCC) have been considered for production and restoration of sculptural elements in historical buildings. For this purpose, fine-graded, multi-component and highly workable mixes were elaborated. Mix compositions were modified with micro-fillers, plasticizing and stabilizing admixtures, as well as fibers to improve material ductility and control shrinkage cracking. Basic mechanical properties and durability (such as water absorption, frost resistance) were determined and two types of HPCC were compared (>50 MPa: HPCC and >120 MPa: UHPCC). It has been confirmed that cement composite mixes are characterized by self-consolidating effect, high compressive strength, extremely high resistance versus freezing and thawing cycles and low water absorption. Surface quality was evaluated and initial water absorption (tube tests) were performed for laboratory samples and real sculptural elements after 5 years of exploitation. The results confirmed good potential for using HPCC for creating more attractive and durable architectural shapes and façade elements compared to elements made using traditional cement and lime mortar.

Keywords: Concrete sculpture, cement composite, durability, flowability.

I. INTRODUCTION

Sculptural and decorative elements are an important component of building façades and urban environment element in modern cities. Their reproduction and restoration are essential for preservation of historical heritage and retention of uniqueness of cities with a rich historical past. From the first civilizations, natural stone has been used as the basic material for creating buildings and their architectural elements. Concrete is not only a popular construction material, but also the material that has been used for producing architectural shapes since ancient times. Concrete based on air hardening binder, like lime and gypsum, has increased porosity and limited mechanical strength. Perfect surface of gypsum sculptural elements is a positive property, but low water resistance and durability are essential drawbacks of gypsum binder [1]. Throughout the centuries, lime putty has been used as mortar binding agent; some lime concrete structures have preserved from ancient times. Lime mortar is a highly capillary porous material, which increases the risk of accelerated degradation of sculptural elements [2]. Ancient Romans discovered hydraulic lime cement, which consists on lime putty with pozzolanic admixtures (volcanic ash). A lot of Roman architecture monuments produced from hydraulic

lime concrete survived in satisfactory conditions till present time, for example, Roman Pantheon and numerous aqueducts.

Golden Age of concrete started in the 19th century, when Portland cement was invented. Its use makes it possible to reach better mechanical strength and durability. First experiments in creating sculptural elements are dated back almost 100 years: in the early 1920th a series of 'technical' experimental cast concrete mini sculptures were created by Henry Moore [3]. The idea of exposed concrete provides for naturally exposed concrete surface. Usually, the surfaces of conventional concrete constructions contain many surface blemishes (bubbles and cavities). The authors [4] proposed the improved method to evaluate surface quality by detecting blemishes in the concrete surfaces using digital analysis of the pictures of these surfaces.

The effect of moisture, freeze-thaw cycles and environment pollution are the basic reasons for degradation of architectural elements. In the maritime climate, ageing is related to chemical attack of salts [5]. In Nordic regions, moisture and freeze-thaw cycles are the dominant destroying agents, but in the Southern regions, especially in desert regions, erosion weathering and sand abrasive effect dominate.

Shrinkage and thermal cracks are another big problem of concrete surfaces. The risk of shrinkage cracking can be minimized by shrinkage compensated admixtures as well as applying special methods of external and internal curing [6]. A lot of work and funds should be spent to repair and rehabilitate concrete using special technologies and materials [7]. Conventional concrete and mortar mixes have water-cement ratio >0.6, it decreases mechanical properties and durability. The results of visual inspection of sculpture elements made from conventional mortar mixes show numerous defects after three years of exploitation: air voids, cavities and surface erosion after freeze-thaw cycling (Fig. 1).



Fig. 1. Vase made from commercially available dry mix after 3 years of exploitation. Typical defects: air voids, cavities and surface erosion after freeze-thaw cycles. (Production – 2011, inspection – 2015).

The use of high performance cement composite for sculptural and decorative elements allows increasing material service time and creating aesthetic sculptural elements characterized by perfect surface and durability [8]. High performance cement composite with low water-cement ratio can provide enhanced workability and good mechanical strength. Dense microstructure is achieved by using micro and nano admixtures in optimal proportions. Insufficient ductility and fragility are compensated by adding different fibers – steel or non-metallic fibers. In accordance with the previous studies [9], steel fibers have the best effect on mechanical strength and post-cracking behaviour. At the same time, some corrosion points in the element surface may appear, but this negative effect can be avoided by using polymer fibers and carbon fibers [10]. It should be noted that polymer fibers are not so effective because they have much lower modulus of elasticity comparing to steel fibers. PVA (polyvinyl alcohol) fibers are the most promotive polymer fibers with E-modulus 30-40 GPa and tensile strength close to 1 GPa. The aim of the investigation is to develop high performance cement composite for fabrication of sculptural elements intended for outdoor application.

II. MATERIALS AND METHODS

A. Materials and Mix Preparation

Two types of mixes were used: the first mix is close in mechanical properties to Ultra-High Performance Cement Composite (UHPCC), the second one is more economical – High Performance Cement Composite (HPCC) – Table 1. In the framework of experimental and practical work, local quartz-based sand (maximum particle size – 1 mm) was used as a fine aggregate and gravel 2/8 mm (basically dolomite) was used as a coarse aggregate.

Silica fume and metakaolin powder were used as a micro-filling and pozzolanic admixture. Used metakaolin is an industrial by-product obtained from the manufacturing of expanded glass granules. PVA (polyvinylalcohol) as well as AR glass fibers were added in order to improve material ductility, bending strength and to decrease the risk of cracking [11]. Air entraining and plasticizing admixtures are introduced in HPCC mixes in order to improve frost resistance and durability [12], at the same time, this admixture is not needed in UHPCC mix thanks to extremely low W/C ratio and dense microstructural packing. Mix components are summarized in Table 1. Fraction volumetric distribution demonstrates paste content 38 % in HPCC and up to 62 % in UHPCC (Fig. 2).

Table I
Type Sizes, Spaces and Intervals

Components	Density	UHPCC	HPCC
White cement CEM I 52.5 R	3.1	850	-
CEM I 42.5 N	3.1	-	400
Sand, fractions 0/1 mm	2.65	1150	200
Sand, fractions 0/4 mm	2.65	-	600
Gravel 2/8 mm	2.65	-	800
Silica fume	2.2	140	10
Metakaolin	2.2	-	50
Fiber PVA	1.1	5	-
Fiber AR glass	-	-	10
Water	1.0	210	200
Superplasticizer	1.2	20	4
Air entraining agent	-	-	0.2
W/C ratio		0.26	0.50

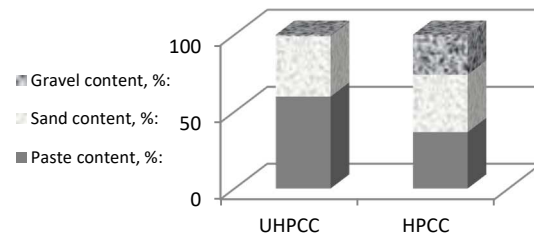


Fig. 2. Fraction volumetric distribution.

Mixing was done in a high shear motion mixer at the speed of 150 rpm. During dry components mixing, 2/3 of the total volume of water was added, the mass was mixed for more than 2 minutes, then adding the rest of the water together with a superplasticizer during the mixing. Samples and sculptural elements were cured in moisture conditions

at the temperature +20±2°C for at least 28 days. Composite mix elaboration, testing and adjusting were carried out in the laboratories of Riga Technical University in collaboration with the sculptor Sandis Aispurs.

Mix flowability was determined by means of flow test, using cylinder with the internal diameter 50 mm and height 100 mm. UHPCC mixes are characterized by flowable consistency (cylinder spread 160-220 mm), this makes it possible to obtain smooth surface of a concrete product. In the sculpture workshop, the elements were produced using the same technology. Numerous experiments were conducted in collaboration with Sandis Aispurs to simulate different mould surfaces and to adjust appropriate mix consistency.

B. Properties Evaluation

Surface water absorption.

Durability of exposed concrete depends on its reaction to water action. There are several standardized methods characterizing material's water absorbing capacity: water absorption by immersing in water (ASTM C140), capillary surface absorption (NT BUILD 368), water permeability under pressure (EN 12390-8), initial surface absorption tube test (RILEM 11.4), etc. Taking into account real exploitation conditions of sculptural elements, the last method may be selected as the most acceptable. The main advantage of RILEM 11.4 test is that it may be realized both in laboratory and field conditions. In accordance with method specification, test Method RILEM II.4 is usually used to check elements temporarily subjected to the action of water.

Compressive strength was determined in accordance with EN 12390-3, using testing machine Controls 50-C56G2.

Frost resistance was tested in accordance with CEN/TS 12390-9. Cubes 100x100x100 mm were produced, matured and sawn into halves. Prior to freezing, the samples were immersed by sawn surface in 3% sodium chloride (NaCl) solution, capillary suction period was 7 days. The samples were subjected to freezing and thawing cycles in accordance with CDF test methodology [13], duration of one cycle was 12 hours and the temperature range -20/+20°C.

III. RESULTS

A. Laboratory sample testing results

Surface water absorption test. The results of surface water absorption test confirm high difference between different types of concrete. The best results were shown by UHPCC samples: water absorption was close to zero during the first hour and only 0.6 ml after 10 days of penetration. After 1 hour water penetration was 0.4 ml for HPCC and close to 1.0 ml for the reference mortar mix (produced from dry mix) (Fig. 3).

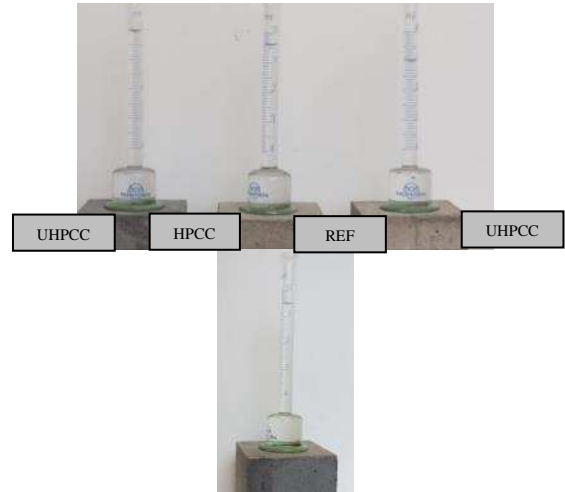


Fig. 3. Water absorption: after 1 h (left), after 10 days for UHPCC (right).

Compressive strength test. Compressive strength tests were performed for mix compositions produced in different times during 2 years. Results of strength and density tests are summarized in Fig. 4. Statistical evaluation shows different values of averaged squared deviation: UHPCC density demonstrates the lowest coefficient of variation (1.7 %), whereas HPCC density demonstrates higher variation (4.2 %). This fact can be explained by the effect of air entrainment, which is difficult to control. Strength results show much higher variations: 13.2 % for UHPCC and 20.3 % for HPCC, it may be associated with the diversity in real regimes of production and possible deviations in the properties of raw materials.

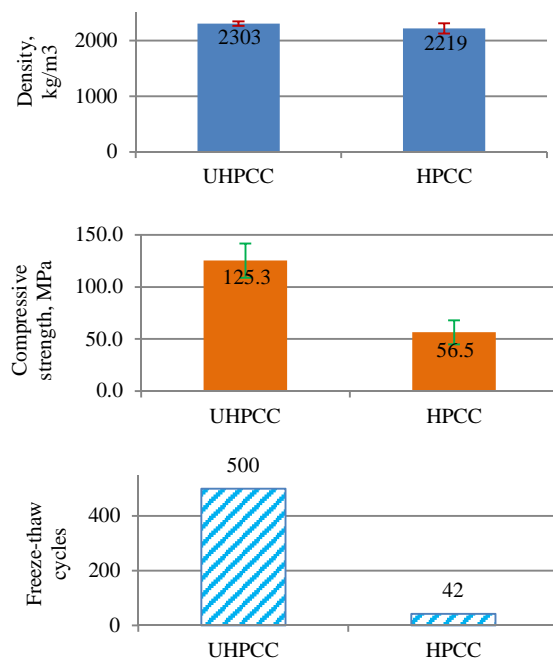


Fig. 4. Comparing density, compressive strength, their average squared deviations and frost resistance results.

Frost resistance test. Concrete scaling resistance usually is evaluated after 28 and 56 freeze-thaw cycles. In this case, the number of cycles for UHPCC was extended up to 500 cycles, it is 18 times more than the standard requirement (Fig. 4). After the test almost no surface damage was detected (mass loss from the surface was not more than 100 g/m²). Test results for HPCC showed lower frost resistance. After 28 cycles, the loss of mass was close to 500 g/m², but considerable destructions were detected after 50 cycles.

B. Results of inspection and testing of the installed sculptural elements

Renovation of sculptural elements was carried out by a professional artist, sculptor Sandis Aispurs [14]. The initial stage of the process included reconstruction of the sculptures in the workshop (fixed together) and modelling of the lost parts. The next stages included production of the mould [15], filling the mould and ensuring the hardening process. Complicated elements were cast in polyurethane or silicon rubber moulds, which are flexible and reusable.

Elaborated HPCC mix compositions were practically used for restoration of sculptural elements in the renovated objects in several historical buildings in Latvia. The first project was the reconstruction of concrete sculptures on the facade of Saldus Secondary School (works finished in 2015). The fronton part of the façade was initially decorated with eight concrete sculptural elements: two spheres, two vases and four sculptures made in putty style. Old elements (see Fig. 5, on the left) were completely reconstructed (Fig. 5 on the right) from UHPCC mix, using silicone moulds. After 5 years of outside use, the same vase was visually inspected and tested using Rilem 11.4 tube test. No important visual surface defects were detected and surface penetration test showed water penetration (1.4 ml after 10 days), it is insignificantly more than for new UHPCC sample produced in laboratory (0.6 ml, Fig.2).



Fig. 5. Saldus Secondary School vase before reconstruction (left), reconstructed UHPCC vase (right).

Riga is one of the few European cities, which retained outstanding examples of Art Nouveau

architecture buildings and design objects built at the beginning of 20th century. Therefore, Riga is included on the UNESCO World Heritage List and this city tends to be called Art Nouveau Metropolis [16]. Nowadays HPCC technology has been used for renovation of several historical Art Nouveau building façades. Usually the façades of these buildings are decorated with sculptural elements, which are considerably damaged or lost, especially the sculptures at the top of the frontons.

Among the first objects the following buildings can be mentioned: a building situated at Alberta Street 2a (described in [8]), architect Michael Eisenstein, construction completed in 1906; façade of the building at Alberta Street 7 (constructed in 1908, architect Hermanis Hilbiks) (Fig. 6); Gertrudes 19/21 (Fig. 7), Matisa Street 44. Partially damaged elements in the vertical parts of the façades were restored in-place, using special Mapei premix restoration composition (Rasa di repara). Significantly damaged elements were completely reconstructed and then



created from UHPCC.

Fig. 6. Reconstruction of a spherical sculptures in Riga, Alberta Street 7.



Fig. 7. Reconstruction of a spherical sculptures in Riga, Gertrudes 19/21.

Discussing the role of PVA fiber, it must be noted that PVA fiber has a minor effect on the compressive strength and modulus of elasticity, but it improves long-term properties, such as shrinkage strains and creep behaviour [17]. It was established that PVA fibers reduce shrinkage deformations, especially in

the early-age stages [18], [19]. At the same time, initial experiments on UHPCC samples confirm strain softening behaviour during bending test.

Current sculptor's Sandis Aispurs object is Brukna St. Apostle Chapel in Byzantine style. Basic architectural elements of the façade – columns, capitals and arches – are created from HPCC (>55 MPa, Fig. 8). The most important current project is the sculptures of 12 apostles, which are being cast from UHPCC (>120 MPa, Fig. 9).



Fig. 8. Current sculptor's Sandis Aispurs object is Brukna St. Apostle Chapel (arch are produced from HPCC) (photo April, 2017).



Fig. 9. Current sculptor's Sandis Aispurs works is Brukna: sculptures of 12 apostles, which are being cast from UHPCC (photo April, 2017).

CONCLUSIONS

Testing of laboratory samples and inspection of the installed sculptures made from cement composites confirm high frost durability (up to 18 times more freezing cycles comparing to traditional concrete).

RILEM 11.4 water absorption test method may be regarded as appropriate test for simple evaluation of durability of HPCC. This method can also be used for evaluating the effect of surface protective (water repellent) agents.

Environment. Technology. Resources, Rezekne, Latvia

The use of High and Ultra High Performance Cement Composites opens new opportunities for creation and reconstruction of sculptural elements permanently subjected to open-air exploitation conditions and preservation of historical heritage.

ACKNOWLEDGMENTS

The financial support of European Regional Development Fund project Nr.1.1.1.1/16/A/007 "A New Concept for Sustainable and Nearly Zero-Energy Buildings" is acknowledged.

REFERENCES

- [1] F. Vegas and At.al., "May a building stand upon gypsum structural wall and pillars?," in *8th International masonry conference in Dresden*, 2017, pp. 1–6.
- [2] C. Rodríguez-navarro, "Binders in historical buildings : Traditional lime in conservation," *Semin. SEM*, vol. 9, pp. 91–112, 2012.
- [3] R. Bailey, "Concrete Thinking for Sculpture," *Parallax*, vol. 21, 2015.
- [4] A. Klovas and M. Daukšys, "The evaluation methods of decorative concrete horizontal surfaces quality," *Medžiagotyra*, vol. 19, no. 3, pp. 343–348, 2013.
- [5] M. Zapoyev, S. Krivoy, and S. Belyayeva, "Salt Corrosion of Masonry Mortar," *Appl. Mech. Mater.*, no. 725–726, pp. 523–528, 2015.
- [6] P. Lura, M. Wyrzykowski, C. Tang, and E. Lehmann, "Internal curing with lightweight aggregate produced from biomass-derived waste," *Cem. Concr. Res.*, vol. 59, pp. 24–33, May 2014.
- [7] W. D. Mangum, A. J. Bermudez-Goldman, D. P. Whitney, D. W. Fowler, and A. H. Meyer, "Repairing Cracks in Portland Cement Concrete Using Polymers. Final Report," no. 2, p. 122 p., 1986.
- [8] G. Šahmenko, S. Aispurs, and A. Krasnikovs, "The Use of High Performance Cement Composite in Renovation and Restoration of Architectural Elements of Buildings Facades," *Procedia Eng.*, vol. 117, no. 1, pp. 317–324, 2015.
- [9] ACI Committee 544, "State-of-the-Art Report on Fiber Reinforced Concrete Reported by ACI Committee 544," *ACI Struct. J.*, vol. 96, no. Reapproved, 2002.
- [10] G. Šahmenko, A. Krasnikovs, and M. Eiduks, "Ultra High Performance Concrete Reinforced with Short Steel and Carbon Fibers," *Proc. 10th Int. Sci. Pract. Conf.*, vol. I, pp. 193–199, 2015.
- [11] A. Macanovskis, A. Krasnikovs, O. Kononova, G. Harjkova, and V. Yevstignejevs, "Mechanical Properties of Glass Fiber Composites Reinforced by Textile Fabric," *Environ. Technol. Resour. Proc. Int. Sci. Pract. Conf.*, vol. 1, no. May, p. 133, 2015.
- [12] Y. Barabanshchikov, S. Belyaeva, A. Avdeeva, and M. Perez, "Fiberglass Reinforcement for Concrete," *Appl. Mech. Mater.*, no. 725–726, pp. 475–480, 2015.
- [13] C. Gehlen and A. Rahimi, "RILEM TC TDC. Compilation of Test Methods to Determine Durability of Concrete. A Critical Review," 2011.
- [14] S. Aispurs, "No Title," 2017. .
- [15] T. J. Niel, "Process and techniques in concrete sculpture," *Concr. Eng. Int.*, vol. 11, no. 4, pp. 46–47, 2007.
- [16] J. Krastiņš, *Jūgendstils Rīgas arhitektūrā*, Zinātne. Riga, 1980.
- [17] A. Sprince, L. Pakrastinsh, B. Baskers, and L. Gaile, "Crack development research in extra fine aggregate cement composites," *Vide. Tehnol. Resur. - Environ. Technol. Resour.*, vol. 1, no. May, p. 17770, 2015.
- [18] A. E. Naaman and K. Wille, "The Path to Ultra-High Performance Fiber Reinforced Concrete (UHP-FRC): Five Decades of Progress," in *Proceedings of HiperMat 2012 (Kassel, March 7-9, 2012)*, 2012, pp. 3–15.

[19] N. Vatin, A. Sprince, L. Pakrastinsh, and N. Vatin, "Long-term Behaviour of Fibre Reinforced Cement Composites," in *Proc. of the Second Intl. Conf. on Advances In Civil,*

Structural and Mechanical Engineering- CSM 2014, 2014, no. November, pp. 116-121.

Nonwoven Development by the Multilayer Structure

Arta Seile, Dana Belakova

Riga Technical University, Faculty of Materials Science and Applied Chemistry, Institute of Design Technologies

Abstract. *the main two directives of the European Commission (EC) has been regulating the automotive industry. The aforementioned directives and education of residents on environmental issues has created the need for new materials that have been produced from renewable resources and should be recycled at the end of product life cycle.*

The objective of this project is to develop a nonwoven materials (NWM) that would incorporate fibers of plants, which could be grown in Latvia because of suitable local climate conditions, for the use in automotive industry. Furthermore, inclusion of polymer fibers in the NWM will expand the areas of use of such material – the NWM can be transformed into a composite material by means of a thermal press.

Manufacturing process of NWM consist of structure modelling and material samples manufacturing. NWM samples production process to be carried out by fibers preparation, fibers mixing, formation by airlaid method, preparation of fiber webs for fixation with a mechanical needle punching method, mechanical fixation of fiber webs, preparation of fixed fiber webs for NWM manufacturing and manufacturing of NWM by mechanical needle punching method.

This article reflects the comparison of two compositions NMW (Polylactid (PLA) (60 wt%) and long flax fibres (40 wt%), and PLA (60 wt%) and technical hemp fibres (40 wt%)) with the same structure by visual appearance, geometrical parameters and tensile strength. The average surface density of hemp NWM varies in the range of 792.09 to 958,71 g·m⁻², thickness varies from 6.91 to 9.23 mm. Flax NWM average surface density is higher than hemp NWM and varies in range of 1,064 to 1,260 g·m⁻², thickness of the material varies from 12.62 to 15.54 mm. For comparison, the surface density of NWM currently used in automotive industry, depending on the use of the material, varies from 100 to 1,400 g·m⁻².

Keywords: *hemp fibers, flax fibers, nonwovens.*

I. INTRODUCTION

The country, where people live, and the legislation of such country regulate the daily life of its residents to a great extent. Not only national legislation, but also the effective directives of the European Union (EU) are binding on the residents of the EU member states. Over the last years, two directives of the European Commission (EC) have been regulated the automotive industry: 2000/53/EC and 2005/64/EC. The first one regulates the proportional amount of details that must be made of recycled resources and the amount of details that could be recycled at the end of product life cycle. The second directive provides that the motor vehicle manufacturers must provide the EU institutions with information on the recycling methods of details used in vehicles. Both directives are based on reduced use of non-renewable resources and wider use of renewable resources.

The aforementioned directives and education of residents on environmental issues has created the need for new materials that have been produced from renewable resources and should be recycled at the end of product life cycle. The objective of this project is to develop a NWM that would incorporate fibres of plants, which could be grown in Latvia as a result of suitable local climate conditions, for the use in

automotive industry. Furthermore, inclusion of polymer fibres in the composition of NWM will expand the areas of use of such material – the NWM can be transformed into a composite material by means of a thermal press. The use of a polymer of biological origin and uniting it with plant fibres allows to obtain a material that conforms to the conditions of sustainable environment management.

II. MATERIALS AND METHODS

Flax, hemp and PLA fibers have been used for the development of samples.

A. Flax fibers

Common flax or linseed (*Linum usitatissimum* L.) is an ancient agrotechnical culture, which has been cultivated in the territory of Latvia as well. Flax is an annual plant that has been cultivated for two principal crops: fiber and seed (i.e. oil linseed). A stalk of a long-stalk flax contains 20 – 30% of fibers. The composition of the fiber is significant for the plant because the principal component of cell membranes is cellulose, which ensures the strength of the fiber. Cellulose is not water-soluble. Cellulose accounts for an average of 60 – 80% of the total flax fiber mass, the rest of the mass consists of lignins, pectins, plant waxes and fats, various water-soluble substances and hygroscopic water. Cellulose, the chemical formula

of which is (C₆H₁₀O₅)_n, is a natural polymer – a macromolecular substance with high degree of polymerisation (300 – 3,000).

The geometrical parameters of the flax fibers used for the research have been determined by laboratory methods: fiber fineness is 3.87 dtex, average length - 139.23 mm.

The average market price of long-fiber flax is approximately 1.39 EUR/kg [1].

B. Hemp fibers

Hemp (*Cannabis sativa*), like flax is an annual plant and a traditional agrotechnical culture in Europe and all regions of Latvia. Similarities between both plant cultures are observed, the structure of the fibers of both plants is in principle similar. Depending on the sort of hemp, the content of fiber in its stalk can reach 25 – 35%. Cellulose forms ~ 77% of the total mass of hemp fibers.

German company BaFa Badische Naturfaseraufbereitung GmbH, which is specialising in hemp fiber cultivation and processing, supplied the hemp fibers used for the development of samples. Company classifies the fibers used for the development of samples as technical fiber with product name Vliesfähige Faser VF6.

The average market price of technical hemp fibers is approximately 0.6 – 0.8 EUR/kg [2].

C. Polylactide fibers

PLA is a natural biopolymer [3], consisting of linear macromolecules with chains containing at least 85 wt% lactic acid esters that are obtained from naturally occurring sugars. The melting temperature thereof is at least 135 °C [4; 5]. PLA is a biodegradable and biologically compatible material that can be processed by using standard manufacturing devices. Depending on the service life of a product with embedded polymer, the time of polymer degradation can be controlled.

The PLA used in the samples has been supplied by the company Ingeo [6], which produces the polymer from corn starch. Sugars generate both principal components of the PLA polymer obtained from corn – carbon dioxide and water. Starch is transformed into glucose by means of fermentative hydrolysis. The glucose is fermented into lactic acid at almost neutral level of pH. The PLA polymer used in the samples has the shape of fibers. Their technical parameters are as follows - type: SLN 2660D, specification: 6.0 dx 64 mm x FB, fiber fineness: 6, 5 ± 0, 5 den, fiber length: 64 ± 4 mm.

The average market price of PLA fibers is 2.12 – 3,5 EUR/kg, for comparison, the price of PP, frequently used for NWM is approximately 1.61 – 1.82 EUR/kg [7].

D. Nonwoven manufacturing

NWM provides the possibility of reaching a textile material with wide functional properties: the porous structure of the material ensures thermal and sound insulation, as well as absorbing properties.

These properties are especially significant for textile materials used in motor vehicle constructions.

Two types of NWM have been developed within the framework of this research: PLA fibers (60 wt%) mixed with long fibers of flax (40 wt%) and PLA fibers (60 wt%) mixed with technical fibers of hemp (40 wt%). The same principle of material structure development and manufacturing technology has been used in both NMW. Mechanical manufacturing method has been used for the creation of both NMW – needle punching. NMW structure has been demonstrated in Fig. 1, in accordance with which the total quantity of fibers is divided into five fiber layers. The three internal layers of fibers are similar in terms of their constituent components, fiber proportion and mass. Uniting these three layers into one would be more economically viable, however, the solution of 3 fiber layers was chosen due to the technological characteristics of the available equipment in order to obtain a material with as equal punch distribution (more homogeneous connection of fibers) as possible. The following operations have been included into the production process:

1. preparation of fibers for work (weighing of the required amount of fibers, loosening of fibers);
2. creation of fiber web layers;
3. punching of fiber web layers:
 - a. preparation of fiber web layers for fixation (in order to reduce the number of punches during the production process and, to prepare three fiber web layers for fixation from five fiber web layers, by placing layers on top of each other);
 - b. fixation of fiber web layers by needle punching;
 - c. arranging of three fiber layers and preparation thereof for the production of NWM.

Production of NWM by means of needle punching method (needle punching of three fixed fiber web layers into a single material).

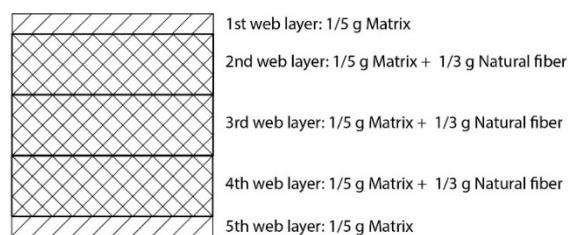


Fig. 1. Structure of nonwoven material.

The fibers were loosened, both types of fiber were mixed (by using the *airlaid* method) and fiber layers were created by using the same device – TRÜTZSCHLER CVT3 1200. In this device, the proportioned amounts of fibers were delivered from the fiber feed-in area via parallel horizontal rollers to the vertical vacuum cylinder, which is connected to the device. In the fiber layer, which was obtained in

the cylinder, the fibers were dispersed in various, indefinite directions. During the NMW production process, the needle punching was performed in two phases. During the first of the phases the fiber layers were fixed and after the second punching phase the finished material was obtained. The same device has been used in both phases of punching: DILO LBM 6. This device has one needle board, which does the work by means of a downwards movement. In order to ensure the minimum number of punches during the production process of NWM, three fiber layers must be prepared for fixation from initially produced five fiber layers by placing one layer on top of another,

see Fig. 2); The following sequence of operations has been observed during the first needle punching procedure:

1. the 1st fiber web layer was punched (PLA fiber layer) together with the 2nd fiber web layer (the layer, where plant fibers were mixed together with PLA fibers);
2. the 3rd fiber web layer was punched separately;
3. the 4th fiber web layer was punched (the layer, where plant fibers and PLA fibers were mixed) together with the 5th fiber web layer (PLA fiber layer).

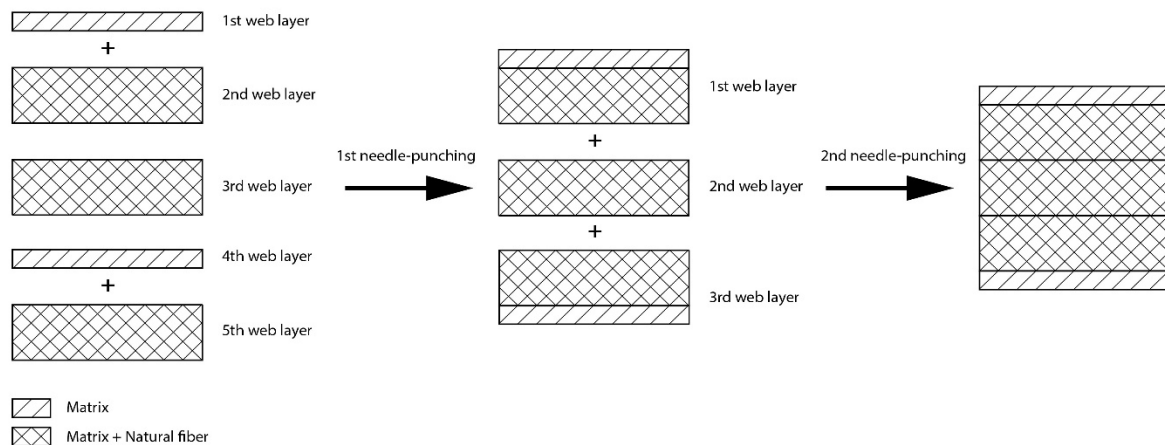


Fig. 2. Needle punching in the manufacturing process of nonwoven material process

The fiber web layers, where two fiber layers were fixed together, were inserted into the needle-punching device with the layer of PLA fibers facing upwards, closer to the needle board. Before the second punching phase, the three previously fixed fiber layers were arranged and placed in accordance with the production scheme of NWM (see Fig. 1 and Fig 2).

III. RESULTS AND DISCUSSION

Different number of samples has been obtained from the both NWM materials within the framework of the research: 5 samples of PLA and hemp NWM (samples labelled with Latin alphabet letters A, B, C, D and E) and 3 samples of PLA and flax NWM (samples labelled with Latin alphabet letters A, B and C). 6 stripes of NWM sized 50 x 300 mm have been cut out of each sample, of which 3 stripes (Fig. 3) from each sample (in the event of Sample D - 1 stripe have been used for the research of NWM. Among the researched samples, the stripes labelled with Latin block capitals and numbers 1 and 3 have been cut out along the direction of operation of the needle punching device, or so called in the machine direction. The sheets that have been labelled with Latin block capitals and number 5 have been cut in the cross-machine direction. Each of the stripes has the same length and width. The average thickness

values between both compositions of NWM differed by approximately 40%, hemp technical fiber containing material is thinner and its thickness varies from 6.91 to 9.23 mm. The thickness of flax fiber containing material ranges from 12.62 to 15.54 mm. The thickness of the produced material samples is directly linked with the quality of fibers binding.

The NWM spicemen strips containing flax fiber are visually lighter - PLA fibers dominate on their surface and the fact that the thickness thereof exceeds that of hemp fiber containing NWM is visible without using technical metering equipment (Fig. 3). The natural colour of hemp fibers is visible in the surface of hemp fiber containing strips, along with the white colour of PLA fibers. Upon the analysis of the obtained breaking strength results and visual appearance of the materials, it can be concluded that the surface density of the material is the factor that mostly affects the durability parameters of the NWM material, including the stretching of the material. The surface density of the hemp containing NWM varies from 792 to 959 g·m⁻², the surface density of the flax containing NWM is higher and varies from 1,064 to 1,260 g·m⁻². For comparison, the surface density of NWM materials currently used in automotive industry, depending on the use of the material, varies from 100 to 1,400 g·m⁻² [8].

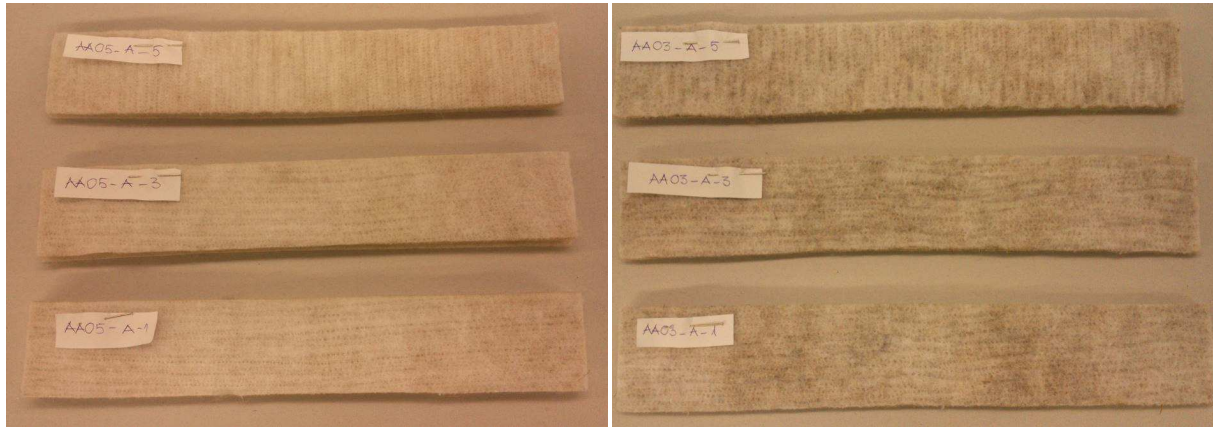


Fig. 3. NWM sample stripes, the lower stripe No. 1 and the medium stripe No. 3 have been cut in the machine direction (0°), the upper stripe No. 5 has been cut in the cross-machine direction (90°): flax fiber containing NWM sample A is on the left, hemp fiber containing NWM sample A is on the right.

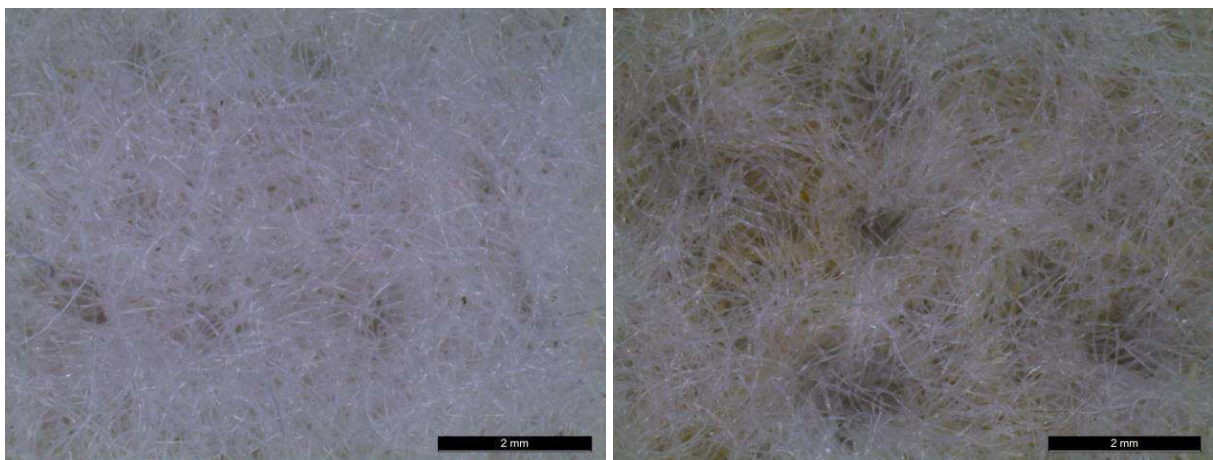


Fig. 4. NWM sample surface in the direction of needle impact, optical magnification 16x: flax fiber containing NWM on the left, hemp technical fiber containing NWM on the right.

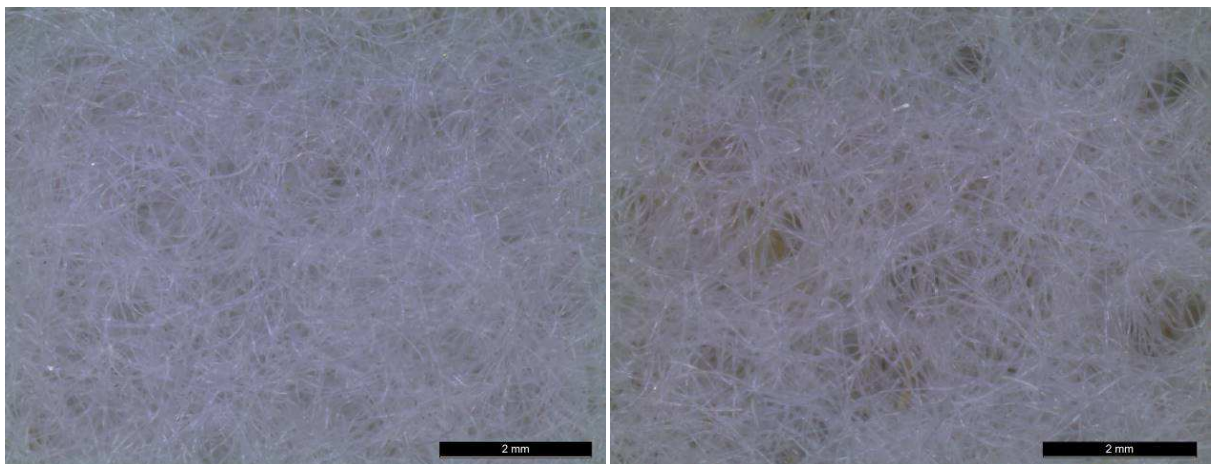


Fig. 5. NWM sample surface that is opposite to the needle impact, optical magnification 16x: flax fiber containing NWM on the left, hemp technical fiber containing NWM on the right.

Upon using the optical microscope for the observation of the samples of NWM materials of both compositions, the traces left by needle punching device are visible as holes of regular shape that recur over regular interval. They are better visualised in the surface of the material that has been directly subject to the impact of the needles (Fig. 4 and Fig 5). After the punching process it can be concluded that more

homogeneous binding of fibers (the fact must be linked with the tighter binding between PLA fiber web layer and mixed fiber web layer (natural and PLA fibers)) has occurred in hemp fiber containing NWM samples. The colour of material isn't as pronouncedly white as in the NWM containing flax fibers. Poorer fiber binding in the flax containing NWM is evidenced by poorly visible traces of needle

punches in the surface of the material that is opposite to the work direction of the needles. Poorer binding of flax fibers containing NWM is visible even

without technical aids and can be checked by trying to separate the strips of samples in the external surface of fiber layer with hands – easily separable.

Table I
PLA and Hemp NWM, PLA and Flax NWM tensile test results

NWM	Sample code	Strip code	Width	Length	Average thickness	Sample section area	Surface density (mA)	Ultimate tensile strength (F _{max})	Breaking load (F _{bruch})	Tensile strength elongation (e F _{max})	Elongation after breaking load (e Bruch)	Sample after testing
			mm	mm	mm	mm ²	g·m ⁻²	MPa	MPa	%	%	
PLA and Hemp	AA03_A	A1	50	300	8,87	443,65	894,69	0,05	0,01	31,79	42,20	Not failed
	AA03_A	A3	50	300	8,46	422,83	918,05	0,06	0,01	28,68	36,28	Not failed
	AA03_A	A5	50	300	8,69	434,70	848,95	0,05	0,01	40,24	47,34	Not failed
	AA03_B	B1	50	300	9,23	461,25	891,19	0,05	0,01	35,88	45,39	Not failed
	AA03_B	B3	50	300	8,21	410,43	873,48	0,06	0,01	29,43	37,99	Not failed
	AA03_B	B5	50	300	7,63	381,45	792,09	0,05	0,01	41,64	50,67	Not failed
	AA03_C	C1	50	300	8,81	440,45	958,71	0,07	0,02	37,08	46,19	Not failed
	AA03_C	C3	50	300	8,78	439,05	923,72	0,06	0,01	31,66	39,14	Not failed
	AA03_C	C5	50	300	8,70	434,95	892,47	0,05	0,01	45,63	51,56	Not failed
	AA03_D	D5	50	300	8,30	415,00	796,67	0,04	0,01	30,69	42,39	Not failed
	AA03_E	E1	50	300	7,02	350,90	891,31	0,10	0,02	35,63	46,24	Not failed
	AA03_E	E3	50	300	7,17	358,70	848,46	0,09	0,02	39,40	45,07	Not failed
AA03_E	E5	50	300	6,91	345,55	858,93	0,08	0,02	35,69	47,10	Not failed	
PLA and flax	AA05_A	A1	50	300	14,58	728,78	1260,51	0,03	0,01	56,24	68,54	Not failed
	AA05_A	A3	50	300	12,62	630,88	1232,53	0,04	0,01	55,54	67,61	Not failed
	AA05_A	A5	50	300	13,53	434,70	1132,70	0,05	0,01	39,88	47,02	Not failed
	AA05_B	B1	50	300	13,15	657,48	1221,27	0,03	0,01	56,50	67,74	Not failed
	AA05_B	B3	50	300	14,68	733,98	1222,01	0,03	0,01	58,96	67,10	Not failed
	AA05_B	B5	50	300	13,96	698,10	1065,74	0,03	0,01	42,40	52,08	Not failed
	AA03_C	C1	50	300	15,54	776,88	1180,77	0,04	0,01	48,99	59,55	Not failed
	AA03_C	C3	50	300	14,35	717,48	1228,77	0,04	0,01	55,79	66,59	Not failed
AA03_C	C5	50	300	14,72	736,15	1138,87	0,03	0,01	46,59	55,35	Not failed	

All tensile test results of NWM are presented in Table 1. Ultimate tensile strength of hemp fibers NWM samples ranges from 0.04 to 0.10MPa and material elongation ranges from 29 to 46%. Tensile strength test results of hemp fibers NWM are higher and elongation amplitude is lower than flax fibers

NWM - tensile strength ranges from 0.03 to 0.05 MPa, material elongation ranges from 40 to 59%.

IV. CONCLUSIONS

As a result of the research a plant fiber and biopolymer NWM structure has been created. A total of two NWM using plant fibers of traditional for the

territory of the Republic of Latvia, but nowadays uncommon flax and hemp agriculture, have been developed and mutually compared.

The NWM samples obtained during the research, according to the colour of the fibers used for manufacturing, are light in colour – due to white-coloured PLA fibers situated in the outer surfaces, the samples are lighter in colour than flax (in PLA and flax fiber samples) and hemp (in PLA and hemp fiber samples) fiber colour. Although the same process and devices have been used for the manufacturing of both materials, better binding of fibers has been observed in hemp fiber containing material samples. Due to better binding of fiber the hemp NWM samples are thinner, ultimate tensile strength have higher while material elongation have lower in comparison with flax NWM of the same structure. The average surface density of both developed NWM (hemp fiber containing material 792.09 to 958,71 g·m⁻² and flax fiber containing material 1,064 to 1,260 g·m⁻²) falls within the amplitude of surface density of NWM that are most frequently used in automotive industry (100-1,400 g·m⁻²). In order to find the best application for the NVM developed in this project, material wear, sound absorption and acoustic tests of the samples must be performed in addition to the tests that have already been implemented.

The comparison of PLA costs with other polymers shows that, for instance, PP, PLA fibers are more expensive. Without the further objective of

reprocessing both NWM into composite materials, the use of PLA is not economically viable.

V. ACKNOWLEDGEMENTS

The authors are grateful to Institute of Textile Technology at RWTH Aachen University for the provided possibility to produce NWM samples and perform the tests of the samples of created materials.

REFERENCES

- [1] Fibre2fashion.com [Online]. Available: http://fibre.fibre2fashion.com/15100550/flax-fibre_suppliers.html [Accessed: June 28, 2016].
- [2] Lauku tīkls [Online]. Available: <http://www.laukutikls.lv/spriez-par-linu-un-kanepju-tirgu> [Accessed: June 28, 2016].
- [3] R.-M. Johnson, Biopolymers, Smithers Rapra, 14 p. [Online]. Available: <http://site.ebrary.com/id/10236793?pgd=12> [Accessed: July 29, 2013].
- [4] *Noteikumi par tekstilšķiedru sastāva norādīšanu tekstilizstrādājumu marķējumā*. MK Noteikumi Nr. 722 [Online]. Available: <http://likumi.lv/doc.php?id=106684> [Accessed: Jan. 1, 2013].
- [5] European Commission Directive 2004/34/EC of 23 March 2004 on textile names (Text with EEA relevance) [Online]. Available: <http://publications.europa.eu/en/publication-detail/-/publication/fb087f8f-9732-4c3e-a810-9e93e35adde4/language-en/format-PDF/source-5039172> [Accessed: Jan. 1, 2013].
- [6] Nature Works™ [Online]. Available: <http://www.natureworkslc.com/news-and-events/press-releases/2005/2-1-05-natureworks-llc-is-new-name.aspx> [Accessed: Feb. 8, 2015].
- [7] Fibre2fashion.com [Online]. Available: http://fibre.fibre2fashion.com/16115623/polypropylene-fibre_suppliers.html [Accessed: June 28, 2016].
- [8] "Clothes make the man" – and nonwovens make the car [tiešsaiste]. Groz-beckert. Newsletter 4 2011. [Online]. Available: http://news.groz-beckert.com/pages/en_n4_nonwovens_in_cars.php5 [Accessed: Nov. 13, 2013].

Analysis Method of Calculation Parameters of Heat and Mass Transfer Processes in the Stirling Engine

Sergej Semyonov, Sergej Tikhonov, Mihail Donchenko,
Jurij Lukyanov, Andrej Perminov

Pskov State University, Faculty of Engineering and Construction Technologies, Pskov State University,
Faculty of Computer Science and Power Engineering.
Address: Russia, g. Pskov, pl. Lenina, d. 2, 180000.

Abstract. The article highlights the optimal calculation methods for determining the parameters of heat and mass transfer processes occurring in the rotary-vane engine with an external supply of heat. It is shown that the mathematical model of working processes must consist of two parts. One part describes the processes occurring in the isolated volume. The second part describes the processes of mass exchange between the working chambers of two modules, as well as a heater or a cooler.

Keywords: rotary-vane, heat and mass transfer processes, expiration process, expansion and contraction, nodal analysis methods, Stirling thermodynamic cycle, analysis of methods of calculation.

I. INTRODUCTION

In recent years greatly increased interest in engines with an external supply of heat, which is associated with the possibility of transformation in these engines in the energy of any kind of heat and low levels of toxicity, which significantly expands the scope of their application compared to the most common currently types of engines (engines of internal combustion, diesel engines). In most cases objects of interest are not the piston engines working on a thermodynamic cycle of Stirling, but rotary engine thermodynamic cycle that differs from a thermodynamic cycle of Stirling a little.

Rotary engines have a number of significant advantages over piston engines, as evidenced by a large number of scientific articles and patents devoted to this subject [1]. One of such engines is a rotary-vane engine with an external supply of heat (RVE), developed the staff of the Pskov State University [2, 3]. Engine unites the advantages of the rotary scheme and the external heat supply. RVE can be a substitute for traditional types of energy unit in areas such as autonomous systems of power supply, including cogeneration unit, electric generators of low power, solar power unit.

Experience designing of a heat engines shows that the creation of adequate experimentally verified mathematical models of processes occurring in the engine can significantly reduce the amount of costly experimental studies. We can say that the creation of an adequate mathematical model is one of the keys to success engine development. The aim of the article is

to determine the optimal method of calculation to determine the parameters of heat and mass transfer processes occurring in RVE.

II. BRIEF DESCRIPTION OF THE THERMODYNAMIC CYCLE

RVE consists of two modules. The two modules have a similar structure and are rotated relative to each other at an angle of 45°. RVE scheme is shown in Figure 1.

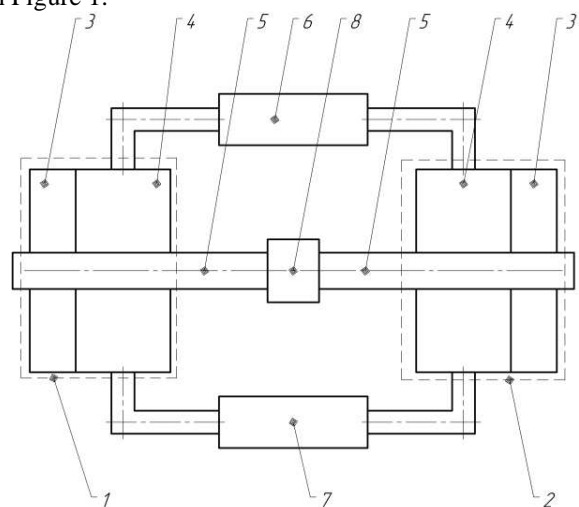


Fig. 1. RVE scheme:
1 – 1st module; 2 – 2nd module; 3 – transformation mechanism; 4 – Vanes group; 5 – output shaft; 6 – heater; 7 – cooler; 8 – coupling.

Vaness group has four working chambers of variable volume. In everyone working chamber

occurs thermodynamic cycle, which is not much different from the thermodynamic cycle of Stirling. Changing the angle between the axes of the pistons ψ and the volume of the working chambers, depending on the output shaft angle α is due to the rotation of the pistons position 2 figure 2 and position 3 figure 2 with different angular velocity. Pistons position 2 figure 2 mounted on the outer rotor have an angular velocity $\omega_1(\alpha)$. Pistons position 3 figure 2 mounted on the internal rotor have angular velocity $\omega_2(\alpha)$.

General view of the vanes group RVE is shown in Figure 2.

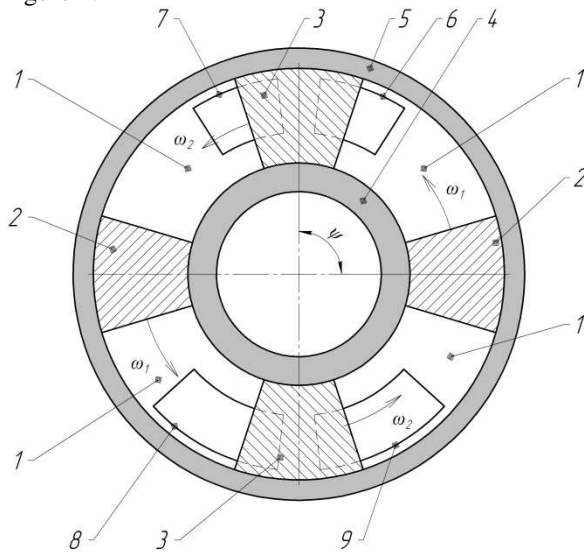


Fig. 2. A general view of a vanes group:
1 – working chamber; 2, 3 – piston; 4 – rotors; 5 – housing; 6 – exhaust port heater; 7 – inlet port heater; 8 – exhaust port cooler; 9 – inlet port cooler.

During one revolution of the output shaft in everyone working chamber of the engine is carried out one complete thermodynamic cycle. Thermodynamic cycle consists of the following processes:

- compression of the working fluid in the isolated volume;
- release of the working fluid through a heater in another module;
- inlet of the working fluid through the heater of another module;
- expansion of the working fluid in the isolated volume;
- release of the working fluid through the cooler in the other module;
- inlet of the working fluid through the cooler from another module.

The thermodynamic cycle that takes place in RVE is closed over the entire engine and opened with respect to one working chamber. The processes of expansion and contraction of the working fluid occurs in isolation. The processes of intake and exhaust of the working fluid occurs with a compound of the

working chambers of two modules with a heater or cooler.

Since in every working chamber RVE passes sequentially through the six thermodynamic processes, some of which takes place in an isolated volume, and some with the release of the working fluid into the working chamber of another module through the heater or cooler, for each of these processes is necessary to develop separate mathematical models that will determine the main parameters of the working fluid (temperature, pressure, weight, etc.) during each processes of cycle, as a function of the angle of rotation of the output shaft, and then to unite model to determine the parameters for all cycle times.

III. IDENTIFICATION OF METHODS FOR CALCULATING THE PARAMETERS OF THE PROCESS OF EXPANSION AND CONTRACTION OF THE WORKING FLUID

The scheme of calculating the expansion and contraction processes that occur in an isolated volume is shown in Figure 3.

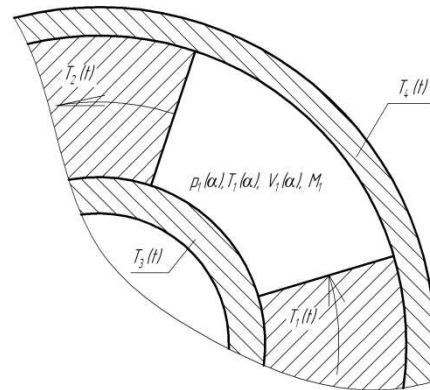


Fig. 3. The scheme of calculating processes of expansion and contraction

In accordance with [4] processes that take place in an isolated volume, described by the equation of the first law of thermodynamics constant weight (1):

$$MC_V dT + pdV + dQ_w = 0, \quad (1)$$

where M – the mass of the working fluid in the chamber; C_V – specific isochoric heat capacity working fluid; T – working fluid temperature in the chamber; dQ_w – heat given (received) the working fluid as a result of heat exchange with the chamber walls; p – pressure; V – volume.

After a series of transformations of the equation (1) is obtained by two differential equations (2) and (3).

$$\frac{dT}{d\alpha} = \frac{(k-1)T}{V} \frac{dV}{d\alpha} - \frac{1}{MC_V} \frac{dQ_w}{d\alpha} \quad (2)$$

$$\frac{dp}{d\alpha} = \frac{kp}{V} \frac{dV}{d\alpha} - \frac{p}{MTC_V} \frac{dQ_w}{d\alpha} \quad (3)$$

Item $\frac{dQ_w(\alpha)}{d\alpha}$ in accordance with [5] equals:

$$\frac{dQ_w(\alpha)}{d\alpha} = \sum_{i=1}^n \frac{\beta_i F_i (T(\alpha) - T_{wi})}{\omega} \quad (4)$$

where β_i – the average value of heat transfer coefficient surface separate part; F_i – heat exchange surface area separate part; T_{wi} – surface temperature separate part; n – number of surfaces, forming a working chamber; i – serial number surface forming a working chamber.

In preliminary calculations, the heat transfer to the walls it is possible to neglect ($dQ_w = 0$) and considered as adiabatic process. For a complete description of the processes of heat and mass transfer during the expansion and compression cycles need to solve equations (2) and (3) for the start of the engine and steady operation engine. At the time of starting the engine wall temperature is 293 K. In the case of the steady operation of the engine for each of the details that form the working chamber should be decided stationary heat conduction differential equation and defined wall temperature T_{wi} . Then it will be possible to determine the heat which is transferred from the working fluid to the walls.

Thus, the processes of expansion and compression of working fluid in the isolated volume may be determined by analytical methods with sufficient accuracy. Numerical study of the processes of expansion and contraction of the working body with sufficient accuracy can be made in systems of computer mathematics (for example, MATLAB, Mathcad, Maple, Mathematica). The results of calculations of the processes of expansion and contraction in computer mathematics system Mathcad are given in [6].

IV. ANALYSIS OF THE MATHEMATICAL MODELS USED TO CALCULATE THE HEAT AND MASS TRANSFER PROCESSES IN PISTON ENGINES STIRLING

Analysis cycles of the supply and removal of heat that occur in piston Stirling engines, has shown their considerable similarity with the cycles of the mass transfer in RVE that allows them to be used as a basis for the development of a methodology of calculation. The main difference is the presence in the construction of the piston Stirling engine regenerator. It may be noted that the mathematical description of mass transfer processes characterized by considerable complexity, as evidenced by the fact that the first Stirling engine was created in 1816, and the

mathematical description of its work has been developed only in 1871.

All the basic mathematical models, which are used to calculate the piston Stirling engines, can be divided into four groups.

- Workflow model of the first order.

These models are used in the preliminary analysis of the piston Stirling engines. Motor parameters are determined on the basis of general relations, which are based on experimental studies. Known ratio to assess the capacity of the Stirling engine, named Bill ratio [7]:

$$P = Z\beta_E V_{SP} P_{cp} N / 6000 \quad (5)$$

P – shaft power; Z – the number of individual thermodynamic cycles; β_E – Bill number, determined by the formula $\beta_E = 0,034 - 0,052\xi$, where ξ – the ratio of the refrigerator temperature to the heater temperature; V_{SP} – a working volume of the compression chamber; P_{cp} – average pressure of the cycle; N – rotational speed.

All found in the literature approximate relations obtained for the piston Stirling engines and their application for the analysis RVE work seems inappropriate, as is significantly different not only engine design, but also the thermodynamic cycle, which implements by the engine.

- Workflow model of the second order.

These models are based on analysis thermodynamic cycle flowing into the engine cylinders, without using heat and mass transfer laws and allow determining the temperature and pressure of the working fluid as a function of the angle of rotation of the engine output shaft. Typically, these models are based on a mathematical model isothermal [6]. This model assumes that the expansion and contraction cycles run at a constant temperature of the working fluid, which is achieved due to supply or remove heat.

The basic admissions of these models are as follows:

- the absence of leaks of the working fluid,
- simplification of heat transfer processes of the working fluid with the walls;
- working fluid temperature in the heater and cooler, equal respectively, is cooler temperature and heater temperature.

Accounting for these factors produced by introducing empirical correction factors.

Workflow model of the second order are used in the preliminary stages of design and allow us to estimate the temperature and pressure in the working chamber of the engine, the output power of the engine and its dimensions. These methods do not allow to accurately determining the parameters of the engine

working process, the error of the results may be around 30-40%. Their main purpose to determine the maximum achievable engine performance. With respect to the piston Stirling engine of the second order model developed by Schmidt, Martini, Finkelstein, Rios, Fejer and others.

- Models workflows third order (nodal analysis methods).

The first study of processes that occur in the piston Stirling engines, method nodal analysis was carried out in 1975, Finkelstein. In models of nodal analysis jointly modeled energy transfer processes and the working fluid flow. To do this, the engine is divided into several sections, for this sections make up and solve a system of ordinary differential equations consisting of the laws of conservation of mass, momentum and energy. The equations are solved by numerical methods, the most common of which is the method of Runge-Kutta methods.

Nodal methods, in contrast to the methods of the first and second order, allow taking into account a number of important factors affecting the operation of the engine. These factors include unsteady heat transfer from the heater and cooler, heat transfer to the walls of the working chamber of the engine. At the same time, the methods of nodal analysis does not take into account the geometric characteristics of each node and the working parameters of the node are considered lumped and depend only on the time.

For piston Stirling engines are best known nodal model workflows Finkelstein, Uriel and the Organ.

As a basis for mathematical model of mass transfer processes in the RVE can be used model, which describes the workflows in the piston Stirling engine with rhombic drive. In this model, the core engine is divided into 13 units. For each of the resulting nodes need to record two ordinary differential equations: the equation of the first law of thermodynamics variable mass (6) and the law of conservation of mass (7):

$$\frac{d}{dt}(MC_V T) = hA(T_w - T) + c_p(w_i T_i - w_0 T_0) - p \frac{dV}{dt} \quad (6)$$

$$\frac{dV}{dt} = G_i - G_0 \quad (7)$$

where h – the working fluid heat transfer coefficient; c_p – isobaric specific heat of the working fluid; G_i – mass flow rate working fluid entering the chamber; G_0 – mass flow rate of the working fluid flowing out of the chamber; T_i – the temperature of the working fluid entering the chamber; T_0 – the temperature of the working fluid out the chamber.

The system of ordinary differential equations must be supplemented by the equation of state of an ideal gas (8):

$$pV = MRT \quad (8)$$

Equations (6) and (7), (8), which are prepared for each of the volumes 13, are solved together, whereby determining pressure, temperature and mass of the working fluid 13 in each of the volumes.

- Computer modeling of the finite element method and finite volume method.

These methods are the most accurate of all the above methods, since they allow taking into account the heat exchange fluid with the walls, geometry of the working chamber, the influence of the intake and exhaust tracts, as well as transients. Also, they allow you to take into account for the flow of the working fluid effects of turbulence and local resistance. To apply these methods require special computer programs (Star CCM +, Flowvision, Ansys Fluent and others). In most cases, these methods are used in the final design stages, together with experimental studies, or instead of them, when you need to calculate the parameters of working processes already designed motor.

V. IDENTIFICATION OF METHODS FOR CALCULATING THE PARAMETERS OF MASS TRANSFER PROCESSES IN RVE

After analyzing the advantages and disadvantages of all basic mathematical models, which are used for the calculation of piston engines, we can conclude that the mathematical model of mass transfer processes in the RVE must be carried out on the basis of nodal analysis methods that provide sufficient accuracy of calculations, and are much smaller in comparison with the methods of computer modeling requirements to computing resources.

The main nodes (control volume), in which will be determined by the parameters of the working body, it is proposed to use the following: The working chamber of the 1st module, inlet manifold the heater or the cooler, tube bundle, and an outlet manifold the heater or the cooler, working chamber 2nd module.

To determine the mass transfer parameters for each node must be written three equations: the equation of the first law of thermodynamics variable mass equation of second mass flow rate and the equation of state [8]:

$$\begin{cases} \sum idM_{ist} = d(Mu) + pdV + dQ_w \\ \frac{dM_{ist}}{dt} = -\mu\rho S_w \\ pV = MRT \end{cases} \quad (9)$$

where i – enthalpy of the working fluid flowing into the control volume or arising from it; dM_{ist} – elementary mass of the working fluid flowing into the control volume or arising from it; u – the internal

energy of the working fluid; μ – expenditure coefficient; ρ – the working fluid density; S – flow section area.

Thus, to describe the parameters of mass transfer processes in the RVE it is necessary to solve differential-algebraic system consisting of 15 equations.

Presentation of the tube bundle as a node with lumped parameters is a clear simplification and can make a significant error in the calculation results, therefore it is necessary to consider separately the processes in the tube bundle and introduce correction factors in the equations (9), if necessary. In general, the processes in the tube bundle described by a

system of the 4 equations: the equation of state, the momentum equation, continuity equation and the energy equation.

Determination of expenditure rate μ , which is included in the system of equations (9), is a complex hydrodynamic task that is complicated by the non-stationary processes occurring in RVE. This problem can be solved by experimental methods or by computer simulation.

The proposed scheme for calculating the parameters of mass transfer process is shown in Figure 4.

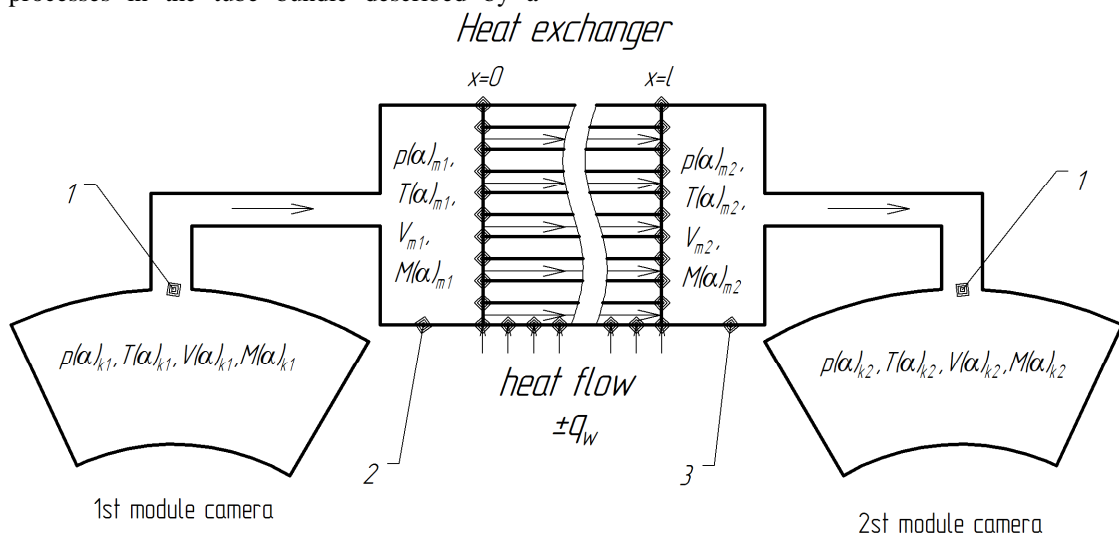


Fig. 4 - Diagram of calculation workflows RVE:
 1 – inlets and outlets of the working chamber; 2 – inlet manifold; 3 – outlet manifold.

$p(\alpha)_{k1}, T(\alpha)_{k1}, V(\alpha)_{k1}, M(\alpha)_{k1}$ – parameters of the working fluid in the working chamber 1st module; $p(\alpha)_{m1}, T(\alpha)_{m1}, V(\alpha)_{m1}, M(\alpha)_{m1}$ – parameters of the working fluid in the inlet manifold; $p(\alpha)_{m2}, T(\alpha)_{m2}, V(\alpha)_{m2}, M(\alpha)_{m2}$ – parameters of the working fluid in the outlet manifold; $p(\alpha)_{k2}, T(\alpha)_{k2}, V(\alpha)_{k2}, M(\alpha)_{k2}$ – parameters of the working fluid in the 2nd module.

Numerical study of the mass transfer processes of the working body is performed in computer mathematics systems (for example, MATLAB, Mathcad, Maple, Mathematica). In the future it is planned to check the adequacy of the assumptions made in the mathematical model to analyze the mass transfer processes of the working body. The check can be carried out by finite element or finite volume methods in special programs (Star CCM +, Flowvision, Ansys Fluent and others).

VI. CONCLUSION

Carried out in this article, the analysis showed that the parameters of the mathematical model of heat exchange and mass transfer processes occurring in the RVE, should consist of two parts. One part describes the processes taking place in an isolated volume based on the differential equations (2) and (3). The second part describes the process of mass transfer based on the system of differential-algebraic equations (9). The

mathematical model includes the following key assumptions: no leakage of the working fluid from the working chamber of the engine; workflow settings in the control volumes are concentrated; the working fluid flow processes are considered quasi-stationary. Built on the basis of recommendations given in this paper, the mathematical model of heat and mass transfer processes in the RVE will significantly reduce the amount of experimental research.

REFERENCES

- [1] Grin'ov D.V. *Structural schemes and principles of rotary vane machines* // Vestnik PskovGU. The economic and technical sciences. Vol. 5. Pskov Publishing house PskovGU, 2014, 142-150.
- [2] RF Patent 2374526 for an invention. Int. Cl. F16H25/04. *Mechanism for converting motion* / Lukyanov Y.N., Zhuravlev Y.N. et al. Publ. 27.11.2009. Bull. Number 33.
- [3] RF Patent 2387844 for an invention. Int. Cl. F01G1/077, F02G1/044. *Rotary-vane engine with an external supply of heat* / Lukyanov Y.N., Zhuravlev Y.N. et al. Publ. 27.04.2010. Bull. Number 12.

- [4] Laushkina L.A., Solohina G.Je., Cherkasova M.V. *Practical Course in Physics. Molecular Physics and Thermodynamics* / Ed. prof. GG Spirin. A manual for schools. M.: VVIA im. prof. N.E. Zhukovskogo, 2008, 156 .
- [5] Tsvetkov F.F., Grigoriev B. A. *Heat and Mass Transfer: A manual for schools. - 2nd ed., Rev. and add.* M: Publishing House of the MEI, 2005, 550.
- [6] Semyonov S.N. *Calculation of temperature and pressure in the rotary-vane engine with external heat supply* // Vestnik PskovGU. The economic and technical sciences. Vol. 5. Pskov Publishing house PskovGU, 2014, 170-176.
- [7] Reader T., Hooper C. *Stirling Engines*. M.: Mir, 1986, 464.
- [8] Petrychenko R.M. *Physical basis intracylinder processes in internal combustion engines*. L.: Publishing House of Leningrad. University, 1983, 244.

Nonlinear Numerical Modelling of Basalt Rebar Reinforced Concrete Structures

Jānis Šlisieris, Līga Gaile, Leonīds Pakrastiņš, Kārlis Rocēns

Riga Technical University, Faculty of Civil Engineering, Institute of Structural Engineering and Reconstruction,
Address: Kļipsalas street 6, Rīga, LV-1048, Latvia.

Abstract. *The ever increasing tendency of more complex architecture and increasing use of basalt fibers in concrete, mainly due to corrosion resistance, requires a suitable, accurate and computationally efficient numerical method for modelling of mechanical behavior. A novel numerical modelling methodology for basalt fiber reinforced concrete structures is proposed. In this paper, the main focus is on modelling concrete beams with basalt longitudinal rebars and steel shear rebars. The proposed method is based on two step simulation method. On the first step a database of flexural stiffness depending on stress-strain state is created using non-linear simulations with continuum finite elements. The database of flexural stiffness is used in second step by performing nonlinear beam finite element simulation of frame structures. The numerical method showed good agreement with experimental results. The use of pre-computed database of flexural stiffness significantly accelerate non-linear simulations and whole building can analyzed by taking into account material non-linearity.*

Keywords: *Basalt fibers, non-linear FEM, concrete structures.*

I. INTRODUCTION

Basalt fiber reinforced concrete have increasing popularity due to corrosion resistance, high tensile strength to weight ratio and good non-magnetization properties. Basalt fiber use in structures where corrosion effects are significant, can be economically and environmentally beneficial. The precise and optimal structural design of basalt fiber reinforced concrete requires an efficient and robust numerical modeling technique.

Numerical modeling of basalt fiber reinforced concrete is complex process. The numerical model must take into account the material non-linearity. Experimental investigations shows that, even for the deflections smaller than serviceability limit state, there are observed highly non-linear material behavior [1].

The flexural testing of single span basalt fiber reinforced concrete beam showed a complex cracking pattern and load-displacement character [1,2,3]. Meanwhile, slip between basalt rebar and concrete for certain circumstances can be observed experimentally [1]. In case of multi-span basalt rebar reinforced concrete plate there are observed bending moment redistribution and highly non-linear material behavior [4].

Those material nonlinearities can be taken into account by appropriate material constitutive law. A thermodynamically consistent non-local damage model for concrete are proposed by [5]. This material model is used in this work. In case of cyclic loading, stiffness recovery and frictional sliding between fiber

and concrete, there are proposed a special constitutive model [6]. A virtual crack monitoring starting from micro-cracks to macroscopic cracks can be achieved by using a combined XFEM- damage mechanic approach [7]. An effective way for calculation of material parameters that are necessary in continuum damage model by using fracture mechanic approach are presented in paper [8]. A convergence problems may arise when non-linear concrete material model is used, therefore non-local theories are recommended. A consistent scheme for calculation of tangential stiffness for non-local damage models are proposed in work [9].

Real-size structures can be mathematically modelled by using extended multi-scale finite element (EMFEM) model, or other sub-structuring methods [10,11,12,13]. In those publications, mainly continuum based finite elements are used. Currently, there are lack of information on modeling using beam finite elements on coarse scale and continuum elements on fine scale. For concrete structures beam finite elements have been widely used to get the whole building structural response. In this work there are proposed a modelling framework of concrete structures with basalt rebars. This technique is based on two scale simulations. On the fine scale simulations, a database with precomputed stiffness characteristics of concrete elements are obtained, depending on deformation state. Furthermore, this database is used for numerical modeling of whole structure on coarse scale by using non-linear beam finite elements.

II. NUMERICAL MODELING

Appropriate numerical modelling technique is dependent on the structural behaviour. For slender beam or frame structures here are proposed a special semi-analytical method that take into account bending moment and axial force when estimating flexural stiffness. When the beam span to cross section height ratio is less than 10 then it is recommended to use EMFEM approach to generate the database with flexural stiffness for necessary cross section. In case of large building frame, both methods can be combined to get maximal performance.

Material constitutive model for concrete is similar as described in publication [5], that include separate damage variable for tension cracking d_t , and for compression damage d_c . As indicated in experimental testing of basalt rebars, they behave nearly linear elastic up to failure [3]. Therefore linear elastic model is used for basalt rebars.

For the tension zones the stiffness was reduced with multiplier $(1 - d_t) * (1 - d_c)$, but in compression zones $(1 - d_c)$ [5]. The evolution of damage variables was defined by exponential laws. For more details see [5].

For beams with complicated geometry, where high stress gradients can appear, it is necessary to use embedded window method [11]. In this case the beam finite element is joined with linear elastic extension (with length L^*) in both ends. This method is recommended for the cases when hypothesis of flat cross sections is not valid.

Concrete is modelled with continuum based finite elements. In this paper a plane stress 4 node finite elements are used. Rebars are modelled by using 2 node link type finite elements.

The obtained database are used in non-linear beam finite element. Only material non-linearity is used for small strain theory.

Extended multi-scale approach

Secant stiffness matrix of beam FE is obtained by performing fine scale simulation with plane stress non-linear finite elements. For beam element with N degrees of freedom (DOF), the nodal displacement vector $\mathbf{d}^0 = \{U^1, U^2, \dots, U^N\}$. From structural mechanics and finite element definition it is clear that i-th column in stiffness matrix is defined by nodal forces of beam finite element from appropriate unit i-th DOF []. Therefore N+1 load cases are necessary for calculation of stiffness matrix of beam finite element. i-th load case is defined by following displacements applied to nodes of finite element $\mathbf{d}^i = \{U^1, U^2, U^{i-1}, 0, U^{i+1}, \dots, U^N\}$. The reaction forces from nodal displacements on coarse scale nodes are denoted in following way $F^i = F(\mathbf{d}^i) = \{F^{i,1}, F^{i,2}, \dots, F^{i,N}\}$. Coefficients of secant stiffness matrix are obtained using following expression:

$$K_{i,j} = \frac{F^{0,j} - F^{i,j}}{\|d^0\|}, \quad (1)$$

where index i- indicate load case number and j- component of reaction force vector.

For relatively slender structures, instead of calculation of whole stiffness matrix, only flexural stiffness EI, axial stiffness EA and shear stiffness GA are necessary to compute. Using appropriate beam theory, for example classical or Timoshenko, stiffness matrix can be assembled.

For slender structures where only EI and EA are important a special semi-analytical approach are presented in next sub-chapter.

Semi-analytical approach

This method is recommended for the structures that have tendency to fail due to bending moment.

Due to non-linear stress-strain relationship the position of neutral axis of cross section is dependent on bending moment and axial force acting in this cross section. It is assumed that classical Euler-Bernoulli hypothesis of flat cross sections are true. Using this hypothesis, deformation field of cross section can be described with tension strains ϵ_{st} , compression strains ϵ_{sp} , and position of neutral axis X (see figure 1). Those three unknowns are calculated by using three non-linear integral equations - R_1, R_2, R_3 .

The first equation states the moment equilibrium of internal stress resultant and bending moment M in current cross section:

$$R_1 = \int_{-X}^{H-X} \sigma(y) * y * b(y) * dy - M = 0 \quad (2)$$

For practical calculations the cross section is divided in many layer (usually 30 to 50), where i-th layer distance to neutral axis is y_i and normal stress in this layer is σ_i , area of i-th layer is A_i . Total height of cross section is H.

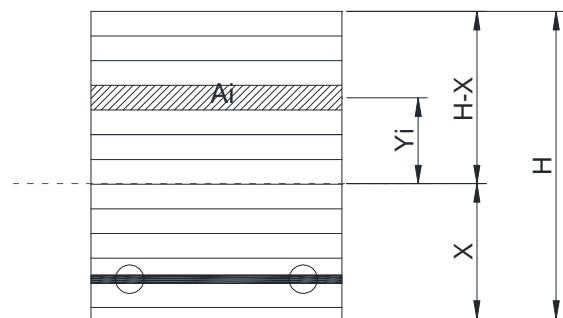


Figure 1. Multi-layer structure of reinforced concrete with smeared rebar's layer.

Rebars are replaced with equal area smeared layer.

Second equation is obtained by using equilibrium of axial forces:

$$R_2 = \int_{-X}^{H-X} \sigma(y) * b(y) * dy - N \quad (3)$$

The third equation is obtained by using assumption that strains on neutral axis ε_N are produced only by axial force:

$$R_3 = \int_{-X}^{H-X} E(y) * \varepsilon_N * b(y) * dy - N \quad (4)$$

where E_i –modulus of elasticity of i-th layer. ε_N is calculated by using linear interpolation of strains through the thickness of cross section:

$$\varepsilon_N = \frac{\varepsilon_{st} * H + X * (\varepsilon_{sp} - \varepsilon_{st})}{H} \quad (5)$$

Resulting system of three non-linear equations is solved by Newton-Raphson iterative method. When the strains and position of neutral axis are known, then flexural stiffness EI and axial stiffness EA are computed and used in non-linear beam finite element.

Non-linear beam finite element

In this work a typical 2 node beam finite element with 3 DOF (two translations and one rotation) per node are used. Total load is divided in N_{steps} load steps. Within each load step there are performed a modified Newton-Raphson iterations. Once the convergence norm of residual vector R is less then tolerance than iterations stops and algorithm moves to next load step.

$$R = F_{int} - F_{ext} \quad (6)$$

where F_{int} - internal forces in nodes, F_{ext} - external forces in nodes.

The secant stiffness matrix C_s is computed using Timoshenko or Euler- Bernoulli theory, depending ratio between span of beam and height of cross section:

$$C_s = F(EI, GA, EA) \quad (7)$$

The convergence difficulties are reduced by using non-local theory. Instead of local flexural stiffness, the smeared flexural stiffness \bar{EI} is used. This can

solve the mesh dependency problem and also can include the tension stiffening effects.

III. RESULTS AND DISCUSSION

The numerical results are validated using experimental measurements from publications [3,4]. Four point bending test of single span 3 m long beam and flexural test of two span beams (each span 2 m long) are analysed.

Single span beam in four point bending

Experimental data of four point bending test was taken from publication [3]. Beam was made using C30/37 concrete, with cube compressive strength 52.3MPa, modulus of elasticity 33.8 MPa and tensile strength 3.6 MPa. Tensile reinforcement was made of 5 Ø9mm basalt rebars. Tensile strength of basalt rebars was 1485 MPa, modulus of elasticity 56.3 GPa, and ultimate strain 2.62 %.

In compression zone 2 Ø8mm B500SP steel rebars was used. Shear reinforcement was made of Ø8mm steel rebars with 100 mm step. Height and width of cross section was 300 and 200 mm, respectively. Distance from center of rebars to surface of beam was 30 mm. Total length of beam was 3050 mm, distance between supports 2700 mm and distance between applied loads was 900 mm. Since the ratio between span and cross section height is 9, extended multiscale approach was used.

The load deflection curve is shown in figure 2. There was performed a 3 alternative numerical simulations- full finite element simulation, extended multiscale with embedding window length $L^* = 0$ and extended multiscale with embedding window length $L^* = 90$ mm. Simulations were done up to serviceability limit state (assumed $L/250$). Up to 10 KN load the full scale finite element simulation showed better agreement with experiments. The simulation with extra window $L^* = 90$ mm, showd slightly overestimated stiffness comparing to experiments, when load exceeds 25 KN. The best agreement with experimetns was showd simulations with window $L^* = 0$, when load exceeds 25 KN.

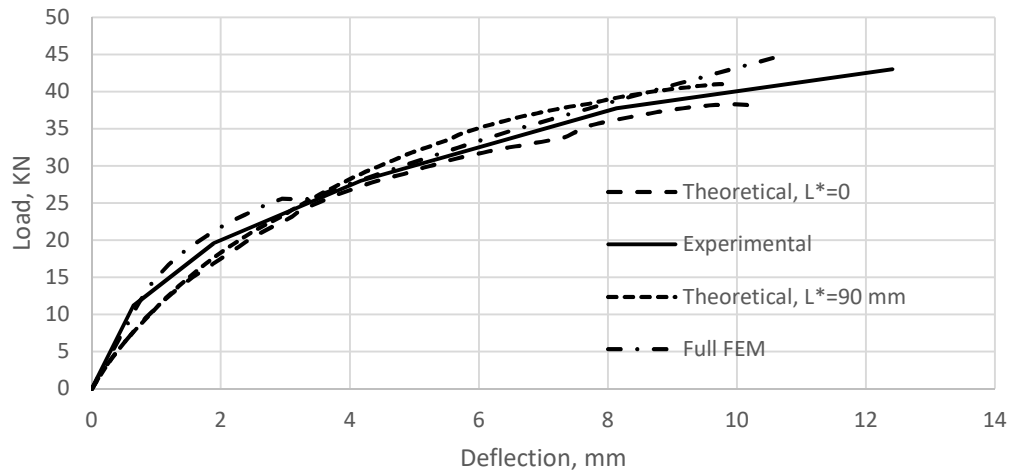


Figure 2. Validation of model with experimental data, load-deflection curve, for beam with 5 basalt fibers, diameter 9 mm.

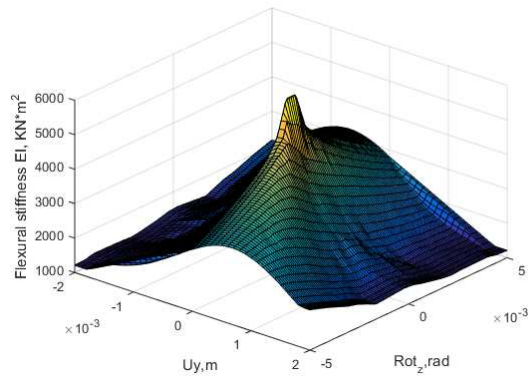


Figure 3. 3D visualization of flexural stiffness EI, depending displacement degrees of freedom of beam FE. Length of finite element was 250 mm. $L^* = 0$

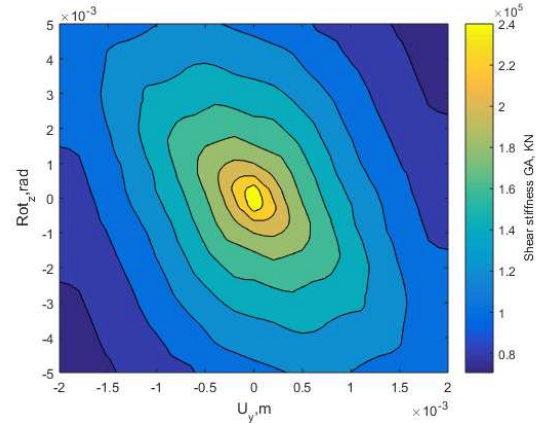


Figure 6. Contour plot of shear stiffness GA, depending displacement degrees of freedom of beam FE. Length of finite element was 250 mm. $L^* = 0$

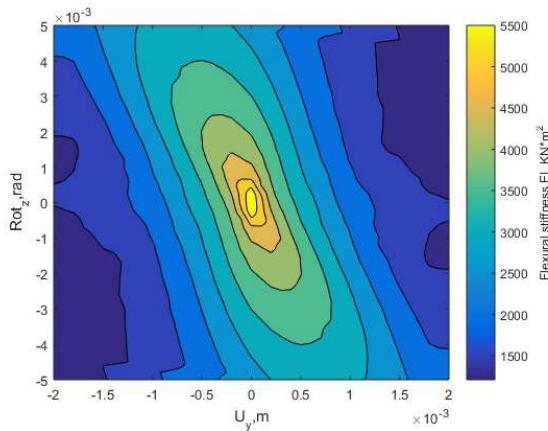


Figure 4. Contour plot of flexural stiffness EI, depending displacement degrees of freedom of beam FE. Length of finite element was 250 mm. $L^* = 0$

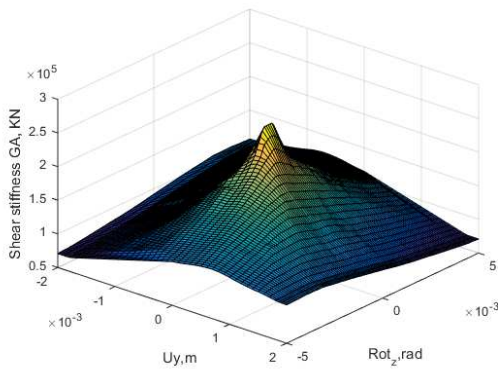


Figure 5. 3D visualization of shear stiffness GA, depending displacement degrees of freedom of beam FE. Length of finite element was 250 mm. $L^* = 0$

Databases of flexural and shear stiffness for beam finite element with length 250 mm and zero extra window length are shown in figures 3-6. Maximal flexural and shear stiffness $6000 \text{ KN} \cdot \text{m}^2$ and 300000 KN , respectively, was observed at nearly zero degrees of freedom. The overall character of shear and flexural stiffness showed a similar tendency.

The visualization of damage evolution is showed in figures 7-8. The damage is represented by damage variable, where 0 indicates no damage and 1 complete damaged area. Experimental observation of damage evolution for similar beams are shown in figure 9. The tensile crack-damage propagation are similar with experimental data. The symmetry of structure was taken into account and only half of beam was modelled.

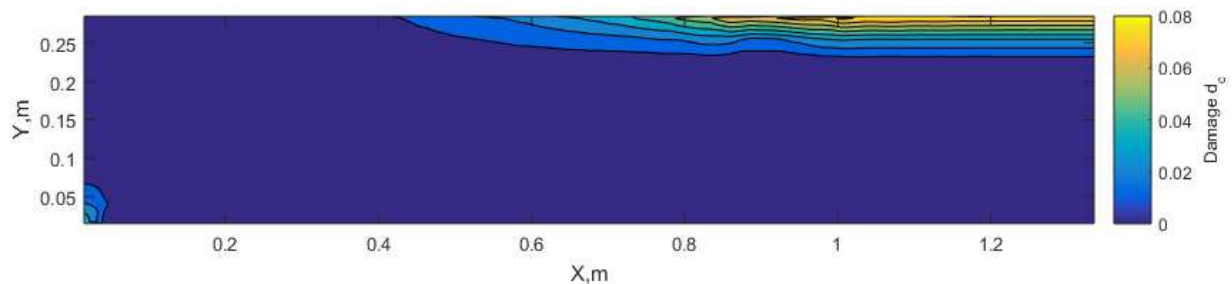


Figure 7. Damage variable in compression d_c .

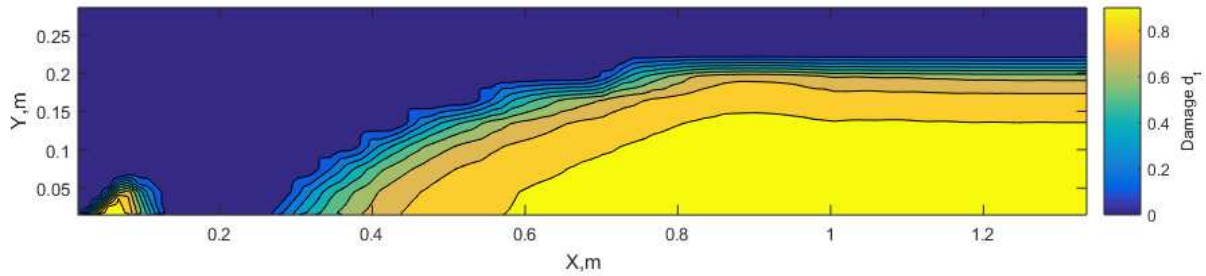


Figure 8. Damage variable in tension d_t .

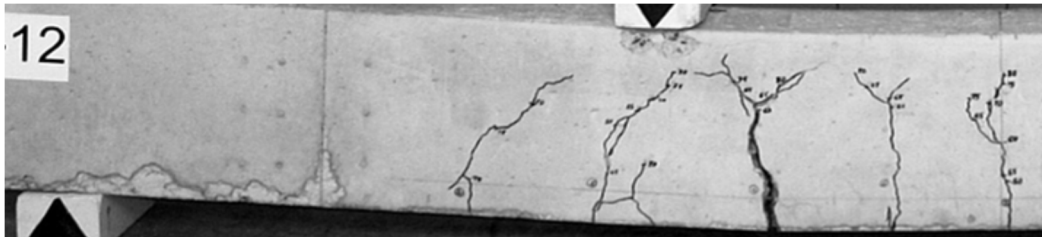


Figure 9. Typical experimental observation of basalt beam failure in four-point bending (figure taken from [1]).

Two-span beam

The numerical model was validated with continuous two 2000 mm span slab. All details are given in publication [4]. A concentrated load was applied in the middle of each span. Thickness of slab was 150mm, width 500mm. Material properties were similar as for single span beam in previous section. Two cross sections were tested. The first cross section was made of 5 \varnothing 10mm basalt rebars and

denoted as C-B-OO. The second cross section was made of 3 \varnothing 8mm basalt rebars and denoted as C-B-UU. Since the span to thickness ratio is 13.3, a semi-analytical approach is used for numerical simulations. In figure 10 is shown the load-displacement curve that shows good agreement between experiments and simulations even for load much higher than serviceability limit state.

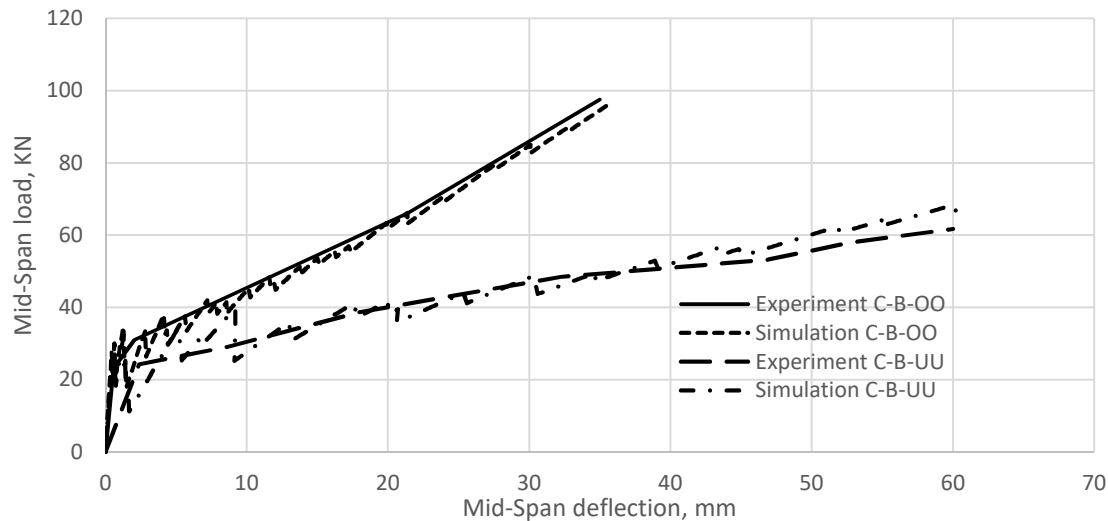


Figure 10. Load deflection curves of 2-span beams (experimental and theoretical)

IV. CONCLUSION

An efficient numerical modelling framework for basalt rebar reinforced concrete is proposed. The method is based on precomputed database with stiffness characteristics such as flexural stiffness EI of the beam. Two alternative methods for computation of database are proposed. The first method is based on extended multi-scale finite element calculations for relatively thick beams, where shear cracks may appear. The second method is based

on semi-analytical approach where the damage and cracks from bending moment and axial force are considered. The method is validated with experimental data from literature and showed good agreement with experiments.

V. ACKNOWLEDGMENTS

The research leading to these results has received the funding from Latvia state research programme under grant agreement "INNOVATIVE

MATERIALS AND SMART TECHNOLOGIES FOR ENVIRONMENTAL SAFETY, IMATEH".

Support for this work was provided by the Riga Technical University through the scientific Research Project Competition for Young Researchers No. ZP-2016/1.

REFERENCES

- [1] Atutis M., Valivonis J., Atutis E. Experimental study of concrete beams prestressed with basalt fiber reinforced polymers. Part I: flexural behavior and serviceability, *Composite Structures*, 2017, doi: <http://dx.doi.org/10.1016/j.compstruct.2017.01.081>
- [2] Atutis E., Atutis M., Budvytis M., Valivonis J. Serviceability and Shear Response of RC Beams Prestressed with a Various Types of FRP Bars, *Procedia Engineering*, 172, 2017, pp 60-67.
- [3] Pawłowski D., Szumigala M. Flexural Behaviour of Full-scale Basalt FRP RC Beams – Experimental and Numerical Studies, *Procedia Engineering*, 108, 2015, pp. 518-525.
- [4] Mahroug M.E.M., Ashour A.F., Lam D. Experimental response and code modelling of continuous concrete slabs reinforced with BFRP bars, *Composite Structures*, 107, 2014, pp. 664-674.
- [5] He W., Wu T.F., Xu Y., Fu T.T. A thermodynamically consistent nonlocal damage model for concrete materials with unilateral effects, *Computer Methods in Applied Mechanics and Engineering*, 297, 2015, pp. 371-391.
- [6] Richard B., Ragueneau F., Cremona C., Adelaide L. Isotropic continuum damage mechanics for concrete under cyclic loading: Stiffness recovery, inelastic strains and frictional sliding, *Engineering Fracture Mechanics*, 77(8), 2010, pp. 1203-1223.
- [7] Roth S.N., Léger P., Soulaïmani A. A combined XFEM–damage mechanics approach for concrete crack propagation, *Computer Methods in Applied Mechanics and Engineering*, 283, 2015, pp. 923-955.
- [8] Kurumatani M., Terada K., Kato J., Kyoya T., Kashiya K. An isotropic damage model based on fracture mechanics for concrete, *Engineering Fracture Mechanics*, 155, 2016, pp. 49-66.
- [9] Jirásek M., Patzák B. Consistent tangent stiffness for nonlocal damage models, *Computers & Structures*, 80(14–15), 2002, pp. 1279-1293.
- [10] Ren M., Cong J., Wang B., Guo X. Extended multiscale finite element method for small-deflection analysis of thin composite plates with aperiodic microstructure characteristics, *Composite Structures*, 160, 2017, pp. 422-434.
- [11] Temizer İ., Wu T., Wriggers P. On the optimality of the window method in computational homogenization, *International Journal of Engineering Science*, 64, 2013, pp. 66-73.
- [12] Liu H., Zhang H.W. A p-adaptive multi-node extended multiscale finite element method for 2D elastostatic analysis of heterogeneous materials, *Computational Materials Science*, 73, 2013, pp. 79-92.
- [13] Liu H., Lv J. An equivalent continuum multiscale formulation for 2D geometrical nonlinear analysis of lattice truss structure, *Composite Structures*, 160, 2017, pp. 335-348.

Spurious Activation Assessment of Thermal Power Plant's Safety-Instrumented Systems

Sergei Trashchenkov¹, Victor Astapov²

Pskov State University, Computer Science and Electric Power Engineering Faculty, Tallinn University of Technology, School of Engineering¹,
Tallinn University of Technology, School of Engineering²

Abstract. Safety-instrumented systems (also called technological protections) play the significant role in prevention and mitigating of major accidents that can occur on thermal power plant. Activations of safety-instrumented system turn the power unit into safe state by shutting it down or reducing its productivity. The power generation process operates continuously. Any unplanned outage of generation equipment leads to undersupply of energy and big commercial losses to generation company. In Russia the values of allowed spurious trip rate for safety-instrumented systems are set by regulatory agency. These values are strict to all technological protections and do not take into account the differences in amounts of losses. This paper presents more flexible approach based on the Farmer's risk criterion. Also risk reduction factor for spurious activation is proposed.

Keywords: Farmer's risk criterion, safety-instrumented systems, spurious activation, thermal power plant.

I. INTRODUCTION

Nowadays thermal power plants (TPPs) are well studied facilities. Decades of operation in thousands of units all around the world produced data for technology development and great amount of studies. Part of those studies are dedicated to reliability issues.

Redundancy of important equipment for safety and reliability is the topic of [1]. The decision about necessity of installing additional lubricate oil pump in these study is based on decision tree approach and costs assessment.

Many papers are focused on maintenance activities. For example, [2] presents genetic algorithm with simulated annealing optimization method. Method helps in increasing reliability and reduce maintenance costs due to changing intervals of planned outages in depending on load demand.

Several papers are about safety-instrumented systems (SIS). In [3] the industrial experience of using IEC 61508 [4] in the thermal power plants is discussed. It was concluded that in most cases TPP equipment does not require very high level of reliability of SIS. In [5] concepts of IEC 61508 was used for Furnace Safety Supervisory System (FSSS) of TPP. Reliability of FSSS was improved by implementing redundant actuator.

Standard [4] uses SIS indexes of unavailability to response on demand (average probability of failure on demand or average frequency of failure) as a measure of reliability to promote the safety state of facility. Failure on demand can lead to the accident. Spurious failures in this approach are not taken into account because the result of such failures is safety

state (shutdown or reduced productivity). In case of power plant such unplanned unavailability or reduced availability lead to big commercial losses. That is why assessment of spurious failures is crucial to TPP. The authors did not find any studies about TPP SIS spurious failures. Research of SIS spurious failures reliability in general is presented in paper [6]. Different approaches of computing spurious trip rate (STR) are described. In addition, the concept of spurious trip levels (STL) is criticized for economical point of view without any assessing of influence to the safety.

This paper introduces the approach for determine acceptable values of STR based of the potential amounts of losses.

II. MATERIALS AND METHODS

A. SIS description

SISs play significant role in accident prevention and mitigation of its consequences for hazardous facilities such as TPP. They perform safety functions by controlling the critical parameters. Crossing the thresholds by those parameters create demands for the SISs to turn off the process of facility or for reducing the productivity.

The structure of SIS can be envisioned as it is shown on Fig. 1. SIS consists of sensors subsystem (S), logic solvers subsystem (LS) and final elements subsystem (FE). Subsystems form series structure. That means that failure of even one subsystem leads to failure of all system. SIS functioning in response to demands mode. Demands are produced by equipment under control (EUC) with frequency λ_{de} . In the case of TPP EUC are power unit itself, steam boiler, steam

ISSN 1691-5402

© Rezekne Academy of Technologies, Rezekne 2017
<http://dx.doi.org/10.17770/etr2017vol3.2529>

turbine, feedwater pumps, etc. [7]. The results of SIS activation can be shutdown, reduction to 50 % productivity, reduction to 30 % or shifting to the idle conditions. If demand occurs, SIS should react. Presence of demand and absence of reaction due to SIS failure lead to the accident. SIS's unavailability can be represented by probability of failure on demand (PFD) for SISs with rare demands (less than one demand per year) or by frequency of failure (PFH) if demands occur more often than once per year. The limits of acceptable/unacceptable level of failures on demand depend on results of risk analysis. Standard [4] recommends several qualitative, quantitative and semi-quantitative methods for risk analysis. Describing these methods is beyond of this paper.

Triggering of SIS without demand is a spurious failure. Probabilistic representation of spurious failures is spurious trip rate (STR).

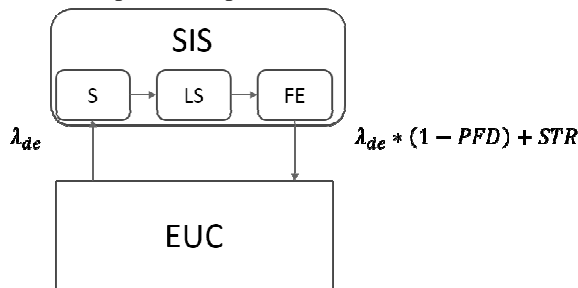


Fig. 1. Safety-instrumented system functioning (based on the concepts described in [4]).

Each subsystem can be designed with different redundancy. Redundancy usually represents as KooN (K out of N), where K is a number of subsystem's elements that is enough to trip subsystem; N is a total number of elements in the subsystem. In addition, $K \leq N$. Subsystems with the same N and different K can have rather different reliability. Lower value of K makes subsystem more reliable to failures on demand just as higher value increases reliability to the spurious failures. Table 1 shows formulas for determining subsystem STR (according to the standard [8]). As it is clear from these formulas, STR values depend on several factors:

- reliability of elements (λ_s – spurious failure rate);
- mean time to repair/ restore (MTTR);
- percent of common cause failures (β_s).

○ STR risk acceptance criteria

In the fundamental paper [10] risk R is described as triplet of scenarios s_i , probabilities p_i (or like in our case frequency f_i) and consequences x_i :

$$R = \{ \langle s_i, f_i, x_i \rangle \}, \quad (1)$$

where $i=1, 2, \dots, N$ is a number of scenario.

Table I
Formulas for str of sis's subsystems with different redundancy [8]

Architecture	Formula
1oo1	$STR_{1oo1} = \lambda_s$
1oo2	$STR_{1oo2} = 2\lambda_s + \beta_s \lambda_s$
2oo2	$STR_{2oo2} = 2\lambda_s^2 + \beta_s \lambda_s$
2oo3	$STR_{2oo3} = 6\lambda_s^2 * MTTR + \beta_s \lambda_s$
2oo4	$STR_{2oo4} = 12\lambda_s^3 * MTTR + \beta_s \lambda_s$

Russian standard [9] requires strict values of STR for each SIS and the total value limitation for all SISs together (0.2 failure per year, no more than 0.065 failure per year for each SIS). The disadvantage of these reliability requirements is that it does not evaluate consequences of spurious trips.

Spurious shutdown or spurious reduced productivity leads to uncertain losses, which value depends on load demand. Authors introduce a risk-orientated approach to determine required values of STR based on load demand.

In our study, according to [9] and other standards, we assumed power unit with 38 SISs that spurious triggering leads to significant changes of availability. The SISs were grouped to consequences categories, as it is shown in Table II. For the sake of space full list is not presented in this paper.

Table II
Categories of SIS

Category of SIS	Amount of SIS
SISs that shut down the unit	28
SISs that reduce efficiency to 50 %	8
SISs that reduce efficiency to 30 %	1
SISs that turn unit into idle mode	1

Such form of risk can be represented in tabular form or graphically as a set of points on x-f-plane. There are two kinds of values to assess consequences x of spurious trip: amount of energy (MW*h) that is not produced due to spurious protection triggering (see Fig. 2). and amount of money losses (EUR). Amount of money losses is more preferable because of its ability to take into account several significant factors, such as changing of cost rate, operational and maintenance costs, penalties to system operator (the main expenditure). Graphical representation involves acceptance criteria (AC) [11]. AC can be straight line, curve or staircase function. The unit of STR is failures per year.

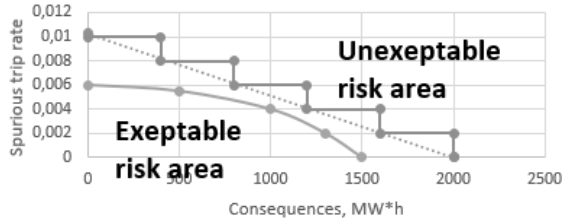


Fig. 2. Examples of the STR risk acceptance criteria.

In the case of straight line (on a logarithmic scale), risk criteria is equation [11]:

$$R_C = F \cdot X^m, \quad (2)$$

where F are all values of frequency on risk criteria line; X are all values of consequences; m is a factor of proportionality.

Then we can implement risk reduction factor (RRF) to measure required improvements for SIS:

$$RRF_i = \frac{STR_U}{STR_A}, \quad (3)$$

where STR_U is unacceptable STR of the SIS; STR_A is acceptable STR of the SIS.

SIS needs reliability improvements if it not satisfied to the risk criteria. For understanding the role of subsystems or even the role single elements in the total SIS reliability authors used importance measures [12].

B. Power unit description

One of the most important parameters of power plants operating on fossil fuel is input cost characteristic. Every generation unit (GU) is unique and has its own parameters, including fuel consumption, which depends on generation power. Generally, input cost characteristic $B(P)$ can be represented as table or described by formula (4):

$$B(P) = a + bP + cP^2, \quad (4)$$

where a, b, c – are coefficients of input cost characteristics; P – output power of GU; P_{min} – minimal amount of power that can be produced by GU. Fuel cost characteristic can show not only how much fuel consumes GU during one hour, but also show how much producer pays for one hour operation and measured in MW/MWh or €/h correspondingly.

The cost rate characteristic $\delta(P)$ evaluates how much fuel is necessary for production of 1 MWh or how much does it cost:

$$\delta(P) = B(P) / P. \quad (5)$$

The efficiency characteristic $\eta(P)$ of GU – is inversely proportional to cost rate characteristic

value, and could be described in few words: the higher load – the higher efficiency.

$$\eta(P) = P / B(P) \quad (6)$$

Fig 3 shows the example GU efficiency characteristic at TPP [13].

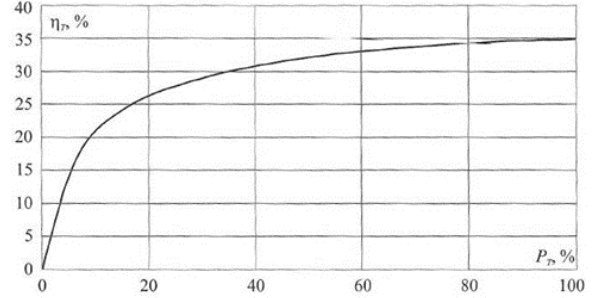


Fig. 3. The relation of GU efficiency from the load.

As result, every power plant, consisting on several GUs, has own optimal load dispatch according to the load profile and GUs' characteristics. In case of one GU, producer try to load it as much, as it possible. That is why some disturbances and changes in unit output lead to losses. Such kind of scenario could occur because of protection spurious triggering and as a result, GU need to reduce its output, unplug from the load or shut down.

With aim to evaluate consequences of the spurious triggering on power plant consisting of one GU, the authors considered following case. Fuel cost characteristics of GU are taken from [14] and presented in Table III.

Table III
Generators Data

Parameter				
P_{min} , MW	P_{max} , MW	a	b	c
30	200	208.4125	9.6506	0.0058

III. RESULTS AND DISCUSSION

A. Losses calculation

Let us assume that in normal regime the load of GU is 90% from nominal. In this case $P_{G0} = 180$ MW, and according to (4-5) the cost rate characteristic is $\delta_0 = 11.85$ €/MWh.

Due to the fault, the output of GU changes to 0.5 $P_{nom} = 100$ MW. As result fuel consumption is changing and fuel price for production $\delta_1 = 12.31$ €/MWh. Depending on restoration time, producer fuel consumption losses appear only because of less effectiveness. It means, that producer lost 0.46 € for every generated 1 MWh with total losses of 83 € per restoration hour.

We can see that fuel cost losses are not significant. However, we need to remember, that in this case, producer pays for other operational and

maintenance costs such salary and own needs as well as do not sell electricity. For example, according to [15] the fixed operational and maintenance costs are 913 €/h. Total amount of generation losses is 996 €.

The most significant problem is, that according to nowadays conditions in electricity market, a producer have official duties to provide electricity to customers or system operator. In case of supplier default, it is obliged to compensate for the expenses incurred. Usually, this amount is registered in the contract. In our case, we consider general numbers taken from [16], where producer pays 0.77 € per none-provided kWh in case of interruption less than 48 hours. In case of generation reduction to $0.5P_{nom}$, the total unsupplied energy is $\Delta W = 80$ MWh, it means, that compensation might be paid is 61 600 €.

Based on these two statements, the Table IV shows possible losses during protection spurious triggering different for scenarios.

The same way calculations for scenarios 2 and 3 are performed and presented in Table IV. Here generation costs are equal, because we assume, that fuel consumption in minimal margin is the same as without load, because generator should rotating.

Table IV
Possible Losses During Fault

No	Regime's changes	Repair duration, h	Generation costs losses, €	Fine to system operator, €	Total, €
1	90 % -> 0.5 P _{nom}	1	996	61600	62596
2	90 % -> P _{min}	1	1 206	100100	101306
3	90 % -> 0 %	1	1 206	138600	139806
4	90 % -> shut down	2	1826	277200	279026

As mentioned before, the time of restoration is varying, but in these particular calculations is taken as one hour for pp. 1-3. Most of the technologies have a limitations regarding to the minimum "rest" time before restarting. If the GU shuts down, the time of restoration is taken as two hours according to the average data for hot start presented at [15]. Here authors apply hot start, because of technology stopped less than 8 hours.

The results show, that TPPs consisting of one GU is very dependent from faults and protection spurious triggering due to high penalties for none supply. Obviously, it is especially critical for TPPs with bigger capacities. That is why there is a reason in additional agreements with more solid producers, who can provide reserve for less money. Installation of second GU, which increase costs (especially investment expenditures), but reduce possible penalties is an alternative option.

B. Construction of risk acceptance curve

According to [17], risk curve construction procedure includes following steps:

- collect relevant data and sort it by the value of consequences;
- calculate the cumulative function;

- show results as diagram.

As we mentioned above, existing reliability requirements [9] establish strict value for the summary STR that is equal to 0.2 failure per year without analysis of consequences. Authors assumed this value as a cumulative STR for the risk acceptance criteria.

Cumulative STR was divided equally to each of four SIS categories from Table II. Individual acceptable STR for single SIS depends on the number of SIS in each category. The values of potential losses, values of STR for single SIS of each category and cumulative STR are presented in Table V.

Table V
Categories of SIS with ranged consequences and cumulative STR

SIS category	Consequences	STR for the single SIS	Cumulative STR
SISs that reduce efficiency to 50 %	62596	0.001786	0.001786
SISs that reduce efficiency to 30 %	101306	0.00625	0.008036
SISs that turn unit into idle mode	139806	0.05	0.058036
SISs that shut down the unit	279026	0.05	0.108036

Diagram in Fig. 3 shows cumulative STR of data in Table V.

Assume the SIS that triggering lead to shut down of GU. As an example, we chose a SIS of controlling pressure in lubricate oil system of turbine. Reliability parameters of SIS's elements for spurious triggering and architectures of subsystems are in Table VI. Total value is computed by using formulas in Table I.

Table VI
Reliability parameters of SIS's elements

Element	λ_s , 1/hour	Architecture	STR, 1/year
Controller	0.0000057	1oo2	0.005
Pressure transmitters	0.0000002	2oo3	0.000183
Solenoid actuated valve	0.00000423	1oo2	0.00371
Total			0.008893

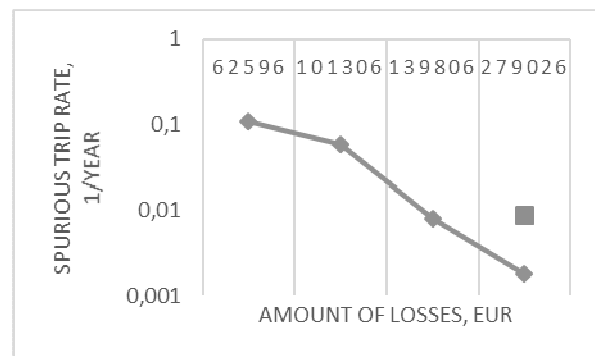


Fig. 3. Cumulative consequences-frequency curve of STR.

Obtained value of the SIS's STR is also presented in Fig. 3 as a single point. Result is unacceptable

according to constructed risk acceptance curve. To make it acceptable based on (3):

$$RRF = \frac{0.008893}{0.001786} = 4.98. \quad (7)$$

That means that obtained STR goes beyond the acceptable value in five times and should be reduced significantly by changing the elements or the architectures of subsystems.

Another way to construct risk acceptance curve is to use power function formula (8) and two scenarios, which STR and amount of losses assumed as acceptable [17].

$$F(L) = aL^{-b}, \quad (8)$$

where a, b > 0 are parameters of the curve, L is amount of losses.

Consider two points of the future risk acceptance curve:

$$\begin{aligned} F(65000) &= 0.1, \\ F(120000) &= 0.01. \end{aligned} \quad (9)$$

These points are rather close to points on acceptance criteria curve in Fig. 3. Parameters a and b can be found as:

$$\begin{aligned} 10^{-1} &= a \cdot 65000^{-b}, \\ 10^{-2} &= a \cdot 120000^{-b}. \end{aligned} \quad (10)$$

Both equations include parameter a. After rearrangement the equation with unknown parameter b is:

$$\begin{aligned} 2^b &= 10, \\ b &= \log_2 10 = 3.322. \end{aligned} \quad (11)$$

With known value of parameter b, parameter a is equal to:

$$a = \frac{10^{-1}}{60000^{-3.322}} \approx 746480476726256. \quad (12)$$

Risk acceptance curve can be described by the formula (13):

$$F(L) = 746480476726256 \cdot L^{-3.322}. \quad (13)$$

Graphical representation of equation (13) in linier scale is presented in Fig. 4. Any value of losses can be examined for maximum acceptable STR value by function (13).

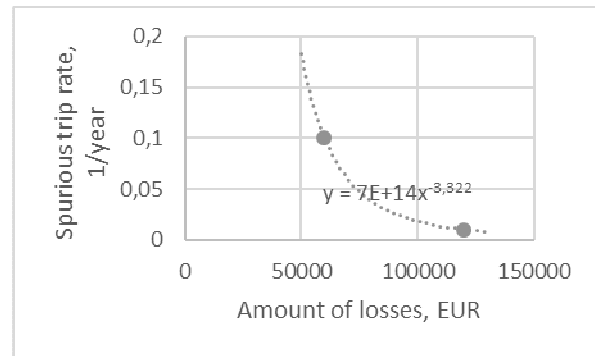


Fig. 4. Example of acceptable STR curve.

IV. CONCLUSION

In this paper, we introduced technique of spurious trip assessment for SIS of thermal power plants. We showed that our technique is more flexible than traditional one [9] and is compatible with it. It can be used as an addition to PFD assessment to improve the decision making process by taking into account such factors as effectiveness of GU regime, fuel costs, maintenance cost and penalties to the system operator.

V. ACKNOWLEDGMENTS

This publication is partially supported by European Regional Development Fund Higher Education Internationalisation, Mobility and Sustainability support program Dora Plus 2014-2020.4.01.16-0025 (contract 36.9-2/59).

REFERENCES

- [1] Carazas, F. G., and Gilberto Francisco Martha de Souza. "Risk-based decision making method for maintenance policy selection of thermal power plant equipment," Energy, vol. 35.2, pp. 964-975, 2010.
- [2] Leou, Rong-Ceng. "A new method for unit maintenance scheduling considering reliability and operation expense," International Journal of Electrical Power & Energy Systems, vol. 28.7, pp. 471-481, 2006.
- [3] P. Rieff, R. Scholing "Power plants in a new safety perspective | Power Engineer," February 21 2013. [Online]. Available: <http://www.engineerlive.com/content/24229> [Accessed: February 21, 2017].
- [4] IEC 61508 Functional Safety of Electrical/electronic/programmable Electronic Safety-related Systems. International Electrotechnical Commission, - Geneva, 2010.
- [5] Wang, Peng, Xiaoyan Chen, and Lei Yu. Application of Functional Safety Theories in Furnace Safety Supervisory System. 2017 9th International Conference on Measuring Technology and Mechatronics Automation (ICMTMA), January 14-15, 2017, Changsha, Hunan, China, pp. 164-167, 2017.
- [6] Jigar, Abraham Almaw, Yiliu Liu, and Mary Ann Lundteigen. "Spurious activation analysis of safety-instrumented systems," Reliability Engineering & System Safety, vol. 156 pp. 15-23, 2016.
- [7] Trashchenkov, S., & Egorov, V. Analysis of emergency situations on the process of thermal power plants using mathematical apparatus of Petri nets. In Environment. Technology. Resources. Proceedings of the International Scientific and Practical Conference, June 2015, Rezekne, Latvia, vol. 2, pp. 307-311, 2015.

- [8] ISA TR 84.00.02. Safety instrumented functions (SIF) safety integrity level (SIL) evaluation techniques. Part 2: determining the SIL of A SIF via simplified equations. Technical report. Instrumentation, Systems, and Automation Society, Research Triangle Park, NC; 2002.
- [9] RD 34.35.124 Technical Requirements for Reliability of Process Protective Means for 800 MW Power Units. ORGRES, - Moscow, 1993.
- [10] Kaplan, Stanley, and B. John Garrick. "On the quantitative definition of risk," *Risk analysis*, vol. 1.1, pp. 11-27, 1981.
- [11] Wang, J. C. et al. *Risk Criterion and Index of Risk. International Topical Meeting on Probabilistic Safety Assessment (PSA'96)*, September 29-October 3, 1996, Park City, UT, 1996.
- [12] Van der Borst, M., and H. Schoonakker. "An overview of PSA importance measures," *Reliability Engineering & System Safety*, vol. 72.3 pp. 241-245, 2001.
- [13] M. Valdma, H. Tammoja, and M. Keel, *Optimization of Thermal Power Plants Operation*. Tallinn: TUT press, 2009.
- [14] M. Valdma, M. Keel, H. Tammoja, and J. Shuvalova, "Economical Dispatch of Power Unit under Fuzziness," vol. 24, no. 2, pp. 249-263, 2007.
- [15] K. Engblom, "Features and parameters of various power plant technologies," *Detail. Wärtsilä's Tech. Mag.*, no. 2, pp. 1-67, 2014.
- [16] "Network service quality requirements and network fees conditions in case of violation," *Võrguteenuste kvaliteedinõuded ja võrgutasude vähendamise tingimused kvaliteedinõuete rikkumise korral*, 2016. [Online]. Available: <https://www.riigiteataja.ee/akt/1039867?leiaKehtiv>. [Accessed: 12-Feb-2017].
- [17] Häring, Ivo, *Risk Analysis and Management: Engineering Resilience*. Springer, 2015.

Poly (Vinyl Alcohol) and Poly (Vinyl Alcohol) /Zinc Oxide Composite Nanofibre Webs: Quality Control with Conductometer

Eva Trumsina, Zane Zelca, Silvia Kukle

Riga Technical University, Faculty of Material Science and Applied Chemistry, Institute of Design Technologies, Kipsalas str. 6, Riga, LV-1048, Latvia

Abstract. In the market a wide variety of products are found that contain/release metal nanoparticles, therefore topical researches on its impacts on the environment and human health. In the textile industry an important step is the development of testing methodology to monitor the quantity of nanoparticles that get into the environment from nanoparticles-containing textile materials. In the study analyzed the method based on the use of conductometer for textiles testing with nano-size metal oxides content to determine the persistence of nanoparticles/ions in the water after textile soaking/washing. Compared results acquired in the experiments with nanofibre webs manufactured by electrospinning from pure polyvinyl alcohol (PVA) and PVA/ZnO composite. The nanofibre webs were soaked in distilled water and obtained samples of water tested with conductometer. The results of the experiments confirm that measurements taken with the conductometer are fairly stable and repeatable; the equipment is suitable for measurements in distilled water for nanoparticles/ions detection. The measurements of the solution's specific electric conductance allow to pinpoint the nanoparticles/ions concentration, but for this purpose, must be created the database that contains the resources needed for the calculations and methodology for sample preparation.

Keywords: conductometer, nanofibre webs, poly(vinyl alcohol), textile testing, zinc oxide.

I. INTRODUCTION

Metals are the oldest of mankind known toxic substances. Lead gained four thousand years ago, but in 370 BC Hippocrates described the lead colic of mining workers. Teofrast described arsenic and mercury in 4th century BC (approximately 372-287 BC). However, many toxic properties of the metals ascertained only today. From 105 periodic system's elements about 80 are metals, but pronounced toxic characteristics have not less than 30 metals or their compounds [1].

Environmental quality may vary according to different geographical, geological, biological and other reasons. These are natural changes that can be quite significant, such as composition of water from the river during flood can be ten and even more times different from the quality indicators of the water in the summer period. Human activity can affect the quality of the environment significantly more than natural processes. Anthropogenic influences disrupt the natural cycle and impact ecosystems.

The industrial activity of the people can greatly shorten the time of metal existence in ores of the Earth crust, creating new combinations and change the distribution of metals in the nature. As such example of impact of human activity can give two hundred time increase of lead amount in the Greenland ice in the 20th century, compared with its

natural levels about 800 years before our era [1]. So the quantity of metals in the environment depends on both natural processes and human industrial activity.

More and more different compounds get into the environment. Currently it is known about 10 million different chemicals, a large part of which does not exist in the nature. About 11 000 chemical compounds are produced in quantities exceeding 500 kg/year, moreover, amount of industrially produced substances are supplemented each year with 1000-3000 new substances [2].

Comparing by different types of water pollution heavy metals are the second main source of contamination after pathogenic micro-organisms [2]. Particularly dangerous pollutants of aquatic environment are lead, mercury, copper, zinc, cadmium, chromium and nickel [2].

In Latvia is carried out monitoring of diffusion of heavy metals in moss and soil. Concentration of heavy metals in mosses suggests that the background level is relatively low. The highest concentrations are found in the Riga region (copper, lead, nickel, cobalt, iron) and near Rezekne (nickel, zinc) [3].

Researching the metal content in the forest soil, detected additional sources of contamination, such as in the soil around the cement factory of Broceni found high levels of the contamination of lead, chromium, zinc and cadmium, but in the soil at

chemical pharmaceutical companies of Olaine – high level of the copper [3].

Heavy metals are found in sediments at the bottom of the Baltic Sea. In addition, greater concentrations of the cadmium, lead, copper and zinc found in port areas of Riga, Liepaja and Ventspils [4], [5].

Main peculiarity of effect from most part of the toxic metals is that, penetrating in the environment, they enter in the human and animal food chains. Thus the heavy metals contaminate food-stuffs [6].

Any material effect on living organisms depends not only on the nature of the exposure (toxicity), but also on the quantity of the substance that gets into the body. Not rare is the situation when taking substances in small quantities, it is showing positive effect on the body, but increased quantities exposed it negative. A typical example of such substances are metal ions, which in microscopic amounts are required for normal operation of enzymes and therefore it is an important ingredient of the multivitamins, but in increased quantities entering in the nature, the same substances works acutely toxic [7].

Exposure to a living organism depends not only on the nature of the substance, but also on the body's age and gender, duration of the exposure and a relapse of the dose, access manner of the substance in the body, the transformation of the substance in the environment and in the body [2].

Mostly exposures of the substances to human are analyzed using obtained information from laboratory experiments with the animals. However, ascribing the results of such experiments to people is as safe as any other extrapolation of substance exposure assessment between species [7].

Nowadays has changed the concept of metal toxicity thresholds. Earlier metal toxicology deals mainly with acute or open metal exposure effects such as lead colic or mercury compounds affected bloody diarrhea. Listed effects of metals exposure must be known and understood in our days too, however, due to strict environmental standards, they now occur less frequently. Now required to find out more subtle chronic or long-term effects that cause-and-effect relationship is not obvious and can be subclinical. For this purpose required to obtain comprehensive information about the doses received and the quantity of metals in the tissues, deeper investigating metal metabolism, especially in tissue and cellular level, as well as found out the metal toxicity affecting factors, such as diet or protein complex formation, which increases or reduces the toxic effect [8].

Most metals effects many organs, their toxicity is determined by the metal ion effects on specific biochemical processes and/or cell membranes or organelles. To assess the effects of metal must be known the concentration in the environment and exposure time. These values have an impact on dose -

the quantity of the metal existing in the cells or organs that determines the toxicological effect. More accessible tissue for dose measurement is blood, urine and hair – sometimes it is called indicator tissue [8].

Toxicological studies show that, compared with the larger size particles, the same chemical composition nanolevel particles cause different toxicological effects on organisms that are most likely related with the large surface area of nanoparticles [9]; [10]. The study [11], which analyses the copper microparticles', nanoparticles' and ionic effects on mice, found that the particle size can greatly affect the toxicity of the substance - the smaller particles, the stronger effect. In referred study used the copper microparticles (17 μm) copper nanoparticles (23.5 nm) and copper ions (0.072 nm). The results of the experiment found that the lethal dose of copper ions (LD_{50}) is 110-118 mg/kg, which belongs to class 3 (moderately toxic) at Hodge and Sterner Scale. The lethal dose of copper nanoparticles is 413 mg/kg, which also applies to class 3, but the lethal dose of copper microparticles is 5610 mg/kg - class 5 (non-toxic).

Toxicological studies of various metal oxides' (zinc oxide, titanium dioxide and aluminium oxide) nanoparticles and larger size particles in aqueous suspension show that ZnO is the most dangerous for the zebra fish embryos and larvae in the early stages of development - the development is delayed, reduced the number of surviving embryos and induced damages of tissue, whereas neither titanium dioxide nor aluminium oxide does not produce toxic effects on zebrafish embryos and larvae [12].

Zinc oxide, titanium dioxide and copper oxide impact studies [13] to freshwater invertebrates (*bacteria Vibrio fischeri*, crustacean *Daphnia magna* and *Thamnocephalus platyurus*) show that zinc oxide and copper oxide is highly toxic compounds, but the titanium dioxide is non-toxic for these freshwater invertebrates, although significantly affects the *Daphnia magna* reproduction system [14].

Verifying effects of various metal oxides (TiO_2 , ZnO, Fe_3O_4 , Al_2O_3 and CrO_3) nanoparticles (size 30-45 nm) on mammalian cells, found that zinc oxide causes significant mitochondrial changes in cells and necrosis. Mitochondrial function results confirm that ZnO displays higher toxicity than other metal oxide nanoparticles. Fe_3O_4 , Al_2O_3 and TiO_2 does not produce any effect on the cells, while the metal oxides concentration reaches 200 $\mu\text{g/ml}$, whereas ZnO toxic effect in mammalian cells is presented already at a concentration of 50 $\mu\text{g/ml}$ [15]. However, analyzing the zinc oxide toxicity to aquatic organisms [16], ascertained that it is important in the freshwater environment (pH 7.6), as the ZnO dissolves in such an environment. The study discusses the nanoparticles of zinc oxide (30 nm), uncrushed ZnO and zinc chloride effects on freshwater algae (*Pseudokirchneriella subcapitata*). As concluded in

the study, particle size don't have an effect on the toxicity of zinc oxide because the ZnO toxicity is associated not with particle size, but with its solubility in the freshwater environment.

Comparing titanium dioxide, silicon dioxide and zinc oxide toxicity on aquatic microorganisms (*Bacillus subtilis*, *Escherichia coli*), concluded that the least toxicity produced silicon dioxide, then titanium dioxide, but the largest zinc oxide. This study found that even light significantly affects bacterial development, but even in the darkness was observed inhibition of bacterial growth [17].

II. MATERIALS AND METHODS

In the article analyzed 9 samples of nanofibre webs - 3 samples of pure poly(vinyl alcohol) (PVA), 3 samples of composite fibres of PVA and zinc oxide (ZnO) nanoparticles with 1 wt.% nanoparticle composition and 3 samples of PVA/ZnO composite fibres with 3 wt.% ZnO nanoparticles content. Considering that the resulting nanoweb area density differs significantly (8-21 g/m²), for obtaining samples important are their weight rather than size. Each nanoweb sample weight is 0.024 g.

Raw materials used in the experiment: PVA (Mowiol 28-99; purity > 99%; MW ~ 145,000; producer Sigma-Aldrich Co, LLC.); ZnO nanoparticles powder (producer Nanjing High Technology Nano material Co., Ltd.; 99.5% purity; D= 20 nm), distilled water (producer SIA "Statoil Fuel & Retail Latvia; the date of manufacture 30.09.2015.; specific electric conductance 2 µS/cm at temperature 22°C).

Spinning solution acquisition technology: 10 wt.% PVA dissolved in distilled water at 80°C, stirred with a magnetic stirrer (BioSan MSH-300) for 2 h at a speed 1000 rpm. Before adding ZnO nanoparticles to PVA solution they were dried at 60°C for 3 h and grinded in mortar to minimize clumping. Then ZnO nanoparticles powder gradually added to PVA solution and sonicated with ultrasonic homogenizer (Hielscher UP200H) for 4 h.

Electrospinning made using the laboratory type Elmarco needle-free (free liquid surface) electrospinning equipment Nanospider LAB 200 with rotating cylindrical electrode. Electrospinning process parameters: electrode rotation speed 4 rpm, distance between the electrodes 150 mm, the applied spinning voltage was 60 kV. For the supporting surface used non-woven polypropylene material (PP spunbond non-woven; area density 30 g/m²). Electrospinning was realized without support material feeding speed, with intervals of 30 seconds, in total 5 min.

Nanofibre samples after electrospinning were heat treated in drying and heating chamber (Binder EU 280) for 15 min at 140°C.

After heat treatment nanofibre webs separated from the supporting material and soaked in distilled water. For each sample used 60 ml distilled water.

Nanofibre webs were stored in distilled water at temperature 22°C for 72 h. The conductivity measurements were made with a time intervals of 24; 48 and 72 h.

Liquid samples were tested with conductometer "Extech EC100". Its electrical conductance range: 0 ÷ 1999 µS/cm; resolution 0.1 µS/cm. Temperature range: 0 ÷ 50 ° C; resolution 0.1 ° C.

III. RESULTS AND DISCUSSION

In Table 1 summarized data are direct measurement results of the experiment. Obtained data shows that, by inserting in distilled water sample without ZnO nanoparticles, the specific electric conductance does not vary. In addition, the same results show all of the parallel samples.

Table 1
 Experimental results

ZnO, wt.%	Sample	Specific electric conductance, µS/cm		
		After 24h	After 48h	After 72h
0%	1.	2	2	2
	2.	2	2	2
	3.	2	2	2
	Average	2	2	2
1%	1.	8	15	24
	2.	9	16	22
	3.	8	17	25
	Average	8,3	16	23,7
3%	1.	12	20	30
	2.	12	21	28
	3.	10	18	24
	Average	11,3	19,7	27,3

Even after 72 h, during which nanofibre samples were in distilled water, water have not changed the specific electric conductance. This means that pure poly(vinyl alcohol) samples does not affect the specific electric conductance of distilled water. Taking into account previous studies [18], the results of this experiment are more appreciated. Otherwise it would be necessary to implement the adjustment of the results, subtracting from the specific electric conductance of the water measurement results of PVA/ZnO composite nanofibre indication that match the measurements of pure PVA nanofibre.

Fig. 1 demonstrates average value changes of the experiment results during time. Inserting the sample with ZnO nanoparticles composition in distilled water after 24 h already observed increase of the specific electric conductance of the water, which evenly augment also after 48 and 72 h.

In Fig. 1 visible differences between the 1 wt.% and 3 wt.% ZnO composition in nanoweb structure –

a higher specific electric conductance of distilled water has sample with 3 wt.% ZnO composition.

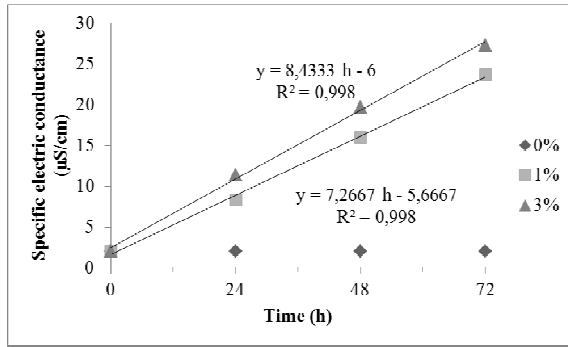


Fig. 1. Changes of the average specific electric conductance after 24, 48 and 72 h of distilled water with nanowebbs placed in it.

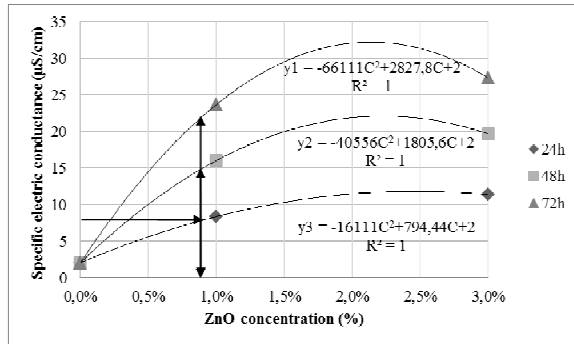


Fig. 2. Influence of the concentration on the results of the specific electric conductance (C-concentration).

The chart in Fig. 2 and incorporated equations can be used not only to determine the percentage of ZnO nanoparticles composition in the nanoweb sample presented in the water, but also to forecast the changes of the specific electric conductance of the water in the longer term. For example, by measuring the specific electric conductance after 24 h and placing a measurement result in the corresponding equations, can be find out specific electric conductance of the same water after 48 and 72 h.

Data summarized in Table 1 are direct indications of measurements, they are raw data. To obtain the specific electric conductance that describes a particular liquid, from the measurement indications must be subtracted initial specific electric conductance of the water - in this case it is 2µS/cm (Table 2). This is necessary because it is not always possible to get distilled water with the same specific electric conductance.

Statistical characteristics of the experimental results were calculated: arithmetic mean, variance, amplitude, standard deviation, average standard error and average relative standard error (Table 2). The average relative standard error with confidence level 0.95 changes from 4.1% to 7.1%, which is satisfactory. Although in this case a maximum matching of the parallel samples' results are not

required, however, for a certain extent it describes the measurement stability.

Compared with the samples without ZnO nanoparticles composition having saved the initial distilled water's specific electric conductance, the nanowebbs composite samples with 1wt.% and 3 wt.% ZnO nanoparticles after 24 h soaking water specific electric conductance has increased on average 6.3 and 9.3 units (Table 2). Prolonging soaking time to 48 h, the specific electric conductance of the water increases even more, up to 14 and 17.7µS/cm, but after 72 h it reaches accordingly 21.7 and 25.3 µS/cm.

Table 2
Summary of adjusted measurements and statistical data

ZnO, wt.%	Sample	Adjusted specific electric conductance, µS/cm		
		24h	48h	72h
0,0%	1.	0	0	0
0,0%	2.	0	0	0
0,0%	3.	0	0	0
Average, µS/cm		0	0	0
Difference, µS/cm		0	0	0
Relative Standarderror, %		0%	0%	0%
1,0%	1.	6	13	22
1,0%	2.	7	14	20
1,0%	3.	6	15	23
Average		6,3	14,0	21,7
Difference, µS/cm		1	2	3
Relative Standarderror, %		5,3%	4,1%	4,1%
3,0%	1.	10	18	28
3,0%	2.	10	19	26
3,0%	3.	8	16	22
Average		9,3	17,7	25,3
Difference, µS/cm		2	3	6
Relative Standarderror, %		7,1%	5,0%	7,0%

To determine the concentration of ZnO nanoparticles and/or ions existing in water, which become detached from the nanoweb sample, in Table2 summarized results of the specific electric conductance must be compared with measurements obtained by adding to distilled water the same size ZnO nanoparticles without nanoweb. Inserting data from Table 2 in the previously calculated equation [19] can be ascertained the percentage of nanoparticles/ions of specific size presented in the water after nanoweb sample soaking and/or washing.

IV. CONCLUSIONS

Analysis of the experimental results demonstrates that the conductometer can be applied to metal oxides

nanoparticles'/ions' concentration determination in distilled water. After soaking in water pure PVA and PVA/ZnO composite nanoweb samples concluded that the specific electric conductance of water is different – the samples without ZnO nanoparticles remain the original specific electric conductance of distilled water, while samples with 1wt.% and 3wt.% composition of ZnO nanoparticles after 24 h soaking specific electric conductance of water has increased to average 6.3 and 9.3 units. The prolonged soaking up to 48 and 72 h causes increase of the specific electric conductance of the water even more, with the exception of pure PVA nanoweb's soaking water, which specific electric conductance remains at the same level during the whole experiment. This proves that the PVA/ZnO composite samples affect the specific electric conductance of distilled water, which can be used to create a testing methodology for textile with metal oxides nanoparticles content, but for this purpose must be created the database that contains the resources needed for the calculations and methodology for sample preparation.

However creating a methodology, it would be necessary to increase the number of parallel measurements to obtain more precise results. The accuracy of the results could also improve higher resolution conductometer.

REFERENCES

- [1] J. Liu, R.A. Goyer and M.P. Waalkes, "Toxic Effects of Metals," in *Casarett and Doull's Toxicology. The Basic Science of Poisons*, C.D. Klaassen, Ed. New York: McGraw-Hill, 2008, pp 931 - 979.
- [2] M. Kļaviņš, *Vides piesārņojums un tā iedarbība*. Rīga: LU Akadēmiskais apgāds, 2012.
- [3] O. Nicodemus and G. Brumelis, "Monitoring of atmospheric heavy metal deposition in Latvia," in *Proceedings of the Latvian Academy of Sciences*, Vol. 52, 1998, pp. 17-24.
- [4] M. Jansons, "Contamination of sediments with trace elements in harbours of Latvia" in *Proceedings of the Latvian Academy of Sciences*, Vol.52, 1998, pp. 72-76.
- [5] Z. Seisuma, B. Pedersen and B. Larsen, "Vertical distribution of heavy metals and total C and N in sediments of the gulf of Riga," *Proceedings of the Latvian Academy of Sciences*, Vol.52, 1998, pp. 77-80.
- [6] M. Kļaviņš *Atmosfēras ķīmija un gaisa piesārņojums*. Rīga: LU, 2000.
- [7] M. Kļaviņš and A. Roska *Toksiskās vielas vidē*. Rīga: LU, 1998.
- [8] M.A. Baķe, "Biological monitoring of metals as indicators of pollution" in *Proceedings of the Latvian Academy of Sciences*, Vol.52, 1998, pp. 24-28.
- [9] K. Donaldson, X.Y. Li and N.W. Mac, "Ultrafine (nanometer) particle mediated lung injury," *Journal of Aerosol Science*, Vol. 29, pp. 553–560, 1998.
- [10] D.B. Warheit, B.R. Laurence, K.L. Reed, D.H. Roach, G.A. Reynolds and T.R. Webb, "Comparative pulmonary toxicity assessment of single-wall carbon nanotubes in rats," *Toxicological Sciences*, Vol. 77, pp. 117–125, 2004.
- [11] Z. Chen, H. Meng, G. Xing, C. Chen, Y. Zhao, G. Jia, T. Wang, H. Yuan, C. Ye, F. Zhao, Z. Chai, C. Zhu, X. Fang, B. Ma and L. Wan, "Acute Toxicological Effects of Copper Nanoparticles in Vivo," *Toxicology Letters*, Vol. 163, pp. 109-120, 2006.
- [12] X. Zhu, L. Zhu, Z. Duan, R. Qi, Y. Li and Y. Lang, "Comparative toxicity of several metal oxide nanoparticle aqueous suspensions to Zebrafish (*Danio rerio*) early developmental stage," *Journal of Environmental Science and Health, Part A: Toxic/Hazardous Substances and Environmental Engineering*, Vol. 43, No. 3, pp. 278-284, 2008.
- [13] M. Heinlaan, A. Ivask, I. Blinova, H.C. Dubourguier and A. Kahru, "Toxicity of nanosized and bulk ZnO, CuO and TiO₂ to bacteria *Vibrio fischeri* and crustaceans *Daphnia magna* and *Thamnocephalus platyurus*," *Chemosphere*, Vol. 71, Issue 7, pp. 1308-1316, 2008.
- [14] K. Wiench, W. Wohlleben, V. Hisgen, K. Radke, E. Salinas, S. Zok and R. Landsiedel, "Acute and chronic effects of nano- and non-nanoscale TiO₂ and ZnO particles on mobility and reproduction of the freshwater invertebrate *Daphnia magna*," *Chemosphere*, Vol.76 (10), pp. 1356-1365, 2009.
- [15] H.A. Jeng, J. Swanson, "Toxicity of metal oxide nanoparticles in mammalian cells," *Journal of Environmental Science and Health, Part A: Toxic/Hazardous Substances and Environmental Engineering*, Vol. 41, No. 12, pp. 2699-2711, 2006.
- [16] N.M. Franklin, N.J. Rogers, S.C. Apte, G.E. Batley, G.E. Gadd and P.S. Casey, "Comparative Toxicity of Nanoparticulate ZnO, Bulk ZnO, and ZnCl₂ to a Freshwater Microalga (*Pseudokirchneriella subcapitata*): The Importance of Particle Solubility," *Environ. Sci. Technol.*, Vol. 41 (24), pp. 8484–8490, 2007.
- [17] L.K. Adams, D.Y. Lyon and P.J. Alvarez, "Comparative ecotoxicity of nanoscale TiO₂, SiO₂, and ZnO water suspensions," *Water Research*, Vol. 40, Issue 19, pp. 3527-3532, 2006.
- [18] E. Trușnița, S. Kukle and G. Zommere, "Metal Coated Textile Testing with GDV Method: Raw Material Influence on the Parameters of GDV Electrograms," *Material Science. Textile and Clothing Technology*, Vol.7, pp.107-112, 2012.
- [19] E. Trușnița and S. Kukle, *Zinc Oxide and Titanium Dioxide Nanoparticles Effect on Specific Electric Conductance of Distilled Water: Magic World of Textiles: 8th International Textile, Clothing and Design Conference (ITC&DC)*, 2-5 October, 2016, Dubrovnik, Croatia, Zagreb: University of Zagreb, 2016.

Using Dynamic Pre-activation of Steel Surfaces for Nitriding Intensification

Yulia Usherenko, Sergei Usherenko, Vladimir Dashkevich, Javad Yazdani

Belarusian National Technical University. Address: Nezavisimosty Ave., 65, Minsk, 220013, Belarus

Abstract. The article considers the possibility of pre-activation of the steel surface before nitriding. A complex dynamic method of material activation with a high-speed flow of powder particles (super deep penetration) was used. To exclude the influence of alloying elements, low-carbon steel (2% wt. C) was chosen as the initial material. Powders of NaF ($> 250 \mu\text{m}$) and Pb ($< 200 \mu\text{m}$) were used as material of powder flow. Research of samples structure revealed the penetration of Pb particles through the depth of samples with the formation of channel elements and the absence of NaF powder traces. Microhardness measurements have shown that using of NaF powder leads to activation of the nitriding process and to increase of hardness of the resulting nitrided layer, while using of Pb powder leads to inhibition of diffusion activity and decrease in the hardness of the nitrided layer. Application of too coarse fraction of NaF resulted in particles sticking to the surface of the sample that reduced the thickness of the nitrided layer. The necessity of using a finer-dispersed fraction of NaF in the future is shown.

Keywords: super-deep penetration, SDP, nitriding, intensification, powders, dynamic loading.

I. INTRODUCTION

Nowadays it has been accumulated vast experience of steel hardening by the different types and methods of chemical and heat treatment. Traditional nitriding allows to form relatively thin, uniformly distributed nitride layers during long processing period. However, production of wear-resistant diffusion layers with a unique morphology and intensification of the process of low-temperature nitrogen saturation of surface layers is an actual scientific problem [1].

Traditional nitriding technologies are characterized by low productivity because of long period of saturation of the surface layer material. One of the reasons that lead to premature failure of the hardened parts is uneven wear of the surface. It's explained, for example, by physical-mechanical and chemical heterogeneity of the diffusion layer after nitriding and the formation of brittle phases therein. Use of traditional nitriding technologies with a sufficiently high degree of probability leads to the formation of an uneven layer with a reduced concentration of saturable substance, low and inhomogeneous hardness of the surface layer, and the appearance of defective areas.

Nitriding intensification can be achieved by variation of some technological parameters in order to reduce duration of preliminary heat treatment [2]-[3]. Such methods of nitriding intensification are only partial solutions of the problem. Many researchers see a fundamental solution to the problem in the fundamental reorganization of the cycle itself. Developments aimed at surface modification using variable electromagnetic fields of different ranges, as

well as using a pulsating discharge look promising. Application of ion-plasma processes in chemical-thermal treatment allows to intensify the process [4]. However, they also have a number of shortcomings.

Effective methods of preparing the surface for coating are complex dynamic operations of the matrix steel activation before nitriding [1]. Therefore, alloying technology for metals and alloys in solid state in the mode of super-deep penetration (SDP) by the flow of powder particles is promising. The specificity of this treatment is an achievement of impulse of high pressure in the range of very short intervals. During SDP process powder particles work as needles and the fibers are formed in metal matrix under dynamic interaction between powder particles and matrix material [5]-[6]. Dynamic loading of surfaces by powder streams may ensure the intensification of subsequent nitriding and increase the wear resistance of the resulting layer.

At SDP process flow of powder particles (striker) move in a volume of the metal body. Behind the strikers in a dense "quasi-liquid" plasma channel cavities are formed, which can slam under the effect of background pressures. Slamming of microcavities under the action of high pressure to a point can lead to energy density $\geq 10^{15} \text{ J/m}^3$. In this case matrix crystal lattice is destroyed with high speed [7], and the matrix material changes from a solid state to a dense plasma, i.e. a dynamic phase transition is realized. Under the influence of this high pressure the cores of material may stick together, i.e. automodel process of inertial confinement fusion [7]-[8] can be realized.

Until now, a common understanding of process of particles penetration at SDP was not found what led many research groups continue working in this direction [9]-[10]. The phenomenon of interaction of cosmic dust particles (diameter less than 100 microns) with the spacecrafts observed in the near-Earth environment. The SDP process is used to determine the possible damages of spacecrafts with flows of cosmic dust and for control systems testing [11]-[12].

II. MATERIALS AND METHODS

Dynamic processing in SDP mode was carried out in the following conditions : particles speed 300-1000 m/s, exposure time \approx 100 microseconds, material of billets: low-carbon steel (0.2% C), material of strikers - various fractions of SiC powders - 3-100 microns, and Pb - \leq 200 microns with addition of powder activator NaF >250 microns.

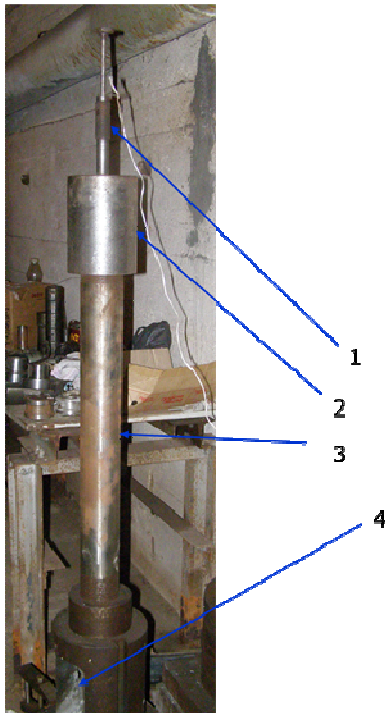


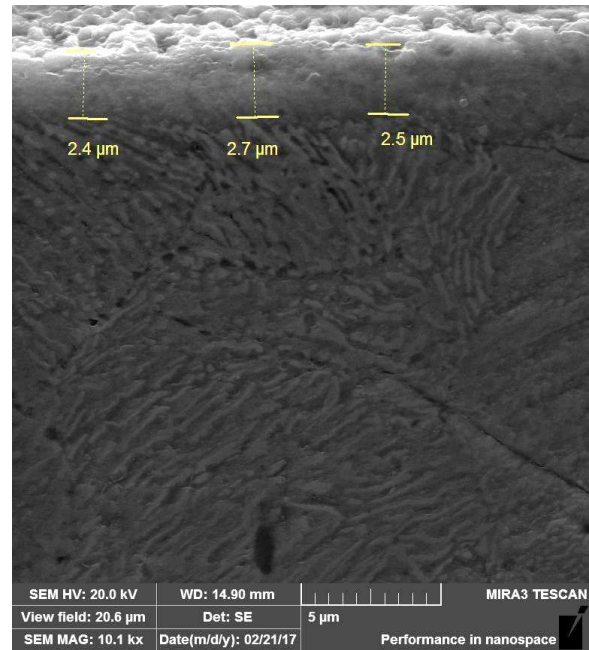
Fig. 1. Indoor cannon accelerator: 1-detonator, 2- explosive chamber, 3 – barrel, 4 – body of sample holder.

The low-temperature nitriding process was carried out in a powder medium at a temperature 560 °C for 10 hours, in containers with a sealing fused shutter. For a low-temperature nitriding the following powder composition (% wt.) was used: $C_6N_6FeK_4$ 20-30%, charcoal 5-10%, $NaHCO_3$ 5-10%, inert filler 50-70%. A shaft electric furnace with selitic heaters was used for the process.

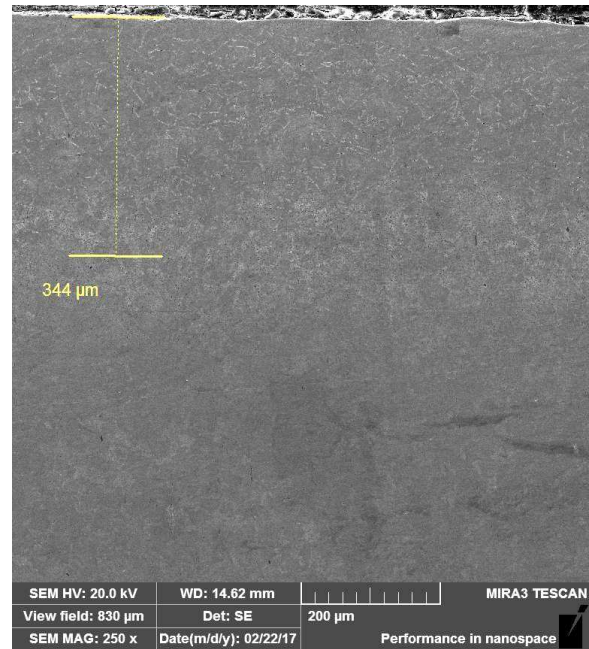
The samples preparation technique includes cutting, polishing and etching in 4% nitric acid. Structures were studied by TESCAN MIRA3 SEM, microhardness was measured by micro durometer PMT-3.

III. RESULTS AND DISCUSSION

To eliminate the influence of alloying elements, low-carbon steel with 0.2% wt. C was used as an initial material. After nitriding, a nitride layer with a thickness of 2.5 μm and a transition zone of 350 μm were formed in the initial steel (Fig. 2).



a)



b)

Fig. 2. Nitride (a) and transition layer (b) on the initial 0.2%C steel.

As a result of the high-energy impact in the SDP mode, activation or inhibition of the matrix material can be realized at different depths. To control the process of preliminary solid-phase doping in the mode of super-deep penetration (SDP), the introduction of chemical elements, which are

certainly absent in the matrix steel, is used. In the low-carbon steel Pb powder was used as a marker of the penetration process. The traces of processing (channel elements) are observed on steel samples after activation by Pb powder (Fig. 3). The nitrated layer is shown on Fig. 4.

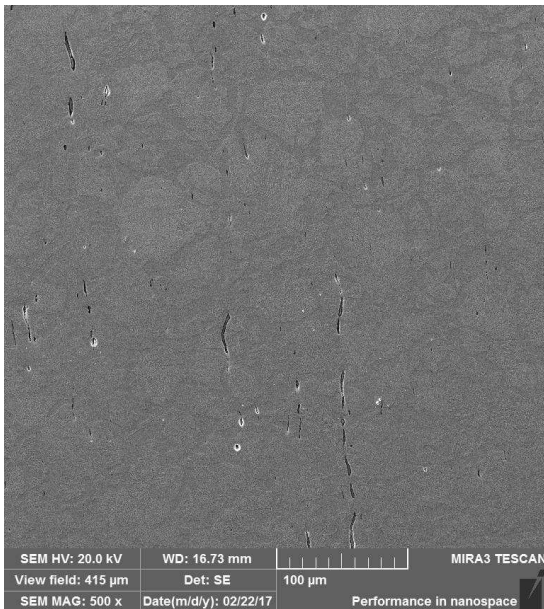


Fig. 3. The structure of low-carbon steel after the activation by Pb powder

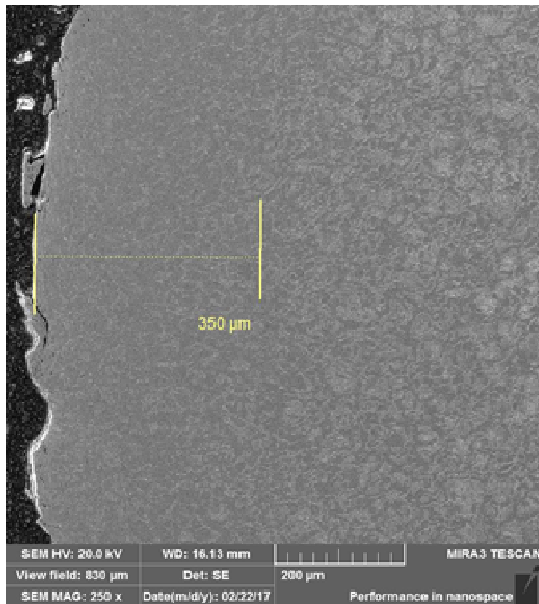
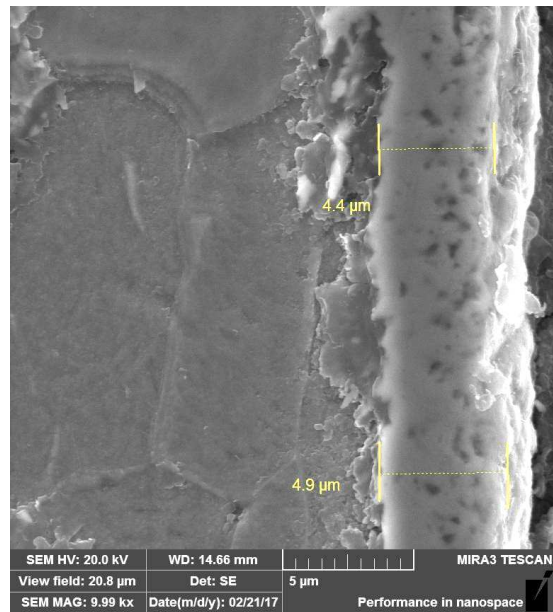
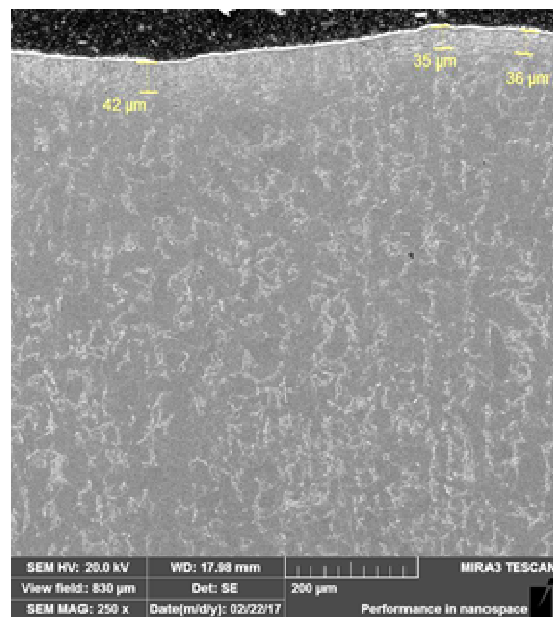


Fig. 4. Structure of a sample activated by Pb after nitriding

Apparently, Pb leads to a decrease in the diffusion activity during subsequent nitriding. In addition, a thin nitride layer mainly of the ϵ -phase ($\text{Fe}_{2.3}\text{N}$) is formed. This layer can be actively cleaved during following sample preparation. Activation of low-carbon steel by NaF powder in SDP mode causes activation of the subsequent nitrogen diffusion process (Fig. 5).



a)



b)

Fig. 5. Structure of steel activated by NaF powder after nitriding: (a) nitride layer, (b) transition layer

Thus, the average thickness of the nitride layer and the transition zone in the initial sample was 2.5 μm and 350 μm , in activated by NaF - 4.6 μm and 40 μm , in the Pb-inhibited sample, the transition zone was 350 μm , the nitride layer was not detected. The transition zone after nitriding of the initial steel (Fig. 3) is much thicker (8.7 times) than the similar zone obtained after nitriding of the NaF-activated steel of the same composition (Fig. 5), while on Pb-activated steel the thickness of the transition zone is equal to the thickness on the initial sample (Fig. 4).

The microhardness of Pb-activated steel at a depth of up to 0.1 mm is 1.4 times lower than that of the initial sample. The microhardness of NaF-activated

steel at a depth of up to 0.1 mm is 1.2 times higher than that of the initial sample (Fig. 6).

The decrease in the thickness of the transition zone at NaF-activated steel is explained by the use of a too coarse powder fraction ($> 250 \mu\text{m}$). This reduced the density of the penetrating flow and caused the sticking of large particles to the surface of the processing sample, which complicated the diffusion of nitrogen during subsequent nitriding. It is confirmed by the fact that in the structure of NaF-activated steel there are practically no channel elements.

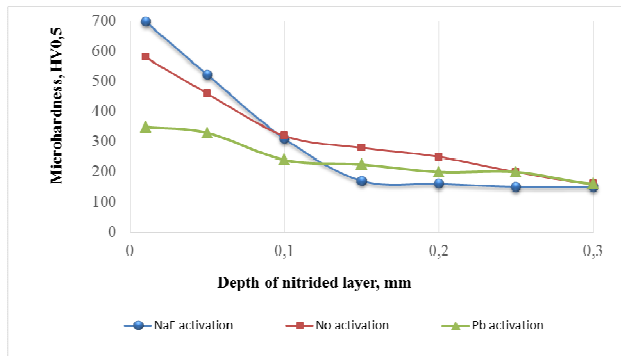


Fig. 6. Microhardness of nitrided samples

IV. CONCLUSION

Based on estimates of changes in the size of nitride layers and transition zones formed on low-carbon steel (0.2% wt. C) without activation, with the activation by NaF powder and by Pb powder, the following conclusions can be drawn:

The use of Pb powder to pre-activation of the steel leads to inhibition of the diffusion activity and to a decrease in the hardness of the layer in 1.4 times.

The use of NaF powder to pre-activation of the steel activates the nitriding process and increases the hardness of the layer 1.2 times

Initial steel and Pb-activated steel after nitriding allow to get the thickness of the transition zone of 350 microns, while at the same time, at NaF-activated

steel, the thickness of the transition zone decreases by 8.7 times. It is necessary to use a finer fraction of NaF to activate the samples to a greater depth.

REFERENCES

- [1] V. A. Kozechko "Nitriding process intensification steel structures", Journal of Engineering Sciences, Vol. 1, Issue 3, pp. F1-F5, 2014
- [2] E.V. Berlin, N.N. Koval and L.A. Seidman, *Plasma chemical-thermal treatment of the surface of steel parts*. Moscow: Technosphaera, 2012.
- [3] Andreev AA, Kunchenko V.V., Sablev L.P., Stupak R.I., Shulaev V.M, "Steel nitriding in the plasma of modified vacuum-arc discharge", Technology of Mechanical Engineering, vol.5 , pp. 27-30, 2002.
- [4] N.K.Krioni, , A.A. Mingazheva and F.F. Musin, "Formation of a nitrided layer during high-energy surface activation of components" Electronic scientific journal "Oil and gas business", vol.5. pp..294-312, 2014.
- [5] S. J. Owsik, K. Jach, S. Usherenko, Y. Usherenko, O. Figovsky and V. Sobolev, , "The physics of superdeep penetration phenomenon", Journal of Technical Physics, vol.49, Issue 1, pp.3-25, 2008.
- [6] Yulia Usherenko, Sergei Usherenko and Javad Yazdani, "High-Energy Method of Transformation of Casting Metals and Alloys to the Composite Materials", Key Engineering Materials, Vol.72 , pp.290-294, 2016.
- [7] Yulia Usherenko, Sergei Usherenko and Javad Yazdani, "Composite Materials for Steel Cutting and Concrete Crushing", Procedia Engineering, vol. 172, pp. 1198 – 1203, 2017.
- [8] V.V. Sobolev and S.M. Usherenko, "Shock-wave initiation of nuclear transmutation of chemical elements", J.Phys, IY, vol.134, pp. 977-982, 2006.
- [9] Chengzhi Qi and Jianjie Chen, "Physical mechanism of super-deep penetration of solid microparticles into solid targets", Journal of the Mechanical Behavior of Materials, vol. 23:1-2 pp.21-27, 2014.
- [10] I. Krestelev, "Simulation of the Process of Entrainment of Powder Particles by Explosive Shock Waves", Vestn. Samar. Gos. Tekhn. Univ. Ser. Fiz.-Mat. Nauki, Issue 2(35), pp. 125 –129, 2014.
- [11] A.I. Belous, V.A. Soloduha and S.V. Shvedov, *Space electronics*, vol.2, Moscow: Technosphaera, 2015.
- [12] V.G. Sitalo "Materials applied. Launch vehicle and spacecraft manufacturing process. New composite materials. Nondestructive quality control" in *EC/ESA/NSAU Workshop on space-related research under FP-6*, 2004, pp. 29-30.

Design of Permanent Magnet Linear Synchronous Motor driving 2D Table for Laser Marking

Peter Uzunov¹, Lyubomir Lazov²

Electricity System Operator, Sofia, Bulgaria¹,
Latvia Academy of Technologies, Rezekne, Latvia²

Abstract. In this paper, the results from design of a permanent magnet linear synchronous motor are published. The motor will drive a table for laser marking of various small details. This table will be part of the equipment of Laser Technologies Laboratory of the Research Centre for Physical Processes and Laser Technologies at Rezekne Academy of Technologies. In the design process, a comprehensive approach was used in which the theory of electric and magnetic circuits was combined with Finite Element Method (FEM). The paper contains the main equations of the design methodology. They were used for the preliminary calculation of motor magnetic system and main electromagnetic parameters via script program. For the specifying of these quantities and motor optimization, the results from modeling and analyzing of the linear motor magnetic field by the FEM were used.

Keywords: Laser Marking, Permanent Magnet Linear Synchronous Motors, Design, Finite Element Analysis.

I. INTRODUCTION

According to the World and European standards the products of mechanical engineering there should be marking such as - matrix code, bar-code, logo of firm, serial numbers, basic technical features etc.

Good quality laser marking is of particular importance to both manufacturers and customers. It is needed by manufacturers so that they could be able to monitor all stages of the production cycle the other hand, it must provide the customer the necessary information about the parameters and characteristics of the products [1, 2, 3].

The laser marking propulsion system must have excellent dynamic performance - speed, acceleration in order to provide high accuracy positioning. Belt, gears and helical gears powered by servomotors with rotation motion does not give good results. A very good solution for industrial laser propulsion systems is the use of Permanent Magnet Linear Synchronous Motors (PMLSMs).

These motors enable direct conversion of electrical energy into mechanical energy of linear motion. This leads to better precision, higher acceleration and higher speed of the moving part.

In laser systems for industrial applications there are two main constructive solutions: a movable laser head and a stationary table with the work piece or stationary laser head and movable table with a detail attached thereon.

The laser system developed by Latvia Academy of Technologies will be used for marking of details with small weight and sizes. Therefore, the second

constructive solution is considered in this work. In this regard, the article presents the results of the design of linear servo motor which drives a two-coordinate table to which the marked detail is affixed.

The designed linear synchronous motor shall have very good dynamics and positioning accuracy. The following dynamic parameters are required: velocity – 3 m/s; acceleration – 60 m/s²; thrust – 180 N; positioning accuracy -100 μm.

As a drive system of this 2D table, an iron core flat type PMLSM is chosen.

PMLSMs are a complex electromechanical system characterized by strong non-linearity in terms of their electromagnetic field. Their design, as well as other electrical machines, is related to solving complex problems caused exactly this non-linearity. An appropriate numerical method (FEM) can be very useful, in the design stage, in order to obtain more information about these non linearities.

In the present work we describe the design and simulations results for the linear synchronous servomotor illustrated and intended for the needs of the laser marking system. The simulations were based on the results of the modeling and analysis of motor magnetic field with FEM. Based on these results, the electromagnetic forces acting on the moving part have been calculated as they are key parameters in motor design.

In the design process a comprehensive approach was used in which the theory of electric and magnetic circuits was combined with FEM. This combination gives excellent results. For this purpose, a special

script program was used, through which, using the theory of electric and magnetic circuits, initial size of the magnetic system was calculated; then physical experiment was simulated based on iteration procedure using FEM. In this simulation, linear motor thrust was calculated using the results from the magnetic field analysis. Its value is used as a criterium for ending the iteration procedure when it reaches the desired value of this force

FEM was also used in the motor final design via random optimization method.

II. DESIGN OF PMLSM

The design of PMLSM was made applying a comprehensive approach comprising three main stages:

1. Initial analytical calculation of the magnetic system, the fundamental electromagnetic loads, and motor main sizes and parameters, using methodology based on the theory of electric and magnetic circuits.

2. Analysis of the motor magnetic field with the resulting geometry and physical experiment simulation with FEM, aimed at clarifying the values of item 1 in one iteration procedure with main criteria the value of the linear motor thrust .

3. Optimization of the resulting motor geometry and determining the final values of motor geometric dimensions and electromagnetic parameters.

A. Selection of construction and control of the linear motor under design

The designed linear motor was selected to be with flat type ferromagnetic core and permanent magnet excitation. Its structure is shown in Fig.1.

The movable part 1 is supported by two linear guides 2, 3 mounted on the stationary motor part 4. The mover includes the core 5 made from silicon steel. On the motor back iron NdFeB permanent magnets 6 (PM-s) are mounted, with alternating polarity N-S-N-S....

A very important issue in linear motors design is the right choice of the number of poles/number of core teeth ratio. The number of poles is directly related to the period of the magnetic detent force. This force disturbs the motor control because generates motor thrust fluctuations and vibrations in motor operation. In order to avoid any adverse effects of the magnetic detent force presence, it was decided that the motor will have 10 poles, i.e. $2p = 10$.

The ultimate target in the design of modern electrical machines aspiration is that they be energy efficient. In order to reduce copper losses of the designed linear motor, two-layer concentric winding was used, wherein each tooth of the mover core has a coil. The individual coils are connected in such a way as to form a three phase winding 7, able to create a "running" magnetic field.

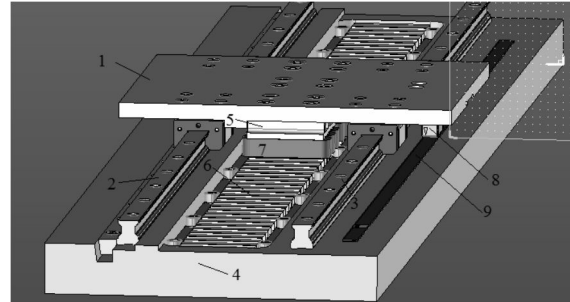


Fig1. 3D CAD model of PMLSM

In the concentric windings the number of slots per pole and per phase q is less than one. To use concentric windings it is very important to choose the correct number of armature slots that correspond to the set number of poles. From [4] a core of the movable part that has $z = 12$ slots was selected.

The vector control of the linear motor was selected. It was implemented with the help of modern digital controller JONI [5], powered by a DC voltage source. It generates a symmetrical three-phase voltage system, supplied to the motor mover via wire connection.

To monitor the position of the motor movable part and the proper work of the digital controller, the linear motor is provided with a magnetic linear encoder [6], which consists of a reading head 8 and a magnetic tape 9.

B. Design Methodology

The methodology applied is based on analytical equations from the theory of electrical and magnetic circuits in integral form and the theoretical mechanics, and from the theory of electromagnetic field in differential form as well.

The starting point for determination of the required motor thrust is Newton's law

$$F = ma + \mu gm . \quad (1)$$

where

m is the mover mass and the mass of the payload;

μ is the friction coefficient of the used linear guide;

a, g is the acceleration of the mover and the earth acceleration.

The calculation of the acceleration a depends on the selected profile of the speed-time curve of the linear motor movable part - triangle or trapezium. It should be borne in mind that the optimal profile is triangular.

Linear synchronous servomotors permit overloading of 3÷4 times. Usually, they work with a small Duty Cycle DC, %. Therefore, they can be designed for a smaller thrust, equal of the continuous force, calculated by the following equation

$$F_{\text{continuous}} = \frac{F_{\text{duty}}}{\sqrt{\frac{DC}{100}}} \quad (2)$$

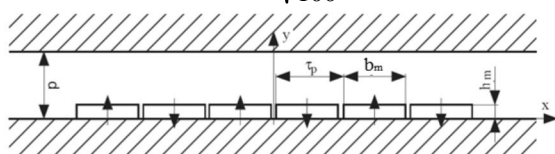


Fig.2. PM magnetic way with one infinite opposite yoke

Output parameter for the calculation of the linear motor magnetic system shown in Fig. 2 is the value of magnetic flux density in the air gap. In order to derive an analytical equation for its calculation, the PM magnetic way must be modeled. This is done by replacing each PM with two current densities of different signs. After using the image theory both B_x and B_y components of the magnetic flux density are obtained.

$$B_{x N_{pm}}(x, y) = \sum_{i=0}^{N_{pm}} (-1)^{i+1} B_{x1_{pm}2p}(x, y, x_i, 0) ; \quad (3)$$

$$B_{y N_{pm}}(x, y) = \sum_{i=0}^{N_{pm}} (-1)^{i+1} B_{y1_{pm}2p}(x, y, x_i, 0) , \quad (4)$$

where

N_{pm} is the number of PM in magnetic way;
 $B_{x N_{pm}}$, $B_{y N_{pm}}$ are the components of magnetic flux density.

The x - coordinate of the PM center is

$$x_i = -\frac{N_{pm}-1}{2} \tau_p + i \tau_p . \quad (5)$$

The preliminary value of magnetic flux in the air gap is

$$\Phi_{\delta} = \tau_p \ell_{\delta} B_{\delta} , \quad (6)$$

where ℓ_{δ} is the width of the mover core and τ_p is the pole pitch.

On the base of magnetic flux value in the air gap, the mover yoke height h_a , and the number of phase turns N_{ph} was calculated

$$h_a = \frac{\Phi_{\delta}}{2k_{Fe}B_a\ell_{\delta}} ; \quad (7)$$

$$N_{ph} = \frac{k_E U_{ph}}{\pi \sqrt{2} f k_w \Phi_{\delta}} , \quad (8)$$

where

B_a is the value of magnetic flux density in the mover yoke;

U_{ph} is the phase voltage, supplied from the inverter;

k_w is the armature winding factor.

The preliminary value of coefficient of induced voltage k_e is

$$k_e = \frac{E_1}{U} . \quad (9)$$

where E_1 is the rms value of motor e.m.f.

The equivalent frequency of the supply voltage received from the motor controller, determining the linear speed of movement v , is

$$f = \frac{v}{2\tau_p} . \quad (10)$$

The height of the back iron is calculated by the next equation [4]

$$h_{\text{backiron}} = \frac{B_r b_m h_m}{B_{\text{back}} (\mu_r (d - h_m) + h_m)} . \quad (11)$$

The MMF for the full magnetic circuit is

$$F_{\text{sum}} = F_a + F_Z + F_{\delta} + F_{\text{backiron}} , \quad (12)$$

where

F_{δ} is the air gap MMF;

F_a - the mover yoke MMF;

F_z - the MMF for the mover core teeth;

F_{backiron} - the backiron MMF.

The coefficient of saturation of the magnetic circuit is

$$k_{\mu} = \frac{F_{\text{sum}}}{F_{\delta}} , \quad (13)$$

In the PMLSM design the fact that it will be supplied and controlled by a digital servo controller, realizing modern vector control was taken into account. This controller provides maximum thrust when the current $I \approx I_{aq}$ is in phase with the e.m.f induced in the winding, and, moreover, its component I_d along the d - axis is zero. Accordingly, the vector diagram was drawn as shown in Fig.3. In Fig.4 the equivalent circuit of one motor phase is shown. It is used for the calculation of basic electrical parameters of the linear motor.

The armature winding resistance for one phase is

$$R_1 = \frac{\rho_{Cu} l_{\text{mean}} N_{ph}}{S_{Cu}} , \quad (14)$$

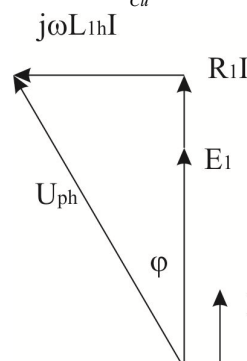


Fig.3. Phasor diagram for the maximum thrust

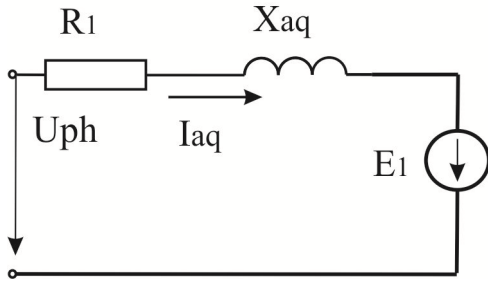


Fig.4. Electrical equivalent circuit for one motor phase

where

ρ_{Cu} is the resistivity of copper;
 l_{mean} - the average length of a turn;
 S_{Cu} - the conductor cross section.

The self inductance for one phase is

$$L_{1h} = \frac{4\mu_0 l_m \tau_p}{\pi^2 p \delta'} (N_{ph} k_w)^2, \quad (15)$$

where

$\delta' = k_\delta \delta$ is the equivalent air gap;
 k_δ - the Carter's coefficient;
 l_m - the axial length of PM.

The value of induced phase voltage is [5]

$$E_1 = 4 f k_\mu \Phi_\delta k_w, \quad (16)$$

The phase voltage is [7]

$$U_{ph} = \sqrt{(E_1 + R_1 I)^2 + (2\pi f L_{ph})^2}. \quad (17)$$

The final value of coefficient of induced voltage

$$k_E = \frac{E_1}{U_{ph}}. \quad (18)$$

With the so calculated value of this coefficient, the number of turns for one phase is recalculated and iteration procedure is organized until reaching its set value.

By the phasor diagram of Fig.3 the power factor is calculated

$$\cos \varphi = \frac{E_1 + R_1 I}{U}. \quad (19)$$

The consumed active power from the PMLSM is

$$P_1 = m U I \cos \varphi, \quad (20)$$

where m is the number of phases.

Iron losses are the sum of hysteresis losses and eddy current losses

$$P_{Fe} = P_h + P_e = \left[k_{Feh} c_h \left(\frac{f}{50} \right) B^2 + k_{Fee} c_e \left(\frac{f}{50} \right)^2 B^2 \right] m_{Fe} \quad (21)$$

where the coefficients of hysteresis losses are $k_{Feh} = 1...2$ и $c_h = 2...5$ Ws/T²kg, and the coefficients of eddy current losses are $k_{Fee} = 2...3$ and $c_e = 0,5...23$ Ws²/T²kg .

The values of all these coefficients are generally given by the manufacturers or they can be deduced from experimental measurements.

The copper losses for the motor winding are

$$P_{Cu} = m I^2 R_1, \quad (22)$$

where $m=3$ is the number of motor phases.

The linear motor mechanical losses are primarily the friction losses in the linear guide and are given by the following equation:

$$P_{meh} = (m_{mover} g + F_{att}) \mu v, \quad (23)$$

In their calculation the great force of attraction to PM should be taken into account. For determining this force, the equation the Maxwell was used [4]

$$F_{att} = \frac{2 p \tau_p w_m B_{ml}^2}{4 \mu_0}. \quad (24)$$

The resistivity of the NdFeB magnets is rather low ($\rho_{PM} \cong 100 \cdot 10^{-6} \Omega/m$). Therefore, the eddy current losses in conductive PM due to magnetic fields produced by the mover slots and the coil MMF cannot be neglected. These losses are generated by the high harmonics of the magnetic flux.

Due to this reason, special attention is paid to the calculation of eddy current losses in PM. This is done basing on the equations of the electromagnetic field in integral form in result of which the following equation is obtained

$$P_{pm} = \frac{\left(\frac{2 l_m \omega_{pm} B_m \tau \pi}{2\sqrt{2}} \sin\left(\frac{b_m \pi}{\tau}\right) \right)^2}{R_{pm}}, \quad (25)$$

where R_{pm} is PM equivalent resistance for eddy currents [7]

$$R_{pm} = \rho_{pm} \frac{2 l_m}{h_m b_m / 2}. \quad (26)$$

For the motor efficiency one can write

$$\eta = \frac{P_1 - P_{Cu} - P_{Fe} - P_{meh} - P_{pm}}{P_1}. \quad (27)$$

In the preliminary design of PMLSM, the approach to analytical calculation of the motor thrust F_x is of particular importance. Various reference sources [8], [6] offer different equations. Practical experience in the design of linear synchronous motors of flat type with ferromagnetic core and excitation of PM proves that the following equation renders very good results [4]

$$F = l_m p \tau_p H_{tm} B_{nm}. \quad (28)$$

It is received on the basis of Maxwell Stress Tensor T_m , which gives the power per unit area, created by the magnetic field acting on the surface S

$$\vec{F} = \iint_S \vec{T}_m d\vec{s}. \quad (29)$$

The normal and tangential components of the tensor T_n and T_t , acting on the surface S with some simplifications can be presented in the following way

$$\begin{aligned} T_n &= \frac{1}{2} \mu (H_n^2 - H_t^2); \\ T_t &= \mu H_n H_t. \end{aligned} \quad (30)$$

In general, the the air gap magnetic field is described by the non-sinusoidal functions because of its unequal magnetic conductivity due to the presence of teeth and slots. As decomposition of functions in Fourier's series is used, sinusoidal distribution of the scalar magnetic potential in the air gap can be assumed. Under this assumption, the tangential component of the magnetic field intensity can be presented as

$$H_{m,v} = \frac{\pi V_{m,v}}{\tau_p}, \quad (31)$$

where v is the harmonic number.

Scalar magnetic potential created by the three-phase motor winding is [4]

$$V_{m,v} = \frac{m \sqrt{2} N_{ph} k_w I^v}{v \pi p}. \quad (32)$$

Equation (31) gives linear current density at $v = 1$, i.e. for the main harmonic.

C. FEM Simulations

At the design stage of the PMLSM, an important question arises - "Do the calculated main motor sizes, its electromagnetic loads and parameters satisfy the technical assignment - i.e. whether it achieved the required thrust (being the most important parameter) acting on the mover?".

To adequately answer of this question, there are two ways:

1. Produce a prototype and experimentally measure its thrust and other parameters of interest - speed, acceleration, efficiency, power factor, etc.
2. Simulate a physical experiment by analyzing the motor magnetic field and, on the basis of the results obtained, calculate adequately this force and these parameters.

The first method is laborious and associated with considerable expenditure of time, labor and money. In the presence of powerful computing equipment and appropriate software nowadays the second method is used, which is commonly called "simulation" of the designed electromagnetic objects. It is much faster and allows for saving significant labor and financial costs. For the purpose of the simulations, the stationary magnetic field of the motor was analyzed. This field is excited by equivalent DC currents equal to the value of the actual peaks of the phase currents. Upon their setting for the three phases, it must be kept in mind that the winding is star-connected, the three phases are shifted 120° , and currents satisfy the first law of Kirchhoff

$$I_A + I_B + I_C = 0. \quad (33)$$

The stationary magnetic field is described by its equations in differential form. After the appropriate transformations, the second degree differential equation for the vector potential of the magnetic field is obtained

$$-\frac{1}{\mu} \nabla^2 \vec{A} = \vec{J}. \quad (34)$$

This equation is solved using FEM, the program FEMM [9] in particular. In its environment, the numerical model for analyzing the linear motor magnetic field is constructed.

To ensure the uniqueness of the solution via FEM, it is necessary to define the relevant boundary conditions, shown in Fig.5.

PMLSM can formally be derived from their rotating counterparts if cut through the axis and extended in one plane. This enables the usage of periodic boundary conditions for the analysis of the magnetic field of linear motors in the FEA.

These boundary conditions make it possible to connect the two end surfaces of motor movable and fixed part - the front and rear surfaces along the direction of movement. Their traces in the XY plane are the contours K2 and K3 in Fig.5. This method allows for the simulation of linear synchronous motors to be reduced to a simulation of rotary motors.

This is true, however, in the case when simulation of the movable part movement is not required.

For this purpose, the vertical boundary contours K_1 and K_3 in Fig.5 must be absolutely identical in structure, i.e. the lengths of the lines shall be equal. Along the other two border contours K_2 and K_4 ,

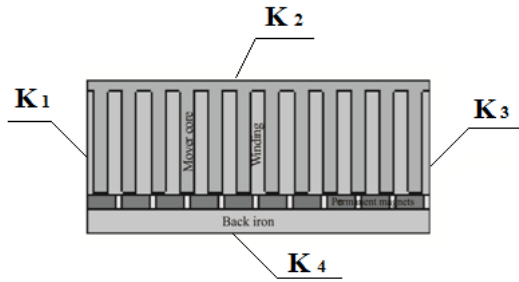


Fig.5 Countours for boundary conditions

Dirichlet boundary conditions for the magnetic vector potential are set.

As a result of the magnetic field analysis the values of the magnetic vector potential, the magnetic flux density, and intensity of the magnetic field of the discretized region are obtained. The distribution of the magnetic flux density is shown in Fig.6.

The main output value for the electromagnetic system, called PMLSM, is the propulsion force it generates. For its calculation the FEA results are used. It is equal to the x-component of the force, calculated via Maxwell Stress Tensor with integration by the volume of the moving part.

For that purpose, iteration cycle is organized over its value by changing the phase currents of the motor. The needed design value of propulsion force is the main criterion for successful fulfillment of the iteration procedure.

Further, in accordance with the phase currents values reached, the final sizes of the mover core and the main motor electromagnetic parameters are specified.

For the design purpose, a scripted program is written running in the medium of the free mathematical software Octave [10].

Its flow chart is shown in Fig. 7.

In the first part of the program, calculation of preliminary sizes of the linear motor magnetic system and its main electromagnetic parameters is performed. In the second part, using the iteration procedure, the value of the propulsion force is calculated basing on the results of the FEA of the motor magnetic field.

The results from the program execution are summarized in Table I.

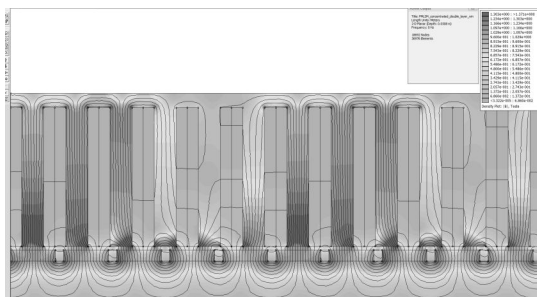


Fig.6 Distribution of the magnetic flux density

A. Optimization of PMLSM

The purpose of the optimization of the designed PMLSM is to optimize the geometry received from the computer aided design, especially the geometry of the moving part so as to reduce its size and weight in order to improve the motor dynamics.

In the present work, the problem of optimal design of PMLSM is reduced to using the method of random optimization (RO) [11]. RO is a family of numerical optimization methods that do not require the gradient of the problem to be optimized and RO can hence be used on functions that are not continuous or differentiable. Such optimization methods are also known as direct-search, derivative-free, or black-box methods.

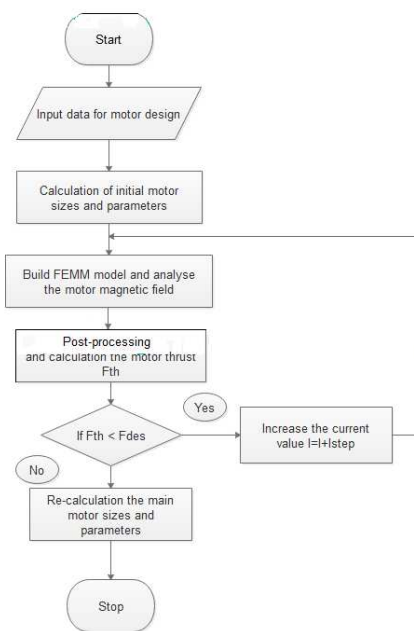


Fig.7 Flowchart of program

Table I
Results from the design of PMLSM

N	QUANTITY	Value
1	Number of phases	3
2	Number of poles	10
3	Slots number	12
4	Rated phase voltage [V]	50
5	Rated phase current [A]	9
6	Efficiency	0.85
7	Power factor	09
8	Air gap [mm]	1
9	Pole pitch [mm]	15
10	Tooth pitch [mm]	12.5
12	Hight of back iron [mm]	8.5
13	Hight of mover yoke [mm]	4
14	PM hight [mm]	6.35
15	PM length [mm]	76
16	PM width [mm]	12.7
17	Speed [m/s]	3
18	Mover mass [kg]	2

Table II
 Optimal values of the optimization variables

N	Variable	Optimal value
1	The height of backiron [mm]	7.9
2	The height of mover yoke [mm]	4.23
3	PM height [mm]	6.11
4	PM length [mm]	7.59
5	The motor active volume [m ³]	0.000506
6	Thrust [N]	180

The objective function which must be minimized is the motor active volume, calculated as follows

$$V_a = 2 p \tau_p l_m (h_{back} + h_m + \delta + h_k + h_a) \quad (36)$$

The vector of optimization variables is

$$\vec{x} = [h_{back} \ h_m \ h_a \ l_m]^T \quad (37)$$

Thus optimal design of PMLSM is reduced to solving of the following problem:

Finding the minimum of the function

$$f(\vec{x}) = V, \quad \vec{x} \in E^4, \quad (38)$$

with the following optimization inequality constraints:

$$\left. \begin{aligned} h_{back} &\leq 10 \text{ mm}; \\ h_a &\leq 9.5 \text{ mm}; \\ h_m &\leq 6.35 \text{ mm}; \\ l_m &\leq 76.2 \text{ mm}. \end{aligned} \right\} \quad (39)$$

These are constraints-inequalities of the kind $g(\vec{x}) \leq g_{lim}$ imposed by technological and structural reasons, mostly related to the motor production. Optimization procedure continues until the extremum of the objective function is reached

$$y(\vec{x}) = y(\vec{x})_{extr}^* \quad (40)$$

defined by the vector with the optimal values of the variables.

The optimal values of the optimization variables are shown in Table II.

III. DESIGN OF 2D LASER TABLE

The designed PMLSM will be used to drive a two-coordinate table, on which the workpiece is attached, subject to laser marking. Its 3D CAD model is shown in Fig.8.

Table III
 Technical data of the table for laser marking

N	Parameter	Value
1	XY Travel distances [mm]	300
2	Maximum linear speed [m/s]	1
3	Maximum pay load [kg]	1
4	Position accuracy [μm]	± 20

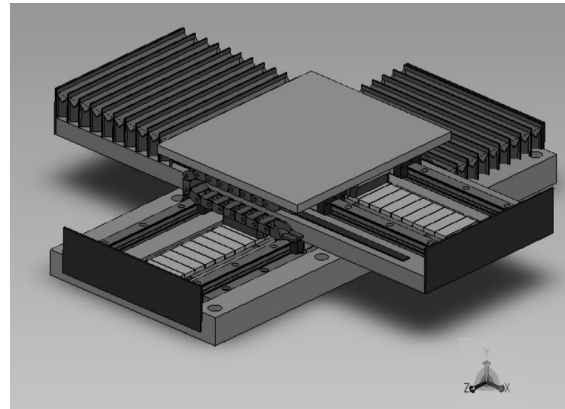


Fig.8. 3D CAD model of the table

Its technical parameters are arranged in Table III.

IV. CONCLUSION

The object of the present work is the design of a PMLSM for linear servo-motor driven XY table for laser marking. The design uses a complex approach in which the theory of electric and magnetic circuits is combined with FEM. This design is computer aided and therein a special script program was used. With the theory of electric and magnetic circuits the initial sizes of the magnetic system are calculated, then, based on iteration procedure using FEM simulations, the linear motor thrust is calculated. Its desired value serves as a criterion for the end of the iteration procedure. FEM was used also in the motor optimal design via the random optimization method.

REFERENCES

- [1] Schuöcker D. Handbook of the Eurolaser Academy, CHAPMAN&HALL, London, 1998
- [2] Валиулин А., С.Горный, Ю.Гречко, М.Патров, К.Юдин, В.Юревич Лазерная маркировка материалов, научно-технический журнал Фотоника, выпуск № 3/2007
- [3] Wolf E. Flexibel und genau, Wolf Productionssysteme, Prooductionic, 4/2006
- [4] S. Majer, Emotor. Electric motor winding calculator. [Online]. Available: <https://www.emotor.com/edit/windings/>
- [5] T. Kotkanen, Granite Device Knowledge Wiki, [Online]. Available: http://granitedevices.com/wiki/IONL_Servo_%26_Stepper_Drive.
- [6] LM10 incremental linear magnetic system encoder, Data sheet, Issue 12, 2014, [Online]. Available: www.rls.si
- [7] S., Chevailler, Comparative study and selection criteria of linear motors, Ph.D. Thesis, EPFL, Suisse, 2006.
- [8] J.F., Gieras, Z. J. Piech, *Linear Synchronous Motors: Transportation and Automation Systems*, 2nd ed., Boca Raton, FL, USA: CRC Press LLC, 2000.
- [9] D. Meeker, (2015, Oct). FEMM reference manual. [Online]. Available: <http://www.femm.info/Archives/doc/manual42.pdf>
- [10] J. Varandas, (2011). GUI Octave. [Online]. Available: http://download.cnet.com/windows/joaquim-varandas/3260-20_4-10128082-1.html
- [11] J. Matyas, Random optimization, *Automation and Remote Control*. 26 (2), 1965, pp. 246–253.

Processes Control with Fuzzy Initial Information in a Complex of Software Design of Digital Control Systems

Sergei Verteshev, Vladimir Konevtsov

Pskov State University,

Faculty of Computer Science and Electrical Power Engineering.

Address: Leo Tolstoy Street 4, Pskov, Russia

Abstract. The relationships between signals and the dependence of signals on time may have not only non-linear character, but non-stationary properties at poor measurability of signals, and hence the difficulty in obtaining an adequate control object model for the purpose of controller synthesis. In such cases, control of the processes takes place under conditions of uncertainty associated with the lack of sufficient information about the behavior of a control object. In this case synthesis of effective control systems can be based on the theory of fuzzy sets (fuzzy logics, infinite logics), allowing the use of empirical knowledge that is difficult to describe by traditional methods.

Application of the theory of fuzzy sets can be effective in the synthesis of control systems of multidimensional objects and objects with distributed parameters, transients, objects in an unpredictable environment. These control objects include, for example, rotational, checkpoints, blast and open-hearth furnaces, processes in biochemical reactors, paraffin installations, braking systems, transport systems, etc.

Keywords: fuzzy logic, fuzzy controller, membership function, operations MAX/MIN.

I. INTRODUCTION

The relationships between signals and the dependence of signals on time may have not only non-linear character, but non-stationary properties at poor measurability of signals, and hence the difficulty in obtaining an adequate control object model for the purpose of controller synthesis. In such cases, control of the processes takes place under conditions of uncertainty associated with the lack of sufficient information about the behavior of a control object. In this case synthesis of effective control systems can be based on the theory of fuzzy sets (fuzzy logic, infinite logic [1-6]), allowing the use of empirical knowledge that is difficult to describe by traditional methods.

Application of the theory of fuzzy sets can be effective in the synthesis of control systems of multidimensional objects and objects with distributed parameters, transients, objects in an unpredictable environment. These control objects include, for example, rotational, checkpoints, blast and open-hearth furnaces, processes in biochemical reactors, paraffin installations, braking systems, transport systems [7-9], etc.

II. FUZZY LOGIC

Fuzzy logic allows to describe mathematically (analytically) tasks formulated linguistically. If the function $y(x)$ and its argument x take values from the

binary set $A = \{0,1\}$, it is called a Boolean. With this definition of the set A any variable x axiomatically belongs ($x \in A$) or does not belong to it ($x \notin A$). Statement $x \in A$ can be expressed by a two-valued membership function $\mu_A(x)$, which reflects the degree of membership of x to the set A :

$$\left. \begin{aligned} x \in A &\Leftrightarrow \mu_A(x)=1 \\ x \notin A &\Leftrightarrow \mu_A(x)=0 \end{aligned} \right\} \quad (1)$$

Sharp distinction between belonging and not belonging to this set is not always the case. The sets in such cases are called fuzzy. The definition of a fuzzy set is based on the assumption that every element to some extent belongs to a given set. Membership function is used to describe a fuzzy set:

$$\mu_A(x) \in \{0,1\} \quad (2)$$

$$\mu_B(x) \in \{0,1\}, \quad (3)$$

where A, B – real sets;

$\{0,1\}$ – the range of variation of a real set.

The simplest example is Temperature (Fig. 1.). In this example, the values of the membership functions

of temperature to sets A (cold), B (heat), C (hot) are the following:

$$\left. \begin{aligned} \mu A(T_1) &= 0,75 \\ \mu B(T_1) &= 0,25 \\ \mu C(T_1) &= 0,0 \end{aligned} \right\} \quad (4)$$

$$\left. \begin{aligned} \mu A(T_2) &= 0,0 \\ \mu B(T_2) &= 0,35 \\ \mu C(T_2) &= 0,5 \end{aligned} \right\} \quad (5)$$

Temperatures T1 and T2 refer with different weights to the elements of the sets A, B, C. Membership functions in Fig. 1 are approximated by piecewise-linear dependencies in various ranges of temperature change (Fig. 2):

$$\mu A = \begin{cases} 1 & \text{at } 0 < T \leq T_1 \\ -\text{tg } \beta & \text{at } T_1 < T \leq T_3 \\ 0 & \text{at } T > T_3 \end{cases} \quad (6)$$

$$\mu B = \begin{cases} 0 & \text{at } (T \leq T_2) \vee (T \leq T_6) \\ \text{tg } \alpha & \text{at } T_2 \leq T < T_4 \\ -\text{tg } \lambda & \text{at } T_4 \leq T < T_6 \end{cases} \quad (7)$$

Example of membership functions of fuzzy sets A, B, C

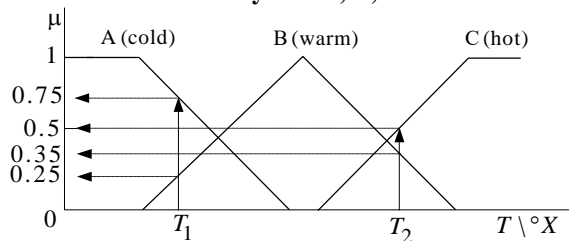


Fig.1

$$\mu C = \begin{cases} 0 & \text{at } T < T_5 \\ \text{tg } \gamma & \text{at } T \geq T_5 \\ 1 & \text{at } T \geq T_7 \end{cases} \quad (8)$$

The example of function calculation program (8.44) is shown in Fig.3. Boolean operations are defined as follows:

Multi conjunction

$$Y = X_1 \wedge X_2 \wedge \dots \wedge X_n = \begin{cases} 1 & \text{at } X_1 = X_2 = \dots = X_n = 1 \\ 0 & \text{otherwise;} \end{cases} \quad (9)$$

Multi-disjunction

$$Y = X_1 \vee X_2 \vee \dots \vee X_n = \begin{cases} 0 & \text{at } X_1 = X_2 = \dots = X_n = 0 \\ 1 & \text{otherwise;} \end{cases} \quad (10)$$

negation NOT

$$Y = \overline{X} = \begin{cases} 1 & \text{at } X = 0 \\ 0 & \text{at } X = 1 \end{cases} \quad (11)$$

where $Y, X_1, X_2, \dots, X_n \in \{0,1\}$, $\{0,1\}$ – a plurality of logical type, $n > 1$.

It is easy to get a fuzzy logic operations, noting that in the generalized case the operation AND means choosing the lesser of n binary numbers, operation OR means selecting the largest of them, and the operation NOT – replacement of the existing number by the number symmetrical with it relating the middle of the set $\{0, 1\}$, but it is of the real form, i.e. It contains an infinite number of values of the elements.

Approximation of membership functions

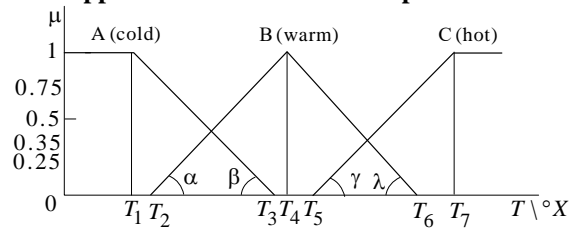


Fig. 2

Three elementary operations are defined in accordance with this:

- the intersection of sets (generalization of the logical AND):

$$Y = X_1 \cap X_2 \cap \dots \cap X_n : \min(\mu X_1(z), \mu X_2(z), \dots, \mu X_n(z)) \quad (12)$$

- the union of sets (generalization of the logical OR):

$$Y = X_1 \cup X_2 \cup \dots \cup X_n : \max(\mu X_1(z), \mu X_2(z), \dots, \mu X_n(z)) \quad (13)$$

- the complement of sets (generalization of the logical NOT):

$$Y = \overline{X}; \mu Y(z) = 1 - \mu X(z), \quad (14)$$

where Y, X_1, X_2, \dots, X_n belong to real sets and membership function μ - to a real set $\{0,1\}$.

Expressions (12) and (13) are realizable by operations MAX and MIN of module MVV or MVVM (MAX and MIN operation), and the expression (14) is feasible by the operation of subtraction of these modules (operation -R).

Definitions of fuzzy logic operations (12) - (14) the so-called MIN / MAX-operators are admissible, if the inputs are independent.

The main element of fuzzy information processing is the so-called production rule. It is knowledge of the form template "condition-action". Such knowledge design is the basis of the design of fuzzy controllers, control of which is carried out not by traditional accurate algorithms, but using a set of linguistic rules of the form:

$$\text{IF } () \text{ TO } (). \quad (15)$$

The left side of (1.15) for each production rule is treated as a conjunction of elementary conditions, and the right one - as a set of elementary actions.

Fuzzy Control System (Fig. 4) is composed mainly of three components:

- Value converter of the reference variable and controlled variable in the form of fuzzy description by means of membership functions;
- Selection algorithm of the solution for determining fuzzy values of the manipulated variable, based on fuzzy description of the controlled variable using linguistic rules knowledge base;
- Converter into a clear value translates fuzzy value of the manipulated variable in a physically realizable exact value of the manipulated variable signal for output to the actuator.

The linguistic rules of fuzzy controllers are usually compiled from expert surveys [2] on the basis of the control object information and its Fuzzy Control Systems.

For example, production rule in the form of a fuzzy controller is suggested in:

$$\text{IF } (e = e_i) \& (\Delta e = \Delta e_i), \text{ then} \\ \Delta u = \Delta u_i. \quad (16)$$

where $i = 1, 2, \dots, n$ - rule number;

- e - error;
- Δe - error rate of change;
- Δu - the change of manipulated variable.

The values of variables $e_i, \Delta e_i, \Delta u_i$ in every rule i is estimated by an expert.

A fuzzy controller is proposed in, whose knowledge base is presented in the form of:

$$\text{IF } (X_1 = A_1^i) \& (X_2 = A_2^i) \& \dots \& (X_n = A_n^i), \\ \text{THAT, } u^i = P_0^i + P_1^i X_1 + \dots + P_n^i X_n \quad (17)$$

where i - rule number;

A_1^i, \dots, A_n^i - fuzzy sets;

X_1, \dots, X_n - clear input values (the error, its speed);

P_0^i, \dots, P_n^i - fixed parameters of each rule;

u^i - the value of the manipulated variable.

The structure of the control system with fuzzy controller

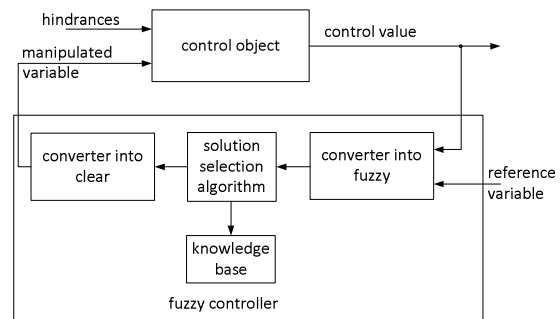


Fig.4

Program calculating the function (17)

If the rules are relevant at the same time, the final control value is defined by the relationship:

$$u = \frac{\sum_{i=1}^k \mu_i u^i}{\sum_{i=1}^k \mu_i}, \quad (18)$$

where μ_i - weighted coefficient that determines the degree of importance of rule i .

The example of the program implementing the relationship (17) and (18) is shown in Fig. 5 [10-16].

Comment. The implementation of a wide variety of corrective devices in the form of completed "standard" functional modules is not appropriate. These modules in the form of circuits can be made by an automation specialist proceeding from his own experience using the calculation modules of MBB and MVVM expressions and shift registers SR providing a deep memory $(k-2), (k-3), \dots, (k-m)$.

Fuzzy Control System Program (17)-(18)

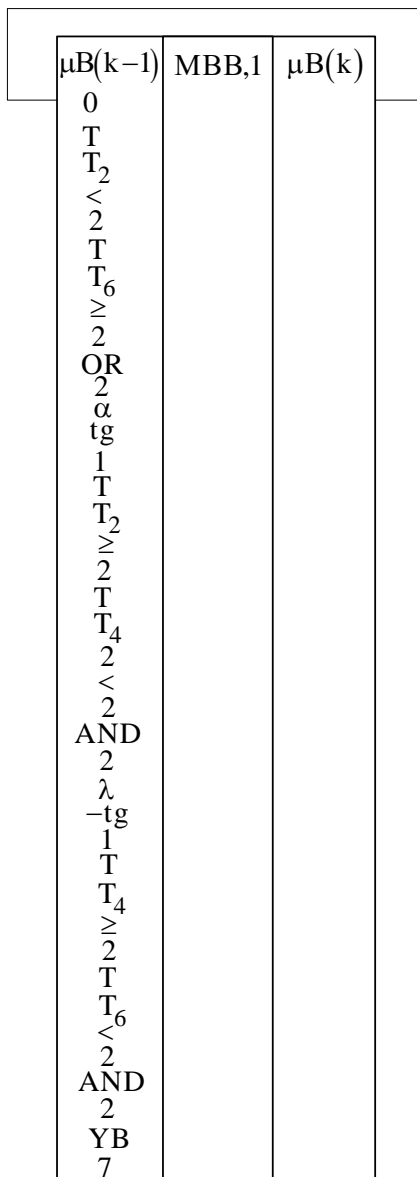


Fig. 3

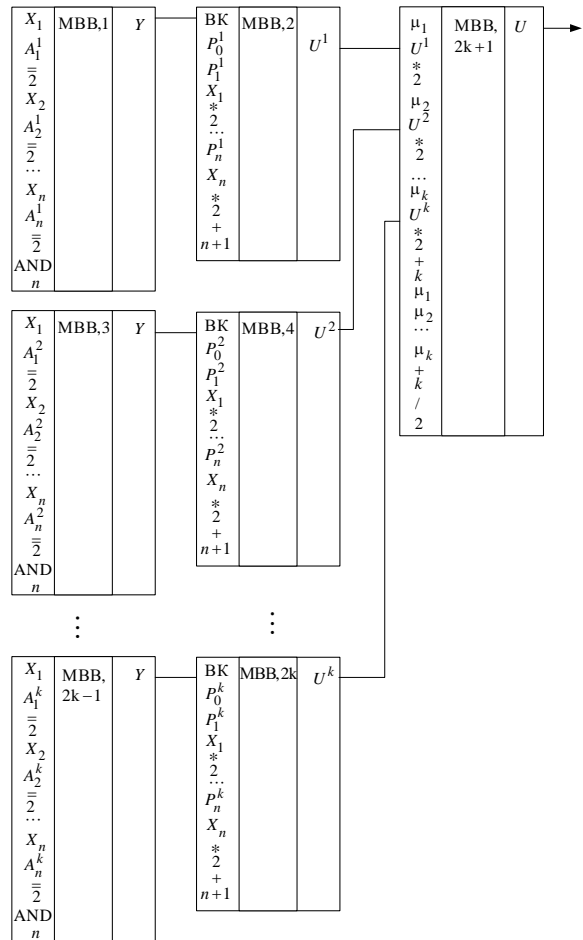


Fig.5

III. CONCLUSION

The paper provides the mathematical description of control in case of fuzzy information with a possibility of its program implementation in the SDSDC complex. This approach allows to expand without any essential expenses the composition of the standardized groups of modules of a fuzzy logic in comparison with the functional requirements of the IEC standard 61131-7. The offered option of program implementation of devices in the SDSDC complex allows to use the technique accepted in the hardware systems development, for example, the technique of developing and mounting of management and regulation systems on the basis of pneumatic automation, hydraulics, electromechanics appliances, the discrete automatic equipment with chips of different integration scale.

IV. ACKNOWLEDGEMENTS

The authors wish to express their sincere thanks to Tatyana Klets, Deputy Dean of Engineering and Construction Technologies Faculty of Pskov State University, for her invaluable foreign language assistance and supportive comments.

REFERENCES

- [1] Алиев Р.А., Церковный А.Э., Мамедова Г.А. Управление производством при нечеткой исходной информации.-М.: Энергоатомиздат, 1991, с. 240.
- [2] Левин В.И. Бесконечнозначная логика в задачах кибернетики.- М.: Радио и связь, 1982, с. 176.
- [3] Левин В.И. Структурно-логические методы исследования сложных систем с применением ЭВМ.- М.: Наука, 1987, с.304.
- [4] Buckley J.J. Fuzzy Controller: Further Limit Theorems for linear Control Rules; in: Fuzzy Sets and Systems, Elsevier Science Publishers B.V. (North-Holland), 36(1990 p.225-233).
- [5] Zadeh L.A. Fuzzy Sets. Inf. Contr. 1965, № 8, p. 338 – 353.
- [6] Takagi T., Sugeno M. Fuzzy Identification of Systems and Its Application to Modelling and Control; in: IEE Transaction on System, Man and Cybernetics, 15.01.1985, p. 116-132.
- [7] Коневцов В.А. САПР цифровых САУ. Кон-цепция: Моногрфия.Псков, Издательство ППИ, 2011. – 256 с.
- [8] Коневцов В.А. САПР цифровых САУ. Кон-цепция: моногрфия. – Изд-е второе, дополн. и испр. – Псков: Издательство ПсковГУ, 2012. – 307 с.
- [9] КОНЕВЦОВ В.А. САПР ЦИФРОВЫХ САУ. КОН-ЦЕПЦИЯ: МОНОГРФИЯ. – ИЗД-Е ТРЕТЬЕ, ДОПОЛН. И ИСПР. – ПСКОВ: ИЗДАТЕЛЬСТВО ПСКОВГУ, 2013 – 317 С.
- [10] AHNERT G: FUZZYSTUERUNG VON VERVAHRENS-TECHNISCHEN PROZESSEN MITTELS BERATUNGSRECHNER AM BEISPIEL DER.AN- UND ABFAHRSTEUERUNG von Pyrolyseöfen; Forschungsbericht, TH Leipzig, 1986
- [11] EICHFELD, H. KÜNEMUND, T.: HARDWARE FOR FUZZY CONTROL SYMPOSIUM, 3. JUNI 1991, FORUM 1, MÜNCHEN, PERLACH, 1991, TAGUNGSBAND
- [12] Hellendoorn H.: Fuzzy Logic and Fuzzy Control; In: van der Vlugten, Rene, et al.(Eds.) Clear Applcition of Fuzzy Logic, Processings IEEE-SymposiumDelft, Delft Delft 17.10.91.S.57-82
- [13] Kawaji. S.; Matsunaga, N.: Fuzzy Control of VSS Type and Its Robustness; In: IFSA'91 Brüssel, 7.-12.8.1991, Preprints, Vol. Engineering S81-84
- [14] Lee C.C. Fuzzy Logic in Control Systems: Fuzzy Logic Controller-Part 1; In: IEEE Transactions on Systems, Man and Cybernetics, 20 (2)(1990), S.404-418
- [15] Lee C.C. Fuzzy Logic in Control Systems: Fuzzy Logic Controller-Part 2; In: IEEE Transactions on Systems, Man and Cybernetics, 20 (2)(1990), S.419-435
- [16] Locke, M.: Fuzzy Modelling in Expert System for Prozess Control; In: Syst., Anal., Model., Simul., Akademie-Verlag Berlin 7 (1990) 9, S.715-719
- [17] Konevtsov V.A., Verteshev S.M: PROGRAMMING OF THE DIGITAL SHEMES. European Science and Technology Germany, Munich April 20th – 21st 2016, p.92 – 100.
- [18] Konevtsov V., Poletaev I., Verteshev S. DISCRETE AUTOMATIC SCHEMES FOR ASC TP. Rösekne, 2015, Environment. Technology Resources, Rezekne, Latvia Proceedings of the 10th International Scientific and Practical Conference, Vol., p. 6 7- 71.
- [19] Konevtsov V.A., Poletaev I.A., Verteshev S.M. EIGENSCHAFTEN VON COMPLEX SDSDC. Germany, Munich European Science and Technology April 23th – 24th 2014, Vol. II, p.493 – 497.
- [20] Konevtsov V.A., Verteshev S.M: PROGRAMMING OF THE DIGITAL SHEMES. European Science and Technology Germany, Munich April 20th – 21st 2016, p.92 – 100.
- [21] Verteshev S.M: Konevtsov V.A., Poletaev I.,A:SOFTWAREMITTEL DER PROJEKTIERUNGDER DIGITALEN STEUERUNG European Science and Technology Germany, Munich October 3rd-4th 20th – 21st 2013, Voi. 1, p. 501 -504.
- [22] Speicherprogrammierbare Steuerungen. Teil 3: Fuzzy Control Programmierung (IEC 61131-7:2000). Deutsche Fassung EN 61131-7:2000.

Direct Digital Control in a Complex of Software Design of Digital Control Systems

Sergei Verteshev, Vladimir Konevtsov

Pskov State University,
Faculty of Computer Science and Electrical Power Engineering.
Address: Leo Tolstoi Street 4, Pskov, Russia

Abstract. This article provides the functionality of creating direct digital control devices in the computer-aided design of digital automatic control systems (CAD of digital ACS), in a complex of software design of digital control systems (SDSDC complex) for automated process control systems. Technical tools are defined by the international standard IEC 61131-1: 2003 (Part 1: General data). The possibility of implementing SDSDC complex in direct digital control, single-cycle and multi-cycle ladder diagrams, identification of objects of management and synthesis of digital controllers in comparison with the international standard IEC 61131-3: 2003 (Part 3: Programming Languages) are evaluated. Users' productivity is estimated as well as the possibility of its separation between the users at different stages of the design of digital systems of automatic control is assessed.

Keywords: closed loop digital control, corrective digital device, direct digital control, proportional-integral-derivative controller.

I. DIGITAL CONTROL CHANNEL

Direct digital control can be used to perform a wide variety of tasks [1]:

- stabilization – ensuring equality of the controlled variable with a given accuracy and constant over time given value;
- program control - ensuring equality of the controlled variable with a given accuracy and previously known function of time;
- tracing control - providing "proximity" of the controlled variable to previously unknown function of any form of time;
- extreme control – retention of the criterion of work quality of the system in the field of proximity to previously unknown and changing in space controlled or specified variable to extreme value of a control quality criterion;
- optimal control - transfer from one state to another with extreme value of selected quality indicators.

The object is controlled by a digital control channel, comprising elements (blocks) of signal processing:

1. Input of values of the controlled variable from the sensor;
2. Input of channel status variables (manual, automatic or program mode, the position of executive body);
3. scaling controlled variable values, the variable of position of the executive body;
4. filtration;

5. verification of signals on the limit values and the rate of change;
6. calculation of control (regulation) error;
7. error limitation and control;
8. calculation of a manipulated variable;
9. the restriction and control of a manipulated variable, ensuring smooth (unstressed) transients in a closed control loop;
10. the zoom of a manipulated variable;
11. output of values of a manipulated variable on the actuator;
12. the digital control channel may comprise units of software and logic control (switches, commutators, signal combiners, etc.) to communicate with other channels and systems.

Synthesis of digital control channel structure is the most objective intuition, rather than "pure" mathematical problem that cannot be solved as standard. Most of the existing "classical" methods of calculation and channel settings are focused on the synthesis of block 8), i.e. algorithm for calculating the manipulated variable (equalizer).

II. CORRECTIVE DIGITAL DEVICES

By corrective device [2,3,4] is implied mathematical dependence, which can be used to achieve the desired behavior of the managed object. A special case of a corrective device is, for example, a conventional proportional-integral-derivative (PID) controller [5,6,7]. Corrective device synthesis is made according to the principle implemented [8-16]:

- direct control,

- feedback control,
- combined control.

The control problem is to achieve with a certain degree of accuracy (quality) the equality between the reference variable $W(z)$ and controlled variable $Y(z)$ in the presence of interference $V(z)$.

In direct management, based on the requirements

$$Y(z) = W(z) \quad (1)$$

transfer function of the corrective device $D(z)$ is equal to the inverse transfer function of the object $G(z)$

$$D(z) = 1/G(z) \quad (2)$$

Direct control principle (the principle of precession or compensation) can be used in cases when in the object controlled:

- there is no hindrance or the values of the hindrance signal are measurable;
- the transfer function of the object corresponds to the entire working range of control action change;
- there are no restrictions in the digital control channel (non-linearity).

For real objects, these conditions are ideal, so the principle of feedback control (the principle of deviation) has got practical application. This principle allows to satisfy the condition (1) with required accuracy, regardless of the cause of the error in a closed control loop. A closed loop digital control generally comprises:

- quantizers of a reference variable $w(t)$, a manipulated variable $u(k)$ and a controlled variable $y(t)$;
- digital corrective device $D(z)$ with the transfer function:

$$D(z) = U(z)/E(z) = \frac{(d_0 + d_1 z^{-1} + \dots + d_n z^{-n})}{(1 + c_1 z^{-1} + \dots + c_n z^{-n})} \quad (3)$$

where $U(z), E(z)$ – images of the manipulated variable signals $u(k)$ and deviation $e(k)$ (control error);

- control object $G(z)$, representing a discrete latch conversion $F(p) = (1 - \exp(-pT))/p$ and continuous transfer function of the object $G(p)$:

$$G(z) = Y(z)/U(z) = (1 - z^{-1}) Z \{ G(p)/p \}, \quad (4)$$

where $Y(z)$ – image of the controlled variable signal $y(t)$.

The order and parameters of the corrective device are selected according to dependencies defined by the applicable method of the synthesis of this device taking into account the properties of the object of control, restrictions, criteria for quality control. The corrective device conventionally used in practice is a PID controller and its modifications, represented by the differential equation:

$$u(t) = K \left[e(t) + \frac{1}{T_I} \int e(t) d\tau + T_d (de(t)/dt) \right], \quad (5)$$

where K – coefficient of controller gain;

T_I – integration time (integral action);

T_d – derivation time (precession);

$e(t)$ – control error (deviation);

$$e(t) = w(t) - y(t); \quad (6)$$

$w(t)$ – reference variable;

$y(t)$ – controlled variable.

Closed-loop digital control

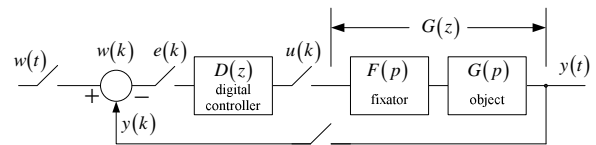


Fig.1

The differential equation (5) can be converted into the form of the equation of differencies by differentiating and replacing the differential relations by difference:

$$du(t)/dt = K \left[de(t)/dt + 1/T_I \cdot e(t) + T_d (d^2e(t)/dt^2) \right], \quad (7)$$

after replacing the first and second derivatives by the first and second differences:

$$de(t)/dt \approx \Delta e(k) = (e(kT) - e(kT - T))/T; \quad (8)$$

$$d^2e(t)/dt^2 \approx \Delta^2 e(k) = \frac{(e(kT) - 2e(kT - T) + e(kT - 2T))}{T^2}; \quad (9)$$

$$du(t)/dt \approx \Delta u(t) = (u(kT) - u(kT - T))/T, \quad (10)$$

where T - period of discreteness chosen small enough, based on the inertia of the controlled object [27].

After substituting the right-hand sides (8) - (10) in (7) instead of corresponding differential relationship with the replacement of real time kT by the relative k , $k = 0, 1, 2, \dots$ difference form of the PID controller is got:

$$u(k) = u(k-1) + K[e(k) - e(k-1) + e(k)T/T_I + Td/T(e(k) - 2e(k-1) + e(k-2))]$$

After grouping the values of the error with respect to timings

$k, k-1, k-2$ the final form of the difference equation of the PID controller is got:

$$u(k) = u(k-1) + d_0e(k) + d_1e(k-1) + d_2e(k-2), \quad (11)$$

$$d_0 = K(1 + T/T_I + T_d/T); \quad (12)$$

$$d_1 = -K(1 + 2T_d/T); \quad (13)$$

$$d_2 = K(T_d/T). \quad (14)$$

From (11) the transfer function of a digital equivalent of the analog controller can be obtained, using the theorem of z-transform delay:

$$D(z) = U(z)/E(z) = (d_0 + d_1z^{-1} + d_2z^{-2}) / (1 - z^{-1}). \quad (15)$$

If not to take into account the expressions (12)-(14), the form of writing (15) does not indicate that it represents the PID controller in the conventional sense, because the PD controller has the same discrete transfer function only with other values of the numerator coefficients in (15), obtained from (12) - (14) at $T_I \rightarrow \infty$:

$$d_0 = K(1 + T_d/T); \quad (16)$$

$$d_1 = -K(1 + 2T_d/T); \quad (17)$$

$$d_2 = K(T_d/T). \quad (18)$$

From the expressions (11)-(14) a digital PI controller can be obtained at $T_d \rightarrow 0$:

$$D(z) = U(z)/E(z) = (d_0 + d_1z^{-1}) / (1 - z^{-1}); \quad (19)$$

$$d_0 = K(1 + T/T_I); \quad (20)$$

$$d_1 = -K. \quad (21)$$

Similarly, P controller is shaped like a PI controller at $T_I \rightarrow \infty$, in which $d_0 = -d_1 = K$.

A variety of digital controllers whose forms and parameters are removed from the molds and parameters of traditional analog controllers is immense. They were derived based on various objects' properties and signals acting on the control circuit. Thus, with significant changes in the reference variable the algorithm (11) will lead to a shock impulse actions on the object, which may cause unwanted transients in a closed control loop. To eliminate this effect suggested the controller structure is suggested in which differentiation of the signal of the reference variable is eliminated by replacing the reference variable differential component of the error by differential component of the controlled variable:

$$du(t)/dt = K \left[dy(t)/dt + 1/T_I e(t) + Td \left(d^2y(t)/dt^2 \right) \right], \quad (22)$$

therefore

$$u(k) = u(k-1) + d_0y(k) + d_1y(k-1) + d_2y(k-2) + d_3w(k), \quad (23)$$

$$d_0 = -K(1 + T/T_I + T_d/T); \quad (24)$$

$$d_1 = K(1 + 2T_d/T); \quad (25)$$

$$d_2 = -K T_d/T. \quad (26)$$

$$d_3 = -K(T_d/T). \quad (27)$$

A block diagram of the connection to the object of equivalent (22) analog controller is shown in Fig. 2. It shows that the abrupt reference variable "is softened" by integrating the error, on the one hand, and the smoothing action of the object, on the other hand, allowing to avoid strong throws of values of differential and proportional part by the reference variable signal.

These effects often occur during channel transitions from manual to automatic or program mode. If the object does not possess adequate smoothing properties, it is possible to use a low pass filter in the differentiation circuit (Fig. 3).

Depending on the properties of the actuator position algorithms (to control actuators that do not have memory) and incremental or speed algorithms of controllers (to control actuators having memory), i.e. able to integrate (stepper motors, valves, integrating amplifiers), are varied.

From (11) we obtain an incremental algorithm of PID-controller:

$$\Delta u(k) = u(k) - u(k-1) = d_0 e(k) + d_1 e(k-1) + d_2 e(k-2)$$

Algorithms of digital controllers whose structures and parameters are determined on the basis of approximation of transfer functions of objects by inertia and integrating links with delay (Ziegler-Nichols [10] Dalin [7], Kalman [7]) are known.

In practice, there are objects that have high inertia.

For example, it may take several minutes to change the temperature in the fermenter medium [8] of 50 cubic meters. One can use a two-position controller with insensitivity to manage a similar subject:

$$u(k) = \begin{cases} U1 & \text{at } (w(k) - \Delta w) > y(k) \\ U2 & \text{at } (w(k) + \Delta w) < y(k) \\ u(k-1) & \text{at } (w(k) - \Delta w) \leq y(k) \leq (w(k) + \Delta w), \end{cases} \quad (28)$$

where $u(k)$ – the value of the manipulated variable;

$w(k)$ – the value of the reference variable;

$y(k)$ – the value of the controlled variable;

Δw – dead zone;

Control contour and «smoothing by the object»

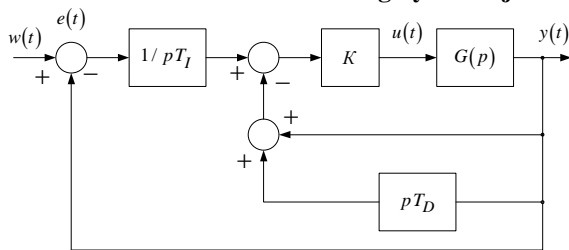


Fig. 2

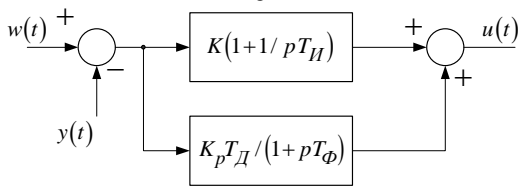


Fig. 3

$U1, U2$ - the values of the manipulated variable outside the dead zone;

$u(k-1)$ – the value of the manipulated variable in the preceding control cycle.

The manipulated variable (28) can be output through the on-off actuators. In this case, $U1$ and $U2$ are the inverse logic signal values.

There is a class of digital controllers, whose structures correspond to the transfer function (3) and

are calculated not from the traditional concepts and methods of tuning digital PID controllers and presentation of object properties in the form of a continuous transfer function. These methods are derived from the representation of the object properties in the form of a differential equation with delay d :

$$y(k) = - \left[\sum_{i=1}^m a_i \cdot y(k-i) + \sum_{i=0}^n b_j \cdot u(k-i-d) \right] \quad (29)$$

or in the form of discrete transfer function:

$$G(z) = Y(z)/U(z) = \frac{(b_0 + b_1 z^{-1} + \dots + b_m z^{-m}) z^{-d}}{(1 + a_1 z^{-1} + \dots + a_m z^{-m})} \quad (30)$$

Only arithmetic operations are used in the considered algorithms of digital controllers. Relations and logical operations usually show a variability of controller or channel structure, the presence of non-linearities, etc. For example, the algorithm [6]:

$$\Delta u(k) = \begin{cases} K[e(k) - e(k-1)] + K \cdot T \cdot e(k) / T_I & \text{at } |e(k)| - |e(k-1)| \geq 0 \\ K \cdot T / T_I \cdot e(k) & \text{at } (|e(k)| - |e(k-1)| < 0) \wedge (|e(k)| > \varepsilon) \end{cases} \quad (31)$$

has a variable structure depending on the nature of changes in the control error: if the absolute value of the control error is reduced, only the integral part of the controller calculating the manipulated variable is used, otherwise, if the absolute value of the control error increases, the proportional component of the controller to calculate the manipulated variable is used.

Piecewise-linear relationship

$$u(k) = \begin{cases} |U_m| \text{ Sign } e(k) & \text{at } |e(k)| \geq \varepsilon \\ 0 & \text{at } t_1 < t < (t_1 + \Delta t) \\ U_1 & \text{at } t > (t_1 + \Delta t) \\ u(k-1) + d_0 e(k) + d_1 e(k-1) + d_2 e(k-2) & \text{at } t > t_2, \end{cases} \quad (32)$$

where U_m – the maximum value of the manipulated variable;

ε – the absolute value of the error;

t_1 – the duration of the forced regime;

Δt – pause duration;

t_2 – controller launch;

U_1 – the value of the manipulated variable before turning the PID controller can be used to implement the forced (relay) modes in the control loop with significant changes in the reference variable.

When handling control loop (manual, program, automatic modes) it is necessary to shock-free switching control circuit (controller channel compensation):

$$Y_1 = \begin{cases} 1 & (\text{mm}=0) \wedge (\text{pm}=0) \text{ auto mode} \\ 0 & \text{otherwise manual or program mode} \end{cases}$$

$$Y_2 = \bar{Y}_1$$

$$Y_3 = \begin{cases} \text{pmm at } = \text{mm} \\ \text{papm at } (\text{mm}=0) \wedge (\text{pm}=1) \\ a = \begin{cases} Y_3(0) + \Delta K |e(k) - \\ -e_0 | \text{Sign } e(k) \text{ at } e(k) > e_0 \\ Y(k-1) \text{ otherwise} \end{cases} \end{cases} \quad (33)$$

$$Y_4 = \begin{cases} X_1(k) \text{ at } \text{mm}=1 \\ X_2(k) \text{ at } (\text{pm}=1) \wedge (\text{mm}=1) \\ Y_0 \text{ otherwise,} \end{cases}$$

where mm – manual mode (mm=1);

pm – program mode (pm=1);

pmm – the position of the actuator in the manual mode;

papm – the position of the actuator in the program mode;

$X_1(k)$ – the controlled variable in the manual mode;

$X_2(k)$ – the controlled variable in the program mode;

$Y(k-1)$ – the manipulated variable in the automatic mode;

$e(k)$ – control error;

e_0 – permissible control error;

ΔK – increment compensation error;

$Y_3(0)$ – the initial value of the compensation channel output;

Y_1 – automatic mode;

Y_2 – manual mode;

Y_3 – the position of the actuator in the manual or

program mode or the value of the manipulated variable;

Y_4 – the value of the controlled variable or control task.

III. CONCLUSION

The paper provides the mathematical description of direct digital control oriented on its program implementation in the SDSDC complex. This approach allows to design and create systems of direct digital control with ampler functional capabilities than it is implied by the requirements of the IEC international standard 611-31-3. So, the program implementation of control in the SDSDC complex provides the creation of controllers' compensation channels and PID – controllers with and without a hysteresis.

IV. ACKNOWLEDGEMENTS

The authors wish to express their sincere thanks to Tatyana Klets, Deputy Dean of Engineering and Construction Technologies Faculty of Pskov State University, for her invaluable foreign language assistance and supportive comments.

REFERENCES

- [1] Волик Б.Г., Буянов Б.Б., Лубков Н.В. Методы анализа и синтеза структур управляющих систем. -М.: Энергоатомиздат, 1988, с. 296.
- [2] Волгин Л.Н. Элементы теории управляющих машин.- М.: Советское радио, 1962, с. 162.
- [3] Волгин Л.Н. Оптимальное дискретное управление динамическими системами. - М.: Наука, 1986, с. 240.
- [4] Федотов С.М., Литвинов А.П. Автоматические системы с цифровыми управляющими машинами (теория и практика).- М., Ленинград: Энергия, 1965, с. 223.
- [5] Емельянов С.В., Матич Б.П., Костылева Н.Е. Универсальная унифицированная система управления переменной структуры.- Приборы и системы управления, 1973, №12, с. 1-3, 1974, №1, с. 12-13.
- [6] Unbehauen H., Böttiger F. Regelalgorithmen für Prozessrechner.- PDV-Berichte, 1974, №26, s. 108.
- [7] Chiu K.C., Corripio A.B., Smith C.L. Digital Control Algorithms: Part I Dahlin-Algorithm; Part II Kalman-Algorithm; Part III Tuning of PI- and PID-Controllers.- Instruments Controlsystems, 1973, №10, p. 57-59; №11, p. 55-59; №12, p. 41-43.
- [8] Бабаянц А.В., Коневцов В.А. Идентификация динамических характеристик процессов микробиологического синтеза с помощью УВК.- Автоматика и телемеханика, 1982, №3, с. 79-86.
- [9] Коневцов В.А. САПР цифровых САУ. Концепция: Монография. Псков: Издательство ППИ, 2011. – 256 с.
- [10] Takahashi Y., Chan C.S., Auslander M.D. Parametereinstellung bei linearer DDC-Algorithmen.- Regelungstechnik und Prozessdatenverarbeitung, 1971, №6, s.237-244.
- [11] Коневцов В.А. САПР цифровых САУ. Концепция: Монография.Псков, Издательство ППИ, 2011. – 256 с.
- [12] Коневцов В.А. САПР цифровых САУ. Концепция: монография. – Изд-е второе, дополн. и испр. – Псков: Издательство ПсковГУ, 2012. – 307 с.
- [13] [3]. Коневцов В.А. САПР цифровых САУ. Концепция: монография. – Изд-е третье, дополн. и испр. – Псков: Издательство ПсковГУ, 2013 – 317 с.
- [14] Коневцов В.А., Казаченко А.П., Литвинова Л.М., Бунин А.Б. Модифицированные средства цифрового

- управления.- М.: Информприбор, Каталог Государственной Системы Приборов СССР, 1987, том 4, вып. 10, 11, 12, с. 112.
- [15] John Karl-Heinz, Tiegelkamp Michael SPS-Programmierung mit IEC 61131-3.- Springer – Verlag Berlin Heidelberg 4. Auflage, 2009, s.402.
- [16] Konevtsov V.A., Verteshev S.M., Poletaev I.A. Eigenschaften von Complex SDSDC // European Science and Technology: 7th International scientific conference. Germany, Munich 2014, Vol.I, p. 493-497.
- [17] Seitz M. Speicherprogrammierbare Steuerungen für die Fabrik- und Prozessautomation.- Fachbuchverlag Leipzig im Carl Hanser Verlag, 3. Auflage, 2012, s. 277.
- [18] Speicherprogrammierbare Steuerungen. Teil 3: Programmiersprachen (IEC 61131-3:2003). Deutsche Fassung EN 61131-3:2003.
- [19] Tröster F. Steuerungs- und Regelungstechnik für Ingenieure.- Oldenburg Verlag München, 3. Auflage, s. 562.
- [20] Verteshev S.M., Konevtsov V.A., Poletaev I.A. Methods of Software Developing of Complex SDSDC // European Science and Technology: 4th International scientific conference. Germany, Munich 2013, p. 377-380.
- [21] Verteshev S.M., Konevtsov V.A., Poletaev I.A. Softwaremittel der Projektierung von Systemen der digitalen Steuerung // European Science and Technology: 5th International scientific conference. Germany, Munich 2013, Vol. I, p. 501-504.
- [22] Wellenreuter G., Zastrow D. Automatisierung mit SPS. Theorie und Praxis.- Vieweg + Teubner, 5. Auflage, 2011, s.870.

New Environmentally Friendly Dust Suppressant Based on Lignocellulosic Biomass from Wood Processing Wastewater

Sanita Vitolina¹, Galia Shulga¹, Brigita Neiberte¹, Skaidrite Reihmane², Elina Zilinska¹

¹Latvian State Institute of Wood Chemistry, 27 Dzerbenes St., Riga, Latvia

²Riga Technical University, 3 Paula Valdena St., Riga, Latvia

Abstract. In this work, the possibility of usage of lignocellulosic biomass derived from wood processing wastewater as an environmentally friendly dust suppressant was studied. To increase the efficiency of the recovery of lignocellulosic biomass, a new developed composite coagulant, representing a polymer-colloid complex of polyethyleneimine with polyvalent metal ions, was applied. The effectiveness of the composite coagulant was examined using a model solution simulating the wastewater of hydrothermal treatment of birch wood. The optimum content of PEI in the composite coagulant was found to be 25-35%. At the optimal composite coagulant dosage and pH value, the yield of the total wood biomass achieved 97%, but the extraction of lignin and lignin-like substances was more than 65%. Due to the polymeric and polyfunctional nature, the recovered wood biomass had glue properties. Taking into account the fact that the dust at the surface of unpaved roads poses considerable environmental problems, the biomass was tested as a structuring agent for sandy and model sandy-clay soils. The obtained results have shown that the separated lignocellulosic biomass was capable of forming large sandy aggregates that were able to decrease the dusty soil blowing off from the unpaved road surface.

Keywords: coagulation, composite coagulant, dust suppressant, lignocellulosic biomass, wastewater.

I. INTRODUCTION

In industrial veneer production, it is common to soak logs at elevated temperature prior to peeling. This hydrothermal pre-treatment is carried out to soften the logs and to ease the cutting during the peeling process [1]. The conditions of soaking depend on the wood species, the manufacturer, and the season of soaking. In Nordic and Eastern European countries, hydrothermal treatment is conducted at temperatures of 40-70°C for 8-48 h [2]. The obtained wastewater contains both suspended and dissolved substances, consisting of hemicelluloses, wood extractives, and lignin and its derivatives. Along with the strengthened public environmental protection awareness, the wastewater discharge regulations all over the world are becoming increasingly strict. Therefore, research on new technologies for wastewater treatment and the improvement of the existing ones becomes increasingly important.

Coagulation/flocculation is an important and established process in water treatment for removing contamination. In this process, coagulants are added to aggregate destabilized dissolved organic matter and colloidal particles into larger-sized flocs that can be effectively removed in subsequent separation processes [3]. Coagulants may be classified into inorganic and organic coagulants. High-charge cations, such as Fe³⁺ or Al³⁺, are among the most

effective reagents for destabilizing the colloids. Therefore, common inorganic coagulants (AlCl₃, Al₂(SO₄)₃, FeCl₃, Fe₂(SO₄)₃) and hydrolyzing metal salts based on aluminum or iron are widely used [4]. The polymers used in coagulation/flocculation treatment are commonly synthetic polyacrylamides, polyacrylic acids and polystyrene sulfonic acids, and their derivatives [5], [6]. To achieve better coagulation efficiency and floc characteristics, in recent years, research has been focused on the development of composite inorganic-organic coagulants. Composite materials pose tremendous potential in treating wastewater due to their better performance compared to that of conventional inorganic-based coagulants, and its lower cost than that of organic-based flocculants [7].

Sludge is a huge source of renewable organic matter that can be considered for sustainable resource recovery. Chemical compositions of the sludge depend on the wastewater quality, the nature of the chemicals used and the treatment processes involved. The results of several studies have indicated that chemical compositions are important while selecting potential reuse options [8]. Hence, prior knowledge of the physical and chemical properties of the sludge is necessary to reuse and recycle it into safe and sustainable disposal alternatives. Depending on the sludge chemical properties, it can be incorporated in

brick and ceramic production [9], [10], used as a raw material for concrete and cement production [11], [12] and in manufacturing lightweight aggregates [13]. Sludge can be used as a low cost adsorbent for removal of contaminants (phosphorus, hydrogen sulfide, fluorides, perchlorate, and glyphosate) and heavy metals from wastewater [14], [15]. It is also applied in agricultural practice and other land based uses for soil structure improvement and pH adjustment [16], [17].

The aim of this work was to study the possibility of using the lignocellulosic biomass derived from wood processing wastewater as an environmentally friendly dust suppressant. To increase the efficiency of the recovery of lignocellulosic biomass, we used a new developed composite coagulant and investigated the chemical composition and yield of the precipitated biomass sludge depending on the environmental pH and the applied dosage of the coagulant.

II. MATERIALS AND METHODS

Materials

The wastewater of the hydrothermal treatment in veneer production was simulated with a model solution obtained by hydrothermal treatment of birch sawdust. The hydrothermal treatment of sawdust was performed with 0.01M NaOH at a 1/50 (mass ratio of the oven dry sawdust to water) hydromodulus and a temperature of 90°C for 4 h. After hydrolysis, the hydrolyzate was separated from the sawdust treated through filtration. The model solution characterization has been published in our previous work [18].

In this study, a new composite coagulant (CC), representing a polymer-colloid complex of polyethyleneimine (PEI, Fluka, molecular mass of 750 kDa) with polyvalent metal ions, was developed. The polymer-colloid complex was formed due to the donor-acceptor interactions between imine atoms and metal cations. Besides, the complex was stabilized by H-linkages, taking into account the hydration shell around the metal ions. The PEI/metal salt mass ratio in the CC varied from 0.16/1 to 1/1.

In order to evaluate the obtained results, we chose the early developed composite coagulant [19] for treatment of the model solution as the control.

Experimental Procedure

The coagulation process was carried out by way of mixing the model wastewater solution and the solution of the CC at a ratio of 1:1 and stirring the suspension with a magnetic stirring bar at 200 rpm for 1 min, followed by slow mixing at 40 rpm for 2 min. The CC was added in the range of 20-140 mg l⁻¹ to the model solution. To characterize the coagulation performance of the CC at different pH values, experiments were conducted at pH values ranging from 5 to 8 by addition of HCl or NaOH. Experiments were conducted in the temperature range

of 13-60°C using a thermostat. The effectiveness of the coagulation was defined after a system settling time of 120 min and filtration. The residual concentration of the biomass and lignin was defined by measuring the obtained filtrate's optical density (A) at 490 and 280 nm using the previously obtained correlation curves for the biomass and lignin. Zeta potential and size measurements were conducted by Malvern Nanosizer SZ (UK).

To fractionate the lignocellulosic biomass and calculate the content of lignin and hemicelluloses therein, the precipitation of the hydrolyzate with concentrated sulfuric acid, with the following treatment of the formed filtrate with ethanol according to Liu and co-authors [20], was employed.

To provide useful information concerning the structure of the biomass sludge, analytical pyrolysis (Py-GC/MS) was applied. The analytical pyrolysis was performed with a Shimadzu GCMS-QP2010 coupled to a Frontier pyrolyzer.

The microstructure of the separated biomass surface was examined by scanning electron microscopy (SEM), using a scanning electron microscope (Tesla, Czech Republic).

Soil structuring experiments were conducted using powdered sand/clay model soil with a clay fraction content varied from 0 to 70%. The clay fraction for this study was taken from the Lielauces quaternary clay deposit (Latvia). Its mechanical composition is shown in Table 1.

Table 1
Average grain size distribution (wt.%)

Sample	>25 0 μm	250- 50 μm	50- 20 μm	20- 10 μm	10-5 μm	5-2 μm	<2 μm
Clay	2.3	9.6	14.3	12.1	13.4	15.5	34.5

The sand was taken from the Baltic Sea coast and had the following mechanical composition: 3.1% of particles ranging from 1.0 to 0.25 mm, 93.9% of particles ranging from 0.25 to 0.05 mm, and 3.0% of particles less than 0.01 mm in size.

In the work, the fraction of soil particles less than 0.25 mm was used. The soil aggregates (> 0.25 mm) were obtained by mixing the soil with 1.0-5.0 g dl⁻¹ biomass water suspensions. The used biomass had a gel form with the content of dry matter less than 10% and was obtained by centrifugation of the precipitated biomass sludge at 6000 rpm during 20 min without its drying. The water suspensions with the defined biomass concentration were prepared by intensive mixing the biomass gel with water at 100 rpm for 10 min using a mechanical mixer. The content of the biomass in the soil samples varied from 0.2% to 0.8% on their dry matter. The fractional composition of the dried structured soil was determined by dry sieving. The structuring coefficients K1 and K2 were found as the mass ratios of the sum of artificial aggregates > 0.25 mm to the initial sandy soil (K1) and of the sum

of aggregates > 3.0 mm to the sum of all aggregates formed in the structured soil after the treatment (K2).

To determine the effect of wind on blowing off the treated soil particles depending on their size, a wind tunnel of original construction at a wind velocity of 5-25 ms⁻¹ was applied. A certain mass of the soil sample was placed in the tunnel, and was subjected to the air flow with a variable speed for one minute. The loss of the mass was expressed as the percentage of the total soil mass.

III. RESULTS AND DISCUSSION

Isolation of Wood Biomass by Coagulation

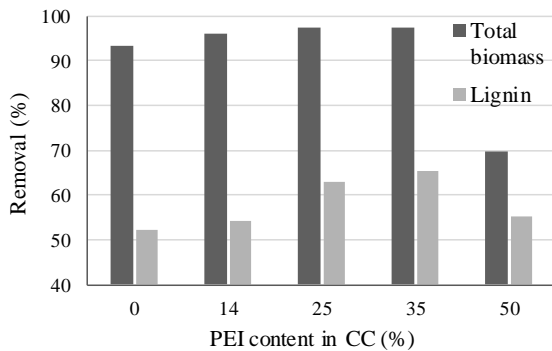


Fig. 1. Total biomass and lignin removal efficiency depending on the PEI content in CC (pH 6, dosage 100 mg l⁻¹).

Fig. 1 shows the total biomass and lignin removal as a function of the PEI content in the CC. The increase of the PEI content in the CC results in improving the efficiency of coagulation and particularly in lignin removal. The best results for the biomass separation occur by using the CC containing 25-35% PEI in its composition. An increase in the PEI content by more than 35% leads to a rapid decrease in the biomass removal efficiency.

For the further study, we used the new developed composite coagulant consisting of 25% and 35% PEI.

The results of the total biomass and lignin removal efficiency depending on the CC and control coagulant dosage at pH 6.0 are shown in Fig. 2. The developed CC demonstrates an overwhelmingly high coagulation efficiency compared with the control coagulant at a given dosage range. The lignocellulosic biomass removal at a dosage of the CC more than 70 mg l⁻¹ is enhanced to a lesser extent. At the same time, the maximal lignin removal with CC-35 and CC-25 is achieved at the dosage close to 100 mg l⁻¹. With the further increase in the dosage of the coagulant more than 100 mg l⁻¹, the removal efficiency of the biomass and lignin is decreased.

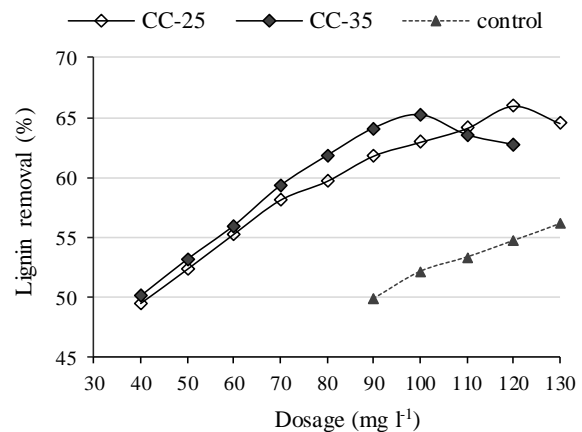
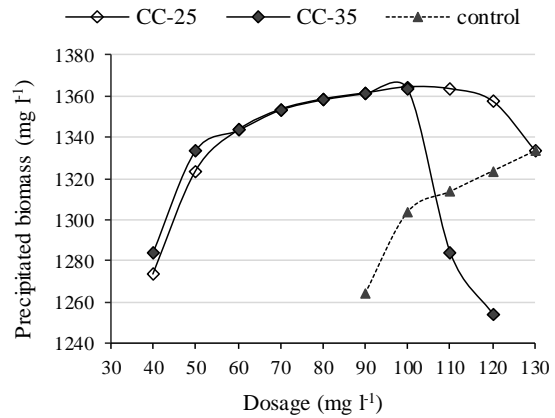


Fig. 2. Total biomass and lignin removal after coagulation treatment as a function of the dosage of CC (pH 6).

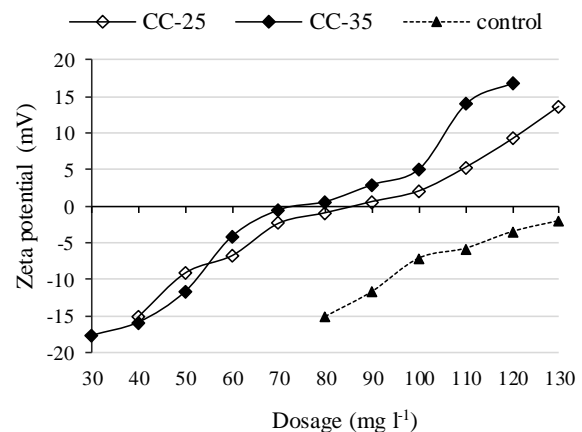


Fig. 3. Zeta potential of the model wastewater after coagulation as a function of coagulant dosage (pH 6).

It is known that zeta potential values indicate the quality of the purification of wastewater. The variations of the zeta potential of the wastewater against the coagulant dosage after the coagulation treatment are shown in Fig. 3. It can be seen that the control coagulant gives a very slight decrease in the negative zeta potential values within the investigated dosages, while the zeta potential of CC-35 and CC-25 increases gradually and reaches the isoelectric points at a dosage of about 70 and 80 mg l⁻¹, respectively.

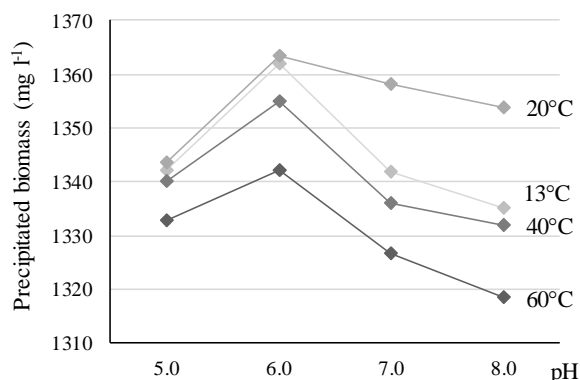


Fig. 4. Total biomass removal efficiency depending on the pH and temperature (CC-35, dosage 100 mg l⁻¹).

According to the obtained results, CC-35 was characterized by a higher total biomass and lignin removal from the wastewater as well as a lower optimal coagulation dosage.

The coagulation ability of CC-35 at different pH was also tested. The investigated pH range varied from 5 to 8. It can be seen (Fig. 4) that the total biomass removal grows slightly from pH 5 to 6, but decreases towards the neutral and alkaline pH values. The optimal pH value for the biomass precipitation is pH 6.

Since the coagulation process is relatively sensitive to the coagulation temperature, it was of interest to compare the coagulation efficiency of CC-35 in the temperature range of 13-60°C. Fig. 4 shows that, over the whole temperature range, the pH relevance remains. The reduction of temperature below 20°C practically does not affect the effectiveness of the CC-35 at the optimal pH 6. At the same time, with increasing temperature up to 40 and 60°C, the biomass removal efficiency decreases.

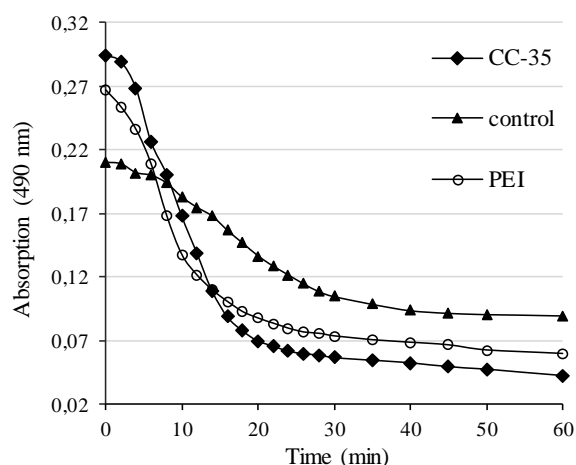


Fig. 5. Effect of coagulation time on the absorption (490 nm) of model wastewater in the coagulation process (pH 6, dosage 100 mg l⁻¹).

A study of sedimentation kinetics, using for this purpose the time-dependence of wastewater absorption at the wavelength 490 nm, shows (Fig. 5)

that the wastewater coagulated with CC-35 has the highest turbidity in comparison with PEI and the control coagulant, and the coagulation process with the participation of CC-35 is completed practically during the first 30 min. The diameter of the flocs obtained with CC-35 after 30 min of the coagulation was in a range of 1114-1242 nm, while these values for the flocs obtained with PEI and the control coagulant were significantly lower, in a range of 664-842 and 331-499 nm, respectively.

Separated Lignocellulosic Biomass Characteristic

The previous studies [18] of the component composition of the biomass with instrumental analysis (FTIR-, UV-, Raman spectroscopy; HPLC) indicated that the dominant wood component in the obtained biomass were hemicelluloses, and the content of hemicelluloses, lignin and water-soluble degraded wood products in the biomass corresponded to the following mass ratio: 6.7/1.2/1.0, respectively.

The study of the composition of the lignocelluloses by analytical pyrolysis indicates that the carbohydrates under investigation represent a mixture of low molecular wood degraded products, in which the content of cyclopentane derivatives is essential (Table 2).

Table 2
Products of carbohydrates pyrolysis

Cyclopentane derivatives	55.60%
Aldehyde, Ketone (Methylglyoxal and Acetone, 2-Butanone, 2-Pentanone, 2-Nonanone, 2-Propanone, 1-hydroxy-2-Butanone, 3-hydroxy-Hexanal)	25.35%
Acid, Alcohol (Acetic acid, 1,2-Ethanediol)	19.05%

At lower temperatures, the thermal decomposition of carbohydrates starts with the depolymerization of the polymer and the cleavage of chemical bonds in the side chains. Therefore, the formation of acetic acid is involved with the primary elimination reaction of the active O-Ac groups in the side chain. At the higher pyrolysis temperature, the products are more complex, including aldehydes, ketones and alcohols from the oxygenation of C2 or C3 in the sugar ring.

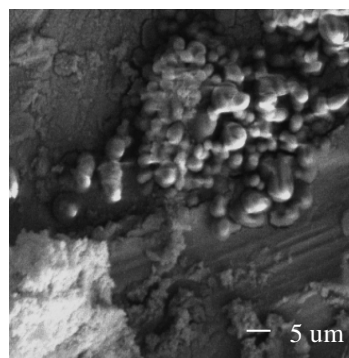


Fig. 6. SEM image of dried lignin and hemicelluloses coagulates.

Precipitated Biomass as a Structuring Agent for Dust Suppression

The reduction in dust emission from unpaved roads can be achieved through the application of chemical dust suppressants. Chemical suppressants such as polymers act as adhesives to bond soil particles together. The resulting agglomerates of soil particles become too heavy to be uplifted and entrained in the atmosphere as dust.

The precipitated lignocellulosic biomass was studied as a structuring agent for dust suppression. The used biomass was applied in the gel form and was obtained by centrifugation of the precipitated biomass sludge without its drying. Stable suspensions with the defined biomass concentration were prepared by intensive mixing the biomass gel with water.

The fractional composition of the treated sandy aggregates is represented in Fig. 7. With growing content of the biomass (0.2-0.8%), the amount of the sandy aggregates in the soil sample increases, and the values of the structure-forming coefficient K1 (Fig. 8) grow. Simultaneously, with increasing amount of the biomass, the structure-forming coefficient K2 also increases.

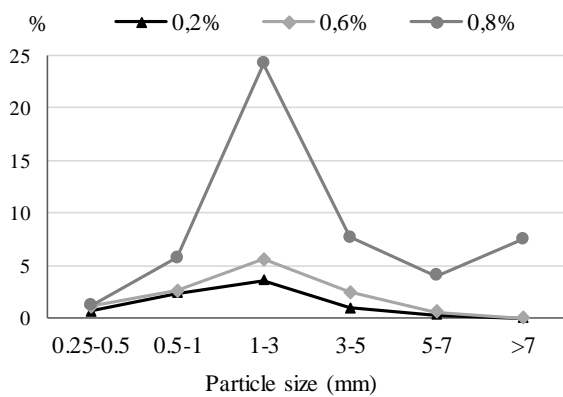


Fig. 7. Fractional composition of sandy soil depending on the added biomass content (100% sand soil).

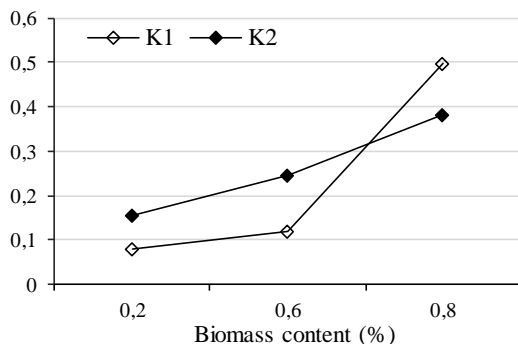


Fig. 8. Structuring coefficients K1 and K2 depending on the added biomass content (100% sand soil).

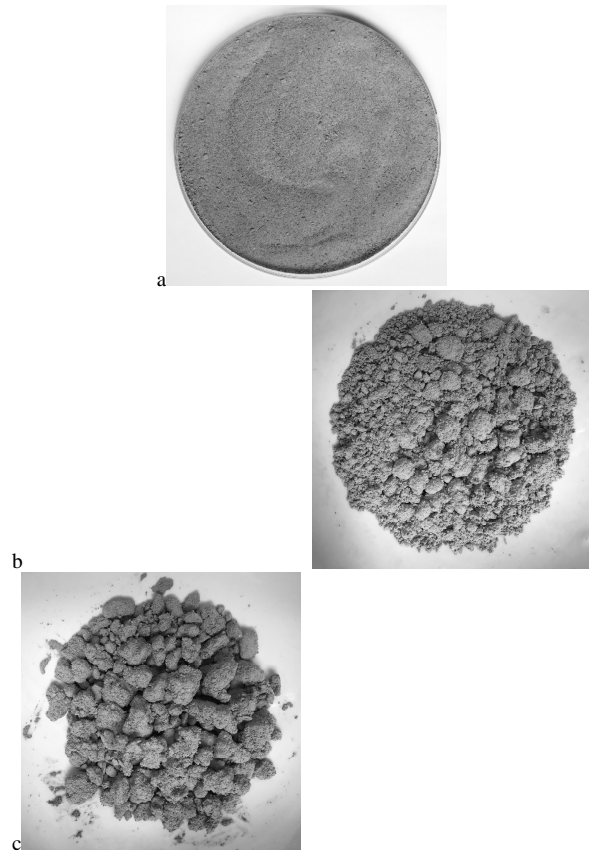


Fig. 9. Sand before (a) and after structuring with precipitated lignocellulosic biomass (b) 0.2%; (c) 0.8%.

Experiments were also conducted using powdered sand/clay model soil, varying the clay content within 0-70% (Fig. 10). Using 0.8% precipitated biomass as a structuring agent, the content and size of the aggregates increase with growing content of clay in the model soil. It verifies the increasing values of the structure-forming coefficients K1 and K2 (Fig. 11).

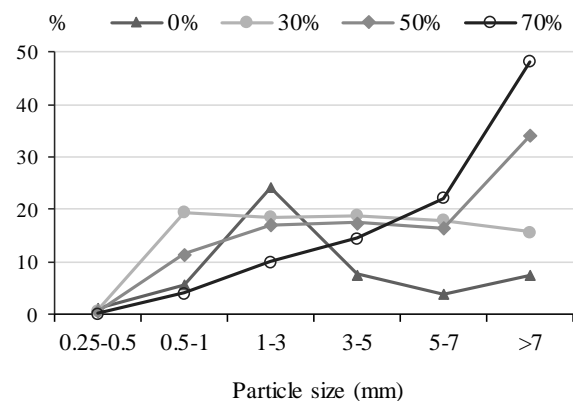


Fig. 10. Fractional composition of model soil depending on the clay content (0.8% biomass).

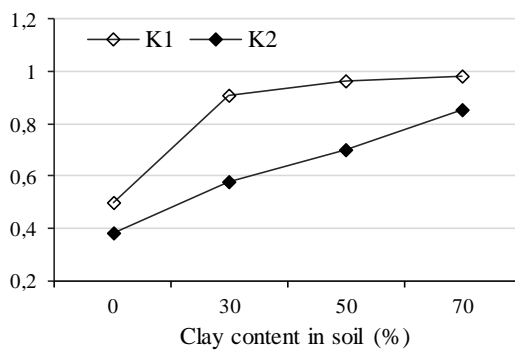


Fig. 11. Structuring coefficients K1 and K2 depending on the clay content in model soil (0.8% biomass).

The maximum amount of the aggregates (98 wt%) is formed with the biomass content of 0.8% in model soil with the clay content of 70%. The dust of the soil particles is exposed to an active transfer by the wind flow. The critical speed at which the movement of soil particles begins depends on the particle size.

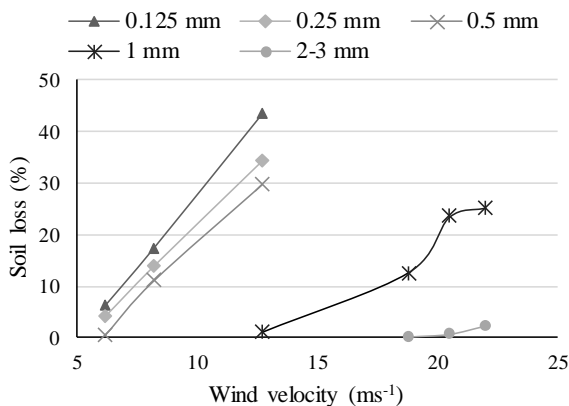


Fig. 12. Soil loss depending on the size of soil particles and wind velocity.

The obtained results show (Fig. 10) that the smaller the particle size, the greater the soil loss of the particles' mass. The movement of soil particles with the diameter below 0.50 mm starts at the wind velocity from 6 ms⁻¹. The critical wind velocity for particles with a diameter of 1 mm is 12 ms⁻¹. Increasing the velocity up to 22 ms⁻¹, the soil loss does not exceed 25%. As can be seen, most resistant against wind erosion are particles with a diameter above 2 mm. The movement of the particles begins only when the wind velocity reaches 18 ms⁻¹ and the loss is around 3%.

IV. CONCLUSION

Using the developed composite coagulant for recovery of birch wood biomass from plywood production model wastewater, at the optimal coagulation parameters, the separation of the total biomass achieves 97%, but the extraction of lignin and lignin-like substances is more than 65%.

The obtained results show that the separated lignocellulosic biomass is able to form large sandy

aggregates, which are able to prevent the dusty soil blowing off from the unpaved road surface.

V. ACKNOWLEDGMENTS

The authors would like to thank the Ministry of Education and Science of the Republic of Latvia for the financial support of the National Research Programme (ResProd).

REFERENCES

- [1] I. Mayer and G. Koch, "Element content and pH value in American black cherry (*Prunus serotina*) with regard to colour changes during heartwood formation and hot water treatment," *Wood Sci. Technol.*, vol. 41, no. 6, 2007, pp. 537-547.
- [2] A. Rohumaa, A. Yamamoto, C. Hunt, C. Frihart, C. Hughes and J. Kers, "Effect of log soaking and the temperature of peeling on the properties of rotary-cut birch (*Betula pendula* Roth) veneer bonded with phenol-formaldehyde adhesive," *Bioresources*, vol. 11 no. 3, 2016, pp. 5829-5838.
- [3] C. Hu, H. Liu, J. Qu, D. Wang and J. Ru, "Coagulation behaviour of aluminium salts in eutrophic water: significance of Al13 species and pH control," *Environ. Sci. Technol.*, vol. 40, 2006, pp. 325-331
- [4] T. Sun, L.-L. Liu, L.-L. Wan and Y.-P. Zhang, "Effect of silicon dose on preparation and coagulation performance of poly-ferric-aluminum-silicate-sulfate from oil shale ash," *Chem. Eng. J.* vol. 163, 2010, pp. 48-54.
- [5] S. Chakrabarti, S. Banerjee, B. Chaudhuri, S. Bhattacharjee and B.K. Dutta, "Application of biodegradable natural polymers for flocculated sedimentation of clay slurry," *Bioresour. Technol.*, vol. 99, 2008, pp. 3313-3317.
- [6] W. Brostow, H. E. H. Lobland, S. Pal and R. P. Singh, "Polymeric flocculants for wastewater and industrial effluent treatment," *J. Mater. Ed.*, vol. 31, 2009, pp. 157-166.
- [7] K. E. Lee, N. Morad, T. T. Teng and B. T. Poh, "Development, characterization and the application of hybrid materials in coagulation/flocculation of wastewater: A review," *Chem. Eng. J.*, vol. 203, 2012, pp. 370-386.
- [8] T. Ahmad, K. Ahmad and M. Alam, "Sustainable management of water treatment sludge through 3'R' concept," *Journal of Cleaner Production*, vol. 124, 2016, pp. 1-13.
- [9] C. Huang, J. R. Pan, K. D. Sun and C. T. Liaw, "Reuse of water treatment plant sludge and dam sediment in brick making," *Water Sci. Technol.*, vol. 44, no. 10, 2001, pp. 273-277.
- [10] O. Kizinievic, R. Zurauskiene, V. Kizinievic and R. Zurauskas, "Utilisation of sludge waste from water treatment for ceramic products," *Constr. Build. Mater.* vol. 41, 2013, pp. 464-473.
- [11] Q. C. Nowasell and J. T. Keavern, "Using drinking water treatment waste as a lowcost internal curing agent for concrete," *ACI Mater. J.*, vol. 112, no. 1, 2015, pp. 69-78.
- [12] J. R. Pan, C. Huang and S. Lin, "Reuse of fresh water sludge in cement making," *Water Sci. Technol.*, vol. 50, no. 9, 2004, pp. 183-188.
- [13] C.-H. Huang and S.-Y. Wang, "Application of water treatment sludge in the manufacturing of lightweight aggregate," *Constr. Build. Mater.*, vol. 43, 2013, pp. 174-183.
- [14] L. Yang, J. Wei, Y. Zhang, J. Wang and D. Wang, "Reuse of acid coagulant recovered drinking waterworks sludge residual to remove phosphorus from wastewater," *Appl. Surf. Sci.*, vol. 305, 2014, pp. 337-346.
- [15] K. C. Makris, D. Sarkar and R. Datta, "Evaluating a drinking water waste byproduct as a novel sorbent for arsenic," *Chemosphere*, vol. 64, 2006, pp. 730-741.
- [16] L. W. Titshall and J. C. Hughes, "Characterization of some South African water treatment residues and implications for land application," *J. Water SA*, vol. 31, no. 3, 2005, pp. 299-307.

- [17] E. A. Dayton and N. T. Basta, "Characterization of drinking water treatment residuals for use as a soil substitute," *Water Environ. Res.*, vol. 73, no. 1, 2001, pp. 52-57.
- [18] G. Shulga, S. Vitolina, J. Brovkina, B. Neiberte, A. Verovkins, M. Puķe and N. Vedernikovs, "Wood biomass from the model wastewater and its fractionation," in *Proceedings of the 9th International Scientific and Practical Conference. Environment. Technology. Resources*, Vol. 1, 2013, pp. 190-194.
- [19] G. Shulga, J. Brovkina, B. Neiberte, J. Ozoliņš and R. Neilands, "A method for wastewater treating from lignin and hemicellulose substances at wood processing plants," LV Patent 14789A, January 20, 2014.
- [20] Z. Liu, Y. Ni, P. Fatehi and A. Saeed, "Isolation and cationization of hemicelluloses from pre-hydrolysis liquor of kraft-based dissolving pulp production process," *Biomass Bioenerg.*, vol. 35, 2011, pp. 1789-1796.

Scientifically Substantiated Guidelines for Physico-mathematical Modelling of Laser Surface-treatment of Wear-resistant Implants for Human Joint Replacements

Uldis Zaimis^{1,2,a}, Sharif E. Guseynov^{1,2,3,b}

¹Institute of Fundamental Science and Innovative Technologies, Liepaja University, Liepaja LV-3401, Latvia;

²Faculty of Science and Engineering, Liepaja University, Kr. Valdemar Street 4, Liepaja LV-3401, Latvia;

³"Entelgine" Research & Advisory Co., Ltd., Kleistu Street 2-53, Riga LV-1067, Latvia; ^auldiss.z@inbox.lv,

^bsh.e.guseinov@inbox.lv

Abstract. This paper presents the main results from a set of guidelines on the physico-mathematical modelling of laser surface-treatment of wear-resistant implants for human joint replacements. These guidelines contain synthesized and documented procedure, theoretical and practical recommendations, which are provided by researchers in the Nanomaterials Laboratory under the Institute of Fundamental Science and Innovative Technologies, Liepaja University. The present paper does not attempt to cover all aspects of physical and mathematical modelling, but draws together many key aspects concerning theoretical and practical difficulties, in the overcoming of what researchers of the Nanomaterials Laboratory, in particular, the authors of the present paper, have sufficient skills.

Keywords: wear-resistant implant, human joint replacement, laser surface-treatment, physico-mathematical modelling, scientifically substantiated guidelines.

I. INTRODUCTION

Modern medicine widely uses artificial materials to replace damaged tissues, bones and organs. Depending on their purpose, the implants involved into the body should be gradually replaced with a living tissue and / or to function for a long time period.

The tissue composition of the human bone has a complex structure. The mechanical strength of bone tissue is based on spatial arrangement of the structural components of bones – bone plates. The composition of the bone includes an organic component – collagen ($\approx 25\%$), inorganic component – calcium phosphates ($\approx 65\%$), water ($\approx 10\%$) ([1]). Artificial materials claiming the role of implants must meet the requirements dictated by the composition and properties of human bone tissue. The main requirements for artificial materials for implantation are resistance to corrosive media and biomechanical compatibility. In addition, the implant material must also possess some mechanical properties, of which the most prestigious are hardness, tensile strength and modulus of elasticity. Since the response of any material to repeated cyclic loads depends on the fatigue strength of the material, it is this property that determines the continuous usage time of the implant ([2]). Because of the fact that the human body is an

aggressive environment for implants, especially those made of metals, when developing new implants, it is necessary to take into account not only their functional characteristics, but also their interaction with the biological environment in where they will be used in. Low wear resistance and low corrosion resistance of metal implants in the corrosive liquid medium of the human body promote the release of metal ions into the body. It has been found ([3]) that Ni^{2+} , Co^{3+} , Al^{3+} , Cr^{3+} ions cause allergic and toxic reactions in the body, and therefore materials used as implants should not have toxicity or should have reliable protective coatings on surfaces that prevent Release of metal ions in the tissues of the human body. For small-size implants, pitting corrosion also poses a risk: for example, the functional integrity of the vascular walls can be destroyed by the presence of only one minor deepen.

On the surface and boundaries of the implant and soft tissues of the body undergo chemical and biological processes, carried out, in particular, on the cell-matrix and nanoscale level. The search for new biocompatible materials with nanostructured characteristics has been implementing according to the biomimetic approach, according to which artificial nanomaterials mimic the properties of biomaterials from living nature. Qualitative progress

in this area is possible only based on interdisciplinary research in medicine, chemistry, biology, materials science, physics and mathematics. Since the 60s of the XX century, specialists in the areas listed above work closely together to understand the complex processes of interaction of body cells with the foreign surface of the implanted material. Biologically active properties of the interface between the tissues of the body and the implanted material reviewed in correlation with its specific properties. The chemical composition of the surface, its physical and chemical characteristics, roughness and morphology, the determination of the activity of various cellular structures acting separately and synergistically. The relationship between the physical and chemical properties of the surface and the cellular response is far from to be clear (for instance, see [1]-[7] and respective references given in these). A firm understanding of the mechanism of this connection will lead to the creation of a new generation of materials that can be more effectively and successfully involved into the human body for therapeutic purposes. The classical concept of bioinert or bioactive materials with the development of materials science and chemical science will shift to the field of creating more advanced biomaterials that could react or facilitate the implementation of various reactions with the biological environment depending on the state of the surface of the implanting material.

Without overlooking of the comparative analysis of the properties, advantages and disadvantages of artificial materials (for instance, see [1], [8], [9]), used in modern implantation surgery, in particular, in endoprosthetics, we list only the types of most frequently used materials, which can be toxic (surrounding tissues die off on contact), bioinert (non-toxic, but biological inactive) and bioactive (non-toxic, fused with bone tissue): composite biomaterials, bioglass and bioceramics; alloys of titanium, zirconium and magnesium. We will investigate only some aspects of laser surface treatment of titanium implants in this paper.

II. BRIEF OVERVIEW OF THE BASIC PROPERTIES OF TITANIUM IMPLANTS

For the first time, the concept of the use of industrially pure titanium and its alloys as implants was put forwarded by Swedish therapist P.-I. Branemark and his scientific group (for instance, see [10], [11] and [12]): from the experimental work carried out in 1952-1969 it is showed the phenomenon of ingrowth of a titanium structure into living bone tissue (now this phenomenon is called osseointegration), and between the implant surface. The fibrous tissue does not form a fibrous or cartilaginous tissue. Since 1965, titanium implants have been used as bio- and mechanically compatible material for the manufacture of implants. Nowadays, numerous fundamental and clinical studies in vitro

and in vivo have shown that industrially pure titanium, titanium-aluminum alloy, titanium-vanadium alloy, and nickel-titanium alloy having shape memory effect have such exceptional qualities as high mechanical strength, low cycle fatigue, plastic, high biocompatibility and biotolerance, antiallergenicity and lack of toxicity, high corrosion resistance due to the formation on the surface of a passivating oxide layer, low thermal conductivity, small coefficient of linear expansion, relatively low specific gravity, the smallest difference between the moduli of elasticity and bone. All listed properties of titanium and its alloys are based on their microstructures. As shown in [13], in order to reduce the modulus of elasticity of industrially pure titanium, the most effective alloying elements for the additive are niobium (Nb), zirconium (Zr), molybdenum (Mo), tantalum (Ta). Nowadays, in the production of implants, industrially pure titanium grades BT1-0 and BT1-00 are used (for instance, see [8], [14]) from so called "commercially pure" titanium grades Ti-6Al-4V, Ti-6Al-7Nb; BT6, Grade-1 ÷ Grade-4, Grade-2H, Grade-6, Grade-7, Grade-7H, Grade-9, Grade-11 ÷ Grade-16, Grade-16H, Grade-17 ÷ Grade-26, Grade-26H, Grade-27 ÷ Grade-38.

It should be noted in conclusion that despite the very high mechanical properties of titanium alloys containing aluminum (Al) and vanadium (V), one should clearly know and distinguish the field of their application, because these elements can accumulate in the human body tissues and, due to the corrosive effect of biological fluids, cause acute allergies and have toxic effects. It is important to note that titanium implants, in spite of the above unique properties and advantages, still: (a) undergo abrasive wear, which often leads to loss of the implant; (B) can cause intolerable pain and pathogenicity due to the fact that wear products are deposited on the human body tissues. Therefore, the unresolved and actual problem is the improvement of existing and development of new methods and technologies for the production of titanium implants and the treatment of their surfaces in order to enhance osseointegration contact, as well as proper biomechanical, chemical-biological (cell-matrix and nanoscale Level) of contacts between the implant and living human bone tissue.

III. LASER TREATMENT OF THE SURFACE OF TITANIUM IMPLANTS

A. *Relevance and status of the issue*

The state of the surface of titanium implants plays a decisive role in cell-cell adhesion. The interaction between the biological environment (hard and soft tissues, blood, body fluids and serum, etc.) and the implant occurs on its surface, and the biological response from the living tissue depends on a variety of surface properties, such as chemical composition, purity, texture and topography, surface energy, corrosion resistance, and the tendency to

denaturalization of surrounding proteins. Nowadays, developed various methods of surface treatment of titanium implants to improve their biocompatible properties and to accelerate the healing process of implants. These methods are based on morphological or biochemical modification of physical, chemical and mechanical properties, in particular, changes in surface energy and surface charge, chemical composition and surface printing of titanium implants. Approximately 20 years ago a new perspective direction arose related to the use of laser technology for surface treatment of biocompatible metallic materials, in particular titanium implants, in order to improve the tribological, biocompatible and corrosive properties of their surfaces. Theoretically, laser processing technology can possibly solve all the above tasks of modifying the complex of surface properties of titanium implants. Application of laser processing technology provides high spatial resolution and high processing speed, and does not affect the bulk properties of the processed material. Recent works (for instance, see [15]-[17] and appropriate references given in these) show that laser treatment of implant surfaces from titanium leads to the formation of a developed surface morphology characterized by a cellular structure, an increase in roughness and the formation of an inert oxide layer, which is necessary for improving the biocompatibility of titanium implants, in particular, enhancing the adhesion of living cells of different scales. In subsection conclusion, in the context of discussing the laser treatment advantages of implant surfaces, let us dwell only on the results of the work [16]: a group of Italian scientists carried out a rather curious experiment with the aim of: (a) studying histomorphometric and biomechanical characteristics (BIC-bone-implant contact; RTV – reverse torque value) of titanium implants, which underwent laser treatment; (B) comparing the ability of laser irradiation to stimulate osseointegration with a similar ability of titanium implants that have been mechanically processed. The results of the experiment showed that RTV for titanium implants treated with a laser was almost 3 times higher than for those that received mechanical treatment; BIC titanium implants treated with a laser proved to be at least 30% better than BIC titanium implants, machined.

B. Mathematical model in terms of spherical trigonometry for describing the transfer of laser radiation during surface treatment of the titanium head of the endoprosthesis

Medical practice, especially in countries formerly part of the USSR, shows that repeated prosthetics of the hip joint of a person is associated with big problems (including due to the relatively high cost of surgery, inaccessible to many needy patients). In many cases, the implementation of such surgical operations becomes virtually impossible and,

therefore, the life of the hip endoprosthesis is extremely important for the patient, especially at a young age. Modern joint endoprosthesis consists of an acetabular cup, a polyethylene liner; an endoprosthesis stem and a ball-shaped head (see Fig. 1). Titanium heads of the human hip joint endoprosthesis, in terms of the nature and magnitude of their load, are in extreme conditions ([6], [18]), and therefore, the problem of improving the accuracy and quality of processing the most significant part of the endoprosthesis – the spherical surface of the head – is one of the most actual problems in modern endoprosthetics. Completely modern equipment for laser processing of materials, which has a Laboratory of Nanomaterials at the Institute of Basic Sciences and Innovative Technologies of the University of Liepaja (Nanomaterials Laboratory under the Institute of Fundamental Science and Innovative Technologies, Liepaja University), has a fixed head-source of laser radiation.

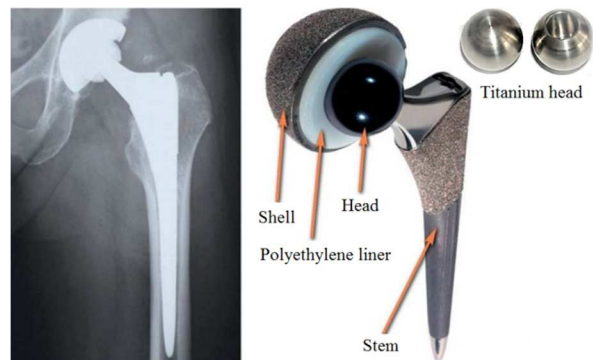


Fig. 1. Main components of a hip joint endoprosthesis.

Therefore, in order to carry out a high-precision uniform laser treatment, the endoprosthesis head, (which has a surface with a 270° angle of the spherical segment) (see Fig. 2, [6]), it is necessary to rotate the endoprosthesis head properly: the endoprosthesis head is fixed with a special holder in the vacuum chamber laser equipment, and this device can rotate the head of the endoprosthesis along two perpendicular axes with constant cycles per unit time (for each rotation axis its constant cycle).

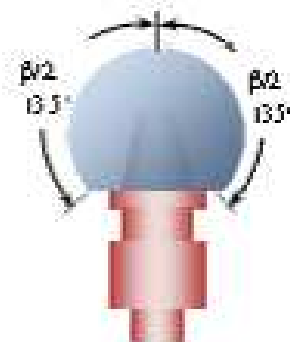


Fig. 2. The head of the endoprosthesis, which has a surface of 270° -angle of the spherical segment.

If the 3D laser-imaged material were a polyhedron, then the necessary calculation formulas for high precision and high-quality laser processing of this polyhedron can be derived from the corresponding mathematical model constructed in the Cartesian coordinate system. Obviously, because of the fact that: (a) the source of laser radiation on the existing laser equipment is stationary; (B) the endoprosthesis head has a spherical surface with a 270 ° angle of the spherical segment being treated; (C) a two-coordinate holder can rotate the endoprosthesis head only in cycles, it is necessary to conduct studies using spherical trigonometry (for instance, see [19], [20]): as the initial construction of the required adequate mathematical model in a Cartesian coordinate system with subsequent derivation from it Of the necessary calculation formulas and the "mechanical" translation of the equations and conditions of the already constructed mathematical model, as well as the resulting computational formulas from the Cartesian coordinate system to the spherical coordinate system, will not provide a correct description of the process of precise, uniform and qualitative treatment of the spherical surface of the head of the hip joint endoprosthesis. In such a case, the work of the exposed (ie, emitting laser radiation) is performed using the Euclidean metric as a measure of closeness between two points (defined in the 3D Cartesian coordinate system) and the work of the affected object. Reception of laser radiation on the spherical surface of the rotating head of the endoprosthesis. The affected object is carried out using a spherical metric as a measure of proximity between two points a priori defined in the 3D spherical coordinate system.

Consider the problem of transferring laser radiation in a parallel vertically inhomogeneous layer of a 3D spherical region (Fig.2), and, for simplicity, assuming the radius equal to 1. We make the following assumptions:

- on the top border $z = 0$ of analyzed layer with width of H and angle $\alpha_0 = \arccos(\mu_0)$ falls laser power F laser irradiation in azimuthal plane $\beta_0, s_0 = \{\alpha_0, \beta_0\}$;
- inside the layer under consideration and at its boundaries there may be diffusion sources of radiation;
- the underlying surface at the lower boundary of the layer under consideration reflects the entire irradiation within a given law
- transfer of irradiation occurs without changing the frequency.

The problem consists in determining the intensity of the multiply incident laser radiation inside the layer $0 \leq z \leq H$, and also in determining the law of the reflected and missed laser radiation.

As was mentioned above, the direction of propagation of multiple laser radiation at an arbitrary point of the layer $0 \leq z \leq H$ It is necessary to describe with spherical coordinates: azimuth

$$\varphi \stackrel{\text{def}}{=} \frac{2}{5} \cdot (4 \cdot \beta - \pi) \in [0, 2 \cdot \pi], \quad \text{where}$$

$$\beta \in \left[\frac{\pi}{4}, \frac{3 \cdot \pi}{2} \right] \quad \text{characterizes the corresponding}$$

azimuth angle for the spherical segment of Fig. 2, and the zenith angle $\alpha \in [0, \pi]$, measured from the direction of the inner normal to the plane $z = 0$ with unit vector \vec{n}_0 , on OZ . In this case, as $\varphi = 0$ accept the azimuth of the external laser beam $\beta_0 = 0$. Then direction $0^\circ \leq \alpha = \alpha^+ < 90^\circ$ will be according the descending / missed radiation, and the direction $90^\circ < \alpha = \alpha^- \leq 180^\circ$ will correspond to the ascending / reflected radiation. We denote by:

$$\mu \stackrel{\text{def}}{=} \cos(\alpha), \quad \mu^+ \stackrel{\text{def}}{=} \cos(\alpha^+) \in (0, 1],$$

$$\mu^- \stackrel{\text{def}}{=} \cos(\alpha^-) \in [-1, 0]. \quad \text{Then the sets } D^+ \text{ and } D^-, \text{ are defined as}$$

$$D^+ \stackrel{\text{def}}{=} \{(\mu, \varphi) : \mu \in [0, 1], \varphi \in [0, 2 \cdot \pi]\};$$

$$D^- \stackrel{\text{def}}{=} \{(\mu, \varphi) : \mu \in [-1, 0], \varphi \in [0, 2 \cdot \pi]\},$$

will characterize the hemispheres of the directions of the descending / missed and ascending / reflected radiations. In this case, obviously, the set

$D \stackrel{\text{def}}{=} D^+ \cup D^-$ is a single sphere of directions for the transfer of laser radiation. If we denote the required intensity of the multiply-incident laser radiation inside the layer $0 \leq z \leq H$ in direction $s = \{\alpha, \varphi\}$

through $I_{RI}(z, \mu, \varphi)$, so it can be written:

$$\mu \cdot \frac{\partial I_{RI}(z, \mu, \varphi)}{\partial z} + (f_t(z) + f_a(z)) \cdot I_{RI}(z, \mu, \varphi) = f_r(z) \cdot \int_D I_{RI}(z, \tilde{\mu}, \tilde{\varphi}) \cdot \rho(z, \omega) d\tilde{\mu} d\tilde{\varphi} + F(z, \mu, \varphi), \quad (1)$$

$$I_{RI}(z, \mu, \varphi) \Big|_{z=0} = g_0(\mu, \varphi) + F(0, \mu, \varphi) \cdot \delta(s - s_0), \quad (2)$$

$$I_{RI}(z, \mu, \varphi) \Big|_{z=H} = g_H(\mu, \varphi) +$$

$$\frac{a \cdot \mu^2}{2 \cdot \pi} \cdot \int_{D^+} \tilde{\mu} \cdot I_{RI}(H, \tilde{\mu}, \tilde{\varphi}) d\tilde{\mu} d\tilde{\varphi}, \quad (3)$$

where

- function $f_t(z)$ and $f_a(z)$, through which the transmission and absorption coefficients of the laser radiation are designated, respectively, mean the physical characteristics of the surface of the endoprosthesis head;

- $\omega \stackrel{def}{=} \cos(\gamma)$, $\int_D \rho(s, \tilde{s}) d\tilde{s} = 1$, $\int_D \rho(\omega) d\tilde{s} = 1$,
 $\int_{-1}^{+1} \rho(\omega) d\omega = \frac{1}{2 \cdot \pi}$, where the transfer angle γ from direction $\tilde{s} = \{\tilde{\mu}, \tilde{\varphi}\}$ in direction $s = \{\mu, \varphi\}$ is defined by the equation
 $\gamma = \arccos(\mu \cdot \tilde{\mu} + \sin(\alpha) \cdot \sin(\tilde{\alpha}) \cdot \cos(\varphi - \tilde{\varphi})$);
- in geometries $\{z, \alpha, \varphi\}$ and $\{z, \alpha\}$ boundary conditions (2) are determined on the following sets, respectively:
 $\partial D_0 = \{(z, \mu, \varphi) : z = 0, s \in D^+\}$,
 $\partial D_0 = \{(z, \mu) : z = 0, \mu \in (0, 1]\}$;
- in geometries $\{z, \alpha, \varphi\}$ and $\{z, \alpha\}$ boundary conditions (3) are determined on the following sets, respectively:
 $\partial D_H = \{(z, \mu, \varphi) : z = H, s \in D^-\}$,
 $\partial D_H = \{(z, \mu) : z = H, \mu \in (-1, 0]\}$.

As in the boundary conditions (3) the required function-intensity itself is present, then the proposed mathematical model (1)-(3) is a specific type of inverse boundary value problem for determining the function $I_{RI}(z, \mu, \varphi)$ in spherical geometry field $\{z, \mu, \varphi\} = [0, H] \times [-1, +1] \times [0, 2 \cdot \pi]$, in which all parameters defined in (1)-(3), but function $I_{RI}(z, \mu, \varphi)$, are assumed to be given, including the laws of the reflected and missed by the layer of laser radiation. We recall that in the complete formulation of the problem formulated above (see, after the enumerated assumptions in this subsection), it was also required to determine the laws of the reflected and missed laser radiation. Unfortunately, the imposed restriction on the size of this article does not allow us to formulate two more mathematical models for determining, respectively, the law of reflected radiation and the law of laser radiation missed by the layer under consideration: both models have a more complex structure than model (1)-(3). In addition, it should be noted that the authors of this paper developed a numerical algorithm based on a combination of the Tikhonov regularization method ([21]) and the method of characteristics ([22]-[24]), which makes it possible to realize the mathematical model (1)-(3).

IV. BRIEF SUMMARY OF OUTCOMES OF EXPERIMENTS

The following results of four experiments on laser surface treatment of biocompatible titanium implants are briefly summarized taking into account the model (1)-(3), which has been implemented using the application package MathCAD 14 (version

Environment. Technology. Resources, Rezekne, Latvia 14.0.0.163) on the basis of a combination of the Tikhonov' regularization method and the method of characteristics. Alongside with a brief results overview for each experiment, there are given the following specifications: the medium type (MEDIUM) with indication of pressure (p), in which the laser treatment was performed; the type of laser used (TYPE); the wavelength of laser emission (λ); the frequency of laser emission (f); the duration of laser pulse (t); the energy density of laser beam (q).

Experiment 1. MEDIUM=high vacuum ($p = 2 \cdot 10^{-4}$ Pa); TYPE=Nd:YAG laser (ns); $\lambda = 1.064 \mu\text{m}$; $f = 30 \text{ kHz}$; $t = 300 \text{ ns}$; $q = 25 \text{ J/cm}^2$ (energy in laser pulse: $E = 2 \text{ mJ}$). Brief results overview: no melting occurs on the titanium surface (Ti-surface) for the given single laser pulse; melting traces are observed only where the number of laser pulses is equal to or more than 240, and from this moment the process of capillary waves emergence begins due to variations in surface thermal stresses. As a result of this process, a characteristic surface relief is formed in the form of ledges, hollows, flutes, etc. An increase in the magnitude of the relief leads to a decrease in the reflective ability of the metal surface, which leads to absorbed laser energy increase. At more than 600 pulses, the microstructure forming of the Ti-surface slows down and islands with a smooth surface containing micro-cracks and pores are formed due to thermal stresses. At more than 1500 pulses, the Ti-surface morphology completely changes: the central zone becomes completely smooth and flat with a polyhedral microstructure sized to several μm and oriented towards the boundary of the laser crater. Any further increase of the laser pulse number leads to a gradual growth of structural non-uniform areas up to several tens of μm , and the modified layer depth becomes equal to 1.5 μm for the 1500 number of pulses, and 4.5 μm for the 21000 number of pulses. The height of ledges depending on the number of pulses increases from 0.5 μm (600 pulses) to 3 μm (21000 pulses). At absorbed energy depth around 1 μm a molten zone is formed and after its crystallization its surface becomes smoother than the original Ti-surface. Deeper melted layers crystallization leads to profiled dendritic relief patterning. This happens due to surface stresses anisotropy caused by temperature gradient. Increase in height of the broken surface zone could be explained by the melt motion, pores formation and phase shifts. The conducted experiment at the above-described characteristics of both medium and laser has resulted in revealing that the role of the oxide layer in the formation of surface morphology is negligible.

Experiment 2. MEDIUM=high vacuum ($p = 2 \cdot 10^{-4}$ Pa); TYPE=Nd: YAG laser (ps); $\lambda = 1064$ nm; $f = 2$ Hz; $t = 40$ ps; $q = \{23.8; 40\}$ J/cm². Brief results overview: both for a single pulse and for 5 laser pulses a crater with a smoothed center relief is formed on the Ti-surface. At pulse number equal to 30, the nano-sized elements of morphology become noticeable and recrystallized titanium droplets are formed at the crater periphery due to the hydrodynamic effect. During the experiment, it has been found out that for the emergence of destruction effect of Ti-surface (i.e. for the crater formation) a minimum energy density of 0.9 J/cm² is required, and the crater depth strongly depends on the laser pulse number: for a single pulse the depth of the crater is equal to 50 μ m, and for the pulse number of 5 is equal to 240 μ m (ablation rate in both cases is around 48 μ m/pulse). At more than 30 pulses and laser energy density of $q = 40$ J/cm², micro-cracks and nanograins are formed (which morphological character is caused by rapid heating and cooling processes), and the hydrodynamic effects at the edge of the crater are weaker. At a laser energy density of $q = 23.8$ J/cm², the absorbed energy exceeds titanium melting temperature threshold and melts appear in the crater center, which is pushed out on the crater periphery.

Experiment 3. MEDIUM=low vacuum ($p = 13.3$ Pa); TYPE=Ti: Al₂O₃ laser (fs); $\lambda = 800$ nm; $f = 1$ kHz; $t = 100$ fs; $q = 0.25 \div 1.5$ J/cm². Brief results overview: the purpose of this experiment was to study the possibility of creating periodic structures on the polished Ti-surface (it is necessary to supplement the model (1)-(3) with the mathematical models described in the articles [25], [26]). During the experiment, it was found that at a constant laser energy density of $q = 0.75$ J/cm², the formed periodic structures morphology depends substantially on the number of laser pulses. In addition, it has been found out that, using the described environment and laser characteristics the minimum laser pulse number, which is required to form a periodic microstructure on the Ti-surface is equal to 10 (in the range $q \in [0.25, 1.5]$ J/cm²). It has been found that in all cases the resulting structures are parallel to the electric polarization vector of the laser. At more than 50 laser pulses, micro-droplets are formed on the vertices of parallel periodic structures. Change in the number of pulses within the range of 10-25 leads to periodic nanostructures formation, which are combined with microstructures.

Experiment 4. MEDIUM=indoor atmosphere ($p = 0.1$ MPa); TYPE=ArF-eximer laser (ns);

$\lambda = 193$ nm; $f = 10$ Hz; $t = 18$ ns; $q = 1.5 \div 5$ J/cm² (energy in pulse: $E = 100$ mJ). Brief results overview: the purpose of this experiment was to study the possibility of polishing the Ti-surface at room indoor environment conditions. To form a texture on the Ti-surface, the laser energy density was increased to $q = 8.5$ J/cm², and the number of laser pulses varied from 250 to 1000. It has been found out that effective Ti-surface polishing occurs only during $q \in [3, 5]$ J/cm²: the treatment completely eliminates traces of machining on the Ti-surface and substantially smoothens the surface, the roughness amplitude decreases from 256 μ m to 25 μ m, and the root cause for this smoothing is either caused by surface layer melting and crystallization processes or by local heating and evaporation of the ledges under laser impacts. X-ray photoelectron spectroscopy revealed that the thickness of the oxide layer has been doubled.

V. CONCLUSION

This paper contains discusses about a relatively new direction related to the use of laser technology for surface treatment of biocompatible titanium implants in order to optimize its topography and physico-chemical properties. The brief overview of some of the results given in this paper demonstrate that laser treatment seems promising both in terms of providing a higher quality of the micromorphology of the surface of the material and in terms of increasing their corrosion resistance. It should be noted that the work aimed at improving the physical and chemical properties of the surface of titanium implants by laser treatment is still at the initial stage of its development within the framework of application in orthopedics. For a deeper understanding of the nature of the change in surface properties under the influence of laser treatment, further investigations are needed with the use of modern surface-sensitive analytical methods that provide quantitative information at the atomic-molecular level.

In addition, in this paper it is proposed a mathematical model in terms of spherical trigonometry for describing the transfer of laser radiation in the surface treatment of the titanium head of the human hip joint endoprosthesis.

VI. ACKNOWLEDGMENTS

For the second co-author the present article was executed within the framework of The State Research Programme "Next generation Information and Communication Technologies" ("NextIT"), Project No. 4.

REFERENCES

- [1] A. V. Puz, "Multifunctional Coatings for alloys of medical purpose", Doctoral Thesis, Institute of Chemistry, Far Eastern Department of the Russian Academy of Sciences, 2014, 164 p.

- [2] L. L.Hench, "Bioceramics", Journal of the American Ceramic Society, vol. 81, pp. 1705-1728, 1998.
- [3] P. Cardaioli, M. Giordan, and G. Rigatelli, "Nickel allergy in interatrial shunt device-based closure patients", Journal of Congenital Heart Disease, vol. 2, No. 6, pp. 416-420, 2007.
- [4] A. L. Gintsburg, A. S. Karyagina, and A. S. Semikhin, "Development of new generation of specimens for efficient repair of bone tissue", Journal of Therapy and Prophylaxis, No. 1, pp. 80-84, 2011.
- [5] S. Takemoto S., Y. Kusudo, K. Tsuru, and S. Hayakawa, "Selective protein adsorption and blood compatibility of hydroxy-carbonate apatites", Journal of Biomedical Materials Research, vol. 69A, No. 3, pp. 544-551, 2004.
- [6] R. S. Turmanidze, T. S. Aptsiauri, and G. Z. Popkhadze, "New Materials for Implants of the Human Hip Joint and Technology of Their Machining With the Achievement of High Precision and Quality of Spherical Surfaces", Journal of Mechanical Engineering, vol. 75, No. 3, pp. 64-71, 2015.
- [7] O. A. Rozenberg, S. V.Sokhan, V. V.Vozny, A. G.Mamalis, J. Gavlik, and D.-J. Kim, "Trends and Development in the Manufacturing of Hip Joints: An Overview", International Journal of Advanced Manufacturing Technology, vol. 27, pp. 537-542, 2006.
- [8] M. A. Vasilev, M. M. Nischenko, and P. A. Gurin, "Laser modification of surface of titanium implants", Progresses of Physical Metallurgy, vol. 11, pp. 209-247, 2010.
- [9] M. M. Nischenko, N. A. Shevchenko, D. V. Schur, V. A. Bogolepov, A. G. Dubovoi, and I. M. Sidorchenko, "Laser-stimulated emission of electrons from carbon nanostructures formed at laser evaporation of oriented carbon nanotubes", Journal of Inorganic Materials: Applied Research, vol. 1, No. 4, pp. 276-278, 2010.
- [10] P.-I. Branemark, B. O. Hansson, R. Adell, U. Breine, J. Lindstrom, O. Hallen, and A. Ohman, "Osseointegrated implants in the treatment of the edentulous jaw. Experience from a 10-year period", Scandinavian Journal of Plastic and Reconstructive Surgery and Hand Surgery, vol. 16, pp. 1-132, 1977.
- [11] R. Adell, U. Lekholm, B. Rockler, and P.-I. Branemark, "A 15-year study of osseointegrated implants in the treatment of the edentulous jaw", International Journal of Oral Surgery, vol 10, No. 6, pp. 387-416, 1981.
- [12] "General statistics about papers of P.-I. Brånemark". [Online]. Available: <http://scicurve.com/author/Br%C3%A5nemark%20P%20I> [Accessed: March 08, 2017].
- [13] G. Wang and H. Zraigat, "Functional Coatings or Films for Hard-Tissue Applications", Journal of Materials, vol. 3, No. 7, pp. 3994-4050, 2010.
- [14] "Titanium alloy". [Online]. Available: https://en.wikipedia.org/wiki/Titanium_alloy [Accessed: March 08, 2017].
- [15] T. Traini, M. Berardini, F. Congedi, B. Sinjari, P. Trisi, and S. Caputi, "Impact of Second Stage Surgery on Bone Remodeling Around New Hybrid Titanium Implants: A Prospective Clinical Study in Humans", Journal of Implant Dentistry, vol. 26, No. 1, pp. 121-128, 2017.
- [16] P. Trisi, M. Berardini, M. Colagiovanni, D. Berardi, and G. L. Perfetti, "Laser-Treated Titanium Implants: An In Vivo Histomorphometric and Biomechanical Analysis", Journal of Implant Dentistry, vol. 25, No. 5, pp. 575-580, 2016.
- [17] M. A. Vasilev, S. P. Chenakin, M. M. Nishchenko, L. F. Yatsenko, "Effect of pulsed laser radiation to the composition of the surface layers of the titanium alloy VT6", Journal of Metal Physics and Advanced Technologies, vol 37, No. 7, pp. 861-870, 2015.
- [18] N. V. Novikov, O. A. Rozenberg, J. Gavlik, S. V. Sohan, V. V. Vozniy, R. S. Turmanidze, D. S. Buchrikidze, and M. D. Beridze, *Implants of Human Joints: Materials and Technologies*. Kiev, Ukraine: Bakul Institute for Superhard Materials, The National Academy of Sciences of Ukraine, 2011, 528 p.
- [19] C. I. Palmer and C.W.Leigh, *Plane and Spherical Trigonometry*. New York & London: McGraw-Hill Book Company, 1934, xiv+229 p.
- [20] M. K. Ventsel, *Spherical Trigonometry*. Moscow, USSR: GeodezIzd, 1934, 154 p.
- [21] A. N. Tikhonov and V. Ya. Arsenin, *Solution of Ill-posed Problems*. Washington, USA: Winston & Sons, 1977, xiii+258 p.
- [22] S. A. Sarra, "The Method of Characteristics with applications to Conservation Laws", Journal of Online Mathematics and its Applications, vol. 3, pp. 1-16, 2003.
- [23] M. Delgado, "The Lagrange-Charpit Method", SIAM Review, vol. 39, No. 2, pp. 298-304, 1997.
- [24] I. M. Gelfand, "Some problems of Theory of Quasi-Linear Equations, Advances of Mathematical Sciences (Russian Mathematical Surveys), vol. 14, No. 2, pp. 97-158, 1959.
- [25] Sh. E. Guseynov and U. Zaimis, "On a physico-mathematical model for controlled formation of periodic nanostructures at solid surfaces irradiated by femtosecond laser pulses", Journal of Nonequilibrium Phase Transformations, No. 3/2016, pp. 17-20, 2016.
- [26] Sh. E. Guseynov and U. Zaimis, "On a physico-mathematical model for controlled formation of periodic nanostructures at solid surfaces irradiated by femtosecond laser pulses", Journal of Machines, Technologies, Materials, No. 7/2016, pp. 23-26, 2016.

Optimization Of Mechanical Strength Of Rotary-Vane Engine

Yury Zhuravlev, Andrey Perminov, Yury Lukyanov, Sergey Tikhonov,
 Alexander Ilyin, Sergey Semyonov,

Pskov State University, Electromechanical Faculty,
 Department of Electric Drive and Automation Systems.
 Address: Lenina 8, Pskov, 180000, Russia

Abstract. The article discusses a rotary-vane heat engine with a lever-cam mechanism motion conversion (an engine may be an internal combustion or external combustion). The output shaft of the engine adds drive torque from the working fluid pressure forces acting on the blade and the inertial moment of the forces of inertia of engine components. The mechanical strength of the motor is dependent on the magnitude and phase of these two torque. The purpose of the article is to determine the conditions under which mechanical strength is minimized.

Keywords: rotary-vane engine, lever-cam motion converter, external supply of heat.

I. INTRODUCTION

It is known that internal combustion engines have almost reached the limit of their energy and environmental characteristics. Therefore, it is necessary to develop engines of a new generation, constructed using other design schemes and implementing new thermodynamic cycles. To solve this problem rotor-vane machines with external heat supply can be used.

The Fig. 1 shows the engine component diagram.

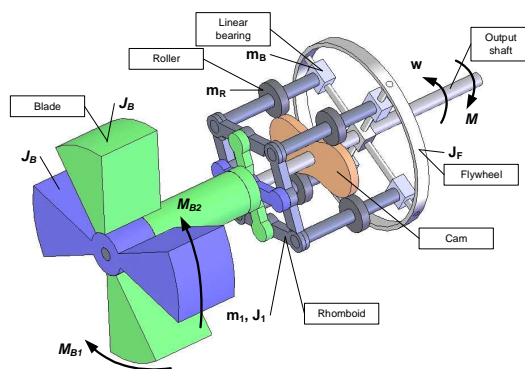


Fig. 1. Engine component diagram.

The engine consists of a driving part, motion converter, output shaft to the flywheel. The driving part consists of two coaxial rotors. Each rotor has the blade of the two diametrically opposite vanes (pistons). Also, the rotors have forks with two diametrically arranged fingers. The fingers are pivotally connected to the midpoints of the sides of the rhomboid links. The pressure of the working fluid between two adjacent vanes create moments on the

blades $M_{B1} = -M_{B2}$, which depend on the output shaft angle.

The tops rhomboid are rollers. The rollers contact with a stationary profiled cam surface. Rhomboid is a motion transformer. It converts cyclic motion of the blade (within the angles ψ_{min}, ψ_{max} between them) into a unidirectional rotation of the output shaft. Thus transmitted torque from the blades. Torque transmission from rhomboid to the output shaft occurs via linear bearings.

To the output shaft of the engine is attached a load torque M .

The motion transformer uses a cam profile which in polar coordinates ρ, α is given by [1]:

$$\rho(\alpha) = 2l \sin(a + b \sin 2\alpha), \quad (1)$$

where $2l$ – rhomboid link length, $a = \pi/4$; $b = \pi/4 - \psi_{min}/2$, where ψ_{min} – angle between the axes of the blades (usually $\psi_{min} = 50^\circ - 55^\circ$).

The vane angles change in a law:

$$\begin{aligned} \varphi_1(\alpha) &= \frac{3\pi}{4} + \alpha + b \cos 2\alpha, \\ \varphi_2(\alpha) &= \frac{\pi}{4} + \alpha - b \cos 2\alpha. \end{aligned} \quad (2)$$

The dynamic system has one degree of freedom, because position of all elements is determined by one coordinate – output shaft angle α .

The motion equation of the system can be written in the form of Lagrange second kind equation:

$$\frac{d}{dt} \frac{\partial T}{\partial \dot{\alpha}} - \frac{\partial T}{\partial \alpha} = M_{DT} - M, \quad (3)$$

where T – the kinetic energy of the system; M_{DT} – the drive torque at the output shaft; M – the load torque.

Equation (3) can also be written as an kinetostatic equilibrium equation:

$$L_z + M_{DT} - M = 0, \quad (4)$$

where L_z – motor torque inertia forces applied to the output shaft:

$$L_z = - \left(\frac{d}{dt} \frac{\partial T}{\partial \dot{\alpha}} - \frac{\partial T}{\partial \alpha} \right). \quad (5)$$

II. TORQUE OF INERTIA FORCES

The kinetic energy of the system includes the kinetic energy of the two blades T_B , four links of the rhomboid T_L , four rollers rhomboid T_R , four linear bearings with fingers T_{LB} , output shaft with a flywheel T_F :

$$T = T_B + T_L + T_R + T_{LB} + T_F. \quad (6)$$

Rotors carrying blades, make a rotary motion around a fixed axis with angular velocity $\dot{\phi}_1, \dot{\phi}_2$. Kinetic energy of rotors carrying blades $T_B = J_B (\dot{\phi}_1^2 + \dot{\phi}_2^2) / 2$, where $J_B = J_{B1} = J_{B2}$ – moments of inertia of the blades B1 and B2; $\dot{\phi}_1 = \dot{\alpha} (1 - 2b \cdot \sin 2\alpha)$; $\dot{\phi}_2 = \dot{\alpha} (1 + 2b \cdot \sin 2\alpha)$.

$$T_B = \frac{1}{2} \dot{\alpha}^2 2J_B (1 + 2b^2 - 2b^2 \cos 4\alpha). \quad (7)$$

Links rhomboid make plane motion, so their kinetic energy is the sum of the kinetic energies of the translational and rotational motions: $T_L = [m_1 (2V_{C1}^2 + 2V_{C2}^2) + J_1 (2\Omega_1^2 + 2\Omega_2^2)] / 2$, where m_1, J_1 – mass and moment of inertia about the central axis of one link; V_{C1}, V_{C2} – linear velocities of the centers; Ω_1, Ω_2 – angular velocities of the centers links 1 and 2. Given that

$$\begin{aligned} V_{C1}^2 + V_{C2}^2 &= \dot{\alpha}^2 l^2 (2 + 4b^2 - 4b^2 \cos 4\alpha), \\ \Omega_1^2 + \Omega_2^2 &= \dot{\alpha}^2 (2 + 4b^2 - 4b^2 \cos 4\alpha) \\ T_L &= \frac{1}{2} \dot{\alpha}^2 4 [(m_1 l^2 + J_1) (1 + 2b^2 - 2b^2 \cos 4\alpha)]. \quad (8) \end{aligned}$$

Four roller rhomboid has kinetic energy

$$T_R = \frac{1}{2} \dot{\alpha}^2 8m_R l^2 (1 + 2b^2 - 2b^2 \cos 4\alpha), \quad (9)$$

where m_R – mass of one roller.

The kinetic energy of the four linear bearings include of the kinetic energy of rotational motion

$T_{rot} = \frac{1}{2} \dot{\alpha}^2 4J_{LB}$ and kinetic energy of translational

motion $T_{tr} = \frac{1}{2} 2m_{LB} (V_A^2 + V_B^2)$, where V_A, V_B – absolute tops speed rhomboid A and B; m_{LB}, J_{LB} – mass and moment of inertia of linear bearings. We obtain

$$\begin{aligned} T_{LB} &= \frac{1}{2} \dot{\alpha}^2 \cdot \\ &\cdot [4J_{LB} + 8m_{LB} l^2 (1 + 2b^2 - 2b^2 \cos 4\alpha)]. \quad (10) \end{aligned}$$

Flywheel together with the output shaft has a kinetic energy:

$$T_F = \frac{1}{2} \dot{\alpha}^2 J_F, \quad (11)$$

where J_F – moment of inertia of flywheel together with the output shaft.

Summing up the values of the kinetic energy (7) – (11), we obtain the kinetic energy of the engine:

$$T = \frac{1}{2} \dot{\alpha}^2 J(\alpha), \quad (12)$$

where $J(\alpha)$ – moment of inertia of engine referred to the output shaft. Moment of inertia includes fixed and variable components

$$J(\alpha) = J_C - J_V \cos 4\alpha. \quad (13)$$

There are J_C – permanent component; J_V – amplitude of the harmonic component with a period of $\pi / 2$:

$$\begin{aligned} J_C &= J_F + 4J_{LB} + 2(1 + 2b^2) \cdot \\ &\cdot [J_B + 2(m_1 l^2 + J_1) + 4l^2 (m_R + m_{LB})]; \quad (14) \end{aligned}$$

$$J_V = 4b^2 [J_B + 2(m_1 l^2 + J_1) + 4l^2 (m_R + m_{LB})]. \quad (15)$$

Expression for the given moment inertia of the engine is:

$$L_z = -\dot{\alpha}^2 2J_V \sin 4\alpha - \ddot{\alpha} (J_C - J_V \cos 4\alpha). \quad (16)$$

III. DEFINITION OF DRIVE TORQUE

Torque of gas pressure forces on the blades $M_{B1} = -M_{B2}$ transmitted through the cam motion transformer to the output shaft create a drive torque M_{DT} .

Work of drive torque at the elementary move $\delta A(M_{DT}) = M_{DT} \delta \alpha$ must be equal to work of torques on the vanes $\delta A(M_{B1}, M_{B2}) = M_{B1} \delta \varphi_1 + M_{B2} \delta \varphi_2$.

The angles of the vanes φ_1 and φ_2 increment

$$\delta \varphi_1 = \frac{d\varphi_1}{d\alpha} \delta \alpha \quad \text{and} \quad \delta \varphi_2 = \frac{d\varphi_2}{d\alpha} \delta \alpha, \quad \text{or using (2),}$$

$$\delta \varphi_1 = (1 - 2b \sin 2\alpha) \delta \alpha, \quad \delta \varphi_2 = (1 + 2b \sin 2\alpha) \delta \alpha.$$

Moments on the vanes make work

$$\delta A(M_{B1}, M_{B2}) =$$

$$[M_{B1} + M_{B2} + 2b(M_{B1} - M_{B2}) \sin 2\alpha] \delta \alpha.$$

Are equal, so the work of the driving torque and torque on the vanes (including $M_{B2} = -M_{B1}$) we obtain an expression for the type of drive torque

$$M_{DT}(\alpha) = 4b M_{B1}(\alpha) \sin 2\alpha. \quad (17)$$

It is periodic function of α with period $T = \pi/2$, which can be expanded in a Fourier series, and represented in the form

$$M_{DT}(\alpha) = M_0 + A_1 \cos 4\alpha + A_2 \cos 8\alpha + A_3 \cos 12\alpha + \dots + B_1 \sin 4\alpha + B_2 \sin 8\alpha + B_3 \sin 12\alpha + \dots \quad (18)$$

where

$$M_0 = \frac{1}{T} \int_0^T M_{DT}(\alpha) d\alpha,$$

$$A_k = \frac{2}{T} \int_0^T M_{DT}(\alpha) \cos k4\alpha d\alpha,$$

$$B_k = \frac{2}{T} \int_0^T M_{DT}(\alpha) \sin k4\alpha d\alpha,$$

$$(k = 1, 2, \dots)$$

M_0 is the average value of $M_{DT}(\alpha)$ for the period, which is a useful driving torque, which is the product of the angular velocity $\omega = \dot{\alpha}$ equal to engine power $N = M_0 \omega$. The remaining terms, as a harmonic function of the shaft angle $\alpha = \omega t$, are classified as disturbing moments with frequencies $4\omega, 8\omega, 12\omega, \dots$. The presence of these harmonics increases the mechanical strength of the engine.

Now we shall find condition under which the mechanical strength of the engine is minimized.

IV. TORQUE ON THE OUTPUT SHAFT

In the steady state acceleration $\ddot{\alpha} = 0$, the angular velocity $\dot{\alpha} = \omega = \text{const}$, and the angle of rotation of the shaft $\alpha = \omega t$.

Inertia moment L_Z , defined by (5) takes the form $L_Z = -\omega^2 2J_V \sin 4\omega t$.

Torque at the output shaft M_S equals the sum of the drive torque M_{DT} defined by (18), and the inertial moment L_Z :

$$M_S = M_{DT} + L_Z = M_0 + (B_1 - 2J_V \omega^2) \sin 4\omega t + \tilde{M}(t), \quad (19)$$

where indicated

$$\tilde{M}(t) = A_1 \cos 4\omega t + A_2 \cos 8\omega t + \dots + B_1 \sin 4\omega t + B_2 \sin 8\omega t + \dots$$

When the condition

$$B_1 - 2J_V \omega^2 = 0 \quad (20)$$

is compensation by inertia forces the most significant component of the disturbing drive torque $B_1 \sin 4\omega t$ and, consequently, to minimize the mechanical strength of the engine.

It follows that the design of its engine parameters should be selected so that the nominal angular velocity ω_n meet the condition (20)

$$\omega_n = \omega^* = \sqrt{\frac{B_1}{2J_V}}. \quad (21)$$

V. RESULTS OF NUMERICAL SIMULATION

Initial data for the simulation: torque on output shaft $M_{DT} = M_0 = 1000 \text{ N} \cdot \text{m}$, speed to 1500 rpm.

Torques on the blades and the drive torque as functions of the angle α are shown in Fig. 3.

Expansion $M_{DT}(\alpha)$ into a Fourier series (18) gives the following coefficients (in $\text{N} \cdot \text{m}$):

$$M_0 = 1075,$$

$$A_1 = -217, A_2 = -468, A_3 = -266, A_4 = -72,$$

$$B_1 = 1690, B_2 = 478, B_3 = 26, B_4 = -96.$$

The most significant component of the disturbing harmonic drive torque is $B_1 \sin 4\omega t$, amplitude of which is 1.5 times higher than the constant M_0 . Compensation of this harmonic by inertia forces must take place according to (21) at the angular speed

$$\omega^* = \sqrt{B_1 / 2J_V} = \sqrt{1690 / 2 * 0,184} = 68 \text{ c}^{-1},$$

or at a frequency rotation $n^* = 30\omega^* / \pi = 650 \text{ rpm}$.

Inertia moment $L_z = -\omega^2 2J_v \sin 4\omega t$ has an amplitude $A_{Lz} = 2J_v \omega^2$, parabolically depending on the speed (Fig. 4). Fig. 5 shows the dependence of the maximum torque on the shaft $(M_s)_{max}$ of the speed. Up to the speed n^* a decrease of $(M_s)_{max} = M_0 + |\tilde{M}|$ take place due to the compensation of the inertial forces components of the drive torque $B_1 \sin 4\omega t$. At speeds $n > n^*$ the torque $(M_s)_{max}$ increases parabolically under the action of the inertial forces.

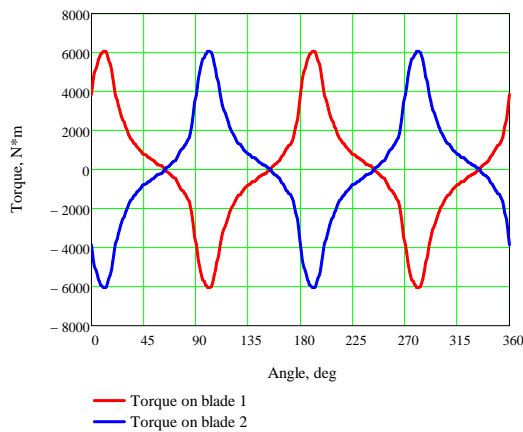


Fig. 2. Torques on the blades.

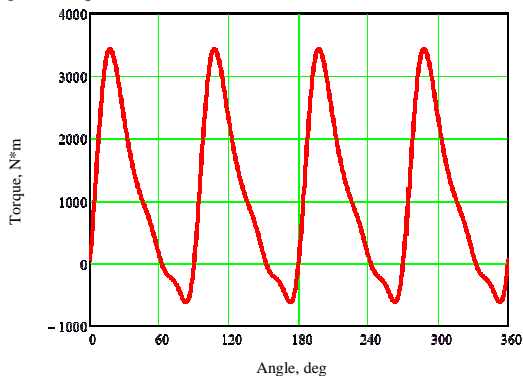


Fig. 3. The drive torque.

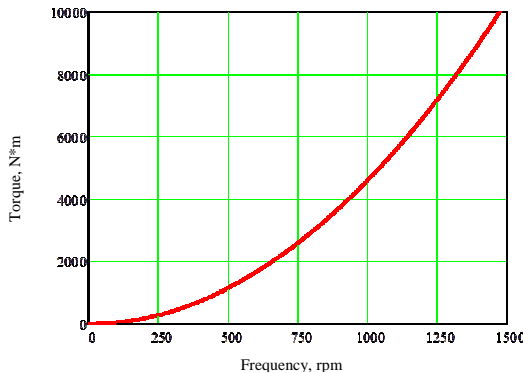


Fig. 4. Inertial moment

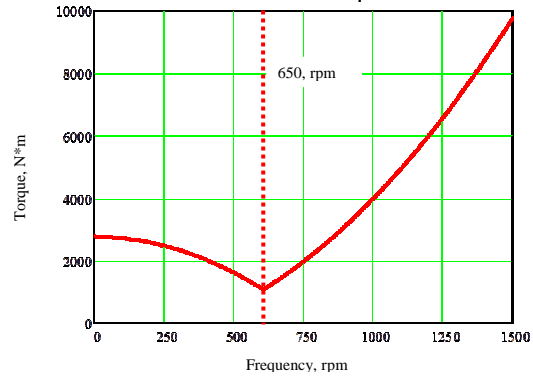


Fig. 5. Torque on the output shaft

VI. CONCLUSION

In this article, we have obtained the analytical expressions for motor driving and inertial moments of the single-module rotary-vane engine with lever-cam referenced to the output shaft, also the condition under which the forces of inertia completely compensate the most significant component of the disturbing drive torque and minimizes the mechanical strength of the engine.

The results of numerical simulation obtained on the example of the engine with internal combustion, which are close to the theoretical prediction.

This results can be used in the preliminary design of the rotary-vane engines.

REFERENCES

- [1] RF Patent 2374526 for an invention. Int. Cl. F16H25/04. Mechanism for converting motion / Lukyanov Y.N., Zhuravlev Y.N., Perminov A.L., Tikhonov S.I. et al. Publ. 27.11.2009. Bull. Number 33.
- [2] RF Patent 2387844 for an invention. Int. Cl. F01G1/077, F02G1/044. Rotary-vane engine with an external supply of heat / Lukyanov Y.N., Zhuravlev Y.N., Perminov A.L., Tikhonov S.I. et al. Publ. 27.04.2010. Bull. Number 12.
- [3] Zhuravlev Y.N., Lukyanov Y.N., Perminov A.L. Mathematical models of physical processes in the swing-piston engine with external heat supply. Collective monograph. Pskov state university. Pskov, 2012.
- [4] Andreev M., Zhuravlev Y., Lukyanov Y., Perminov A. Autonomous Power Station Based on Rotary-Vane Engine with an External Supply of Heat. Environment. Technology. Resources. Proceedings of the 9th International Scientific and Practical Conference. Volume 2. 2013.

PRINCIPLES OF PUBLICATION USE AND ETHICS

The Publisher states the following principles of publication use and ethics:

1. Only original works, that have not been previously published and in which the data do not infringe the copyright of another person or organization, are accepted for publishing.
2. Every submitted paper is reviewed anonymously by 2 reviewers.
3. Publisher has the right to use plagiarism detection software to screen submitted papers.
4. Authors retain copyright over their work, while allowing the conference to place this unpublished work under a Creative Commons Attribution License, which allows others to freely access, use.
5. Publisher undertakes to publish articles accepted after reviewing and, according to the scientific quality of an article, publish them electronically and include them in various international scientific paper data bases.
6. Publisher undertakes to use author's personal data only for the needs of identification of authors and co-authors, as well as to preserve data in accordance with the restrictions determined in the current regulations of the Republic of Latvia.

The author (-s) of original article confirms and guarantees that:

1. A paper has been written by the Author (s) who has (have) been stated in the Paper and in this statement and there is no any other person who would have any rights to this Paper.
2. The Paper is original; it has not been previously published and is not under simultaneous consideration by another publications.
3. The Paper will not later be submitted elsewhere.
4. There are references for all the pictures, data and other materials used in the Paper.
5. The results of the Paper are genuine; they do not infringe on the original work of another person or organisation. The Author (-s) have taken all the necessary measures to ensure the requirements of the sponsors' who finance the Paper.
6. If author finds a significant error after the publishing of the paper, it is the author's obligation to promptly notify the editor.
7. The Author (-s) has (have) been authorised to submit the Paper for publication; the intellectual property rights will not be infringed according to the 14th, 15th articles of the Copyright law and other normative acts of the Republic of Latvia and international normative acts binding for the Republic of Latvia.
8. The Author (-s) take (-s) the sole responsibility related to the third parties' objections and demands concerning the publishing or using the Paper.
9. The Author (s) take (-s) all the responsibility and promptly, irrevocably and unconditionally undertakes to independently at his (their) own expenses and risk if there will be objections or demands from the third parties' concerning the publishing or using the Paper.

Publication editor:

1. Ensures double-blind peer-review of the submitted paper.
2. Until the publishing, ensures the confidentiality of information concerning the submitted article.
3. Strives to prevent any possible conflict of interests between authors and reviewers or editors.

Reviewer:

1. Evaluates the content of the article according to the scientific article criteria, without regard to ethnic origin, gender, sexual orientation, citizenship, religious beliefs or political views of the authors.
2. Keeps confidential all the information related to submitted paper.
3. Notifies the editor if there is a suspicion of plagiarism or copyright infringement.
4. If the reviewer feels unqualified to review or knows that it is impossible to provide review in time, he should notify the Editor-in-Chief and ask to exempt him from reviewing.

